UQAC
Université du Québec
à Chicoutimi

Geochemical variation of oxide-apatite mineralization associated with Proterozoic massif-type anorthosites in the Central Grenville Province, Quebec, Canada

by

Pedro Miloski Guimarães

Under the direction of Sarah Dare

Thesis presented to the Université du Québec à Chicoutimi as partial fulfillment of requirements for the degree of Doctor of Philosophy (Ph.D) in Earth and Atmospheric Sciences

Québec, Canada

Jury:

Renée-Luce Simard, Professor, Department of Applied Sciences/ UQAC, President of the Jury

Sarah Dare, Professor, Department of Applied Sciences/ UQAC, Supervisor

Nolwenn Coint, Researcher in Geology, Geological Survey of Norway

Michael Higgins, Professor, Department of Applied Sciences/ UQAC

Bertrand Rottier, Professor, Department of Geology and Geological Engineering/ ULaval

RESUMÉ

Une variété de minéralisations magmatiques d'oxyde-apatite sont associées spatialement et temporellement aux suites AMCG (Anorthosite – Mangerite – Charnockite – Granite) protérozoïques, présentant un intérêt à la fois économique et scientifique, abritant des quantités importantes de métaux critiques et stratégiques, tels que Ti, V et P. Cependant, l'origine et la relation génétique entre la minéralisation oxyde-apatite et l'hôte AMCG sont encore très controversées, ainsi que le cadre tectonique exact. La minéralisation en oxyde-apatite est communément interprétée comme une cristallisation à partir de liquide résiduel riche en Fe-Ti-V-P (composition ferrodiorite/jotunite), après une cristallisation polybarique étendue de plagioclase et de silicates mafiques lors de la formation de massifs d'anorthosite. Les deux suites AMCG plus jeunes de la province centrale du Grenville (suites AMCG Pipmuacan 1082-1045 Ma et Valin 1020-1008 Ma) ont une évolution pétrogénétique complexe, présentant une variation géochimique de la minéralisation en oxyde-apatite (de la minéralisation dominée par la Ti-magnétite à l'hémo-minéralisation à dominante ilménite) selon la composition de l'anorthosite encaissante (type labradorite ou andésine) et son âge. Les massifs d'anorthosite de type andésine datant de moins de 1100 Ma sont à orthopyroxène et contiennent des minéralisations à hémo-ilménite (± apatite), tandis que les massifs d'anorthosite de type labradorite, plus âgés que 1100 Ma, sont à olivine et contiennent des minéralisations à Ti-magnétite (± apatite). La raison de cette variation minéralogique et géochimique de la minéralisation d'oxyde-apatite avec le temps n'est pas comprise, mais pourrait être due à un changement dans les magmas parentales et/ou aux degrés de contamination crustale ou de cristallisation fractionnée. Cette thèse vise à mieux caractériser cette variation géochimique à l'échelle du gisement et à l'échelle régionale dans la Province du Grenville, en comprenant les processus qui contrôlent leur variation de composition (ex. source de magma, contamination crustale, évolution des magmas résiduels de ferrodiorite/jotuntite) utilisant la chimie minérale du plagioclase, de l'ilménite, de la magnétite et de l'apatite, ainsi que des isotopes U-Pb-Hf dans le zircon. Cette méthodologie a été appliquée à la minéralisation Fe-Ti-(P) (dominée par l'hémo-ilménite) à trois échelles différentes afin de mieux caractériser la variation géochimique au sein: I) d'un seul gisement lenticulaire d'oxyde-apatite-norite (Lac à l'Orignal); à plus grande échelle jusqu'à II) plusieurs lentilles minéralisées composées des différents cumulâtes de Fe-Ti-P (ex. oxydes massifs, nelsonite et oxyde-apatite-norite au Lac Mirepoix); une échelle régionale, III) comparant les différentes localisations de minéralisation Fe-Ti-P encaissées dans les anorthosites et mangérites aux Suites AMCG de Pipmuacan (Lac de l'Abbondance, L'Étang, Lac Périgny) et Valin (Lac Brûlé, Mattawa et La Hache) avec minéralisation au Lac à l'Orignal et au Lac Mirepoix (Anorthosite de Vanel), ainsi que les données publiées des gisements Fe-Ti-P de la Province du Grenville (ex. Lac Tio, Grader Intrusion, Saint Urbain).

Le gisement Fe-Ti-P du Lac à l'Orignal, encaissé dans l'anorthosite de Vanel)1080 (±2) Ma) près de la limite nord de l'anorthosite de Mattawa (1016 (±2) Ma), comprend une structure lenticulaire d'oxide-apatite-norite (OAN) avec de fines couches d'anorthosite à apatite et des quantités mineures de nelsonite (oxydes massifs de Fe-Ti et apatite). La minéralisation est dominée par l'hémo-ilménite, accompagnée d'apatite et d'une quantité mineure de magnétite aux bordures, tandis que le noyau est dominé par l'ilménite, la magnétite et l'apatite. La datation U-Pb in situ des zircons magmatiques de la minéralisation indique que le gisement du Lac à l'Orignal est une intrusion multi-injection avec deux âges de cristallisation différents entre le noyau le plus jeune (993 ± 13 Ma) et la bordure supérieure la plus ancienne (1069 ± 12 Ma) de l'intrusion. Ces âges sont similaires à ceux des massifs d'anorthosite voisins (anorthosites de Mattawa et Vanel, respectivement). L'analyse in situ des éléments traces du plagioclase, de l'apatite et des oxydes révèle de

subtiles variations de Cr, Ni et V liées à la différenciation dans des conditions de fO_2 relativement élevées (FMQ = +0,9 à +1,7). Les compositions de la fonte calculées à partir de l'apatite indiquent un magma parental similaire pour la bordure et le noyau qui correspond à la composition des dykes de ferrodiorite à haute teneur en Fe-Ti-P du Lac à l'Original. L'équilibrage d'inter-oxydes sous-solidus a modifié la composition originale des différentes cumulâtes de l'intrusion. L'absence de cumulus de massifs d'oxydes étendus et la présence de quantités plus élevées des cumulus de magnétite et d'apatite, soutenues par la chimie minérale, dénotent un caractère plus évolué du gisement du Lac à l'Orignal par rapport aux autres gisements de Fe-Ti-(P) de la Province du Grenville (ex. Lac Tio, Grader Intrusion). Pétrogénétiquement, le gisement de Fe-Ti-P du Lac à l'Orignal correspond à une partie évoluée d'un système pauvre en Ti/Fe de la Province du Grenville aux derniers stades de différenciation des magmas ferrodiorite/jotunite.

La minéralisation Fe-Ti-P du Lac Mirepoix, située à proximité, est également dominée par l'(hémo)-ilménite, accompagnée de magnétite et d'apatite. Cette intrusion litée est subdivisée en trois zones différentes en raison de l'apparition de différentes phases des cumulâtes: la zone I comprend principalement des couches d'oxyde massif (>70 % d'hémo-ilménite ± magnétite) encaissées dans l'anorthosite. Vers le centre (zone II), les couches d'oxydes massifs sont moins fréquentes tandis que des cumulâtes d'apatites apparaissent, formant de la nelsonite massive (50-70 % de magnétite ± ilménite et 25-30 % d'apatite) et d'oxyde-apatite norite (OAN, 15-25 % hémo-ilménite ± magnétite et 8-20% d'apatite). Enfin, la zone III est marquée par l'alternance de couches d'OAN (10-25m), plus riches en magnétite, en plus de l'(hémo)-ilménite et de l'apatite, et par une absence d'oxyde massif et de nelsonite. L'analyse in situ des éléments traces du plagioclase, de l'apatite et des oxydes révèle des variations cryptiques liées à la différenciation du magma et à des injections multiples de magmas parentaux de ferrodiorite de composition similaire à partir desquels l'OAN et la nelsonite ont cristallisé. Semblable au Lac à l'Orignal, la datation U-Pb in situ des zircons de la minéralisation OAN elle-même indique deux âges de cristallisation différents entre la zone III (1048 ± 8 Ma) et la zone I (964 ± 9 Ma), favorisant un modèle de multi-injections plutôt que la cristallisation in situ d'une intrusion litée, qui est soutenue par la géochimie des éléments traces. La minéralisation du Lac Mirepoix enregistre la séquence de cristallisation fractionnée suivante d'un magma à haute teneur en Ti-P, résiduel après la formation de l'anorthosite: d'abord, des oxydes massifs d'hémo-ilménite cristallisés (haute Ti/Fe) par accumulation d'oxydes, avec des compositions primitives, similaires à le gisement de classe mondiale du Lac Tio. La minéralisation d'oxyde-apatite (nelsonite et OAN) s'est cristallisée à partir du liquide résiduel (Ti/Fe inférieur, compositions évoluées) dans lequel la magnétite et l'apatite étaient plus abondantes, semblable à la minéralisation voisine dans la région (ex. Lac à l'Orignal Fe-Ti-P). La diminution observée de la teneur en Ti du magma en évolution est soutenue par la ligne de descente liquide de plusieurs dykes de ferrodiorite au sein des roches encaissantes et de la minéralisation.

L'étude régionale de plusieurs minéralisations Fe-Ti-P dans les deux suites AMCG plus jeunes de Pipmuacan et Valin démontre une évolution géochimique similaire liée à la cristallisation fractionnée du magma ferrodiorite parental, avec des oxydes massifs (hémo-ilménite ± magnétite) cristallisant d'abord à partir de niveaux élevés de Ti/Fe, suivies par les nelsonites contenant de l'apatite ((hémo)-ilménite + magnétite + apatite), la norite d'oxyde d'apatite ((hémo)-ilménite + magnétite + apatite + silicates) qui cristallisent à partir de liquides résiduelles (ferrodiorite) à faible teneur en Ti/Fe. Les magmas les plus évolués (composition de jotunite) ont formé des mangérites minéralisées (ilménite + magnétite + apatite + oligoclase + feldspath potassique + quartz). La majeure partie de la minéralisation Fe-Ti-P dans cette étude se situe dans la plage des âges précédents pour les suites AMCG Pimuacan et Valin (1080 – 950Ma). Cependant, la datation U-Pb des cumulâtes minéralisés dans cette étude a donné des âges assez différents (> 50 Ma) par rapport aux publications

précédentes sur chaque AMCG hôte respectif. Nous proposons un modèle complexe d'injections multiples de liquides résiduels riches en Fe-Ti-P drainés ou filtrés dans des diapirs de bouillies riches en plagioclase qui ont été mises en place à plus de 80 Mys d'intervalle le long de la même zone de détachement crustale.

Les isotopes U-Pb-Hf in situ dans le zircon de la minéralisation Fe-Ti-P dans cette étude ont principalement des valeurs εHf chondritiques à légèrement positives et négatives, dans lesquelles la minéralisation des anorthosites de Labrieville et Mattawa présente une signature Hf plus suprachondritique (εHf: + 3,0 à +7,0 ; datation U-Pb : 1065 (± 5Ma) à 990 (± 7Ma)), reflétant peut-être une contamination par une croûte juvénile, similaire à la minéralisation de l'anorthosite de Saint Urbain. Les minéralisations associées à l'anorthosite Vanel et aux mangérites de La Hache et Poulin de Courval présentent une signature Hf plus enrichie (εHf: -5,0 à +7,4 ; datation U-Pb: 964 (± 9Ma) à 1115 (± 11Ma)), soit étant relativement plus contaminés et/ou associés à des sources mantelliques plus enrichies par rapport à la minéralisation de Labrieville et de Mattawa. Les patrons d'éléments traces de l'apatite de toutes les minéralisations Fe-Ti-P ont des patrons enrichis en LREE très similaires à l'apatite provenant d'intrusions litées, associées aux panaches du manteau, avec une contamination crustale négligeable. Cela indique l'implication d'une source de manteau asthénosphérique enrichi dans la formation des magmas riches en Fe-Ti-P pour les différentes minéralisations en Fe-Ti-P dans cette étude, plutôt qu'une source de manteau appauvrie ou un manteau lithosphérique sous-continental enrichi comme communément proposé dans les études précédentes de modèles tectoniques pour le magmatisme AMCG de Grenville. De plus, les données Lu-Hf révèlent que la minéralisation Fe-Ti-P dans l'anorthosite de Vanel et les mangérites de La Hache et Poulin de Courval ont probablement subi une contamination crustale inférieure faible à modérée. Ainsi, nous montrons pour la première fois que la géochimie de l'apatite et du zircon fournit des contraintes importantes sur la source mantellique et le rôle de la contamination dans la pétrogenèse des suites AMCG de la Province du Grenville, qui devraient être prises en compte pour le modèle tectonique du Grenville.

ABSTRACT

A variety of magmatic oxide-apatite mineralization is spatially and temporally associated with Proterozoic AMCG (Anorthosite–Mangerite–Charnockite–Granite) suites, being of both economic and scientific interest, hosting significant amounts of critical and strategic metals, such as Ti, V and P. However, the origin and genetic relationship of both AMCG host and oxide-apatite mineralization are still highly debated, as well as the exact tectonic setting. Oxide-apatite mineralization is commonly interpreted as crystallizing from residual Fe-Ti-V-P rich melts (ferrodiorite/jotunite composition), after extensive polybaric crystallization of plagioclase and mafic silicates during the formation of anorthosite massifs. The two younger AMCG suites in the Central Grenville Province (1082-1045 Ma Pipmuacan and 1020-1008 Ma Valin) have a complex petrogenetic evolution, presenting a geochemical variation of oxide-apatite mineralization (from Ti-magnetite-dominated to hemo-ilmenite-dominated mineralization) according to the host anorthosite composition (labradorite- or andesine-type) and its age. Andesine-type anorthosite massifs that are younger than 1100 Ma are orthopyroxene-bearing and host hemo-ilmenite (± apatite) mineralization, whereas labradorite-type anorthosite massifs which are older than 1100 Ma, are olivine-bearing and host Ti-magnetite (± apatite) mineralization. The reason for this mineralogical and geochemical variation of oxide-apatite mineralization with time is not understood but could be due change in parental melts and/or degrees of crustal contamination or fractional crystallization. This thesis aims to better characterize this geochemical variation in both ore-deposit and regional scales in the Central Grenville Province, understanding the processes that control their compositional variation (e.g., source of magma, crustal contamination, evolution of residual ferrodiorite/jotuntite magmas) through LA-ICP-MS whole rock and mineral chemistry of plagioclase, ilmenite, magnetite and apatite, as well U-Pb-Hf isotopes in zircon. This methodology was applied to Fe-Ti-(P) mineralization (hemo-ilmenite dominated) at three different scales to better characterize the geochemical variation within: I) a single lenticular oxide-apatite-norite deposit (Lac à l'Orignal); a larger scale through II) several mineralized lenses composed by different Fe-Ti-P cumulates (e.g., massive oxides, nelsonite and oxide-apatite-norite at Lac Mirepoix); a regional scale, III) comparing the different locations of Fe-Ti-P mineralization hosted in the anorthosites and mangerites of the Pipmuacan (Lac de l'Abbondance, L'Étang, Lac Périgny) and Valin (Lac Brûlé, Mattawa and La Hache) AMCG suites with mineralization at Lac à l'Orignal and Lac Mirepoix (Vanel Anorthosite), as well as published data from Fe-Ti-P deposits from the Grenville Province (e.g, Lac Tio, Grader Intrusion, Saint Urbain).

The Lac à l'Orignal Fe-Ti-P deposit, hosted in the 1080 (±2) Ma Vanel Anorthosite near the northern border of the 1016 (±2) Ma Mattawa Anorthosite, comprises a lenticular structure of oxide apatite norite (OAN) with thin layers of apatite-bearing anorthosite and minor amounts of nelsonite (massive Fe-Ti oxides and apatite). The mineralization is dominated by hemo-ilmenite, accompanied by apatite and a minor amount of magnetite at the borders, whereas the core is dominated by ilmenite, magnetite, and apatite. In-situ U-Pb dating of magmatic zircon from the mineralization indicates that the Lac à l'Orignal deposit is a multi-injection intrusion with two different crystallization ages between the younger core (993 ± 13 Ma) and the older upper border (1069 ± 12 Ma) of the intrusion. These ages are similar to those of nearby anorthosite massifs (Mattawa and Vanel anorthosites, respectively). In-situ trace element analysis of plagioclase, apatite and oxides reveals subtle variations in Cr, Ni and V related to differentiation under relatively high-fO_2 conditions (FMQ = +0.9 to +1.7). Calculated melt compositions from apatite indicates a similar parental magma for both the border and core that matches the composition of high-Fe-Ti-P ferrodiorite dykes at Lac à l'Original. Sub-solidus inter-oxide equilibration modified the original composition of the different cumulates in the intrusion. The absence of extensive

massive oxide cumulates and the presence of higher amounts of cumulus magnetite and apatite, supported by mineral chemistry, denotes a more evolved character for the Lac à l'Orignal deposit compared with other Fe-Ti-(P) deposits in the Grenville Province (e.g., Lac Tio, Grader intrusion). Petrogenetically, the Lac à l'Orignal Fe-Ti-P deposit corresponds to an evolved part of a low-Ti/Fe system in the Grenville Province in the late stages of differentiation of ferrodiorite/jotunite magmas.

The nearby Lac Mirepoix Fe-Ti-P mineralization is also (hemo)-ilmenite-dominated, accompanied by magnetite and apatite. This 'layered intrusion' is subdivided in three different zones due to the appearance of different cumulate phases: zone I comprises mainly massive oxide (>70% hemo-ilmenite ± magnetite) layers hosted in anorthosite. Towards the center (zone II), massive oxide layers are less common whereas apatite-bearing cumulates appear, forming massive nelsonite (50-70% magnetite ± ilmenite and 25-30% apatite) and oxide apatite norite (OAN, 15-25% hemo-ilmenite ± magnetite and 8-20% apatite). Finally, zone III is marked by the alternance of OAN layers (10-25m), richer in magnetite, in addition to (hemo)-ilmenite and apatite, and an absence of massive oxide and nelsonite. In-situ trace element analysis of plagioclase, apatite and oxides reveals cryptic variations related to magma differentiation and multiple injections of ferrodiorite parental magmas of similar composition from which the OAN and nelsonite crysatllized from. Similar to Lac à l'Orignal, in-situ U-Pb dating of zircon from the OAN mineralization itself indicates two different crystallization ages between zone III (1048 ± 8Ma) and zone I (964 ± 9 Ma), favoring a model of multi-injections rather than in-situ crystallization of a single layered intrusion, which is supported by trace element geochemistry. The Lac Mirepoix mineralization records the following fractional crystallization sequence of a high-Ti-P magma, residual after the anorthosite formation: first, massive oxides of hemo-ilmenite crystallized (high Ti/Fe) by oxide settling, with primitive compositions, similar to the world-class Lac Tio deposit. The oxide-apatite mineralization (nelsonite and OAN) crystallized from the residual liquid (lower Ti/Fe, evolved compositions) in which magnetite and apatite were more abundant, similar to nearby mineralization in the area (e.g. Lac à l'Orignal Fe-Ti-P mineralization). The observed decrease in Ti content of the evolving melt is supported by the liquid line of descent of several ferrodiorite dykes within the host-rocks and mineralization.

The regional study of several Fe-Ti-P mineralization in the two younger Pipmuacan and Valin AMCG suites demonstrates a similar geochemical evolution related to fractional crystallization of parental ferrodiorite magma, with massive oxides (hemo-ilmenite ± magnetite) crystallizing first from high Ti/Fe residual melts followed by apatite-bearing nelsonites ((hemo)-ilmenite + magnetite + apatite), oxide apatite norite ((hemo)-ilmenite + magnetite + apatite + silicates) crystallizing from low-Ti/Fe melts. The most evolved melts (jotunite composition) formed mineralized mangerites (ilmenite + magnetite + apatite + oligoclase + K-feldspar + quartz). Most of the Fe-Ti-P mineralization in this study is within the range of previous ages for the Pimuacan and Valin AMCG suites (1080 – 950Ma). However, U-Pb dating of the mineralized cumulates in this study resulted in quite different ages (>50Ma) from previously publications on each respective host-AMCG. We propose a complex model of multiple injections of residual Fe-Ti-P-rich liquids drained from or filter-pressed within diapirs of plagioclase-rich mushes that were emplaced over 80 Mys apart along the same crustal detachment zone.

In-situ U-Pb-Hf isotopes in zircon from Fe-Ti-P mineralization in this study have mainly chondritic to slightly positive and negative εHf values, in which mineralization in the Labrieville and Mattawa anorthosites present more suprachondritic Hf signature (εHf: +3.0 to +7.0; U-Pb dating: 1065 (± 5Ma) to 990 (± 7Ma)), possibly reflecting contamination from juvenile crust, similar to mineralization in the Saint Urbain Anorthosite. Mineralization associated with the Vanel Anorthosite and the mangerites of La Hache and Poulin de Courval present a more enriched Hf signature (εHf: -5.0 to +7.4; U-Pb dating: 964 (± 9Ma)

to 1115 (± 11Ma)), either being relatively more contaminated, and/or associated with more enriched mantle source(s) in relation to the mineralization at Labrieville and Mattawa. The trace element patterns of apatite from all of the Fe-Ti-P mineralization have LREE enriched patterns very similar to apatite from mafic layered intrusions, associated with mantle plumes, with negligible crustal contamination. This indicates the involvement of an asthenospheric enriched mantle source in forming the Fe-Ti-P rich melts for the different Fe-Ti-P mineralization in this study, rather than a depleted mantle source or enriched subcontinental lithospheric mantle as commonly proposed in previous tectonic models for the Grenville AMCG magmatism. Moreover, the Lu-Hf data reveal that Fe-Ti-P mineralization in Vanel Anorthosite and the mangerites of La Hache and Poulin de Courval probably underwent low- to moderate lower crustal contamination. Therefore, we show for the first time that apatite and zircon geochemistry provide important constraints on the mantle source and role of contamination in the petrogenesis of AMCG suites in the Grenville Province, which should be taken into account for the tectonic model of the Grenville.

ACKNOWLEDGEMENTS

Several people played a decisive role in helping me during all my journey to become a geologist, and now, a Ph.D. I am extremely grateful to my parents, Cristiane and Eduardo, and grandparents, Eloyr and Sonia, for loving me unconditionally all over my life and for always trying to give me a daily emotional support even living in another country. When I made the decision to move to Canada, they directly supported me and believed that I would be doing the right thing. If today I am concluding a Ph.D. in the science that I love so much, that is due to all the love, knowledge, education and discipline that I have received from them during all my life. Thanks for teaching me the right direction. I love you.

"If a child is trained up in the right way, even when he is old he will not be turned away from it."

Proverbs 22:6

I would like to kindly thank my friends Bianca and Raphael, who were my family in Chicoutimi while I was far from Brazil. The life in Quebec does not only gave me the opportunity to complete a Ph.D, but also made me make two really nice friends for all life. This project would not be possible without your help.

I would like to specially thank Sarah Dare for believing in my potential, and for giving me the opportunity to come to Canada. This decision changed my life. I do not have enough words to express how I am grateful for all your help supervising me during the four years of research, and financially supporting my research through the Fonds de recherche du Quebec - Nature and Technologie (FRQNT grant for new academics 2020-NC-271033 and 2021-NC-309329) and the Canada Research Chair in Geochemistry Applied to Ore Deposits (CRC-2017-0286). Thank you very much Sarah.

I also thank my co-authors, Caroline-Emmanuelle Morisset (CSA), for her orientation and support; and Morgann Perrot and Joshua Davies (UQAM) for their kindness helping with the isotopic data analysis and interpretation.

I thank Christian Tremblay (TRCM-UQAC), Leopold Tremblay and Randolph Maier for their assistance with field work; Frank Guillemette (MRBoreal) for access and sampling of drillcore; Audrey Lavoie, Dany Savard and Pape Doudou Tague for helping with LA-ICP-MS analytical procedures at LabMaTer, UQAC; Marc Choquette and Suzie Côté for their SEM, microprobe and uXRF work at Université Laval and André Poirier who helped with LA-ICP-MS data acquisition on zircons at GEOTOP, UQAM.

The long journey of a Ph.D and the life in a foreign country unfortunately make us feel a little bit far from the ones we love. The choice of moving to another country also has some price. During the second year of my research, I lost one of the most important people that I have ever met, my grandfather Eloyr. If someone on Earth ever believed in my potential since the beginning, this one was my grandfather. He was my truly friend, but I was far when he passed away during Covid time. So I dedicate this thesis and all this work to his memory. I am sure that wherever he is, he might be happy and proud right now.

Thank you all.

TABLE OF CONTENTS

LIST OF FIGURES

CHAPTER 1

CHAPTER 2

CHAPTER 4

LIST OF TABLES

CHAPTER 1

CHAPTER 2

CHAPTER 3

CHAPTER 4

LIST OF APPENDICES

CHAPTER 2

CHAPTER 3

CHAPTER 4

CHAPTER 1

INTRODUCTION

1.1 Introduction

Magmatic Fe-Ti-V-P mineralization have spatial and temporal connections with Proterozoic massif-type anorthosite suites (Ashwal, 1993). The majority of known oxide-apatite deposits are concentrated within exposed rocks of the Grenville Province, from southwestern United States through eastern Canada (Québec), and also in its extension into the Rogaland Anorthosite Province, Norway (Ashwal, 1993). These magmatic oxide–apatite deposits are of both economic and scientific interest, providing important resources for critical and strategic elements as titanium (Ti), from ilmenite ($FeTi_2O_4$) and hemo-ilmenite (ilmenite with extensive hematite (Fe_2O_3) exsolution lamellae); vanadium (V), from magnetite (Fe_3O_4) and titanomagnetite; and for phosphorus (P), from apatite ($Ca_5(PO_4)_3(OH,F,Cl)$). For example, about 90% of the world's commercial TiO_2 produced (an important chemical constituent of white-color paints and corrosion-resistant steel) is exploited from ilmenite and hemo-ilmenite (Charlier et al. 2015), of which 30% are related with two active mines in world-class hemo-ilmenite deposits associated with massif-type anorthosites (e.g., Lac Tio, Québec). Moreover, significant resources for phosphorus are hosted in Proterozoic anorthosites of Quebec (e.g., Lac à Paul deposit, Lac-Saint-Jean Anorthosite Suite), and for vanadium in Poland (e.g., Suwalki Anorthosite; Charlier et al. 2006).

However, the origin of both the host anorthosite rocks and oxide-apatite mineralization, and their genetic relationship to one another, are still highly debated (see below for details). This debate involves some fundamental processes in igneous petrology and ore deposit studies, such as the role of magma source (mantle or crust-derived), crustal contamination, liquid immiscibility and fractional crystallization. Understanding the formation of magmatic Fe-Ti-oxide deposits relies on a better understanding of the genesis of anorthosite and related rocks hosting these deposits, the evolution of the liquid from which oxide and silicate minerals crystallized, the role of

crustal contamination and the tectonic setting of anorthosite massifs (Woodruff et al. 2013).

Anorthosite suites hosting these deposits require an extensive history of voluminous plagioclase crystallization to develop. According to accepted models (Ashwal, 1993; Duchesne et al. 1999), plagioclase diapirs with entrained Fe-Ti-rich residual melt rise from the base of the lithosphere to mid- and upper-crustal levels (Charlier et al. 2015) (Fig. 1.1), along deep-crustal shear zones (Hébert et al. 2005; 2009; Indares & Moukhsil, 2013). The timing and style of oxide mineralization are related to magmatic and dynamic evolution of these diapiric systems and to development and movement of oxide cumulates and related melts.

In the Grenville province, Quebec, anorthosite magmatism was long-lived (> 300 Ma) ranging from the active continental collision (1.3Ga) through three episodes of collision (Shawinigan, 1190 – 1140Ma; Ottawan, 1080 – 1020Ma and Rigolet, 1000 – 850Ma), separated by periods of crustal extension/within-plate magmatism, towards post-collisional regime (River, 1997; Indares & Moukhsil, 2013; Groulier et al. 2018). Fe-Ti-V-P mineralization is hosted in all four episodes of anorthosite magmatism. However, the mineralization presents a clear geochemical and mineralogical variation (from Ti-magnetite-dominated to hemo-ilmenite-dominated mineralization) according to the host anorthosite composition (labradorite- or andesine-type) and its age (Hébert et al. 2005; 2009). However, no previous work explained why.

In this PhD we apply mineral chemistry (oxides, apatite, zircon and plagioclase) to better understand the petrogenesis of the different Fe-Ti-P mineralization (dominated by hemo-ilmenite) in the younger anorthosite suites of the Central Grenville. This work has shed new insights into the roles of source of magma, crustal contamination and magma evolution by fractional crystallization, which control the geochemical and mineralogical variation of Fe-Ti-P mineralization.

1.2. Proterozoic massif-type anorthosites and related Fe-Ti-P mineralized cumulates

Massif-type anorthosites are igneous bodies of mainly Proterozoic age, being composed of at least 90% of plagioclase feldspar of fairly restricted composition (labradorite [50-63%An] or andesine [30-50%An]), with the remaining mineralogy of mafic silicates and Fe-Ti oxide minerals (Ashwal, 1993). Fe-Ti oxides are common accessory phases and can be either primary, early liquidus minerals, or late-stage concentrations. Anderson & Morin (1969) distinguished two different groups of massif anorthosites: andesine- and labradorite-types, suggesting that both types could not be related by continuous fractionation. The andesine-type is characterized by antiperthitic plagioclase (An23-50), orthopyroxene and hemo-ilmenite. Labradorite-type (An50-63) anorthosites may contain olivine or orthopyroxene, and also low-Fe_2O_3 ilmenite and magnetite (Anderson & Morin, 1969; Hébert et al. 2005). In cases where the two anorthosite-types occur together, the andesine-type is commonly younger (e.g., Central Grenville Province), although some exceptions are described in other anorthosite provinces (e.g., Morse, 1982; for Nain anorthosite complex, Labrador), in which andesine-bearing anorthosites are older, and not younger than more labradorite-type anorthosite (Woodruff et al. 2013). For Longhi et al. (1999), the two anorthosite sub-types differ in the compositions of their parental magmas, with labradorite-type parental magmas containing higher Mg#, and lower TiO_2, K_2O and P_2O_5, whereas magmas parental to andesine anorthosites are more evolved, containing lower Mg#, and higher TiO_2, K_2O and P_2O_5. Differences between the two anorthosite types and correlations with their parental magmas should be argued in relation to isotopic compositions between these anorthosite types, to consider crustal contamination as an important factor in anorthosite petrogenesis (Bybee & Ashwal, 2015).

Anorthosites *strictu-sensu* are generally associated with some mafic rock-types (olivine and orthopyroxene-bearing), that include leucotroctolite, leuconorite, troctolite

(Morse, 1980), norite, gabbronorite and Fe-Ti-P enriched rocks: oxide-apatite gabbronorite (OAGN, Owens & Dymek, 1992), nelsonite (Fe-Ti oxides + subordinate apatite: Dymek & Owens, 2001), semi-massive and massive ilmenite and magnetite rocks (magnetitite & ilmenitite), ferrogabbro, ferrodiorite and jotunite (hypersthene monzodiorite: Owens et al. 1993; Vander Auwera et al. 1998; Duchesne, 1999). Anorthosites can also be associated with coeval Si-rich rocks, as quartz-mangerite (hypersthene quartz monzonite), mangerite (hypersthene monzonite), charnockite (hypersthene granite) and granite (Duchesne & Wilmart, 1997). This has led to the collective term “AMCG suite” (Anorthosite – Mangerite – Charnockite – Granite) as a common descriptor.

The structures of AMCG suites range from composites of multiple diapiric intrusions (e.g. Havre-Saint-Pierre Anorthositic Suite, Quebec; Van Breemen & Higgins, 1993) to dozens of discrete layered troctolite, gabbro and anorthosite intrusions (e.g. Damiao, China; Zao et al. 2009); to large, layered mafic intrusions (e.g. Bjerkreim-Sokndal intrusion, Norway; Wilson et al. 1996; Kiglapait, Nain, Labrador; Morse, 1980), many of which can host significant concentrations of magmatic Fe-Ti oxides and P mineralization.

1.2.1 Overview on the petrogenesis of AMCG-suites

Despite the relatively simple, plagioclase-dominated mineralogy of anorthosite massifs, the origin of anorthosite remains an outstanding unsolved petrological problem for over a century (Ashwal, 1993). Some questions concerning the composition of the parental magmas, i.e., whether these melts were generated within the crust or mantle, the relationship between anorthosite, Fe-Ti-P rocks and coeval felsic rocks, and also the tectonic setting are still debated (Ashwal, 1993; Duchesne, 1999).

The two-source model of mantle for the anorthosite members and crust for the felsic rocks (e.g. Emslie, 1985; Scoates & Mitchell 2000; McLelland et al. 2010) has been

challenged by two competing single-source hypotheses that advocate either the mantle (Turner et al. 1992; Frost et al. 2002) or the continental crust (Duchesne & Wilmart 1997; Duchesne et al. 1999; Schiellerup et al. 2000) as the only source for the entire AMCG suite. The nature of the mantle source is still debated, with models ranging from depleted mantle (Ashwal & Wooden, 1985; Ashwal et al. 1986; Francis et al. 2000; Morisset, 2008; Morisset et al. 2013; Owens et al. 1994) to enriched metasomatized subcontinental lithospheric mantle (SCLM, Owens & Tomascak, 2002; Bickford et al. 2010; Groulier et al. 2018) to even an enriched asthenospheric mantle for the origin of some anorthosite lithologies (Francis et al. 2000; Regan et al. 2011) and including Fe-Ti rich (jotunite) dykes (Icehower et al. 1998) with some similarities to continental flood basalts.

A generic two-stage model (Fig. 1.1a) for anorthosite massifs is generally accepted by all (Duchesne et al. 1985, 1999; Emslie, 1985; Ashwal, 1993; Charlier, 2007). First, there is stagnation of magma at the crust-mantle interface (MOHO; Ashwal, 1993; 2010; Bybee et al. 2014), with crystallization of plagioclase and mafic silicates in deep-seated magma chambers. Ponding of magmas at the MOHO is evidenced by the presence of high-Al (4-10 wt.%) orthopyroxene megacrysts (HAOMs; Bybee et al. 2014), in which experimental geobarometers show crystallization pressures of around 30–40km below the surface. Density separation of plagioclase (which float to the top of magma chambers) from mafic minerals results in diapiric upwelling of a plagioclase-melt mush and sinking of ultramafic cumulates back into the mantle. This is followed by a stage of vertical emplacement of a plagioclase-melt mush, with polybaric fractional crystallization (Charlier et al. 2015; Fig.1.4) of the residual liquid dominated by plagioclase, Fe-Ti oxides, and Fe-Mg silicates (Ashwal, 2010). The intrusion of plagioclase-rich diapirs are probably favored by zones of weakness such as major lineaments and/or deep-level shear zones (Corrigan & Hanmer, 1997; Scoates & Chamberlain, 1997; Duchesne et al. 1999; Ryan, 2000; Bogdanova et al. 2004; Hébert et al. 2005; 2009; Indares & Moukhsil, 2013).

An alternative model (Fig. 1.1b) proposes that basaltic parental magmas of massif-type anorthosites were derived by melting of mafic lower continental crustal "tongues" (Duchesne et al. 1999; Vander Auwera et al. 2011, 2014). These would be underthrust into the upper mantle, and heated to their solidus temperatures, during or shortly after collisional events. Support for this model comes mainly from observations and measurements made in the Rogaland Anorthosite Province, Norway, where crustal-scale zones of weakness and terrane boundaries extending to Moho offsets are argued to have facilitated ascent and emplacement of anorthosite magmas (Duchesne et al. 1999). The crustal source model is supported by high-pressure experimental work on Al-rich basaltic melt compositions, which show a thermal divide on the plagioclase-pyroxene liquidus at 10–13 Kbar, implying that a mantle-derived melt could not produce the observed range of olivine- and orthopyroxene-bearing mineral assemblages in the Rogaland Anorthosite Province (Longhi et al. 1999). Isotopic results for these anorthosite massifs, including U-Pb geochronology and whole rock Re-Os measurements (Schiellerup et al. 2000), have also been interpreted to endorse a mafic lower crustal source for the parental magmas.

According to Bybee & Ashwal (2015), the broadly tholeiitic mineralogy of the anorthosites, related residua and associated fine-grained gabbros are the main lines of reasoning supporting the mantle source model (Morse, 1982). Stable and radiogenic isotope data support the proposals that the magmas were derived from melting of the depleted mantle, which then experienced strong crustal contamination as function of polybaric magma emplacement/crystallization (Ashwal et al. 1986; Emslie et al. 1994; Peck and Valley, 2000; Frost et al. 2010; Peck et al. 2010; Bybee & Ashwal, 2015).

Concerning the petrogenesis of the intermediate (Fe-Ti-P enriched) and evolved felsic rocks (MCG) commonly associated with anorthosite massifs, their origin is also contentious, with a divergence of opinion regarding the source of the magmas, and their relationship with the anorthosites *strictum sensum*. As explained by Ashwal (1993), the

main hypotheses involved for the origin of rocks associated with massif-type anorthosites are: (1) the voluminous acidic plutons associated with anorthosites mostly formed by anatexis at the base of the lower crust, due to the increase of heat from the crystallizing mafic magmas, which would facilitate ascent of anorthosite diapirs through the crust (Ashwal, 1993); (2) ferrodiorites, jotunites (orthopyroxene-bearing monzonorite) and related intermediate Fe-Ti-P rocks are residual liquids after the crystallization of anorthosite (Morse, 1982; Owens et al. 1993; Emslie et al. 1994; Mitchell et al. 1996), favoured by their occurrence as dykes or small intrusions, commonly at or near the margins of massifs; (3) both mafic intermediate and felsic rocks are the direct product of partial melting of a lower gabbronoritic crust and are the parental magmas of andesine anorthosites (Longhi et al. 1999).

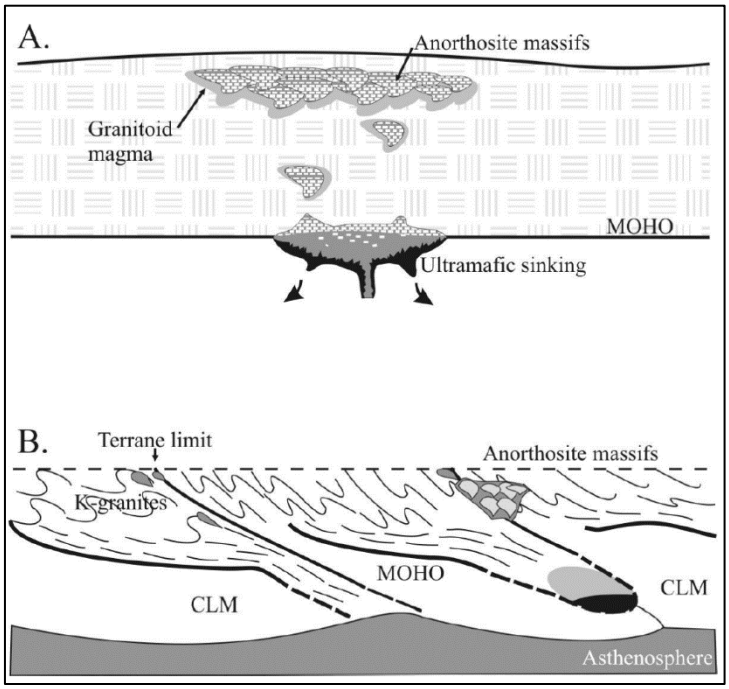

Figure 1.1. Models of massif-type anorthosite petrogenesis. A. Anorogenic two-stage model of Ashwal (1993). B. Post-collisional crustal tongue model of Duchesne (1999). CLM – Continental lithospheric mantle. Extracted from Charlier et al. (2010) with the permission of © Oxford University Press.

According to Charlier et al. (2015) however, these hypotheses are not mutually exclusive. Most authors agree that these Fe-Ti-P rocks represent intermediate compositions in the comagmatic sequence from anorthosite to mangerite and even to

granitoids (Vander Auwera et al. 1998). These authors, using experiments, have shown that evolved monzonitic and mangeritic rocks can be produced by closed-system fractional crystallization from jotunitic-ferrodioritic magmas, although increasing degrees of crustal contamination might also be involved. The comagmatic origin of jotunitic to charnockitic melts is also illustrated by the Tellnes dyke, Rogaland, Norway (Charlier et al. 2006), which is made up of this continuous series of compositions and can be modeled by closed-system fractional crystallization (Wilmart et al. 1989).

1.2.2 The role of crustal contamination

The large and growing database of variable radiogenic and stable isotopic compositions for massif-type anorthosites and related rocks was initially interpreted in terms of derivation from mantle sources with differing degrees of incompatible element enrichment (e.g., Ashwal & Wooden, 1983; Icenhower et al. 1998). It is now clear, however, that variable assimilation of lower and mid-upper continental crustal components by mantle-derived magmas has played a crucial role in massif-type anorthosite composition (Bybee & Ashwal, 2015), in association with polybaric crystallization (Figs. 1.2 & 1.4: Charlier et al. 2009; Chen et al. 2013). Also, the isotopic signatures of Proterozoic anorthosite rocks and minerals can be correlated with the ages of the crustal basement rocks through and/or into which they were emplaced. For example, ~1.3 Ga anorthosite rocks of the Nain Plutonic Suite (Labrador), that intruded through and into Archean basement gneisses with ages up to 3.9 Ga (Morse, 1980; Ryan, 2000), all have highly negative εNd values (as low as −13), whereas massifs emplaced into more juvenile Proterozoic crust of the Grenville Province (e.g. Adirondacks, Morin, Lac-Saint-Jean, Mealy Mountains) are generally characterized by positive εNd values (Emslie & Hegner, 1993) close in value to depleted mantle (Frost et al. 2010; Bybee & Ashwal, 2015).

The effects of crustal assimilation in anorthosite plutons are also reflected in the

mineral assemblages of these rocks (Morse, 2006; Frost et al. 2010). According to these authors, crustal assimilation will increase both the silica activity and oxygen fugacity of mafic magmas, modifying the silica-dependent equilibria existing among Fe–Ti oxides, orthopyroxene, olivine, and quartz. Less contaminated magmas would be related with labradorite-type anorthosites and coeval olivine-bearing troctolite and olivine-gabbros, enriched in magnetite. In contrast, mantle-derived magmas exposed to higher degrees of crustal assimilation would generate andesine-type anorthosite massifs and associated orthopyroxene-bearing rocks, dominated by ilmenite and hemo-ilmenite oxides. Therefore, crustal contamination seems to be a crucial factor in controlling the mineralogy and geochemistry of oxide-apatite deposits related to AMCG suites.

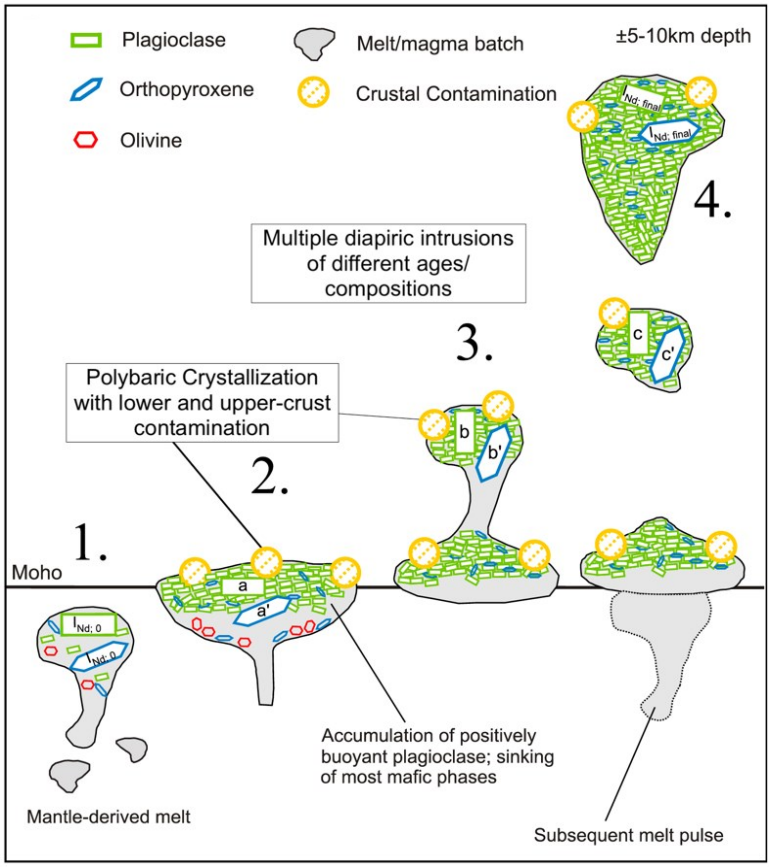

Figure 1.2. Schematic diagram documenting internal mineral composition changes in a ponding magma assimilating lower crust. Extracted from Bybee & Ashwal (2015) with the permission of © Elsevier.

1.2.3 Fe-Ti-V-P-rich deposits: geochemical variation of oxide mineralogy in relation to AMCG-suites

Magmatic rocks containing mineralization of Fe-Ti-V-P are commonly associated with massif-type anorthosites and related mafic (ferrodiorite, jotunite, gabbronorite) and felsic rocks. A single anorthosite suite may be composed of multiple anorthosite lobes with varying ages/different plagioclase compositions (e.g., Lac-Saint-Jean & Havre-Saint-Pierre Anorthositic Suites; Quebec) and host different styles of Fe-Ti-oxide mineralization (Gobeil et al. 2002), in which several controls and mechanisms can concentrate ilmenite ± magnetite ± apatite during cooling of the parental magma (Pang et al. 2008; Charlier et al. 2015). Ilmenite, hemo-ilmenite (ilmenite with exsolution of hematite) and Ti-magnetite occur with apatite and minor silicate phases as plagioclase and orthopyroxene, forming nelsonites (oxide-apatite massive rocks) and related oxide-apatite gabbronorite (OAGN) (Owens & Dymek, 1992; Dymek & Owens, 2001). Fe-Ti cumulates at some locations are devoid of apatite, forming massive oxide mineralization, as well as mineralized olivine-bearing troctolites (e.g., Kiglapait, Labrador; Morse, 1986) or orthopyroxene-bearing norites, dominated either by (hemo)ilmenite (e.g., Lac Tio, Quebec; Charlier et al. 2010) or magnetite (Fedorivka deposit, Ukraine; Charlier et al., 2006). Fe-Ti-P oxide deposits associated with anorthosite massifs, according to Charlier et al. (2015), generally exhibit four distinct modes of occurrence: (1) massive deposits; (2) stratiform deposits; (3) massive to layered tabular bodies; (4) lenticular ore bodies. Several classification schemes have been proposed to subdivide Fe-Ti-P mineralization, most of them based on the observation of two deposit types in the Grenville anorthosites, which contains the world's highest concentration of Fe-Ti-P mineralization (Anderson & Morin, 1969). The first type is dominated by Ti-magnetite (a Ti-rich magnetite with > 2 wt.% Ti and commonly containing exsolutions of ilmenite) and occurs in labradorite-type anorthosite whereas the second type has hemo-ilmenite as the principal mineral and is found exclusively in andesine-type anorthosite (Anderson & Morin, 1969). Studies on the

Lac-Saint-Jean Anorthositic Suite in Quebec, the largest anorthosite massif in the world, support this suggestion (Hébert et al. 2005; 2009), showing also that Ti-magnetite deposits are usually devoid of apatite. However, Grant (2020) shows that nelsonite does occur in magnetite-dominated deposits (e.g., Lac Perron and Saint Charles de Bourget) but associated with andesine-type rather than labradorite-type anorthosite of the 1.15 – 1.12Ga Lac-Saint-Jean Anorthositic Suite. Conversely, the younger anorthosites in the Central Grenville are exclusively andesine in composition and are dominated by hemo-ilmenite (+ magnetite ± apatite) and can include nelsonite or oxide-rich apatite gabbronorite (Owens & Dymek, 1992, 2005; Dymek & Owens, 2001; Morisset et al. 2010; 2013). For the Rogaland anorthosite province, in Norway, the following classification was therefore adopted: Type I: hemo-ilmenite alone; Type II: (hemo)-ilmenite + Ti-poor magnetite; and Type III: Ti-magnetite + (hematite-free) ilmenite + apatite, including nelsonite, without being necessarily linked to an andesine- or labradorite-type plagioclase (Duchesne, 1972; 1973; 1999).

More recently, Charlier et al. (2015) proposed a general subdivision of four deposit types based on mineralogical criteria, separating ilmenite and Ti-magnetite deposits, but not precluding the existence of transitional types: I) (Gabbro)-noritic (hemo) ilmenite ore ± apatite ± magnetite, which includes the two world-class Ti deposits of Lac Tio, Havre-Saint-Pierre (Québec) and Tellnes, Rogaland Province (Norway), being dominated by massive hemo-ilmenite with extensive exsolution lamellae of hematite. Other localities include the Big Island (Morisset et al. 2009), the Grader Intrusion (Charlier et al. 2008) deposits of the Havre-Saint-Pierre Anorthositic Suite in addition to several occurrences in the Saint Urbain Anorthosite, both in Québec; II) Ti-magnetite ± apatite-dominated ore, not currently viable for Ti, but with significant resources of V, such as the Magpie Mountain (Lac-Saint-Jean Anorthositic Suite, Québec; Perreault, 2003), the Suwalki Anorthosite (Poland; Charlier et al. 2009) and the Fedorivka layered intrusion (Korosten Complex, Ukraine; Duchesne et al. 2006); III) Nelsonite ore, as observed in Lac à Paul deposit in the Lac-Saint-Jean Anorthositic Suite, Québec (Corriveau et al.

2007), or in association with OAGN (oxide-apatite gabbro-norite), as observed in Labrieville and Saint Urbain anorthosites, Quebec (Owens & Dymek, 1992); IV) Rare rutile-ilmenite ore, being only described in association with andesine-type anorthosites in the Saint Urbain and Big Islands deposits, Havre-Saint-Pierre Anorthositic Suite, Québec (Morisset & Scoates, 2008; Morisset et al. 2009; 2010).

Morse (2006) proposed a model (Fig. 1.3) from studying the anorthosite suites of Nain (Labrador), which Frost et al. (2010) tested for the Laramie Anorthosite (U.S.A). These authors concluded that changes in the mineral assemblage of both host anorthosite and oxide-deposit rocks are a function of I) distinct parental magma compositions and/or II) different degrees of crustal assimilation in anorthosite diapirs. Assimilation will increase both silica activity (and stabilise orthopyroxene over olivine) and oxygen fugacity (and stabilise hemo-ilmenite over magnetite) of high-Ti-P mafic magmas, modifying the silica-dependent equilibria existing among Fe–Ti oxides, orthopyroxene, olivine, and quartz. The activities are coupled as long as olivine and pyroxene remain in the system at equilibrium. In general, assimilation of silicic country rocks increases the activity of oxygen as well as that of silica (thus making noritic magmas). If the magma is contaminated by crustal rocks (high Si activity), more orthopyroxene is generated until olivine is exhausted (noritic anorthosites). If the system is less contaminated (low Si activity and reduced fO_2), more olivine is generated until pyroxene is exhausted (troctolitic anorthosites). Lack of crustal contamination helps to preserve mantle-like, olivine-rich, low activities of silica and oxygen, resulting in troctolitic magmas (e.g. Voisey's Bay, Kiglapait, Nain Plutonic Suite– Labrador).

Moreover, the initial magma composition shows some fundamental role. The initial crystallization of ilmenite is normally related with low fO_2 conditions (Toplis & Carrol, 1995), with increasing of oxidation conditions favoring magnetite formation. However, ilmenite as a first liquidus phase with lack of magnetite, even in more oxidized conditions, is frequent in some important deposits (e.g., Lac Tio, Tellnes) and seems to be dependent of the initial magma composition (Charlier et al. 2006; 2008; 2014).

Enriched Fe-Ti parental magmas can possibly generate ilmenite-dominated mineralization, not necessarily related with dependent fO_2 conditions. These enriched magmas being exposed to more oxidizing condition (e.g., as a function of crustal contamination), would crystallize hemo-ilmenite preferentially. Also, high-P_2O_5 content of parental magmas would favor magnetite destabilization, leading to more ilmenite crystallization (Toplis & Carrol, 1994).

In summary (Fig.1.3), for a system where an enriched Fe-Ti-P mafic magma reacts with a silica-rich assimilant: I) Oxygen fugacity will also increase, along with $aSiO_2$; II) Magnetite/olivine will be consumed; III) Ilmenite/orthopyroxene will become more abundant; IV) Ilmenite will become enriched in Fe^{+3} (Hemo-ilmenite).

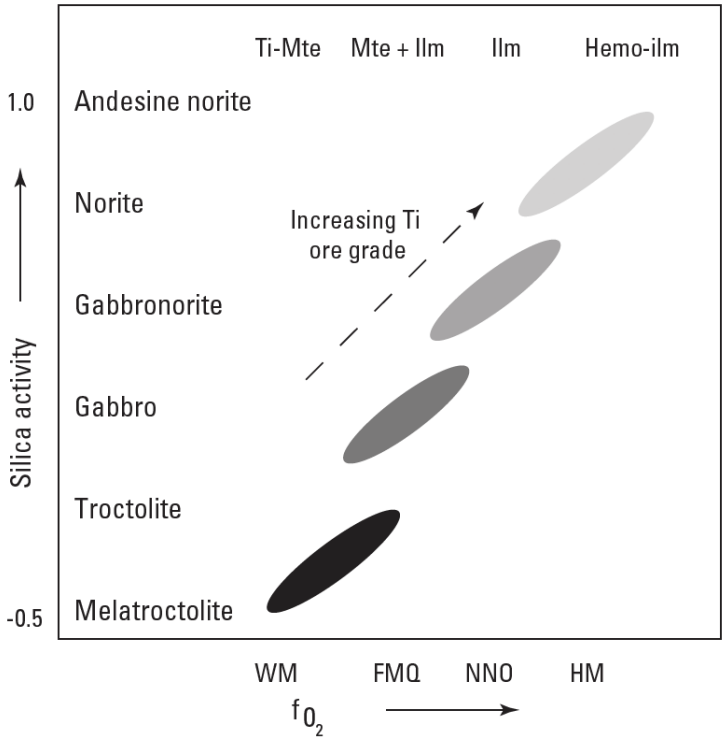

Figure 1.3. Rock association and Fe-Ti oxide mineralogy classification scheme for massif -type anorthosites based on silica activity and oxygen fugacity for idealized lithologies after Morse (2006). Ti-Mte: Ti-Magnetite; Me: magnetite; Ilm: ilmenite; Hemo-ilm: Hemo-ilmenite; WM: wustite - magnetite; FMQ: fayalite – magnetite – quartz; NNO: nickel-nickel-oxide; HM: hematite-magnetite. Extracted from Morse (2006) with the permission of © Elsevier.

Less contaminated magmas thus, would be related with labradorite-anorthosites and coeval olivine-bearing troctolite and olivine gabbros, enriched in magnetite. On the other side, mantle-derived magmas after exposing to higher degrees of assimilation

would generate andesine-anorthosite massifs and associated orthopyroxene-bearing rocks, dominated by ilmenite and hemo-ilmenite oxides. This appears to explain well the variation in oxide and anorthosite lithologies of the Central Grenville, but no one has yet tested this hypothesis.

1.2.4 Main magmatic controls and ore forming processes on the crystallization of oxide-apatite mineralization

Several experimental studies on Fe-Ti rich magmas (Buddington & Lindsley, 1964; Snyder et al. 1993; Toplis & Carroll, 1995) have confirmed that the timing and nature of oxide saturation in a crystallizing magma will determine the type and style of oxide mineralization. These studies demonstrate the strong influence of oxygen fugacity (fO_2) and temperature on the stability fields of Fe-Ti oxides, as important factors influencing the timing of magnetite-ilmenite crystallization (Charlier et al. 2006; 2015).

Toplis & Carroll (1995) have shown, with one-atmosphere experiments on ferrobasalts, that the stability field of magnetite expands with increasing fO_2. Consequently, at high fO_2 (above FMQ conditions), the appearance of magnetite would precede that of ilmenite. These experiments also show that the initial TiO_2 content of magmas is equally crucial in controlling the primary type of oxide crystallization. According to these authors, the fO_2 only affects the stability field of magnetite whereas the saturation point of ilmenite is controlled by the TiO_2 content of the melt. Consequently, the enlarged stability field of ilmenite as the only early cumulus oxide under reduced conditions is a consequence of magnetite destabilization, and thus iron-enrichment in the melt. On the other hand, even in oxidizing conditions, melts with a high-TiO_2 content might reach ilmenite saturation before magnetite, and in some cases, with prior hemo-ilmenite crystallization without magnetite (Charlier et al. 2008). The high hematite content in ilmenite would be thus, an indicator of both high fO_2 and high-TiO_2 content of the parental magma (Toplis & Carroll, 1995).

Besides the TiO_2 content, different concentrations of P_2O_5 also seem to have an important role on differentiation of ferrobasalt magmas (Toplis et al. 1994a; Toplis et al. 1994b). This leads to the formation of silicate melts with much higher Fe contents than is possible for P-poor compositions, allowing the concentration of Fe and Ti at higher levels. At a given temperature, the increasing P_2O_5 content decreases the stability field of magnetite while the relative abundance of ilmenite remains approximately constant. The high P_2O_5 content of ferrodioritic or jotunitic liquids associated with anorthosites (e.g. Mitchell et al. 1996; Vander Auwera et al. 1998) is thus probably responsible for some characteristics of anorthosite suites, such as the common early saturation of ilmenite compared to magnetite. However, the reason for high-Ti-P concentrations in these magmas is not well understood.

A change in pressure may have a significant influence on the formation of Fe-Ti oxide mineralization, as melt phase equilibria depend strongly on the crystallization pressure (Vander Auwera & Longhi, 1994). The dynamic and polybaric crystallization (Fig. 1.4) of massif-type anorthosites is strictly related with its petrogenesis and may mechanically sort disseminated crystals of Fe-Ti oxides during the ascent of plagioclase-rich mushes (Charlier et al. 2009; Chen et al. 2013). According to these authors, the oxides crystallize continuously as the anorthosite diapir ascends, and the occurrence of different cumulus assemblages may thus result from different pressures of crystallization. Phase equilibria experiments (Vander Auwera et al. 1998; Longhi et al. 1999) on plausible parental magmas of massif-type anorthosite show initial saturation in plagioclase + orthopyroxene at 10-13 kbar, whereas the assemblage plagioclase + ilmenite (± magnetite) may crystallize at lower pressure, 8-5 kbar, from the same parental magma.

Although there is a consensus on the igneous origin of Fe-Ti-P deposits associated with massif anorthosite, questions remain about the complex magmatic processes creating ilmenite ± magnetite ± apatite accumulations in economic quantities

in both layered intrusions and anorthosite massifs. The most popular models are fractional crystallization with oxide settling (possibly accompanied by plagioclase flotation) and liquid immiscibility (Ashwal, 1993), although the combination of accumulation processes, solid-state remobilization, filter-pressing, slumping, magma mixing and cotectic crystallization were also attributed to explain the formation of large massive ilmenite-dominated deposits, such as Lac Tio and Tellnes (Charlier et al. 2006; Woodruff et al. 2013).

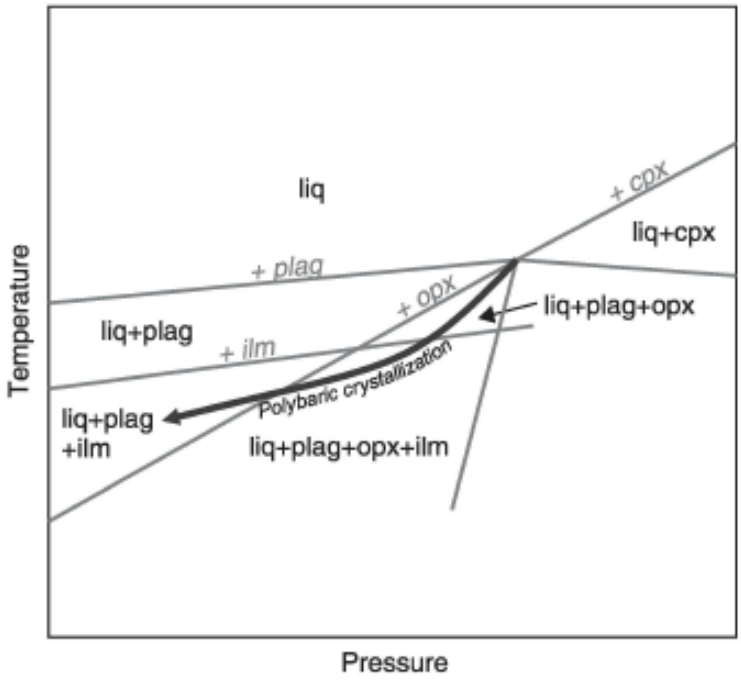

Figure. 1.4. Schematic phase equilibria showing the stability of plagioclase, clinopyroxene, orthopyroxene and ilmenite in relation to pressure and temperature. Extracted from Charlier et al. (2015) with the permission of © Elsevier.

The fractional crystallization model (Fig. 1.5) involves crystallization of Fe-Ti oxides and silicates in cotectic proportions (i.e. magnetite:silicate = 15:8 wt.%, Toplis and Carroll, 1995; ilmenite:silicate = 20:8 wt.%, Charlier et al. 2007; 2008; 2010) followed by settling, whereby the different densities of these minerals can result in flotation of plagioclase (Namur et al. 2011) and sinking of dense Fe-Ti oxide crystals to produce massive cumulate layers (Wager and Brown, 1968). This cumulate sorting produces Fe-Ti oxide abundance greater than the cotectic proportions would suggest (Charlier et al.

2006; Tollari et al. 2008). Plagioclase can float vertically (Fig. 1.5a) and form also a layer of anorthosite (Namur et al. 2011) or be transported laterally (Fig. 1.5b) to form leucocratic rocks in other parts of the magma chamber (Charlier et al. 2015).

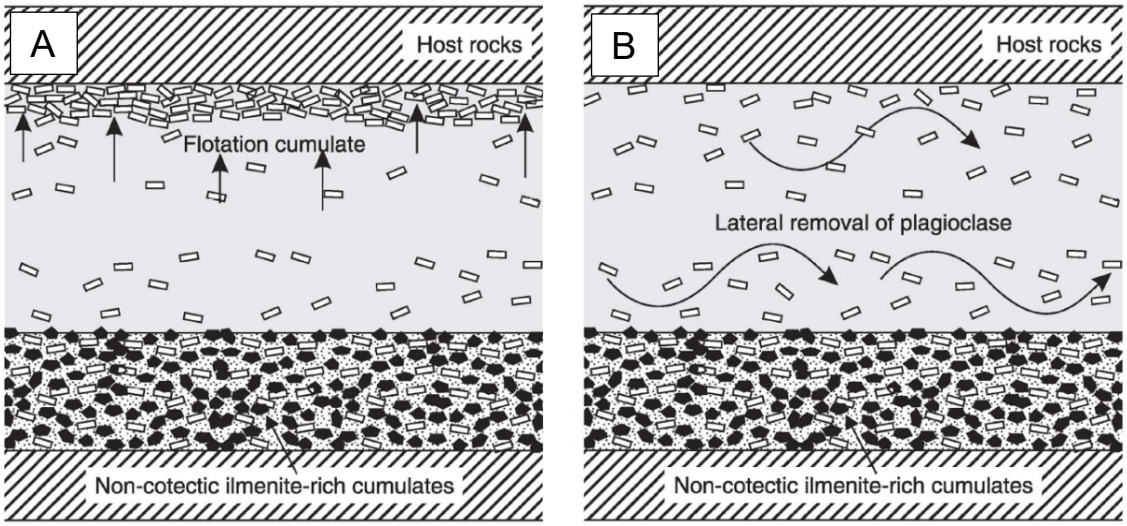

Figure 1.5. Schematic illustrations of fractional crystallization combined with plagioclase segregation processes: (a) by flotation of light plagioclase in a dense Fe-Ti-rich melt; (b) by lateral removal driven by convection. Extracted from Charlier et al. (2015) with the permission of © Elsevier.

Magmas parental to anorthosite, and their residual liquids, are Ti-rich, commonly having more than 4 wt.% TiO_2 (Mitchell et al. 1996; Vander Auwera et al. 1998). This may promote early ilmenite saturation (Toplis and Carroll, 1995), as observed in Lac Tio and Tellnes for example, where ilmenite is considered to be a first liquidus phase. In these deposits, fractional crystallization with oxide settling and plagioclase flotation, together with other processes, would promote the primary accumulation of hemo-ilmenite crystals (Charlier et al. 2006; 2007; 2008; 2015).

Anorthosite-massifs are emplaced as diapirs and crystallize polybarically during the ascent of the plagioclase mush (Ashwal, 1993), undergoing polybaric crystallization (Bybee & Ashwal, 2014). This dynamic emplacement provides the conditions necessary to produce stress-driven residual melt segregation (Fe-Ti-P-rich ferrodiorite; Fig. 1.6) in partially molten rocks (Kohlstedt et al. 2010).

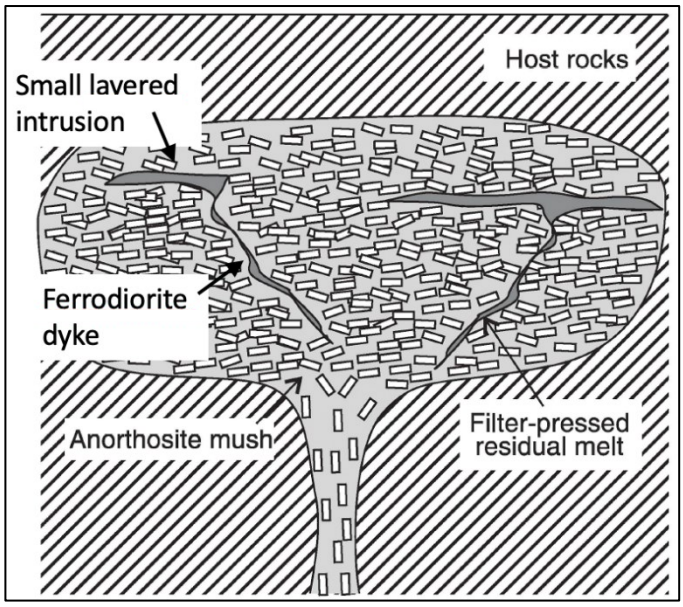

Figure 1.6. Schematic illustration of filter-pressing process: segregation of Fe-Ti-enriched residual melts from uprising anorthosite mush. Modified from Charlier et al. (2015) with the permission of © Elsevier.

According to Scoates et al. (2010), these residual melts are pressed out and segregated into regions of lower pressure (fractures and margins) inside the newly generated massif anorthosite, forming small layered mafic intrusions commonly observed (Vander Auwera et al. 2006), such as at Grader Lake deposit (Charlier et al. 2008), or as discordant dykes/lenses (Dymek & Owens, 2001) of massive ore in host anorthosite. Multiple pulses of magma emplacement, with alternating periods of fractional crystallization and magma mixing, are common processes described in many layered intrusions around the world (Namur et al. 2010; Charlier et al. 2010) and may also induce the formation of Fe-Ti oxide deposits in massif-type anorthosites (Robinson et al. 2003; Charlier et al. 2006).

Immiscibility between two silicate melts (Fe-Ti-P-rich ferrobasalt/Si-rich rhyolite) has been recognized experimentally and in natural systems as a potential differentiation mechanism in evolved basaltic magmas (Roedder, 1978; Philpotts, 1967; 1982; Charlier & Grove, 2012; Charlier et al. 2011, 2013; Zhou et al. 2013; Hou et al. 2018; Coint et al. 2020). Philpotts (1967) proposed that immiscibility is responsible for the origin of certain Fe-Ti oxide and apatite rocks. A similar process was involved by Force (1991) to

generate ilmenite deposits in general, while Kolker (1982) favored this model for the origin of nelsonites, mainly to explain field evidence such as discordant veins and dykes intruding the host anorthosite (Fig. 1.7). However, more recent studies proposed instead that nelsonites represent cumulates (Duchesne, 1999); Dymek & Owens (2001); Charlier et al. 2008). Another hypothesis is that nelsonites represent cumulates crystallized from Fe-rich immiscible silicate melts, rather than crystallized Fe-oxide immiscible melts (Namur et al. 2012; Kieffer et al. 2023).

According to Charlier et al. (2011), immiscibility is supported by the presence of contrasting Fe-rich and Si-rich melt inclusions trapped in cumulus apatite. Phase diagrams and well-documented occurrences of small-scale immiscibility confirm that liquid-liquid unmixing and the separation of Fe-rich and Si-rich liquids may contribute significantly to the absence of some intermediary mafic compositions along the tholeiitic liquid line of descent (e.g. Sept Iles, Namur et al. 2010). Hou et al. (2018) have recently shown that increasing pH_2O and fO_2 enlarges the "two-liquid field" thus allowing a Fe–Ca–P melt to separate easily from host silicic magma and produce Fe-Ti oxide-apatite ores.

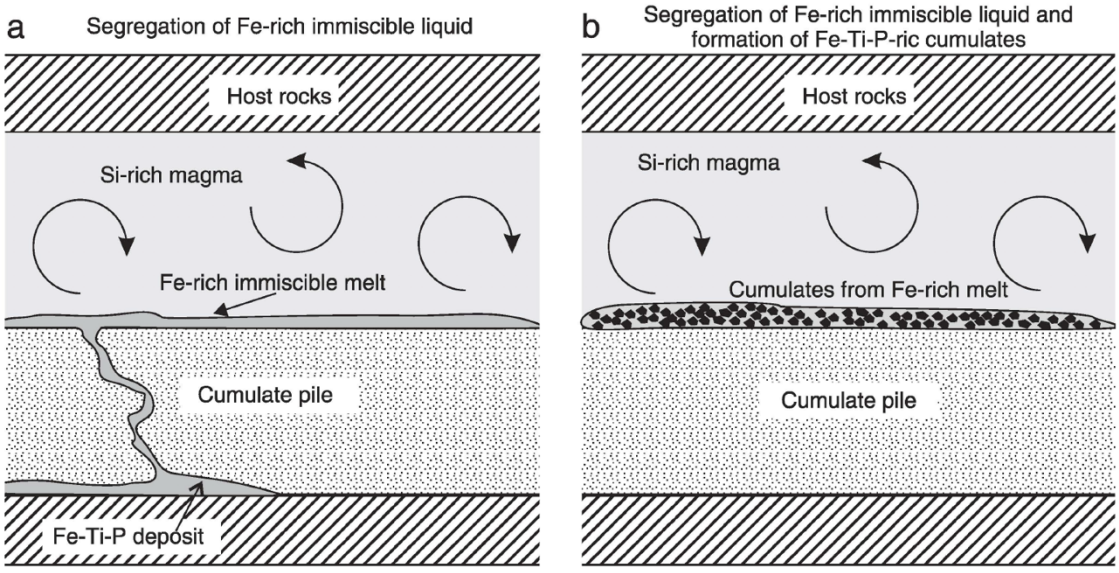

Figure 1.7. Schematic illustrations of ore-forming processes by immiscibility. a) Segregation and accumulation of Fe-rich immiscible melt with potential downward percolation of the dense melt into partially molten cumulate; b) Segregation of an immiscible Fe-rich melt and crystallization of an Fe-Ti oxide-rich cumulate. Extracted from Charlier et al. (2015) with the permission of © Elsevier.

Coint et al. (2020) also emphasize the importance of silicate-liquid immiscibility in the evolution of intermediate to felsic alkalic ferroan systems and generation of Fe-Ti-P-rich rocks in the Raftsund Intrusion, Norway. Concerning the petrogenesis of massive oxide-deposits, Zhou et al. (2013) have proposed a model involving the crystallization of massive magnetite bodies from an Fe-Ti oxide liquid, by two stages of liquid immiscibility: the first stage represents the unmixing of a mafic magma into a Si-rich and Fe-rich conjugate silicate melts; the second is defined by unmixing of the Fe-rich silicate liquid into a Fe-Ti oxide liquid (ore) and a mafic liquid (Fig. 1.8).

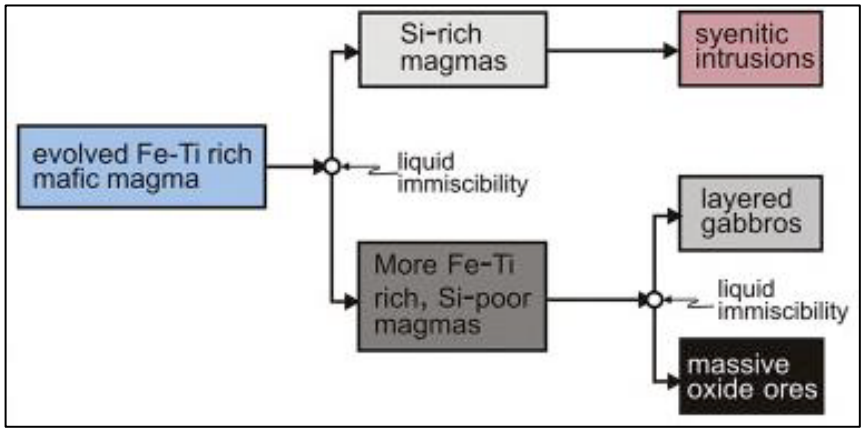

Figure 1.8. Schematic diagram illustrating the model of Zhou et al. (2013) for the formation of Fe-Ti-V oxide deposits by liquid immiscibility at Panzihua, Emeishan LIP. Extracted from Zhou et al. (2013) with the permission of © Elsevier.

However, according to Veksler et al. (2007), the most iron-rich immiscible liquids produced experimentally do not exceed 28 w.t.% FeO and 5 w.t.% TiO_2 contents, which is not enough to generate massive deposits (which normally contains upwards of 95 w.t.% FeO and TiO_2, Charlier et al. 2015). Furthermore, Fe-Ti immiscible liquids strongly partition P (Toplis & Carroll, 1995); the absence of apatite in many massive bodies therefore suggests they were not formed from an Fe-Ti-P oxide liquid. Besides that, according to Charlier & Groove (2012), immiscibility in evolved ferrobasalts do not produce melts saturated with a single-phase. A liquid of ilmenite composition would melt at 1360°, while magnetite melts at 1590ºC, both unrealistically high temperatures for crustal conditions. According to Charlier et al. (2006), pure massive ores, such as that in

Tellnes (Duchesne, 1999) and Lac Tio (Charlier et al. 2010), cannot be produced by immiscibility, favoring instead the fractional crystallizing model.

1.3. Area of study: AMCG suites and related Fe-Ti-P mineralization in the Central Grenville Province

The Grenville Province is a Mesoproterozoic orogenic belt along the southeastern margin of the Canadian Shield (Corriveau et al. 2007), in which numerous episodes of AMCG are recorded (Higgins & van Breemen, 1996; Gobeil et al. 2002; Hébert et al. 2005; 2009). These AMCG suites (Figs. 1.9 and 1.10) and coeval Fe-Ti-P mineralization (Table 1.1) have been emplaced for over 300 million years (1343-1008 Ma, Hébert et al. 2009) recording a complex petrogenetic, tectonic and temporal evolution.

Hébert et al. (2009), compiling previous work and generating new geochronological data for the Central-South Grenville anorthosites (Fig. 1.10), proposed four distinct pulses of magmatism, with major occurrences in the region of Saguenay-Lac-Saint-Jean: I) the 1327 ± 16 Ma labradorite-type De La Blache Mafic Plutonic Suite (Gobeil et al. 2002); II) the 1160-1135 Ma labradorite- and andesine-type Lac-Saint-Jean Anorthosite Suite (Higgins & Van Breemen, 1992; Higgins et al. 2002); III) the 1082-1045 Ma andesine and labradorite-type Pipmuacan Anorthosite Suite, including the Vanel anorthosite, the Poulin de Courval Mangerite and the coeval Saint Urbain andesine anorthosite (Higgins & van Breemen, 1996); IV) the 1020-1008 Ma andesine-type Valin Anorthosite Suite, including the Mattawa Anorthosite (Hébert et al. 2005), Labrieville Alkalic Anorthosite Massif (Owens et al. 1994), the Gouin Charnockite (Hébert et al. 2005), and the La Hache Monzonite (Hébert et al. 2005).

Other chrono-correlated occurrences include the important 1139-1062 Ma Havre-Saint-Pierre Anorthositic Suite to the northeast (Van Breemen & Higgins, 1993), which hosts the massive hemo-ilmenite Lac Tio deposit, and the 1155 ± 3 Ma Morin Massif (Doig, 1991) to the southwest (Fig. 1.9).

As previously mentioned, a variation in the oxide assemblage (from magnetite to hemo-ilmenite) and apatite trace element patterns (Grant, 2020; Dymek & Owens, 2002) seems to be directly related with the host anorthosite composition. In the central Grenville Province: I) labradorite-type anorthosites are exclusively older than 1130 Ma and their Fe-Ti oxide deposits are dominated by Ti-magnetite; II) andesine anorthosites are typically younger than 1160 Ma (except for the 1354-Ma Rivière-Pentecôte Anorthosite and 1150 Ma Lac-Saint-Jean Anorthosite Suite, which contains both labradorite- and andesine-type anorthosite); and III) no hemo-ilmenite mineralization occurs in anorthosite plutons older than 1160 Ma, and are restricted to andesine-type anorthosite and associated oxide–apatite-rich gabbronorites (OAGN) and nelsonites (Fig. 1.10).

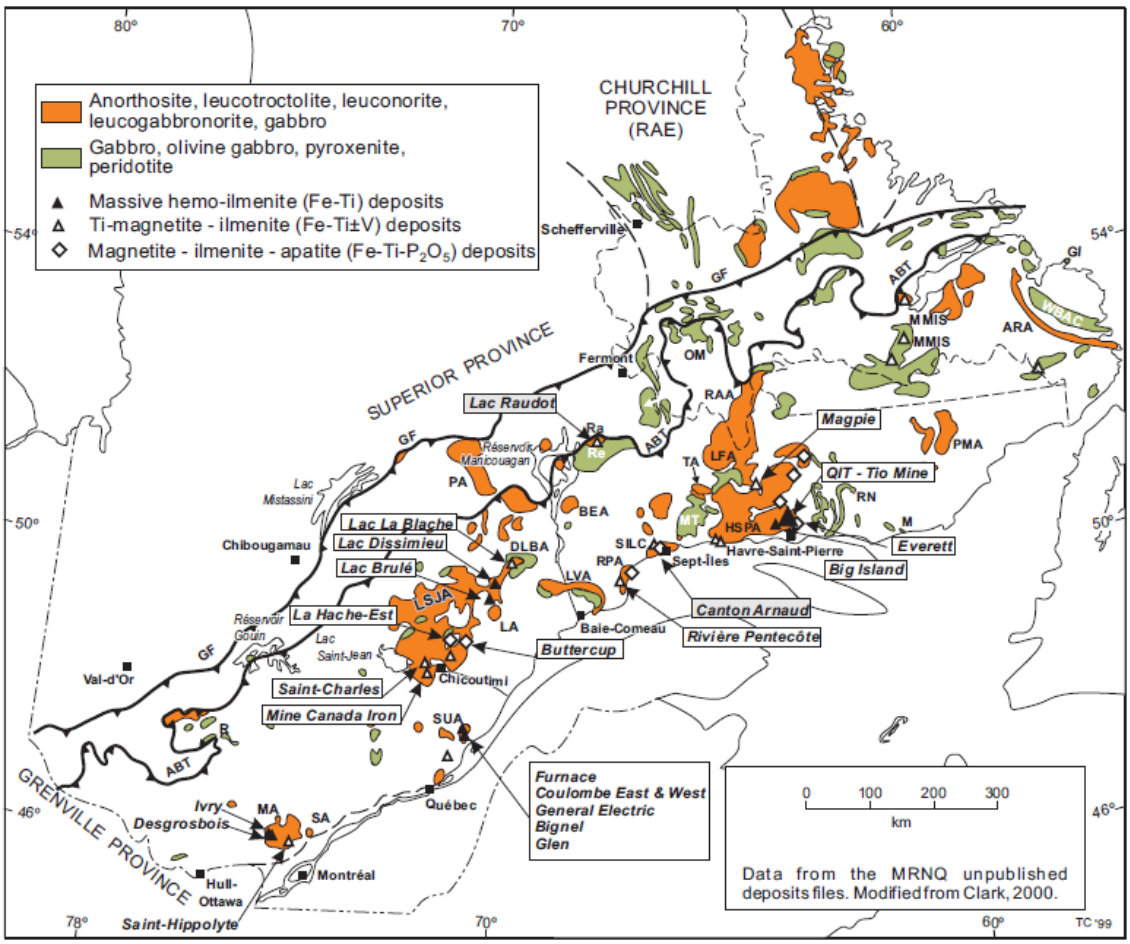

Figure 1.9. Distribution of anorthosite massifs and major mafic intrusions and their Fe-Ti deposits in the Quebec and Labrador segments of the Grenville Province. Extracted from Corriveau et al. 2007 with the permission of © Economic Geology and Society of Economic Geologists. Anorthosite massifs: ARA, Alexis River; BEA, Berte; LA, Labrie; DLBA, De La Blache; HSPA, Havre-Saint-Pierre; LFA, Lac Fournier; LSJA, Lac-Saint-Jean; LVA, Lac Vaillant; MA, Morin; PA, Pambrun; PMA, Petit Mecatina; RAA, Atikonak River; RPA, Riviere Pentecote; SA, Shawinigan; SUA, Saint-Urbain; TA, Tortue; . Mafic intrusions and intrusive complexes: GI, Grady Island; M, Musquaro; MMIS, Mealy Mountains; MT, Matamec; OM, Ossok Mountain; R, Raudot; SILC, Sept-Iles; WBA, White Bear Arm. Sills: R, Renzy; RN, Robe Noire. GF, Grenville Front.

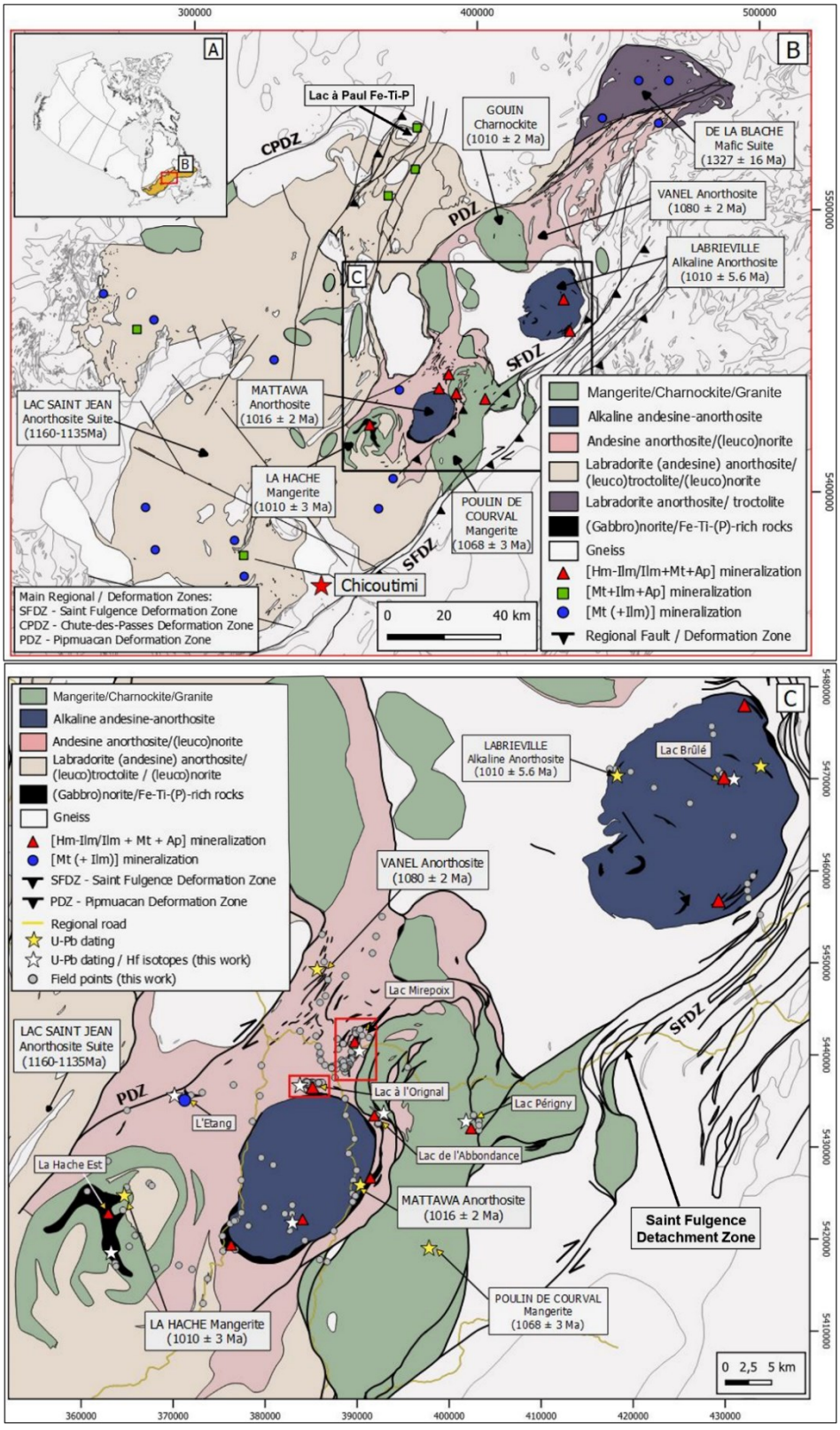

Figure 1.10. Geological map of the Central Grenville Province, showing the different AMCG suites and associated Fe-Ti-P mineralization (table 1.1), divided in four different magmatic pulses, defined by Hébert et al. (2005); (2009). Geological maps modified from SIGEOM (Quebec System of Geomining Information; Gobeil et al. 2002; Hébert & Cadieux, 2003).

Table 1.1. Major AMCG suites and coeval Fe-Ti-P mineralization in the Grenville province, Québec

Location				Age (Ma)	Anorthosite Type	Deposit Rock Type	Oxide Minerals	Deposit Type
Region	**Suite**	**Deposit Name**						
Western	Morin	Desgrobois		1155±3[1]	Labradorite-Andesine	Fe-Ti oxide-rich gabbro	Ti-Mgt + ilm + apt	Tabular/dyke-like bodies
		Ivry				Ilmenitite	Hm-ilm (Hm 33%)	Parallel layers/lenses
Central	De La Blache	Lac de La Blache		1327±16[2]	Labradorite	Magnetitite, leucotroctolite, leuconorite	Ti-Mgt ± ilm (Hm <6%)	Tabular/dyke-like bodies
	Lac-Saint-Jean	Saint Charles, Buttercup, Lac Perron		1156±2[3]	Labradorite - Andesine	Magnetitite, leuconorite	Ti-mgt + ilm + (apt)	Dyke-like massive bodies
		Lac à Paul*			Andesine	Leuconorite, nelsonite	Ilm + Ti-mgt + apt	Lenses/dyke-like and disseminated ores
	Pipmuacan	**Poulin de Courval Mangerite**	**Lac Périgny, Lac L'abbondance**	1068±3[4]	-	Gabbro, norite, nelsonite, magnetitite, ilmenitite	Ti-mgt + ilm + apt	Lenses/sill-like massive layers
		Vanel Anorthosite	**Lac à Original, Lac Vanel, Lac Mirepoix, L'Étang**	1080±2[5]	Andesine	OAGN, ferrogabbro, nelsonite, ilmenitite	(Hm)-ilm + Ti-mgt + apt	Lenses/dykes/sill-like massive layers
		Saint Urbain Anorthosite	Bignell, Coulomb, Fourneau, G. Electric, Lac Ontario, Glen	1053±3[6] 1080±2[7]	Andesine	Ilmenitite, nelsonite, OAGN	Hm-ilm (Hm 11-27%) + Rut + Apt	Lenses/sill-like massive layers
	Valin	**Mattawa Anorthosite**	**Mineralization within**	1016±2[3]	Andesine	OAGN, nelsonite, ilmenitite	Hm-ilm + Ti-mgt + apt	Lenses/dykes/sill-like massive layers
		Labrieville Alkaline Anorthosite	**Lac Brulé,** Lac Sault Aux Cochons, Lac Catherine	1010±2[8] 1016±2[9]	Andesine	OAGN, nelsonite, ilmenitite	Hm-ilm + Ti-mgt + apt	Lenses/sill-like massive layers
		La Hache Mangerite	**La Hache Est**, Lac du Braconnier, Moncouche	1010±3[9]	-	OAGN, gabbro	Ti-Mgt + ilm + apt	Lenses/sill-like massive and disseminated layers
		Gouin Charnockite	Lac Gouin	1010±2[9]	-	Magnetitite, ferrogabro, ferrodiorite	Ti-Mgt + ilm + apt	Lenses/sill-like massive layers
Eastern	Havre-Saint-Pierre	Lac Tio** (Lac Allard Anorthosite)		1060±3[10]	Andesine	Ilmenitite, ilmenite-rich norite	Hm-ilm (Hm 23-29%)	Funnel shape massive ore intrusion
		Big Island				Ilmenitite	Hm-ilm (Hm 20-30%) + rut	Dyke-like massive bodies
		Grader Intrusion				OAGN, ilmenitite	Hm-ilm (Hm 20-32%) ± mgt ± apt	Layered intrusion

Studied areas in this study in bold. * Lac à Paul is a world-class resource of P waiting to be exploited. ** Lac Tio is the biggest currently Ti mine in the world. Mineral abbreviations: mgt: magnetite; ilm: ilmenite; apt: apatite; rut: rutile; hm: hematite. References: 1- Morriset et al. (2013); 2- Gobeil et al. (2002); 3- Higgins & Van Breemen (1996); 4- Hébert et al. (1998); 5- Van Breemen (2009); 6 - Morriset et al. (2009); 7- Hébert et al. (2009); 8- Owens et al. (1994); 9- Hébert *et al.* (2005); 10- Morrisset *et al.* (2009).

Detailed work on the Havre-Saint-Pierre anorthosite also demonstrates a variation in oxide mineralogy, with age: older (1139-1129Ma) labradorite-type anorthosite lobes containing Ti-magnetite and ilmenite (± apatite) whereas the younger andesine-type anorthosites contain abundant hemo-ilmenite (± apatite) (Hébert et al. 2009)

The Grenville province contains several occurrences of Fe-Ti-P mineralization associated with more silicic members of AMCG suites, such as mangerites and charnockites, a case almost absent in others anorthosite provinces worldwide. These appear in association with andesine-anorthosite, in the last stages of magmatism in the region of Saguenay-Lac-Saint.-Jean (e.g., La Hache Mangerite, Gouin Charnockite).

Making a detailed look into the andesine-ilmenite dominated Pipmuacan and Valin suites (table 2), it is possible to observe a variation in the oxide mineralogy even within these younger anorthosites. Anorthosite massifs such as Vanel, Mattawa and Labrieville are hemo-ilmenite dominated, but occur in association with Ti-magnetite and apatite. On the other hand, the coeval Saint Urbain Anorthosite is hemo-ilmenite + apatite + rutile dominated, with absence of magnetite, similar to Lac Tio deposit. More evolved Si-rich lithologies, such as Gouin and La Hache, however, host the association Ti-magnetite + ilmenite + apatite.

The long-lived AMCG magmatism (more than 300Ma) in the Grenville was generated from different tectonic settings (from Andean-type margin to continental collision and even post-collisional collapse/lithospheric thinning) that can allow for considerable changes in the petrogenetic factors, such as the sources of magma, crustal contamination, and subsequent processes of evolution/differentiation. The exclusive concentration of massive hemo-ilmenite/apatite-rich deposits in the two younger anorthosite pulses denotes enriched Ti-P parental magmas for the

Pipmuacan and Valin suites, whose origins is not yet understood. A complex genetic relationship of Fe-Ti-P mineralization to host anorthosite and more evolved, related rocks, especially in the Central Grenville province is thus, unclear and remains debated.

1.4 Hypothesis

The hypotheses proposed for this PhD is based on the geochemical differences observed between distinct host AMCG and respective Fe-Ti-P mineralization in the Central Grenville, that would be due to changes in:

1) Parental magma composition (distinct Ti, P, fO_2 sources);
2) Degrees of crustal contamination (modifying directly fO_2 and silica activity, and thus the type of Fe-Ti deposit formed) or
3) Both.

We further propose that the geochemical variation occurs on different scales related to either:

1) A big scale change of tectonic setting with time in the Grenville from pre-syn- to post-collisional regimes. For example, the younger (syn-post) anorthosite-massifs in the Central Grenville (Pipmuacan and Valin suites) would be related to high-Ti-P parental magmas due to a more-enriched source(s) and/or higher degrees of crustal assimilation than the older pre-syn Lac-Saint-Jean and De La Blache Anorthositic suites respectively.

2) A smaller scale variation (massif/ore-deposit scale), in which changes in the oxide mineralogy (from hemo-ilmenite to magnetite) even within coeval AMCG of the same suite could be related to fractionation processes of Fe-Ti-P enriched magmas, with

initial crystallization of hm-ilmenite/ilmenite oxides, followed by magnetite and apatite, i.e., residual mineralization associated with evolved MCG. In this case, mineralized mangerites, (e.g., La Hache Mangerite) would represent the most evolved/residual part of fractionated Fe-Ti-P enriched magmas, rather than anatexis of crustal rocks.

1.5 Objectives

The main goals of this Ph.D. project are to enhance our understanding of:

1) The petrogenesis of magmatic oxide deposits associated with anorthosite complexes.
2) The processes that control their compositional (mineralogical and geochemical) variation and how they vary with time. To achieve this goal the specific objectives are:

I) Characterize the Fe-Ti-P mineralization, i.e. furnish a detailed analysis of the geochemical variation of Fe-Ti-P mineralization associated with AMCG suites in an ore-deposit scale (e.g. Lac à Orignal deposit and Lac Mirepoix Fe-Ti-P mineralization), to further compare with data acquired in the nearby areas of study (geochemical variation in a regional scale).

II) Evaluate the roles in controlling the composition of magmatic oxide deposits and their associated anorthosite complexes:

I) source of melting;

II) crustal contamination;

III) magma composition;

IV) redox conditions (fO_2)

III) Determine the age of the mineralization itself, associated with different AMCG suites in the Grenville Province, Quebec.

1.6 Methodology

This section presents a summary of the methods used to investigate the aforementioned hypotheses and thus achieve the set objectives. More details on the analytical methods are provided in the individual chapters.

This Ph.D. project is the first attempt to reconcile the temporal variation in the composition of both oxide-apatite mineralization and associated anorthosite rocks using a multi-tool geochemical approach that combines trace element chemistry of the ore minerals (Fe-Ti oxides and apatite) and plagioclase, with radiogenic isotopes in zircon. The Fe-Ti oxides provide information on magma differentiation and redox conditions (Andersen et al. 1993; Dare et al. 2014). Trace element in apatite is used to calculate the magma composition (Charlier et al. 2008) and has the potential to track crustal contamination and constrain the mantle source (Kieffer et al. *in review*). The U-Pb dating and Lu-Hf isotopes in zircon help to constrain the age, magma source and degree of crustal contamination (Bickford et al. 2010) of the oxide-apatite mineralization, for the first time.

1.6.1 Area of study

The area of study of this PhD focuses on the AMCG and related mineralization in the central part of the Grenville Province, in Québec (Fig.1.9; Table 1.1), where four main periods of anorthosite magmatism co-exist. More specifically, the PhD concentrated on the younger magmatism in the region (<1100 Ma), with mineralization dominated by hemo-ilmenite and associated with andesine-type anorthosite. The following Fe-Ti-(P) mineralization covering the 2 main periods of younger magmatism were studied: 1) The syn-collisional (1080-1045 Ma) Pipmuacan AMCG suite, comprising the relatively unknown Vanel Anorthosite and related Fe-Ti-P mineralization (Lac à Orignal, Lac Mirepoix, Lac de l'Abbondance Fe-Ti-P

mineralization and L'Étang Fe-Ti mineralization) and the Poulin de Courval Mangerite hosting the Lac Périgny Fe-Ti-P mineralization. None of the mineralization has been dated; and 2) Post-collisional (1016-1008 Ma) Valin AMCG suite, containing the Mattawa Anorthosite (with several Fe-Ti-P occurrences), the Labrieville Alkaline Anorthosite (Lac Brulé Fe-Ti-P mineralization) and the La Hache Mangerite (Fe-Ti-P mineralization occurrences within).

The Lac à l'Orignal deposit (Fig.1.10c) is one of a number of Fe-Ti-P mineralized lenses located approximately 100km northeast of Chicoutimi, outcropping near the border of the Vanel and Mattawa anorthosites. This deposit is the focus of chapter 2 and was selected for detailed study of a Fe-Ti-P mineralization in an ore-deposit scale, through the stratigraphic section (borehole LO-14-21) of the intrusion that is dominated by oxide-apatite-norite cumulates. Based on drilling by Glen Eagle resources, the Lac à l'Orignal Fe-Ti-P mineralized zone has a E-W lenticular structure, approximately 10-100 m thick and 1.5 km in length, with an average grade of 5.1 wt.% P_2O_5, locally up to 7.0 wt.% P_2O_5 (Laverdière, 2013; 2016). The deposit has recently been claimed by First Phosphate Corp., with a Mineral Resources Estimate (MRE) indicating 15.8 Mt at 5.2% P_2O_5, 4.2% TiO_2 and 23.90% Fe_2O_3, with inferred values of 33.2 Mt at 5.06% P_2O_5, 4.2% TiO_2 and 22.5% Fe_2O_3 (Yassa, 2022).

The Lac Mirepoix Fe-Ti-P mineralization is located around 15km northeast of Lac à l'Orignal in the Vanel anorthosite and is discussed in chapter 3. Lac Mirepoix was selected to evaluate the geochemical variation of Fe-Ti-P mineralization through different types of oxide-apatite cumulates (e.g., massive oxides, nelsonite, oxide-apatite-norite) across a larger intrusion, combining samples from outcrops and short drillcores. Previous work based on mapping, drilling and regional analysis (Bouldreault, 2000; Morisset, 2000; Boulianne, 2001; Lefebvre, 2014) proposed that

the Lac Mirepoix mineralization is a sill-like layered intrusion hosted in massive pink anorthosite, where a series of different layers/lenses of oxide-apatite-(gabbro)-norite, leuconorite, nelsonite and massive oxides occur along approximately 2000m. Drilling campaigns by Arianne Phosphate (Boulianne, 2001) identified several 10-25m-thick mineralized horizons, with oxide-apatite-(gabbro)-norite levels (average of 4.3% of TiO_2 and 3.1% of P_2O_5), and massive oxide bands in anorthosite (up to 25.1% TiO_2).

Other Fe-Ti-P mineralization in this study (Fig. 1.9; Lac de l'Abbondance, L'Étang, Lac Périgny, Mattawa, Lac Brulé and La Hache) occur as lenses near the borders and/or form dykes/layers within the Pipmuacan (Lac de l'Abbondance, L'Étang, Lac Périgny) and Valin (Mattawa, Lac Brulé and La Hache) AMCG suites in the Central Grenville. These suites of mineralized samples were selected to investigate the variation of mineralization at a more regional scale and how it varied with time, being the focus of chapter 4. The Lac de l'Abbondance mineralization, initially described by the Mapping Campaign of the Ministère des Ressources Naturelles et des Forêts(Hébert & Cadieux, 2003), is composed of a massive nelsonite (magnetite dominated) of approximately 5 m wide and more than 1 km of extension and hosted in the Vanel anorthosite. The single report for the area gives an average grade of 6.3% TiO_2 and 5.0 % P_2O_5 for the massive nelsonite (Hébert & Cadieux, 2003). The L'Étang area is located in the western portion of the Vanel Anorthosite, where Fe-Ti mineralized lenses of oxide-rich leuconorite occur with high concentration of magnetite + ilmenite (hematite exsolution free), but no apatite. Few publications have given basic descriptions of these smaller mineralization zones in the Vanel Anorthosite (e.g., Hébert & Cadieux, 2003; Hébert et al. 2009). The Lac Périgny occurrence (Girard, 2001) is composed of a 1km thick ilmenite-rich layered gabbro and leucogabbro unit (3.5 % P_2O_5), containing some thin nelsonite layers (up to 9.3 %

P_2O_5), in association with ultramafic (wehrlite), anorthosite and mangerite lithologies, hosted nearby to the Poulin de Courval Mangerite. The Mattawa Anorthosite (Owens & Dymek, 2005) contains seceral where lenses of Fe-Ti-P mineralization at the interface of the Vanel Anorthosite. In this study, we found Fe-Ti-P mineralization within the Mattawa Anorthosite itself. It contains hemo-ilmenite + magnetite + apatite as lenses of oxide-apatite-norite, similar to the cumulates observed at Lac Mirepoix and Lac à l'Orignal of the nearby Vanel Anorthosite. The Lac Brulé Fe-Ti-P mineralization is located on the outer core of the Labrieville Anorthosite, comprising several lenticular massive nelsonite/ilmenitite bodies with approximately 530m of extension and 23m of thickness, exposing grades of 24.5 – 59.2% Fe_2O_3t, 17.2 – 35.9% TiO_2 and 8.9 – 12.4 % P_2O_5 (Forbes, 2006). Fe-Ti-P Mineralization at the La Hache Mangerite contains some stratiform gabbroic layers with massive and disseminated magnetite, ilmenite and apatite mineralization. A previous exploration report in the area (Raby, 1968) gives an average grade of 24.6% Fe_2O_3t, 5.1 % TiO_2 and 5.2 % P_2O_5.

1.6.2 Field work

Two-hundred and sixty samples from mineralization and host-AMCGs were taken in the different areas of study in the Central Grenville Province (Fig.1.9), during twelve days of field work between 2020-2022, and also from previous drillcore sampling, available at some locations (e.g., Lac Mirepoix, Lac à l'Orignal). Outcrop samples have been collected not just near the mineralization itself, but also within the different anorthosites in the region, to better characterize Vanel, Mattawa, Labrieville and La Hache massifs (Fig.1.9).

1.6.3 Optical microscopy

Petrographic description on 158 thin sections containing silicates, oxides and apatite, between the different ore deposits and host-AMCGs, were done using optical

microscope (transmitted and reflective light) at UQAC, to determine the mineral proportions, textures and the selection of grains for mineral analysis.

1.6.4 Mineral chemistry by LA-ICP-MS

Forty-eight trace element concentrations [Li, Na, Mg, Al, Si, P, Cl, K, Ca, Sc, Ti, V, Cr, Mn, Fe, Co, Ni, Cu, Zn, Ga, Ge, Rb, Sr, Y, Zr, Nb, Cs, Ba, La, Ce, Pr, Nd, Sm, Eu, Gd, Tb, Dy, Ho, Er, Tm, Yb, Lu, Hf, Ta, W, Pb, Th and U] in plagioclase, magnetite, ilmenite and apatite were determined in-situ using an Excimer 193nm Resolution M-50 laser ablation system, equipped with a double volume cell S-155, and coupled with an Agilent 7900 mass spectrometer at LabMaTer, UQAC. Line scans across the surface of 3-5 grains (per mineral) per polished thin section were made with beam sizes ranging from 33-55µm according to the size of the grain. International reference materials were used for calibration (NIST-610 glass for plagioclase and apatite; Fe-rich GSE glass for ilmenite and magnetite) and to monitor the data quality for each mineral protocol (e.g., NIST-612, G-PROBE-6 and GSD for plagioclase; with MAPS-4 and UQAC-APA in addition for apatite; G-PROBE-6 and GSD for oxides as well as in-house reference materials BC-28 (massive magnetite) and AMIS-0454 (massive ilmenite)).

Data reduction was carried out using Iolite 4 (Iolite Software, The University of Melbourne), based on semi-quantitative data reduction scheme, normalized to 100% oxides (Paton et al. 2011) for plagioclase and ilmenite as they often contained exsolutions. Magnetite data was treated using the traditional internal standard of Fe value, close to stoichiometry, obtained by electron microprobe (EPMA) at University Laval for a few samples. In the same way, apatite data was normalized using Ca value (close to stoichiometry) obtained by electron microprobe for a few samples. For the oxide minerals the recalculation of Fe total to FeO and Fe_2O_3 contents,

required to balance the total to 100%, was carried out using the EPMA charge balance spreadsheet. The Xhem content in ilmenite was calculated using the QUILF program (Andersen et al. 1993). For plagioclase, the molar proportions of An-Ab-Or was calculated using the EPMA spreadsheet for charge balance. Details are given Appendix 2.2

1.6.5 Electron microprobe analysis (EMPA)

Analyses of major and minor elements were determined in plagioclase, orthopyroxene, magnetite, ilmenite and apatite by electron microprobe analysis at Université Laval (ULaval), Quebec, using a CAMECA SX-100 EPMA, equipped with five wavelength-dispersive spectrometers (WDS). Beam size was 10 µm with a voltage of 15 kV and a current of 20 nA.. The calculated cationic proportion, the recalculation of Fe^{+2}/Fe^{+3} ratios, and molar proportions of An-Ab-Or contents in plagioclase were done using charge balance spreadsheets provided by the probe operator. Details are given Appendix 2.2.

1.6.6 U-Pb geochronology

Zircon separation (on about 2kg per sample), preparation and U-Pb analysis were conducted in GEOTOP labs at the Université du Québec à Montréal. Laser ablation U-Pb analysis was performed using a Nu Attom single collector mass spectrometer attached to a photon machines G2 193nm excimer laser following a procedure adapted from Perrot et al. (2017). Data processing, and down-hole fractionation correction were done using Iolite 4 software, using 91500 (Wied
et al. 1995) as a primary reference material for calibration. Two secondary reference materials were analysed: Plešovice and OG1 for quality control and validation

purposes. Concordia diagrams and weighted mean ages were plotted and treated through Isoplot R (Vermeesch, 2018) software. Details are given Appendix 4.1

1.6.7 Hf isotopes

Hf isotope measurements were carried out at the University of Geneva, Switzerland, using a Termo Neptune Plus multi-collector-ICP-MS coupled to a NWR 193 HE laser ablation system, following a procedure similar to that described in Ruiz et al. (2022). Zircons were ablated with a fluence of 3.5 J/cm2 fluence, a repetition rate of 5 Hz and a spot size of 40 µm. The zircon reference materials used were Mud Tank, GJ-1 and synthetic MUN. Data reduction was conducted offline using an in-house Excel spreadsheet. Initial $^{176}Hf/^{177}Hf$ ratios and εHf values were calculated using the $^{207}Pb/^{206}Pb$ date of the sample. Details are given Appendix 4.1.

1.6.8 Whole-rock lithogeochemistry by fusion-LA-ICP-MS

Whole-rock major and trace element analyses were carried out by fusion – LA-ICP-MS at LabMaTer, UQAC, following the protocol of Barnes & Mansur (2020). First, the sample powder was fused into glass disks following a conventional XRF major element fusing technique. The glass disks were mounted in epoxy mounts and polished for analysis by LA-ICP-MS using an Excimer 193nm Resolution M-50 laser ablation system equipped with a double volume cell S-155 and coupled with an Agilent 7900 mass spectrometer. Data reduction was carried out using the Iolite software based on semi-quantitative data reduction scheme normalized to 100% oxides for major elements and including loss on ignition (LOI) (Paton et al. 2011). A series of reference materials, international and in-house were prepared using the same fusion method to 1) us for calibration (an in-house MIX-KPT-610) and 2) monitor the quality of the results for silicate rocks and glasses (KPT-1, OKUM, LK-NIP, GEOPT-23,

GEOPT-25, GEOPT-34, AN-G, GSE, NIST 610), Fe-Ti oxides (BC-28, AMIS-0454, NIST27f) and 3) Fe-Ti-P mineralized rocks. Details are given Appendix 2.2.

1.6.9 pXRF (Portable XRF)

Analyses of Ca, Si, Al, K, Ba and Sr were determined in plagioclase crystals of cut slabs (10 x 10cm) of anorthosite host rocks and mineralization by portable (p)XRF (Niton XL3t, Thermo Scientific) at LabMaTer, UQAC following the protocol developed by Tondoh (2021) and Gueye (2023). 3-5 grains of plagioclase were analyzed for each sample. Due to the coupled substitution of Ca-Na and Al-Si in plagioclase, the Anorthite contents were calculated from the Ca/Si ratio following the method of Tondoh (2021). Matrix-matched plagioclase reference materials, which were characterised using LA-ICP-MS and EMPA at UQAC, were used to correct the instrumental bias of Si, Ca and Sr values of the pXRF method. Repeated analysis of these reference materials indicates that the pXRF method is accurate and precise to within 2 – 5% (Tondoh 2021; Gueye, 2023). Details are given Appendix 2.2.

1.7 Format of the thesis

This thesis consists of an introduction (chapter 1) with general problematic and three research articles (chapters 2, 3 and 4) that have been published, or will be submitted, and a brief conclusion (chapter 5). The introduction in chapter 1 provides a general overview about Proterozoic AMCG suites and associated oxide-apatite mineralization, including aspects on anorthosite petrogenesis (source of magma, magma evolution, fractional crystallization and crustal contamination), Fe-Ti-P ore-formation as well as the peculiarities of Fe-Ti-P mineralization in the Central Grenville Province, followed by a description of the hypothesis, objectives, overall methodology and the area of study.

Chapter 2 consists of a manuscript published in the journal *Mineralium Deposita* in October 2023 as: *Miloski, P., Dare, S., Morisset, C-E., Davies, J., Perrot, M., Savard. Petrogenesis of Fe-Ti-P mineral deposits associated with Proterozoic anorthosite massifs in the Grenville Province: insights from oxide and apatite trace element geochemistry at Lac à l'Orignal, Quebec, Canada*. This study provides for the first time U-Pb dating of zircon in Fe-Ti-P mineralized rocks of the region, coupled with detailed trace element geochemistry of plagioclase, ilmenite, magnetite and apatite of oxide-apatite-norite across the stratigraphic section of the deposit. It is compared to other Fe-Ti-P mineralization from the Grenville, such as the world-class Ti deposit of Lac Tio and Grader layered intrusion from Havre-Saint-Pierre, Quebec.

Chapter 3 consists of a manuscript submitted (in revision) for publication in the journal *Ore Geology Reviews* as: *Miloski, P., Dare, S., Morisset, C-E., Perrot, M., Davies, J. Petrogenesis of oxide-apatite mineralization associated with Proterozoic anorthosite massifs at Lac Mirepoix, Quebec, Canada: a multi-stage model of evolution for Fe-Ti-P mineralization in the Central Grenville Province*. This manuscript integrates new U-Pb dating of zircon in Fe-Ti-P mineralized rocks from Lac Mirepoix, coupled with detailed trace element geochemistry of plagioclase, ilmenite, magnetite and apatite for different oxide-apatite-rich cumulates (massive oxides, nelsonite, leuconorite and oxide-apatite norite), allowing a broader comparison of the geochemical variation of Fe-Ti-P mineralization in the Vanel Anorthosite and the evolution of residual ferrodiorite/jotuntite magmas, comparing with previous published data of Lac à l'Orignal (Chapter 2) and other Fe-Ti-P mineralization worldwide.

Chapter 4 consists of a manuscript submitted to the journal *Precambrian Research* as: *Miloski, P., Dare, S., Perrot, M., Davies, J. Geochemical variation of Fe-Ti-(P) mineralization associated with the younger Grenvillian AMCG-suites (1080 –*

950Ma): new evidence for mantle source and crustal contamination constrained from zircon and apatite chemistry. This study provides for the first time Hf isotopes in zircon for mineralized Fe-Ti-P mineralized rocks, coupled with new U-Pb dating of zircon and detailed trace element geochemistry of plagioclase, ilmenite, magnetite and apatite using LA-ICP-MS. A regional comparison with previous U-Pb-Hf-Nd isotope data and oxide-apatite trace element data associated with different AMCG suites/mineralization in the Central Grenville Province allowed interpretations on the petrogenesis of Fe-Ti-P mineralization (source of magma, crustal contamination, evolution of residual ferrodiorite/jotuntite magmas) at a more regional scale. Moreover, apatite trace element are used to help interpret the Lu-Hf data from zircon to better constrain the mantle source and role of contamination in the petrogenesis of AMCG suites in the Grenville Province, which has significant implications for the tectonic model for the Grenville Province.

The conclusion consists of a concise summary of the major findings presented in this thesis. Supplementary data information regarding samples, methodology and chemical analysis referred to in the other chapters are presented in the Appendices.

1.8 Declaration of original contribution

Each manuscript was submitted to peer-reviewed journals for original publication. The data presented in the three manuscripts were acquired during this project and were supplemented by a compilation of whole-rock, mineral and isotope chemistry data from the literature, carried out during this project.

This Ph.D. project is the first attempt to reconcile the temporal variation in the composition of both oxide-apatite mineralization and associated anorthosite rocks using a multi-tool geochemical approach that combines trace element chemistry of the

ore minerals (Fe-Ti oxides and apatite) and plagioclase, with radiogenic isotopes in zircon of the mineralization itself.

1.9 Contributions of the co-authors

The author of this thesis is the main author of each of the three articles/manuscripts constituting chapters 2, 3 and 4. For each contribution, the main author is responsible for the collection and treatment of data (including both field work and laboratory analyses for whole rock and mineral chemistry), their interpretation, the production of figures, tables and writing of the manuscripts and thesis.

Sarah Dare initiated the original idea and supervised this thesis, providing advice, teaching and support throughout its completion, as well as providing funding for this study. She reviewed each of the manuscripts and helped improve them before submission.

Caroline-Emanuelle Morisset provided thin sections and additional chemical data for comparison/confection of chapter 3 (Lac Mirepoix mineralization). She provided useful discussions and reviewed the first 2 manuscripts (chapters 2 and 3) and helped improve them before submission.

Morgann Perrot was responsible for generation/treatment of the U-Pb-Hf data from zircon grains applied in the three manuscripts. She gave advice how to generate U-Pb ages and provided useful discussions on the interpretation of the zircon data. She reviewed each of the manuscripts, provided the methodology and helped improve them before submission.

Joshua Davies helped in the interpretation of the U-Pb-Hf data. He provided useful discussions on the interpretation of the zircon data and reviewed each of the manuscripts and helped improve them before submission.

Dany Savard was responsible for the generation of the trace element map of oxides by LA-TOF-ICP-MS data for chapter 2 (Lac à l'Orignal mineralization) and provided the methodology.

2. References

Anderson, A. T., Morin, M., & Isachsen, Y. E. 1969. Two types of massif anorthosites and their implications regarding the thermal history of the crust. Origin of anorthosite and related rocks, NY State Mus. and Sci. Service, Mem, 18, 57-69.

Andersen, D.J., Lindsley, D.H., Davidson, P.M., 1993. QUIIF: a PASCAL program to assess equilibria among Fe–Mg–Ti oxides, pyroxenes, olivine, and quartz.Computers & Geosciences 19, 1333–1350.

Ashwal, L. D., & Wooden, J. L. 1985. Sm-Nd isotopic studies of Proterozoic anorthosites: systematics and implications. In The Deep Proterozoic Crust in the North Atlantic Provinces (pp. 61-73). Dordrecht: Springer Netherlands.

Ashwal, L. D., Wooden, J. L., & Emslie, R. F. 1986. Sr, Nd and Pb isotopes in Proterozoic intrusives astride the Grenville Front in Labrador: Implications for crustal contamination and basement mapping. Geochimica et Cosmochimica Acta, 50(12), 2571-2585.

Ashwal, LD., 1993. Anorthosites. Springer, Heidelberg.

Ashwal, L. D. 2010. The temporality of anorthosites. The Canadian Mineralogist, 48(4) 711-728.

Barnes, S. J., Mansur, E. T., Pagé, P., Meric, J., & Arguin, J. P. 2020. Major and trace element compositions of chromites from the Stillwater, Bushveld and Great Dyke intrusions compared with chromites from komatiites, boninites and large igneous provinces.

Bickford, M. E., McLelland, J. M., Mueller, P. A., Kamenov, G. D., & Neadle, M. 2010. Hafnium isotopic compositions of zircon from Adirondack AMCG suites: Implications for the petrogenesis of anorthosites, gabbros, and granitic members of the suites. The Canadian Mineralogist, 48(4), 751-761.

Bogdanova, S. V., Pashkevich, I. K., Buryanov, V. B., Makarenko, I. B., Orlyuk, M. I., Skobelev, V. M., ... & Legostaeva, O. V. 2004. The 1.80–1.74-Ga gabbro–anorthosite–rapakivi Korosten Pluton in the Ukrainian Shield: a 3-D geophysical reconstruction of deep structure. Tectonophysics, 381(1-4), 5-27.

Buddington, A. F., & Lindsley, D. H. 1964. Iron-titanium oxide minerals and synthetic equivalents. Journal of petrology, 5(2), 310-357.

Bybee, G. M., & Ashwal, L. D. 2015. Isotopic disequilibrium and lower crustal contamination in slowly ascending magmas: Insights from Proterozoic anorthosites. Geochimica et Cosmochimica Acta, 167, 286-300.

Charlier, B., Grove, T.L., 2012. Experiments on liquid immiscibility along tholeiitic liquid lines of descent Contrib. Mineral. Petrol. 164 (1), 27-44

Charlier, B., Namur, O., Malpas, S., de Marneffe, C., Duchesne, j.C., Vander Auwera, J.,Bolle, O, 2010b. Origin ofthe giant Allard Lake ilmenite ore deposit (Canada) by fractional crystallization, multiple magma pulses and mixing. Litho 119-134.

Charlier, B., Namur, O., Toplis, M. J., Schiano, P., Cluzel, N., Higgins, M. D., & Auwera, J.V. 2011. Large-scale silicate liquid immiscibility during differentiation of tholeiitic basalt to granite and the origin of the Daly gap. Geology, 39(10), 907-910.

Charlier, B., Duchesne, J.-C., Vander Auwera, J., 2006. Magma chamber processes in the Tellnes ilmenite deposit (Rogaland Anorthosite Province, SW Norway) and the formation of Fe–Ti ores in massif-type anorthosites. Chemical Geology 234, 264–290.

Charlier, B., Sakoma, E., Sauve, M., Stanaway, K., Vander Auwera, J., Duchesne, J.-C.,2008. The Grader layered intrusion (Havre-Saint-Pierre Anorthosite, Quebec) and genesis of nelsonite and other Fe–Ti–P ores. Lithos 101, 359–378.

Charlier, B., Namur, O., Duchesne, J.-C., Wiszniewska, J., Parecki, A., Vander Auwera, J.,2009. Cumulate origin and polybaric crystallization of Fe–Ti oxide ores in the Suwalki anorthosite, Northeastern Poland. Economic Geology 104, 205–221.

Charlier, B., Namur, O., Malpas, S., de Marneffe, C., Duchesne, j.C., Vander Auwera, J.,Bolle, O, 2010b. Origin ofthe giant Allard Lake ilmenite ore deposit (Canada) by fractional crystallization, multiple magma pulses and mixing. Lithos 117, 119-134.

Charlier, B., Namur, O., & Grove, T. L. (2013). Compositional and kinetic controls on liquid immiscibility in ferrobasalt–rhyolite volcanic and plutonic series. Geochimica et Cosmochimica Acta, 113, 79-93.

Charlier B, Namur O, Bolle O, et al 2015. Fe-Ti-V-P ore deposits associated with Proterozoic massif type anorthosites and related rocks. Earth Science Reviews, 141:56–81. doi: 10.1016/j.earscirev.2014.11.005.

Coint, N., Keiding, J. K., & Ihlen, P. M. 2020. Evidence for silicate–liquid immiscibility in monzonites and petrogenesis of associated Fe–Ti–P-rich rocks: example from the Raftsund intrusion, Lofoten, Northern Norway. Journal of Petrology, 61(4).

Corrigan, D., & Hanmer, S. 1997. Anorthosites and related granitoids in the Grenville orogen: a product of convective thinning of the lithosphere?. Geology, 25(1), 61-64.

Corriveau, L., Perreault, S., Davidson, A., 2007. Prospective metallogenic settings of the Grenville Province. In: Goodfellow, W.D. (Ed.), Mineral Deposits of Canada: a Synthesis of Major Deposit-types, District Metallogeny, the Evolution of Geological Provinces, and Exploration Methods: Geological Survey of Canada, Mineral Deposits Division, Special Publication, pp. 819–847.

Dickin, A. P. 2000. Crustal formation in the Grenville Province: Nd-isotope evidence. Canadian Journal of Earth Sciences, 37(2-3), 165-181.

Duchesne, J. C., & Wilmart, E. 1997. Igneous charnockites and related rocks from the Bjerkreim–Sokndal layered intrusion (Southwest Norway): a jotunite (hypersthene monzodiorite)-derived A-type granitoid suite. Journal of petrology, 38(3), 337-369.

Duchesne, J. C., Liégeois, J. P., Vander Auwera, J., & Longhi, J. 1999. The crustal tongue melting model and the origin of massive anorthosites. Terra Nova, 11(2-3), 100-105.

Duchesne, J.C., Shumlyanskyy , L, Charlier, B., 2006. The Fedorivka layered intrusion (Korosten Pluton, Ukraine) : an example ofhighly differentiated ferrobasaltic evolution. Lithos 89, 353-376.

Duchesne, J.C. 1972. Iron-titanium oxide minerais in the Bjerkrem-Sogndal Massif, South-western Norway. J. Petrol. 13, 57-81 .

Duchesne, J. C. 1999. Fe-Ti deposits in Rogaland anorthosites (South Norway) geochemical characteristics and problems of interpretation. Mineralium Deposita, 34, 182-198

Dymek, R.F., Owens, B.E., 2001. Petrogenesis of apatite-rich rocks (nelsonites and oxide apatite gabbronorites) associated with massif anorthosites. Economic Geology 96, 797–815.

Emslie, R. F.,& Hegner, E. 1993.Reconnaissance isotopic geochemistry of anorthosite mangerite-charnockite-granite (AMCG) complexes, Grenville Province, Canada. Chemical Geology, 106(3-4), 279-298.

Fisher, C. M., Vervoort, J. D., & Hanchar, J. M. (2014). Guidelines for reporting zircon Hf isotopic data by LA-MC-ICPMS and potential pitfalls in the interpretation of these data. Chemical geology, 363, 125-133.

Francis, D., Scowen, P., Panneton, G., & Doig, R. 2000. Contrasting Si-saturation in troctolite–anorthosite intrusions along the Manicouagan corridor of the Abitibi–Grenville transect. Canadian Journal of Earth Sciences, 37(2-3), 271-289.

Frost, C. D., Frost, B. R., Lindsley, D. H., Chamberlain, K. R., Swapp, S. M., & Scoates, J. S. 2010. Chemical and isotopic evolution of the anorthositic plutons of the Laramie Anorthosite Complex: Explanations for variations in silica activity and oxygen fugacity of massif anorthosites. The Canadian Mineralogist, 48(4), 925-946.

Gobeil, A., Brisebois, D., Clark, T., Verpaelst, P., Madore, L., Wodicka, N., Cheve, S., 2003. Geologie de la moyenne Cote-Nord. In: Brisebois, D., Clark, T. (Eds.), Geologie et ressources minerales de la partie est de la Province de Grenville. Ministere des Ressources naturelles, de la Faune et des Parcs, Quebec, pp. 9–58. DV 2002-03.

Grant, M. 2020. Formation of magmatic Fe-Ti-V-P deposits within the Lac St. Jean area Saguenay, Québec, Canada: Insights from trace element composition of Fe-oxides and apatite. (Unpublished masters thesis). University of Ottawa, Ontario, Canada, pp. 343.

Groulier, P. A., Indares, A.,Dunning, G., Moukhsil, A., & Jenner, G. 2018. Syn-orogenic magmatism over 100 my in high crustal levels of the central Grenville Province: characteristics, age and tectonic significance. Lithos, 312, 128-152.

Gueye, B. 2023 Répartition spatiale de la composition de plagioclase de la Suite anorthositique de Lac-Saint-Jean, secteur Nord-Ouest du Lac-Saint-Jean : implications pour exploration minérale. Undergraduate thesis (UQAC), 55 pp.

Hébert, C., & Cadieux, A. M. 2003. Géologie de la région des lacs Portneuf et Maria Chapdelaine (22E/01 et 22E/02). Géologie Québec [Ressources naturelles].
Hébert, C., Van Breemen, O., & Cadieux, A. 2009. Région du reservoir Pipmuacan, (SNRC 22E): Synthese Geologique. RG 2009-01. Ministère des ressources naturelles et de la faune, Gouvernement du Québec.

Hébert, C., Cadieux, A.-M., Van Breemen, O., 2005. Temporal evolution and nature of Ti–Fe–P mineralization in the anorthosite–mangerite–charnockite–granite (AMCG) suites of the South–central Grenville Province, Saguenay – Lac St. Jean area, Quebec, Canada. Canadian Journal of Earth Sciences 42, 1865–1880.

Higgins, M.D., Van Breemen, O., 1996. Three generations of Anorthosite–Mangerite–Charnockite–Granite magmatism, contact metamorphism and tectonism in the Saguenay – Lac–St-Jean region, Grenville Province, Canada. Precambrian Research 79, 347–362.

Higgins, M. D., Ider, M., & Breemen, O. V. 2002. U-Pb ages of plutonism, wollastonite formation, and deformation in the central part of the Lac-Saint-Jean anorthosite suite. Canadian Journal of Earth Sciences, 39(7), 1093-1105.

Horstwood, M. S., Košler, J., Gehrels, G., Jackson, S. E., McLean, N. M., Paton, C., ... & Schoene, B. 2016. Community-derived standards for LA-ICP-MS U-(Th-) Pb geochronology–Uncertainty propagation, age interpretation and data reporting. Geostandards and Geoanalytical Research, 40(3), 311-332.

Hou, T., Charlier, B., Holtz, F., Veksler, I., Zhang, Z., Thomas, R., & Namur, O. 2018. Immiscible hydrous Fe–Ca–P melt and the origin of iron oxide-apatite ore deposits. Nature communications, 9(1), 1-8.

Icenhower, J. P., Dymek, R. F., & Weaver, B. L. 1998. Evidence for an enriched mantle source for jøtunite (orthopyroxene monzodiorite) associated with the St. Urbain anorthosite, Quebec. Lithos, 42(3-4), 191-212.Indares, A., & Moukhsil, A. 2013. Geon 12 crustal extension in the central Grenville Province, implications for the orogenic architecture, and potential influence on the emplacement of anorthosites. Canadian Journal of Earth Sciences, 50(9), 955-966.

Kolker, A. 1982. Mineralogy and geochemistry of Fe-Ti oxide and apatite (nelsonite) deposits and evaluation of the liquid immiscibility hypothesis. Economic Geology, 77(5), 1146-1158.

Laverdière, G. 2013. Rapport de travaux d'exploration. Propriété Lac Orignal, Région du Saguenay-Lac Saint Jean. Glen Eagle Resources Inc.

Laverdiere, G. 2016. Rapport de travaux d'exploration. Propriete Lac Original, Region du Saguneay-Lac Saint Jean. Glen Eagle Resources Inc.

Lizuka, T., Yamaguchi, T., Hibiya, Y., & Amelin, Y. 2015. Meteorite zircon constraints on the bulk Lu− Hf isotope composition and early differentiation of the Earth. Proceedings of the National Academy of Sciences, 112(17), 5331-5336.

Longhi, J., Auwera, J. V.,Fram, M.S., & Duchesne, J. C. 1999. Some phase equilibrium constraints on the origin of Proterozoic (massif) anorthosites and related rocks. Journal of Petrology, 40(2), 339-362.

Mitchell, J., Scoates, J., Frost, C.D., Kolker, A., 1996. The geochemical evolution of anorthosite residual magmas in the Laramie Anorthosite Complex, Wyoming.j. Petrol. 37, 637-660.

Morel, M. L. A., Nebel, O., Nebel-Jacobsen, Y. J., Miller, J. S., & Vroon, P. Z. 2008. Hafnium isotope characterization of the GJ-1 zircon reference material by solution and laser-ablation MC-ICPMS. Chemical geology, 255(1-2), 231-235.

Morisset, C.-E., Scoates, J.S., Weis, D., Friedman, R.M., 2009. U–Pb and 40Ar/39Ar geochronology of the Saint-Urbain and Lac Allard (Havre-Saint-Pierre) anorthosites and their associated Fe–Ti oxide ores, Quebec: evidence for emplacement and slow cooling during the collisional Ottawan orogeny in the Grenville Province. Precambrian Research 174, 95–116.

Morisset, C.-E., Scoates, J.S., Weis, D., Friedman, R.M., 2009. U–Pb and 40Ar/39Ar geochronology of the Saint-Urbain and Lac Allard (Havre-Saint-Pierre) anorthosites and their associated Fe–Ti oxide ores, Quebec: evidence for emplacement and slow cooling during the collisional Ottawan orogeny in the Grenville Province. Precambrian Research 174, 95–116.

Morisset, C.-E., Scoates,J.S., Weis, D., Sauve, M., Stanaway, K.J., 2010. Rutile-bearing ilmenite deposits associated with the Proterozoic Saint-Urbain and Lac Allard anorthosite massifs, Grenville Province, Québec. Can. Mineral. 48, 821-849.

Morisset, C. E., Williamson, M. C., & Hipkin, V. 2013. Investigation of three Fe–Ti oxide deposits associated with Grenvillian anorthosite massifs as potential source for lunar analogue ilmenite. Canadian Journal of Earth Sciences, 50(1), 64-77.

Morse, S. A. 1982. A partisan review of Proterozoic anorthosites. American Mineralogist 67(11-12), 1087-1100.

Morse, S. A. 2006. Labrador massif anorthosites: chasing the liquids and their sources.Lithos, 89(1-2), 202-221.

Namur, O., Charlier, B., Toplis, M. J., Higgins, M. D., Liégeois, J. P., & Vander Auwera, J.2010. Crystallization sequence and magma chamber processes in the ferrobasaltic Sept Iles layered intrusion, Canada. Journal of Petrology, 51(6), 1203-1236.

Namur, O., Charlier, B., Pirard, C., Hermann, J., Liégeois, J. P., & Vander Auwera, J. 2011. Anorthosite formation by plagioclase flotation in ferrobasalt and implications for the lunar crust. *Geochimica et Cosmochimica Acta*, *75*(17), 4998-5018.

Namur, O., Charlier, B., Holness, M.B., 2012. Dual origin of Fe-Ti-P gabbros by immiscibility and fractional crystallization of evolved basalts in the Sept Iles layered intrusion. Lithos 154, 100-114.

Norman, M. D., Borg, L. E., Nyquist, L. E., & Bogard, D. D. 2003. Chronology, geochemistry, and petrology of a ferroan noritic anorthosite clast from Descartes breccia 67215: Clues to the age, origin, structure, and impact history of the lunar crust. Meteoritics & Planetary Science, 38(4), 645-661.

Owens, B.E., Dymek, R.F., 1992. Fe-Ti-P-rich rocks and massif anorthosite: problems of interpretation illustrated from the Labrieville and St-Urbain plutons, Quebec. Can. Mineral. 30, 163-190

Owens, B.E., Dymek, R.F., 2005. Rediscovery of the Mattawa anorthosite massif, Grenville Province, Quebec. Canadian Journal of Earth Sciences 42, 1699–1718.

Owens, B. E., Dymek, R. F., Tucker, R. D., Brannon, J. C., & Podosek, F. A. 1994. Age and radiogenic isotopic composition of a late-to post-tectonic anorthosite in the Grenville Province: the Labrieville massif, Quebec. Lithos, 31(3-4), 189-206.

Owens, B.E., Rockow, M.W., Dymek, R.F., 1993. Jotunites from the Grenville Province, Quebec: petrological characteristics and implications for massif anorthosite petrogenesis. Lithos 30, 57–80.

Owens, B. E., & Tomascak, P. B. 2002. Mesoproterozoic lamprophyres in the Labrieville Massif, Quebec: clues to the origin of alkalic anorthosites?. Canadian Journal of Earth Sciences, 39(6), 983-997.

Pang, K.-N., Li, C., Zhou, M.-F., Ripley, E.M., 2007. Abundant Fe–Ti oxide inclusions in olivine from the Panzhihua and Hongge layered intrusions, SW China: evidence for early saturation of Fe–Ti oxides in ferrobasaltic magma. Contributions to Mineralogy and Petrology 156, 307–321.

Patchett, P. J., & Tatsumoto, M. (1980). Hafnium isotope variations in oceanic basalts. Geophysical Research Letters, 7(12), 1077-1080.

Paton, C., Hellstrom, J., Paul, B., Woodhead, J., & Hergt, J. (2011). Iolite: Freeware for the visualisation and processing of mass spectrometric data. Journal of Analytical Atomic Spectrometry, 26(12), 2508-2518.

Peck, W. H., & Valley, J. W. 2000. Large crustal input to high δ 18 O anorthosite massifs of the southern Grenville Province: new evidence from the Morin Complex, Quebec. Contributions to Mineralogy and Petrology, 139, 402-417.

Peck, W. H., Clechenko, C. C., Hamilton, M. A., & Valley, J. W. 2010. Oxygen isotopes in the Grenville and Nain AMCG suites: Regional aspects of the crustal component in massif anorthosites. The Canadian Mineralogist, 48(4), 763-786.

Perreault, S. (2003). Contrasting styles of Fe-Ti mineralization in the Havre-Saint-Pierre anorthosite suite, Quebec's North Shore, Canada. SPECIAL PUBLICATION 9, 87.

Philpotts, A.R., 1967. Origin of certain iron-titanium oxide and apatite roeks. Econ. Geol. 62, 303-315.

Philpotts, A.R., 1982. Compositions of immiscible liquids in volcanic roeks. Contrib. Mineral. Petrol. 80, 201-218.

Regan, S. P., Chiarenzelli, J. R., McLelland, J. M., & Cousens, B. L. 2011. Evidence for an enriched asthenospheric source for coronitic metagabbros in the Adirondack Highlands. *Geosphere*, *7*(3), 694-709.

Rocha, B. C., Davies, J. H., Janasi, V. A., Schaltegger, U., Nardy, A. J., Greber, N. D., ... & Polo, L. A. 2020. Rapid eruption of silicic magmas from the Paraná magmatic province (Brazil) did not trigger the Valanginian event. Geology, 48(12), 1174-1178.

Roedder, E. 1978. Silicate liquid immiscibility in magmas and in the system K2O-FeO-Al2O3-SiO2: an example of serendipity. Geochimica et Cosmochimica Acta, 42(11) 1597-1617.

Ryan, B. 2000. The Nain-Churchill boundary and the Nain Plutonic Suite: A regional perspective on the geologic setting of the Voisey's Bay Ni-Cu-Co deposit. Economic Geology, 95(4), 703-724.

Schiellerup, H., Lambert, D. D., Prestvik, T., Robins, B., McBride, J. S., & Larsen, R. B. 2000. Re–Os isotopic evidence for a lower crustal origin of massif-type anorthosites. Nature, 405(6788), 781-784.

Scoates, J. S., & Chamberlain, K. R. 1997. Orogenic to post-orogenic origin for the. 1.76 Ga Horse Creek anorthosite complex, Wyoming, USA. The Journal of Geology, 105(3), 331-344.

Sláma, J., Košler, J., Condon, D. J., Crowley, J. L., Gerdes, A., Hanchar, J. M., ... & Whitehouse, M. J. 2008. Plešovice zircon—a new natural reference material for U–Pb and Hf isotopic microanalysis. Chemical Geology, 249(1-2), 1-35.

Snyder, D., Carmichael, I.S.E., Wiebe, RA., 1993. Experimental study of liquid evolution in an Fe-rich, layered mafic intrusion: constrains of Fe-Ti oxide precipitation on the T-}02 and T-p paths of tholeiitic magmas. Contrib. Mineral. Petrol. 113, 73-86.

Söderlund, U., Patchett, P. J., Vervoort, J. D., & Isachsen, C. E. 2004. The 176Lu decay constant determined by Lu–Hf and U–Pb isotope systematics of Precambrian mafic intrusions. Earth and Planetary Science Letters, 219(3-4), 311-324.

Thirlwall, M. F., Anczkiewicz, R., Platt, J. P., & Wakabayashi, J. (2004). Franciscan subduction off to a slow start: evidence from high-precision Lu–Hf garnet ages on high grade-blocks. Earth and Planetary Science Letters, 225(1-2), 147-161.

Tondoh, A. 2022. Développement d'une méthode d'analyse chimique de plagioclase par fluorescence X portative appliquée à la répartition spatiale des faciès de la Suite anorthositique du Lac-Saint-Jean. Projet de fin d'etudes. UQAC, Chicoutimi, Quebec, Canada.

Toplis, MJ., Dingwell, D., Libourel, G., 1994a. The effect of phosphorous on the iron redox ratio, viscosity, and density of an evolved ferrobasalt. Contrib. Mineral. Petrol. 117, 293-304.

Toplis, M. J., Libourel, G., & Carroll, M. R. 1994b. The role of phosphorus in crystallisation processes of basalt: an experimental study. Geochimica et Cosmochimica Acta, 58(2), 797-810.

Toplis, MJ, Carroll, M.R., 1995. An experimental study of the influence of oxygen fugacity on Fe-Ti oxide stability, phase relations, and mineral-melt equilibria in ferro-basaltic systems. J. Petrol. 36, 1137-1170.

Breemen, O. V., & Higgins, M. D. 1993. U–Pb zircon age of the southwest lobe of the Havre-Saint-Pierre anorthosite complex, Grenville Province, Canada. Canadian Journal of Earth Sciences, 30(7), 1453-1457.

Vander Auwera, J., Longhi, J., 1994. Experimental study of a jotunite (hypersthene monzodiorite): constraints on the parent magma composition and crystallization conditions (P, T, fO2,) of the Bjerkreim-Sokndal layered intrusion (Norway) . Contrib. Mineral. Petrol. 118, 60-78.

Vander Auwera, J., Longhi, J, Duchesne, J.C., 1998. A liquid line of descent of the jotunite (hypersthene monzodiorite) suite. J. Petrol. 39, 439-468.

Vander Auwera, J., Bolle, O., Bingen, B., Liégeois, J. P., Bogaerts, M., Duchesne, J. C., ...& Longhi, J. 2011. Sveconorwegian massif-type anorthosites and related granitoids result from post-collisional melting of a continental arc root. Earth-Science Reviews, 107(3-4), 375-397.

Veksler, I. V., Dorfman, A. M., Borisov, A. A., Wirth, R., & Dingwell, D. B. 2007. Liquid immiscibility and the evolution of basaltic magma. Journal of Petrology, 48(11), 2187-2210.Vermeesch, P. (2018). IsoplotR: A free and open toolbox for geochronology. Geoscience Frontiers, 9(5), 1479-1493.

Duchesne, J. C., Wilmart, E., Demaiffe, D., & Hertogen, J. 1989. Monzonorites from Rogaland (Southwest Norway): a series of rocks coeval but not comagmatic with massif-type anorthosites. Precambrian research, 45(1-3), 111-128.

Wilson, J. R., Robins, B., Nielsen, F. M., Duchesne, J. C., & Vander Auwera, J. (1996). The Bjerkreim-Sokndal layered intrusion, Southwest Norway. In Developments in Petrology (Vol. 15, pp. 231-255). Elsevier.

Woodhead, J. D., & Hergt, J. M. 2005. A preliminary appraisal of seven natural zircon reference materials for in situ Hf isotope determination. Geostandards and Geoanalytical Research, 29(2), 183-195.

Woodruff, L. G., Nicholson, S. W., & Fey, D. L. 2013. A Deposit Model for Magmatic Iron-titanium-oxide Deposits Related to Proterozoic Massif Anothosite Plutonic Suites. US Department of the Interior, US Geological Survey.

Zhao, T. P., Chen, W., & Zhou, M. F. 2009. Geochemical and Nd–Hf isotopic constraints on the origin of the~ 1.74-Ga Damiao anorthosite complex, North China Craton. Lithos, 113(3-4), 673-690.

Zhou, M. F., Chen, W. T., Wang, C. Y., Prevec, S. A., Liu, P. P., & Howarth, G. H. 2013.Two stages of immiscible liquid separation in the formation of Panzhihua-type Fe-Ti-V oxide deposits, SW China. Geoscience Frontiers, 4(5), 481-502.

CHAPTER 2

PETROGENESIS OF FE-Ti-P MINERAL DEPOSITS ASSOCIATED WITH PROTEROZOIC ANORTHOSITE MASSIFS IN THE GRENVILLE PROVINCE: INSIGHTS FROM OXIDE AND APATITE TRACE ELEMENT GEOCHEMISTRY AT LAC À L'ORIGNAL, QUEBEC, CANADA

Pedro Miloski[1], Sarah Dare[1], Caroline-Emmanuelle Morisset[2], Joshua H.F.L. Davies[3], Morgann G. Perrot[3], Dany Savard[1]

1. Département des Sciences Appliquées, Université du Québec à Chicoutimi (UQAC), 555 Boulevard de l'Université, Chicoutimi, Québec, Canada, G7H 2B1

2. Agence Spatiale Canadienne, 6767 Rte de l'Aéroport, Saint-Hubert, Québec, Canada, J3Y 8Y9

3. Département des Sciences de la Terre et de l'Atmosphère/GEOTOP, Université du Québec à Montréal (UQAM), 405 Rue Sainte-Catherine Est, Montréal, Québec, Canada, H2L 2C4

Mineralium Deposita (2023)
DOI: 10.1007/s00126-023-01216-5

Résumé

Les massifs d'anorthosite protérozoïques peuvent héberger des quantités importantes de métaux critiques et stratégiques, tels que Ti, V et P, associés aux oxydes magmatiques de Fe-Ti et à l'apatite. Pourtant, leur pétrogenèse est beaucoup moins comprise que celle des gisements de Fe-Ti-V-P hébergés dans des intrusions litées au sein de grandes provinces ignées. Plusieurs lentilles minéralisées de Fe-Ti-P affleurent près de la frontière des massifs d'anorthosite de Vanel et de Mattawa, dans la province du Grenville, Québec, Canada. Par exemple, le gisement Fe-Ti-P du Lac à l'Orignal, encaissé dans l'anorthosite Vanel près de la limite nord de l'anorthosite de Mattawa, comprend une structure lenticulaire d`oxyde-apatite norite (OAN) avec de fines couches d'anorthosite à apatite et quantités mineures de nelsonite (oxydes massifs de Fe-Ti et apatite), indiquant une accumulation par différences de densité. La sédimentation des oxydes a généré les cumulâts mélanocratiques d'OAN et la nelsonite. La flottation du plagioclase a généré des couches d'anorthosite leucocrates contenant de l'apatite. La minéralisation est dominée par l'hémo-ilménite, accompagnée d'apatite et d'une quantité mineure de magnétite aux bordures, le noyau est dominé par l'ilménite, la magnétite et l'apatite. La datation U-Pb in situ de zircons magmatiques indique que le gisement Lac à l'Orignal est une intrusion à plusieurs étages avec deux âges de cristallisation différents entre le noyau plus jeune (993 ± 13 Ma) et la bordure supérieure plus ancienne (1069 ± 12 Ma) de l'intrusion. Ces âges sont similaires à ceux des massifs d'anorthosite voisins (anorthosites de Mattawa et Vanel, respectivement). L'analyse in situ des éléments traces du plagioclase, de l'apatite et des oxydes, par ablation laser ICP-MS, révèle de subtiles variations de certains éléments traces (par exemple Cr, Ni, V) liés à la différenciation dans des conditions de fO_2 relativement élevées (FMQ = +0,9 à +1,7). Les compositions de la fonte calculées à partie de l'apatite indiquent un magma parental similaire pour la

bordure et le noyau qui correspond à la composition des dykes de ferrodiorite à haute teneur en Fe-Ti-P du Lac à l'Original. Ce magma de ferrodiorite à haute teneur en Ti-P était probablement résiduel après la formation de l'anorthosite. L'équilibrage inter-oxydes sous-solidus a modifié la composition originale des différentes cumulâts de l'intrusion. L'absence d'oxydes massifes importants et la présence de quantités plus élevées de cumulus de magnétite et d'apatite, soutenues par la chimie minérale, dénotent un caractère plus évolué au gisement Lac à l'Orignal par rapport aux autres gisements de Fe-Ti-(P) de la Province du Grenville (p. ex., gisements de Fe-Ti-P du Lac Tio et de l'intrusion Grader dans l'anorthosite de Havre-Saint-Pierre, dans l'est du Québec). Pétrogénétiquement, le gisement Fe-Ti-P du Lac à l'Orignal correspond à une partie évoluée d'un système pauvre en Ti/Fe de la Province du Grenville aux derniers stades de différenciation des magmas ferrodiorite/jotunite.

Abstract

Proterozoic anorthosite massifs can host significant amounts of critical and strategic metals, such as Ti, V and P, associated with magmatic Fe-Ti oxides and apatite. Yet their petrogenesis is much less understood than Fe-Ti-V-P deposits hosted in layered intrusions within large igneous provinces. Several mineralized lenses of Fe-Ti-P outcrop near the border of the 1080 (±2) Ma Vanel and the 1016 (±2) Ma Mattawa anorthosite massifs, in the Central Grenville Province, Quebec, Canada. For example, the Lac à l'Orignal Fe-Ti-P deposit, hosted in the Vanel anorthosite near the northern border of the Mattawa Anorthosite, comprises a lenticular structure of oxide apatite norite (OAN) with thin layers of apatite-bearing anorthosite and minor amounts of nelsonite (massive Fe-Ti oxides and apatite), indicating accumulation by density differences. Oxide settling generated the melanocratic OAN cumulates and nelsonite. Plagioclase flotation generated the leucocratic apatite-bearing anorthosite layers. The mineralization is dominated by hemo-ilmenite, accompanied by apatite and a minor amount of magnetite at the borders, whereas the core is dominated by ilmenite, magnetite, and apatite. In-situ U-Pb dating of magmatic zircon indicates that the Lac à l'Orignal deposit is a multi-stage intrusion with two different crystallization ages between the younger core (993 ± 13 Ma) and the older upper border (1069 ± 12 Ma) of the intrusion. These ages are similar to those of nearby anorthosite-massifs (Mattawa and Vanel anorthosites, respectively). In-situ trace element analysis of plagioclase, apatite and oxides, by laser ablation ICP-MS, reveals subtle variations in certain trace element (e.g., Cr, Ni, V) related to differentiation under relatively high-fO_2 conditions (FMQ = +0.9 to +1.7). Calculated melt compositions from apatite indicates a similar parental magma for both the border and core that matches the composition of high-Fe-Ti-P ferrodiorite dykes

at Lac à l'Original. This high-Ti-P ferrodiorite magma was probably residual after anorthosite formation. Sub-solidus inter-oxide equilibration modified the original composition of the different cumulates in the intrusion. The absence of extensive massive oxide cumulates and the presence of higher amounts of cumulus magnetite and apatite, supported by mineral chemistry, denotes a more evolved character for the Lac à l'Orignal deposit compared with other Fe-Ti-(P) deposits in the Grenville Province (e.g., Lac Tio Fe-Ti and Grader intrusion Fe-Ti-P deposits in the Havre-Saint-Pierre Anorthositic Suite, eastern Quebec). Petrogenetically, the Lac à l'Orignal Fe-Ti-P deposit corresponds to an evolved part of a low-Ti/Fe system in the Grenville Province in the late stages of differentiation of ferrodiorite/jotunite magmas.

2.1 Introduction

Magmatic oxide-apatite (Fe-Ti-V-P) mineralization/deposits are spatially and temporally associated with Proterozoic AMCG (Anorthosite – Mangerite – Charnockite - Granite) suites (Ashwal, 1993; Charlier et al. 2015). They provide important resources for several critical and strategic elements, in particular Ti (from hemo-ilmenite: Fe_2O_3-$FeTiO_3$), but also V (from magnetite: Fe_3O_4) and P (from apatite: $Ca_5(PO_4)_3(OH,F,Cl)$). For example, there are only two currently active magmatic Ti mines in the world, both associated with massif-type anorthosites and hemo-ilmenite-dominated mineralization: Lac Tio (Havre-Saint-Pierre Anorthositic Suite, Quebec (Charlier et al. 2010)), the world's largest producer of TiO_2; and Tellnes (Rogaland Anorthosite Province, Norway (Charlier et al. 2006)). However, the origin of oxide-apatite mineralization and its genetic relationship to the host anorthosite rocks are still debated (Owens & Dymek, 1992; Dymek & Owens, 2001; Charlier et al. 2008). Oxide-apatite minerals can form stratiform layers in layered mafic intrusions at the margins of massif-type anorthosites, such as the Bjerkrein Sokndal Layered Intrusion, Norway

(Wilson et al. 1996); Grader intrusion, Quebec (Charlier et al. 2008) and Fedorivka Layered Intrusion, Ukraine (Duchesne et al. 2006). However, mineralized zones can also take the form of lenses of massive oxides, such as Lac Tio, Quebec (Charlier et al. 2010), Saint Urbain, Quebec (Morisset et al. 2009) or nelsonite (oxide and apatite), such as at Damiao, China (Chen et al. 2013) within anorthosite. In some cases, the lenses of oxides may have formed in a magma conduit cross cutting the anorthosite (Charlier et al. 2010). Finally, some deposits form by emplacement of sills containing ilmenite-plagioclase-(orthopyroxene) cumulates, such as the Tellnes Ti deposit, Norway (Charlier et al. 2006, 2007) or as dykes/layers along or near the outer boundaries of anorthosite massifs.

Anorthosite massifs were emplaced as diapiric intrusions of plagioclase-rich mushes into the middle-crust, along major crustal shear zones, that formed after crystallization and sinking of ultramafic cumulates in deep-seated magma chambers at or near the base of the continental crust (Ashwal, 1993; Bybee & Ashwal, 2015; Slagstad et al. 2022). Oxide-apatite mineralization is commonly interpreted as crystallizing from residual Fe-Ti-V-P rich melts (ferrodiorite/jotunite composition), after extensive polybaric crystallization of plagioclase and mafic silicates (e.g., olivine, orthopyroxene, clinopyroxene) during the formation of anorthosite massifs (Vander Auwera et al. 2006; Charlier et al. 2008; Ashwal 2010). However, a number of mechanisms have been proposed to concentrate the oxides (± apatite) into Fe-Ti(±P) deposits, such as fractional crystallization with oxide settling and plagioclase flotation (Charlier et al. 2006; 2007; 2008; 2015), filter pressing or draining of jotunite/ferrodiorite residual melts into tension fractures of margins of the massifs (Dymek & Owens, 2001 Vander Auwera et al. 2006; Scoates et al. 2010), magma

mixing (Charlier et al. 2006; 2010; Namur et al. 2010) and/or liquid immiscibility (Philpotts, 1967; 1982; Charlier & Grove, 2012; Hou et al. 2018; Coint et al. 2020).

Previous studies on Fe-Ti-(P) mineral deposits worldwide, such as in the Bjerkrein-Sokndal in Norway (Charlier et al. 2005), Lac Tio (Charlier et al. 2010) and Grader (Charlier et al. 2008) in Canada, Fedorivka in Ukraine (Duchesne et al. 2006) and Damiao (Chen et al. 2013) in China, have successfully used the trace element composition of Fe-Ti oxides, apatite and silicates (where present) to investigate the role of magmatic processes (e.g. fractional crystallization, magma replenishments, parental magma composition) involved in the formation of these oxide-apatite deposits. Numerous Fe-Ti-P showings occur in the Central Province of the Grenville, including the world-class phosphate deposit of Lac à Paul. However, only a few publications have focused on the petrological aspects of oxide-apatite cumulate rocks for the Central Grenville Province (e.g., Owens & Dymek, 1992; Dymek & Owens, 2001; Morisset et al. 2010). In this paper, we present a detailed whole-rock and in-situ trace element stratigraphical study of plagioclase, oxides, and apatite, as well as in-situ U-Pb dating of zircon, from oxide-apatite norite cumulates associated with the Lac à l'Orignal Fe-Ti-P deposit, in the Central Grenville Province, Quebec.

Based on drilling by Glen Eagle resources, the Lac à l'Orignal Fe-Ti-P mineralized zone has a E-W lenticular structure, approximately 10-100 m thick and 1.5 km in length (Fig.2.1e), with an average grade of 5.1 wt.% P_2O_5 (Fig.2.1d), locally up to 7 wt.% P_2O_5 (Laverdière, 2013; 2016). The deposit has recently been claimed by First Phosphate Corp., with a Mineral Resources Estimate (MRE) indicating 15.8 Mt at 5.18% P_2O_5, 4.23% TiO_2 and 23.90% Fe_2O_3, with inferred values of 33.2 Mt at 5.06% P_2O_5, 4.16% TiO_2 and 22.55% Fe_2O_3. (Yassa, 2022). Similar to the two hard-rock deposits in anorthosites presently exploited, the Lac Tio mine, Quebec (Charlier

et al. 2008) and the Tellnes deposit, Norway (Charlier et al. 2006; 2007), the Lac à l'Orignal deposit is ilmenite-dominated with geochemical and mineralogical variation related to magma differentiation within a multi-stage mineralized body. The oxide-apatite rich rocks at Lac à l'Orignal thus constitute an important opportunity to study the Fe-Ti-P ore-forming processes and the controlling factors on ore composition (i.e., processes e.g., fractional crystallization; fO_2 conditions, subsolidus re-equilibration) in the Central Grenville Province.

2.2 Regional geological setting

The Grenville Province in Eastern Canada (Fig.2.1a) is a Mesoproterozoic orogenic belt that represents the southeastern margin of the Paleocontinent of Laurentia (Corriveau et al. 2007). The Paleo to Late Mesoproterozoic rocks of the Grenville Province represent an active continental margin with more than 400 m.y. of tectonic activity and extensive episodes of subduction-accretion and arc formation (Rivers, 1997). Subsequent stages of continent-continent collision (Shawinigan, 1190 – 1140Ma; Ottawan, 1080 – 1020Ma and Rigolet, 1000 – 850Ma) took place during the Grenvillian Orogeny, separated by periods of crustal extension and several occurrences of within-plate magmatism. During this Himalayan-type event, crustal thickening and tectonic extrusion led to widespread high-grade metamorphism (Ludden and Hynes, 2000b) and reactivation of deep-level shear zones in the Grenville Province, such as the Saint Fulgence and Pipmuacan Deformation Zones in the Central Grenville (Fig.2.1b) (Corriveau et al. 2007).

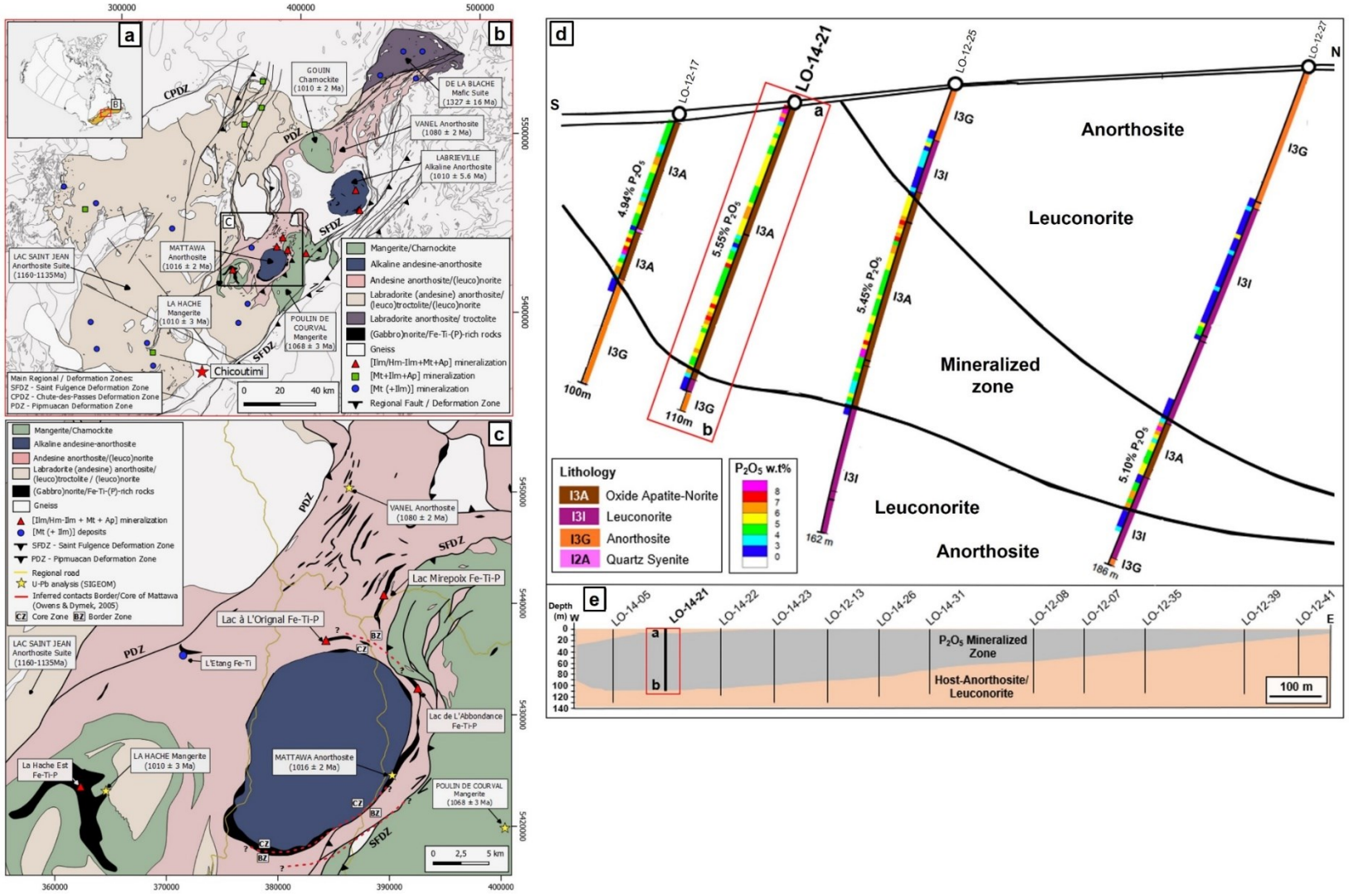

Figure 2.1. a Location of the Grenville Province in Quebec, Canada. Red square represents the Central Grenville shown in "b". b Regional geological map of the AMCG suites in the Central Grenville Province, Quebec with the location of the Fe-Ti-(P) deposits and regional deformation zones (DZ). c Close up of the AMCG suites and Fe-Ti-(P) mineral deposits in the Lac à l'Orignal area. Red dotted lines indicate the inferred limit between core (CZ) and border (BZ) of the Mattawa Anorthosite Massif, according to Owens & Dymek (2005), based on geochemical criteria. Geological maps modified from SIGEOM (Quebec System of Geomining Information; Gobeil et al. 2002; Hébert & Cadieux, 2003). d-e Schematic geology sections of the Lac à l'Orignal Fe-Ti-P deposit: d N-S section showing the oxide-apatite mineralized zone (average P_2O_5 around 5 wt.%) hosted by anorthosite and leuconorite. Cut-off grade is 3 wt.%. (Laverdière, 2013; 2016). e Schematic W-E section showing the approximate lens-shape of the mineralized zone, dipping around 30° to the north. The large thickness of the LO-14-21 drillcore was chosen for this study.

The Grenville Province experienced numerous episodes of AMCG magmatism with coeval Fe-Ti-P mineralization, that occurred over 300 m.y. (1327 – 1000 Ma), recording a complex petrogenetic, tectonic and temporal evolution (Emslie, 1985; Higgins & Van Breemen, 1996; Gobeil et al. 2002; Hébert et al. 2005; 2009). The emplacement of most of the AMCG suites and other mafic magmas described in the Central Grenville Province are coeval with periods of either crustal shortening or crustal extension during the Grenvillian Orogeny and associated with the presence of deep-level shear zones (Higgins & Van Breemen, 1996; Gobeil et al. 2002). In the Central-South Grenville (Fig.2.1b), Hébert et al. (2009) summarized four distinct pulses of magmatism, with major occurrences in the region of Saguenay-Lac-Saint-Jean, Quebec: I) the 1327 ± 16 Ma labradorite-type De La Blache Mafic Suite (Gobeil et al. 2002); II) the 1160-1135 Ma labradorite- and andesine-type Lac-St.-Jean Anorthosite Suite (Higgins & Van Breemen, 1992; 1996; Higgins et al. 2002), which is the largest anorthosite suite in the world (Ashwal, 1993); III) the 1082-1045 Ma Pipmuacan Anorthosite Suite, including the andesine-type Vanel Anorthosite, the Poulin de Courval Mangerite and the coeval Saint-Urbain Anorthosite (Higgins & Van Breemen, 1996; Morisset et al. 2009); IV) the 1020-1008 Ma andesine-type Valin Anorthosite Suite, including the Mattawa Anorthosite (Hébert et al. 2005; Owens & Dymek, 2005), the Labrieville Alkalic Anorthosite Massif (Owens & Dymek, 1992; 1995; Owens et al. 1993; 1994), the Gouin Charnockite (Hébert et al. 2005) and the La Hache Mangerite (Hébert et al. 2005).

Among the AMCG suites observed in the Central Grenville Province, a variation in the assemblage of oxide (from magnetite to hemo-ilmenite), mafic silicates (olivine to orthopyroxene) and plagioclase composition (from labradorite to andesine) (Dymek & Owens, 2002; Hébert et al. 2005; 2009; Grant, 2020) seems to be directly

related to the age of the anorthosite suite: I) labradorite-type anorthosites are exclusively older than 1130 Ma, can be olivine-bearing or orthopyroxene-bearing and host Fe-Ti-V mineralization, dominated by magnetite; II) anorthosites younger than 1130 Ma are exclusively andesine in composition and dominated by orthopyroxene (olivine is absent) and host Fe-Ti mineralization; and III) the presence of hemo-ilmenite is also exclusive to anorthosite suites younger than 1130 Ma. Phosphate mineralization is spatially associated with anorthosites of all ages.

2.3 Local geology of the Lac à l'Orignal Fe-Ti-P deposit

The Lac à l'Orignal deposit is one of a number of Fe-Ti-P mineralized lenses located approximately 100km northeast of Chicoutimi (Quebec, Canada), within the Central part of the Grenville Province. It outcrops near the border of two anorthosite intrusions (Vanel and Mattawa), both of which were emplaced near lower-crustal shear zones of the Saint Fulgence and the Pipmuacan Deformation Zone in the northeast margin of the Lac-Saint-Jean Anorthositic Suite (Fig.2.1c). Lac à l'Orignal is located within the 1080 (±2) Ma Vanel Anorthosite (Hébert & Van Breemen, 2004; Hébert et al. 2009) near the northern margin of the younger, dome-shaped 1016 (±2) Ma Mattawa Anorthosite (Owens & Dymek, 2005; Hébert et al. 2009). The limit of the two anorthosites was drawn on the geological map with the aid of geophysics (Mattawa has distinctive low magnetitic response compared to Vanel). However, based on the An content of plagioclase Owens & Dymek (2005) showed that the core of Mattawa (with the low magnetite response) has much lower An contents (29-37) than the border zone (An39 – 45) which hosts several lenses of leuconorite and Fe-Ti-P-rich rocks (Fig.2.1c); the latter was used to date the Mattawa anorthosite (Hébert et al. 2005). However, the 'border zone' is designated as the Vanel Anorthosite on the geological map. Indeed, the plagioclase composition of the Vanel Anorthosite away from Mattawa

has similar compositions (Miloski et al. 2023 *in review*). This illustrates how complex it can be to distinguish different types of anorthosite massifs in the field.

Observations from surface outcrops and drillcore in this study (Fig.2.2) indicate that the deposit is comprised of oxide apatite norite (OAN) with approximate mineral proportions of Fe-oxides (15 - 25%), apatite (8 - 20%) and orthopyroxene surrounding coarser plagioclase (Figs.2.2a-b). Locally there are patches (20-30cm) of pegmatitic-OAN (Fig.2.2c). Layering occurs between OAN and thin (10 – 20 cm thick) anorthosite layers (Fig.2.2d), which are sometimes apatite-bearing. These anorthosite levels within the mineralization contain similar to even higher amounts of apatite in comparison with the OAN cumulates. One portion of the analyzed drillcore contains a 40cm-thick anorthosite layer with a 20 cm-thick massive apatite portion (Fig.2.2e). Finally, several 30 cm thick fine-grained OAN dykes crosscut the mineralization. The mineralization is hosted by pink anorthosite and leuconorite, the latter containing up to 3 wt.% P_2O_5 (Fig.2.1d). Small massive oxides (20-40 cm) occur as lenses or together with blocks of anorthosite (Fig.2.2f) near the contact with the main mineralized zone, both on outcrop and in drill core.

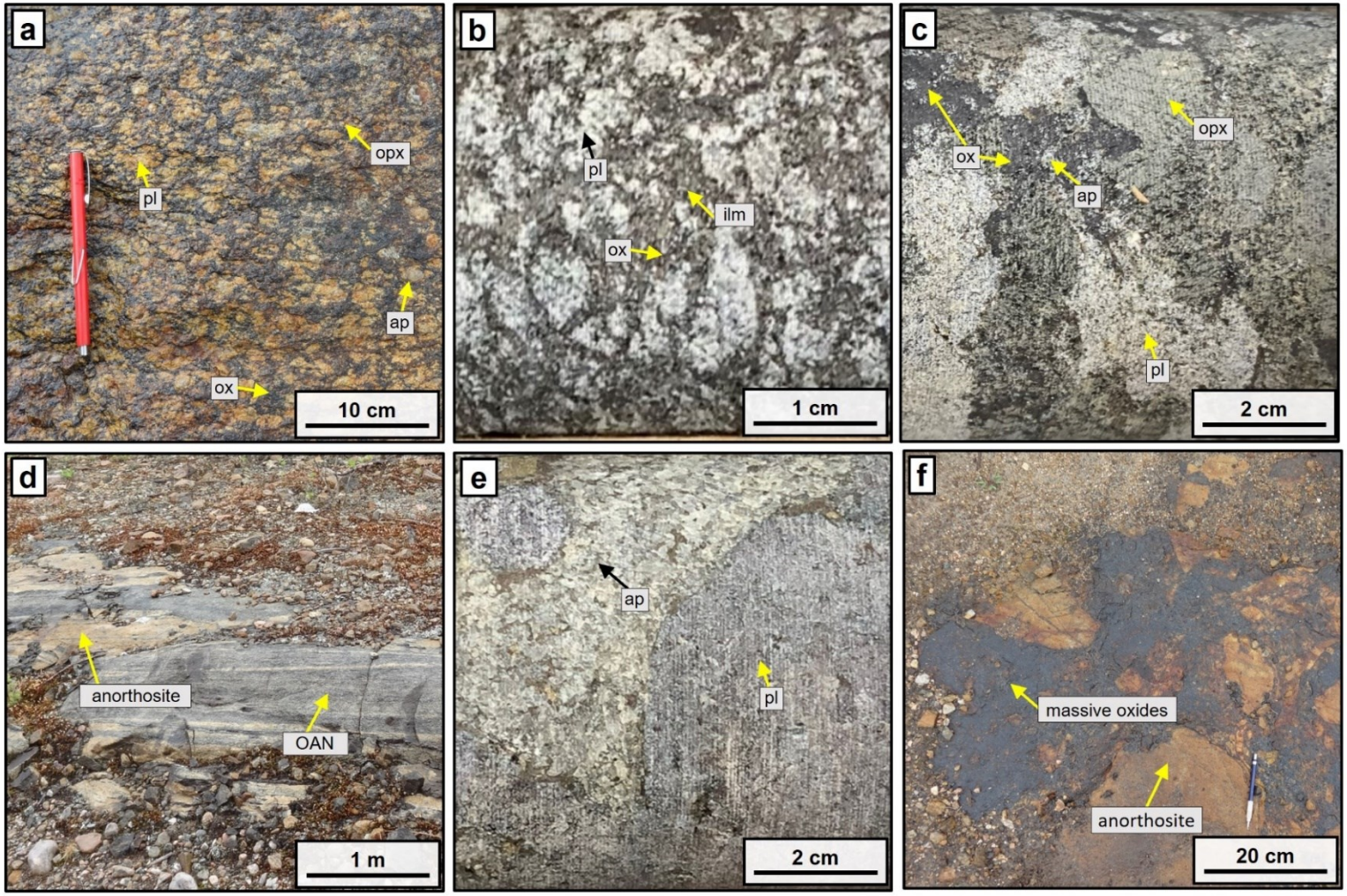

Figure 2.2. Photographs of representative lithologies of the Lac à l'Orignal Fe-Ti-P deposit from surface and drillcore. a Coarse-grained oxide-apatite-norite (OAN) (sample 20PM02). b Oxide-apatite-norite (LO-24, 28m). c Pegmatitic OAN (LO-41, 71m). d Layering of OAN with plagioclase-rich (anorthosite) layers. e Massive apatite layer within pink-anorthosite layers (LO-03, 5m). f Massive oxides (ilmenite + magnetite) containing blocks of the host anorthosite (sample 20PM03). Mineral abbreviations: pl = plagioclase; opx = orthopyroxene; ox = oxides; ilm = ilmenite; ap = apatite.

2.4 Sampling and analytical methods

Fifty-eight samples spanning the entire sequence of one of the thickest portions (around 100m) of the mineralized zone (drillcore LO-14-21, Fig. 2.3) were selected for detailed lithological description. In addition, three samples from surface outcrops (Fe-Ti-P zones, massive oxides and host anorthosite) were included. From these, thirty-eight samples were selected for petrographic descriptions and modal mineral abundances estimates from polished thin sections using an optical microscope. A subset of eleven samples covering the entire drillcore stratigraphy were selected for chemical mapping using the Bruker - Tornado M4 micro-X-Ray fluorescence (μXRF) analysis at Université Laval, Quebec.

Thirty-eight samples were selected for major and trace element determinations by whole rock and by in-situ analysis of the rock-forming minerals. Details of the following analytical methods, instrumentation and evaluation of the data quality are discussed in Appendix 2.2. The samples were cut, crushed, and further reduced to powder (~10 g) in an alumina mill at LabMaTer, Université du Québec à Chicoutimi (UQAC). Whole-rock analysis was carried out by fusion of rock powder to form a lithium-borate glass bead that was then analyzed for major and trace element, in situ, by laser ablation inductively coupled plasma mass spectrometry (LA-ICP-MS) at LabMaTer, UQAC, following the protocol of Barnes & Mansur (2020). The major and trace element geochemistry of plagioclase (n=168), apatite (n=132), ilmenite (n=108) and magnetite (n=88), in-situ by LA-ICP-MS at LabMaTer, UQAC was also carried out on polished thin sections from the same 38 samples. In addition, one sample was selected for detailed LA-ICP-MS 2D mapping of the oxides using a time of flight (TOF) ICP-MS at LabMaTer, UQAC

Fifteen samples were selected for the analysis of major and minor elements of plagioclase (n=57), orthopyroxene (n=59), magnetite (n=41), ilmenite (n=81), apatite (n=54) and biotite (n=27) by electronprobe microanalysis (EPMA) at Université Laval, Quebec. This was done to verify the value for the internal standard necessary for some minerals during the LA-ICP-MS data reduction, as well as to compare with major element results obtained by LA-ICP-MS (Appendix 2.2, Fig.2.2). Thirteen samples containing hemo-ilmenite were also analyzed by EDX analysis, using a scanning electron microscope (SEM) at Université Laval, of a 500 x 500µm area covering exsolutions of hematite in ilmenite. This was carried out in order to determine the major element composition of hemo-ilmenite that better approximates the results from the LA-ICP-MS raster lines, due to the presence of abundant hematite exsolutions in ilmenite. Whole-rock CIPW norm was done using standard calculations. Recalculation of An*/Or* contents following Owens & Dymek (2005). The calculated cationic proportions, the recalculation of Fe^{+2}/Fe^{+3} ratios and the An content of plagioclase were done using mass balance equations/spreadsheets (Appendix 2.1 & 2.2).

Two samples of mineralized rocks, one from each of the core and border of the intrusion, were selected for U-Pb dating of zircon (see samples location on Fig.2.3). Zircon separation, preparation and U-Pb analysis, determined by LA-High Resolution-ICP-MS, following the protocol of Perrot et al. (2017), were conducted at the GEOTOP labs in the Université du Québec à Montréal (UQAM).

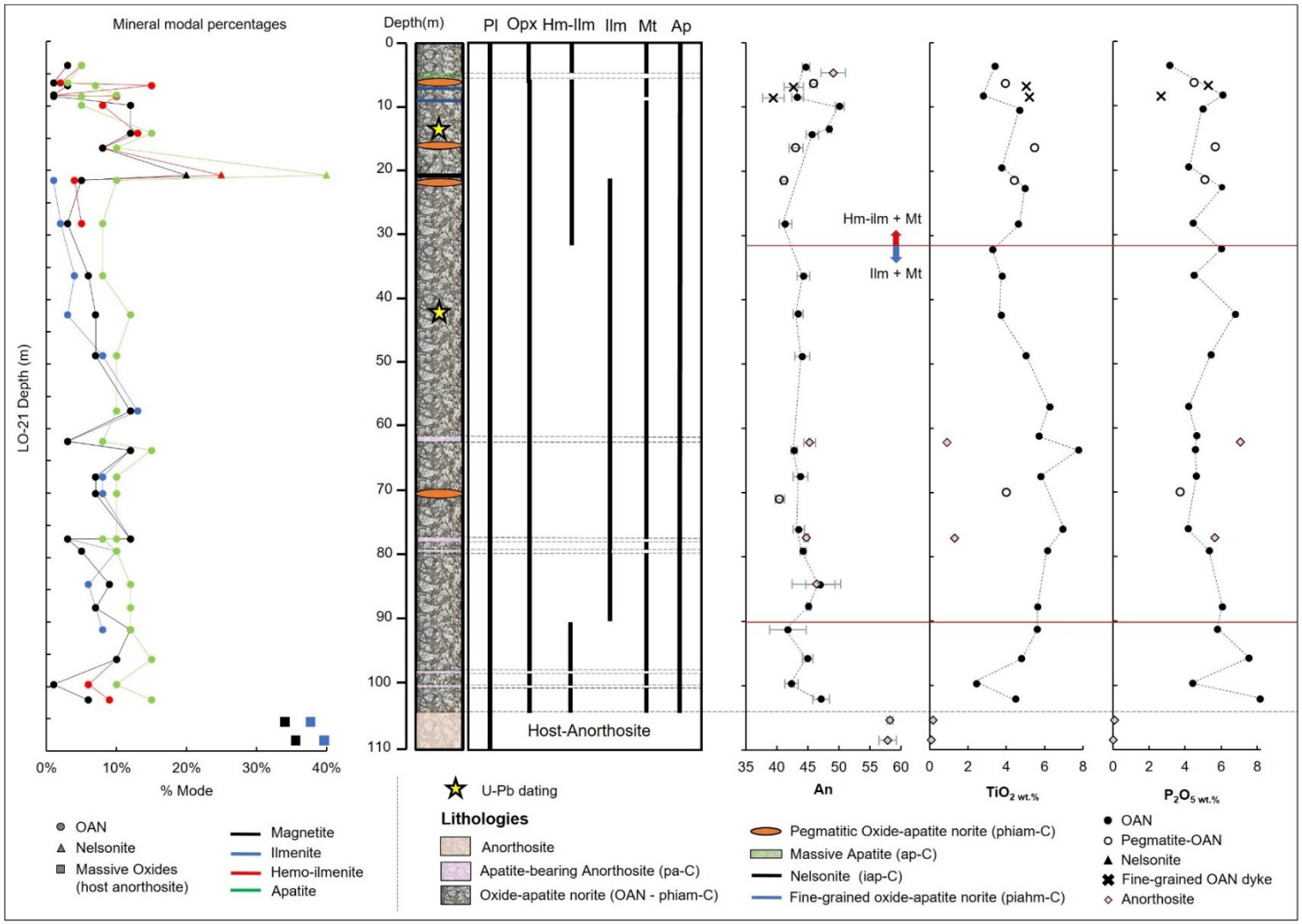

Figure 2.3. Stratigraphic subdivision of the Lac à l'Orignal intrusion based on the distribution of different cumulus phases from the borders to the core. Modal proportion of oxides and apatite (left). Cryptic variation in plagioclase of anorthite (An) content (An=100 [Ca/ (Ca+Na)]) and TiO_2 and P_2O_5 values of whole-rock analysis are shown. Cumulus (-C) assemblages follow the nomenclature of Irvine (1982). Mineral abbreviations: p = plagioclase (pl); i = ilmenite (ilm); a = apatite (ap); h = orthopyroxene (opx); m = magnetite (mt); hm-ilm = hemo-ilmenite. Error bars = 1 standard deviation of the average value and represents the natural variation within the thin section.

2.5 Results

2.5.1 Petrography and cumulate stratigraphy

The stratigraphic variation of the mineralized zone (from drillcore LO-14-21) is displayed in Figure 2.3, based on petrographic (both macro and microscale, Appendix 2.1; Figs.2.4 & 2.5) observations, whole rock data, μXRF maps and the An content of plagioclase. The presence of layering within the Lac à l'Orignal mineralized zone (Fig.2.2d) suggests a cumulate origin. Thus, the nomenclature of Irvine (1982) is used whereby the first letter of their cumulus phases are followed by -C, meaning 'cumulus'.

The Lac à l'Orignal deposit is dominated by medium to coarse-grained oxide-apatite-norite (OAN) cumulates (phiam-C, Fig.2.4a), comprising plagioclase (30-40%), orthopyroxene (15-35%), Fe-oxides (15-25%) and apatite (5-20%) as major phases. Accessory minerals include fine-grained exsolutions of Al-spinel from oxide phases (Fig.2.5h) and sulfides (Fig.2.5e-g). Apatite is homogeneously present throughout the entire cumulate succession, from the bottom to the top of the mineralized interval, being most commonly associated with oxide phases (Fig.2.3). Samples are fresh and well-preserved without hydrothermal alteration.

Overall, the cumulus phases (plagioclase, orthopyroxene, apatite, magnetite (hemo)-ilmenite) are present throughout the mineralized zone, but with varying modal proportions (Fig.2.3 & Appendix 2.1). In particular, the oxide mineralogy reveals a distinct zonation (discussed in more detail below): hemo-ilmenite (ilmenite with hematite exsolutions) is restricted to the borders whereas ilmenite, free of hematite-exsolutions, occurs in the core. In general, the lower part of the intrusion (50-90m depth) is characterized by higher amounts of orthopyroxene (melanocratic) than the upper part (above 40m depth), where plagioclase is the predominant mineral phase,

forming leucocratic oxide-apatite-norite (Fig.2.3). In a few places (between 12-25m and around 70m depth), the OAN gradually coarsens towards a pocket (10-20cm thick) of pegmatitic coarse-grained OAN (phiam-C, Figs.2.2c & 2.4b), with centimetric-scale orthopyroxene containing rutile exsolutions (Fig.2.4c). Massive nelsonite (oxide and apatite) is uncommon in the studied drillcore: one small (10cm-thick) nelsonite layer (55%: hemo-ilmenite + ilmenite + magnetite and 35% apatite) (iamph-C) was observed in the upper border (at 20.9m, Fig.2.4d). Several medium-grained anorthosite layers (10-50cm) occur throughout the mineralized zone, most of them containing high-amounts (7-20%) of apatite (pa-C) within plagioclase but low proportions of Fe-Ti oxides and orthopyroxene (Figs.2.4e-f). A massive apatite (ap-C) layer (20cm thick) that lacks oxides, with euhedral/medium-grained apatite crystals, occurs at the top of the stratigraphy (4.6m, Fig.2.5g) in sharp contact with an apatite-bearing anorthosite layer. Apatite crystals are euhedral. This is unexpected because massive apatite without oxides has never been reported. Plagioclase throughout the mineralized zone, in both OAN and ap-bearing anorthosite layers, is andesine in composition (An 40–50: Fig.2.4) with exsolutions of K-rich phase (Fig.2.4e).

Two fine-grained oxide-apatite-norite (phiam-C, Fig.2.4h) dykes/sills (30cm thick each) occur in sharp contact within the upper 10m of the upper border of the intrusion. They share similar mineralogy, and plagioclase composition, with the coarser-grained OAN mineralization and represent rapidly cooled, thin injections of ferrodiorite/jotunite magma. Hemo-ilmenite is the main oxide phase in these fine-grained dykes, whereby magnetite is nearly or completely absent.

The lower contact of the mineralized zone comprises the host pink anorthosite (Fig.2.4i), which is distinct in composition from the apatite-bearing anorthosite layers (andesine) within the mineralized zone. The host anorthosite is labradorite (An > 50)

in composition and contains anti-perthite textures with no apatite. Surface outcrops adjacent to the mineralized zone, contain irregular lenses of massive oxides (magnetite + ilmenite; hemo-ilmenite with no apatite) hosting andesine-anorthosite blocks (sample 20PM03, An 50-51, Fig.2.2f). Grant (2020) previously described similar massive oxides within the anorthosite-host at the lower contact of drill core LO-12-13 (sample MG-LO-04).

2.5.2 Oxide petrography

The Lac à l'Orignal deposit is (hemo)-ilmenite-dominated, similar to other Fe-Ti-(P) occurrences associated with the younger anorthosites in the Grenville province (e.g., Grader intrusion (Charlier et al. 2008); Lac Tio (Charlier et al. 2010)). However, the oxide mineralogy changes from the borders to the core (Figs.2.3 & 2.5). Both the top (0-30m, Figs.2.5a & 2.5e) and bottom (30-105m, Fig.2.5d) borders of the mineralized zone are dominated by cumulus hemo-ilmenite, hosting large hematite exsolution lamellae. In contrast, the core (30 - 90m, Figs.2.5c & 2.5g) contains Fe-poor ilmenite that is devoid of hematite exsolutions. Magnetite is also present as a cumulus oxide throughout the OAN mineralized zone, commonly as a minor cumulus phase at the borders (ilm/mt ratios = 6.0 to 0.7, decreasing towards the core) or in similar proportions to ilmenite in the core of the intrusion (ilm/mt ratios = 2.4 -0.4).

At the transition between the border and the core (20 – 30m, Fig. 2.5f), ilmenite and hemo-ilmenite coexist, the latter typically contains finer hematite lamellae. In this case, hemo-ilmenite also presents a depletion in hematite exsolutions (size and quantity) towards the contact with adjacent magnetite (Figs.2.5f & 2.5h). Al-spinel is an accessory oxide phase. Re-equilibration between magnetite and ilmenite produces fine-grained irregular Al-spinel exsolutions at the contact of magnetite and ilmenite

(Figs.2.5g-h). Fine-grained Al-spinel exsolution lamellae, following preferential crystallographic directions, also occur in magnetite and Al-spinel commonly forms external granules in ilmenite.

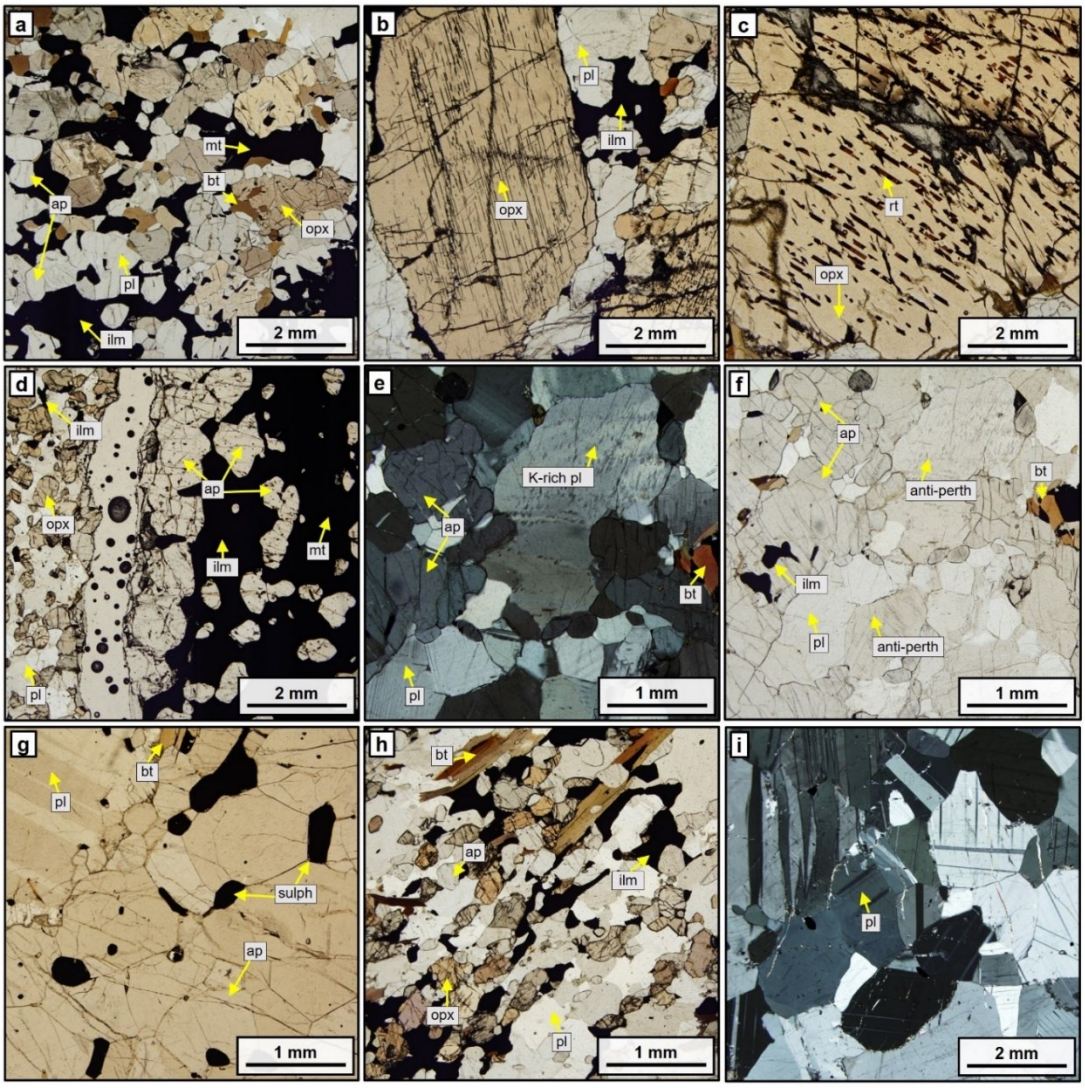

Figure 2.4. Photomicrographs of the main lithologies of the Lac à l'Orignal Fe-Ti-P mineralized zone. a Medium-grained oxide-apatite-norite (OAN) (LO-24, 28m). b Pegmatitic coarse-grained OAN. Note the appearance of centimetric-scale orthopyroxene (LO-41, 71m). c Orthopyroxene megacrystal with rutile exsolution lamellae (LO-41, 71m). d Contact between medium-grained OAN and massive nelsonitic layer (LO-21, 20.8m). e-f Accumulation of apatite crystals within anorthosite layer (apatite-bearing anorthosite, LO-38, 62m) containing plagioclase with exsolutions of K-rich phase. (LO-38, 62m). g Massive apatite layer (LO-02, 4.7m). h Fine-grained OAN dyke (LO-06, 6.7m). i Coarse-grained host anorthosite lacking apatite and exsolutions in plagioclase (LO-58, 105.3m). Mineral abbreviations: pl = plagioclase; opx = orthopyroxene; bt = biotite; hm-ilm = hemo-ilmenite; ilm = ilmenite; mt = magnetite; rt = rutile; ap = apatite; spl = Al-spinel; sulph = sulfides.

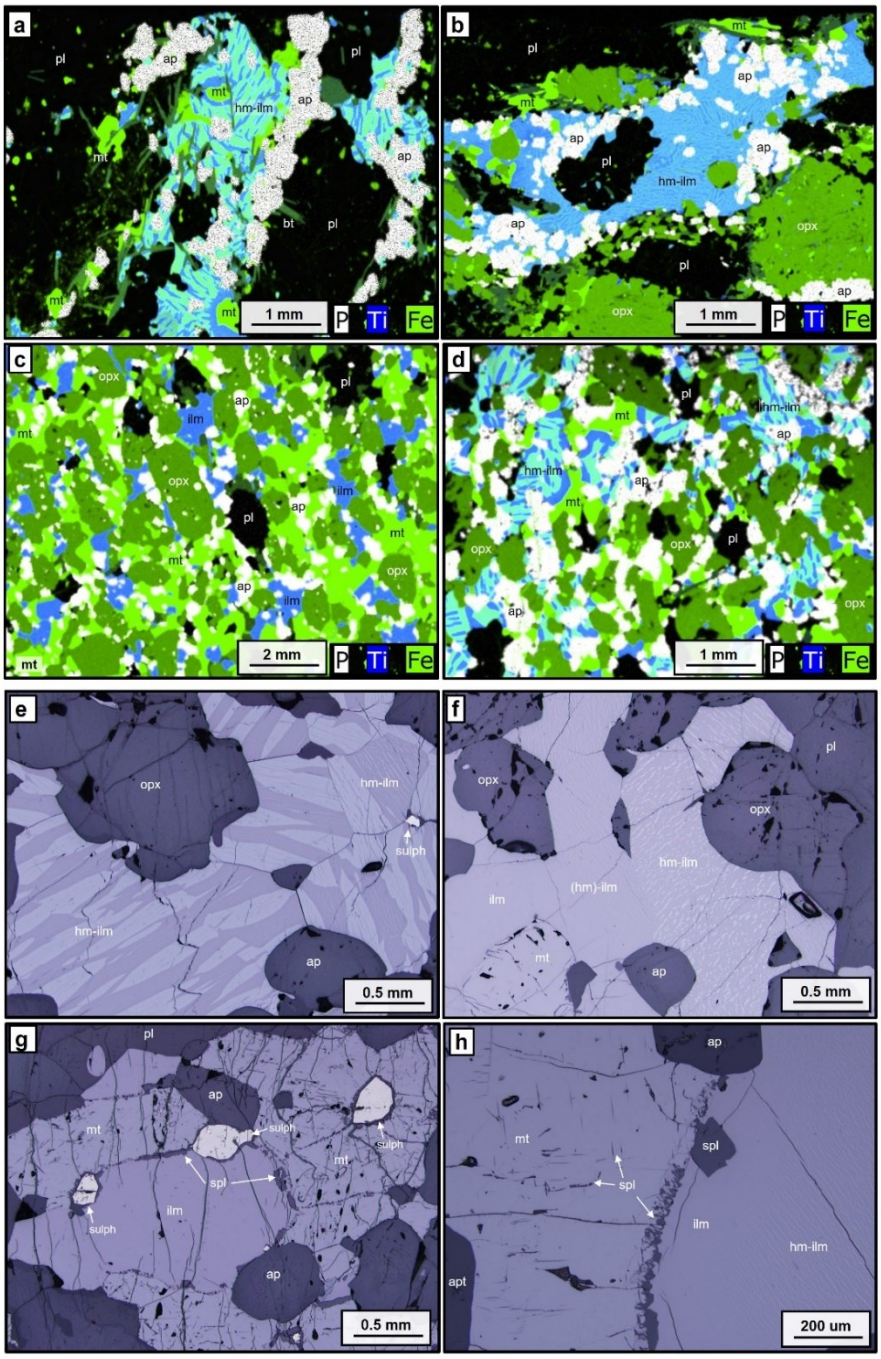

Figure 2.5. a-d µXRF-maps, combining P (white), Ti (blue) and Fe (green), showing the different proportions of oxides and apatite from the Lac à l'Orignal Fe-Ti-P mineralized zone. Ilmenite is blue, where as hematite-rich part of ilmenite is cyan. Magnetite is bright green. Orthopyroxene/biotite is dark green. a Medium grained-OAN dominated by hemo-ilmenite containing coarse exsolution lamellae of hematite, and minor magnetite (top border zone, LO-01, 3.7m). b Coarse grained-OAN dominated by hemo-ilmenite containing thin exsolution lamellae of hematite, and magnetite (transition zone, LO-22, 21.5m). c Medium grained-OAN dominated by magnetite and ilmenite (Hemo-ilmenite is absent) from core zone (LO-43, 75.7m). d Medium grained-OAN dominated by hemo-ilmenite, containing coarse exsolution lamellae of hematite, and minor magnetite, from the bottom border zone (LO-57, 102.1m). Note the higher presence of apatite near the oxide crystals. e-h Photomicrographs (reflected light) of the oxide assemblages. e Medium grained oxide-apatite norite (OAN) dominated by hemo-ilmenite containing coarse exsolution lamellae of hematite (pale) and ilmenite (dark) and minor magnetite (border zone, LO-10, 10.5m). f Medium grained-OAN dominated by hemo-ilmenite, with fine exsolutions of hematite, and ilmenite (exsolution-free) close to magnetite (transition zone, sample LO-24, 28m). g Medium grained-OAN dominated by magnetite, ilmenite and Al-spinel exsolutions. Hemo-ilmenite is absent (core zone, LO-32, 48.5m). h Evidence of sub-solidus re-equilibration between magnetite and ilmenite, with depletion of hematite exsolutions in ilmenite towards the border with magnetite. Note the higher presence of Al-spinel exsolutions at the contact between magnetite and ilmenite grains (LO-29, 42m). Mineral abbreviations: pl = plagioclase; opx = orthopyroxene; hm-ilm = hemo-ilmenite; ilm = ilmenite; mt = magnetite; ap = apatite; spl = Al-spinel; sulph = sulfides; bt = biotite.

2.5.3 U-Pb dating

The U–Pb results for zircon analyzed from the upper border and core of the mineralized zone are presented in Table 2.1. The Concordia diagrams for these 2 samples are shown in Figure 2.6a, where all the ages are presented with the calculated 2σ uncertainties. Representative cathode luminescence photomicrographs of the zircon grains selected for dating are also displayed in Figure 2.6b. The complete cathode luminescence photomicrographs (Appendix 2.3) show that they comprise single grains of subhedral prismatic to anhedral igneous zircons with simple, magmatic zoning. Although some show darker cores (e.g., in LOR1) their ages are similar to those of the paler borders. Weighted mean diagrams (Appendix 2.3) show a normal distribution of a single population of zircons for each sample. Zircon grains are U poor and associated with a large error.

Sample LOR-1 is a leucocratic oxide-apatite norite (OAN) located at the upper border of the intrusion (14m – 16m depth), dominated by hemo-ilmenite (± magnetite). The calculated Concordia age, based on all the zircon grains (n=14) is 1069 ± 13 Ma, which is within the range of crystallization ages of the Pipmuacan Anorthosite Suite (1080 – 1060Ma) and the nearby Vanel Anorthosite (1080.0 ± 2.0 Ma, Hébert et al. 2009). Sample LOR-2 is a melanocratic oxide-apatite norite from the core of the intrusion (41m and 43m depth), dominated by ilmenite + magnetite. The calculated Concordia age for all the concordant zircon grains (n=16) is 993 ± 13 Ma, which is significantly younger than the age of the border, and closer to the crystallization age of the nearby Mattawa Anorthosite (1016 ± 2 Ma, Hébert et al. 2005). These new dates indicate that the Lac à l'Orignal intrusion is multi-phase with an older border and a younger core.

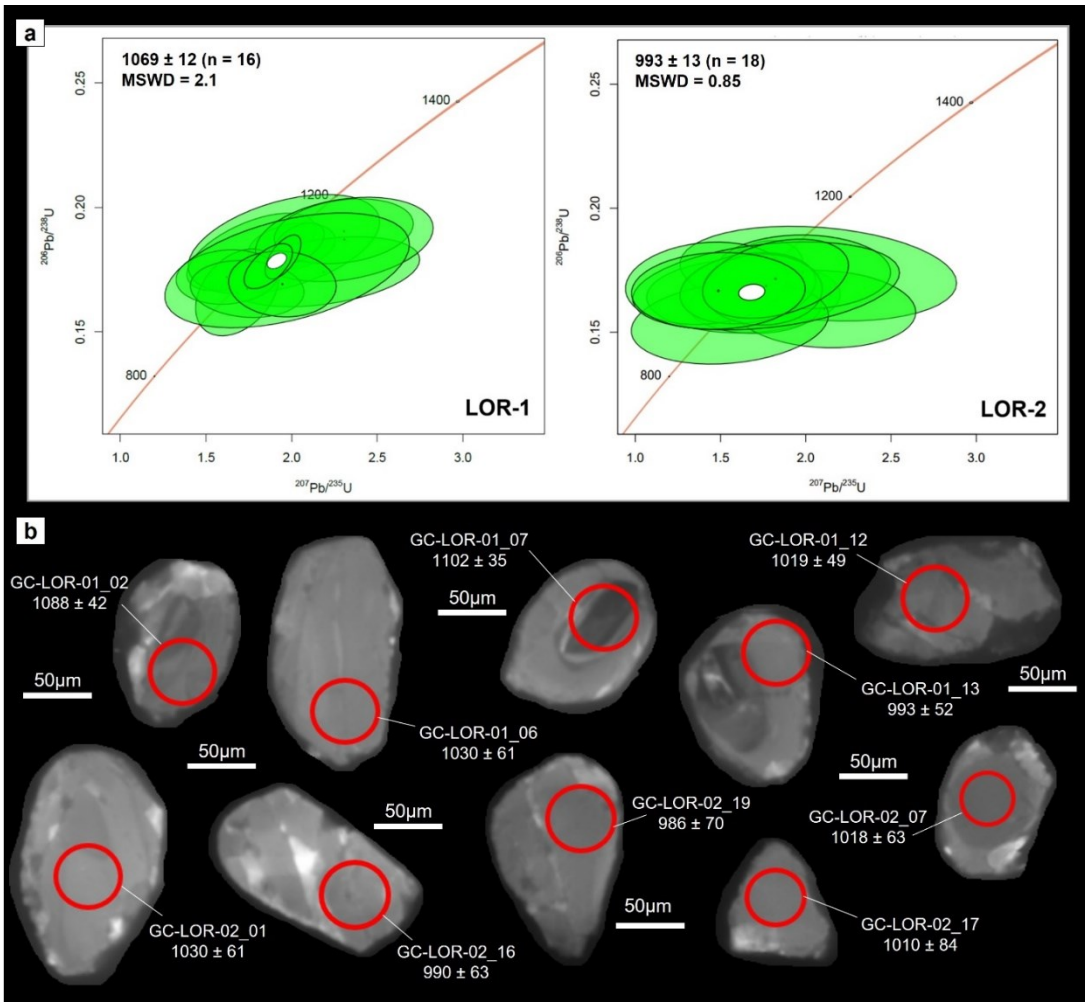

Figure 2.6. a Concordia diagrams for in situ LA-ICP-MS U–Pb data from analyzed zircons in the Lac à l'Orignal Fe-Ti-P mineralization. Each ellipse represents the result of the analysis of a single grain, as identified in Table 1, and corresponds to the associated 2σ uncertainties. b Representative cathodoluminescence images from magmatic grains of zircon of the Lac à l'Orignal Fe-Ti-P mineralization in the Central Grenville Province, Quebec. Red circles show the location of the 50 µm beam for U–Pb microanalysis.

Table 2.1. Zircon U–Pb LA-ICP-MS analytical data of samples in hole LO-14-21 from the Lac à l'Orignal Fe-Ti-P deposit

#Analysis	U_{ppm}	Pb_{ppm}	Th/U	$^{206}Pb/^{204}Pb$	Isotopic ratios ±1s%			Apparent ages ±2s%			Rho
					$^{206}Pb/^{238}U$	$^{207}Pb/^{235}U$	$^{207}Pb/^{206}Pb$	$^{206}Pb/^{238}U$	$^{207}Pb/^{235}U$	$^{207}Pb/^{206}Pb$	
Oxide-apatite norite (hemo-ilmenite + magnetite bearing) – 14.0 – 16.0m depth											
GC-LOR-01_2	49.1	1814.4	0.9	-180.6	0.18432 ± 2.1	2.00082 ± 5.2	0.07858 ± 4.9	1088 ± 42	1079 ± 75	991 ± 225	0.27242
GC-LOR-01_3	23.8	848.2	0.8	-793.5	0.18209 ± 3.5	1.76384 ± 8.7	0.07136 ± 8.3	1071 ± 69	925 ± 111	465 ± 396	0.57702
GC-LOR-01_5	30.8	1087.1	1.1	189.0	0.18524 ± 4.4	1.9547 ± 11.7	0.08215 ± 9.7	1084 ± 86	1038 ± 148	1179 ± 322	0.45058
GC-LOR-01_6	15.1	505.4	0.5	68.8	0.17415 ± 3.3	2.18625 ± 10.5	0.09371 ± 9.9	1030 ± 61	1030 ± 168	1466 ± 330	0.34580
GC-LOR-01_7	233.2	8207.0	1.4	1113.5	0.15861 ± 1.8	2.04052 ± 3.1	0.07945 ± 2.7	1102 ± 35	1119 ± 42	1098 ± 118	0.45140
GC-LOR-01_10	49.8	1784.2	1.0	170.5	0.19041 ± 2.8	2.30463 ± 7.2	0.08391 ± 7.1	1119 ± 57	1126 ± 99	903 ± 326	0.22514
GC-LOR-01_11	64.5	2279.9	2.3	66.0	0.18714 ± 3.7	2.30761 ± 9.2	0.08902 ± 8.9	1103 ± 73	1166 ± 117	1142 ± 361	0.26715
GC-LOR-01_12	24.8	811.6	1.0	20.8	0.17201 ± 2.6	1.62206 ± 7.5	0.06738 ± 7.5	1019 ± 49	890 ± 110	630 ± 357	0.09702
GC-LOR-01_13	28.5	910.3	0.9	13.2	0.16721 ± 2.8	1.74013 ± 7.8	0.07373 ± 7.3	993 ± 52	934 ± 104	642 ± 357	-0.11120
GC-LOR-01_15	7.4	239.2	0.5	1.7	0.17471 ± 5.4	1.97317 ± 14.8	0.07303 ± 16.8	1021 ± 101	892 ± 253	1991 ± 331	0.45490
GC-LOR-01_16	31.9	1026.7	0.9	6.1	0.16922 ± 3.2	1.94567 ± 6.6	0.08358 ± 6.9	1002 ± 59	1041 ± 95	1089 ± 287	-0.07291
GC-LOR-01_17	484.2	15990.8	0.8	121.8	0.18008 ± 2.1	1.94987 ± 2.2	0.07732 ± 2.1	1065 ± 40	1090 ± 29	1085 ± 82	0.60867
GC-LOR-01_19	6.1	187.8	0.6	2.3	0.16846 ± 5.1	1.66545 ± 17.1	0.08767 ± 17.9	990 ± 91	640 ± 347	2178 ± 324	0.02042
GC-LOR-01_20	444.6	14541.9	0.7	175.2	0.17638 ± 2.1	1.86342 ± 3.1	0.07378 ± 2.5	1044 ± 40	1059 ± 40	998 ± 101	0.59924
Oxide-apatite norite (ilmenite + magnetite bearing) – 41.0 – 43.0m depth											
GC-LOR-02_1	24.0	752.2	2.2	11.6	0.16758 ± 3.1	1.58629 ± 8.3	0.07237 ± 8.2	1000 ± 57	864 ± 125	809 ± 347	0.15626
GC-LOR-02_2	176.5	5446.0	0.4	145.1	0.16328 ± 1.7	1.65135 ± 3.2	0.07164 ± 3.3	968 ± 30	973 ± 41	892 ± 144	0.18780
GC-LOR-02_3	85.5	2745.2	1.4	-7.8	0.16952 ± 2.4	1.69575 ± 4.3	0.07203 ± 4.4	1006 ± 44	986 ± 55	851 ± 193	0.17176
GC-LOR-02_5	8.4	273.2	1.1	3.8	0.16461 ± 3.7	1.63427 ± 14.2	0.07538 ± 15.1	975 ± 68	628 ± 232	1898 ± 323	0.04278
GC-LOR-02_6	6.2	193.5	0.8	3.2	0.16931 ± 5.5	2.16737 ± 18.6	0.14402 ± 20.1	991 ± 102	759 ± 291	2386 ± 408	-0.16299
GC-LOR-02_7	47.9	1466.1	1.3	16.5	0.17219 ± 3.5	1.72061 ± 6.3	0.07098 ± 5.9	1018 ± 63	953 ± 79	687 ± 303	0.31096
GC-LOR-02_8	7.1	226.0	0.6	-0.1	0.17361 ± 4.5	2.07287 ± 16.1	0.09835 ± 16.7	1020 ± 86	710 ± 278	2333 ± 346	-0.20157
GC-LOR-02_9	23.6	695.2	1.1	0.1	0.16049 ± 2.8	1.70196 ± 9.3	0.07683 ± 9.5	956 ± 49	878 ± 134	866 ± 390	0.01493
GC-LOR-02_10	15.8	462.1	1.9	5.3	0.15928 ± 4.1	2.10853 ± 10.4	0.10365 ± 11.6	945 ± 69	953 ± 155	1445 ± 388	-0.08488
GC-LOR-02_12	15.3	474.4	2.3	15.8	0.17428 ± 3.5	1.98305 ± 10.6	0.08587 ± 11.9	1028 ± 67	920 ± 171	1224 ± 384	-0.01054
GC-LOR-02_14	12.8	395.2	0.5	9.1	0.16971 ± 4.1	1.41787 ± 13.7	0.06286 ± 15.6	1020 ± 82	728 ± 195	1163 ± 373	0.12923
GC-LOR-02_15	20.8	597.4	1.0	5.0	0.16774 ± 3.5	1.66007 ± 9.8	0.07706 ± 9.9	993 ± 64	962 ± 142	969 ± 370	0.20728
GC-LOR-02_16	30.0	832.7	1.1	18.0	0.16721 ± 3.5	1.74633 ± 8.2	0.07661 ± 7.9	990 ± 63	903 ± 115	935 ± 339	0.00805
GC-LOR-02_17	7.7	221.7	0.6	5.8	0.16865 ± 4.3	1.76706 ± 18.1	0.07941 ± 18.4	1010 ± 84	683 ± 303	1951 ± 333	0.29674
GC-LOR-02_18	20.7	593.1	1.1	12.1	0.17156 ± 3.8	1.82227 ± 9.6	0.07824 ± 9.3	1013 ± 71	880 ± 154	1173 ± 331	0.33830
GC-LOR-02_19	15.9	433.5	1.7	2.8	0.16671 ± 3.8	1.48753 ± 14.1	0.07406 ± 14.1	986 ± 70	647 ± 207	1380 ± 392	0.05748

2.5.4 Whole-rock geochemistry

The whole rock geochemistry of mineralized samples (n = 33), fine-grained dykes (n = 2) and host anorthosite (n = 4), containing massive oxides (n = 2), is presented in Table 2.2 (complete data and CIPW norm calculations are presented in Appendix 2.1) and confirms our petrographic observations. The stratigraphic variation in whole-rock composition is presented in Figure 2.3 & Appendix 2.3 and binary variation diagrams in Figure 2.7. As expected, the oxide-apatite norite cumulates from the mineralized zone are characterized by relatively high-Fe_2O_{3t} (14.2 – 47.1%), TiO_2 (2.8 – 7.7%), V (181 – 722ppm), P_2O_5 (3.1 – 8.1%) and MgO (2.8 – 10.8%) contents and low-SiO_2 (20.2 – 42.5%), Al_2O_3 (7.1 – 16.7%) and Na_2O (0.1 – 3.4%), reflecting much higher proportions of Fe-Ti oxides, apatite (CIPW norm: 7.4 -19.3 wt.% ap.) and orthopyroxene, and lower proportions of plagioclase in the mineralized cumulates when compared to the host anorthosites. The CIPW norm confirms a K-rich andesine-type plagioclase (An* = 45.60, Or* = 7.78) for the OAN mineralization on average. The ilmenite-bearing OAN in the core tends to have higher Fe_2O_{3t}, TiO_2, V, MgO and lower SiO_2, CaO, Na_2O and K_2O confirming that this part of the mineralization is more melanocratic, with higher proportions of oxides and orthopyroxene and lower plagioclase, respectively, than the hemo-ilmenite bearing border zones which tend to me more leucocratic.

The apatite-bearing anorthosite layers (pa-C) have similar P_2O_5 contents (4.5 – 5.6 wt.%) as the OAN zone, but much lower Fe_2O_{3t} (6.5 -7.3 wt.%), MgO (1.6 – 1.7 wt.%) and TiO_2 (0.9 – 1.3 wt.%), confirming the low proportions of orthopyroxene and oxides. The plagioclase is also K-rich andesine-type (CIPW norm: An* 42, Or* 7.8). The fine-grained OAN dykes (phiam-C) are chemically very similar to the leuco-OAN border group for all elements (Fig.2.7). There are two types of host anorthosite (p-C)

based on An and K contents, determined by CIPW-norm (Appendix 2.1): 1) a K-poor (0.36 to 0.46 wt.% K_2O), labradorite-type (An > 50) anorthosite (CIPW norm: An* = 57.1 – 59.1, Or* = 2.3 – 2.8) with higher CaO (10.8 – 11.0%) and Al_2O_3 (28.0 – 28.1%), sampled below the mineralized zone; 2) a K-rich (1.4 – 1.5% K_2O), andesine-type (An < 50) anorthosite (CIPW norm: An* = 40.9 – 43.3, Or* = 10.0 – 10.7) with lower CaO (7.1 – 8.4%) and Al_2O_3 (22.7 – 23.2%), sampled above the mineralized zone on surface. Both host anorthosites are P-poor (< 0.1 wt.% P_2O_5) in comparison to apatite-bearing anorthosite layers within the mineralized zone.

The massive oxides in the host anorthosite (andesine-type) have the highest Fe_2O_{3t} (54.5 – 71.4 wt.%), TiO_2 (9.5 – 12.1 wt.%) and V (1769 ppm) contents and lowest CaO and P_2O_5 values among all mineralized samples, due to a much higher proportion of magnetite to ilmenite (Fig.2.2) and the lack of plagioclase and apatite, respectively. In Figure.2.7, massive oxides plot on the same trends for Fe_2O_{3t} and TiO_2 as OAN cumulates, but not for V, for example, due to their higher concentration of ilmenite and magnetite.

Chondrite-normalized REE diagrams (Fig.2.8) show similar patterns between the OAN cumulates from the border (leucocratic, Hm-ilm + mt) and core (melanocratic, Ilm + mt), suggesting that they formed from similar magma compositions. These mineralized rocks are enriched in LREE (80 – 300x chondrite) relative to HREE (10 – 30x chondrite), presenting a smooth pattern with weak, negative Eu-anomalies (Eu* between 0.7 and 0.8). Moreover, leucocratic OAN tend to have a slightly higher abundance of REE in comparison with melanocratic OAN. The apatite-bearing anorthosite layers also have the same REE patterns as that of the OAN mineralization (Fig.2.8b), indicating that cumulus apatite controls the distribution of REE and also formed from a similar magma as the mineralization. Finally, the fine-grained OAN

dykes have very similar patterns to that of the OAN and have the highest REE abundance.

The host anorthosite samples have distinct REE patterns (Fig.2.8b) compared to the OAN mineralization, presenting enrichment in LREE and positive Eu-anomalies, typical of plagioclase accumulation, and lower overall REE concentrations. The labradorite-type anorthosite below the mineralization has lower REE values in comparison to the andesine-type anorthosite (associated with massive oxides) above the mineralization, which has a flatter distribution between light and heavy-REE due to the slightly higher amounts of apatite in relation to the other host anorthosite samples (P_2O_5 < 0.1 wt.%). Massive oxide samples, absent of apatite, have much lower REE abundances compared to the other cumulates (Fig.2.8a).

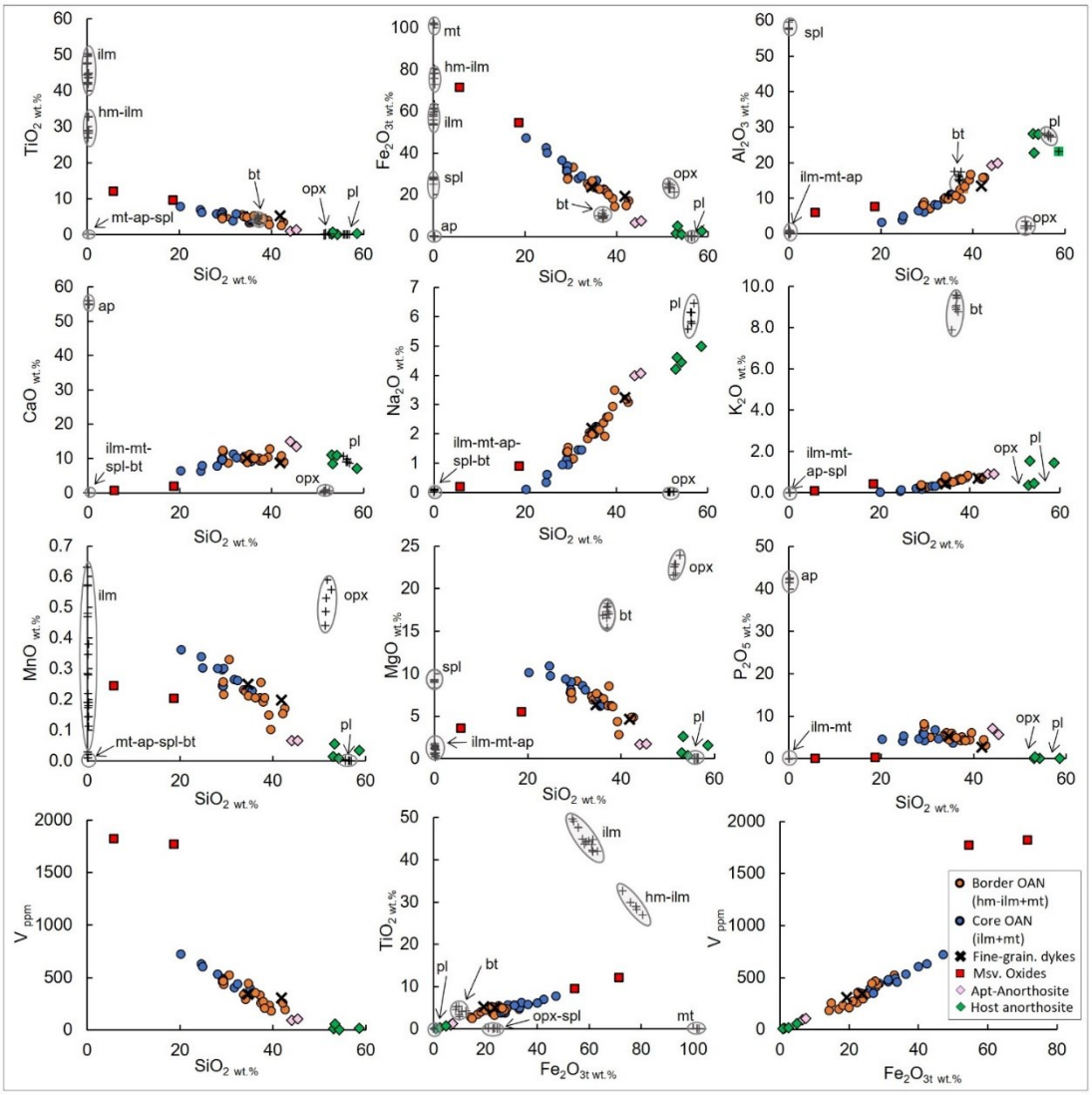

Figure 2.7. Whole-rock variation diagrams for the Lac à l'Orignal Fe-Ti-P deposit with the major mineral compositions plotted from electron microprobe and SEM data. Mineral abbreviations: pl = plagioclase; opx = orthopyroxene; bt = biotite; hm-ilm = hemo-ilmenite; ilm = ilmenite; mt = magnetite; ap = apatite; spl = Al-spinel; hbl = hornblende. OAN = oxide-apatite-norite; Msv.oxides = massive oxides; Fine-grain. Dykes = fine-grained ferrodiorite dykes.

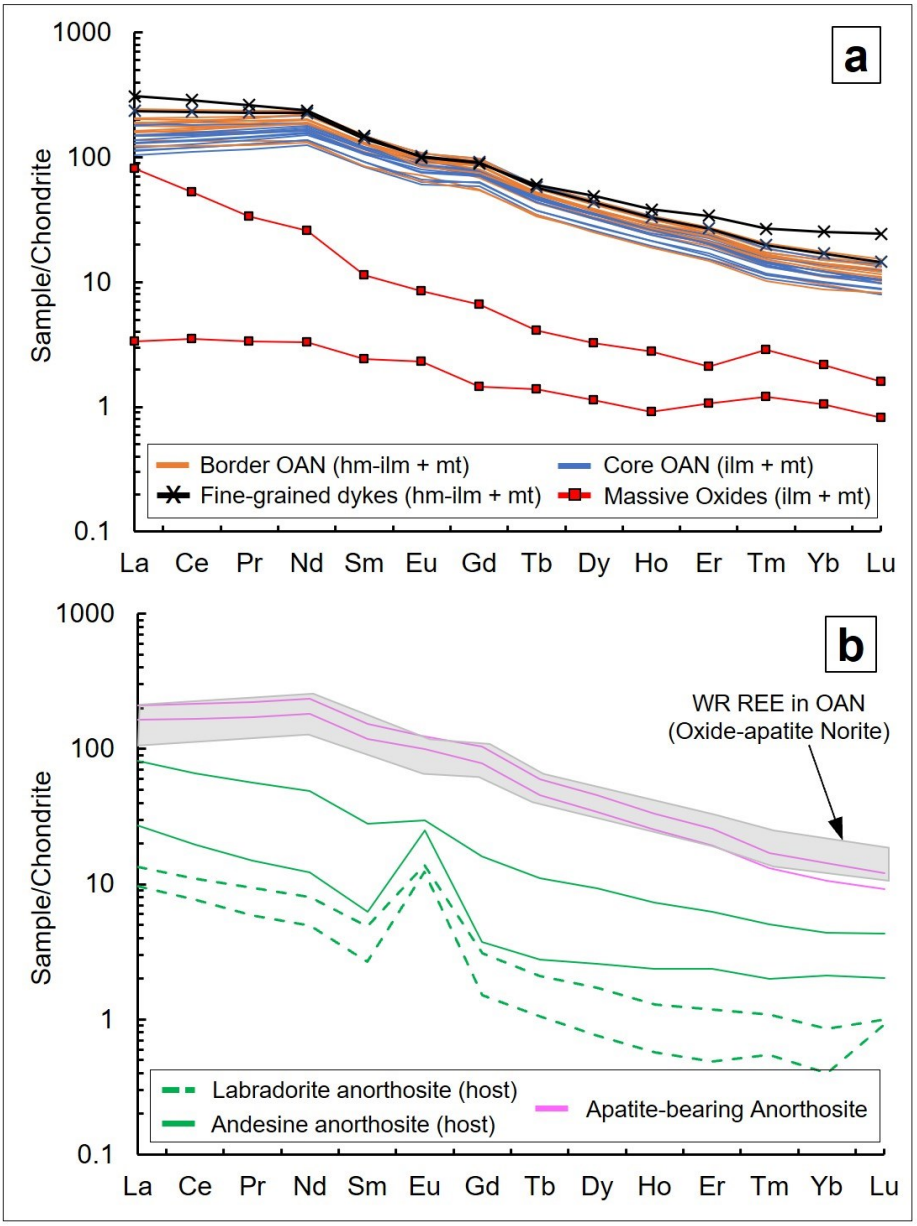

Figure 2.8. Chondrite-normalized REE compositions of whole-rock samples (normalized to chondrite; Sun and McDonough, 1989). a Mineralized samples: border and core OAN, massive oxides and fine-grained dykes. b Comparison between anorthosite samples (host and apatite-bearing layers) and the mineralized OAN from Fig. 8b (grey field). Mineral abbreviations: hm-ilm = hemo-ilmenite; ilm = ilmenite; mt = magnetite.

Table 2.2. Representative LA-ICP-MS Whole-rock major and trace element compositions (by LA-ICP-MS)

Sample	Depth (m)	Location	Lithology	Oxides	SiO_2	TiO_2	Al_2O_3	Fe_2O_{3t}	MnO	MgO	CaO	Na_2O	K_2O	P_2O_5	LOI	Total
LO-01	3.70	LO-14-21	Medium-grained OAN	Hm-ilm + Mt	42.6	3.4	15.8	17.0	0.2	4.9	9.1	3.1	0.7	3.1	0.3	100.0
LO-05	6.40	LO-14-21	Coarse-grained OAN	Hm-ilm + Mt	39.2	4.0	15.2	18.2	0.1	4.3	10.4	2.9	0.7	4.5	0.4	100.0
LO-06	6.80	LO-14-21	Fine-grained OAN dyke	Hm-ilm + Mt	34.6	5.1	10.9	23.7	0.2	6.3	10.2	2.2	0.4	5.3	1.1	100.0
LO-07	8.50	LO-14-21	Medium-grained OAN	Hm-ilm + Mt	39.6	2.8	16.8	14.2	0.1	2.8	12.8	3.5	0.8	6.1	0.4	100.0
LO-08	8.60	LO-14-21	Fine-grained-OAN dyke	Hm-ilm	41.8	5.2	13.5	19.3	0.2	4.6	8.8	3.2	0.7	2.7	0.0	100.0
LO-10	10.50	LO-14-21	Medium-grained OAN	Hm-ilm + Mt	30.6	4.7	7.1	33.1	0.3	9.1	8.7	1.1	0.3	5.0	0.0	100.0
LO-16	16.40	LO-14-21	Coarse-grained OAN	Hm-ilm + Mt	33.7	5.5	9.8	25.2	0.2	7.3	10.0	1.8	0.5	5.7	0.2	100.0
LO-18	19.50	LO-14-21	Medium-grained OAN	Hm-ilm + Mt	37.2	3.8	12.4	22.6	0.2	6.2	10.1	2.4	0.6	4.2	0.3	100.0
LO-22	21.50	LO-14-21	Coarse-grained OAN	Hm-ilm + Mt	37.4	4.4	9.8	22.2	0.3	8.5	9.3	1.9	0.6	5.1	0.5	100.0
LO-23	22.70	LO-14-21	Medium-grained OAN	Hm-ilm + Mt	34.1	5.0	10.2	23.9	0.2	6.9	10.6	2.0	0.5	6.1	0.5	100.0
LO-24	28.20	LO-14-21	Medium-grained OAN	Hm-ilm + Mt	37.9	4.6	12.6	21.0	0.2	6.2	9.3	2.6	0.7	4.4	0.4	100.0
LO-25	32.20	LO-14-21	Medium-grained OAN	Ilm + Mt	35.2	3.3	10.9	23.4	0.2	7.3	11.1	2.0	0.4	6.0	0.1	100.0
LO-26	36.30	LO-14-21	Medium-grained OAN	Ilm + Mt	35.2	3.8	11.1	26.0	0.2	7.2	9.5	2.0	0.5	4.5	0.1	100.0
LO-29	42.40	LO-14-21	Medium-grained OAN	Ilm + Mt	31.7	3.8	8.2	27.6	0.3	8.6	11.3	1.5	0.3	6.8	0.0	100.0
LO-32	48.70	LO-14-21	Medium-grained OAN	Ilm + Mt	29.1	5.0	7.2	33.2	0.3	8.9	9.5	1.1	0.3	5.4	0.0	100.0
LO-34	56.70	LO-14-21	Medium-grained OAN	Ilm + Mt	29.4	6.3	6.1	33.8	0.3	9.0	9.8	0.9	0.2	4.2	0.0	100.0
LO-37	61.20	LO-14-21	Medium-grained OAN	Ilm + Mt	32.4	5.7	8.1	28.7	0.3	8.1	10.3	1.4	0.3	4.7	0.0	100.0
LO-38	62.20	LO-14-21	Apatite-bearing Anorthosite	-	44.1	0.9	19.2	6.5	0.1	1.7	15.0	4.0	0.9	7.1	0.6	100.0
LO-39	63.40	LO-14-21	Medium-grained OAN	Ilm + Mt	20.2	7.8	3.3	47.2	0.4	10.1	6.4	0.1	0.0	4.6	0.0	100.0
LO-40	67.50	LO-14-21	Medium-grained OAN	Ilm + Mt	28.1	5.8	6.5	36.3	0.3	9.3	7.8	0.9	0.2	4.6	0.0	100.0
LO-41B	70.10	LO-14-21	Coarse-grained-OAN	Ilm + Mt	35.6	4.0	11.0	26.9	0.2	6.2	9.1	2.3	0.6	3.7	0.4	100.0
LO-43	75.70	LO-14-21	Medium-grained OAN	Ilm + Mt	24.6	7.0	3.9	42.5	0.3	10.9	6.2	0.3	0.1	4.2	0.0	100.0
LO-44-2	77.00	LO-14-21	Apatite-bearing Anorthosite	-	45.4	1.3	19.9	7.4	0.1	1.7	13.5	4.1	0.9	5.6	0.2	100.0
LO-46	79.00	LO-14-21	Medium-grained OAN	Ilm + Mt	24.8	6.2	5.0	40.0	0.3	9.7	7.9	0.6	0.1	5.3	0.0	100.0
LO-49	87.80	LO-14-21	Medium-grained OAN	Ilm + Mt	29.1	5.7	8.3	31.2	0.2	7.8	10.0	1.4	0.3	6.1	0.0	100.0
LO-50	91.20	LO-14-21	Medium-grained OAN	Ilm + Mt	29.2	5.6	8.4	31.2	0.2	8.1	9.6	1.4	0.3	5.8	0.0	100.0
LO-51	95.80	LO-14-21	Medium-grained OAN	Hm-ilm + Mt	29.4	4.8	8.9	28.2	0.2	7.0	12.0	1.5	0.4	7.5	0.0	100.0
LO-55	99.70	LO-14-21	Medium-grained OAN	Hm-ilm + Mt	42.2	2.5	15.8	14.8	0.2	4.8	10.8	3.2	0.7	4.4	0.6	100.0
LO-57	102.10	LO-14-21	Medium-grained OAN	Hm-ilm + Mt	29.3	4.5	8.1	27.5	0.3	7.7	12.4	1.4	0.4	8.2	0.4	100.0
LO-58	105.40	LO-14-21	Anorthosite	-	53.0	0.2	28.1	1.3	0.0	0.7	11.1	4.2	0.4	0.1	1.0	100.0
LO-59	108.50	LO-14-21	Anorthosite	-	54.2	0.1	28.0	0.9	0.0	0.3	10.9	4.4	0.5	0.0	0.6	100.0
20PM02	0.00	Surface	Medium-grained OAN	Hm-ilm + Mt	34.7	4.9	9.8	26.6	0.2	7.7	8.8	2.0	0.8	4.5	-0.1	100.0
20PM03	0.00	Surface	Massive oxides in anorthosite	Ilm + Mt	18.7	9.5	7.6	54.5	0.2	5.5	1.9	0.9	0.4	0.3	-0.4	100.0
20PM03B	0.00	Surface	Anort. Hosting massive oxides	-	53.3	0.7	22.7	4.8	0.1	2.6	8.5	4.6	1.5	0.4	0.7	100.0

OAN = Oxide-apatite norite; Anort = Anorthosite; Hm-ilm = hemo-ilmenite; Ilm = ilmenite; Mt = magnetite. UTM Coordinates: borehole LO-14-21: 384535E/5437021N; LO-12-10: 384713E/5436961N; LO-12-25: 384445E/5436975N; LO-12-31: 385824E/5436863N; LO-12-13: 384730E/5436854N; 20PM02: 384943E/5436888N; 20PM03: 386644E/5436738N. Eu/Eu* = (Eu)n/[(Sm)n x (Gd)n]0.5 calculated with Chondrite normalization values of Sun & McDonough (1989).

Table 2.2. (cont.) Representative LA-ICP-MS Whole-rock major and trace element compositions (by LA-ICP-MS)

Sample	Depth (m)	Location	Lithology	Oxides	V	Cr	Ni	Sr	Y	Zr	La	Ce	Eu/Eu*
LO-01	3.70	LO-14-21	Medium-grained OAN	Hm-ilm + Mt	195	30	29	1296	28	75	33	84	1.0
LO-05	6.40	LO-14-21	Coarse-grained OAN	Hm-ilm + Mt	234	31	50	1320	38	101	42	109	1.0
LO-06	6.80	LO-14-21	Fine-grained OAN dyke	Hm-ilm + Mt	342	31	53	891	48	110	56	142	0.9
LO-07	8.50	LO-14-21	Medium-grained OAN	Hm-ilm + Mt	181	18	42	1514	55	53	62	161	1.0
LO-08	8.60	LO-14-21	Fine-grained-OAN dyke	Hm-ilm	307	44	41	1126	56	412	73	176	0.8
LO-10	10.50	LO-14-21	Medium-grained OAN	Hm-ilm + Mt	522	180	239	542	47	124	37	102	0.7
LO-16	16.40	LO-14-21	Coarse-grained OAN	Hm-ilm + Mt	338	23	39	899	43	72	45	118	0.9
LO-18	19.50	LO-14-21	Medium-grained OAN	Hm-ilm + Mt	333	80	168	1023	37	23	35	93	0.9
LO-22	21.50	LO-14-21	Coarse-grained OAN	Hm-ilm + Mt	259	17	25	811	49	370	58	148	0.8
LO-23	22.70	LO-14-21	Medium-grained OAN	Hm-ilm + Mt	292	15	45	959	46	117	49	128	0.9
LO-24	28.20	LO-14-21	Medium-grained OAN	Hm-ilm + Mt	272	16	41	1164	35	161	38	98	1.0
LO-25	32.20	LO-14-21	Medium-grained OAN	Ilm + Mt	350	137	141	912	41	39	39	105	0.9
LO-26	36.30	LO-14-21	Medium-grained OAN	Ilm + Mt	395	125	115	870	36	90	35	92	0.9
LO-29	42.40	LO-14-21	Medium-grained OAN	Ilm + Mt	405	152	134	721	48	53	43	118	0.9
LO-32	48.70	LO-14-21	Medium-grained OAN	Ilm + Mt	493	161	114	555	38	40	33	90	0.9
LO-34	56.70	LO-14-21	Medium-grained OAN	Ilm + Mt	455	36	42	437	38	66	28	78	0.9
LO-37	61.20	LO-14-21	Medium-grained OAN	Ilm + Mt	441	30	46	621	38	163	31	83	0.9
LO-38	62.20	LO-14-21	Apatite-bearing Anorthosite	-	91	38	16	1617	47	28	50	131	1.0
LO-39	63.40	LO-14-21	Medium-grained OAN	Ilm + Mt	722	146	102	162	31	128	27	73	0.8
LO-40	67.50	LO-14-21	Medium-grained OAN	Ilm + Mt	533	66	58	471	30	70	27	73	0.9
LO-41B	70.10	LO-14-21	Coarse-grained-OAN	Ilm + Mt	350	23	20	947	42	26	44	112	0.9
LO-43	75.70	LO-14-21	Medium-grained OAN	Ilm + Mt	632	70	77	241	28	69	25	68	0.8
LO-44-2	77.00	LO-14-21	Apatite-bearing Anorthosite	-	107	32	23	1626	37	77	39	102	1.0
LO-46	79.00	LO-14-21	Medium-grained OAN	Ilm + Mt	604	34	53	365	34	113	31	85	0.8
LO-49	87.80	LO-14-21	Medium-grained OAN	Ilm + Mt	460	50	61	678	38	95	36	97	0.9
LO-50	91.20	LO-14-21	Medium-grained OAN	Ilm + Mt	478	30	52	688	37	128	35	95	0.9
LO-51	95.80	LO-14-21	Medium-grained OAN	Hm-ilm + Mt	435	35	51	782	47	64	44	121	0.9
LO-55	99.70	LO-14-21	Medium-grained OAN	Hm-ilm + Mt	256	70	72	1231	35	102	41	101	1.0
LO-57	102.10	LO-14-21	Medium-grained OAN	Hm-ilm + Mt	466	30	92	697	40	65	38	102	0.8
LO-58	105.40	LO-14-21	Anorthosite	-	14	22	19	639	2	10	3	7	3.5
LO-59	108.50	LO-14-21	Anorthosite	-	6	16	13	663	1	3	2	5	5.9
20PM02	0.00	Surface	Medium-grained OAN	Hm-ilm + Mt	442	24	21	698	28	110	29	76	0.9
20PM03	0.00	Surface	Massive oxides in anorthosite	Ilm + Mt	1769	943	337	247	4	59	19	32	0.9
20PM03B	0.00	Surface	Anort. Hosting massive oxides	-	58	87	56	510	11	134	19	41	1.3

2.5.5 Mineral chemistry

The mineral compositions of plagioclase, apatite, (hemo)ilmenite and magnetite determined by LA-ICP-MS, for mineralized rocks and host rocks of Lac à l'Orignal, are presented in Tables 2.3 - 2.6 (with full results in Appendix 2.1 & 2.3). The stratigraphic variation of selected elements is presented in Figure 2.9.

Plagioclase from the OAN mineralization (both coarse-grained and pegmatitic pockets) are K-rich andesine in composition (Fig.2.9a), varying from $An_{39.4}$ to $An_{50.1}$ and from $Or_{0.7}$ to $Or_{7.9.}$ They have Sr (1501 to 2337 ppm) and Ba (193 to 1016 ppm) compositions that are higher compared to plagioclase (An_{58}, $Or_{1.3}$ to $Or_{2.9}$) in the host labradorite-type anorthosite below the mineralization (Sr contents of 631 -644 ppm and Ba of 90 – 93 ppm). Plagioclase from the apatite-bearing anorthosite layers within the mineralized zone ($An_{44.7}$ to $An_{45.3}$, $Or_{3.2}$ to $Or_{3.4}$, Sr = 2005 -2154 ppm and Ba = 322 – 343 ppm) are similar in composition to plagioclase from the OAN. However, at the same stratigraphic level, the Sr and Ba content of plagioclase from the apatite-bearing anorthosite layers are significantly lower than those from the adjacent OAN. Comparing the borders (dominated by hm-ilmenite + magnetite) with the core of the intrusion (dominated by Fe-poor ilmenite + magnetite) relatively constant An, Or and Sr values are observed, whereas Ba is relatively enriched in the core of the intrusion (Fig.2.9a). However, Or contents are erratically higher (< 10) in the lower-border of the intrusion, due to the presence of K-rich exsolutions. Apatite trace element concentrations (Fig.2.9b) are overall fairly similar for the coarse-grained OAN, pegmatitic OAN and apatite-bearing anorthosite levels within the mineralized zone.

The Sr values in apatite varies from 679 to 1501 ppm, with the lowest values at the outer borders of the intrusion and relatively higher Sr values (1300 ppm) in the

core of the intrusion (around 65 – 78m). This subtle variation for Sr in apatite matches that for Sr in plagioclase, which has higher Sr content than that of apatite. The massive nelsonite layer has apatite with an exceptionally high Sr content within the upper border (1501 ppm) but contains no plagioclase to compare with. The REE content of apatite slightly increases up-section from the bottom (1407 ppm: sample LO-57) to the upper border (2769 ppm: LO-01). Moreover, Eu/Eu* values are constant throughout the core and reaches lower values in the borders, particularly where overall abundance in REE is higher.

The REE contents of apatite, normalized to chondrite (Fig.2.10a), show very similar shaped patterns for the OAN samples from the border (hm-ilm + mt) and core (ilm + mt) indicating that they probably formed from a similar magma composition. Both are characterized by weak negative Eu anomalies (Eu/Eu^{*} = 0.63 – 0.83) and LREE enrichment (La/Yb_N = 12.7 - 17.7), typical of igneous apatite. The apatite REE patterns from the fine-grained OAN dykes are similar to apatite REE patterns from the mineralization (Fig.2.10a). In particular, the dyke with the lower abundance of REE (sample LO-06) has identical REE and Sr composition as the most REE-enriched apatite from the border zone, indicating that this is similar to the parental melt of the mineralization. However, the dyke (sample LO-08) that is most enriched in REE, has a larger negative Eu anomaly (Eu/Eu^{*} = 0.51 and La/Yb_N = 9.5) and lower Sr (680 ppm), typical of a more evolved melt. The similarity of the chondrite-normalized REE patterns of whole-rock analyses with the apatite analyzes (Fig.2.10b) indicates that the REE content of the Lac a l'Orignal deposit is controlled by apatite crystallization.

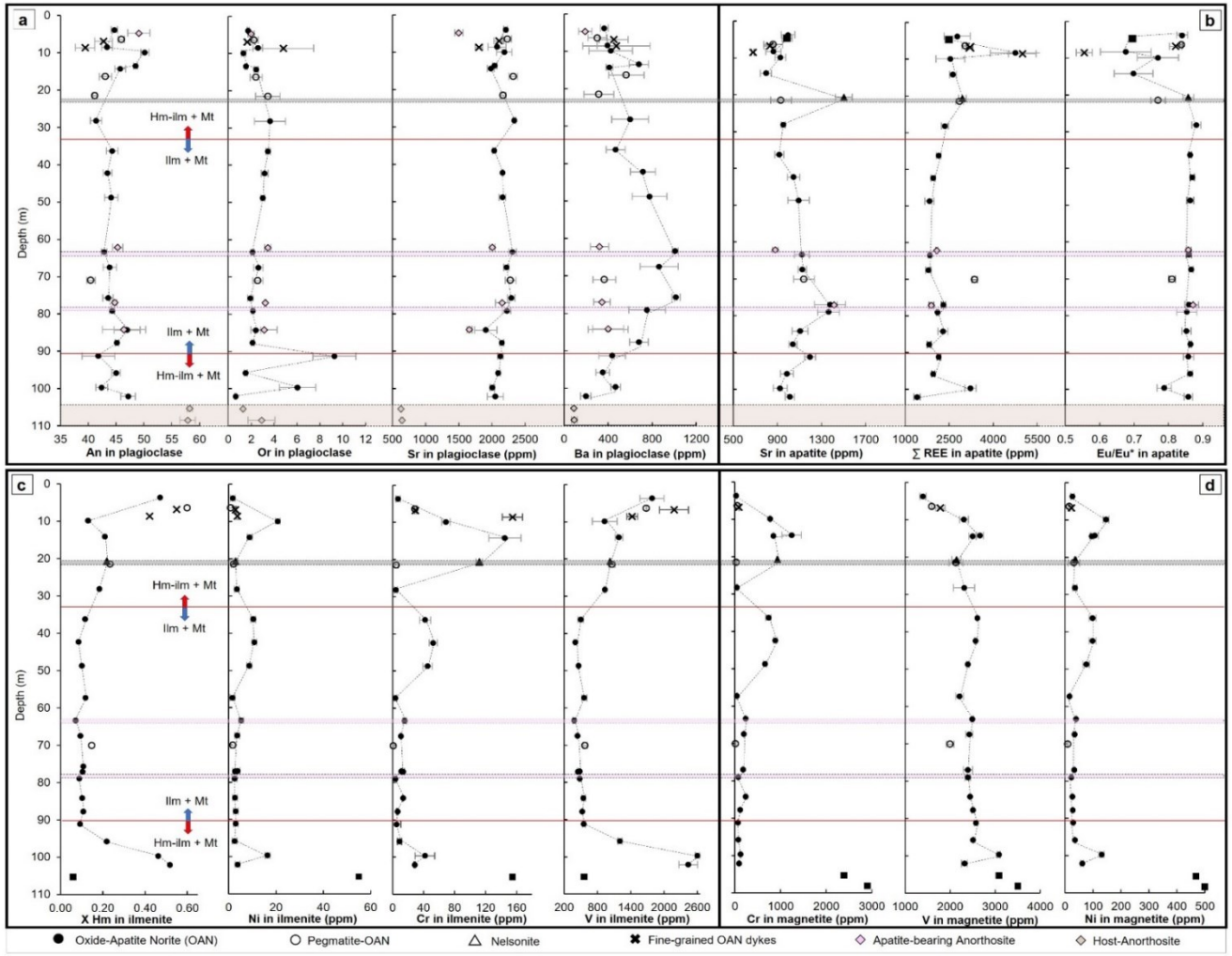

Figure 2.9. Stratigraphic variation of plagioclase (a), apatite (b), ilmenite (c) magnetite (d) compositions in drillcore LO-14-21. The grey horizon represents the nelsonite (iap-C) layer. The pink horizons represent the apatite-bearing anorthosite (pa-C) layers and the brownish horizon the host anorthosite. Red lines indicate the oxide assemblage changing from Hm-ilmenite to Fe-poor ilmenite towards the core of the intrusion. Error bars = 1 standard deviation and represents the natural variation within the thin section. Mineral abbreviations: hm-ilm = hemo-ilmenite; ilm = ilmenite; mt = magnetite.

Table 2.3. Representative LA-ICP-MS major and trace element analyses of plagioclase for samples the Lac à l'Orignal Fe-Ti-P deposit

Detection Limits (33-55µm)														0.058-0.245	0.515-0.809	0.005-0.013	0.003-1.838	0.001-0.023
Sample	Depth (m)	Lithology	Oxides	# analysis	SiO_2	Al_2O_3	CaO	Na_2O	K_2O	Total	An	Ab	Or	^{88}Sr	^{137}Ba	^{139}La	^{140}Ce	^{153}Eu
LO-01	3.7	Medium-grained OAN	Hm-ilm + Mt	n=5	56.1	28.1	8.7	5.7	0.3	99.0	44.7	53.6	1.7	2209	365	6	9	2
LO-02	4.7	Anorthosite	-	n=5	54.8	29.2	9.4	5.2	0.3	99.1	49.1	48.9	2.0	1501	193	7	11	1
LO-05	6.4	Coarse-grained OAN	Hm-ilm + Mt	n=5	56.2	28.1	8.8	5.5	0.4	99.2	45.9	51.8	2.3	2233	303	8	11	2
LO-06	6.8	Fine-grained OAN dyke	Hm-ilm + Mt	n=5	56.6	28.0	8.3	6.0	0.3	99.3	42.7	55.6	1.7	2106	450	8	11	2
LO-07	8.5	Medium-grained OAN	Hm-ilm + Mt	n=5	56.7	27.8	8.4	5.8	0.4	99.2	43.3	54.1	2.6	2078	393	11	16	2
LO-08	8.6	Fine-grained-OAN dyke	Hm-ilm		57.7	27.0	7.6	5.9	0.8	99.1	39.4	55.7	4.8	1803	475	16	21	2
LO-09	9.9	Medium-grained OAN	Hm-ilm + Mt	n=5	54.6	29.3	9.6	5.2	0.2	99.1	50.1	48.5	1.3	2187	424	7	10	1
LO-15-1	14.2	Medium-grained OAN	Hm-ilm + Mt	n=4	55.0	29.0	9.4	5.3	0.3	99.1	48.5	50.0	1.5	2040	680	6	9	1
LO-15-2	14.4	Medium-grained OAN	Hm-ilm + Mt	n=5	55.7	28.5	8.8	5.5	0.4	99.1	45.7	51.8	2.4	1985	412	7	11	1
LO-16	16.4	Coarse-grained-OAN	Hm-ilm + Mt	n=5	56.8	27.7	8.3	5.8	0.4	99.2	43.1	54.5	2.4	2322	566	6	8	2
LO-22	21.5	Coarse-grained OAN	Hm-ilm + Mt	n=5	57.1	27.5	8.0	5.9	0.6	99.2	41.2	55.4	3.5	2171	315	6	9	2
LO-24	28.2	Medium-grained OAN	Hm-ilm + Mt	n=4	56.9	27.8	8.0	5.9	0.6	99.3	41.4	55.0	3.6	2337	600	5	8	2
LO-26	36.3	Medium-grained OAN	Ilm + Mt	n=5	56.3	28.1	8.5	5.5	0.6	99.2	44.3	52.2	3.5	2035	468	5	7	2
LO-29	42.4	Medium-grained OAN	Ilm + Mt	n=5	56.4	28.1	8.4	5.7	0.5	99.2	43.5	53.4	3.2	2158	715	5	8	1
LO-32	48.7	Medium-grained OAN	Ilm + Mt	n=6	56.2	28.2	8.5	5.6	0.5	99.2	44.1	52.9	3.0	2159	776	4	7	1
LO-38	62.2	Apatite-bearing Anorthosite	-	n=5	56.2	28.4	8.6	5.4	0.6	99.3	45.3	51.3	3.4	2006	322	4	6	2
LO-39	63.4	Medium-grained OAN	Ilm + Mt	n=5	56.3	28.1	8.3	5.9	0.3	99.1	42.8	55.1	2.1	2309	1008	4	7	1
LO-40	67.5	Medium-grained OAN	Ilm + Mt	n=6	56.1	28.3	8.5	5.7	0.4	99.2	43.8	53.5	2.6	2218	863	4	7	1
LO-41B	70.1	Coarse-grained OAN	Ilm + Mt	n=6	57.2	27.6	7.8	6.1	0.4	99.4	40.5	56.9	2.6	2279	366	8	11	2
LO-43	75.7	Medium-grained OAN	Ilm + Mt	n=4	56.3	28.2	8.3	5.8	0.3	99.1	43.5	54.5	1.9	2290	1016	4	7	1
LO-44-2	77.0	Apatite-bearing Anorthosite	-	n=5	56.6	28.1	8.5	5.5	0.5	99.3	44.7	52.0	3.2	2154	343	4	7	2
LO-46	79.0	Medium-grained OAN	Ilm + Mt	n=5	56.5	28.2	8.5	5.7	0.3	99.4	44.3	53.6	2.1	2224	753	4	7	1
LO-47-1	84.2	Medium-grained OAN	Ilm + Mt	n=5	55.6	28.7	9.0	5.3	0.4	99.2	47.0	50.6	2.4	1907	402	5	7	1
LO-47-2	84.3	Anorthosite	-	n=5	56.0	28.7	8.8	5.3	0.5	99.4	46.4	50.5	3.1	1661	401	7	10	2
LO-49	87.8	Medium-grained OAN	Ilm + Mt	n=5	56.2	28.4	8.6	5.6	0.3	99.3	45.2	52.7	2.1	2150	679	4	7	1
LO-50	91.2	Medium-grained OAN	Ilm + Mt	n=4	56.5	27.8	8.5	5.7	1.4	99.9	41.8	50.3	7.9	2127	436	4	6	1
LO-51	95.8	Medium-grained OAN	Hm-ilm + Mt	n=6	56.4	28.2	8.6	5.7	0.2	99.3	45.0	53.5	1.5	2096	351	4	7	1
LO-55	99.7	Medium-grained OAN	Hm-ilm + Mt	n=4	56.5	27.7	8.4	5.6	1.0	99.3	42.4	51.6	6.1	2006	467	7	10	2
LO-57	102.1	Medium-grained OAN	Hm-ilm + Mt	n=6	55.4	28.9	9.1	5.6	0.1	99.2	47.1	52.2	0.7	2053	197	4	6	1
LO-58	105.4	Anorthosite	-	n=6	52.3	31.2	11.0	4.2	0.2	99.2	58.2	40.5	1.3	631	90	1	3	1
LO-59	108.5	Anorthosite	-	n=4	53.4	30.2	11.5	4.3	0.5	100.1	57.9	39.2	2.9	645	93	1	3	Below DL
20PM02	0.0	Medium-grained OAN	Hm-ilm + Mt	n=5	56.4	29.3	9.5	5.6	0.4	101.3	47.1	50.7	2.2	2274	414	5	8	2
20PM03B	0.0	Massive oxides in anorthosite	Ilm + Mt	n=5	55.6	30.7	10.6	5.4	0.1	102.4	49.7	49.6	0.7	2129	189	13	21	2

Major elements in wt.%, An=100 [Ca/(Ca+Na+K)]; Ab=100 [Na/(Ca+Na+K)]; Or=100 [K/(Ca+Na+K)]; trace element in ppm. OAN = Oxide-apatite norite; Hm-ilm = hemo-ilmenite; Ilm = ilmenite; Mt = magnetite.

Table 2.4. Representative LA-ICP-MS major and trace element analyses of apatite for samples the Lac à l'Orignal Fe-Ti-P deposit

Detection Limits (33-55µm bean size)					0.01-0.07	0.01-0.02	0.003-0.014	0.003-0.012	0.002-0.008	0.012-0.030	0.013-0.021	0.003-0.009	0.015-0.057	0.002-0.004	0.006-0.015	0.002-0.004	0.009-0.027	0.002-0.003
Sample	Depth (m)	Lithology	Oxide Mineralogy	# analysis	^{88}Sr	^{89}Y	^{139}La	^{140}Ce	^{141}Pr	^{146}Nd	^{147}Sm	^{153}Eu	^{157}Gd	^{159}Tb	^{166}Er	^{169}Tm	^{172}Yb	^{175}Lu
LO-01	4	Medium-grained OAN	Hm-ilm + Mt	n=4	997	369	326	957	155	799	168	42	151	17	32	3	17	2
LO-02	5	Massive Apatite	-	n=4	987	268	356	952	140	655	126	25	109	12	24	3	14	2
LO-05	6	Coarse-grained OAN	Hm-ilm + Mt	n=4	862	379	388	1095	171	852	176	44	155	17	33	3	18	2
LO-06	7	Fine-grained OAN dyke	Hm-ilm + Mt	n=4	831	414	408	1140	179	889	183	44	161	18	38	4	23	3
LO-07	9	Medium-grained OAN	Hm-ilm + Mt	n=6	864	609	690	1825	263	1210	237	45	201	24	57	7	37	5
LO-08	9	Fine-grained OAN dyke	Hm-ilm	n=3	679	763	637	1794	281	1351	283	45	247	30	72	8	46	6
LO-09	10	Medium-grained OAN	Hm-ilm + Mt	n=4	928	336	344	911	140	687	143	32	129	14	29	3	17	2
LO-15-1	14	Medium-grained OAN	Hm-ilm + Mt	n=4	796	333	353	955	146	713	148	29	130	15	30	3	17	2
LO-21	21	Medium-grained Nelsonite	Hm-ilm + Mt	n=4	1501	381	404	1052	161	794	170	43	150	17	34	4	22	3
LO-22	22	Coarse-grained-OAN	Hm-ilm + Mt	n=4	933	349	394	1031	160	771	159	36	139	16	31	3	18	2
LO-24	28	Medium-grained OAN	Hm-ilm + Mt	n=4	953	289	307	826	129	655	138	36	122	13	26	3	14	2
LO-26	36	Medium-grained OAN	Ilm + Mt	n=4	917	286	265	720	117	620	132	34	119	13	25	3	14	2
LO-29	42	Medium-grained OAN	Ilm + Mt	n=4	1047	251	241	662	108	566	121	31	109	12	22	2	11	1
LO-32	49	Medium-grained OAN	Ilm + Mt	n=4	1092	234	227	620	100	532	114	29	102	11	20	2	10	1
LO-38	62	Apatite-bearing Anorthosite	-	n=4	881	263	260	708	113	597	128	33	114	12	23	2	12	2
LO-39	63	Medium-grained OAN	Ilm + Mt	n=4	1123	229	232	630	101	532	112	29	101	11	20	2	10	1
LO-40	68	Medium-grained OAN	Ilm + Mt	n=4	1126	227	221	609	99	522	111	29	100	11	20	2	10	1
LO-41B	70	Coarse-grained-OAN	Ilm + Mt	n=4	1141	419	458	1203	186	925	191	46	168	18	37	4	21	3
LO-43	76	Medium-grained OAN	Ilm + Mt	n=4	1377	281	289	785	125	664	142	36	127	13	25	2	14	2
LO-44-2	77	Apatite-bearing anorthosite	-	n=4	1414	238	235	647	104	547	115	30	103	11	21	2	11	1
LO-46	79	Medium-grained OAN	Ilm + Mt	n=4	1364	254	264	714	115	605	129	33	117	12	23	2	12	1
LO-47	84	Medium-grained OAN	Ilm + Mt	n=4	1105	285	298	786	124	641	140	36	127	13	27	3	15	2
LO-49	88	Medium-grained OAN	Ilm + Mt	n=4	1040	228	226	625	101	524	111	29	99	11	20	2	10	1
LO-50	91	Medium-grained OAN	Ilm + Mt	n=3	1196	259	271	734	116	616	131	34	119	13	23	2	12	2
LO-51	96	Medium-grained OAN	Hm-ilm + Mt	n=4	986	249	244	671	108	562	120	31	107	12	22	2	11	2
LO-55	100	Medium-grained OAN	Hm-ilm + Mt	n=4	924	382	447	1159	175	872	180	42	158	18	36	4	21	3
LO-57	102	Medium-grained OAN	Hm-ilm + Mt	n=4	1013	187	163	463	77	423	91	23	82	9	15	2	8	1
20PM02	0	Medium-grained OAN	Hm-ilm + Mt	n=13	872	281	277	766	120	643	136	34	132	14	24	3	13	2

OAN = Oxide-apatite norite; Hm-ilm = hemo-ilmenite; Ilm = ilmenite; Mt = magnetite

Table 2.5. Representative LA-ICP-MS major and trace element analyses of ilmenite for samples the Lac à l'Orignal Fe-Ti-P deposit

Detection Limits (33-55µm)															0.035-0.296	0.952-3.179	0.551-1.198
Sample	Depth (m)	Lithology	Oxides	# analysis	TiO_2	Fe_2O_3	FeO	MnO	MgO	Total	X_{geik}	X_{pyr}	X_{hem}	X_{ilm}	^{51}V	^{53}Cr	^{60}Ni
LO-01	3.7	Medium-grained OAN	Hm-ilm + Mt	n=4	28.22	50.27	25.17	0.12	0.24	99.27	0.009	0.003	0.472	0.522	1781.3	7.1	1.7
LO-05	6.4	Coarse-grained OAN	Hm-ilm + Mt	n=3	21.53	64.50	19.00	0.20	0.36	99.52	0.013	0.004	0.600	0.389	1683.2	29.0	0.8
LO-06	6.8	Fine-grained OAN dyke	Hm-ilm + Mt	n=4	24.37	59.09	21.85	0.13	0.22	100.00	0.008	0.003	0.549	0.445	2179.9	29.6	2.9
LO-08	8.6	Fine-grained OAN dyke	Hm-ilm	n=4	31.09	45.06	26.57	0.24	0.79	99.43	0.029	0.005	0.421	0.564	1428.3	154.8	3.7
LO-09	9.9	Medium-grained OAN	Hm-ilm + Mt	n=3	46.15	12.71	38.97	0.75	1.59	100.52	0.059	0.016	0.131	0.859	931.9	68.8	20.7
LO-15-1	14.2	Medium-grained OAN	Hm-ilm + Mt	n=4	42.38	22.23	35.06	0.58	1.64	100.10	0.060	0.012	0.211	0.772	1188.2	144.9	8.8
LO-21	20.7	Medium-grained Nelsonite	Hm-ilm + Mt	n=3	41.60	23.22	34.45	0.46	1.49	98.98	0.055	0.010	0.219	0.765	1030.4	111.9	2.8
LO-22	21.5	Coarse-grained-OAN	Hm-ilm + Mt	n=3	40.55	24.70	35.09	0.28	0.75	99.08	0.028	0.006	0.235	0.757	1061.8	5.0	2.0
LO-24	28.2	Medium-grained OAN	Hm-ilm + Mt	n=4	43.72	19.58	36.83	0.51	1.24	100.13	0.046	0.011	0.185	0.804	937.0	4.2	3.4
LO-26	36.3	Medium-grained OAN	Ilm + Mt	n=4	47.26	12.35	38.42	0.87	1.91	99.83	0.071	0.018	0.117	0.871	503.7	42.2	10.4
LO-29	42.4	Medium-grained OAN	Ilm + Mt	n=3	50.97	9.35	41.11	1.00	2.22	104.01	0.079	0.020	0.086	0.904	399.3	52.5	10.9
LO-32	48.7	Medium-grained OAN	Ilm + Mt	n=3	49.36	10.95	39.68	0.98	2.22	102.43	0.080	0.020	0.102	0.887	463.2	45.1	8.6
LO-35	57.3	Medium-grained OAN	Ilm + Mt	n=3	47.17	12.44	38.33	0.78	2.01	99.70	0.074	0.016	0.119	0.869	562.2	3.7	1.6
LO-39	63.4	Medium-grained OAN	Ilm + Mt	n=4	53.34	8.05	42.28	0.99	2.79	106.90	0.096	0.019	0.073	0.918	384.2	15.5	5.2
LO-40	67.5	Medium-grained OAN	Ilm + Mt	n=3	50.08	10.54	40.04	0.87	2.35	102.92	0.084	0.018	0.096	0.893	438.6	10.8	3.6
LO-41B	70.1	Coarse-grained-OAN	Ilm + Mt	n=3	43.15	14.83	36.19	0.64	1.20	94.66	0.047	0.014	0.148	0.842	578.3	1.2	1.7
LO-43	75.7	Medium-grained OAN	Ilm + Mt	n=4	48.02	11.47	39.21	0.83	1.86	100.41	0.068	0.017	0.108	0.882	478.1	11.4	3.7
LO-44-1	77.1	Medium-grained OAN	Ilm + Mt	n=3	48.95	11.37	39.29	1.02	2.15	101.75	0.078	0.021	0.105	0.883	446.2	13.5	2.7
LO-46	79.0	Medium-grained OAN	Ilm + Mt	n=3	50.49	9.76	40.75	0.81	2.27	103.33	0.081	0.016	0.090	0.900	483.9	3.8	2.4
LO-47	84.2	Medium-grained OAN	Ilm + Mt	n=3	47.83	10.96	39.66	0.80	1.50	99.82	0.056	0.017	0.104	0.888	548.6	13.4	2.6
LO-49	87.8	Medium-grained OAN	Ilm + Mt	n=3	48.25	0.00	49.53	0.70	2.08	100.99	0.076	0.015	0.108	0.881	530.1	6.3	2.9
LO-50	91.2	Medium-grained OAN	Ilm + Mt	n=3	49.98	2.19	47.56	0.81	2.19	103.09	0.079	0.017	0.094	0.896	556.7	5.0	2.9
LO-51	95.8	Medium-grained OAN	Hm-ilm + Mt	n=4	41.77	23.34	34.94	0.51	1.29	99.71	0.048	0.011	0.220	0.767	1206.0	9.0	2.4
LO-55	99.7	Medium-grained OAN	Hm-ilm + Mt	n=5	28.94	49.41	25.76	0.12	0.40	100.12	0.015	0.003	0.463	0.529	2603.0	41.7	16.4
LO-57	102.1	Medium-grained OAN	Hm-ilm + Mt	n=5	25.87	55.35	22.61	0.13	0.53	99.19	0.020	0.003	0.518	0.470	2437.6	28.6	3.7
20PM02	0.0	Medium-grained OAN	Hm-ilm + Mt	n=5	44.60	14.99	36.73	0.60	1.62	98.75	0.062	0.013	0.145	0.843	772.5	5.6	2.6
20PM03	0.0	Massive oxides in anorthosite	Ilm + Mt	n=5	46.70	10.72	40.57	0.61	0.55	99.36	0.021	0.013	0.105	0.892	937.6	166.9	60.1

Major elements in wt.%, FeO and Fe2O3 recalculated from FeOt by charge balance equations; molar fractions of geikielite, pyrophanite, hematite and ilmenite (Xgeik, Xpyr, Xhem, Xilm) calculated following QUILF algorithm (Andersen et al.1993); trace element in ppm. OAN = Oxide-apatite norite; Hm-ilm = hemo-ilmenite; Ilm = ilmenite; Mt = magnetite.

Table 2.6. Representative LA-ICP-MS major and trace element analyses of magnetite for samples the Lac à l'Orignal Fe-Ti-P deposit

Detection Limits (33-55µm)														0.047-0.242	1.527-9.987	0.719-2.736
Sample	Depth (m)	Lithology	Oxides	# analysis	SiO_2	TiO_2	Al_2O_3	FeO_t	Fe_2O_3	FeO	MnO	MgO	Total	^{51}V	^{53}Cr	^{60}Ni
LO-01	3.7	Medium-grained OAN	Hm-ilm + Mt	n=3	0.40	0.06	0.40	91.98	67.47	31.27	0.01	0.06	99.98	1732.9	29.0	26.9
LO-05	6.4	Coarse-grained OAN	Hm-ilm + Mt	n=3	0.64	0.08	0.50	91.98	68.69	30.17	0.03	0.11	100.52	1596.8	54.6	14.6
LO-06	6.8	Fine-grained OAN dyke	Hm-ilm + Mt	n=3	0.20	0.09	0.49	91.98	67.30	31.42	0.01	0.07	99.89	1781.4	86.8	23.0
LO-09	9.9	Medium-grained OAN	Hm-ilm + Mt	n=3	0.41	0.10	0.62	91.98	68.97	29.92	0.02	0.16	100.66	2307.9	769.6	146.5
LO-15-1	14.2	Medium-grained OAN	Hm-ilm + Mt	n=3	0.04	0.09	0.47	91.98	67.70	31.06	0.02	0.14	100.11	2662.0	1243.9	105.4
LO-15-2	14.4	Medium-grained OAN	Hm-ilm + Mt	n=3	0.15	0.09	0.51	91.98	68.12	30.68	0.02	0.20	100.26	2499.7	842.8	95.8
LO-21	20.7	Medium-grained Nelsonite	Hm-ilm + Mt	n=3	0.00	0.09	0.49	91.98	67.39	31.35	0.01	0.14	99.94	2142.9	930.9	37.1
LO-22	21.5	Coarse-grained OAN	Hm-ilm + Mt	n=4	0.35	0.09	0.58	91.98	68.26	30.56	0.02	0.13	100.31	2133.3	28.1	31.8
LO-24	28.2	Medium-grained OAN	Hm-ilm + Mt	n=4	0.53	0.09	0.54	91.98	68.66	30.20	0.02	0.11	100.52	2313.0	39.5	35.4
LO-26	36.3	Medium-grained OAN	Ilm + Mt	n=3	0.04	0.60	1.03	91.98	70.97	28.12	0.05	0.30	101.61	2604.2	735.8	98.5
LO-29	42.4	Medium-grained OAN	Ilm + Mt	n=3	0.26	0.90	1.19	91.98	73.00	26.29	0.06	0.39	102.61	2568.4	886.3	98.6
LO-32	48.7	Medium-grained OAN	Ilm + Mt	n=3	0.16	0.24	0.64	91.98	68.80	30.08	0.03	0.20	100.59	2395.2	657.3	75.4
LO-35	57.3	Medium-grained OAN	Ilm + Mt	n=3	0.23	0.26	0.56	91.98	68.55	30.30	0.02	0.19	100.47	2206.2	43.9	15.7
LO-39	63.4	Medium-grained OAN	Ilm + Mt	n=4	0.27	0.90	1.02	91.98	72.18	27.04	0.06	0.36	102.23	2492.7	232.5	39.4
LO-40	67.5	Medium-grained OAN	Ilm + Mt	n=3	0.08	0.37	0.72	91.98	69.11	29.80	0.04	0.23	100.72	2426.5	194.7	33.8
LO-41B	70.1	Coarse-grained-OAN	Ilm + Mt	n=3	0.18	0.11	0.58	91.98	67.78	30.99	0.02	0.12	100.09	1999.2	14.5	9.3
LO-43	77	Medium-grained OAN	Ilm + Mt	n=3	0.09	0.46	0.76	91.98	69.49	29.45	0.04	0.24	100.91	2394.6	179.1	32.7
LO-44-1	77.1	Medium-grained OAN	Ilm + Mt	n=3	0.13	0.37	0.83	91.98	69.72	29.25	0.04	0.27	100.97	2219.5	200.3	26.7
LO-46	79	Medium-grained OAN	Ilm + Mt	n=3	0.14	0.43	0.86	91.98	70.08	28.92	0.03	0.30	101.14	2394.9	69.4	22.3
LO-47	84.2	Medium-grained OAN	Ilm + Mt	n=3	0.26	0.35	0.82	91.98	69.83	29.15	0.02	0.21	101.06	2444.8	232.1	26.8
LO-49	87.8	Medium-grained OAN	Ilm + Mt	n=3	0.46	0.34	0.88	91.98	70.83	28.25	0.03	0.30	101.48	2508.3	110.0	27.1
LO-50	91.2	Medium-grained OAN	Ilm + Mt	n=3	0.27	0.17	0.81	91.98	70.50	28.54	0.02	0.29	101.39	2575.6	64.1	29.2
LO-51	95.8	Medium-grained OAN	Hm-ilm + Mt	n=3	0.15	0.08	0.48	91.98	67.48	31.26	0.02	0.12	99.97	2510.4	71.3	35.4
LO-55	99.7	Medium-grained OAN	Hm-ilm + Mt	n=3	0.29	0.10	0.49	91.98	68.20	30.61	0.03	0.12	100.33	3080.4	121.2	197.9
LO-57	102.1	Medium-grained OAN	Hm-ilm + Mt	n=3	0.15	0.08	0.51	91.98	67.73	31.03	0.02	0.16	100.06	2318.5	90.5	61.1
20PM02	0.0	Medium-grained OAN	Hm-ilm + Mt	n=5	0.15	0.09	0.46	92.38	68.18	31.04	0.01	0.12	100.04	2254.3	64.1	26.2
20PM03	0.0	Massive oxides in anorthosite	Ilm + Mt	n=5	0.09	0.08	0.49	92.09	68.05	30.85	0.01	0.05	99.63	3041.1	1960.8	470.2

Major elements in wt.%, FeO and Fe2O3 recalculated from FeOt by charge balance equations; trace element in ppm; OAN = Oxide-apatite norite; Hm-ilm = hemo-ilmenite; Ilm = ilmenite; Mt = magnetite.

The fraction of hematite in ilmenite (Xhm) varies from 0.07 to 0.60, with the lower values in the core of the intrusion (31-92m depth), where hematite exsolutions are almost absent in ilmenite (Fig.2.9c). Higher Xhm contents are observed in the lower and upper borders of the intrusion, where coarse hematite exsolutions in hemo-ilmenite are common (Fig 2.5). The V (384 to 2603 ppm) concentrations of ilmenite follow an identical behaviour to that of the Xhm values, with higher V contents corresponding to higher hematite contents at the borders. In general, Ni (0.8 to 20.7 ppm) and Cr (3.7 to 157 ppm) are also higher in hemo-ilmenite from the borders, whereas MgO (0.2 to 2.8 wt.%) and MnO (0.12 to 1.0 wt.%) are typically lower in the borders than the core. Therefore, the trace element variation for (hemo)-ilmenite in the Lac à l'Orignal intrusion appears to be directly related with the presence or absence of hematite exsolutions, marking distinct geochemical patterns between the borders and the center of the intrusion. In the core some grains of hm-ilm (e.g., from 35 – 58m) have relatively high Ni, V and Cr contents that are similar to those observed at the borders, although lacking elevated Xhm. Relatively higher MgO, MnO, Ni and Cr values are observed above the nelsonite (iap-C) layer, at the top border of the intrusion. Such irregular patterns with reversals to more primitive compositions within the intrusion may indicate the presence of magma reinjections. Ilmenite in the massive oxide within the host anorthosite has the lowest Xhm (0.07-0.10) and V contents (859-937 ppm) of all and are almost absent of hematite exsolutions. However, their Cr (167-180 ppm) and Ni (50-60 ppm) contents are much higher in comparison with the values for ilmenite in the OAN mineralization.

Similar to ilmenite, magnetite shows cryptic variation for Cr (14 - 1244 ppm) and Ni (9.3 – 197.9 ppm) (Fig.2.9d). This includes higher values of Cr (1961-2544 ppm) and Ni (470 – 507 ppm) in the oxide minerals from the massive oxides. In

contrast to ilmenite, V in magnetite behaves more similarly to Ni and Cr with higher V (3041 – 3536 ppm) concentrations in magnetite from the massive oxides compared to that from the OAN mineralized zone (9.3 – 197.9 ppm V).

2.6 Discussion

Our study reveals that the Lac à l'Orignal Fe-Ti-P deposit is a multi-phase lenticular intrusion comprising cumulates of oxide-apatite norite (OAN). The older border (1069 ± 12 Ma) is dominated by hemo-ilmenite (± magnetite) and is more leucocratic whereas the younger core (993 ± 13 Ma) is dominated by ilmenite and magnetite and more melanocratic. Weighted mean diagrams (Appendix 2.3) show a normal distribution of a single population of zircons, precluding the occurrence of inheritance. This is confirmed with the CL images of zircons which although some show darker cores (e.g., in LOR1) their ages are similar to those from the paler borders. Also zircon is most likely undersaturated in magmas of ferrodiorite composition until it reaches a high degree of crystallinity therefore not preserving a lot of inherited zircon (e.g. Watson & Harrison, 1983). Therefore, the difference in ages of the border and core is unlikely due to inheritance of zircons. However, chondrite-normalized REE compositions (of whole rock and apatite) present similar patterns between the border and core of the mineralized OAN-body, indicating that at least two magma injections of similar composition, formed the Lac à l'Orignal mineralized intrusion over a period of 80 Ma. Exceptionally, the older intrusion is preserved at the border of the younger intrusion. Furthermore, the Lac à l'Orignal intrusion is layered, with thin horizons of apatite-bearing anorthosite and, less commonly, massive nelsonite of similar plagioclase and apatite chemistry as that of the OAN mineralization. This suggests that it formed as cumulate segregation from the magmas. The border is crosscut by fine-grained OAN dykes of similar mineralogy and

apatite chemistry to the mineralization, suggesting a co-genetic link which is demonstrated below.

According to Dymek & Owens (2001), OAGN (oxide-apatite-gabbro-norite) in the Grenville Province, Canada, occurs as 1) discordant to concordant sill-like bodies within anorthosite massifs, 2) as layers along or near the outer boundaries of anorthosite massifs, or 3) as layers within associated jotunite or mangerite. The Lac à l'Orignal mineralized intrusion is located near the boundary of two massif-type anorthosites: Vanel and Mattawa, whose ages are similar to those obtained in our study for the border and core of the intrusion, respectively. Furthermore, OAGN can form at various stages in the evolution of a particular massif anorthosite complex and represent mainly cumulate segregation from jotunite/ferrodiorite liquids, with the proportion of oxide-apatite-pyroxene reflecting a cotectic assemblage (Owens & Dymek, 1992). According to these authors, OAGN host more evolved mineral compositions than anorthosites and massive nelsonite/oxide layers, indicating generation from more evolved magmas, i.e., in latter stage of fractionation after massive oxide/plagioclase crystallization, from which jotunite liquids would form (Vander Auwera & Longhi, 1994; Vander Auwera et al. 1998). In the Lac à l'Orignal deposit, in contrast to most of the hemo-ilmenite dominated OAGN occurrences described above, there is a lack of massive oxide and or massive nelsonite layers at the base of the main mineralized body. Also, cumulus apatite and magnetite are present throughout the intrusion, in addition to hemo-ilmenite, thus suggesting a more evolved character for these cumulates in relation to other Fe-Ti-(P) occurrences in the Grenville Province (e.g., Grader intrusion, Charlier et al. 2008; Lac Tio, Charlier et al. 2010; Saint-Urbain Anorthosite, Morisset et al. 2009) which contain less magnetite.

2.6.1 Parental magma

Apatite is an important phase in the late-stage evolution of layered intrusions and massif-type anorthosite complexes where it crystallizes, along with Fe-Ti oxides, from an evolved magma, enriched in Fe, Ti and P (Toplis et al. 1994) and can accumulate to form, in some cases, Fe-Ti-P mineralization (McLelland et al. 1994; Dymek & Owens, 2001; Tollari et al. 2008; Charlier et al. 2008; Namur et al. 2010; 2012). Evolved magmas, such as ferrodiorite and/or jotunite, are commonly interpreted as liquids associated with massif-type anorthosites and have been shown to be co-genetically related to the Fe-Ti-P mineralization either as a parental or residual magma (Owens et al. 1993; Vander Auwera et al. 1998). These melts are unusually enriched in Fe_2O_{3t} (13.2-21.9 %), TiO_2 (3.1-6.0%) and P_2O_5 (0.8-3.9%) (Appendix 2.1). High concentrations of P_2O_5 in evolved magmas leads to the formation of silicate melts with much higher Fe contents than is possible for P-poor compositions, allowing for concentration of Fe and Ti at higher levels (Toplis et al. 1994). This is partially because the increasing P_2O_5 content decreases the stability field of magnetite whereas the relative abundance of ilmenite remains approximately constant. Thus, the high P_2O_5 content of ferrodioritic or jotunitic liquids associated with anorthosite suites (e.g., Mitchell et al. 1996; Vander Auwera et al. 1998) is responsible for some their characteristics, such as the common early saturation of ilmenite compared to magnetite (Charlier et al. 2015).

The fine-grained dykes at Lac à l'Orignal (LO-06 and LO-08: Table 2.2) are very similar in bulk composition to fine-grained ferrodiorite/jotunite dykes compiled from other Fe-Ti-(P) mineralization and anorthosite massifs, in particular the dykes from the Grader intrusion (Appendix 2.1). Moreover, at Lac à l'Orignal these fine-grained lithologies present the same mineralogy and similar geochemistry (whole rock

and apatite REE patterns) as the border-OAN cumulates in the mineralization, suggesting they are co-genetic with the mineralization, although dykes present more evolved apatite compositions (higher REE and Y and lower Sr). The relationship between the fine-grained dykes and melt compositions in equilibrium with the cumulates can be evaluated from the composition of cumulus apatite in the intrusion, by inverting the composition of apatite using the equation C$Liq\ REE = \frac{CAp\ REE}{DAp\ REE}$. The REE contents of the ferrodiorite dykes (samples LO-06 and LO-08) are plotted (Appendix 2.3) along with REE patterns calculated for liquids in equilibrium with apatite from the OAN cumulates of Lac à l'Orignal, using empirically determined D$Ap\ REE$ values (Table 2.7) obtained from the gabbronorite cumulates of the Bjerkreim–Sokndal layered intrusion (Charlier et al. 2005). This approach was previously applied by Charlier et al. (2008) to the oxide-apatite gabbronorites of the Grader intrusion, Quebec, which has similar mineralogy to the Lac à l'Orignal deposit. The calculated liquids in equilibrium with apatite show similar REE contents and patterns as those of the fine-grained ferrodiorite (OAN) dykes, suggesting that these dykes could represent melts that were in equilibrium with the oxide-apatite-norites, and related apatite-bearing cumulates. However, the calculated liquids have slightly positive Eu anomalies, and do not match the small-negative Eu anomalies observed in both of the fine-grained dykes from Lac à l'Orignal. A similar mismatch for Eu was also observed for the melt composition calculated from apatite of the Grader intrusion compared to their dykes (Charlier et al. 2008). As pointed out by Charlier et al. (2008), the D$Ap\ Eu$ value (3.9) of Charlier et al. (2005) overestimates the value for the calculated melt of the Grader intrusion, because the D$Ap\ Eu$ is too low. Europium is sensitive to redox conditions. At high fO_2, the relative proportion of Eu^{3+} and Eu^{2+} is also higher in apatite because D$Ap\ Eu3+$ > D$Ap\ Eu2+$ (Roelandts & Duchesne, 1979). Thus, the

mismatch in Eu at the Grader intrusion indicated that crystallization of apatite occurred under higher fO_2 conditions (between NNO +0.5 + & 1.0) at Grader intrusion than that at Bjerkrein-Sokndal layered intrusion. This is supported by higher hematite content in ilmenite in Grader (X_{hem} = 0.20 – 0.32, Charlier et al. 2008) compared to that in the Bjerkrein-Sokndal layered intrusion (X_{hem} = 0.03 – 0.19, Duchesne, 1972). At Lac à l'Orignal, the high hematite content of ilmenite in the dykes (Xhem = 0.42 – 0.55) and that preserved in the border of the OAN mineralization (X_{hem} = 0.10 – 0.60) also indicates similar or even higher fO_2 conditions of the melt (see below). Higher fO_2 conditions would thus result in a higher ratio of Eu^{3+}/Eu^{2+} in the melt and higher D^{Ap}_{Eu}, explaining the mismatch in Eu anomalies observed in Appendix 2.3. To avoid possible inconsistences in using partition coefficients determined from Bjerkrein-Sokndal, in particular for D^{Ap}_{Eu}, new D^{Ap}_{REE} values were determined for this study using whole rock REE and apatite REE values of the fine-grained OAN dykes from Lac à l'Orignal itself, using the equation: $D^{Ap}_{REE} = \frac{CAp\ REE}{CLiq\ REE}$ (Table 2.7).

Liquids in equilibrium with apatite from the OAN mineralization were then recalculated applying the new D^{Ap}_{REE} values from the least evolved (sample LO-06; Fig.2.10c) and most evolved (sample LO-08; Appendix 2.3) dykes. The REE patterns, including Eu anomalies, and abundance of REE of the calculated liquids perfectly match the fine-grained OAN dykes when applying partition coefficients from the least-evolved dyke (Fig.2.10c). However, when using partition coefficients from the more evolved dyke, the calculated liquids have lower-REE concentrations in comparison with the fine-grained dykes, due to higher D^{Ap}_{REE} obtained from the evolved dyke. These results indicate that the composition of the least-evolved fine-grained dyke (LO-06) better reflects an initial liquid in equilibrium with the OAN cumulates (i.e., parental melt), whereas the dyke LO-08 would represent a more-

evolved, residual liquid at further stages of differentiation. Increased polymerization of a more evolved liquid may explain the higher D$Ap\ REE$ calculated for this dyke.

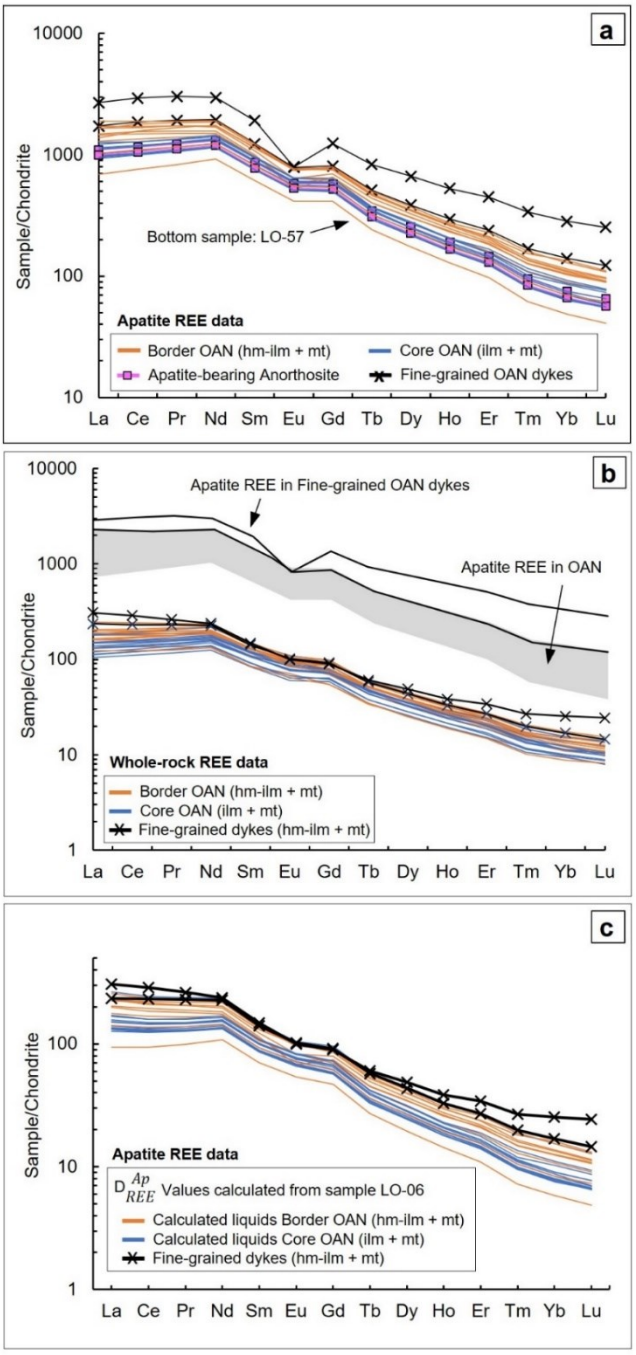

Figure 2.10. Chondrite-normalized REE compositions (after Sun and McDonough, 1989). a Apatite REE-data. b Whole-rock REE data in comparison with apatite (grey field – Fig.10-A) showing the REE behavior controlled by apatite concentration. c Apatite REE patterns for fine-grained OAN dykes (samples LO-06 and LO-08) compared to calculated liquids from the inversion of apatite compositions of border (orange lines) and core (blue lines) samples. Calculated liquids applying D$Ap\ REE$ values obtained from bulk and apatite compositions of dyke sample LO-06.

Table 2.7. Representative LA-ICP-MS major and trace element analyses of apatite for samples the Lac à l'Orignal Fe-Ti-P deposit

	REE geochemical analysis of fine-grained OAN dykes					Calculated D_{ap} values			Compilation of D_{ap} values		
	Whole-rock REE values			Apatite REE values		Lac à l'Orignal Fe-Ti-P			Bjerkrein Sokndal Layered Intrusion		
Element	LO-06	LO-08		LO-06	LO-08	D_{ap}[a]	D_{ap}[b]		D_{ap}[c]	D_{ap}[d]	D_{ap}[e]
La	55.82	73.09		408.0	637.3	7.3	8.7		3.9	4.3	12.0
Ce	141.88	176.40		1139.6	1794.3	8.0	10.2		4.7	5.5	15.0
Pr	21.27	24.38		178.5	280.9	8.4	11.5		5.4	-	-
Nd	103.48	108.58		888.8	1350.7	8.6	12.4		6.0	6.9	19.0
Sm	20.88	21.92		182.6	282.7	8.7	12.9		6.6	7.3	20.0
Eu	5.75	5.60		44.4	44.8	7.7	8.0		3.9	7.5	13.0
Gd	18.30	17.85		161.2	247.2	8.8	13.8		6.8	7.9	20.0
Tb	2.08	2.18		18.4	29.9	8.8	13.8		6.1	7.7	19.0
Dy	10.72	12.02		94.9	163.9	8.9	13.6		5.3	-	-
Ho	1.80	2.09		16.2	28.8	9.0	13.8		4.6	6.6	16.8
Er	4.33	5.46		38.0	71.6	8.8	13.1		4.0	-	-
Tm	0.50	0.67		4.2	8.3	8.4	12.4		3.4	-	-
Yb	2.72	4.10		22.6	45.5	8.3	11.1		2.7	4	13.0
Lu	0.36	0.60		3.0	6.2	8.4	10.3		2.2	3.25	10.0

a Calculated partition coefficients between apatite and melt from sample LO-06. b Calculated partition coefficients between apatite and melt from sample LO-08.
c Partition coefficients between apatite and melt from Charlier et al.(2005). d Partition coefficients between apatite and melt from Roelandts & Duchesne (1979).
e Partition coefficients between apatite and melt from Vander Auwera et al.(1998).

2.6.2 Oxygen fugacity

To better constrain the probable high fO_2 conditions of the ferrodiorite magma forming the mineralization at Lac à l'Orignal we used the QUILF program of Andersen et al. (1993) and input the mineral compositions of magnetite-hemo-ilmenite pairs from the fine-grained OAN dyke. Given that the dykes cooled faster than the main body, subsolidus modification should be less important and thus these samples are the best estimate for magmatic conditions of the mineralization. Following Charlier et al. (2008), the fO_2 values at equilibrium between oxides were obtained by fixing the liquidus temperatures between 1100 and 1200°C (Vander Auwera & Longhi, 1994; Vander Auwera et al. 1998), and pressures between 1-5Kbar (Charlier et al. 2008; Lin & Sawyer, 2018). The calculations give values of fO_2 between - 6.97 and –7.85 and Δ log fO_2 (relative to FMQ) values between +0.9 and +1.7 (Appendix 2.1).

Plotting the calculated fO_2 values relative to the Fe content of orthopyroxene, in Appendix 2.3, shows that the Lac à l'Orignal deposit falls into the ilm – hm + mt + opx field, which is compatible with the mineralogy present in the OAN cumulates. Furthermore, it illustrates that the crystallization conditions of the Lac à l'Orignal deposit was more oxidizing than the olivine-magnetite-bearing Kiglapait Intrusion of the Nain Plutonic Suite, Labrador (Morse, 1982) but not as oxidizing as the hemo-ilmenite-orthopyroxene-bearing Labrieville Anorthosite (Owens and Dymek, 2001; Frost et al. 2010). In addition, we have determined the oxygen fugacity from the experimental calibration of the Fe–Ti oxide thermo-oxybarometer of Lattard et al. (2005), applying the same range of temperature (1100-1200°C), pressure (1-5Kbar) and the hematite content of ilmenite (Charlier et al. 2008). Applying the ilmenite composition of the fine-grained OAN dykes (X_{Hm} between 0.45-0.56) to this range of values, calculations give FMQ between +1.34 and +1.71 (NNO between +0.57 and

+0.95), confirming the values obtained using QUILF. Furthermore, such high-fO_2 values of the parental ferrodiorite liquid at Lac à l'Orignal are compatible with the inference of high fO_2 previously suggested above from the Eu* chemistry of apatite. Similar high oxygen fugacity (fO_2) conditions (>+1 FMQ) were reported for the formation of hemo-ilmenite dominated OAGN cumulates at the Grader intrusion (Charlier et al. 2008).

For mafic-basaltic systems, experimental studies on the stability fields of Fe–Ti oxides (Snyder et al. 1993; Toplis & Carroll, 1995) have shown that at high-fO_2 (>+1 FMQ) the magnetite–ulvöspinel solid solution precedes the appearance of the ilmenite–hematite solid solution, whereas the reverse occurs at low-fO_2 (<+1 FMQ). However, according to Toplis & Carroll (1995), the fO_2 only affects the stability field of magnetite, whereas the crystallization of ilmenite as the first oxide is controlled primarily by the TiO_2 content of the melt. The crystallization of hematite-rich ilmenite in the Lac a l'Orignal Fe-Ti-P deposit is thus a reflection of the initial high-TiO_2 content of the parental magma coupled with high-fO_2 conditions, as observed for the Grader intrusion (Charlier et al. 2008; Morisset et al. 2009; 2010).

2.6.3 Fractional crystallization

In addition to the An content of plagioclase, trace element in apatite and Fe-Ti oxides are useful, and sometimes more sensitive, in tracing fractional crystallization processes (Fig. 2.11 and Appendix 2.3) and magma injections (Namur et al. 2010; Tollari et al. 2008; Kieffer et al. 2022). In a magma chamber behaving as a closed system (i.e. one that does not experience successive inputs of magma), elements that are highly compatible into Fe-Ti oxides, such as Cr should be strongly enriched in the most primitive magnetite and ilmenite (associated with Fe-Ti-V deposits).

Subsequently crystallizing Fe-Ti oxides (associated with Fe-Ti-P deposits) would continuously decrease (Fig.2.11) the concentration in highly compatible elements due to their progressive removal from the residual magma (Barnes et al. 2004; Klemme et al. 2006; Tegner et al. 2006; Namur et al. 2010; Dare et al. 2014; Grant, 2020). In more open systems, sharp reversals to higher concentrations of compatible elements are often attributed to reinjections of a more primitive magma (Namur et al. 2010). However, the primary magmatic composition of oxides can be modified, after crystallization, by sub-solidus processes both during cooling of the intrusion and later by metamorphism (Duchesne, 1972; Arguin et al. 2018; Grant, 2020; Dare et al. 2019). In contrast, sub-solidus re-equilibration processes seems to have minor influence on the trace element distribution in apatite (Tollari et al. 2008).

Binary diagrams (Appendix 2.3) display some trace element concentrations in plagioclase, apatite and oxides as a function of the An content of plagioclase, used here as a proxy for tracking fractional crystallization. Data from the Grader intrusion (Charlier et al. 2008) are plotted in comparison. Although plagioclase from Lac à l'Orignal varies from An 50 to An 40, only the Or content significantly increases as An content decreases (Appendix 2.3), whereas Sr and Ba contents in plagioclase do not vary with increasing degree of fractionation, suggesting a global KD of around 1. This behaviour of K, Sr and Ba in plagioclase is similar to that from Grader, except the latter has higher K and lower Sr concentrations. Similarly, the Sr, and Mn contents, of apatite also do not vary with fractionation (Appendix 2.3), whereas the REE content shows a very slight increase with decreasing An content at both Lac à l'Orignal and Grader, however there is significant scatter in REE for the borders of Lac à l'Orignal. Overall, the Lac à l'Orignal deposit is similar to the upper portion of the Grader intrusion

(Appendix 2.3), suggesting a more evolved character, although the Sr contents of apatite and plagioclase in the former, are higher.

Cr and Ni contents in both magnetite and ilmenite of the Lac à l'Orignal deposit decrease together with the An content of plagioclase (Appendix 2.3), behaving as compatible elements during fractional crystallization, although there is some scatter. Nb and Zr values in ilmenite (Appendix 2.3), as expected, behave incompatibly, slightly increasing with lower An contents. However, the V content of magnetite and ilmenite remains constant, and V has higher concentrations, but more scattered distribution in hemo-ilmenite than in ilmenite. This is probably because $V^{3+, 4+}$ substitutes more easily into the Fe^{3+} site of the hematite component of hemo-ilmenite than the Fe^{2+} site of ilmenite, which explains the correlation between V and Xhem content of ilmenite in Fig.2.11c. Toplis & Corgne (2002), applying experiments on ferrobasalts, showed that V and Cr partitioning into magnetite is strongly dependent on fO_2, resulting in a decrease in both partition coefficients with increasing oxidizing conditions. In phosphorous-bearing systems, such as for the Lac à l'Orignal mineralization, $D^{mt/liq}\,Cr$ decreases from 291 to 27 with increasing oxygen fugacity (from NNO -0.7 to NNO +2.6), whereas $D^{mt/liq}\,V$ decreases from 29 to 2. Consequently, even at high-fO_2, Cr remains compatible during fractional crystallization whereas for the same proportion of magnetite, V could remain unchanged (Duchesne et al. 2006; Charlier et al. 2009). The constant V content in magnetite (V around 0.30 wt.%) in relation to the An content of plagioclase (Appendix 2.3) and with Cr in magnetite (Fig.2.11a), implies a $D^{bulk/liq}\,V$ around 1 in the OAGN cumulates, thus indicating a relatively low-$D^{mt/liq}\,V$. We interpret this to be the result of a relatively high-fO_2 of the magma that formed the Lac à l'Orignal oxide-apatite mineralization. This is due to the high proportion of V^{4+} and V^{5+} in the melt at high-fO_2 which partition less well into magnetite

compared to V^{3+} (Toplis & Corgne, 2002). High-fO_2 is also responsible in part for the similarly low and constant V content in magnetite from both Grader OAGN (Fig.2.11a; Charlier et al. 2008) and the Fe-Ti ores of the Suwalki Anorthosite (Charlier et al. 2009).

The high Cr and Ni contents in ilmenite and magnetite as well as the lower Nb and Zr values in ilmenite of the massive oxide sample (within the host anorthosite, Appendix 2.3) indicate that this sample has a more primitive composition in comparison with the main OAN mineralization, as previously noted by Owens & Dymek (1992) in other locations in the Grenville Province. Fractional crystallization from ferrodiorite magmas initially dominated by oxide (settling) + plagioclase (flotation) could explain the presence of massive layers of ilmenite + magnetite within the host anorthosite. In further stages, fractional crystallization of the residual liquid, dominated by Fe-Ti oxides, silicates and apatite would generate the OAN cumulates observed in the main intrusion.

The Lac à l'Orignal norite cumulates have a large range of V and Cr variation for ilmenite and magnetite (Fig.2.11). In comparison, ilmenite in the Grader intrusion has higher Cr, Ni and V values in relation to Lac à l'Orignal. During crystallization, Cr, V and Ni preferentially partition into magnetite over ilmenite (Dare et al. 2014; Arguin et al. 2018). The lower abundance of magnetite at Grader could result in higher Cr values for ilmenite at this location, as well as a more primitive character (an initial high-Cr value) of its parental magma (s) in relation to Lac à l'Orignal. The An content of Lac à l'Orignal (An50 – 40) is similar to that at Grader (An50-45) but decreases to lower values, suggesting a more evolved magma.

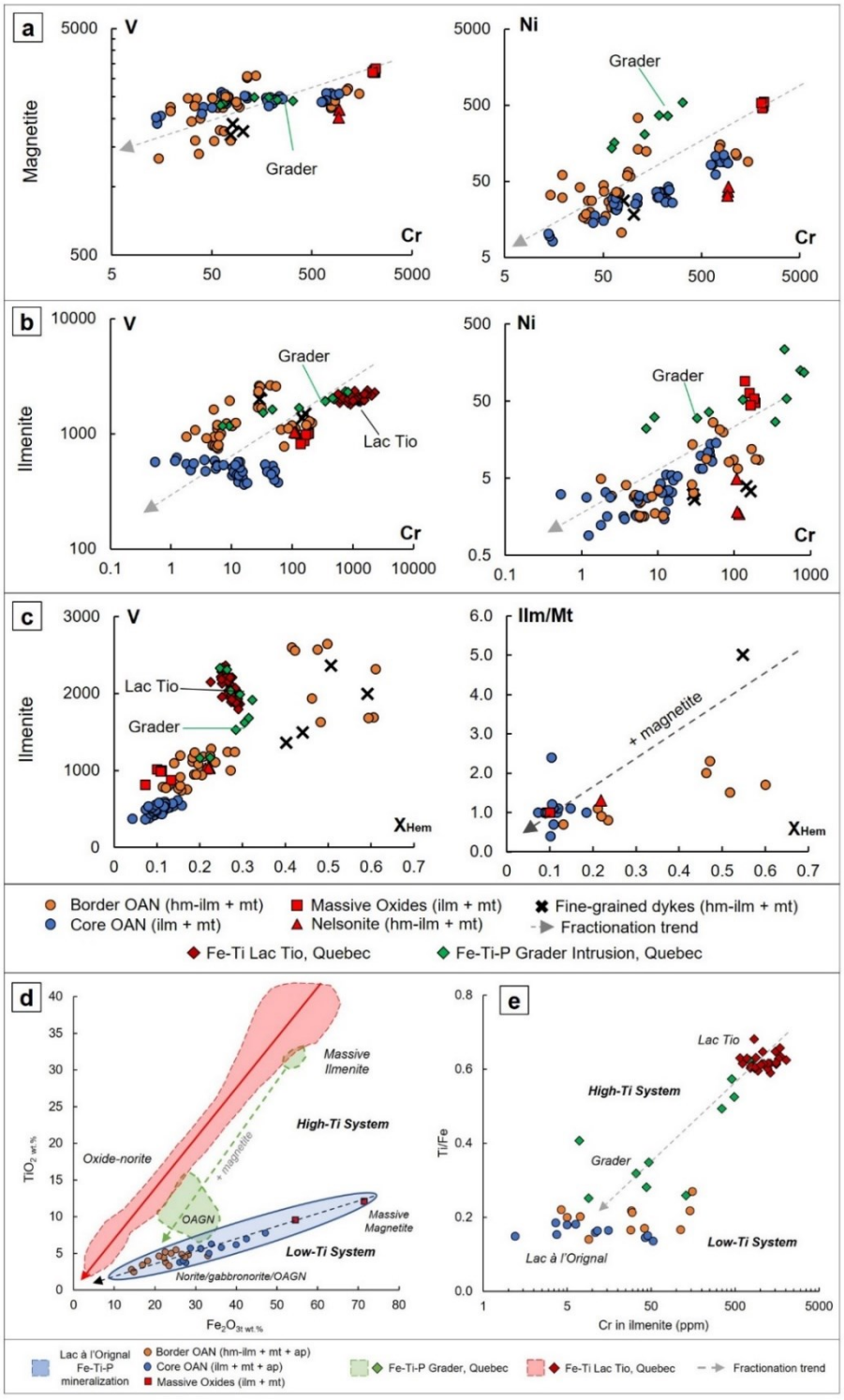

Figure 2.11. Binary diagrams displaying concentrations of compatible elements in magnetite (a) and ilmenite (b), using Cr as a proxy for fractional crystallization. c Hematite content in ilmenite in relation to the V concentration in ilmenite (left) and the modal proportion of magnetite (right). Comparison between geochemical data of the Lac à l'Orignal Fe-Ti-P deposit (this work), the Grader intrusion Fe-Ti-P, Quebec (Charlier et al. 2008) and the world-class ilmenite deposit of Lac Tio Fe-Ti, Quebec (Charlier et al. 2010). d-e Geochemical comparison of the Lac à l'Orignal Fe-Ti-P deposit (blue field – this study) with the Lac Tio Ti deposit (red field) and the Fe-Ti-P mineralization at Grader intrusion (green field), in the Havre-Saint-Pierre Anorthositic Suite, Quebec (data from Charlier at al. 2010; 2008). e Whole-rock Fe_2O_{3t} vs. TiO_2. e Ti/Fe whole rock ratio vs. Cr content of ilmenite (in

Cumulates in Lac à l'Orignal present a higher Cr for both magnetite and ilmenite from the core in relation to the upper border (Figs.2.9c-d), pointing for a more primitive character to the former in relation to the latter. However, apatite trace element concentrations have a discrete REE enrichment up-section (Fig.2.9b), with slightly lower Eu/Eu* values at the top border of the succession. The leuco-OAN's in the older border zone are more plagioclase concentrated, which could have an influence on the behavior of certain elements that are controlled by plagioclase, such as Eu and Sr. Moreover, the top border could have been affected by trapped liquid effect, in which could have modified the concentration of REE at this portion, as previously described for the Fedorivka intrusion (Duchesne et al. 2006). The more scatter distribution of REE compositions for the OAN-border, as previously pointed in Figure 2.9b, corroborates that.

The role of liquid immiscibility in forming Fe-Ti-P-rich and Si-rich silicate melts has recently shown to be fairly common in the late stages of fractionation of mafic melts (Namur et al. 2010; 2011; Charlier & Groove, 2012). Undisputed evidence for this is the presence of melt inclusions in apatite that record the 2 immiscible melts (e.g., Charlier et al. 2008). At Lac a l'Orignal, no melt inclusions occur in apatite. Furthermore, bulk whole-rock compositions of fine-grained OAN dykes, interpreted as liquidus compositions of Fe-Ti-P mineralization, were projected onto ternary diagrams for liquid immiscibility evaluation, as previously applied to the Sept Iles Layered Intrusion (Appendix 2.3, modified from Tollari et al. 2008; Charlier & Grove, 2012). Overall, the composition of ferrodiorite dykes associated with Fe-Ti-P mineralization at Lac a l'Orignal, Quebec, fall outside of the liquid immiscibility field (Appendix 2.2), supporting the model of fractional crystallization of a single magma as the main process in the petrogenesis of these cumulates.

2.6.4 Post-cumulus modification in magnetite and ilmenite

The fractionation trends recorded by oxides at Lac à l'Orignal are more scattered than those from the Grader intrusion (Fig.2.11 & Appendix 2.3) which could point to secondary modification of the primary composition of the oxides. Alteration of a primary chemical composition of a mineral can occur through several modes of 'diffusive modification', a term used by Tanner et al. (2014) to describe the diffusive interchange occurring either between compositional zones within a mineral, or between a mineral and the adjacent media (i.e., melts, minerals, or volatile-rich fluids) as they attempt to attain equilibrium. In the Bushveld Complex, for example, both the 'trapped liquid shift' and subsolidus re-equilibration, during prolonged cooling of the intrusion, have been identified as important modifiers of the trace element concentrations on cumulate minerals (Cawthorn, 2007; Tanner et al. 2014).

Fe-Ti oxides can be modified by 3 different processes; 1) re-equilibration between magnetite and ilmenite (inter-oxide re-equilibration), 2) re-equilibration between Fe-oxides and Fe-Mg silicates (oxide-silicate re-equilibration), and 3) re-equilibration between magnetite/ilmenite and internal exsolution phases (intra-oxide re-equilibration), which can directly affect the concentration of elements in these minerals (Frost et al. 1988; Frost 1991; Frost & Lindsley 1992; Pang et al. 2007). Therefore, exsolution and/or re-equilibration within magnetite, ilmenite and/or Al-spinel must be considered when interpreting the cryptic layering in these minerals as indicator of magmatic crystallization conditions. Magnetite and hemo-ilmenite at Lac à l'Orignal have both been affected by subsolidus re-equilibration, similar to that described for the ilmenite cumulates of the Tellnes Deposit (Charlier et al. 2007) and Bjerkrein Sokndal (Duchesne, 1972). At the grain-scale, coronas of Al-spinel (pleonaste) are commonly observed at the contact between ilmenite and magnetite

(Fig.2.5). The Al_2O_3 and MgO content of magnetite and ilmenite vary in the same way indicating an alteration of a primary ilmenite/magnetite chemical composition to generate Al-spinel grains. Also, the proportion of hematite exsolutions in ilmenite is locally reduced when magnetite is present, with the hematite content (Fe_2O_3) of ilmenite decreasing towards the margin with magnetite (Figs.2.5b & 2.5f). This is explained by a two-step process: the first step is the exsolution of pleonaste in magnetite most notably at the border of the grains. The exsolutions are incorporated, in a second step, to the ilmenite grain by the formation of new ilmenite at the contact of magnetite-ilmenite. This new ilmenite is formed by oxidation of the ulvöspinel component of magnetite. The oxidation is caused by reaction with the hematite contained in the ilmenite (Buddington & Lindsley, 1964, Duchesne, 1972). Because of this process, Al_2O_3 and MgO from magnetite are incorporated as pleonaste in ilmenite and the TiO_2 content of magnetite and the hematite content of ilmenite both decreases. According to Frost et al. (1988), the smaller proportion of magnetite relative to ilmenite means that this reaction has mainly changes the primary composition of magnetite into a Ti-poor variety, without significantly affecting the composition of the ilmenite.

At Lac à l'Orignal, there is a marked but gradual change in the oxide mineralogy from the border (hemo-ilmenite) towards the core of the intrusion (ilmenite). We attribute this to varying degrees of subsolidus re-equilibration between hemo-ilmenite and magnetite, resulting in the decrease of hematite exsolutions, as previously described, with less re-equilibration at the border and more in the core of the intrusion. Therefore, it is crucial to better understand how much inter-oxide re-equilibration has influenced the concentration/distribution of key trace element, such as V, Cr and Ni between the different oxide phases.

High resolution element mapping, using LA-TOF-ICP-MS (Fig.2.12, Appendix 2.1), was performed at the contact area between magnetite and hemo-ilmenite, where it is evident that subsolidus, inter-oxide re-equilibration has occurred. In this example, the hemo-ilmenite “core’’ portion, which is not in contact with magnetite, preserves more hematite exsolutions than the ilmenite “edge”, in contact with magnetite. Also, fine-grained exsolutions of ilmenite (enriched in Ti, Sc, Mn; depleted in Fe and V) and pleonaste (enriched in Al and Co; depleted in V and Sc) in magnetite and at the edge of ilmenite are visible using the TOF mapping technique.

The inter-oxide re-equilibration at the contact of hemo-ilmenite and magnetite causes a depletion of Fe and a relative increase of Ti content of ilmenite at the edge in comparison with ilmenite in the core which is dominated by hematite exsolutions. There is no significant difference (Relative Difference (RD) < 15%, which is within precision of analyses) between the hematite-rich core and the hematite-poor edge for Ni, Co, Mn, Sc and Mg (Fig.2.12). Although V and Cr concentrations show significant differences, with a strong depletion (RD 20-50%) in ilmenite from the core (e.g., 54 ppm Cr) towards the edge of the grain (e.g., 40 ppm Cr) in contact with magnetite, this difference is relatively small compared to the variation between the different samples shown in Figure 2.12 (e.g., Cr varies from 200 to 1 ppm). Sub-solidus reequilibration of magnetite at the border with ilmenite had an even less of an effect on the primary composition of magnetite for most elements including Cr, Ni and V (RD<15%) especially in relation with the Ti content that increases from the core to the edge portion. Therefore, inter-oxide reequilibration might have influenced some of the geochemical variation of major and trace element between ilmenite and magnetite, especially for V concentrations of ilmenite.

A series of binary diagrams comparing the V, Cr and Ni contents of magnetite and ilmenite (Fig.2.11) should therefore exhibit positively correlated differentiation trends if the cumulates were unmodified by inter-oxide reequilibration as they reflect the evolving composition of the parental magma during differentiation (Charlier et al. 2008; Polivchuk, 2017). This is the case at the Grader intrusion, where the V and Cr contents of ilmenite are well correlated (Fig.2.11b), with the slope of the trend varying according to their respective partition coefficients (Charlier et al. 2008). The hemo-ilmenite dominated Grader intrusion hosts much less magnetite (< 5% cumulus magnetite) in comparison with Lac à l'Orignal (10 – 15% cumulus magnetite), resulting in negligible inter-oxide reequilibration. However due to the presence of substantial magnetite with hemo-ilmenite at Lac à l'Orignal, inter-oxide reequilibration is probably more important (Fig.2.12), resulting in larger scatter for some of these differentiation trends (Figs.2.11 & Appendix 2.3). In detail, the V, Cr and Ni contents of magnetite (Fig.2.11a) are fairly well correlated with relatively low dispersion. In particular, the correlation of V and Cr of magnetite from both border and core of Lac à l'Orignal is similar to that of Grader. The Cr and Ni contents of ilmenite (Fig.2.11b) also show good correlation and relatively low dispersion. In contrast, the behaviour of V in ilmenite is different to that of magnetite: for hemo-ilmenite the V-Cr trend is similar to that of Grader but with a lot of scatters. However, the V content of Fe-poor ilmenite is much lower and does not vary with Cr. There is a positive correlation between the V content of ilmenite and the hematite component (Xhm), and thus the amount of hematite exsolutions, in ilmenite (Fig.2.11c). The hematite component provides an Fe^{3+} site in (hemo)-ilmenite into which $V(^{3+, 4+, 5+})$ can partition into more easily than the Fe^{2+} site in ilmenite. The enrichment of V in hematite exsolutions in ilmenite are visible from the TOF elemental mapping in Figure 2.12.

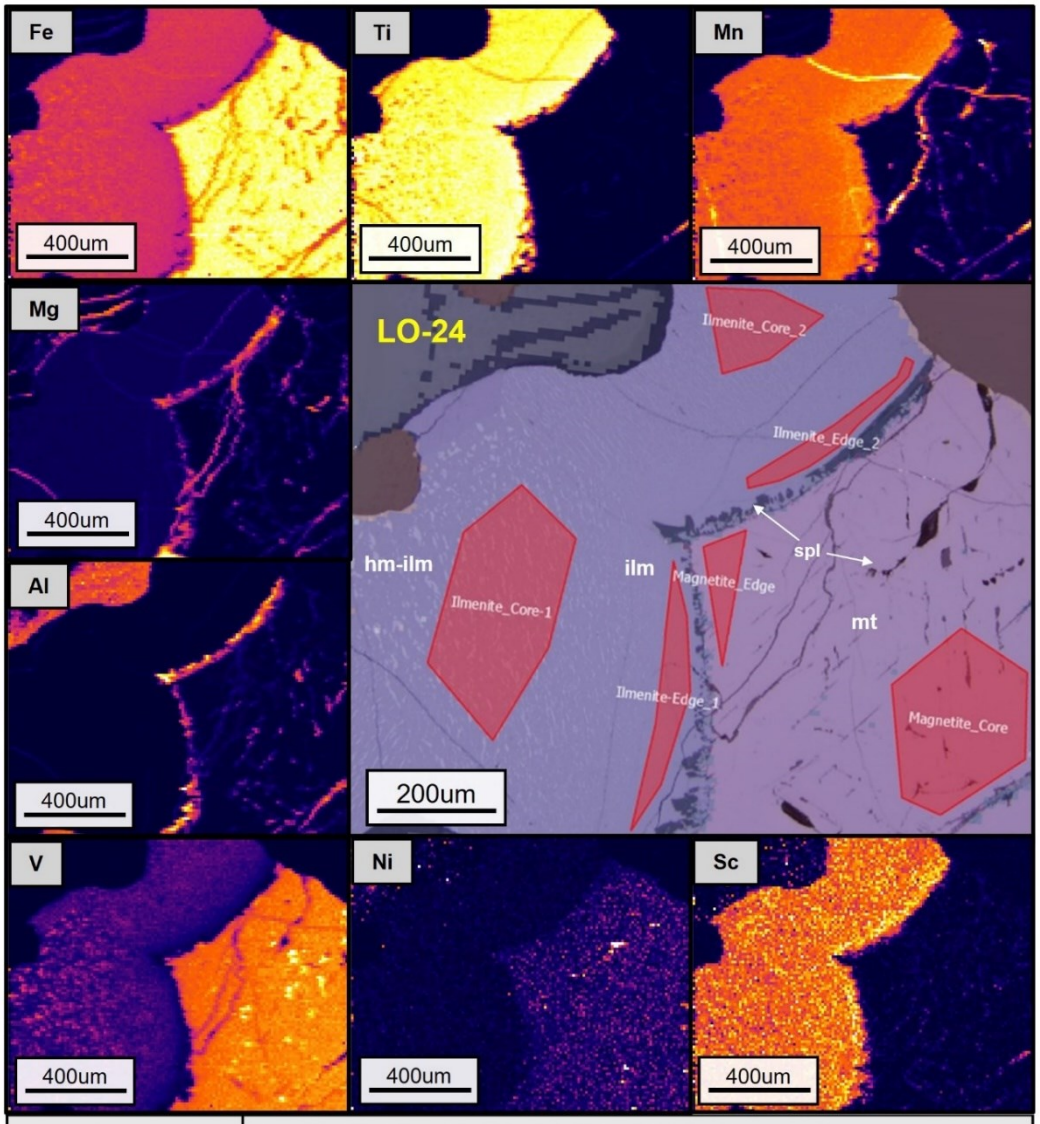

Sample	FeOt (%)	TiO_2 (%)	Al_2O_3 (%)	MgO (%)	MnO (%)	Sc ppm	V ppm	Cr ppm	Ni ppm
Ilmenite Core 1	43.29	54.33	0.08	1.63	0.61	103.41	976.17	47.15	15.92
Ilmenite Edge 1	38.43	58.38	0.26	1.87	0.72	120.41	781.38	39.66	15.93
Relative Difference (%)	-12.65	6.94	69.86	12.76	14.80	14.12	-24.93	-18.89	0.07
Ilmenite Core 2	43.40	54.06	0.11	1.62	0.63	110.06	979.87	54.72	14.13
Ilmenite Edge 2	38.33	58.50	0.33	1.85	0.76	132.48	646.20	40.34	15.26
Relative Difference (%)	-13.23	7.59	66.27	12.64	16.65	16.93	-51.64	-35.66	7.38
Magnetite Core	89.59	0.27	1.63	0.50	0.04	5.21	3101.33	87.80	59.33
Magnetite Edge	89.30	0.83	1.91	0.50	0.03	4.82	2656.28	94.54	52.74
Relative Difference (%)	-0.32	67.48	14.68	0.61	-27.63	-8.13	-16.75	7.13	-12.49

Figure 2.12. Fully quantified, high resolution element maps, using LA-Time of Flight-ICP-MS, showing the distribution of some major and trace element at the contact between ilmenite and magnetite crystals (sample LO-24). Any significant relative difference (%) in the element concentrations of selected core and edge areas in ilmenite and magnetite are due to sub-solidus, inter-oxide reequilibration. Red-yellow colors representing higher concentration of an element. Blue-white colors representing lower concentration.

Therefore, the hematite component of ilmenite, which is affected by subsolidus re-equilibration, directly controls the V content of ilmenite, thus resulting in large scatter for our samples from Lac à l'Orignal. Finally, the diagram Xhm vs Ilm/Mt ratio (Fig.2.11c) confirms that the hematite component in ilmenite is related in part to the abundance of, and thus inter-oxide exchange with magnetite: hemo-ilmenite bearing samples at the border of the Lac à l'Orignal mineralized zones have slightly lower magnetite concentrations (higher ilm/mt rations) in comparison with the ilmenite-bearing core, which has more magnetite and lower ilm/mt ratio.

On the diagram XHm vs. V content of ilmenite (Fig.2.11c), some of the OAN border samples (with larger hematite exsolutions and higher-V contents) plot close to the ilmenite from the fine-grained dykes (fast-cooled rocks) and could represent samples that also suffered a relatively fast-cooling history of crystallization, with negligible re-equilibration. In Figure 2.9c the higher Xhm content of ilmenite occurs at the very edges of the older borders of the intrusion (samples LO-01, 05, 55 & 57). It is known that sub-solidus re-equilibration processes are higher during long-cooling rates (Tanner et al. 2014). So, the hemo-ilmenite border samples with high-V contents probably suffered lower amounts of inter-oxide modification due to a faster cooling-rate and also a lower content of magnetite. Otherwise, the younger core of the intrusion, due to slower-cooling rates and/or higher amounts of magnetite, observed higher amounts of sub-solidus re-equilibration, consuming the hematite exsolutions and leading to a higher cationic exchange between magnetite and ilmenite. This difference in the cooling rates could be associated to different volume of magmas, the size of the different dykes/intrusions or even the difference of temperature between the new magma injection and the host-rocks (anorthosite and/or mineralized norites).

2.6.5 Insights on the petrogenesis of the Lac à l'Orignal Fe-Ti-P deposit

The Lac à l'Orignal deposit presents a complex history of evolution, being formed by at least two different injections of similar ferrodiorite compositions but with different ages (border: 1069 ± 12 Ma and core: 993 ± 13 Ma). These cumulates were formed through fractional crystallization of a residual high-Ti-P magma with oxide settling generating oxide-apatite norite cumulates, with occasional small nelsonite layers, and plagioclase flotation generating apatite-bearing anorthosite layers (Fig.2.13). The oxide chemistry of the massive oxides, hosted in andesine-anorthosite, has a more primitive signature. We thus suggest that the ferrodiorite magmas, that formed the oxide-apatite norite cumulates were residual (evolved) liquids after extensive plagioclase + oxide crystallization that formed the host anorthosites and massive oxides, respectively (Fig.2.13). A similar petrogenetic model was applied for the two other Fe-Ti-(P) occurrences previously studied in the Grenville Province: the Grader intrusion (OAGN and massive hemo-ilmenite) and the Lac Tio hemo-ilmenite deposit (Charlier et al. 2008; 2010). However, in contrast, the Lac à l'Orignal deposit does not contain extensive massive oxide cumulates within the mineralized zone as is the case for the Grader intrusion.

In detail, Figure 2.13 illustrates a schematic petrogenetic model for the formation of Fe-Ti-P mineralization at Lac à l'orignal to illustrate the occurrence of multiple diapiric intrusions of different ages, each with their respective residual Fe-Ti-P rich melts. Firstly, the Vanel Anorthosite (1080 ± 2 Ma) was emplaced and the residual Fe-Ti-P-rich liquid (ferrodiorite) drained/filterpressed (Scoates et al. 2010; Charlier et al. 2015) into zones of lower pressure (margins and or fractures) in the semi-consolidated anorthosite (plagioclase-rich mush diapir). Fractional crystallization of plagioclase, orthopyroxene, hemo-ilmenite, magnetite and apatite, as cumulus

phases from the ferrodiorite liquid, formed the oxide-apatite norite (OAN) mineralization (1069 ± 12 Ma), nelsonite (oxide + apatite settling) and apatite-bearing anorthosite (flotation of plagioclase-rich accumulation with intergranular apatite) layers. Around 70Ma later, the younger Mattawa Anorthosite (1016 ± 2 Ma) was emplaced nearby, probably using the same deep-crustal shear zones (e.g., Saint Fulgence Detachment Zone) that allowed the Vanel Anorthosite diapirs to ascend. Similar processes of segregation and accumulation of ferrodiorite liquid and emplacement of a younger OAN intrusion (993 ± 13 Ma) occurred forming the cumulates at the core of Lac à l'Orignal, intruding the previous cumulates associated to Vanel Anorthosite. The younger cumulates in the core (OAN and anorthosite-layers) evolved through similar fractionation processes, generating different cumulates due to crystal settling/flotation. The higher amount of magnetite in the core (Fig. 2.13) probably led to a higher degree of inter-oxide reequilibration (Fig.2.12) between the oxides in the core, resulting in ilmenite rather than hemo-ilmenite that are dominant in the older borders.

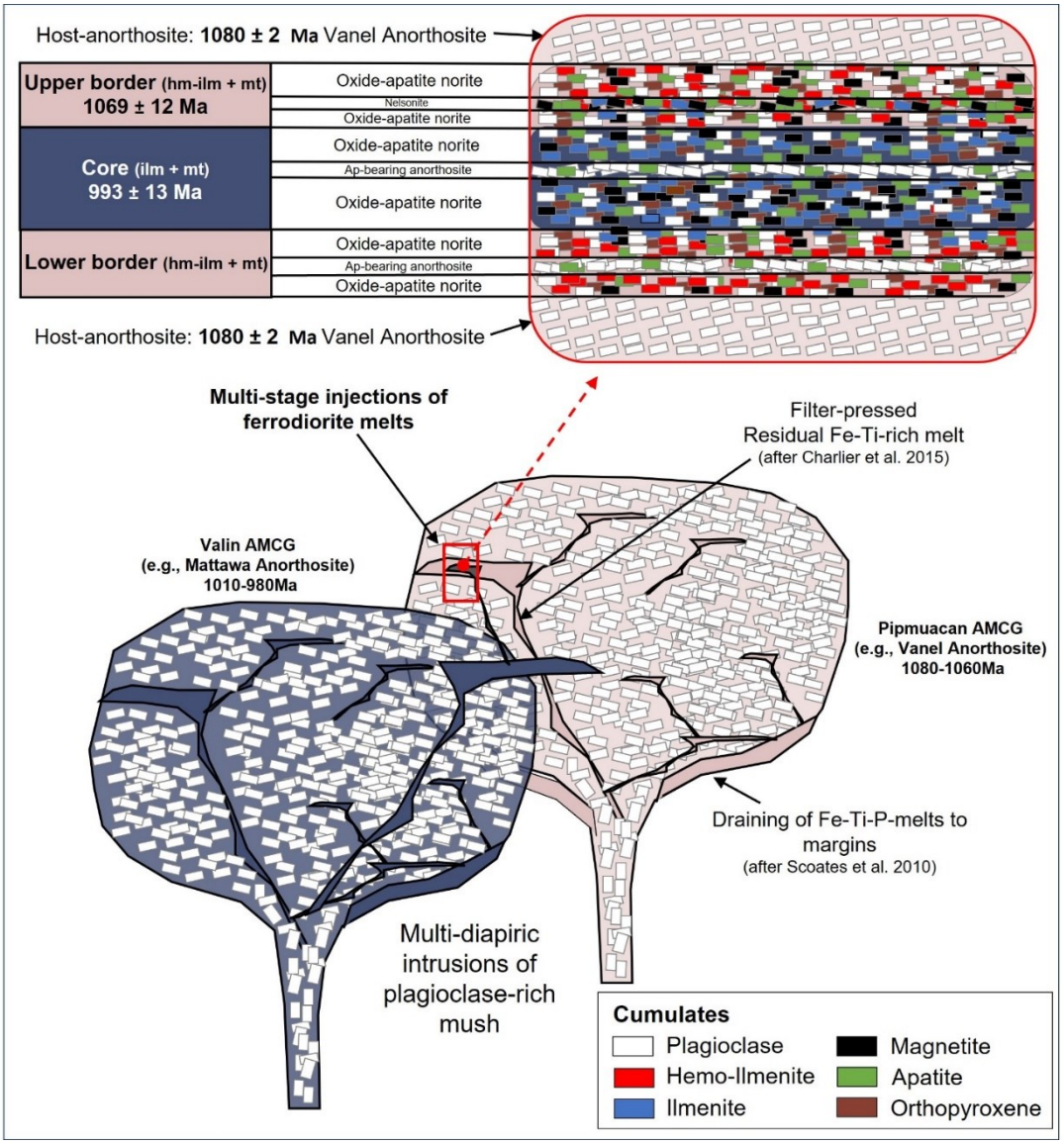

Figure 2.13. Schematic simplified model for the generation of Fe-Ti-P mineralization, exemplified by the Lac à l'Orignal Fe-Ti-P deposit in the Central Grenville Province. Fractionation of residual Fe-Ti-P rich ferrodiorite melts generated after anorthosite crystallization. Multi-diapiric emplacement of mafic mantle-derived magmas forming the Pipmuacan AMCG suite (e.g. Vanel Anorthosite) favored by deep-seated shear zones like the Saint Fulgence Detachment Zone. Segregation of ferrodiorite residual liquids filter-pressed into fractures/zones of lower pressure, generating the accumulation of oxide-apatite cumulates in dykes/sill-like structures and/or around the anorthosite-massifs. Emplacement and crystallization of the Valin AMCG suite and segregation of ferrodiorite residual magmas as previously described. Note that the intrusion of the Valin AMCG Suite within the previous Pipmuacan AMCG suite possibly the generation of conduits interconnecting different residual magma accumulation of different ages. Fractionation of evolved Fe-Ti-P melts with apatite as a liquids phase, dominated by (hemo)-ilmenite + magnetite + apatite initially (older border), and subsequently dominated by ilmenite + magnetite + apatite (younger core). Formation of local oxide-apatite-rich layers (nelsonite) by settling; residual oxide-apatite-norite (apatite + apatite + silicates) and apatite-bearing anorthosite (plagioclase + apatite) by relatively flotation.

Although Lac à l'Orignal shares some similarities with the Grader intrusion, the former contains higher amounts of cumulus magnetite. Along with the range of An content (extending to lower An) in plagioclase, higher REE content in apatite as well as similar to lower Cr, Ni and V concentrations in the Lac à l'Orignal in comparison to the Grader intrusion and Lac Tio (Figs.2.11 & Appendix 2.3), this denotes a more evolved character for the OAN mineralization at Lac à l'Orignal. To illustrate this, whole rock Ti and Fe contents are plotted in Figure 2.11d and show that overall, the Lac à l'Orignal cumulates have a lower Ti/Fe ratio (up to 12 wt.% TiO_2 in massive oxides), in comparison with Lac Tio and the base of the Grader intrusion (up to 30 - 40 wt.% TiO_2 in massive oxides). However, the OAGN of Grader plots between the two trends. The Ti/Fe reflects the relative proportion of their main cumulate phases (hemo-ilmenite, ilmenite and magnetite), with a minor contribution of Fe coming from orthopyroxene (low-abundance). The low-Ti/Fe trend of Lac à l'Orignal is due to lower proportions of ilmenite and higher magnetite, whereas Lac Tio and Grader intrusion form a high-Ti/Fe trend with hemo-ilmenite-rich cumulates containing much lower proportions of magnetite. Using Cr in ilmenite to trace the degree of differentiation in Figure 2.11e, it is clear that the Ti/Fe ratio decreases from high-Ti/Fe systems (dominated by hemo-ilmenite only) to low-Ti/Fe systems (hemo-ilmenite and magnetite) with fractional crystallization, i.e., that Ti behaves as a compatible element due to the extensive crystallization of hemo-ilmenite from the Ti-rich melt. Petrogenetically, Lac Tio and the base of the Grader intrusion could be part of a high-Ti system in the Grenville Province (Fig.2.11d), forming from a more primitive melt, with high Ti/Fe ratio and high-Cr-V in ilmenite, dominated by massive ilmenite and ilmenite-rich norite cumulates, with low-magnetite concentrations and absence of apatite-bearing cumulates. The Grader intrusion would correspond to a transition from

the high-Ti/Fe to the low-Ti/Fe system during continued fractional crystallization in response to decreasing Ti/Fe ratio, with the appearance of cumulus apatite forming massive nelsonite layers as well as minor cumulus magnetite generating oxide-apatite norite cumulates at the top part of the succession (Charlier et al. 2008). The OAN-dominated Lac à l'Orignal deposit, part of a low-Ti/Fe system, with the lowest Ti/Fe ratios, represents the most evolved, oxide-apatite norite cumulates, due to the presence of hemo-ilmenite + magnetite + apatite as first liquidus phases, in the late stages of differentiation of ferrodiorite/jotunite magmas. Similar features are also observed in the uppermost megacyclic units of the Bjerkreim-Sokndal Layered Intrusion (Duchesne & Charlier, 2005), where a progressive upward evolution is present from ilmenite-bearing cumulates to ilmenite-magnetite-bearing cumulates, being the appearance of cumulus magnetite due to fractional crystallization.

2.7 Conclusions

The Lac à l'Orignal Fe-Ti-P deposit is a multi-stage intrusion dominated by oxide-apatite norite cumulates where the marked feature is the change in the oxide mineralogy from hemo-ilmenite (+ minor magnetite) at the older border (1069 ± 12 Ma) to Fe-poor ilmenite + magnetite towards the younger core (993 ± 12 Ma). Although core and border have different ages, their range of ages are coeval with those previously described for the two youngest AMCG magmatic events in the region, and both cumulates have been generated under similar high-fO_2 conditions. Both intrusions were derived from high-Ti-P ferrodiorite magmas with similar REE compositions that evolved through extensive crystallization of hemo-ilmenite, magnetite and apatite. Petrogenetically, the Lac à l'Orignal Fe-Ti-P deposit corresponds to an evolved part of a low-Ti/Fe system in the Grenville Province,

evolved through extensive crystallization of ilmenite, and further magnetite, in the late stages of differentiation of ferrodiorite/jotunite magmas.

The variation and spatial distribution of hemo-ilmenite (Xhem) between the border and core of Lac à l'Orignal must account for higher amounts of magnetite at the core of the intrusion (more evolved) in relation to border (more primitive). Border and core have had variable degrees of subsolidus inter-oxide re-equilibration, which had influence on the compositional evolution of the analyzed cumulates, especially within the core portion, modifying its original composition.

The variation of trace element in oxides and apatite as well as new U-Pb ages for Fe-Ti-rich mineralized rocks at Lac à l'Orignal, indicate the complex petrogenesis of oxide-apatite mineralization related to anorthosite-massifs in the Central Grenville Province. Understanding the petrogenesis of Fe-Ti-P mineralization and their relationship to the host AMCG suite is essential for helping to predict the occurrence of similar deposits in nearby locations, which can guide exploration efforts, saving time and resources.

2.8 Acknowledgments

This research was supported financially from the Fonds de recherche du Québec – Nature and Technologie (FRQNT) grant for new academics No 2020-NC-271033 & 2021-NC-309329 and the Canada Research Chair in Geochemistry Applied to Ore Deposits No CRC-2017-0286 of Sarah Dare. The authors thank Christian Tremblay (TRCM-UQAC) and Leopold Tremblay for their assistance with field work; to Frank Guillemette (MRBoreal) for access and sampling of drillcore; Audrey Lavoie and Pape Doudou Tague for helping with LA-ICP-MS analytical procedures at LabMaTer, UQAC; Marc Choquette and Suzie Côté for their SEM, microprobe and

uXRF work at Université Laval and André Poirier who helped with LA-ICP-MS data acquisition on zircons at GEOTOP, UQAM. The authors also thank the reviewers that revised the original version of the manuscript for their suggestions that helped to improve the paper.

2.9 References

Andersen, D.J., Lindsley, D.H., Davidson, P.M., 1993. QUILF: a PASCAL program to assess equilibria among Fe–Mg–Ti oxides, pyroxenes, olivine, and quartz. Computers & Geosciences 19, 1333–1350.

Arguin J-P, Pagé P, Barnes S-J, Girard R, Duran C. 2018. An Integrated Model for Ilmenite, Al-Spinel, and Corundum Exsolutions in Titanomagnetite from Oxide-Rich Layers of the Lac Doré Complex (Québec, Canada). Minerals. 2018; 8 (11):476.

Ashwal, LD., 1993. Anorthosites. Springer, Heidelberg.

Ashwal, L. D. 2010. The temporality of anorthosites. The Canadian Mineralogist, 48 (4), 711-728.

Barnes, S. J., Maier, W. D., & Ashwal, L. D. 2004. Platinum-group element distribution in the main zone and upper zone of the Bushveld Complex, South Africa. Chemical Geology, 208(1-4), 293-317.

Barnes, S. J., Mansur, E. T., Pagé, P., Meric, J., & Arguin, J. P. 2020. Major and trace element compositions of chromites from the Stillwater, Bushveld and Great Dyke intrusions compared with chromites from komatiites, boninites and large igneous provinces.

Buddington, A. F., & Lindsley, D. H. 1964. Iron-titanium oxide minerals and synthetic equivalents. Journal of petrology, 5(2), 310-357.

Bybee, G. M., & Ashwal, L. D. 2015. Isotopic disequilibrium and lower crustal contamination in slowly ascending magmas: Insights from Proterozoic anorthosites. Geochimica et Cosmochimica Acta, 167, 286-300.

Cawthorn, R. G. 2007. Cr and Sr: Keys to parental magmas and processes in the Bushveld Complex, South Africa. Lithos, 95(3-4), 381-398.

Charlier, B., Grove, T.L., 2012. Experiments on liquid immiscibility along tholeiitic liquid lines ofdescent Contrib. Mineral. Petrol. 164 (1), 27-44

Charlier, B., Vander Auwera, J., & Duchesne, J. C. 2005. Geochemistry of cumulates from the Bjerkreim–Sokndal layered intrusion (S. Norway): Part II. REE and the trapped liquid fraction. Lithos, 83(3-4), 255-276.

Charlier, B., Duchesne, J.-C., Vander Auwera, J., 2006. Magma chamber processes in the Tellnes ilmenite deposit (Rogaland Anorthosite Province, SW Norway) and the formation of Fe–Ti ores in massif-type anorthosites. Chemical Geology 234, 264–290.

Charlier, B., Skar, O., Korneliussen, A., Duchesne, J.-C., Vander Auwera, J., 2007. Ilmenite composition in the Tellnes Fe–Ti deposit, SW Norway: fractional crystallization, postcumulus evolution and ilmenite–zircon relation. Contributions to Mineralogy and Petrology 154, 119–134.

Charlier, B., Sakoma, E., Sauve, M., Stanaway, K., Vander Auwera, J., Duchesne, J.-C., 2008. The Grader layered intrusion (Havre-Saint-Pierre Anorthosite, Quebec) and genesis of nelsonite and other Fe–Ti–P ores. Lithos 101, 359–378.

Charlier, B., Namur, O., Duchesne, J.-C., Wiszniewska, J., Parecki, A., Vander Auwera, J., 2009. Cumulate origin and polybaric crystallization of Fe–Ti oxide ores in the Suwalki anorthosite, Northeastern Poland. Economic Geology 104, 205–221.

Charlier, B., Namur, O., Malpas, S., de Marneffe, C., Duchesne, j.C., Vander Auwera, J., Bolle, O, 2010b. Origin ofthe giant Allard Lake ilmenite ore deposit (Canada) by fractional crystallization, multiple magma pulses and mixing. Lithos 117, 119-134.

Charlier B, Namur O, Bolle O, et al 2015. Fe-Ti-V-P ore deposits associated with Proterozoic massif type anorthosites and related rocks. Earth Science Reviews, 141:56–81. doi: 10.1016/j.earscirev.2014.11.005.

Chen, W., Zhou, M.-F., Zhao, T.-P., 2013. Differentiation of nelsonitic magmas in the formation of the - 1.74 Ga Damiao Fe-Ti-P ore deposit, North China. Contrib. Mineral. Petrol. 165, 1341-1362.

Coint, N., Keiding, J. K., & Ihlen, P. M. 2020. Evidence for silicate–liquid immiscibility in monzonites and petrogenesis of associated Fe–Ti–P-rich rocks: example from the Raftsund intrusion, Lofoten, Northern Norway. Journal of Petrology, 61(4).

Corriveau, L., Perreault, S., Davidson, A., 2007. Prospective metallogenic settings of the Grenville Province. In: Goodfellow, W.D. (Ed.), Mineral Deposits of Canada: a Synthesis of Major Deposit-types, District Metallogeny, the Evolution of Geological Provinces, and Exploration Methods: Geological Survey of Canada, Mineral Deposits Division, Special Publication, pp. 819–847.

Dare S.A, Barnes S-J, Beaudoin G, et al 2014. Trace element in magnetite as petrogenetic indicators. Mineralium Deposita, 49:785–796.

Dare, S., Bethell, E., & Barnes, S. J. 2019. Constraining the formation of Fe-Ti-VP deposits using trace element in Fe-Ti oxides: insights from the chemostratigraphic variation of magnetite and ilmenite in the Upper Zone of the Bushveld Igneous Complex. GAC-MAC-IAH Québec 2019.

Duchesne, J.C. 1972. Iron-titanium oxide minerais in the Bjerkrem-Sogndal Massif, South-western Norway. J. Petrol. 13, 57-81 .

Duchesne, J.C., Charlier, B., 2005. Geochemistry of cumulares from the Bjerkreim-Sokndal layered intrusion (S. Norway). Part 1: constraints from major elements on the mechanism of cumulate formation and on the jotunite liquid line of descent. Lithos, 83, 229-254.

Duchesne, J.C., Shumlyanskyy , L, Charlier, B., 2006. The Fedorivka layered intrusion (Korosten Pluton, Ukraine) : an example ofhighly differentiated ferrobasaltic evolution. Lithos 89, 353-376.

Dymek, R.F., Owens, B.E., 2001. Petrogenesis of apatite-rich rocks (nelsonites and oxide apatite gabbronorites) associated with massif anorthosites. Economic Geology 96, 797–815.

Emslie, R.F., 1985. Proterozoic anorthosite massifs. In: Tobi, A.C., Touret, J.L.R. (Eds.), The Deep Proterozoic Crust in the North Atlantic Provinces. Reidel, Dordrecht, pp. 39–60.

Frost, B. R. & Lindsley, D. H. 1992. Equilibria among Fe-Ti oxides, pyroxenes, olivine, and quartz: Part I. Theory. American Mineralogist, 77(9-10), 987-1003.

Frost, B. R. (1991). Magnetic petrology: factors that control the occurrence of magnetite in crustal rocks. Reviews in Mineralogy and Geochemistry, 25(1), 489-509.

Frost, B.R., Lindsley, D.H., Andersen, D.J, 1988. Fe-Ti oxide-silicate equilibria: assemblages with fayalitic olivine. Am. Mineral. 73, 727-740.

Frost, C. D., Frost, B. R., Lindsley, D. H., Chamberlain, K. R., Swapp, S. M., & Scoates, J. S. 2010. Chemical and isotopic evolution of the anorthositic plutons of the Laramie Anorthosite Complex: Explanations for variations in silica activity and oxygen fugacity of massif anorthosites. The Canadian Mineralogist, 48(4), 925-946.

Gobeil, A., Brisebois, D., Clark, T., Verpaelst, P., Madore, L., Wodicka, N., Cheve, S., 2003. Geologie de la moyenne Cote-Nord. In: Brisebois, D., Clark, T. (Eds.), Geologie et ressources minerales de la partie est de la Province de Grenville. Ministere des Ressources naturelles, de la Faune et des Parcs, Quebec, pp. 9–58. DV 2002-03.

Grant, M. 2020. Formation of magmatic Fe-Ti-V-P deposits within the Lac St. Jean area Saguenay, Québec, Canada: Insights from trace element composition of Fe-oxides and apatite. (Unpublished masters thesis). University of Ottawa, Ontario, Canada, pp. 343.

Hébert, C., Cadieux, A.-M., Van Breemen, O., 2005. Temporal evolution and nature of Ti– Fe–P mineralization in the anorthosite–mangerite–charnockite–granite (AMCG) suites of the South–central Grenville Province, Saguenay – Lac St. Jean area, Quebec, Canada. Canadian Journal of Earth Sciences 42, 1865–1880.

Hébert, C., Van Breemen, O., & Cadieux, A. 2009. Région du reservoir Pipmuacan, (SNRC 22E): Synthese Geologique. RG 2009-01. Ministère des ressources naturelles et de la faune, Gouvernement du Québec.

Higgins, M. D., & Van Breemen, O. 1992. The age of the Lac-Saint-Jean anorthosite complex and associated mafic rocks, Grenville Province, Canada. Canadian Journal of Earth Sciences, 29(7), 1412-1423.

Higgins, M.D., Van Breemen, O., 1996. Three generations of Anorthosite–Mangerite–Charnockite–Granite magmatism, contact metamorphism and tectonism in the Saguenay – Lac–St-Jean region, Grenville Province, Canada. Precambrian Research 79, 347–362.

Higgins, M. D., Ider, M., & Breemen, O. V. 2002. U-Pb ages of plutonism, wollastonite formation, and deformation in the central part of the Lac-Saint-Jean anorthosite suite. Canadian Journal of Earth Sciences, 39(7), 1093-1105.

Hou, T., Charlier, B., Holtz, F., Veksler, I., Zhang, Z., Thomas, R., & Namur, O. 2018. Immiscible hydrous Fe–Ca–P melt and the origin of iron oxide-apatite ore deposits. Nature communications, 9(1), 1-8.

Irvine, T.N., 1982. Terminology for layered intrusions. Journal of Petrology 23 (2), 127–162.

Jensen, J. C., Nielsen, F. M., Duchesne, J. C., Demaiffe, D., & Wilson, J. R. 1993. Magma influx and mixing in the Bjerkreim-Sokndal layered intrusion, South Norway: evidence from the boundary between two megacyclic units at Storeknuten. Lithos, 29(3-4), 311-325.

Klemme, S., Gunther, D., Hametner, K., Prowatke, S., Zack, T., 2006. The partitioning of trace element between ilmenite, ulvospinel, armalcolite and silicate melts with implications for the early differentiation of the moon. Chemical Geology 234, 251–263.

Kieffer, M. A., Dare, S. A., & Namur, O. 2022. The use of trace element in apatite to trace differentiation of a ferrobasaltic melt in the Sept-Iles Intrusive Suite, Quebec, Canada: Implications for provenance discrimination. Geochimica et Cosmochimica Acta.

Lattard, D., Sauerzapf, U., Kasemann, M., 2005. New calibration data for the Fe-Ti oxide thermo-oxybarometers from experiments in the Fe-Ti-O system at 1 bar, 1,000- 1,300 ºC and a large range of oxygen fugacities . Contrib . Mineral. Petrol. 149, 735-754.

Laverdière, G. 2013. Rapport de travaux d'exploration. Propriété Lac Orignal, Région du Saguenay-Lac Saint Jean. Glen Eagle Resources Inc.

Laverdiere, G. 2016. Rapport de travaux d'exploration. Propriete Lac Original, Region du Saguneay-Lac Saint Jean. Glen Eagle Resources Inc.

Leeman, W. P., Ma, M. S., Murali, A. V., & Schmitt, R. A. 1978. Empirical estimation of magnetite/liquid distribution coefficients for some transition elements. Contributions to mineralogy and petrology, 65(3), 269-272.

Lin, L & Sawyer, E. 2019. Microstructure and compsotional changes across biotite-rich reaction selvedges around mafic schollen in a semppelitic diatexite migmatite. Journal of Metamorphic Geology, 37:539-566.

McLelland,J., Ashwal, L, Moore, L, 1994. Composition and petrogenesis of oxide-, apatite-rich gabbronorites associated with Proterozoic anorthosite massifs: examples from the Adirondack Mountains, New York. Contrib. Mineral. Petrol. 116, 225-238.

Mitchell, J.N., Scoates, j.S., Frost, C.D., Kolker, A., 1996 . The geochemical evolution of anorthosite residual magmas in the Laramie Anorthosite Complex, Wyoming.j. Petrol. 37, 637-660.

Morisset, C.-E., Scoates, J.S., Weis, D., Friedman, R.M., 2009. U–Pb and 40Ar/39Ar geochronology of the Saint-Urbain and Lac Allard (Havre-Saint-Pierre) anorthosites and their associated Fe–Ti oxide ores, Quebec: evidence for emplacement and slow cooling during the collisional Ottawan orogeny in the Grenville Province. Precambrian Research 174, 95–116.

Morisset, C.-E., Scoates,J.S., Weis, D., Sauve, M., Stanaway, K.J., 2010. Rutile-bearing ilmenite deposits associated with the Proterozoic Saint-Urbain and Lac Allard anorthosite massifs, Grenville Province, Québec. Can. Mineral. 48, 821-849.

Morse, S. A. 1982. A partisan review of Proterozoic anorthosites. American Mineralogist, 67(11-12), 1087-1100.

Namur, O., Charlier, B., Toplis, M. J., Higgins, M. D., Liégeois, J. P., & Vander Auwera, J. 2010. Crystallization sequence and magma chamber processes in the ferrobasaltic Sept Iles layered intrusion, Canada. Journal of Petrology, 51(6), 1203-1236.

Namur, O., Charlier, B., Holness, M.B., 2012. Dual origin of Fe-Ti-P gabbros by immiscibility and fractional crystallization of evolved tholeiitic basalts in the Sept Iles layered intrusion. Lithos 154, 100-114.

Owens, B.E., Dymek, R.F., 1992. Fe-Ti-P-rich rocks and massif anorthosite: problems of interpretation illustrated from the Labrieville and St-Urbain plutons, Quebec. Can. Mineral. 30, 163-190

Owens, B.E., Dymek, R.F., 2005. Rediscovery of the Mattawa anorthosite massif, Grenville Province, Quebec. Canadian Journal of Earth Sciences 42, 1699–1718.

Owens, B.E., Rockow, M.W., Dymek, R.F., 1993. Jotunites from the Grenville Province, Quebec: petrological characteristics and implications for massif anorthosite petrogenesis. Lithos 30, 57–80.

Pang, K.-N., Li, C., Zhou, M.-F., Ripley, E.M., 2007. Abundant Fe–Ti oxide inclusions in olivine from the Panzhihua and Hongge layered intrusions, SW China: evidence for early saturation of Fe–Ti oxides in ferrobasaltic magma. Contributions to Mineralogy and Petrology 156, 307–321.

Perrot, M., Tremblay, A., & David, J. (2017). Detrital zircon U-Pb geochronology of the Magog Group, southern Quebec–stratigraphic and tectonic implications for the Quebec Appalachians. American Journal of Science, 317(10), 1049-1094.

Philpotts, A.R., 1967. Origin of certain iron-titanium oxide and apatite roeks. Econ. Geol. 62, 303-315.

Philpotts, A.R., 1982. Compositions of immiscible liquids in volcanic roeks. Contrib. Mineral. Petrol. 80, 201-218.

Polivchuk, M., & Dare, S. A. S. 2017. The formation of vanadium deposits of the Archean Bell River Complex, Quebec, Canada: Insights from Fe Ti oxide chemistry.

Rivers, T., 1997. Lithotectonic elements of the Grenville Province: review and tectonic implications. Precambrian Research 86, 117–154.

Scoates, J.S., Lindsley, D.H., Frost, B.R., 2010. Magmatic and structural evolution of an anorthositic magma chamber: the Poe Mountain intrusion, Laramie Anorthosite complex, Wyoming. Can. Mineral. 48, 851-885.

Slagstad, T., Henderson, I. H., Roberts, N. M., Kulakov, E. V., Ganerød, M., Kirkland, C. L. & Coint, N. 2022. Anorthosite formation and emplacement coupled with differential tectonic exhumation of ultrahigh-temperature rocks in a Sveconorwegian continental back-arc setting. Precambrian research, 376, 106695.

Snyder, D., Carmichael, I.S.E., Wiebe, RA., 1993. Experimental study of liquid evolution in an Fe-rich, layered mafic intrusion: constrains of Fe-Ti oxide precipitation on the Tf02 and T-p paths of tholeiitic magmas. Contrib. Mineral. Petrol. 113, 73-86.

Tanner, D., Mavrogenes, J. A., Arculus, R. J., & Jenner, F. E. 2014. Trace element stratigraphy of the Bellevue Core, Northern Bushveld: multiple magma injections obscured by diffusive processes. Journal of Petrology, 55(5), 859-882.

Tegner, C., Cawthorn, R. G., & Kruger, F. J. 2006. Cyclicity in the Main and Upper Zones of the Bushveld Complex, South Africa: crystallization from a zoned magma sheet. Journal of Petrology, 47(11), 2257-2279.

Tollari, N., Barnes, S. J., Cox, R. A., & Nabil, H. 2008. Trace element concentrations in apatites from the Sept-Îles Intrusive Suite, Canada—implications for the genesis of nelsonites. Chemical Geology, 252(3-4), 180-190.

Toplis, MJ., Dingwell, D., Libourel, G., 1994a. The effect of phosphorous on the iron redox ratio, viscosity, and density of an evolved ferrobasalt. Contrib. Mineral. Petrol. 117, 293-304 .

Toplis, M. J., Libourel, G., & Carroll, M. R. 1994b. The role of phosphorus in crystallization processes of basalt: an experimental study. Geochimica et Cosmochimica Acta, 58(2), 797-810.

Toplis, MJ, Carroll, M.R., 1995. An experimental study of the influence of oxygen fugacity on Fe-Ti oxide stability, phase relations, and mineral-melt equilibria in ferrobasaltic systems. J. Petrol. 36, 1137-1170.

Toplis, M., Corgne, A., 2002. An experimental study of element partitioning between magnetite, clinopyroxene and iron-bearing silicate liquids with particular emphasis on vanadium Contrib. Mineral. Petrol. 144, 22-37.

Toplis, M. J., & Dingwell, D. B. (1996). The variable influence of P2O5 on the viscosity of melts of differing alkali/aluminium ratio: Implications for the structural role of phosphorus in silicate melts. Geochimica et Cosmochimica Acta, 60(21), 4107-4121.

Vander Auwera, J., Longhi, J., 1994. Experimental study of a jotunite (hypersthene monzodiorite): constraints on the parent magma composition and crystallization conditions (P, T, fO2) of the Bjerkreim-Sokndal layered intrusion (Norway) . Contrib. Mineral. Petrol. 118, 60-78.

Vander Auwera, J., Longhi, J, Duchesne, J.C., 1998. A liquid line of descent of the jotunite (hypersthene monzodiorite) suite. J. Petrol. 39, 439-468.

Vander Auwera, J., Weis, D., Duchesne,j.C., 2006. Marginal mafic intrusions as Indicators of downslope draining of dense residual melts in anorthositic diapirs? Lithos 89, 329-352.

Wilson, J. R., Robins, B., Nielsen, F. M., Duchesne, J. C., & Vander Auwera, J. 1996. The Bjerkreim-Sokndal layered intrusion, Southwest Norway. In Developments in Petrology (Vol. 15, pp. 231-255). Elsevi

Yassa, A. 2022. Technical report and initial mineral resource estimate of the Lac Orignal phosphate property, Saguenay-Lac-Saint-Jean region, Northern Québec. First Phosphate Corp.

CHAPTER 3

PETROGENESIS OF OXIDE-APATITE MINERALIZATION ASSOCIATED WITH PROTEROZOIC ANORTHOSITE MASSIFS AT LAC MIREPOIX, QUEBEC, CANADA: A MULTI-STAGE MODEL OF EVOUTION FOR FE-TI-P MINERALIZATION IN THE CENTRAL GRENVILLE PROVINCE

Pedro Miloski[1], Sarah Dare[1], Caroline-Emmanuelle Morisset[2], Joshua H.F.L. Davies[3], Morgann G. Perrot[3]

1. Département des Sciences Appliquées, Université du Québec à Chicoutimi (UQAC), 555 Boulevard de l'Université, Chicoutimi, Québec, Canada, G7H 2B1

2. Agence Spatiale Canadienne, 6767 Rte de l'Aéroport, Saint-Hubert, Québec, Canada, J3Y 8Y9

3. Département des Sciences de la Terre et de l'Atmosphère/GEOTOP, Université du Québec à Montréal (UQAM), 405 Rue Sainte-Catherine Est, Montréal, Québec, Canada, H2L 2C4

Ore Geology Reviews (2023)
Under Review

Résumé

La minéralisation Fe-Ti-P du Lac Mirepoix présente plusieurs lentilles minéralisées qui affleurent près de la frontière des massifs d'anorthosite de Vanel et Mattawa, dans la province du Grenville, Québec, Canada. La minéralisation est dominée par l'(hémo)-ilménite, accompagnée de magnétite et d'apatite. Elle est subdivisée en trois zones différentes en raison de l'apparition de différentes phases de cumulâts: la zone I comprend principalement des couches d'oxydes massifs (>70 % hémo-ilménite ± magnétite) encaissées dans l'anorthosite. Vers le centre de la minéralisation (zone II), les couches d'oxydes massifs sont moins fréquentes tandis que des cumulâts apatites apparaissent, formant de la nelsonite massive (50-70 % de magnétite ± ilménite et 25-30 % d'apatite) et de la norite d'apatite oxydée (OAN, 15 - 25% hémo-ilménite ± magnétite et 8-20% apatite). Enfin, la zone III est marquée par l'alternance de couches d'OAN (10-25m), plus riches en magnétite, en plus de l'(hémo)-ilménite et de l'apatite, et par une absence d'oxyde massif et de nelsonite. L'analyse in situ des éléments traces du plagioclase, de l'apatite et des oxydes par ablation laser ICP-MS, révèle des variations cryptiques liées à la différenciation du magma et à des injections multiples de magmas parentaux de ferrodiorite de composition similaire. La datation U-Pb in situ des zircons de la minéralisation OAN elle-même indique deux âges de cristallisation différents entre la zone III (1048 ± 8 Ma) et la zone I (964 ± 9 Ma), favorisant un modèle à multi-injections plutôt que cristallisation in situ d'une seule intrusion litée, soutenue par la géochimie des éléments traces. La minéralisation du Lac Mirepoix enregistre la séquence de cristallisation fractionnée suivante d'un magma à haute teneur en Ti-P (ferrodiorite), résiduel après la formation de l'anorthosite: d'abord, des oxydes massifs d'hémo-ilménite cristallisés (haute Ti/Fe) par accumulation d'oxydes, avec des compositions primitives, similaires au gisement de classe mondiale du Lac Tio. La minéralisation

d'oxyde-apatite (nelsonite et OAN) s'est cristallisée à partir du liquide résiduel (Ti/Fe inférieur, compositions évoluées) dans lequel la magnétite et l'apatite étaient plus abondantes, semblable à la minéralisation voisine dans la région (ex. Lac à l'Orignal Fe-Ti -P minéralisation). La diminution observée de la teneur en Ti du magma en évolution est soutenue par la ligne de descente liquide de plusieurs dykes de ferrodiorite au sein des roches encaissantes et de la minéralisation. Enfin, nous proposons un modèle d'injections multiples de liquides résiduels riches en Fe-Ti-P drainés ou filtrés dans des diapirs de bouillies riches en plagioclase qui ont été mises en place à plus de 80 Mys d'intervalle le long de la même zone de détachement crustale.

Abstract

The Lac Mirepoix Fe-Ti-P mineralization presents several mineralized lenses that outcrop near the border of the 1080 (±2) Ma Vanel and the 1016 (±2) Ma Mattawa Anorthosite massifs, in the Central Grenville Province, Quebec, Canada. The mineralization is (hemo)-ilmenite-dominated, accompanied by magnetite and apatite. It is subdivided in three different zones due to the appearance of different cumulate phases: zone I comprises mainly massive oxide (>70% hemo-ilmenite ± magnetite) layers hosted in anorthosite. Towards the center of the mineralization (zone II), massive oxide layers are less common whereas apatite-bearing cumulates appear, forming massive nelsonite (50-70% magnetite ± ilmenite and 25-30% apatite) and oxide apatite norite (OAN, 15-25% hemo-ilmenite ± magnetite and 8-20% apatite). Finally, zone III is marked by the alternance of OAN layers (10-25m), richer in magnetite, in addition to (hemo)-ilmenite and apatite, and an absence of massive oxide and nelsonite. In-situ trace element analysis of plagioclase, apatite and oxides by laser ablation ICP-MS, reveals cryptic variations related to magma differentiation and multiple injections of ferrodiorite parental magmas of similar composition. In-situ U-Pb dating of zircon from the OAN mineralization itself indicates two different crystallization ages between zone III (1048 ± 8Ma) and zone I (964 ± 9 Ma), favouring a model of multiple injections of similar Fe-Ti-P-rich melts of similar composition over a period of 80 Mys rather than in-situ crystallization of a single intrusion, which is supported by trace element geochemistry. The Lac Mirepoix mineralization records the following fractional crystallization sequence of a high-Ti-P magma, residual after the anorthosite formation: first, massive oxides of hemo-ilmenite crystallized (high Ti/Fe) by oxide settling, with primitive compositions, similar to the world-class Lac Tio deposit. The oxide-apatite mineralization (nelsonite and OAN) crystallized from the

residual liquid (lower Ti/Fe, evolved compositions) in which magnetite and apatite were more abundant, similar to nearby mineralization in the area (e.g. Lac à l'Orignal Fe-Ti-P mineralization). The observed decrease in Ti content of the evolving melt is supported by the liquid line of descent of several ferrodiorite dykes within the host-rocks and mineralization. Finally, we propose a model of multiple injections of residual Fe-Ti-P-rich liquids drained from or filter-pressed within diapirs of plagioclase-rich mushes that were emplaced over 80 Mys apart along the same crustal detachment zone.

3.1 Introduction

Examples of magmatic oxide-apatite mineralization within massif-type anorthosites and related layered intrusions are found throughout the world (Ashwal, 1993). These magmatic oxide–apatite ores are of both economic and scientific interest, providing important resources for several critical and strategic substances/metals, such as TiO_2 (from hemo-ilmenite: Fe_2O_3-$FeTiO_3$), V (from magnetite: Fe_3O_4) and P (from apatite: $Ca_5(PO_4)_3(OH,F,Cl)$). For example, the world's largest producer of TiO_2, Lac Tio mine, is a hemo-ilmenite-deposit within the massif-type anorthosite of Havre-Saint-Pierre, Quebec (Corriveau et al. 2007; Charlier et al. 2008). The Lac Mirepoix Fe-Ti-P mineralization is situated in the Vanel Anorthosite (Hébert et al. 2005) that is part of the AMCG suites (Anorthosite–Mangerite–Charnockite–(rapakivi) Granite) of the Grenville Province (Quebec), where there are the major occurrences of Fe–Ti–P ores (Owens & Dymek, 1992; 2005; Owens et al. 1993; Morisset et al. 2009; 2010; Charlier et al. 2008; 2010). AMCG suites hosting these deposits require an extensive and complex history of voluminous plagioclase crystallization to develop (Ashwal, 1993; Woodruff et al. 2013), with accumulation of mantle-derived (Emslie, 1985; Ashwal, 1993; 2010; Bybee et al. 2015) or mafic crust-

derived (Duchesne, 1999) magmas at the crust-mantle interface (MOHO), followed by multiple diapiric upwelling of plagioclase-melt mushes (Barnichon et al. 1999) with extensive effects of crustal assimilation (Bybee & Ashwal, 2015). Most of the oxide-apatite mineralization is then generated by further fractional crystallization of the residual liquid (jotunite/ferrodiorite composition, Vander Auwera et al. 1998; Owens et al. 1993), dominated by plagioclase, Fe-Ti oxides, and Fe-Mg silicates. These multiple diapiric intrusions are probably favored by zones of weakness such as major deep-seated lineaments (Corrigan & Hanmer, 1997; Duchesne, 1999; Ryan, 2000; Bogdanova et al. 2004; Hébert et al. 2005; 2009), as clearly observed near several anorthosite intrusions in the Central Grenville Province. According to Charlier et al. (2015), the timing and style of oxide mineralization are related to the magmatic and dynamic evolution of these diapiric systems and to development and movement of oxide cumulates and related melts. These cumulate rocks enriched in Fe-Ti-P can be observed either as massive deposits (e.g Lac Tio deposit, Quebec); as a part of layered stratigraphic deposits (e.g. Bjerkrein Skondal Layered Intrusion, Norway; Grader Intrusion, Quebec); massive to layered tabular bodies (e.g. Tellnes, Norway) and as lenticular ore bodies (e.g. Suwalki Anorthosite, Poland; Damiao deposit, China) (Charlier et al. 2015 and references within).

However, the origin of oxide-apatite mineralization and its genetic relationship to the host anorthosite rocks are still highly debated. Understanding the formation of magmatic Fe-Ti-oxide deposits relies on better knowing the nature of anorthosites and related rocks hosting these deposits, the evolution of the residual liquid from which oxide and silicate minerals crystallized, the role of crustal contamination and the tectonic setting of massif-type anorthosite (Woodruff et al. 2013; Ashwal & Bybee, 2017).

Several factors can concentrate ilmenite ± magnetite ± apatite during cooling of the parental magma, such as oxygen fugacity (fO_2), initial TiO_2 and P_2O_5 contents of the magma, temperature and/or pressure (Toplis et al. 1994a,b; Toplis & Carroll, 1995; Charlier et al. 2006; 2008; 2015; Mitchell et al. 1996; Vander Auwera et al. 1998; Vander Auwera & Longhi, 1994; Miloski et al. 2023), and mechanisms (e.g. fractional crystallization with oxide settling and plagioclase flotation (Charlier et al. 2006; 2007; 2008; 2015; Miloski et al. 2023); filter pressing of jotunite/ferrodiorite residual melts (Scoates et al. 2010; Vander Auwera et al. 2006; Dymek & Owens, 2001); magma mixing (Namur et al. 2010; Charlier et al. 2006; 2010; 2015) and/or liquid immiscibility (Roedder, 1978; Philpotts, 1967; 1982; Charlier & Grove, 2012; Charlier et al. 2011; Hou et al. 2018; Coint et al. 2020). Previous studies (Duchesne et al. 2006; Charlier et al. 2005; 2006; 2007; 2008; 2009; 2010; Chen et al. 2013; Miloski et al. 2023) on different Fe-Ti-(P) mineralization worldwide (e.g. Tellnes, Bjerkrein-Skondal, Lac Tio, Grader Intrusion, Fedorivka, Damiao) have successfully used trace element of Fe-Ti oxides, apatite and silicates (where present) to track magmatic processes (e.g fractional crystallization, magma replenishments, chemostratigraphic variation, calculation of parental magma composition using apatite, oxide sub-solidus reequilibration).

However, only a few publications are available regarding the petrological aspects of oxide-apatite cumulate rocks for the Central Grenville Province (e.g. OAGN - oxide-apatite gabbronorite, Owens & Dymek, 1992; Miloski et al. 2023; and nelsonite - Fe-Ti oxides + subordinate apatite, Dymek & Owens, 2001). In this paper, we present a detailed whole-rock and in-situ trace element study of plagioclase, oxides, and apatite, and in-situ U-Pb dating into the different cumulates of the Lac Mirepoix Fe-Ti-P mineralization, in the Central Grenville Province, Quebec. This mineralization is ilmenite-dominated like the two hard-rock deposits in anorthosites presently exploited,

the Lac Tio mine, Quebec (Charlier et al. 2008), and the Tellnes deposit, Norway (Charlier et al. 2006, 2007), and contains variable concentrations of Fe-Ti oxides and apatite from massive oxides to nelsonites, as well as oxide-apatite norites cumulates. The oxide-apatite rich rocks of the Lac Mirepoix mineralization thus constitute an important opportunity to achieve a comprehensive understanding of the mechanisms responsible for the formation of Fe-Ti-P mineralization, the relationship between massive oxides, massive nelsonites and oxide-apatite-norites, the nature of the parental magmas, and the controlling factors on ore composition in the Central Grenville Province.

3.2 Regional geological setting

The Grenville Province (Fig.3.1) is a Mesoproterozoic orogenic belt that represents the southeastern margin of the Laurentian Paleocontinent, comprising a significant portion of the Eastern Canadian Shield (Corriveau et al. 2007). The Archean to Late Mesoproterozoic rocks of the Grenville Province evidence the existence of an active continental margin with more than 400Ma years of tectonic activity. Substantial growth events have been documented in the Labradorian (1680 - 1660 Ma), Pinwarian (1500 - 1450 Ma), and Elzevirian (1250 - 1190 Ma) periods. Subsequent stages of continent-continent collision (Shawinigan, 1190 – 1140Ma; Ottawan, 1080 – 1020Ma and Rigolet, 1000 – 850Ma) took place during the Grenvillian Orogeny, separated by periods of crustal extension and several occurrences of within-plate magmatism. The emplacement of most of the AMCG-suites in the Central Grenville Province are coeval to periods of either crustal shortening or crustal extension during the Grenvillian Orogeny, being associated with the presence of lower crustal-type shear zones (Fig.3.1), such as the Saint Fulgence Deformation Zone and Pipmuacan Deformation

Zone (Higgins & Van Breemen, 1996; Gobeil et al. 2002; Hébert et al. 2005; 2009; Corriveau et al. 2007).

The Grenville Province hosts numerous episodes of AMCG magmatism, and coeval Fe-Ti-P mineralization, that were emplaced for over 300 million years (1327 – 1000 Ma) recording a complex petrogenetic, tectonic and temporal evolution (Emslie, 1985; Higgins & Van Breemen, 1996; Gobeil et al. 2002; Hébert et al. 2005; 2009). In the Central-South Grenville (Fig.3.1b), Hébert et al. (2009) summarised four distinct pulses of magmatism, with major occurrences in the region of Saguenay-Lac-Saint Jean, Quebec: I) the 1327 ± 16 Ma labradorite-type De La Blache Mafic Suite (Gobeil et al. 2002); II) the 1160-1135 Ma labradorite- and andesine-type Lac-Saint-Jean Anorthosite Suite (Higgins & Van Breemen, 1992; 2004; Higgins et al. 2002); III) the 1082-1045 Ma andesine and labradorite-type Pipmuacan Anorthosite Suite, including the Vanel Anorthosite, the Poulin de Courval Mangerite and the coeval Saint Urbain anorthosite (Higgins & Van Breemen, 1996; Morisset et al. 2009); IV) the 1020-1008 Ma andesine-type Valin Anorthosite Suite, including the Mattawa Anorthosite (Hébert et al. 2005; Owens & Dymek, 2005), the Labrieville Alkalic Anorthosite Massif (Owens & Dymek, 1992; Owens et al. 1993), the Gouin Charnockite (Hébert et al. 2005), and the La Hache Mangerite (Hébert et al. 2005).

3.3 Fe-Ti-P mineralization in the Central Grenville Province

A large number of Fe-Ti oxide + apatite mineralization occurrences are present in the central Grenville Province (Fig.3.1), hosted in the aforementioned AMCG-massifs. The Fe-Ti-P mineralization normally occurs in the form of lenses, dykes and small layered intrusions at the margins, or within, these different AMCG-massifs (Hébert et al. 2005; 2009; Corriveau et al. 2007), containing mainly the ilmenite/hemo-ilmenite (ilmenite with extensive hematite exsolution) + Ti-magnetite + apatite

association. These minerals, in association with other cumulus phases as plagioclase and orthopyroxene, constitute oxide-apatite (gabbro)norites, leuconorites, and nelsonite (massive oxides + apatite) lithologies. However, a few localities do not contain apatite, being dominated by massive hemo-ilmenite/ilmenite + magnetite rocks. The variation in the oxide assemblage (from magnetite to hemo-ilmenite) and apatite trace element patterns appears to be related to the composition and age of the host anorthosites (Dymek & Owens, 2002; Hébert et al. 2005; 2009; Grant, 2020): I) labradorite-type anorthosites are predominantly older than 1130 Ma (such as the Lac-Saint.-Jean Anorthosite Suite) and host Fe-Ti-V-P oxide mineralization dominated by Ti-magnetite and olivine; II) hemo-ilmenite-dominated mineralization occurs exclusively with andesine-type anorthosites younger than 1130 Ma, such as the Pipmuacan and Valin suites, and when it forms Fe-Ti-P mineralization, such as nelsonites (massive oxides-apatite) and oxide–apatite (gabbro)norites (OAGN), it is associated with orthopyroxene instead of olivine.

Variation in the oxide mineralogy also exists within the younger andesine anorthosites of the Pipmuacan (1082-1045 Ma) and Valin suites (1020-1008 Ma). Mineralization spatially associated with the anorthosite massifs (Fig.3.1) of Vanel (1080 ± 2 Ma), Mattawa (1016 ± 2 Ma) and Labrieville (1010 ± 5 Ma) are hemo-ilmenite dominated but contain variable proportions of magnetite and apatite (Owens & Dymek, 1992; Corriveau et al. 2007; Miloski et al. 2023), similar to the Grader Intrusion (Charlier et al. 2008) in the Havre-Saint-Pierre Anorthosite of the northeastern Grenville Province. On the other hand, the Saint Urbain Anorthosite (1055 ± 2 Ma), 100 km south of Mattawa, hosts mineralization dominated by hemo-ilmenite (± Al-spinel ± apatite ± rutile) with notable absence of magnetite, similar to Lac Tio deposit of Havre-Saint-Pierre (Morisset et al. 2009). The presence of Ti-rich ilmenite

(hematite-exsolution-free), when associated with magnetite, is also commonly observed within the different Fe-Ti-P mineralization occurrences, as a result of subsolidus re-equilibration of hemo-ilmenite with magnetite (Charlier et al. 2007; Morisset et al. 2010; Miloski et al. 2023). Minor amounts of Al-spinel occur with the oxide mineralization either as exsolutions from magnetite and ilmenite (Charlier et al. 2007; Miloski et al. 2023) and/or crystallizes with hemo-ilmenite in the absence of magnetite (Morisset et al. 2013).

Fe-Ti-P mineralization associated with more silicic members of AMCG suites, such as mangerites and charnockites, is fairly rare in anorthosite provinces worldwide, except for the Lofoten-Vesteralen AMCG suite (e.g., Coint et al. 2020). However, in the Central Grenville, there is some Fe-Ti-P mineralization associated with the (1010 ± 3 Ma) La Hache Mangerite in the northern region of the Saguenay-Lac-Saint-Jean area (Fig.3.1; Miloski et al. 2023a).

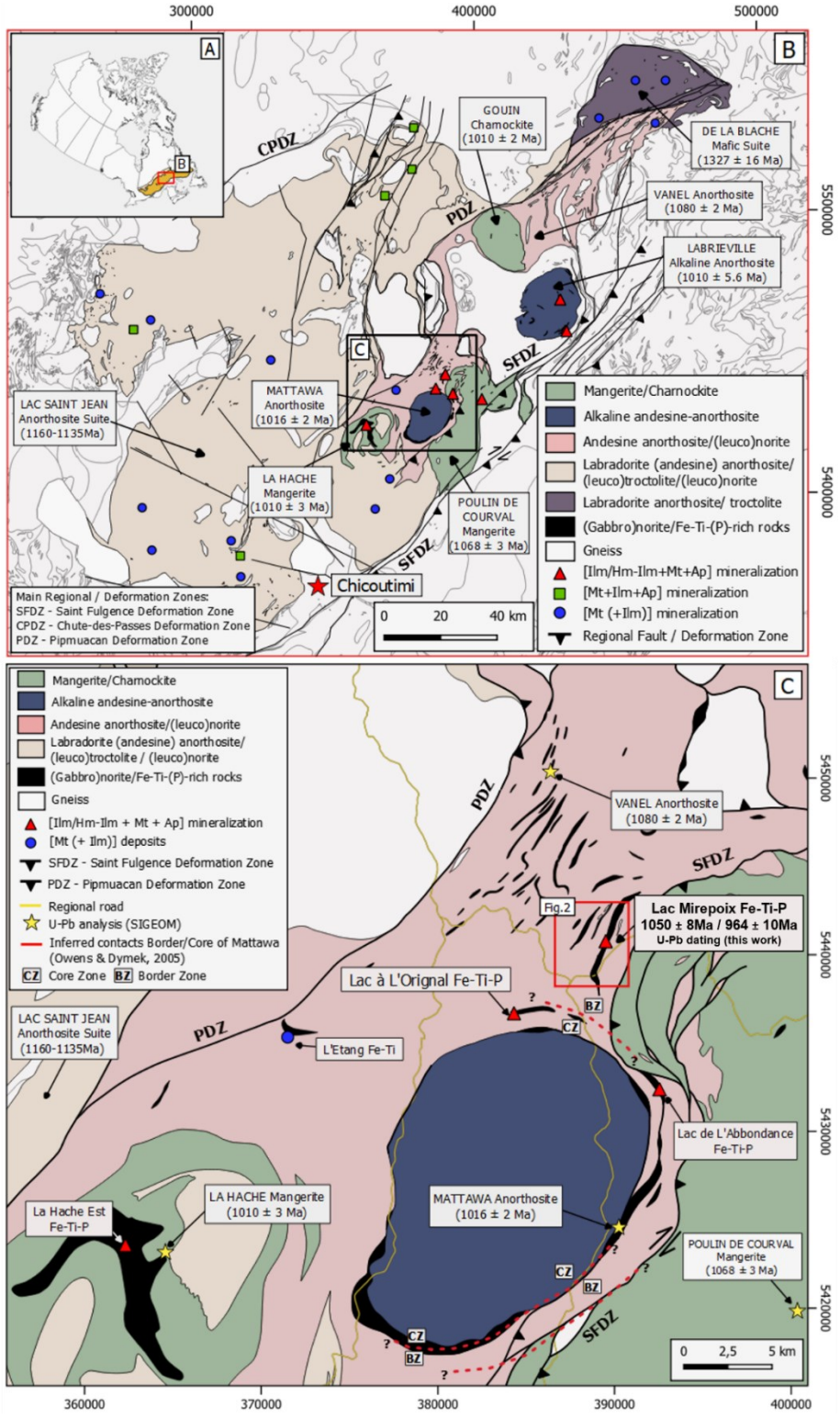

Figure 3.1. a. Location of the Grenville Province in Quebec, Canada. Red square representing the Central Grenville exposed in detail in Figure b. b. Detailed map of the AMCG-suites in the Central Grenville Province, Quebec with the location of the main Fe-Ti-(P) mineralization and regional deformation zones. c. Regional geological map of the AMCG-suites in the Lac Mirepoix Fe-Ti-P mineralization area. Note the occurrence of several lenses/sill-like Fe-Ti-(P) (gabbro)norite intrusions around/within the Mattawa, Poulin de Courval and Vanel massifs (e.g Lac à l'Orignal, Lac de L'Abbondance, L'Etang, La Hache Est mineralization). Red dotted lines indicating the inferred limit between core (CZ) and border (BZ) of the Mattawa Anorthosite Massif, according to Owens & Dymek (2005), based on geochemical criteria. Geological maps modified from SIGEOM (Quebec System of Geomining Information; Gobeil et al. 2002; Hébert & Cadieux, 2003), after Miloski et al. 2023a.

3.4 Local geology of the Lac Mirepoix Fe-Ti-P mineralization

The Lac Mirepoix Fe-Ti-P mineralization is located around 100km northeast of Chicoutimi (Quebec, Canada) and is hosted within the eastern margin of the (1080 ± 2 Ma) Vanel Anorthosite (Hébert & Van Breemen, 2004; Hébert et al. 2009), 3 km to the north of the dome-shaped, andesine-type (1016 ± 2 Ma) Mattawa Anorthosite (Owens & Dymek, 2005; Hébert et al. 2009) (Fig.3.1; Miloski et al. 2023a). Both anorthosites and the Fe-Ti-P mineralization of Lac Mirepoix are emplaced near lower crust-type shear zones (e.g., Saint Fulgence Deformation Zone; Pipmuacan Deformation Zone) in the northeast margin of the 1160-1135 Ma Lac-Saint-Jean Anorthositic Suite (Fig.3.1b), the latter being the largest anorthosite suite in the world (Ashwal, 1993). An extensive network of logging roads exposes several lenses of Fe-Ti-(P) mineralization that occur around the border of the Mattawa Anorthosite massif (Fig.3.1), such as at Lac à l'Orignal (Miloski et al. 2023). Recent U-Pb dating of zircon from the nearby Fe-Ti-P mineralization at Lac à l'Orignal (Miloski et al. 2023) revealed two ages, indicating the occurrence of multi-stage injections in the area: 1) an older (1068 ± 12 Ma) age for the border of the mineralization, correlating in age with the Vanel Anorthosite of the Pipmuacan ACMG Suite, and 2) a younger (993 ± 13 Ma) age for the core of the mineralized intrusion, coeval to the Mattawa Anorthosite of the Valin AMCG Suite. Both the border and core of the mineralization have very similar mineralogy (OAN cumulates) and mineral chemistry, indicating that they formed from similar parental melts (ferrodiorites) but over a prolonged (80 Ma) period of time (Miloski et al. 2023). Therefore, it is important to date Lac Mirepoix mineralization in this study as well (see below).

Previous work based on geological mapping, drilling and regional analysis (Bouldreault, 2000; Boulianne, 2001; Morisset, 2001, 2002) proposed that the Lac

Mirepoix mineralization is a sill-like layered intrusion hosted in massive pink anorthosite (Fig.3.2), where a series of different layers/lenses of oxide-apatite-(gabbro)-norite, leuconorite, nelsonite and massive oxides occur (Morisset 2000). Drilling campaigns by Arianne Phosphate (Boulianne, 2001) identified several 10-25m-thick mineralized horizons, with oxide-apatite-(gabbro)-norite levels (average of 4.26 wt.% of TiO_2 and 3.10 wt.% of P_2O_5), and massive oxide bands in anorthosite (up to 25.1 wt.% TiO_2). However, the extension of the entire mineralization body is difficult to assess because most of the contacts with the enclosing anorthosite are not exposed and outcrops occur only in road sections due to dense vegetation and the presence of quaternary deposits overlying the basement. Also, there is no deep-seated drillcores (more than 35m length) in the area.

A series of different lenses (layers), tilted at 15° to 30° N-NW, are exposed in outcrops, and previous drilling campaigns, along the road for approximately 2500m in the southeastern portion of the area (Fig.3.2). Based on a schematic section of this SE exposure of the mineralization (Fig.3.2b), we propose a division of the Lac Mirepoix Fe-Ti-P mineralization into three different zones (Figs.3.3 & 3.4) as follows, according to the main lithologies observed. The southernmost portion (zone I) of Lac Mirepoix comprises mainly massive to semi-massive (> 50% Fe-Ti oxides) oxide mineralization, dominated by hemo-ilmenite and minor silicates (plagioclase and orthopyroxene) and the absence of visible apatite in the field (Fig.3.3a). The layers of massive oxides (10-15m-thick, Boulianne, 2001) are hosted in medium to coarse-grained pink anorthosite that outcrops mostly in the southwestern portion of Lac Mirepoix (Figs.3.2 & 3.3a). Enclaves of host anorthosite (5 cm to 2 m) occur with the massive mineralization (Figs.3.3a-b), which in places forms a matrix of hemo-ilmenite and coarse-grained plagioclase (Fig.3.3b). Also, one outcrop (20PM04) located southwestern of zone I

(Fig.3.2) represents massive oxide layers unusually enriched in magnetite (Fig.3.4b). Towards the center of the mineralization (zone II), massive oxide layers are less common whereas layers/lenses of apatite-bearing cumulates appear, forming massive nelsonites (50-70% oxides and 25-30% apatite) and oxide apatite norite (OAN, approximately 15-25% Fe-oxides and 8-20% apatite,Figs.3.3c-d). The medium to coarse-grained OAN of Lac Mirepoix is characterized by a matrix formed of orthopyroxene, Fe-oxides (hemo-ilmenite, magnetite) and apatite surrounding coarser plagioclase. Nelsonitic horizons (10-30cm-thick) occur within the OAN layers (Fig.3.3d). In detail, the OAN horizons reveal cumulate textures with compositional layering due to the different modal proportions of plagioclase and orthopyroxene, forming a sequence of several plagioclase-rich (leuco-OAN) and mafic-rich (melano-OAN) layers (Figs.3.3e-f). Finally, the zone III is marked by the alternance of OAN layers (10-25m-thick) and the host anorthosites, and an absence of massive oxides and nelsonites. A number of fine-grained OAN dykes (20-50cm thick) crosscut the mineralization and the host anorthosites (Figs.3.3g-h).

3.5 Sampling and analytical methods

A hundred and twenty-two samples covering the different portions of the mineralized zone (Fig.3.2), including outcrops and boreholes, were selected for detailed lithological description of the massive oxides, nelsonite, oxide-apatite norite (OAN) and anorthosite units. From these, fourty-eight samples were selected for petrographic descriptions and modal mineral abundance estimates from polished thin sections using an optical microscope. A subset of ten samples, covering the different zones, were selected for element mapping using the Bruker - Tornado M4 micro-X-Ray fluorescence (μXRF) analysis at Université Laval, Quebec (Appendix 3.2). Thirty samples were selected for the determination of their whole-rock major and trace

element concentrations. Details of the following analytical methods, instrumentation and evaluation of the data quality are discussed in detail in Appendix 3.3. In summary the samples were cut, crushed, and further reduced to powder (~10 g) in an alumina mill at LabMater, Université du Quebec à Chicoutimi (UQAC). Whole-rock analysis was carried out by fusion of rock powder to form a lithium-borate glass bead which was then analyzed for major and trace element, in situ, by laser ablation inductively coupled plasma mass spectrometry (LA-ICP-MS) at LabMater, UQAC, following the protocol of Barnes & Mansur (2020). Another thirty-seven samples of mineralization and anorthosites were analyzed for whole-rock by X-ray fluorescence by Morisset (2002) and incorporated into this dataset. The major and trace element geochemistry of plagioclase (n=140), apatite (n=144), ilmenite (n=174) and magnetite (n=136) were determined in-situ by LA-ICP-MS at LabMater, UQAC on polished thin sections from 39 samples. Two samples were selected for the analysis of plagioclase (n=10) and orthopyroxene (n=10) by electron probe microanalysis (EPMA) at Université Laval, Quebec. A subset of seven samples of the host anorthosite were analyzed by portable XRF for major and minor element geochemistry. The calculated cationic proportions, Fe^{2+}/Fe^{3+} ratios, whole-rock CIPW norms and the An*/Or* contents in plagiolcase were determined using mass balance equations/spreadsheets. Two samples of oxide-apatite norite, one from the SE portion (zone 1) and another from the NE portion (zone III) of the intrusion, were selected for U-Pb dating of zircon. Zircon separation, preparation and U-Pb analysis, determined by LA-high resolution-ICP-MS following the protocol of Perrot et al. (2017), were conducted in the GEOTOP labs at the Université du Québec à Montréal (UQAM).

3.6 Results

3.6.1 Petrography of Lac Mirepoix

3.6.1.1 Cumulate stratigraphy of the Fe-Ti-P mineralization

The stratigraphic profile (a-b in Fig.3.2) of the mineralized zone in the SE area of Lac Mirepoix is displayed in Figure 3.4, based on petrographic (both macro and microscale) observations (Appendix 3.1; Figs.3.5 & 3.6), uXRF mineral maps, whole rock data and the An content of plagioclase. As observed at the Grader Intrusion (Charlier et al. 2008) and the Lac à l'Orignal mineralization (Miloski et al. 2023), the presence of igneous layering in the Lac Mirepoix lithologies is consistent with a cumulate origin for the rocks. However, in contrast to the Grader intrusion, the lack of continuous outcrops in the Lac Mirepoix Fe-Ti-P mineralization and the absence of boreholes crosscutting the entire stratigraphy makes it more difficult to understand the relationship between the different layers/lenses of mineralization and whether it forms a layered intrusion or multiple injections of lenses into host anorthosite.

Overall, the same cumulate phases (plagioclase, orthopyroxene, apatite, magnetite ilmenite and hemo-ilmenite are present throughout the profile, but with varying modal proportions (Fig.3.4; Appendix 3.1). The whole-rock compositions (Fig.3.4) of Fe_2O_3, TiO_2 (decreasing towards zone III) and P_2O_5 (abrupt increase in zone II) reflect the changes in the main cumulus phases between the three zones. Zone I is mainly dominated by massive oxides (phi(m)-C according to Irvine (1982)) hosted in anorthosite, with predominantly hemo-ilmenite (>70%) and minor (<5%) Fe-poor ilmenite, Ti-poor magnetite (absent of ilmenite exsolutions), Al-spinel, plagioclase, orthopyroxene and biotite (Figs.3.5a & 3.6a). Where small amounts of magnetite are observed (5-10%), ilmenite is absent of hematite exsolutions. An unusually magnetite-rich (50-55%) massive oxide layer (sample 20PM04, Fig.3.6b)

containing hematite-free ilmenite (40-45%) occurs in the southwestern portion of zone I (Fig.3.2). The massive oxides in zone I are apatite poor (P_2O_5 < 0.5 wt.%, Fig.3.4). However, in three outcrops (samples 20PM06, Fig.3.6c and 20PM18), lenses of medium to coarse-grained oxide-apatite-norite cumulates, comprising plagioclase (30-45%), orthopyroxene (35-50%), hemo-ilmenite + magnetite (5-10%) and apatite (3-5%), occur at the contact of the massive oxides and host anorthosite in zone I.

Zone II is characterized by the appearance of abundant cumulus apatite, forming massive nelsonite layers (piam-C, Figs.3.5b-c & 3.6d), dominated by cumulus (hematite-free) ilmenite (25-35%), magnetite (25-30%), apatite (20-30%) and minor plagioclase (5-10%), orthopyroxene (10-15%) and Al-spinel (1-3%). The massive nelsonites occur within oxide-apatite-norite layers/lenses (phiam-C, Fig.3.3c-d), the latter comprising abundant plagioclase (30-40%), orthopyroxene (15-35%), hemo-ilmenite (10-15%), apatite (5-15%) and a minor amount (<5%) of magnetite.

Zone III is marked by the absence of massive oxides and nelsonite lithologies, and the mineralization is strictly dominated by medium to coarse-grained oxide-apatite-norite (OAN) cumulates (phiam-C, Figs.3.5d-e & 3.6e-f), similar to those described in zone II, but with higher amounts of magnetite (10-15%). Minor amounts of biotite and hornblende (<1%) occur as an intergranular texture in the different OAN cumulates and are considered primary in origin as they do not replace orthopyroxene (Appendix 3.1). Accessory minerals include fine-grained exsolutions of Al-spinel from oxide phases and sulphides. Plagioclase from the OAN mineralization is andesine in composition (40 < An < 50) throughout all three zones, with high Or contents, but without visible K-rich exsolutions. OAN mineralization in the Lac Mirepoix is quite similar in mineralogy and plagioclase composition in relation to the nearby Lac à

l'Orignal Fe-Ti-P mineralization (Miloski et al. 2023). An exception in the absence of K-rich exsolution in plagioclase, which is abundant in the latter.

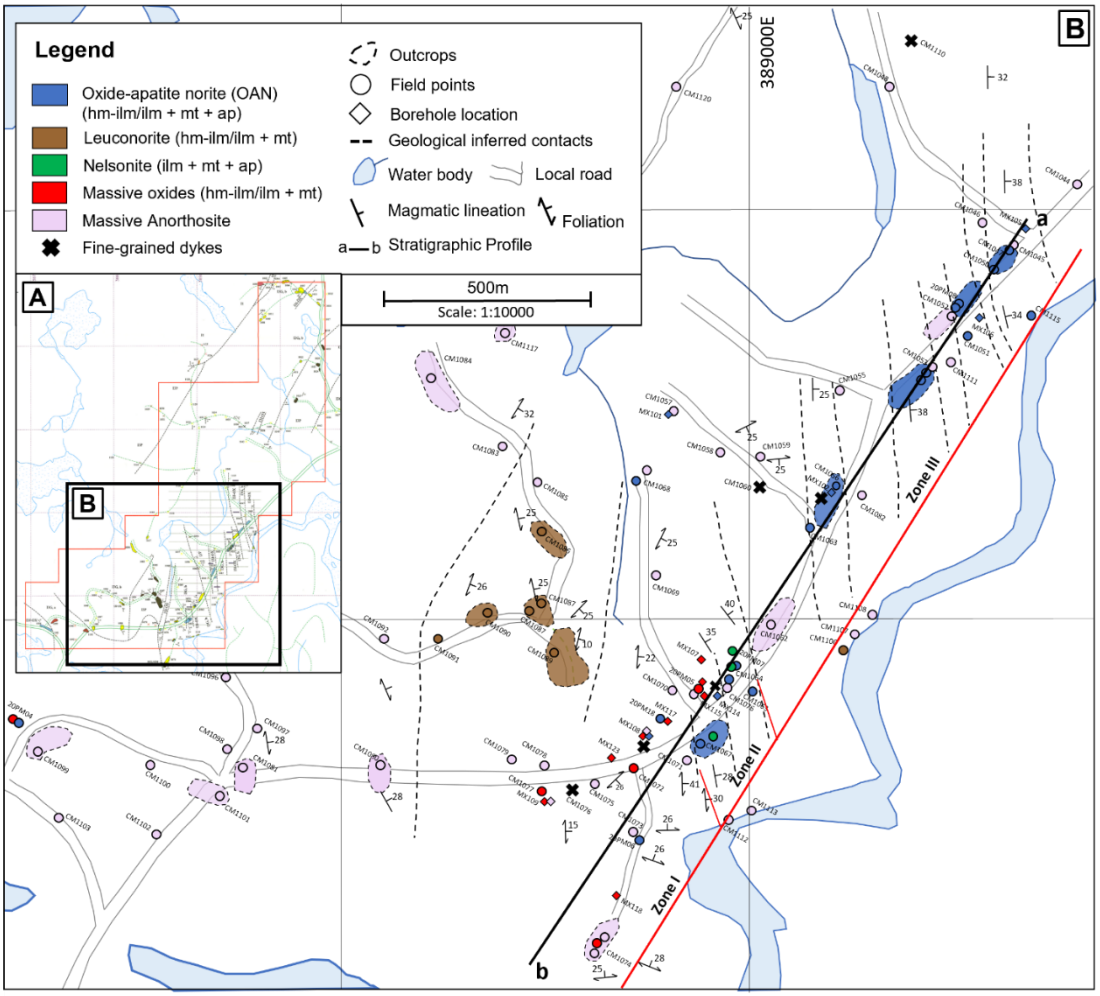

Figure 3.2. a. Geological map of the Lac Mirepoix Fe-Ti-P mineralization area (modified from Morisset, 2000). The entire map (a) in presented in Appendix 3.2.2. b. Detail for the SE portion where most of the mineralized outcrops and drill cores are located. Black doted lines for inferred contacts between the different cumulates (after Morisset, 2000). Red doted lines representing the proposed section a-b and the contact between the mineralized zones I, II and III.

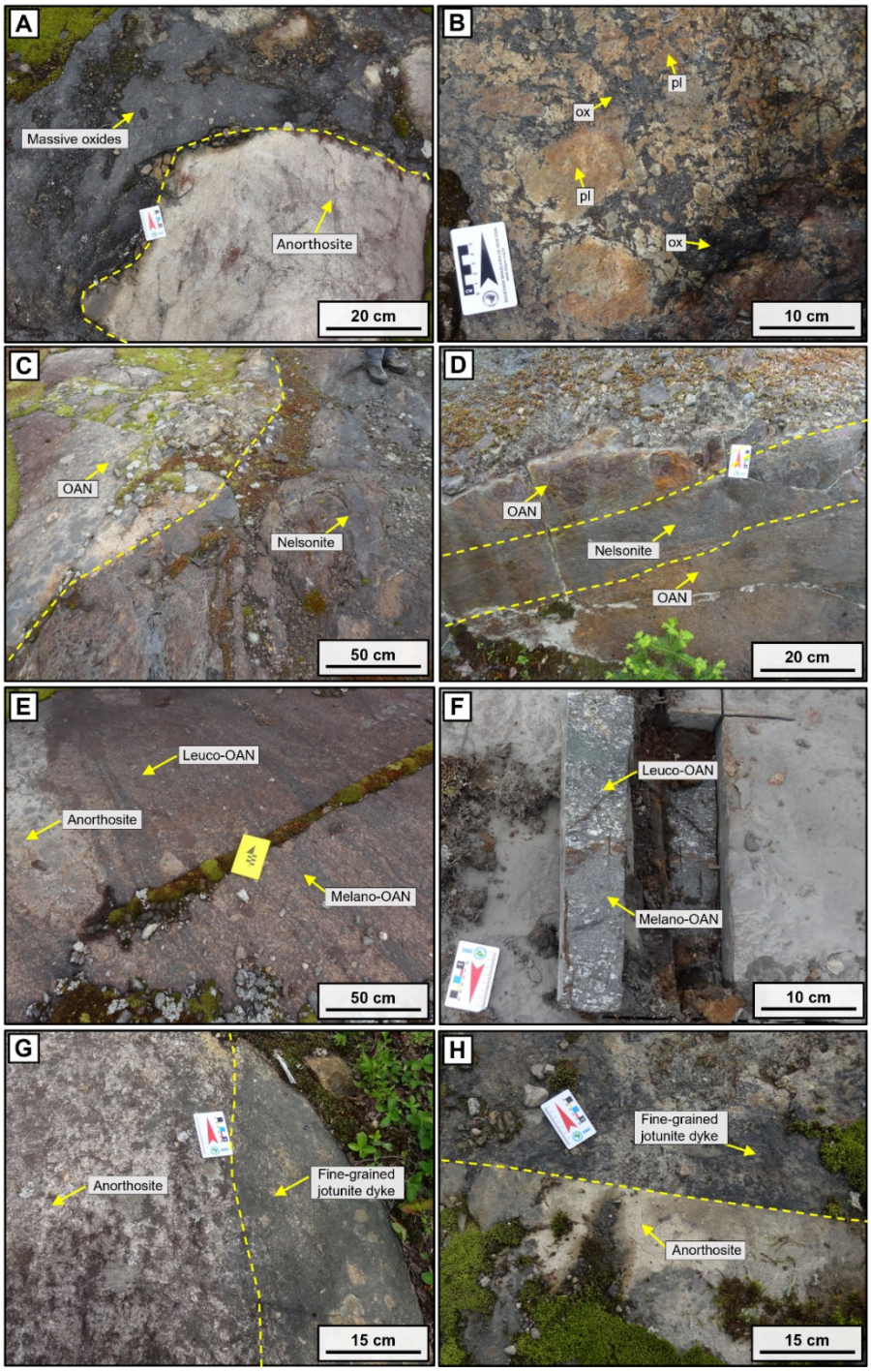

Figure 3.3. Photographs of representative outcrops and lithologies of the Lac Mirepoix Fe-Ti-P mineralization. a. Contact between the host anorthosite and massive ilmenitite (hemo-ilmenite) lens containing blocks of anorthosite (zone I, 20PM05A-C). b. Semi-massive mineralization containing blocks of anorthosite within a matrix formed by coarse-grained plagioclase and hemo-ilmenite (zone I, 20PM05-B). c-d. Contact between layered oxide-apatite-norite (OAN) and massive nelsonite (zone II, 20PM07). e. Layering of OAN with plagioclase-rich (leuco-OAN) and mafic-rich (melano-OAN) layers (zone III, 20PM08-B). f. Fresh-outcrop sample exposing the igneous layering between leuco- and melano-OAN layers (zone III, 20PM08-B). g-h. Contact between the host anorthosite and fine-grained jotunite dyke (sample 20PM19-B). Mineral abbreviations: pl = plagioclase; ox = oxides.

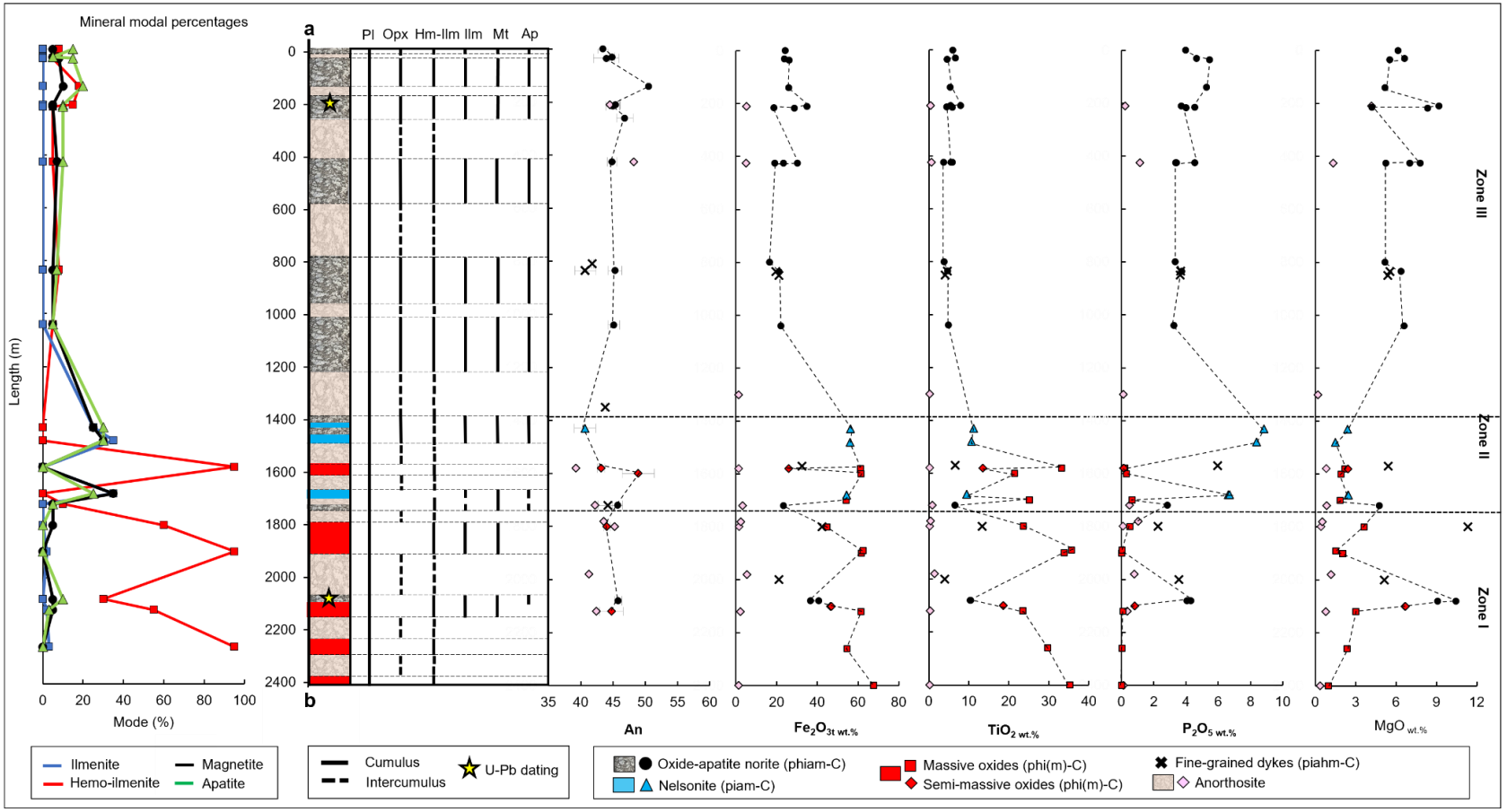

Figure 3.4. Geochemical variation of the Lac Mirepoix mineralization showing the distribution of the different cumulate phases along the SE section a-b from Figure 3.2. Cryptic layering of anorthite (An=100 [Ca/ (Ca+Na)]) in plagioclase for mineralized samples determined by LA-ICP-MS. An content in the host anorthosite (CIPW norm), Fe2O3, TiO2 P2O5 and MgO from bulk whole-rock LA-ICP-MS analysis. Cumulus assemblages following the nomenclature of Irvine (1982). Mineral abbreviations: p / pl = plagioclase; i / ilm = ilmenite; a / ap = apatite; h / opx = orthopyroxene; m / mt = magnetite; -C = cumulus. Bars representing the standard deviation. Error bars = 1 standard deviation and represents the natural variation within the thin section.

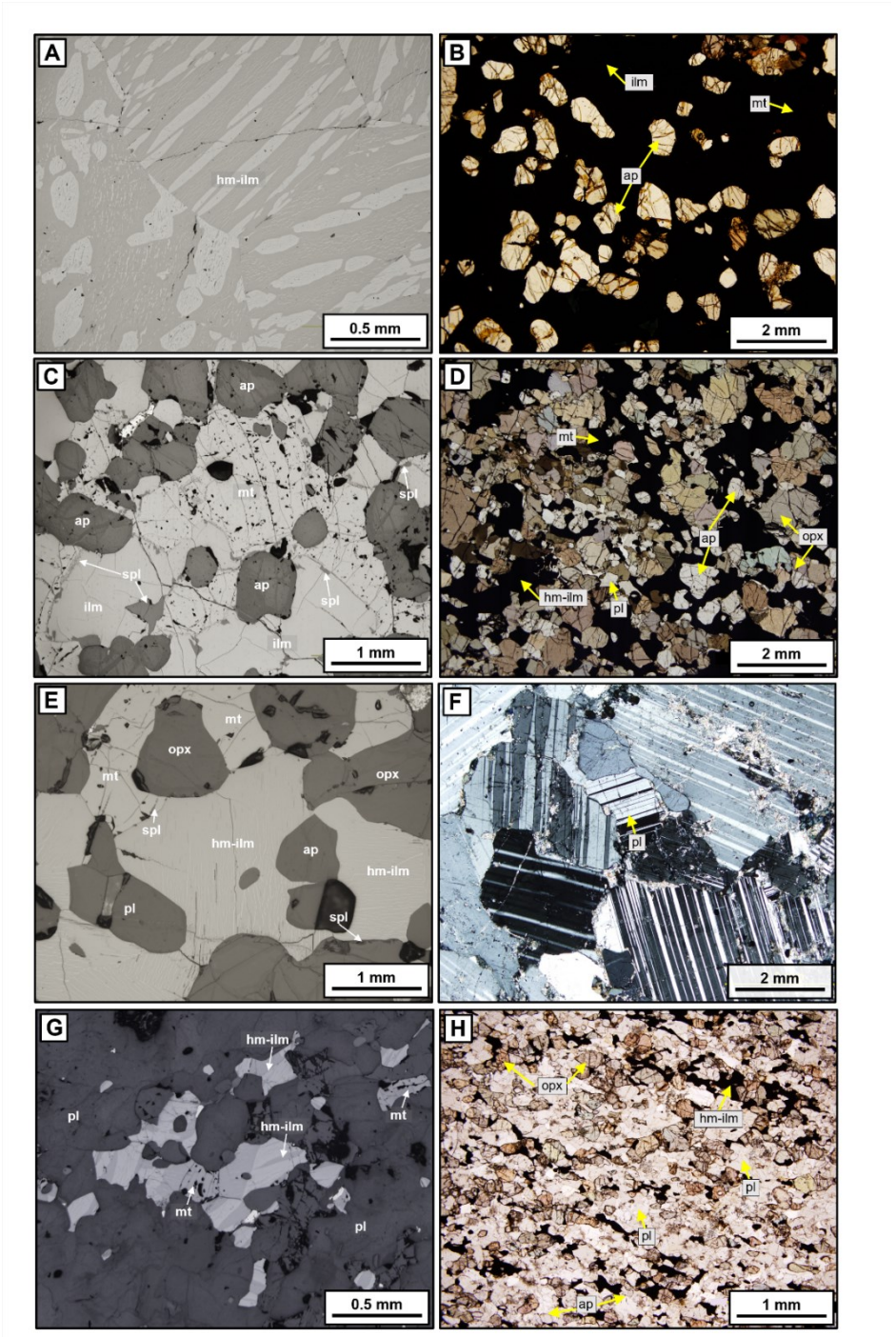

Figure 3.5. Photomicrographs of the main lithologies that characterize the different zones of the of the Lac Mirepoix Fe-Ti-P mineralization in transmitted (figures 3.5b, d, f, h) and reflected (figures 3.5a, c, e, g) light. a. Massive oxides dominated by hemo-ilmenite with coarse exsolutions of hematite (pale) and ilmenite (dark) (zone I, 20PM05-A). b-c. Medium-grained nelsonite dominated by ilmenite (hematite exsolution-free), magnetite and small exsolved spinel crystals at the contacts between oxides (zone II, 20PM07). d-e. Medium grained-OAN dominated by hemo-ilmenite with fine exsolutions, and ilmenite (exsolution-free) when close to magnetite. Presence of exsolved spinel crystals in the contact between the oxides. Evidence of sub-solidus reequilibration between magnetite and ilmenite, with depletion of hematite exsolutions in ilmenite towards the border with magnetite (zone III, 20PM08-B1). f. Coarse-grained massive anorthosite-host with well-preserved plagioclase crystals and minor hemo-ilmenite crystals. g-h. Fine-grained leuco-OAN dyke dominated by hemo-ilmenite and magnetite (20PM19-B). Mineral abbreviations: pl = plagioclase; opx = orthopyroxene; hm-ilm = hemo-ilmenite; ilm = ilmenite; mt = magnetite; ap = apatite; bt = biotite; spl = Al-spinel.

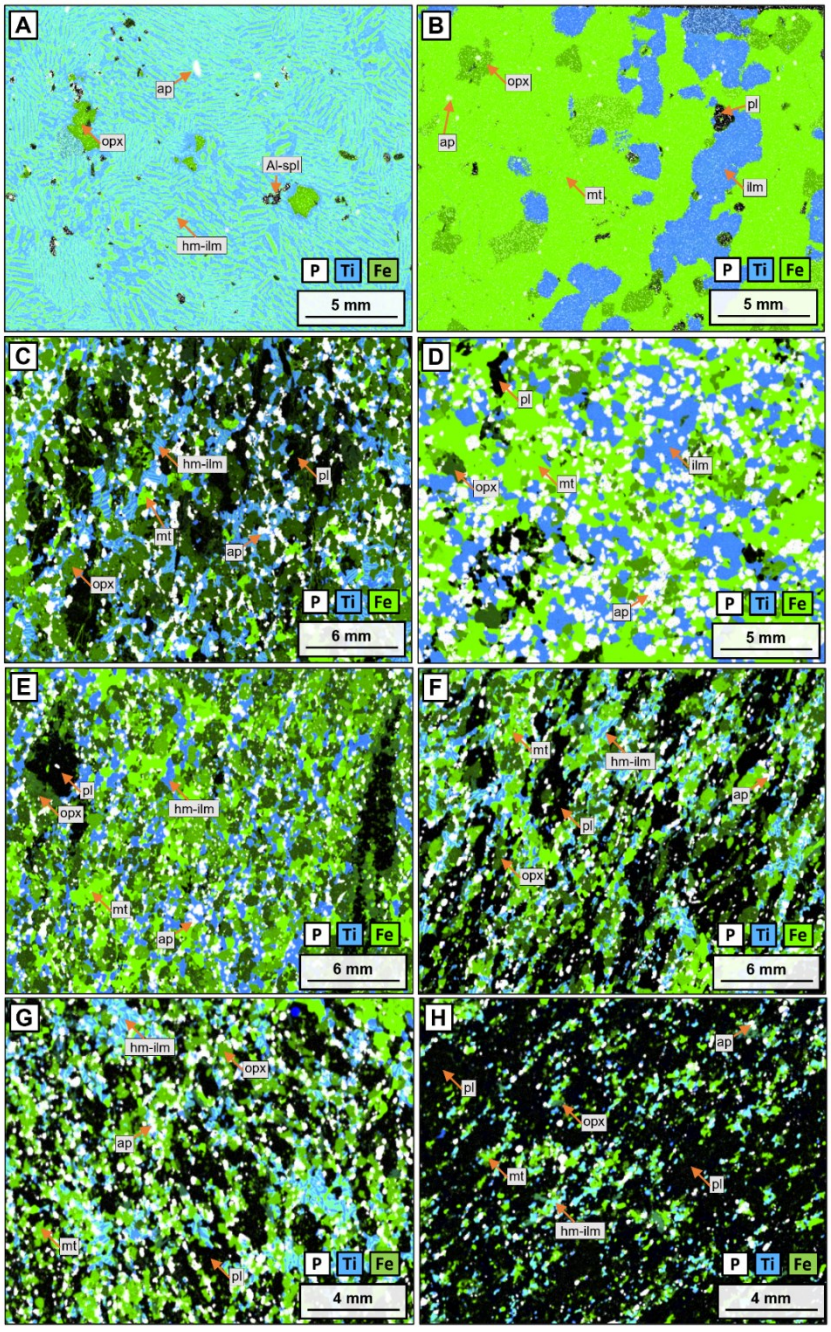

Figure 3.6. µXRF-maps, combining P (white), Ti (blue) and Fe (green), showing the different proportions of oxides and apatite from the Lac Mirepoix Fe-Ti-P mineralization. Ilmenite is blue, where hematite-rich part of ilmenite is cyan. Magnetite is bright green. Orthopyroxene is dark green. a. Massive ilmenitite with coarse hemo-ilmenite crystals and absence of of cumulus magnetite and apatite (zone I, 20PM05-A). b. Massive oxides layer within the anorthosite-host, dominated by ilmenite (hematite-free) and magnetite (20PM04-B). c. Medium grained-OAN dominated by hemo-ilmenite and minor magnetite (zone I, 20PM06-B). d. Massive nelsonite dominated by magnetite and ilmenite (hematite exsolutions-free) (zone II, 20PM07). e-f. Medium grained-OAN equally dominated by hemo-ilmenite and magnetite (zone III, E: 20PM08-B1; F: MX-105-1). g. Fine-grained OAN dyke, dominated by hemo-ilmenite and magnetite (MX-114-1). h. Fine-grained jotunite dyke, with higher modal proportion of plagioclase and magnetite in relation to hemo-ilmenite and orthopyroxene (20PM19-B). Mineral abbreviations: pl = plagioclase; opx = orthopyroxene; hm-ilm = hemo-ilmenite; ilm = ilmenite; mt = magnetite; ap = apatite; spl = Al-spinel; sulph = sulphides; bt = biotite. See Appendix B.2 for compilation of all elements mapped by uXRF.

Ilmenite contains variable amounts of hematite exsolutions in the mineralized samples. In zone I, the mineralization is dominated by hemo-ilmenite hosting large hematite exsolution lamellae, and minor magnetite (Figs.3.5a & 3.6a). In contrast, zone II (nelsonite-rich) and a few OAN layers in zone I contain higher amounts of magnetite and Fe-poor ilmenite, absent of hematite exsolutions (Figs.3.5c & 3.6e). Magnetite is present as a cumulus oxide throughout the mineralized zones II and III, and at the top of zone I, normally as minor cumulus phase or in equal proportion to ilmenite crystals (Figs.3.5c & 3.6d). Al-spinel is an accessory oxide phase, occurring as small irregular grains that exsolved near the contact of ilmenite and magnetite crystals (Fig.3.5c). When ilmenite and hemo-ilmenite coexist, the latter typically contains finer hematite lamellae (Figs.3.5c & 3.5e). In this case, hemo-ilmenite also presents a depletion in hematite exsolutions (size and quantity) towards the contact with adjacent magnetite. This most likely results from post-magmatic re-equilibration processes within these cumulates, as previously described in other Fe-Ti mineralized occurrences dominated by hemo-ilmenite (± magnetite), such as Lac à l'Orignal (Miloski et al. 2023) and the Tellnes deposit (Charlier et al. 2006). Compositional re-equilibration between magnetite and ilmenite also produces fine-grained irregular Al spinel exsolutions at the contact of magnetite and ilmenite (Figs.3.5c & 3.5e).

3.6.1.2 Fine-grained dykes

Fine-grained oxide-apatite-norite (ferrodiorite) occurs as dykes (with sharp contacts), that crosscut all 3 zones of the mineralization and the host anorthosite (Figs.3.3f-g). As previously described at the nearby Lac a l'Orignal mineralization (Miloski et al. 2023a), these dykes have a similar mineralogy (Figs.3.6g-h) and plagioclase composition (An 40-50) as the OAN mineralization. Hemo-ilmenite is the main oxide phase (10-15%) in these fine-grained lithologies (e.g., MX-114-1, Fig.3.6g;

& MX-102-3) with minor magnetite (<5%) being accompanied by higher amounts of plagioclase (>40%) and apatite (3-15%). They likely represent rapidly cooled, thin injections of ferrodiorite parental magma. However, one of them (sample 20PM19-B (Fig.3.6h) has higher amounts of magnetite, plagioclase, as well as quartz and K-feldspar, and lower amounts of ilmenite (Appendix 3.2) and may represent a more evolved jotunite (opx-bearing monzodiorite) magma. Such ferrodiorite/jotunite dykes, are commonly observed with other Fe-Ti-P mineralization associated with AMCG worldwide (e.g Grader Intrusion and Lac Tio, Quebec - Charlier et al. 2008; Bjerkrein Skondal, Norway - Vander Auwera et al. 1994; Duchesne & Charlier, 2005; Lac à l'Orignal, Quebec – Miloski et al. 2023) where they have been shown to be co-genetically related to the Fe-Ti-P mineralization either as parental or residual magmas (Owens et al. 1993; Vander Auwera et al. 1998).

3.6.1.3 Host anorthosite

Throughout the three different mineralized zones, a pinkish, coarse-grained anorthosite (Fig.3.5e) hosts the mineralized layers/lenses. Its plagioclase composition is similar to that of the mineralization (andesine, 40 < An < 50, Fig.3.4) and also do not contain K-rich exsolutions. The host anorthosite contains minor amounts of orthopyroxene (< 5%), hemo-ilmenite (<5%) and apatite (<1% P_2O_5, Fig.3.4). This low-P_2O_5 content is different from that observed in the nearby Lac à l'Orignal Fe-Ti-P mineralization (Miloski et al. 2023), where thin (10-20cm-thick) apatite-bearing anorthosites (P_2O_5 3-5%) are interlayered with the OAN mineralization.

3.6.2 Whole-rock geochemistry

The whole rock geochemistry of the Lac Mirepoix area, comprising Fe-Ti-P mineralization (n = 45), fine-grained dykes (n = 9) and host anorthosite (n = 15), is

presented in Table 3.1 (complete data is presented in Appendix 3.1 and confirms our petrographic observations (Fig.3.4)). The successive appearance of phases in the Lac Mirepoix mineralization is observed in the whole-rock geochemistry (Figs.3.4 & 3.7 and Appendix 3.2). Chondrite-normalized whole-rock REE compositions are presented in Figure 3.8.

3.6.2.1 Fe-Ti-P mineralization

The abrupt increase in P_2O_5 between zones I and II, and in MgO, between zones II and III, mark the appearance of high concentrations of cumulus apatite and orthopyroxene, respectively, in the mineralized layers/lenses (Fig.3.4). The massive oxides have the highest Fe_2O_{3t} (54.1 – 81.2 wt.%), TiO_2 (10.7 - 35.7 wt.%) and V (1316 - 2541 ppm) contents and lowest CaO (0.1 – 2.8 wt.%) and P_2O_5 (0.1 – 0.7 wt.%) values among all of the mineralized samples (Figs.3.4 & 3.8), due to a much higher proportion of ilmenite and magnetite and very low proportions of plagioclase and apatite (CIPW norm, Appendix 3.1: Ap = 0.1 – 1.6%), respectively. Semi-massive oxides have higher concentrations of cumulus plagioclase and orthopyroxene, and as such contain higher contents of CaO (1.5 – 5.2 wt.%) and MgO (1.5 – 8.6 wt.%) and lower Fe_2O_{3t} (26.0 – 61.3 wt.%) and TiO_2 (18.0 – 23.6 wt.%) in comparison with massive oxides. This confirms that plagioclase and orthopyroxene crystallize with Fe-Ti-oxides before apatite. The massive nelsonite horizons contain, as expected, the highest P_2O_5 (6.6 – 8.8 wt.%) and CaO values (10.7 – 13.2 wt.%) due to their high concentration of apatite (CIPW norm, Ap = 15.7 – 20.6%). The comparatively low-TiO_2 (9.5 – 11.2 wt.%) and V (1219 – 1412 ppm) values, at similar high Fe_2O_{3t} (54.3 – 56.4 wt.%) values, in comparison with the massive oxides (dominated by hemo-ilmenite) from zone I reflects the higher concentrations of magnetite than ilmenite in the nelsonite samples (Figs. 3.6d & 3.7). The massive oxide (dominated by magnetite:

Fig.3.6b) occurring to the west of the mineralized profile “a-b” (20PM04 - Fig.3.2), also has similar low-TiO_2 (10.7 wt.%) values, but the highest Fe_2O_{3t} (81.7 wt.%) and V (2541ppm) values. The oxide-apatite-norite cumulates have the lowest Fe_2O_{3t} (13.6 – 40.7 wt.%), TiO_2 (3.8 – 10.4 wt.%), V (77 – 543 ppm), and the highest SiO_2 (24.7 – 46.7 wt.%), MgO (4.2 – 10.4 wt.%) and K_2O (0.1 – 0.8 wt.%) contents among all the mineralized samples, reflecting lower proportions of Fe-Ti oxides and higher concentrations of plagioclase and orthopyroxene. Also, the OAN cumulates systematically contain high proportions of cumulus apatite (average P_2O_5 = 2.53 wt.%; CIPW norm: Ap = 4.0 – 13.5%) throughout zone III.

Chondrite-normalized REE diagrams (Fig.3.8a) show similar patterns between the OAN and nelsonite cumulates, suggesting that they contain apatite of similar composition. These mineralized rocks are enriched in LREE (OAN: 70 – 200x Chondrite; Nelsonite: 300x Chondrite) relative to HREE (OAN: 5 – 20x Chondrite; Nelsonite: 15x Chondrite), presenting a smooth pattern with similar weakly negative Eu anomalies (OAN: Eu* between 0.81 and 1.04; Nelsonite: Eu* = 0.78). Moreover, very similar patterns and abundances are observed when comparing the Lac Mirepoix OAN with the nearby Lac à l’Orignal Fe-Ti-P mineralization (Miloski et al. 2023). The massive oxides, with very low concentration of apatite, as expected have much lower REE abundances compared to the other cumulates (Fig.3.8a).

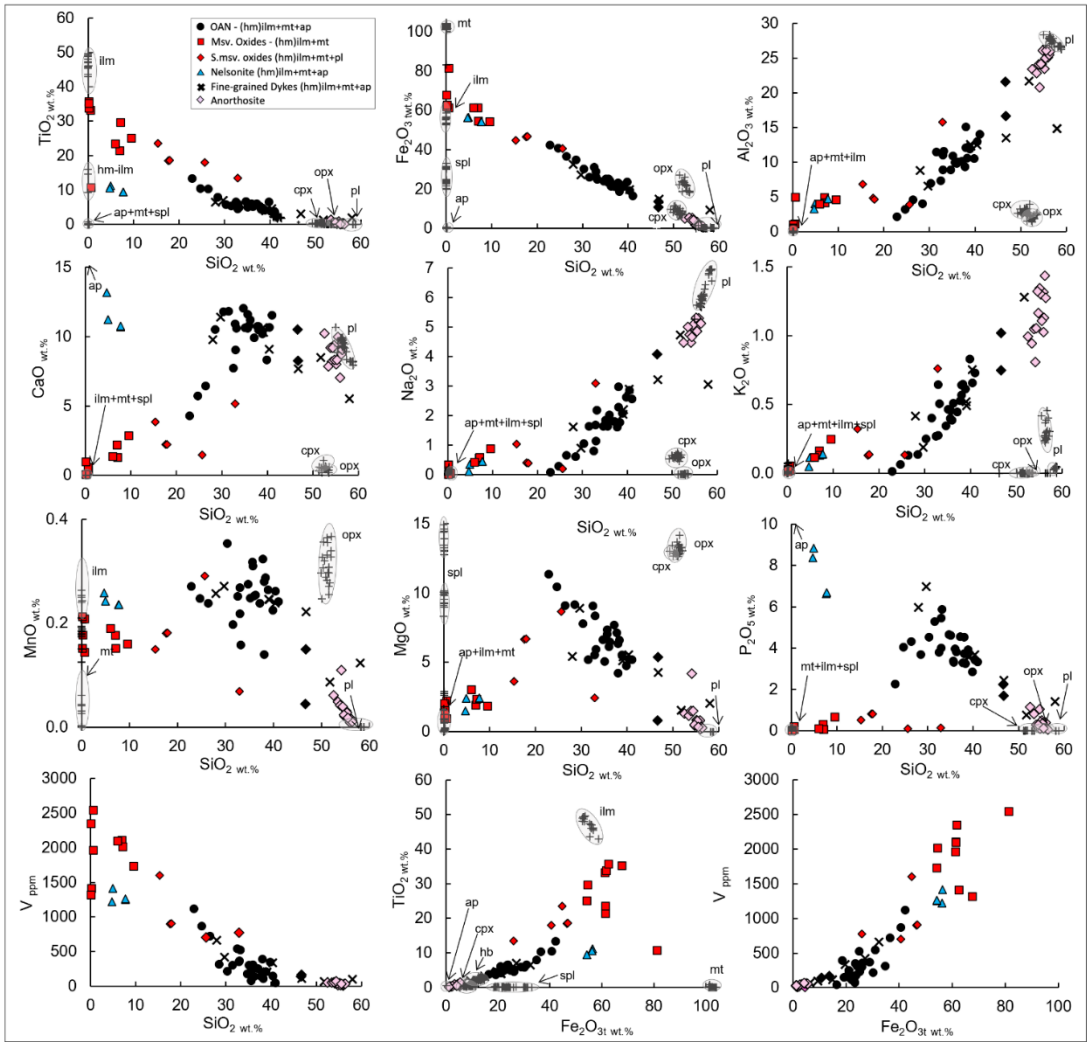

Figure 3.7. Whole-rock variation diagrams for the Lac Mirepoix Fe-Ti-P mineralization with the major mineral compositions by electron microprobe, including the dataset of Morisset (2001). Mineral abbreviations: pl = plagioclase; opx = orthopyroxene; bt = biotite; hm-ilm = hemo-ilmenite; ilm = ilmenite; mt = magnetite; ap = apatite; spl = Al-spinel. OAN = oxide-apatite norite.

Table 3.1. LA-ICP-MS Whole-rock major and trace element compositions in the Lac Mirepoix Fe-Ti-P mineralization

Sample	Depth (m)	Lithology	Oxides	SiO_2	TiO_2	Al_2O_3	Fe_2O_{3t}	MnO	MgO	CaO	Na_2O	K_2O	P_2O_5	LOI	Total
20PM04A	-	Medium-grained OAN	Ilm+Mt	33.20	4.92	11.61	24.91	0.16	5.94	10.60	2.19	0.51	5.87	0.00	100.00
20PM04B	-	Massive oxides	Ilm+Mt	0.64	10.66	4.96	81.27	0.21	0.92	0.36	0.04	0.02	0.06	0.00	100.00
20PM05A	-	Massive oxides	Hm-Ilm	0.64	10.66	4.96	81.27	0.21	0.92	0.36	0.04	0.02	0.06	0.00	100.00
20PM05B	-	Semi-massive oxides	Hm-Ilm+Mt	32.89	13.46	15.81	25.93	0.07	2.42	5.17	3.10	0.76	0.14	0.00	100.00
20PM05C	-	Anorthosite	-	56.03	0.26	24.85	1.77	0.01	1.09	7.24	4.78	1.24	0.14	2.58	100.02
20PM06A		Medium-grained OAN	Hm-ilm	24.68	10.42	3.21	40.70	0.25	10.44	5.73	0.29	0.07	4.05	0.00	100.00
20PM06B	-	Medium-grained OAN	Hm-Ilm	26.42	10.28	4.63	36.57	0.24	9.09	6.46	0.66	0.13	4.31	1.07	100.00
20PM07	-	Nelsonite	Ilm+Mt	4.93	11.16	4.03	56.39	0.24	2.38	11.25	0.35	0.12	8.83	0.00	100.00
20PM08A	-	Anorthosite	-	54.13	0.39	20.78	5.24	0.11	4.17	8.21	4.47	0.81	0.22	1.44	100.00
20PM08B1	-	Medium-grained OAN	Hm-Ilm+Mt	29.86	7.40	4.19	33.16	0.40	9.40	10.51	0.86	0.46	3.69	-0.39	100.00
20PM08B2	-	Medium-grained OAN	Hm-Ilm+Mt	37.64	5.08	10.34	23.05	0.29	7.36	10.46	1.99	0.74	3.02	-1.46	100.00
20PM17	-	Anorthosite	-	55.96	0.31	26.28	1.32	0.01	0.23	9.37	5.09	1.03	0.40	0.00	100.00
20PM18A	-	Anorthosite	-	55.14	0.85	23.49	3.22	0.03	0.83	8.00	4.97	1.34	0.50	1.62	100.00
20PM18B	-	Medium-grained OAN	Hm-Ilm+Mt	39.81	6.49	10.51	23.46	0.23	4.75	8.32	2.63	0.83	2.85	0.05	100.00
20PM19A	-	Fine-grained ferrodiorite	Hm-Ilm+Mt	51.76	1.35	21.72	6.40	0.09	1.53	8.51	4.73	1.28	0.76	1.85	100.00
20PM19B	-	Fine-grained jotunite	Hm-Ilm+Mt	58.02	2.00	14.83	9.40	0.12	2.05	5.53	3.06	3.51	1.41	0.04	100.00
MX102-3	13.50	Fine-grained ferrodiorite	Hm-Ilm+Mt	40.38	4.57	12.51	19.62	0.24	5.55	9.09	2.89	0.75	3.68	0.72	100.00
MX102-5	21.00	Medium-grained OAN	Hm-Ilm+Mt	38.01	4.66	12.08	21.16	0.28	6.36	10.75	2.29	0.57	3.74	0.11	100.00
MX105-1	0.50	Medium-grained OAN	Hm-Ilm+Mt	35.99	5.98	9.88	24.16	0.25	6.13	10.79	2.03	0.39	3.96	0.44	100.00
MX106-1	5.00	Medium-grained OAN	Hm-Ilm+Mt	38.05	4.40	15.07	18.59	0.14	4.21	10.49	2.98	0.64	4.53	0.90	100.00
MX108-4	12.00	Fine-grained OAN	Hm-Ilm+Mt	22.87	13.35	2.17	42.24	0.27	11.35	4.28	0.09	0.01	2.27	1.10	100.00
MX108-6	20	Semi-massive oxides	Hm-Ilm+Mt	15.34	23.56	6.84	44.75	0.15	3.63	3.85	1.03	0.32	0.51	-0.36	100.00
MX-108-8	31	Anorthosite	-	54.77	0.25	26.12	1.73	0.02	0.42	8.34	4.99	1.17	0.11	2.08	100.00
MX-109-3	9	Massive oxides	Hm-Ilm+Mt	6.01	23.47	4.00	61.34	0.19	3.01	1.34	0.42	0.12	0.09	-1.17	100.00
MX109-7	35	Anorthosite	-	55.34	0.29	24.98	2.21	0.03	0.77	8.33	5.32	1.30	0.38	1.05	100.00
MX114-1	8.50	Fine-grained ferrodiorite	Hm-Ilm+Mt	27.98	6.52	8.82	32.44	0.26	5.42	9.78	1.62	0.42	5.96	0.78	100.00
MX-115	16.50	Massive oxides	Hm-Ilm+Mt	7.01	21.38	4.95	61.35	0.18	1.90	2.20	0.56	0.16	0.31	-1.13	100.00
MX-117	13.50	Massive oxides	Hm-Ilm+Mt	9.55	25.07	4.62	54.14	0.16	1.84	2.84	0.87	0.25	0.66	-1.27	100.00
MX-118	4.00	Massive oxides	Hm-ilm	7.11	29.65	4.21	54.47	0.15	2.35	1.29	0.59	0.13	0.05	-0.88	100.00
MX-123	0.50	Massive oxides	Hm-ilm	0.15	33.82	1.08	61.72	0.15	2.03	0.97	0.03	0.02	0.02	-1.85	100.00

OAN = Oxide-apatite norite; Hm-ilm = hemo-ilmenite; Ilm = ilmenite; Mt = magnetite. Eu/Eu* = (Eu)n/[(Sm)n x (Gd)n]0.5 calculated with Chondrite normalization values of Sun & McDonough (1989).

Table 3.1. (Cont.) LA-ICP-MS Whole-rock major and trace element compositions in the Lac Mirepoix Fe-Ti-P mineralization

Sample	Depth (m)	Lithology	Oxides	V	Cr	Ni	Sr	Y	Zr	Nb	Ba	La	Ce	Eu	Yb	Eu/Eu*
20PM04A	-	Medium-grained OAN	Ilm+Mt	526	111	48	32	882	30	56	3	32	83	4	2	0.91
20PM04B	-	Massive oxides	Ilm+Mt	2541	1878	525	16	14	1	22	5	1	2	0	0	0.57
20PM05A	-	Massive oxides	Hm-Ilm	2541	1878	525	16	14	1	22	5	1	2	0	0	0.60
20PM05B	-	Semi-massive oxides	Hm-Ilm+Mt	777	654	272	95	942	3	208	12	7	14	1	0	2.53
20PM05C	-	Anorthosite	-	12	27	33	13	1379	3	18	1	13	24	1	0	2.89
20PM06A		Medium-grained OAN	Hm-ilm	871	59	41	44	168	19	155	6	16	45	2	1	0.81
20PM06B	-	Medium-grained OAN	Hm-Ilm	723	51	34	37	299	21	82	6	17	47	2	1	0.82
20PM07	-	Nelsonite	Ilm+Mt	1412	209	320	137	340	60	238	10	65	167	6	3	0.78
20PM08A	-	Anorthosite	-	45	87	32	3	763	14	75	4	31	62	2	1	1.55
20PM08B1	-	Medium-grained OAN	Hm-Ilm+Mt	341	23	27	26	295	53	213	6	33	95	6	3	0.88
20PM08B2	-	Medium-grained OAN	Hm-Ilm+Mt	228	20	24	19	775	47	138	5	162	268	6	3	0.96
20PM17	-	Anorthosite	-	19	88	26	8	1976	7	32	1	13	29	2	0	1.62
20PM18A	-	Anorthosite	-	47	20	20	9	1589	10	93	5	20	43	2	1	1.72
20PM18B	-	Medium-grained OAN	Hm-Ilm+Mt	350	17	21	28	721	48	208	30	43	109	5	4	0.87
20PM19A	-	Fine-grained ferrodiorite	Hm-Ilm+Mt	71	23	13	5	1637	18	71	7	28	63	3	1	1.45
20PM19B	-	Fine-grained jotunite	Hm-Ilm+Mt	100	19	12	11	1034	62	1173	25	102	235	6	5	0.75
MX102-3	13.50	Fine-grained ferrodiorite	Hm-Ilm+Mt	337	22	56	1001	60	256	18	1047	74	180	7	4	0.89
MX102-5	21.00	Medium-grained OAN	Hm-Ilm+Mt	183	6	10	1071	50	175	5	1042	40	109	7	3	1.04
MX105-1	0.50	Medium-grained OAN	Hm-Ilm+Mt	314	3	5	972	52	244	11	617	46	121	7	3	0.94
MX106-1	5.00	Medium-grained OAN	Hm-Ilm+Mt	395	14	65	1245	36	206	8	806	44	108	5	2	0.99
MX108-4	12.00	Fine-grained OAN	Hm-Ilm+Mt	1119	142	318	78	13	206	10	32	9	25	1	1	0.77
MX108-6	20	Semi-massive oxides	Hm-Ilm+Mt	1602	888	378	355	9	297	21	303	11	27	1	1	0.98
MX-108-8	31	Anorthosite	-	14	4	18	1519	3	13	1	1055	12	22	3	0	4.68
MX-109-3	9	Massive oxides	Hm-Ilm+Mt	2098	1015	470	121	1	428	19	95	2	4	0	0	1.68
MX109-7	35	Anorthosite	-	20	5	8	1845	8	17	2	1085	16	34	3	1	2.51
MX114-1	8.50	Fine-grained ferrodiorite	Hm-Ilm+Mt	662	40	71	780	57	361	13	487	65	164	6	3	0.80
MX-115	16.50	Massive oxides	Hm-Ilm+Mt	2106	1693	334	182	4	386	23	127	5	11	1	0	1.16
MX-117	13.50	Massive oxides	Hm-Ilm+Mt	1730	1261	127	290	9	620	46	209	11	26	1	1	0.93
MX-118	4.00	Massive oxides	Hm-ilm	2014	1556	240	160	1	476	30	103	2	4	0	0	2.03
MX-123	0.50	Massive oxides	Hm-ilm	2349	1630	309	12	1	918	34	28	0	1	0	0	1.13

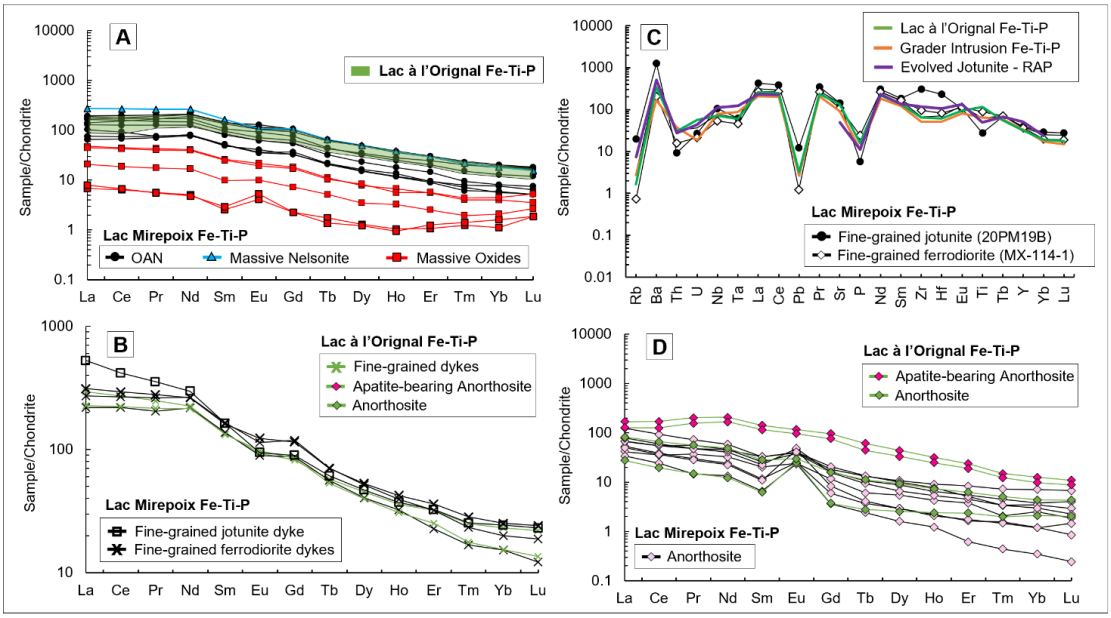

Figure 3.8. Chondrite-normalized whole-rock compositions (after Sun and McDonough, 1989). Comparison with the nearby Fe-Ti-P Lac à l'Orignal mineralization (Miloski et al. 2023a): a. Mineralized samples along the section a-b, including the dataset on Morisset (2001). b. Fine-grained dykes. c. Multi-element diagram comparing the fine-grained lithologies in the Lac Mirepoix with the average composition of dykes in the Fe-Ti-P Lac à l'Orignal mineralization, the Fe-Ti-P Grader Intrusion (Charlier et al. 2008) and a reference evolved jotunite dyke from the Rogaland Anorthosite Province, Norway (Wilmart et al. 1989). d. Anorthosites. Abbreviations: OAN = oxide-apatite norite. $Eu/Eu^* = (Eu)_n/[(Sm)_n \times (Gd)_n]^{0.5}$.

3.6.2.2 Fine-grained dykes and liquid line of descent

The ferrodiorite fine-grained dykes from Lac Mirepoix are enriched in Fe_2O_3 (27.1 – 6.4 wt.%), TiO_2 (7.0 – 1.3 wt.%) and P_2O_5 (7.0 – 0.8 wt.%) whereas their SiO_2 contents vary from 28.0 – 51.8 wt.%, characteristic of other ferrodiorite dykes associated with anorthosite massifs compiled from the literature (Appendix 3.1; Fig.3.13). The low-SiO_2 content of the most primitive dyke (MX-114) could also denote some accumulation of oxides and orthopyroxene in the dyke, although texturally this sample is fine-grained. The jotunite dyke (sample 20PM19B) presents more evolved compositions, with higher SiO_2 (58.02 wt.%), K_2O (3.51 wt.%) and lower Fe_2O_{3t} (9.40 wt.%) and TiO_2 (2.0 wt.%) contents in relation to the ferrodiorite dykes. This is similar

to other jotunite dykes previously presented in the literature (Fig.3.8b), reflecting higher proportions of plagioclase, K-feldspar and lower amounts of oxides, apatite and orthopyroxene compared to Fe-Ti-P-rich ferrodiorites. Moreover, it is important to note that low P fine-grained dykes, i.e., parental to oxide-plag-px cumulates (massive oxides) were not observed within the mineralization.

The fine-grained dykes in Lac Mirepoix have very similar REE and multi-element patterns to the ferrodiorite dykes from Lac à l'Orignal and the Grader Intrusion (Figs.3.8b-c). Ferrodiorite dykes (e.g. MX-114-1) have more primitive trace element compositions (lower REE, Y, Zr and Hf, Fig.3.8c) in relation to evolved jotunite dykes (e.g. 20PM19B). Jotunite dykes in the Lac Mirepoix present similar patterns to the evolved jotunite dykes (Fig.3.8c) analyzed in the Rogaland Anorthosite Province (Wilmart et al. 1989), except for the slightly enrichment in Zr and Hf of the former.

A compilation of bulk whole-rock analysis of different lithologies (ferrodiorite/jotunite dykes and granites) interpreted as evolved liquid compositions in mafic layered intrusions (Sept Iles) and associated with Fe-Ti-P mineralization hosted in anorthosite massifs (e.g. Lac Tio Fe-Ti deposit, the Grader Intrusion and the Lac à l'Orignal Fe-Ti-P mineralization in Quebec), are plotted as a series of Harker diagrams in Appendix 3.2 to illustrate the behaviour of elements during the liquid line of descent. As mentioned above, Lac Mirepoix fine-grained dykes plot similar to other ferrodiorites/jotunites from anorthosite massifs and indicate compatible behaviour for TiO_2, FeO, MgO, CaO, P_2O_5, Sr, V and Cr, whereas K_2O, REE (e.g., La) and Nb behave incompatibly. At Lac Mirepoix, a liquid line of descent can be traced from the primitive ferrodiorite MX-114-1 dyke composition (Ti-rich, hemo-ilmenite dominated), from which cumulate phases (plagioclase, pyroxene, ilmenite, magnetite and apatite) would be continuously extracted to form nelsonites and OAN. This cumulate extraction

would then lead to the formation of a residual evolved jotunite liquid in equilibrium with the cumulates enriched in plagioclase, magnetite and normative K-feldspar and quartz (dyke sample 20PM19-B). The less evolved liquids, i.e., the ferrodiorites of Lac Mirepoix and Grader Intrusion, exhibit a higher Ti/Fe ratio in relation to more evolved jotunite dykes of the Rogaland Province, and Si-rich members of the Sept-Iles Layered Intrusion, which have the lowest Ti/Fe ratio (Appendix 3.2). However, at Lac Mirepoix, the Ti/Fe ratio remains constant from ferrodiorite to jotunite.

3.6.2.3 Host anorthosite

The anorthosite samples, from both the host anorthosite and enclaves (e.g. sample 20PM05C) within massive/semi-massive mineralization, have a similar geochemical signature, being andesine in composition (CIPW norm: An* = 40.4 – 48.2, Or* = 5.4 – 9.0) and display lower MgO (< 4.17 wt.%), Fe_2O_3 (< 5.46 wt.%), TiO_2 (< 0.85 wt.%) and P_2O_5 (< 1.15 wt.%) contents in relation to the mineralized cumulates. The host anorthosite has the typical pattern of plagioclase-rich cumulates, exhibiting lower overall REE concentrations with positive Eu-anomalies (Fig.3.8d). These patterns and REE-abundances are very similar to the host anorthosite samples analyzed from Lac à l'Orignal (Fig.3.8d) but distinct from the apatite-bearing anorthosite layers, present within the mineralization at Lac à l'Orignal, which have much higher REE abundances and an overall flat-pattern (Fig.3.8d) due to the presence of cumulus apatite.

3.6.3 U-Pb dating

U–Pb zircon results from two samples within the Fe-Ti-P mineralization at Lac Mirepoix are presented in Table 3.2 (complete data in Appendix 3.1). Concordia diagrams for each sample are shown Figure 3.9, where all ages are presented with their associated 2σ analytical uncertanties. Cathodoluminescence photomicrographs

of the zircon grains selected for U-Pb dating (Fig.3.9; Appendix 3.1) show that they are mostly subhedral prismatic to anhedral igneous zircons with magmatic oscillatory zoning. The two samples from Lac Mirepoix produced two different crystallization ages, which are similar to the two U-Pb zircon ages of Fe-Ti-P (OAN) mineralization at the nearby, sill-like Lac à l'Orignal intrusion (Miloski et al. 2023). At Lac Mirepoix, sample LMX-1 is an OAN (20PM06, hemo-ilmenite + magnetite dominated) layer located in zone I, where massive oxides are the dominant cumulate assemblage (Fig.3.4). The calculated weighted mean Concordia age for all the zircon grains, is 964 ± 9 Ma (MSWD = 1.3 n=24). This age is younger than the range of crystallization ages from the youngest Valin AMCG Suite (1020-1008 Ma) in the region, including the nearby Mattawa Anorthosite (1016 ± 2 Ma, Hébert et al. 2005), but similar to the young core of Lac à l'Orignal OAN mineralization (993 ± 13 Ma: Miloski et al. 2023). Sample LMX-2 represents an OAN (20PM08B, hemo-ilmenite + magnetite dominated) layer located in zone III, where oxide-apatite norites are the main cumulate rocks (Fig.3.4). The calculated weighted mean Concordia age for all the zircon grains, is 1048 ± 8 Ma (MSWD = 1.0, n=19), which is close but younger than the youngest ages from the Pipmuacan Anorthosite Suite (1080 – 1060Ma), including the nearby Vanel Anorthosite (1080.0 ± 2.0 Ma, Hébert et al. 2009). It is also similar to the older, upper border of Lac à l'Orignal OAN mineralization (1069 ± 12 Ma: Miloski et al. 2023). This indicates that the Lac Mirepoix mineralization is multi-phase, being formed by at least two different pulses of magmas of distinct ages – 80 Ma apart, similar to the Fe-Ti-P mineralization at Lac à l'Orignal.

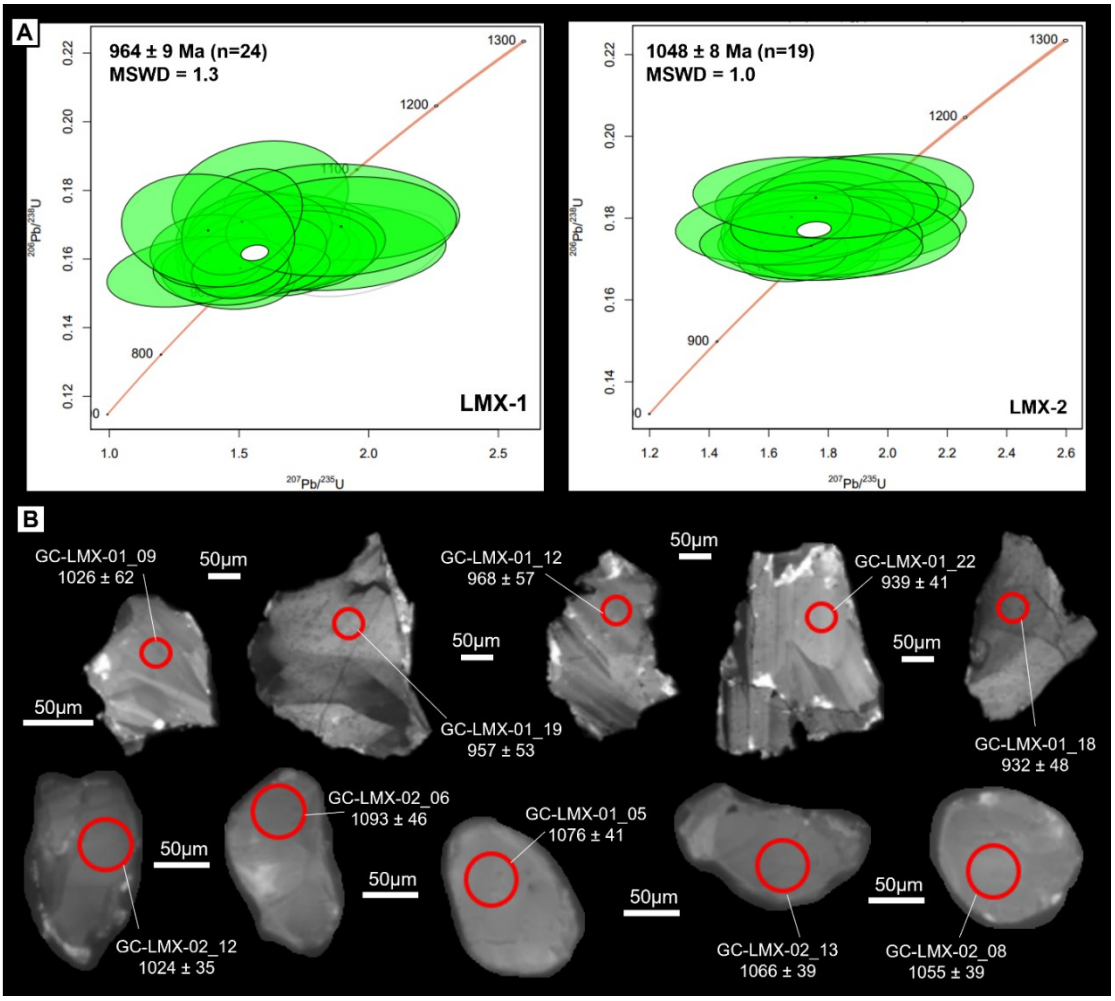

Figure 3.9. a. Concordia diagrams for in situ LA-ICP-MS U–Pb data from analyzed zircons in the Lac Mirepoix Fe-Ti-P mineralization. Each ellipse represents the result of the analysis of a single grain, and corresponds to the associated 2σ uncertainties. b. Representative cathodoluminescence images from detrital magmatic grains of zircon of the Lac Mirepoix Fe-Ti-P. Red circles show the location of the 50 µm beam for U–Pb microanalysis. Sample LMX-1 representing an oxide-apatite norite in the Zone I, dominated by massive oxides (20PM06). Sample LMX-2 representing an oxide-apatite norite in the zone III portion dominated by oxide-apatite norites (20PM08B1 & 2).

Table 3.2. Zircon U–Pb LA-ICP-MS analytical data in Lac Mirepoix Fe-Ti-P mineralization

#Analysis	U_{ppm}	Pb_{ppm}	Th/U	$^{206}Pb/^{204}Pb$	Isotopic ratios ±1s%			Apparent ages ±2s%			Rho
					$^{206}Pb/^{238}U$	$^{207}Pb/^{235}U$	$^{207}Pb/^{206}Pb$	$^{206}Pb/^{238}U$	$^{207}Pb/^{235}U$	$^{207}Pb/^{206}Pb$	
Sample LMX-01 (20PM06) - Oxide-apatite norite. Concordia age: 964 ± 10Ma											
GC-LMX-01_2	20.2	1222.7	0.5	-35.7	0.1614 ± 3	1.6933 ± 6	0.0748 ± 6	960 ± 55	975 ± 90	905 ± 285	0.15
GC-LMX-01_3	14.4	883.7	0.4	-28.7	0.1636 ± 3	1.8285 ± 11	0.077 ± 10	972 ± 57	964 ± 134	642 ± 445	0.04
GC-LMX-01_4	13.6	836.1	0.3	-43.2	0.1654 ± 3	1.6595 ± 10	0.0764 ± 10	981 ± 62	863 ± 153	807 ± 477	0.01
GC-LMX-01_5	15.2	960.9	0.6	-70.9	0.1774 ± 4	1.5811 ± 9	0.0666 ± 8	1045 ± 73	868 ± 135	689 ± 373	0.16
GC-LMX-01_6	47.7	2842.4	0.5	-327.1	0.1604 ± 3	1.7209 ± 6	0.0749 ± 5	956 ± 45	978 ± 70	831 ± 229	0.31
GC-LMX-01_7	20.8	1284.4	0.5	-130.5	0.1624 ± 3	1.5432 ± 7	0.0679 ± 7	967 ± 44	836 ± 115	760 ± 314	0.44
GC-LMX-01_8	30.0	1869.7	0.6	-548.5	0.1660 ± 3	1.6694 ± 6	0.0707 ± 6	986 ± 53	953 ± 72	658 ± 273	0.43
GC-LMX-01_9	9.1	600.1	0.4	139.4	0.1737 ± 3	1.8963 ± 10	0.0856 ± 11	1026 ± 62	890 ± 169	815 ± 468	-0.07
GC-LMX-01_10	16.4	991.0	0.5	136.2	0.1633 ± 3	1.5888 ± 9	0.0719 ± 8	972 ± 46	902 ± 103	567 ± 406	0.19
GC-LMX-01_11	30.7	1922.2	0.3	180.3	0.1682 ± 3	1.5358 ± 6	0.0675 ± 6	998 ± 51	909 ± 76	446 ± 308	0.22
GC-LMX-01_12	13.5	808.0	0.4	72.8	0.1629 ± 3	1.6722 ± 10	0.0846 ± 10	968 ± 57	866 ± 151	1036 ± 398	0.21
GC-LMX-01_13	15.4	904.1	0.6	53.1	0.1556 ± 3	1.4589 ± 7	0.0695 ± 7	929 ± 46	849 ± 95	526 ± 378	-0.09
GC-LMX-01_14	91.0	5301.3	0.6	495.9	0.1585 ± 3	1.5256 ± 4	0.0708 ± 3	954 ± 47	919 ± 46	880 ± 151	0.37
GC-LMX-01_15	18.3	1136.3	0.4	98.5	0.1654 ± 3	1.5664 ± 8	0.0733 ± 7	981 ± 59	860 ± 102	945 ± 322	0.30
GC-LMX-01_16	21.6	1267.7	0.6	25.4	0.1625 ± 3	1.7393 ± 7	0.0815 ± 7	967 ± 52	955 ± 80	935 ± 311	0.07
GC-LMX-01_17	39.7	2250.8	0.6	44.8	0.1568 ± 2	1.6138 ± 6	0.0757 ± 6	937 ± 35	933 ± 72	855 ± 244	0.26
GC-LMX-01_18	12.8	716.7	0.4	7.7	0.1562 ± 3	1.3071 ± 10	0.0685 ± 10	932 ± 48	774 ± 131	550 ± 409	0.29
GC-LMX-01_19	19.5	1116.7	0.5	2.9	0.1606 ± 3	1.5632 ± 7	0.0722 ± 7	957 ± 53	890 ± 104	759 ± 344	0.32
GC-LMX-01_20	28.7	1599.5	0.5	-1.1	0.1565 ± 3	1.4350 ± 8	0.0706 ± 8	934 ± 46	844 ± 97	695 ± 344	-0.03
GC-LMX-01_21	27.7	1550.7	0.4	-2.5	0.1622 ± 3	1.3874 ± 7	0.0640 ± 7	965 ± 49	843 ± 82	538 ± 302	0.08
GC-LMX-01_22	35.7	1991.5	0.3	-33.7	0.1573 ± 2	1.5043 ± 5	0.0687 ± 5	939 ± 41	893 ± 62	667 ± 233	0.19
GC-LMX-01_23	10.5	596.2	0.5	-5.6	0.1694 ± 4	1.8939 ± 10	0.0821 ± 10	1002 ± 64	945 ± 156	1192 ± 343	0.14
GC-LMX-01_24	19.5	1115.9	0.5	-10.1	0.1708 ± 4	1.5115 ± 6	0.0670 ± 6	1021 ± 71	919 ± 77	682 ± 266	0.31
GC-LMX-01_25	12.8	712.7	0.5	-9.4	0.1683 ± 4	1.3806 ± 10	0.0657 ± 10	994 ± 73	749 ± 157	531 ± 432	-0.13

Table 3.2. (Cont.) Zircon U–Pb LA-ICP-MS analytical data in Lac Mirepoix Fe-Ti-P mineralization

#Analysis	U_{ppm}	Pb_{ppm}	Th/U	$^{206}Pb/^{204}Pb$	Isotopic ratios ±1s%			Apparent ages ±2s%			Rho
					$^{206}Pb/^{238}U$	$^{207}Pb/^{235}U$	$^{207}Pb/^{206}Pb$	$^{206}Pb/^{238}U$	$^{207}Pb/^{235}U$	$^{207}Pb/^{206}Pb$	
Sample LMX-02 (20PM08B) - Oxide-apatite norite. Concordia age: 1050 ± 8Ma											
GC-LMX-02_3	6.0	1105.4	0.7	5.2	0.1847 ± 2	1.8094 ± 9	0.0743 ± 9	1089 ± 46	1047 ± 117	1126 ± 300	0.17
GC-LMX-02_4	11.5	1962.3	0.9	20.4	0.1723 ± 2	1.6995 ± 7	0.0708 ± 7	1023 ± 34	951 ± 83	700 ± 319	-0.14
GC-LMX-02_5	9.4	1710.6	0.6	17.2	0.1822 ± 2	1.7784 ± 7	0.0724 ± 6	1076 ± 41	961 ± 99	987 ± 256	0.04
GC-LMX-02_6	8.6	1484.1	1.1	7.4	0.1853 ± 2	1.9136 ± 8	0.0773 ± 8	1093 ± 46	1040 ± 109	1030 ± 293	0.23
GC-LMX-02_8	11.5	1832.6	1.4	11.8	0.1782 ± 2	1.9533 ± 2	0.0818 ± 7	1055 ± 39	1052 ± 82	995 ± 298	0.10
GC-LMX-02_9	13.6	2156.1	0.8	-7.7	0.1800 ± 2	1.7158 ± 2	0.0713 ± 6	1065 ± 40	970 ± 93	946 ± 227	0.25
GC-LMX-02_10	25.7	3870.6	3.3	11.1	0.1758 ± 2	1.7895 ± 2	0.0757 ± 4	1042 ± 38	1020 ± 57	956 ± 181	0.07
GC-LMX-02_11	22.7	3429.5	2.4	-7.7	0.1771 ± 2	1.7354 ± 2	0.0723 ± 4	1050 ± 32	1009 ± 60	849 ± 198	0.25
GC-LMX-02_12	21.7	3125.0	1.9	-38.2	0.1725 ± 2	1.7395 ± 2	0.0735 ± 5	1024 ± 35	997 ± 76	842 ± 234	0.33
GC-LMX-02_13	13.6	2027.2	1.8	-10.3	0.1802 ± 2	1.9454 ± 2	0.0809 ± 6	1066 ± 39	1058 ± 94	1028 ± 254	0.37
GC-LMX-02_14	9.5	1340.7	0.9	-13.7	0.1753 ± 2	1.8610 ± 2	0.0767 ± 6	1039 ± 45	954 ± 130	1163 ± 274	0.05
GC-LMX-02_15	11.1	1581.6	0.6	-27.1	0.1758 ± 2	1.7773 ± 2	0.0782 ± 8	1041 ± 45	1002 ± 107	1039 ± 307	-0.01
GC-LMX-02_17	46.4	6284.9	0.8	213.3	0.1717 ± 1	1.7100 ± 1	0.0700 ± 3	1021 ± 26	1006 ± 46	921 ± 147	0.09
GC-LMX-02_19	19.4	2659.3	1.7	-19.9	0.1788 ± 2	1.8286 ± 2	0.0756 ± 5	1066 ± 39	1000 ± 86	817 ± 276	0.34
GC-LMX-02_20	17.7	2365.3	1.8	-10.5	0.1764 ± 2	1.6601 ± 2	0.0679 ± 5	1046 ± 34	961 ± 65	678 ± 219	0.34
GC-LMX-02_21	12.0	1651.8	1.1	20.9	0.1776 ± 2	1.6501 ± 2	0.0663 ± 9	1052 ± 40	932 ± 122	859 ± 315	0.10
GC-LMX-02_22	10.0	1334.1	0.6	37.0	0.1732 ± 2	1.7426 ± 2	0.0721 ± 9	1028 ± 39	926 ± 123	1209 ± 271	-0.04
GC-LMX-02_24	27.9	3855.9	2.0	-45838.3	0.1802 ± 2	1.6769 ± 2	0.0676 ± 4	1066 ± 38	960 ± 65	668 ± 244	0.27
GC-LMX-02_25	9.3	1386.2	1.2	-28.9	0.1849 ± 2	1.7580 ± 2	0.0691 ± 9	1091 ± 44	973 ± 131	996 ± 331	-0.10

3.6.4 Mineral chemistry

3.6.4.1 Plagioclase

Plagioclase is the first cumulus mineral of the Lac Mirepoix mineralization, accompanied by hemo-ilmenite, and is present throughout the 3 zones (Fig.3.4). Plagioclase compositions, determined by LA-ICP-MS for the mineralisation, fine-grained dyke and a few host anorthosites, are presented in Table 3.3 and Appendix 3.1. Microprobe and pXRF plagioclase data, from a subset of mineralization and host anorthosite, is also presented in Appendix 3.1. Overall, plagioclase An content is andesine in composition (An 40 – 50) throughout Lac Mirepoix but Sr and Ba are more variable among the different zones (Fig.3.10a). Plagioclase from the semi-massive oxide mineralization in zones I and II varies from An44.1 to An48.9 and from Or0.4 to Or1.4. Sr contents vary from 1876 to 1956 ppm and Ba from 141 to 360 ppm. Nelsonite in zone II has a slightly more evolved plagioclase composition (An40.7) and higher Sr (2614 ppm) content. The An content of plagioclase from OAN mineralization in all 3 zones varies from 41.4 to 50.5, but those in zone III typically have higher Sr (1988 to 2964 ppm) and Ba (400 – 1315 ppm) contents than those from OAN in zones I and II (<2000 ppm Sr and <400 ppm Ba). Also, a large variability in the plagioclase composition is observed at zone III (Fig.3.10a).

Plagioclase from the fine-grained ferrodiorite dykes (An31.8 to An48.5, Or0.9 to Or4.3, Sr = 1434 -2615 ppm and Ba = 133 – 7842 ppm) have similar ranges to those from the OAN mineralization. However, the more evolved jotunite dyke (20PM19B) contains lower An (31.8-33-7) and Sr (1433-1613 ppm) values in comparison to the more primitive ferrodiorite dykes and the OAN samples, confirming the evolved nature of these dykes. Plagioclase from the host anorthosite is also andesine in composition,

with similar An (35.0-47.0) and Sr (1679 - 2847 ppm) but higher Ba (827 - 1938 ppm) values in relation to the mineralized samples.

3.6.4.2 Apatite

Apatite trace element composition is presented in Table 3.4 and the geochemical variation for selected elements (Sr, Total REE, Y and Eu/Eu*) in Figure 3.9b. The complete data is presented in Appendix 3.2. The REE-contents of apatite from OAN, nelsonite and semi-massive oxides have a similar overlapping range of Total REE (1575 – 4715 ppm) concentrations. Apatite from OAN of zones II and III are slightly enriched in REE than those from zone I. Apatite from nelsonite samples have higher Sr (1296 – 1346 ppm) values in relation to apatite from the other mineralized samples (670 – 1247 ppm). The fine-grained dykes contain a large range of trace element concentrations in apatite, presenting the highest total REE (1195 - 10275 ppm) and the lowest Sr values (561 – 1054 ppm) amongst all of the analyzed samples.

The REE contents of apatite, normalized to chondrite (Fig.3.11; Table 3.4), show very similar shaped patterns for the OAN (Fig.3.10a, La/Yb_N = 11.4 – 17.6 and Eu/Eu^* = 0.6 – 0.8), nelsonite (La/Yb_N = 13.6 – 14.6 and Eu/Eu^* = 0.7 – 0.8) and fine-grained OAN dykes (Fig.3.11b, La/Yb_N = 9.1 – 17.5 and Eu/Eu^* = 0.5 – 0.8), characterized by small negative Eu anomalies and LREE enrichment. Overall, the patterns and REE abundance of both OAN and fine-grained dykes are similar to those observed in the nearby Lac à l'Orignal Fe-Ti-P mineralization (Figs.3.11a-b: Miloski et al. 2023). Apatite from a few OAN samples from zone III, as well as the evolved jotunite (20PM19B) have higher-REE concentrations in relation to the other Lac Mirepoix samples and from those present in the nearby Lac à l'Orignal (Figs.3.11a-b).

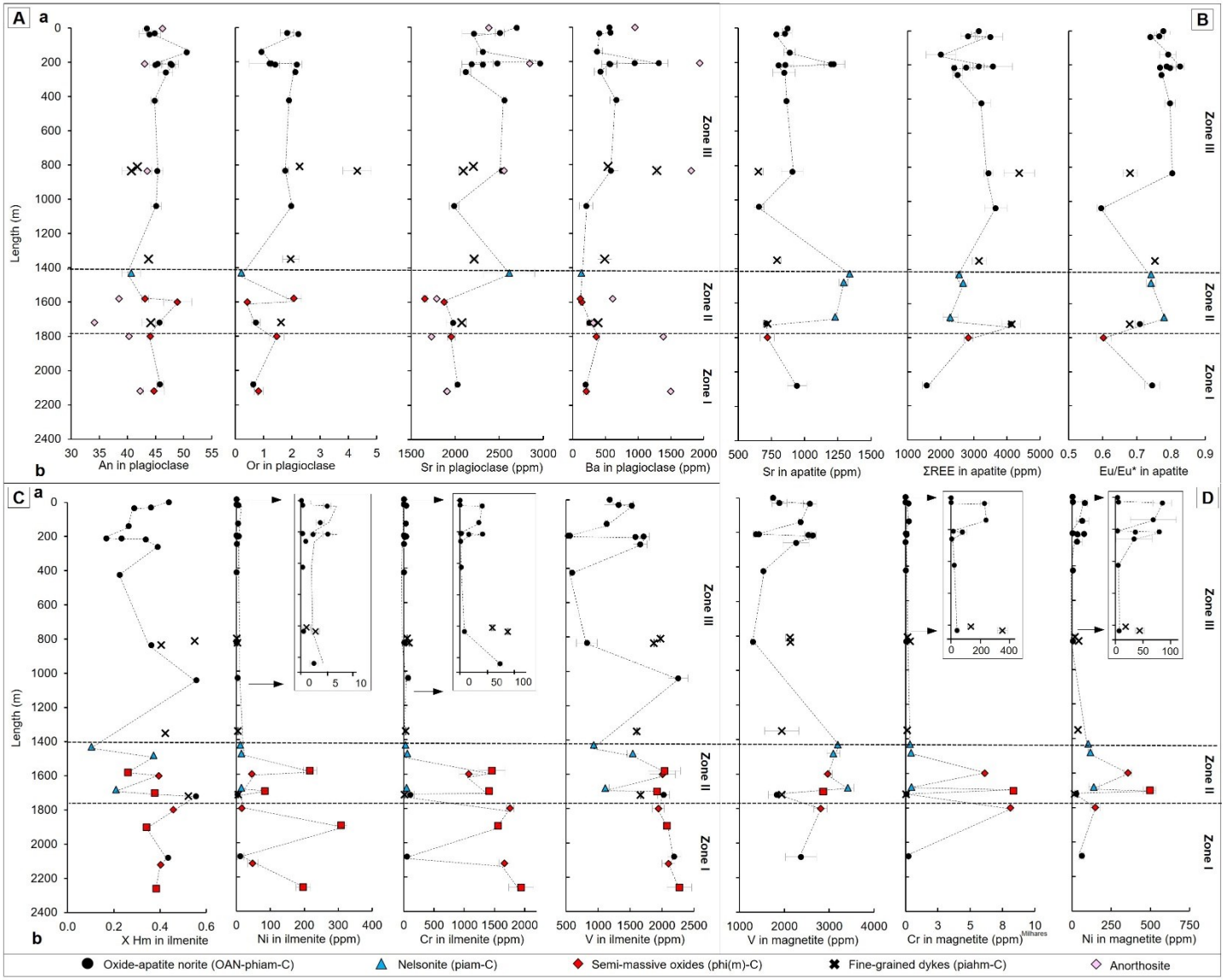

Figure 3.10. Geochemical variation of plagioclase (a), apatite (b), ilmenite (c) and magnetite (d) compositions in the Lac Mirepoix Fe-Ti-P mineralization along the stratigraphic profile of Fig. 3.2 (SE section a-b), with black horizontal lines separating the three petrographic zones (I – III). Error bars = 1 standard deviation and represents the natural variation within the thin section. Mineral abbreviations: hm-ilm = hemo-ilmenite; ilm = ilmenite; mt = magnetite. XHm=hematite content in ilmenite.

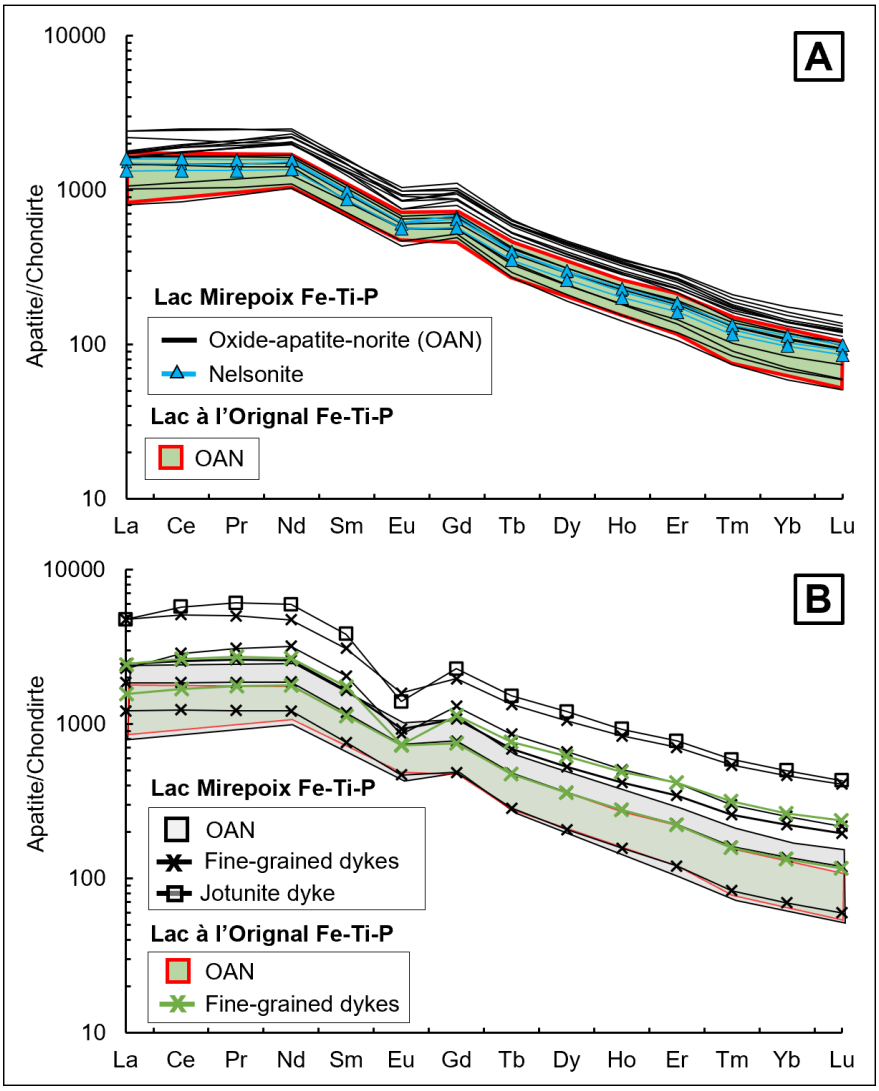

Figure 3.11. Chondrite-normalized REE compositions of apatite (after Sun and McDonough, 1989) from the Lac Mirepoix Fe-Ti-P mineralization. Comparison (green field) with the nearby Lac à l'Orignal Fe-Ti-P mineralization (Miloski et al. 2023a). a. Mineralized oxide-apatite norite (OAN) and nelsonite samples. b. Fine-grained dykes compared to fields (grey and green) for the OAN compositions of Fig.3.10-a.

Table 3.3. LA-ICP-MS major and trace element analyses of plagioclase in the Lac Mirepoix Fe-Ti-P mineralization

Sample	Depth (m)	Lithology	Oxides	# analysis	SiO_2	Al_2O_3	FeO_t	CaO	Na_2O	K_2O	Total	An	Ab	Or
20PM05C	-	Anorthosite enclaves	-	n=6	56.69	28.14	0.13	8.38	5.87	0.34	99.56	43.16	54.76	2.07
20PM06B	-	Medium-grained OAN	Hm-Ilm+Mt	n=6	56.69	29.06	0.23	8.89	5.75	0.10	100.75	45.80	53.56	0.64
20PM07	-	Nelsonite	Ilm+Mt	n=6	58.45	28.18	0.19	8.10	6.50	0.03	101.48	40.67	59.12	0.21
20PM08B1	-	Medium-grained OAN	Hm-Ilm+Mt	n=6	56.41	29.79	0.12	9.34	5.52	0.21	101.53	47.70	51.04	1.26
20PM08B2	-	Medium-grained OAN	Hm-Ilm+Mt	n=6	57.36	27.88	0.08	8.29	5.39	0.19	99.19	45.40	53.39	1.22
20PM18B	-	Medium-grained OAN	Hm-Ilm+Mt	n=6	58.68	26.64	0.15	7.99	5.17	0.11	98.73	45.71	53.57	0.73
20PM19B	-	Fine-grained jotunite	Hm-Ilm+Mt	n=6	61.13	25.27	0.18	6.14	6.49	0.28	99.48	33.70	64.45	1.86
CM1001A	-	Fine-grained OAN dyke	Hm-Ilm	n=4	59.51	24.37	0.11	4.42	5.35	4.59	98.94	31.78	66.34	1.89
CM1007	-	Medium-grained OAN	Hm-Ilm+Mt	n=4	55.25	27.96	0.20	8.38	6.26	0.42	98.52	41.44	56.06	2.50
CM1012	-	Medium-grained Anort-OAN	Hm-Ilm+Mt	n=4	55.35	28.09	0.14	8.32	6.16	0.41	98.49	41.68	55.86	2.47
CM1013	-	Medium-grained OAN	Hm-Ilm+Mt	n=4	55.00	28.12	0.18	8.57	6.16	0.44	98.53	42.30	55.10	2.60
CM1038	-	Medium-grained OAN	Hm-Ilm+Mt	n=4	54.61	28.00	0.61	8.77	6.12	0.42	98.62	43.08	54.49	2.43
CM1045	-	Medium-grained OAN	Hm-Ilm+Mt	n=4	54.61	28.53	0.11	9.01	5.91	0.31	98.55	44.87	53.30	1.83
CM1047	-	Medium-grained OAN	Hm-Ilm+Mt	n=4	54.58	28.46	0.45	8.74	5.92	0.37	98.56	43.95	53.82	2.23
CM1050	-	Medium-grained OAN	Hm-Ilm+Mt	n=4	53.02	29.64	0.08	10.21	5.42	0.16	98.57	50.53	48.55	0.92
CM1051	-	Medium-grained OAN	Hm-Ilm+Mt	n=4	54.02	28.93	0.11	9.41	5.67	0.36	98.55	46.81	51.07	2.12
CM1052	-	Medium-grained OAN	Hm-Ilm+Mt	n=4	53.56	29.34	0.09	9.64	5.64	0.24	98.58	47.88	50.71	1.41
CM1053	-	Medium-grained OAN	Hm-Ilm+Mt	n=4	54.35	28.70	0.09	9.07	5.96	0.32	98.56	44.84	53.26	1.90
CM1060	-	Fine-grained ferrodiorite	Hm-Ilm+Mt	n=4	55.10	28.06	0.13	8.51	6.29	0.39	98.53	41.80	55.93	2.27
CM1063B	-	Medium-grained OAN	Hm-Ilm	n=4	53.94	28.94	0.16	9.18	5.95	0.34	98.53	45.11	52.91	1.98
CM1076B	-	Fine-grained ferrodiorite	Hm-Ilm+Mt	n=4	54.74	28.39	0.19	8.87	6.02	0.27	98.53	44.19	54.20	1.61
CM1110	-	Fine-grained ferrodiorite	Hm-Ilm+Mt	n=4	53.64	29.29	0.08	9.72	5.62	0.15	98.54	48.48	50.60	0.92
MX102-3	13.50	Fine-grained ferrodiorite	Hm-Ilm+Mt	n=4	55.74	27.68	0.20	8.09	6.04	0.71	98.60	40.71	54.98	4.31
MX102-5	21.00	Medium-grained OAN	Hm-Ilm+Mt	n=4	53.61	29.06	0.16	9.34	6.03	0.31	98.58	45.32	52.91	1.77
MX105-1	0.50	Medium-grained OAN	Hm-Ilm+Mt	n=4	54.50	28.51	0.10	8.87	6.16	0.33	98.55	43.44	54.62	1.95
MX106-1	5.00	Medium-grained OAN	Hm-Ilm+Mt	n=4	53.80	28.93	0.15	9.25	6.01	0.38	98.57	44.97	52.85	2.18
MX108-6	3.00	Semi-massive Oxides	Hm-Ilm+Mt	n=4	54.31	28.50	0.33	8.98	6.14	0.25	98.55	44.04	54.50	1.46
MX109-2	4.50	Semi-massive Oxides	Hm-Ilm	n=4	53.89	29.08	0.31	9.03	6.07	0.14	98.55	44.75	54.42	0.82
MX114-1	8.50	Fine-grained ferrodiorite	Hm-Ilm+Mt	n=4	54.62	28.36	0.22	8.87	6.08	0.33	98.55	43.77	54.27	1.96
MX-115	16.50	Semi-massive Oxides	Hm-Ilm+Mt	n=4	52.04	30.27	0.12	10.21	5.85	0.07	98.57	48.91	50.66	0.42

Major elements in wt.%, An=100 [Ca/(Ca+Na+K)]; Ab=100 [Na/(Ca+Na+K)]; Or=100 [K/(Ca+Na+K)]; trace element in ppm. OAN = Oxide-apatite norite; Hm-ilm = hemo-ilmenite; Ilm = ilmenite; Mt = magnetite.

Table 3.3. (Cont.) LA-ICP-MS major and trace element analyses of plagioclase in the Lac Mirepoix Fe-Ti-P mineralization

Detection Limits (33-55µm)						0.058-0.245	0.515-0.809	0.005-0.013	0.003-1.838	0.008-0.476	0.010-0.057	0.005-0.058	0.001-0.023
Sample	Depth (m)	Location	Lithology	Oxides	# analysis	^{88}Sr	^{137}Ba	^{139}La	^{140}Ce	^{141}Pr	^{146}Nd	^{147}Sm	^{153}Eu
20PM05C	-	Surface Outcrop	Anorthosite enclaves	-	n=6	1656.8	114.9	8.6	14.5	1.5	5.0	0.5	1.3
20PM06B	-	Surface Outcrop	Medium-grained OAN	Hm-Ilm+Mt	n=6	2026.6	193.5	3.1	4.7	0.5	1.8	0.0	0.8
20PM07	-	Surface Outcrop	Nelsonite	Ilm+Mt	n=6	2614.2	133.3	5.3	7.6	0.7	2.6	0.0	0.8
20PM08B1	-	Surface Outcrop	Medium-grained OAN	Hm-Ilm+Mt	n=6	2964.9	1315.7	7.2	10.9	1.1	3.8	0.0	2.4
20PM08B2	-	Surface Outcrop	Medium-grained OAN	Hm-Ilm+Mt	n=6	2478.2	947.5	6.2	9.9	1.0	3.4	0.0	2.0
20PM18B	-	Surface Outcrop	Medium-grained OAN	Hm-Ilm+Mt	n=6	1975.3	251.4	8.5	12.2	0.9	0.0	0.0	2.4
20PM19B	-	Surface Outcrop	Fine-grained jotunite	Hm-Ilm+Mt	n=6	1433.9	133.1	30.0	38.9	3.2	9.2	0.0	2.9
CM1001A	-	Surface Outcrop	Fine-grained OAN dyke	Hm-Ilm	n=4	1613.3	7842.0	12.8	12.8	0.9	2.6	0.2	3.5
CM1007	-	Surface Outcrop	Medium-grained OAN	Hm-Ilm+Mt	n=4	2607.9	436.6	10.2	14.5	1.4	4.6	0.5	3.0
CM1012	-	Surface Outcrop	Medium-grained Anort-OAN	Hm-Ilm+Mt	n=4	2083.1	242.1	12.4	16.5	1.5	4.8	0.4	2.5
CM1013	-	Surface Outcrop	Medium-grained OAN	Hm-Ilm+Mt	n=4	2384.6	498.8	10.2	14.2	1.4	4.6	0.5	2.6
CM1038	-	Surface Outcrop	Medium-grained OAN	Hm-Ilm+Mt	n=4	2317.6	603.0	14.3	24.5	3.0	12.7	2.2	3.7
CM1045	-	Surface Outcrop	Medium-grained OAN	Hm-Ilm+Mt	n=4	2506.6	575.0	8.3	11.4	1.1	3.6	0.4	2.2
CM1047	-	Surface Outcrop	Medium-grained OAN	Hm-Ilm+Mt	n=4	2211.1	405.4	8.8	11.9	1.1	3.6	0.4	2.1
CM1050	-	Surface Outcrop	Medium-grained OAN	Hm-Ilm+Mt	n=4	2313.6	373.3	5.4	7.9	0.8	2.8	0.3	1.3
CM1051	-	Surface Outcrop	Medium-grained OAN	Hm-Ilm+Mt	n=4	2118.6	422.6	7.0	10.0	1.0	3.3	0.3	1.8
CM1052	-	Surface Outcrop	Medium-grained OAN	Hm-Ilm+Mt	n=4	2312.9	571.6	7.1	9.8	0.9	3.1	0.3	1.5
CM1053	-	Surface Outcrop	Medium-grained OAN	Hm-Ilm+Mt	n=4	2560.4	667.0	8.0	11.8	1.2	4.3	0.4	3.1
CM1060	-	Surface Outcrop	Fine-grained ferrodiorite	Hm-Ilm+Mt	n=4	2204.5	536.9	12.8	16.8	1.5	4.9	0.4	2.8
CM1063B	-	Surface Outcrop	Medium-grained OAN	Hm-Ilm	n=4	1988.3	205.6	10.8	14.9	1.4	4.5	0.4	2.1
CM1076B	-	Surface Outcrop	Fine-grained ferrodiorite	Hm-Ilm+Mt	n=4	2076.8	388.1	10.0	13.8	1.3	4.2	0.4	2.3
CM1110	-	Surface Outcrop	Fine-grained ferrodiorite	Hm-Ilm+Mt	n=4	2614.8	307.7	6.3	8.9	0.9	2.9	0.3	1.3
MX102-3	13.50	Boregole MX-102	Fine-grained ferrodiorite	Hm-Ilm+Mt	n=4	2091.5	1283.9	13.7	17.2	1.6	4.9	0.4	2.8
MX102-5	21.00	Boregole MX-102	Medium-grained OAN	Hm-Ilm+Mt	n=4	2530.5	580.3	8.8	13.4	1.4	4.9	0.5	3.3
MX105-1	0.50	Boregole MX-105	Medium-grained OAN	Hm-Ilm+Mt	n=4	2697.2	559.6	8.4	11.8	1.1	3.8	0.4	2.6
MX106-1	5.00	Boregole MX-106	Medium-grained OAN	Hm-Ilm+Mt	n=4	2186.0	562.2	7.5	10.8	1.1	3.5	0.3	1.9
MX108-6	3.00	Boregole MX-108	Semi-massive Oxides	Hm-Ilm+Mt	n=4	1956.5	359.7	8.8	13.5	1.4	4.6	0.5	1.8
MX109-2	4.50	Boregole MX-109	Semi-massive Oxides	Hm-Ilm	n=4	1904.9	204.5	11.6	18.5	1.9	6.4	0.7	1.8
MX114-1	8.50	Boregole MX-114	Fine-grained ferrodiorite	Hm-Ilm+Mt	n=4	2213.2	489.2	7.9	10.5	1.0	3.2	0.3	2.0
MX-115	16.50	Boregole MX-115	Semi-massive Oxides	Hm-Ilm+Mt	n=4	1876.5	140.9	13.6	21.0	2.1	7.0	0.7	1.6

Major elements in wt.%, An=100 [Ca/(Ca+Na+K)]; Ab=100 [Na/(Ca+Na+K)]; Or=100 [K/(Ca+Na+K)]; trace element in ppm. OAN = Oxide-apatite norite; Hm-ilm = hemo-ilmenite; Ilm = ilmenite; Mt = magnetite

Table 3.4. LA-ICP-MS major and trace element analyses of apatite in the Lac Mirepoix Fe-Ti-P mineralization

Detection Limits (33-55µm bean size)						0.01-0.07	0.01-0.02	0.003-0.014	0.003-0.012	0.002-0.008	0.012-0.030	0.013-0.021	0.003-0.009	0.015-0.057	0.002-0.004
Sample	Depth (m)	Location	Lithology	Oxides	# analysis	^{88}Sr	^{89}Y	^{139}La	^{140}Ce	^{141}Pr	^{146}Nd	^{147}Sm	^{153}Eu	^{157}Gd	^{159}Tb
20PM06B	-	Surface Outcrop	Medium-grained OAN	Hm-Ilm + Mt	n=6	943.4	200.2	190.1	514.7	85.4	469.7	98.9	24.4	98.2	9.8
20PM07	-	Surface Outcrop	Nelsonite	Ilm + Mt	n=6	1339.9	306.2	355.0	903.5	135.9	695.6	143.2	34.5	135.9	14.4
20PM08B1	-	Surface Outcrop	Medium-grained OAN	Hm-Ilm + Mt	n=6	1200.1	456.2	413.7	1180.0	193.5	1050.9	229.0	58.5	218.9	23.3
20PM08B2	-	Surface Outcrop	Medium-grained OAN	Hm-Ilm + Mt	n=6	1246.7	402.1	391.7	1094.4	177.5	924.1	201.5	51.3	175.0	19.2
20PM18B	-	Surface Outcrop	Medium-grained OAN	Hm-Ilm + Mt	n=6	712.2	493.0	568.4	1528.0	231.0	1099.1	219.2	48.3	187.2	21.7
20PM19A		Surface Outcrop	Fine-grained ferrodiorite	Hm-Ilm + Mt	n=6	779.2	746.4	577.7	1843.3	297.5	1518.0	318.5	51.0	272.9	32.3
20PM19B	-	Surface Outcrop	Fine-grained jotunite	Hm-Ilm + Mt	n=6	618.1	1350.7	1222.7	3740.0	594.9	2891.7	597.7	83.8	476.8	58.1
CM1001A	-	Surface Outcrop	Fine-grained ferrodiorite	Hm-ilm	n=4	560.9	1251.5	1194.5	3302.4	491.8	2284.6	483.5	94.1	410.9	51.0
CM1007	-	Surface Outcrop	Medium-grained OAN	Hm-Ilm + Mt	n=4	936.4	506.2	442.4	1267.4	203.5	1055.9	227.6	49.9	203.3	22.6
CM1012	-	Surface Outcrop	Medium-grained OAN	Hm-ilm	n=4	766.8	569.3	621.3	1679.5	254.3	1240.0	253.1	46.8	218.6	25.1
CM1013	-	Surface Outcrop	Medium-grained OAN	Hm-Ilm + Mt	n=4	862.8	443.4	433.1	1197.0	187.8	937.6	200.4	44.1	175.9	19.8
CM1038	-	Surface Outcrop	Medium-grained OAN	Hm-Ilm + Mt	n=4	830.9	540.5	600.2	1569.2	241.4	1200.3	247.7	58.1	214.4	23.8
CM1045	-	Surface Outcrop	Medium-grained OAN	Hm-Ilm + Mt	n=4	882.2	350.0	407.6	1051.8	158.9	794.4	164.2	39.5	143.9	15.8
CM1047	-	Surface Outcrop	Medium-grained OAN	Hm-Ilm + Mt	n=4	832.0	431.0	545.9	1366.2	199.5	966.4	193.4	44.5	166.0	18.6
CM1050	-	Surface Outcrop	Medium-grained OAN	Hm-Ilm + Mt	n=4	1005.0	292.4	278.7	767.9	122.1	637.4	139.6	35.0	125.4	13.7
CM1051	-	Surface Outcrop	Medium-grained OAN	Hm-Ilm + Mt	n=4	888.4	335.7	362.1	948.7	143.7	712.9	145.9	35.5	129.2	14.6
CM1052	-	Surface Outcrop	Medium-grained OAN	Hm-Ilm + Mt	n=4	839.6	280.9	363.2	926.8	136.9	673.5	133.1	33.2	115.7	12.4
CM1053	-	Surface Outcrop	Medium-grained OAN	Hm-Ilm + Mt	n=4	909.7	465.1	404.5	1131.6	184.6	989.0	215.8	55.0	197.9	21.8
CM1060	-	Surface Outcrop	Fine-grained ferrodiorite	Hm-Ilm + Mt	n=4	768.4	522.2	645.0	1650.8	242.6	1155.7	229.7	48.6	197.0	22.7
CM1063B	-	Surface Outcrop	Medium-grained OAN	Hm-ilm	n=4	684.8	476.8	533.7	1413.7	210.6	1014.4	203.8	38.2	179.2	20.8
CM1064	-	Surface Outcrop	Nelsonite	Ilm + Mt	n=4	1295.9	347.4	398.5	1030.1	153.9	757.9	154.0	36.0	135.9	15.2
CM1067	-	Surface Outcrop	Nelsonite	Ilm + Mt	n=4	1310.5	309.0	335.7	872.7	132.2	662.8	136.9	33.6	121.0	13.5
CM1076B	-	Surface Outcrop	Fine-grained ferrodiorite	Hm-Ilm + Mt	n=4	809.4	483.1	518.0	1381.2	212.6	1058.6	212.5	47.6	186.4	20.9
CM1110	-	Surface Outcrop	Fine-grained ferrodiorite	Hm-Ilm + Mt	n=4	1021.3	235.4	300.0	788.2	118.1	578.3	116.9	27.5	100.5	10.7
MX102-3	13.50	Borehole MX-102	Fine-grained ferrodiorite	Hm-Ilm + Mt	n=4	669.7	609.9	595.7	1616.2	250.1	1216.5	250.5	53.4	219.3	25.6
MX102-5	21.00	Borehole MX-102	Medium-grained OAN	Hm-Ilm + Mt	n=4	669.6	638.9	635.8	1708.3	261.5	1265.2	260.8	54.9	227.2	26.8
MX105-1	0.50	Borehole MX-105	Medium-grained OAN	Hm-Ilm + Mt	n=4	886.5	426.6	385.5	1112.3	176.9	924.0	196.7	48.6	176.9	19.4
MX106-1	5.00	Borehole MX-106	Medium-grained OAN	Hm-Ilm + Mt	n=4	887.5	360.8	404.9	1044.3	157.2	768.8	156.9	37.8	136.8	15.5
MX108-6	3.00	Borehole MX-108	Semi-massive Oxides	Hm-Ilm + Mt	n=4	742.1	401.9	377.4	1050.0	162.8	810.5	170.4	32.4	150.9	17.2
MX108-4	12.00	Borehole MX-108	Fine-grained OAN	Hm-ilm	n=4	1054.3	155.7	146.5	402.8	65.5	349.9	74.3	18.2	67.6	7.0
MX114-1	8.50	Borehole MX-114	Fine-grained ferrodiorite	Hm-Ilm + Mt	n=4	825.6	418.1	457.2	1186.7	180.5	892.4	183.0	43.3	160.8	18.1

[La/Yb]n and Eu/Eu* = (Eu)n/[(Sm)n x (Gd)n]0.5 calculated with Chondrite normalization values of Sun & McDonough (1989). OAN = Oxide-apatite norite; Hm-ilm = hemo-ilmenite; Ilm = ilmenite; Mt = magnetite.

Table 3.4. (Cont.) LA-ICP-MS major and trace element analyses of apatite in the Lac Mirepoix Fe-Ti-P mineralization

Detection Limits (33-55µm bean size)						0.008-0.014	0.002-0.003	0.006-0.015	0.002-0.004	0.009-0.027	0.002-0.003	Total REE	[La/Yb]n	Eu/Eu*
Sample	Depth (m)	Location	Lithology	Oxides	# analysis	^{163}Dy	^{165}Ho	^{166}Er	^{169}Tm	^{172}Yb	^{175}Lu			
20PM06B	-	Surface Outcrop	Medium-grained OAN	Hm-Ilm + Mt	n=6	46.8	7.7	17.0	1.8	9.5	1.3	1575.2	13.7	0.7
20PM07	-	Surface Outcrop	Nelsonite	Ilm + Mt	n=6	71.1	12.0	28.1	3.1	16.6	2.2	2551.2	14.6	0.7
20PM08B1	-	Surface Outcrop	Medium-grained OAN	Hm-Ilm + Mt	n=6	111.3	18.3	42.4	4.4	22.5	3.0	3569.7	12.6	0.8
20PM08B2	-	Surface Outcrop	Medium-grained OAN	Hm-Ilm + Mt	n=6	93.1	15.7	35.3	3.5	19.4	2.4	3204.0	13.7	0.8
20PM18B	-	Surface Outcrop	Medium-grained OAN	Hm-Ilm + Mt	n=6	112.5	19.0	46.2	5.2	28.1	3.8	4117.7	13.8	0.7
20PM19A		Surface Outcrop	Fine-grained ferrodiorite	Hm-Ilm + Mt	n=6	170.4	29.2	69.9	7.8	43.4	5.5	5237.4	9.1	0.5
20PM19B	-	Surface Outcrop	Fine-grained jotunite	Hm-Ilm + Mt	n=6	311.8	54.0	131.2	15.6	85.7	11.2	10275.1	9.5	0.5
CM1001A	-	Surface Outcrop	Fine-grained ferrodiorite	Hm-ilm	n=4	272.9	48.1	118.7	14.1	78.6	10.6	8855.7	11.1	0.6
CM1007	-	Surface Outcrop	Medium-grained OAN	Hm-Ilm + Mt	n=4	115.4	19.4	44.9	4.9	25.9	3.4	3686.6	11.8	0.7
CM1012	-	Surface Outcrop	Medium-grained OAN	Hm-ilm	n=4	130.5	22.3	52.9	6.0	33.0	4.3	4587.8	12.8	0.6
CM1013	-	Surface Outcrop	Medium-grained OAN	Hm-Ilm + Mt	n=4	100.8	17.1	39.6	4.4	23.5	3.1	3384.1	12.5	0.7
CM1038	-	Surface Outcrop	Medium-grained OAN	Hm-Ilm + Mt	n=4	122.6	20.6	47.7	5.2	27.5	3.6	4382.3	14.8	0.7
CM1045	-	Surface Outcrop	Medium-grained OAN	Hm-Ilm + Mt	n=4	79.4	13.5	31.1	3.3	17.8	2.4	2923.4	15.5	0.8
CM1047	-	Surface Outcrop	Medium-grained OAN	Hm-Ilm + Mt	n=4	95.5	16.3	38.3	4.3	23.8	3.1	3682.0	15.6	0.7
CM1050	-	Surface Outcrop	Medium-grained OAN	Hm-Ilm + Mt	n=4	67.2	11.1	24.2	2.5	12.7	1.6	2239.0	14.8	0.8
CM1051	-	Surface Outcrop	Medium-grained OAN	Hm-Ilm + Mt	n=4	75.1	12.9	30.4	3.4	18.6	2.4	2635.4	13.3	0.8
CM1052	-	Surface Outcrop	Medium-grained OAN	Hm-Ilm + Mt	n=4	62.0	10.4	24.1	2.6	14.0	1.9	2509.9	17.6	0.8
CM1053	-	Surface Outcrop	Medium-grained OAN	Hm-Ilm + Mt	n=4	110.1	18.5	42.1	4.5	23.4	3.1	3402.0	11.8	0.8
CM1060	-	Surface Outcrop	Fine-grained ferrodiorite	Hm-Ilm + Mt	n=4	118.9	20.6	49.6	5.6	31.0	4.1	4421.8	14.1	0.7
CM1063B	-	Surface Outcrop	Medium-grained OAN	Hm-ilm	n=4	107.7	18.5	44.1	5.0	27.7	3.6	3820.9	13.1	0.6
CM1064	-	Surface Outcrop	Nelsonite	Ilm + Mt	n=4	77.7	13.3	31.3	3.5	19.3	2.6	2828.9	14.0	0.7
CM1067	-	Surface Outcrop	Nelsonite	Ilm + Mt	n=4	68.6	11.7	27.6	3.1	16.8	2.2	2438.4	13.6	0.8
CM1076B	-	Surface Outcrop	Fine-grained ferrodiorite	Hm-Ilm + Mt	n=4	106.3	18.0	42.5	4.7	25.9	3.4	3838.5	13.6	0.7
CM1110	-	Surface Outcrop	Fine-grained ferrodiorite	Hm-Ilm + Mt	n=4	53.7	8.9	20.0	2.1	11.7	1.5	2138.1	17.5	0.8
MX102-3	13.50	Borehole MX-102	Fine-grained ferrodiorite	Hm-Ilm + Mt	n=4	133.9	23.3	56.6	6.5	36.6	4.9	4489.2	11.0	0.7
MX102-5	21.00	Borehole MX-102	Medium-grained OAN	Hm-Ilm + Mt	n=4	140.9	24.5	59.2	6.8	38.0	5.1	4715.0	11.4	0.7
MX105-1	0.50	Borehole MX-105	Medium-grained OAN	Hm-Ilm + Mt	n=4	96.6	16.4	37.9	4.1	21.6	2.9	3219.6	12.1	0.8
MX106-1	5.00	Borehole MX-106	Medium-grained OAN	Hm-Ilm + Mt	n=4	79.5	13.5	31.9	3.6	19.7	2.6	2873.0	14.0	0.8
MX108-6	3.00	Borehole MX-108	Semi-massive Oxides	Hm-Ilm + Mt	n=4	89.4	15.3	36.3	4.1	22.2	2.9	2941.7	11.6	0.6
MX108-4	12.00	Borehole MX-108	Fine-grained OAN	Hm-ilm	n=4	33.9	5.7	12.9	1.4	7.9	1.1	1194.5	12.7	0.8
MX114-1	8.50	Borehole MX-114	Fine-grained ferrodiorite	Hm-Ilm + Mt	n=4	92.8	15.8	37.6	4.2	23.0	3.1	3298.5	13.5	0.8

[La/Yb]n and Eu/Eu* = (Eu)n/[(Sm)n x (Gd)n]0.5 calculated with Chondrite normalization values of Sun & McDonough (1989). OAN = Oxide-apatite norite; Hm-ilm = hemo-ilmenite; Ilm = ilmenite; Mt = magnetite.

Table 3.5. LA-ICP-MS major and trace element analyses of ilmenite in the Lac Mirepoix Fe-Ti-P mineralization

Sample	Depth (m)	Lithology	Oxides	# analysis	SiO_2	TiO_2	Al_2O_3	FeO_t	Fe_2O_3	FeO	MnO	MgO	Total
20PM04B		Massive Oxides	Ilm + Mt	n=6	0.02	48.19	0.09	50.43	10.34	41.12	0.83	0.87	101.63
20PM05A	-	Massive Oxides	Hm-Ilm	n=6	0.04	47.42	0.08	64.67	29.43	38.19	0.21	2.59	118.47
20PM06B	-	Medium-grained OAN	Hm-Ilm + Mt	n=6	0.05	28.46	0.11	63.90	42.64	25.53	0.20	0.15	97.46
20PM07	-	Nelsonite	Ilm + Mt	n=6	0.02	47.62	0.05	47.81	9.71	39.07	0.83	1.73	99.17
20PM08B1	-	Medium-grained OAN	Hm-Ilm + Mt	n=6	0.02	44.07	0.05	50.34	15.95	35.99	0.81	1.65	98.63
20PM08B2	-	Medium-grained OAN	Hm-Ilm + Mt	n=6	0.16	42.06	0.07	55.18	23.05	34.44	0.76	1.59	102.16
20PM18B	-	Medium-grained OAN	Hm-Ilm + Mt	n=6	1.78	23.79	0.30	71.67	55.79	21.47	0.48	0.19	104.01
20PM19B	-	Fine-grained jotunite	Hm-Ilm + Mt	n=6	0.21	22.27	0.12	76.34	63.14	19.53	0.23	0.31	105.88
CM1001A	-	Fine-grained ferrodiorite	Hm-ilm	n=4	0.16	26.82	0.24	71.99	10.89	62.19	0.19	0.18	100.91
CM1007	-	Medium-grained OAN	Hm-Ilm + Mt	n=4	0.11	34.74	0.19	63.58	8.43	55.99	0.42	0.64	100.67
CM1012	-	Medium-grained OAN	Hm-ilm	n=4	0.04	30.66	0.15	68.48	10.67	58.88	0.20	0.41	101.19
CM1013	-	Medium-grained OAN	Hm-Ilm + Mt	n=4	0.07	38.64	0.14	59.69	7.18	53.23	0.38	0.69	100.57
CM1036	-	Massive Oxides	Hm-ilm	n=4	0.05	37.40	0.12	60.70	7.42	54.02	0.22	1.09	100.77
CM1038	-	Medium-grained OAN	Hm-Ilm + Mt	n=4	0.20	29.51	0.18	69.33	10.87	59.55	0.26	0.38	101.14
CM1045	-	Medium-grained OAN	Hm-Ilm + Mt	n=4	0.07	34.87	0.10	64.03	9.29	55.68	0.31	0.58	101.09
CM1047	-	Medium-grained OAN	Hm-Ilm + Mt	n=4	0.06	38.57	0.17	60.16	8.11	52.86	0.46	0.56	101.03
CM1050	-	Medium-grained OAN	Hm-Ilm + Mt	n=4	0.08	40.25	0.14	58.84	9.79	50.03	0.54	0.83	101.83
CM1051	-	Medium-grained OAN	Hm-Ilm + Mt	n=4	0.09	33.55	0.15	65.91	11.56	55.51	0.23	0.57	101.91
CM1052	-	Medium-grained OAN	Hm-Ilm + Mt	n=4	0.06	36.53	0.10	62.67	10.74	53.01	0.35	0.86	101.89
CM1053	-	Medium-grained OAN	Hm-Ilm + Mt	n=4	0.03	42.72	0.07	55.97	9.32	47.58	0.78	1.28	101.86
CM1060	-	Fine-grained ferrodiorite	Hm-Ilm + Mt	n=4	0.23	24.75	0.23	74.50	13.54	62.31	0.19	0.28	101.86
CM1063B	-	Medium-grained OAN	Hm-ilm	n=4	0.07	24.42	0.15	75.05	13.37	63.02	0.12	0.35	101.84
CM1064	-	Nelsonite	Ilm + Mt	n=4	0.11	34.66	0.15	64.27	10.86	54.50	0.62	0.89	101.67
CM1067	-	Nelsonite	Ilm + Mt	n=4	0.08	43.72	0.14	54.31	8.86	46.34	0.75	1.72	101.78
CM1076B	-	Fine-grained ferrodiorite	Hm-Ilm + Mt	n=4	0.16	26.11	0.15	73.49	13.25	61.56	0.27	0.13	101.90
CM1110	-	Fine-grained ferrodiorite	Hm-Ilm + Mt	n=4	0.06	37.87	0.10	60.48	8.27	53.04	0.30	1.10	101.04
MX102-3	13.50	Fine-grained ferrodiorite	Hm-Ilm + Mt	n=4	0.29	32.18	0.17	66.03	8.57	58.32	0.27	0.43	100.56
MX102-5	21.00	Medium-grained OAN	Hm-Ilm + Mt	n=4	0.06	34.53	0.29	61.76	3.71	58.42	0.57	0.96	98.68
MX105-1	0.50	Medium-grained OAN	Hm-Ilm + Mt	n=4	0.23	30.22	0.26	66.45	4.85	62.09	0.34	0.55	98.72
MX106-1	5.00	Medium-grained OAN	Hm-Ilm + Mt	n=4	0.09	30.50	0.22	67.89	9.13	59.67	0.20	0.50	100.58
MX108-6	3.00	Semi-massive Oxides	Hm-Ilm + Mt	n=4	0.06	29.17	0.21	67.04	2.93	64.41	0.22	0.67	98.23
MX108-4	12.00	Fine-grained OAN	Hm-ilm	n=4	0.04	31.57	0.18	65.21	3.17	62.36	0.18	0.53	98.36
MX109-2	4.50	Semi-massive Oxides	Hm-ilm	n=4	0.13	31.81	0.15	64.30	1.32	63.11	0.24	0.58	97.89
MX114-1	8.50	Fine-grained ferrodiorite	Hm-Ilm + Mt	n=4	0.21	31.01	0.19	67.55	8.89	59.55	0.22	0.22	100.53
MX-115	16.50	Semi-massive Oxides	Hm-Ilm + Mt	n=4	0.06	33.04	0.10	63.96	4.77	59.67	0.24	0.95	99.29
MX-117	13.50	Massive Oxides	Hm-Ilm + Mt	n=4	0.03	34.00	0.14	63.18	5.28	58.44	0.21	1.02	99.61
MX-118	4.00	Massive Oxides	Hm-ilm	n=4	0.03	33.87	0.07	62.33	2.95	59.67	0.17	1.39	98.78
MX-123	0.50	Massive Oxides	Hm-ilm	n=4	0.03	36.50	0.09	59.99	4.59	55.86	0.16	1.81	99.58

Major elements in wt.%, FeO and Fe2O3 recalculated from FeOt by charge balance equations; molar fractions of geikielite, pyrophanite, hematite and ilmenite (Xgeik, Xpyr, Xhem, Xilm) calculated following QUILF algorithm (Andersen et al.1993); trace element in ppm. OAN = Oxide-apatite norite; Hm-ilm = hemo-ilmenite; Ilm = ilmenite; Mt = magnetite.

Table 3.5. (Cont.) LA-ICP-MS major and trace element analyses of ilmenite in the Lac Mirepoix Fe-Ti-P mineralization

Detection Limits (33-55µm)							0.111-0.411	0.648-4.274	0.035-0.296	0.252-3.179	0.463-1.920	0.251-1.198
Sample	Depth (m)	Lithology	Oxides	# analysis	X_{hem}	X_{ilm}	^{25}Mg	^{27}Al	^{51}V	^{53}Cr	^{55}Mn	^{60}Ni
20PM04B		Massive Oxides	Ilm + Mt	n=6	0.1	0.9	5264.56	519.3	952.67	198.0	1652876.0	98.66
20PM05A	-	Massive Oxides	Hm-Ilm	n=6	0.26	0.74	15647.1	350.1	2037.3	1457.7	1587.4	216.8
20PM06B	-	Medium-grained OAN	Hm-Ilm + Mt	n=6	0.43	0.57	899.6	228.9	2189.7	48.8	1580.5	11.8
20PM07	-	Nelsonite	Ilm + Mt	n=6	0.10	0.90	10430.2	214.8	934.4	27.1	6453.4	11.7
20PM08B1	-	Medium-grained OAN	Hm-Ilm + Mt	n=6	0.17	0.83	9957.2	85.6	527.3	1.6	6294.0	0.5
20PM08B2	-	Medium-grained OAN	Hm-Ilm + Mt	n=6	0.23	0.77	9599.4	353.7	560.0	2.8	5868.8	0.4
20PM18B	-	Medium-grained OAN	Hm-Ilm + Mt	n=6	0.55	0.45	1135.8	1591.1	2024.5	103.9	5272.1	4.0
20PM19B	-	Fine-grained jotunite	Hm-Ilm + Mt	n=6	0.60	0.40	1893.0	635.2	1364.3	40.7	1768.6	0.4
CM1001A	-	Fine-grained ferrodiorite	Hm-ilm	n=4	0.50	0.50	1095.3	1268.2	1544.9	1.4	1467.7	0.8
CM1007	-	Medium-grained OAN	Hm-Ilm + Mt	n=4	0.36	0.64	3859.2	979.7	1066.0	1.9	3222.8	0.2
CM1012	-	Medium-grained OAN	Hm-ilm	n=4	0.44	0.56	2502.3	788.9	1129.3	0.6	1541.2	0.2
CM1013	-	Medium-grained OAN	Hm-Ilm + Mt	n=4	0.29	0.71	4175.4	759.8	1095.6	1.6	2944.3	0.3
CM1036	-	Massive Oxides	Hm-ilm	n=4	0.32	0.68	6591.6	623.7	2140.3	842.7	1729.8	17.5
CM1038	-	Medium-grained OAN	Hm-Ilm + Mt	n=4	0.46	0.54	2278.9	954.1	1186.9	19.6	2028.9	0.7
CM1045	-	Medium-grained OAN	Hm-Ilm + Mt	n=4	0.36	0.64	3480.2	545.3	1320.9	0.4	2391.6	0.5
CM1047	-	Medium-grained OAN	Hm-Ilm + Mt	n=4	0.29	0.71	3394.5	895.2	1525.1	39.1	3539.4	6.3
CM1050	-	Medium-grained OAN	Hm-Ilm + Mt	n=4	0.26	0.74	4993.2	717.3	1133.4	33.1	4163.4	4.7
CM1051	-	Medium-grained OAN	Hm-Ilm + Mt	n=4	0.39	0.61	3451.0	789.2	1656.9	1.7	1785.5	1.2
CM1052	-	Medium-grained OAN	Hm-Ilm + Mt	n=4	0.34	0.66	5209.8	551.6	1581.0	15.5	2689.5	3.0
CM1053	-	Medium-grained OAN	Hm-Ilm + Mt	n=4	0.23	0.77	7689.4	358.6	594.4	2.6	6011.8	0.5
CM1060	-	Fine-grained ferrodiorite	Hm-Ilm + Mt	n=4	0.55	0.45	1713.3	1238.5	1974.1	56.7	1460.0	1.4
CM1063B	-	Medium-grained OAN	Hm-ilm	n=4	0.56	0.44	2101.2	776.6	2255.3	70.5	913.3	3.2
CM1064	-	Nelsonite	Ilm + Mt	n=4	0.37	0.63	4589.4	770.1	1543.9	56.4	3839.6	14.8
CM1067	-	Nelsonite	Ilm + Mt	n=4	0.21	0.79	10348.1	744.4	1113.8	42.9	5815.1	14.7
CM1076B	-	Fine-grained ferrodiorite	Hm-Ilm + Mt	n=4	0.52	0.48	771.1	813.2	1663.6	12.4	2099.3	5.0
CM1110	-	Fine-grained ferrodiorite	Hm-Ilm + Mt	n=4	0.31	0.69	6662.4	549.1	1979.4	18.5	2320.2	10.2
MX102-3	13.50	Fine-grained ferrodiorite	Hm-Ilm + Mt	n=4	0.41	0.60	2571.0	909.8	1872.5	83.7	2066.2	3.5
MX102-5	21.00	Medium-grained OAN	Hm-Ilm + Mt	n=4	0.36	0.64	5785.8	1552.9	824.7	8.2	4441.5	0.7
MX105-1	0.50	Medium-grained OAN	Hm-Ilm + Mt	n=4	0.44	0.56	3300.3	1357.1	1181.5	0.3	2660.6	0.2
MX106-1	5.00	Medium-grained OAN	Hm-Ilm + Mt	n=4	0.44	0.56	2984.9	1179.1	1712.6	39.9	1537.2	6.4
MX108-6	3.00	Semi-massive Oxides	Hm-Ilm + Mt	n=4	0.46	0.54	4052.9	1121.9	1943.3	1758.3	1710.7	16.0
MX108-4	12.00	Fine-grained OAN	Hm-ilm	n=4	0.41	0.59	3220.1	932.3	1900.5	280.2	1413.8	50.3
MX109-2	4.50	Semi-massive Oxides	Hm-ilm	n=4	0.40	0.60	3483.6	767.4	2099.9	1663.5	1851.2	47.9
MX114-1	8.50	Fine-grained ferrodiorite	Hm-Ilm + Mt	n=4	0.42	0.58	1316.7	996.2	1605.6	29.8	1708.1	3.9
MX-115	16.50	Semi-massive Oxides	Hm-Ilm + Mt	n=4	0.39	0.61	5754.5	545.8	2009.2	1070.9	1869.9	45.7
MX-117	13.50	Massive Oxides	Hm-Ilm + Mt	n=4	0.38	0.62	6133.2	738.6	1923.3	1412.0	1629.0	83.7
MX-118	4.00	Massive Oxides	Hm-ilm	n=4	0.38	0.62	8400.5	394.8	2272.7	1941.4	1289.6	197.0
MX-123	0.50	Massive Oxides	Hm-ilm	n=4	0.34	0.66	10933.7	478.3	2077.9	1557.6	1242.8	307.9

Major elements in wt.%, FeO and Fe2O3 recalculated from FeOt by charge balance equations; molar fractions of geikielite, pyrophanite, hematite and ilmenite (Xgeik, Xpyr, Xhem, Xilm) calculated following QUILF algorithm (Andersen et al.1993); trace element in ppm. OAN = Oxide-apatite norite; Hm-ilm = hemo-ilmenite; Ilm = ilmenite; Mt = magnetite.

Table 3.6. LA-ICP-MS major and trace element analyses of magnetite in the Lac Mirepoix Fe-Ti-P mineralization

Detection Limits (33-55µm)														0.047-0.242	1.527-9.987	0.719-2.736
Sample	Depth (m)	Lithology	Oxide Mineralogy	# samples	SiO_2	TiO_2	Al_2O_3	FeO_t	Fe_2O_3	FeO	MnO	MgO	Total	^{51}V	^{53}Cr	^{60}Ni
20PM04B	-	Massive Oxides	Ilm + Mt	n=6	0.05	0.08	0.51	91.91	67.98	30.73	0.01	0.05	100.34	3662.00	2560.48	647.35
20PM06B	-	Medium-grained OAN	Hm-Ilm + Mt	n=6	0.02	0.07	0.40	91.98	66.30	32.25	0.00	0.03	99.46	2366.76	219.38	62.03
20PM07	-	Nelsonite	Ilm + Mt	n=6	0.05	0.09	0.41	91.98	67.67	31.25	0.02	0.13	100.12	3193.96	329.67	103.37
20PM08B1	-	Medium-grained OAN	Hm-Ilm + Mt	n=6	0.12	0.09	0.45	91.98	67.77	31.30	0.02	0.15	100.12	1368.96	16.80	3.79
20PM08B2	-	Medium-grained OAN	Hm-Ilm + Mt	n=6	0.43	0.07	0.44	91.98	67.76	31.01	0.03	0.41	100.37	1429.50	19.96	5.77
20PM18B	-	Medium-grained OAN	Hm-Ilm + Mt	n=6	0.65	0.08	0.44	91.98	68.39	30.44	0.01	0.10	100.41	1826.54	89.29	27.06
20PM19B	-	Fine-grained jotunite	Hm-Ilm + Mt	n=6	1.00	0.07	0.45	91.98	69.88	29.10	0.05	0.22	101.04	1375.04	89.75	9.13
CM1007	-	Medium-grained OAN	Hm-Ilm + Mt	n=4	0.11	0.09	0.00	91.98	65.19	33.32	0.01	0.10	99.05	1652.34	7.84	1.60
CM1013	-	Medium-grained OAN	Hm-Ilm + Mt	n=4	0.11	0.18	0.00	91.98	66.30	32.33	0.01	0.06	99.60	1911.66	9.63	2.74
CM1038	-	Medium-grained OAN	Hm-Ilm + Mt	n=4	0.69	0.17	0.01	91.98	67.20	31.51	0.01	0.14	100.00	1408.18	72.07	9.66
CM1045	-	Medium-grained OAN	Hm-Ilm + Mt	n=4	0.24	0.14	0.00	91.98	65.59	32.96	0.01	0.06	99.28	1892.09	1.66	5.63
CM1047	-	Medium-grained OAN	Hm-Ilm + Mt	n=4	0.12	0.12	0.04	91.98	65.57	32.98	0.01	0.05	99.28	2567.07	238.86	82.46
CM1050	-	Medium-grained OAN	Hm-Ilm + Mt	n=4	0.26	0.14	0.04	91.98	66.13	32.48	0.01	0.09	99.53	2360.00	250.00	66.38
CM1051	-	Medium-grained OAN	Hm-Ilm + Mt	n=4	0.41	0.17	0.00	91.98	66.35	32.28	0.01	0.10	99.64	2257.59	4.74	32.75
CM1052	-	Medium-grained OAN	Hm-Ilm + Mt	n=4	0.26	0.20	0.01	91.98	66.26	32.36	0.01	0.11	99.60	2638.68	81.41	35.14
CM1053	-	Medium-grained OAN	Hm-Ilm + Mt	n=4	0.31	0.24	0.00	91.98	66.44	32.20	0.03	0.19	99.63	1530.67	23.36	4.85
CM1060	-	Fine-grained ferrodiorite	Hm-Ilm + Mt	n=4	0.37	0.13	0.02	91.98	66.23	32.39	0.01	0.08	99.57	2122.77	141.06	18.33
CM1064	-	Nelsonite	Ilm + Mt	n=4	0.36	0.20	0.07	91.98	67.02	31.68	0.02	0.12	99.97	3092.18	419.53	117.11
CM1067	-	Nelsonite	Ilm + Mt	n=4	0.27	0.08	0.08	91.98	67.43	31.30	0.02	0.32	100.05	3413.26	457.45	139.48
CM1076B	-	Fine-grained ferrodiorite	Hm-Ilm + Mt	n=4	0.23	0.12	0.01	91.98	65.69	32.87	0.01	0.08	99.31	1940.02	32.32	17.56
CM1110	-	Fine-grained ferrodiorite	Hm-Ilm + Mt	n=4	0.24	0.13	0.02	91.98	66.27	32.35	0.01	0.12	99.59	3044.65	107.51	94.26
MX102-3	13.50	Fine-grained ferrodiorite	Hm-Ilm + Mt	n=4	0.44	0.08	0.06	91.98	66.83	31.85	0.02	0.16	99.81	2129.68	365.68	42.88
MX102-5	21.00	Medium-grained OAN	Hm-Ilm + Mt	n=4	0.37	0.12	0.01	91.98	66.37	32.26	0.03	0.20	99.56	1300.03	43.00	6.54
MX105-1	0.50	Medium-grained OAN	Hm-Ilm + Mt	n=4	0.61	0.24	0.00	91.98	66.89	31.79	0.03	0.08	99.90	1743.68	n.a	4.03
MX106-1	5.00	Medium-grained OAN	Hm-Ilm + Mt	n=4	0.57	0.19	0.01	91.98	67.30	31.42	0.05	0.15	100.08	2532.67	81.26	76.73
MX108-6	3.00	Semi-massive Oxides	Hm-Ilm + Mt	n=4	0.15	0.12	1.44	91.98	72.63	26.63	0.01	0.12	102.62	2805.12	8089.88	148.32
MX114-1	8.50	Fine-grained ferrodiorite	Hm-Ilm + Mt	n=4	0.47	0.13	0.02	91.98	66.58	32.07	0.02	0.05	110.88	1942.41	115.95	38.30
MX-115	16.50	Semi-massive Oxides	Hm-Ilm + Mt	n=4	0.18	0.08	1.09	91.98	71.30	27.82	0.02	0.19	101.94	2968.76	6106.91	356.56
MX-117	13.50	Massive Oxides	Hm-Ilm + Mt	n=4	0.15	0.06	1.49	91.98	73.13	26.17	0.01	0.23	102.81	2863.30	8321.16	496.44

Major elements in wt.%, FeO and Fe2O3 recalculated from FeOt by charge balance equations; trace element in ppm; OAN = Oxide-apatite norite; Hm-ilm = hemo-ilmenite; Ilm = ilmenite; Mt = magnetite

3.6.4.3 Ilmenite and hemo-ilmenite

Ilmenite and hemo-ilmenite compositions, determined by LA-ICP-MS, are presented in Table 3.5 and Appendix 3.1. The trace element concentrations of (hemo)-ilmenite from Lac Mirepoix are plotted on multi-element diagrams (Figs.3.12a-b) and shows that overall, ilmenite has similar trace element patterns for the different types of cumulates in the three mineralized zones (Fig.12A), but different concentrations according to lithology. In particular, Cr, Ni, V, Co and Pb decrease in ilmenite from the massive (apatite-free) oxides to the apatite-bearing nelsonite and OAN whereas Zn, W and Y increase. Moreover, similar to other studies (Dare et al. 2014; Arguin et al. 2018), the High Field Strength Elements (HFSE; Zr, Hf, Nb, Ta, Ti) are preferentially enriched in ilmenite over co-existing magnetite.

An irregular cryptic variation between the different zones for XHm, Ni, Cr, V (Fig.3.10c) and MgO, MnO (Appendix 3.2) is observed. The fraction of hematite in ilmenite (XHm) varies from 0.10 to 0.60, with higher XHm contents generally observed in the massive oxide samples of zone I and in the fine-grained dykes, where hemo-ilmenite is predominantly the main oxide phase due to the lower abundance of magnetite. Lower XHm values occur in some of the nelsonites and OAN samples where magnetite has higher modal proportions (e.g., sample 20PM04B). (Hemo) ilmenite from massive oxides and nelsonites have similar high MgO contents (up to 2.5 wt.%) (Appendix 3.2), whereas most of the (hemo-)ilmenite from OAN samples of zone III and the fine-grained dykes have lower values (< 1.6 wt.%). This feature is mainly due to Fe-Mg exchange between oxides and pyroxene, as previously pointed in the literature (Dare et el. 2019; Grant, 2020; Miloski et al. 2023). A large variation in the V, Cr and Ni concentrations of (hemo-)ilmenite is observed among the three zones (Fig.3.12a), with the highest contents occurring in the massive oxides of zone I,

whereas both OAN and nelsonite, in zones II and III, show progressively lower amounts (Figs.3.9c & 3.12). The Ni and Cr contents of (hemo-)ilmenite behave very similarly, with the lowest values (< 50 ppm) in OAN from zone III. The OAN ilmenite patterns, and the range of trace element concentrations are similar to those observed in the Lac à l'Orignal OAN mineralization (Fig.3.12b). The V and XHem contents of (hemo-)ilmenite are well correlated (Fig.3.13c) with V enrichment in the hematite exsolutions, as previously observed in the nearby Lac à l'Orignal intrusion (Miloski et al. 2023). The Mn content of (hemo)-ilmenite presents the opposite behaviour due to Mn^{+2} exchange with Fe^{+2}, with values decreasing with higher amounts of hematite exsolutions in ilmenite (Fig.3.9c).

The fine-grained dykes also show very similar ilmenite trace element patterns as the OAN mineralization at both Lac Mirepoix and Lac à l'Original. In particular, their low Cr (1 – 280 ppm) and Ni (0.3 – 50 ppm) values are similar to the more primitive OAN cumulates of zone III and the OAN presented in the nearby Lac à l'Orignal mineralization. However, the ferrodiorite dykes samples present higher V (1364 – 1974 ppm) concentrations, closer to the values observed within the hemo-ilmenite from massive oxides (Fig.3.9c), due to their high Xhem contents (0.30 – 0.60).

3.6.4.4 Magnetite

Magnetite compositions (Table 3.6) show a very restricted range of low Ti values (TiO_2 < 0.25 wt.%), being absent of ilmenite exsolutions. The trace element concentrations of magnetite from Lac Mirepoix are plotted on multi-element diagrams (Figs.3.12c-d) and show that magnetite presents similar trace element patterns for the different types of cumulates in the three mineralized zones (Fig.3.12c), but different concentrations according to lithology. Similar to ilmenite, Cr, Ni, V, Co and Mn

decrease in magnetite from the massive (apatite-free) oxides to the apatite-bearing nelsonite and OAN whereas Zn increases in ilmenite from OAN. Moreover, the range of trace element concentrations in magnetite observed at Lac Mirepoix are similar in comparison to those observed in the OAN cumulates of the nearby Lac à l'Orignal mineralization (Fig.3.12c). Along with being Ti poor, magnetite is also unusually poor in other HFSE (Nb, Ta, Sc, Zr, Hf) compared to Ti-rich magnetite from layered intrusions, where normally higher magnetite/ilmenite ratios are observed. Fe-Ti-P mineralization at Lac Mirepoix and Lac à l'Orignal (Miloski et al. 2023) contain bigger proportions of ilmenite than normally observed in mafic layered intrusions associated with Fe-Ti-V and Fe-Ti-P mineralization (e.g. Dare et al. 2014, Fig.3.12).

The stratigraphic variation of magnetite composition for selected elements (V, Cr and Ni) is presented in Figure 3.10d. In general, Cr and Ni concentrations in magnetite show a similar behaviour, co-varying together as compatible elements, in a similar way to that of ilmenite. The values are typically highest in magnetite from the massive/semi-massive oxides in zone I (Cr = 6107 - 8321 ppm; Ni = 148 - 496 ppm), intermediate for magnetite from the nelsonites in zone II (Cr = 330 - 457 ppm; Ni = 103 - 139 ppm) and lowest in those from the OAN (Cr = 2 - 250 ppm; Ni = 2 - 82 ppm). V concentrations are also highest in both massive oxides and nelsonites (2805 - 2969 ppm) in relation to OAN (1300 - 2639 ppm) and fine-grained dykes (1375 - 3044 ppm). Similar to ilmenite, magnetite from the fine-grained dykes also has evolved compositions (Cr = 32 - 366 ppm; Ni = 9 - 94 ppm) similar to the more primitive OAN cumulates from both Lac Mirepoix and Lac à l'Orignal (Fig.3.12d).

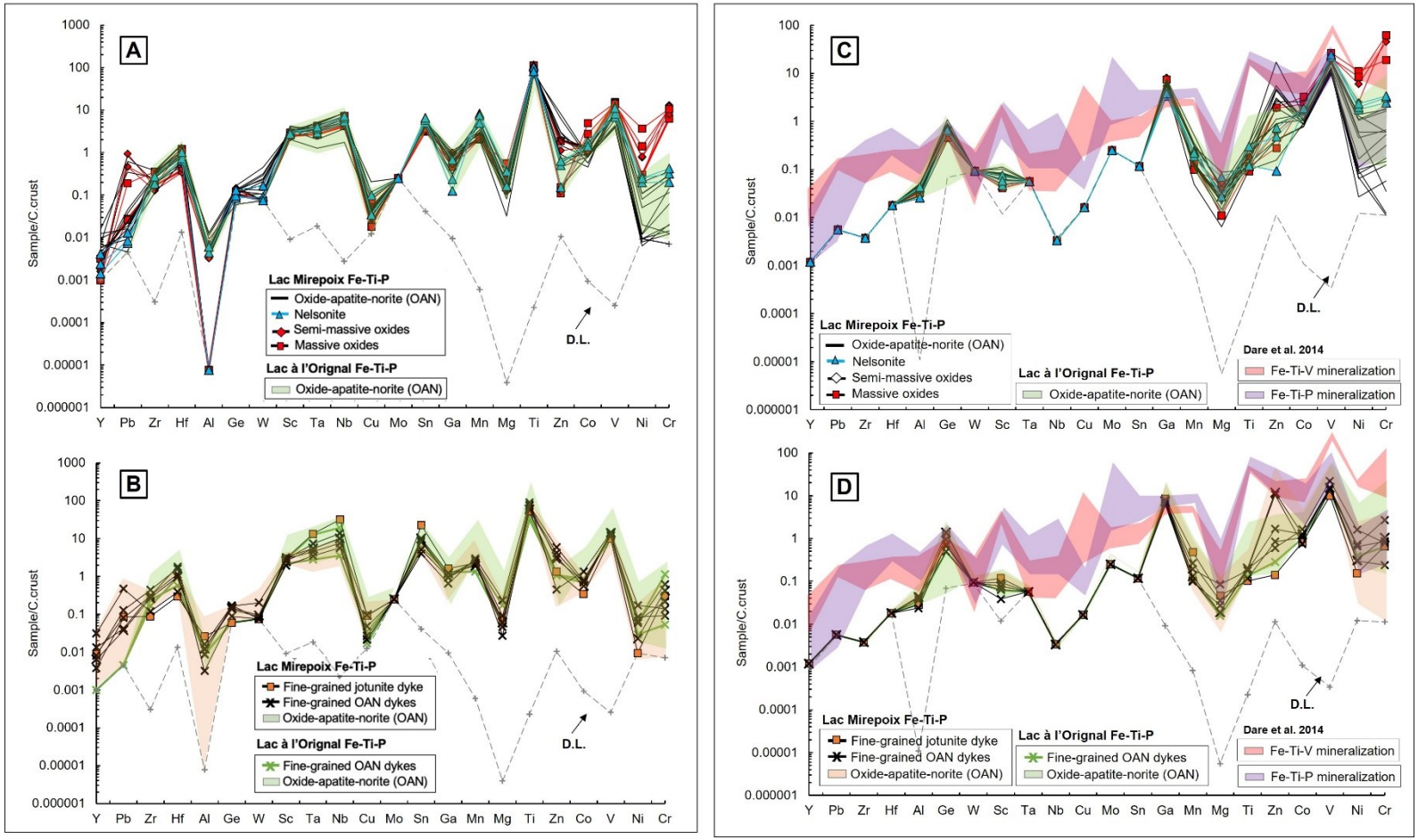

Figure 3.12. Continental-crust-normalized trace element compositions of ilmenite (a-b) and magnetite (c-d) (after Rudnick & Gao, 2003) from the Lac Mirepoix Fe-Ti-P mineralization. Comparison with the nearby Lac à l'Orignal Fe-Ti-P mineralization (green field, Miloski et al. 2023a), and other Fe-Ti-V mineralization (red field) and Fe-Ti-P mineralization (purple field) of the Grenville Province (Dare et al. 2014). ilmenite: a. Mineralized massive oxides, oxide-apatite norite (OAN) and nelsonite samples. b. Fine-grained dykes compared to OAN compositions of Fig.11A. Magnetite: c. Mineralized massive oxides, oxide-apatite norite (OAN) and nelsonite samples. d. Fine-grained dykes compared to fields for the OAN compositions of Fig.3.12c. Abbbreviations: D.L. Detection limits.

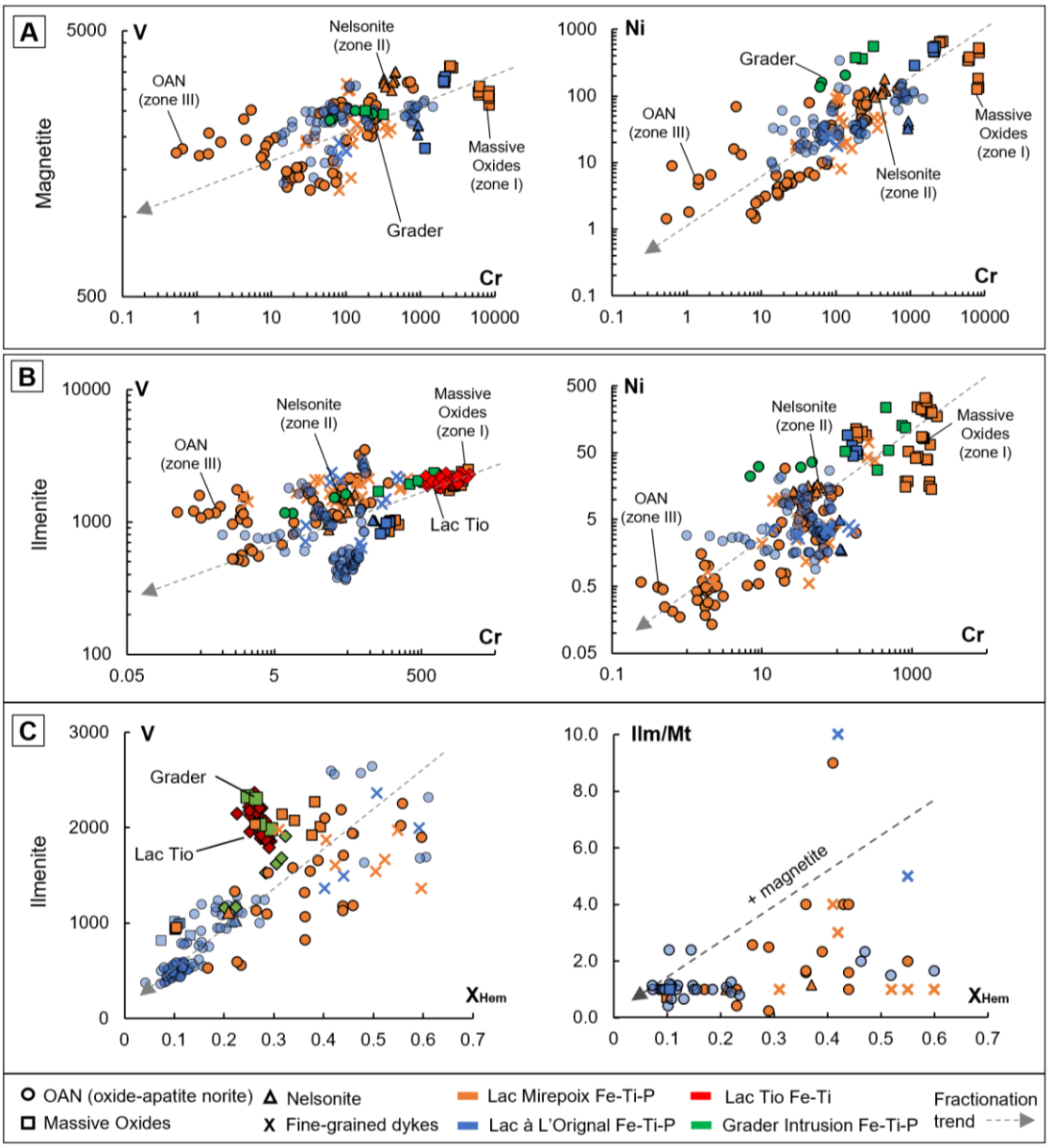

Figure 3.13. Binary diagrams displaying concentrations of compatible elements in magnetite (a) and ilmenite (b), using Cr as a proxy for fractional crystallization. c. Hematite content in ilmenite in relation to the V concentration in ilmenite (left) and the modal proportion of magnetite (right). Comparison between geochemical data of the Lac Mirepoix Fe-Ti-P mineralization (this work) with the Lac à l'Orignal Fe-Ti-P mineralization (Miloski et al. 2023a), the Grader Intrusion Fe-Ti-P, Quebec (Charlier et al. 2008) and the world-class ilmenite deposit of Lac Tio Fe-Ti, Quebec (Charlier et al. 2010).

3.6.5 Comparison of oxide composition ith other Fe-Ti-P mineralization in the Grenville Province

The oxide chemistry (Cr, Ni and V contents) of Lac Mirepoix is compared to that from other locations in the Grenville Province where Fe-Ti-(P) mineralization was previously described: the Lac Tio Fe-Ti deposit (Charlier et al. 2010), the Grader Intrusion (Charlier et al. 2008) and the Lac a l'Original Fe-Ti-P mineralization (Miloski et al. 2023) (Figs.3.13a-b). From this, it is clear that both magnetite and ilmenite from the massive oxides of Lac Mirepoix (zone I) have the highest Cr, Ni and V contents, similar to the massive hemo-ilmenite cumulates of Lac Tio, Quebec. This confirms a more primitive composition of the massive oxides in relation to apatite-bearing cumulates, as previously noted by Owens & Dymek (1992), Charlier et al. (2008) and Miloski et al. (2023). The nelsonites of Lac Mirepoix (zone II) have intermediate Cr, Ni, V compositions, similar to those described at the base of the Grader Intrusion. In contrast, the content of Cr, Ni and V compositions of oxides from the oxide-apatite-norites (zone III) of Lac Mirepoix are lower than those from Grader Lake OAN, and most similar to the OAN cumulates at the nearby Lac a l'Original mineralization (Miloski et al. 2023). The V concentration is directly related to the XHem on ilmenite (Fig.3.13c), with V enrichment in the hematite exsolutions of different Fe-Ti-P mineralization in the Grenville Province.

3.6.6 Calculation of melt composition from apatite

At Lac Mirepoix, the ferrodiorite dykes are mineralogically and chemically very similar to the leuco-OAN mineralization. As such, they might represent the liquid from which the separation of denser mafic silicates/oxides/apatite by crystal settling and flotation of plagioclase (+ apatite) to form the nelsonite and melano-OAN cumulates. To test this, the REE concentrations in apatite were used to evaluate the relationship

between the fine-grained dykes and melt compositions in equilibrium with the cumulates, following the approach of Charlier et al. (2005) andMiloski et al. (2023a). This is achieved by inverting the composition of apatite from the Fe-Ti-P mineralization, using the equation $C\mathrm{Liq}\ \mathrm{REE} = \frac{C\mathrm{Ap}\ \mathrm{REE}}{D\mathrm{Ap}\ \mathrm{REE}}$ (details are presented in Miloski et al. 2023a), to calculate melt compositions from which apatite crystallized. The fine-grained dyke samples were selected to calculate $D\mathrm{Ap}\ \mathrm{REE}$ values (Table 3.7; Fig.3.14), ranging from the most primitive (ferrodiorite) to the most evolved (jotunite) dyke composition. The newly obtained D values are within range of published partition coefficients for similar intrusions, except for Eu (Charlier et al. 2005; Bedard, 2023; Miloski et al. 2023a). The calculation of new D values for the dykes in the Lac Mirepoix mineralization was preferable as Eu is sensitive to magmatic fO_2 and the published values from Bjerkreim Sokndal (Charlier et al. 2005) are not suitable since they come from less oxidized magmas (Miloski et al. 2023; Appendix 3.1). Liquids in equilibrium with apatite from the mineralization were then recalculated applying the newly calculated $D\mathrm{Ap}\ \mathrm{REE}$ values obtained from the two selected dykes (Table 3.7; Fig.3.14).

The REE patterns, including Eu anomalies, and abundance of REE of the liquids calculated from the nelsonite and OAN samples in zones II and III match the REE patterns of fine-grained OAN dykes when applying partition coefficients from the least-evolved dyke (Fig.3.14a). This confirms that the ferrodiorite dykes are likely the parental melt of the OAN mineralization, both at Lac Mirepoix and Lac à l'Original (Miloski et al. 2023). However, when using partition coefficients from the most evolved jotunite dyke (20PM19-B, Fig.3.14b), the calculated liquids have lower-REE concentrations in comparison with the fine-grained dykes (Appendix 3.1), due to higher $D\mathrm{Ap}\ \mathrm{REE}$ obtained. These results indicate that the composition of the least-evolved

ferrodiorite dykes better reflects the initial liquid in equilibrium with the OAN cumulates (i.e., parental melt), whereas the jotunite dyke 20PM19-B would represent a more-evolved, residual liquid at further stages of differentiation.

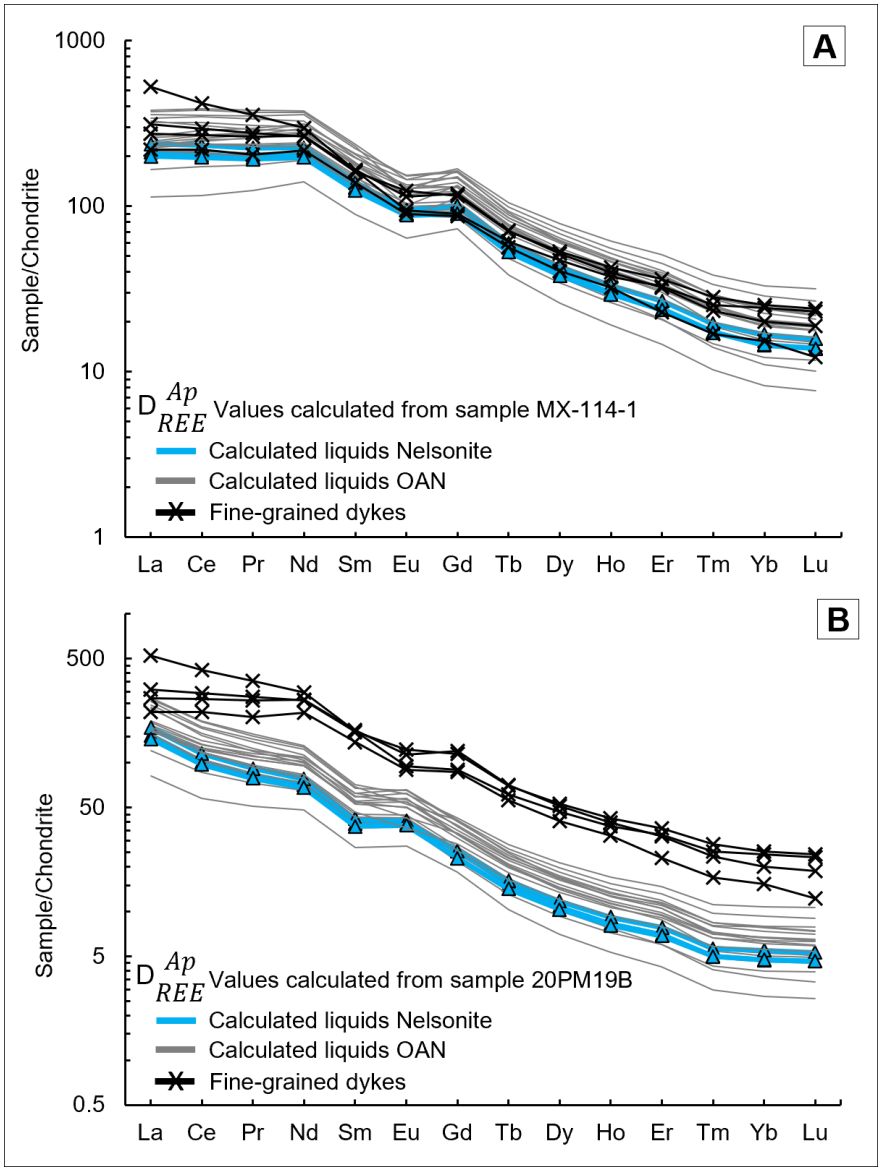

Figure 3.14. Chondrite normalized (after Sun and McDonough, 1989) apatite REE patterns for fine-grained dykes (primitive MX-114-1 and evolved 20PM19-B) compared to calculated liquids from the inversion of apatite compositions of nelsonites (blue lines) and OAN (grey lines) samples. a. Calculated liquids applying D$Ap\ REE$ values obtained from bulk and apatite compositions of ferrodiorite dyke MX-114-1. b. Calculated liquids applying D$Ap\ REE$ values from bulk and apatite compositions of jotunite dyke 20PM19-B.

Table 3.7. REE concentrations of the fine-grained dykes and respective calculated partition coefficients between apatite and melt

Element	REE geochemical analysis of fine-grained OAN dykes				Calculated D_{ap} values		Compilation of D_{ap} values					
	Whole-rock REE values		Apatite REE values		Lac Mirepoix Fe-Ti-P		Lac à L'Orignal Fe-Ti-P		Bjerkrein Sokndal Layered Intrusion			Naim Plutonic Suite
	MX-114-1	20PM19B	MX-114-1	20PM19B	MX-114-1[a]	20PM19B[b]	D_{ap}[c]	D_{ap}[c]	D_{ap}[d]	D_{ap}[e]	D_{ap}[f]	D_{ap}[g]
La	64.6	124.7	457.2	1222.7	7.1	9.8	7.3	8.7	3.9	4.3	12.0	3.4
Ce	164.2	255.9	1186.7	3740.0	7.2	14.6	8.0	10.2	4.7	5.5	15.0	7.0
Pr	24.3	32.8	180.5	594.9	7.4	18.1	8.4	11.5	5.4	-	-	9.0
Nd	121.1	135.6	892.4	2891.7	7.4	21.3	8.6	12.4	6.0	6.9	19.0	11.0
Sm	24.4	24.1	183.0	597.7	7.5	24.8	8.7	12.9	6.6	7.3	20.0	12.0
Eu	6.4	5.3	43.3	83.8	6.8	15.8	7.7	8.0	3.9	7.5	13.0	9.6
Gd	23.7	17.8	160.8	476.8	6.8	26.7	8.8	13.8	6.8	7.9	20.0	10.0
Tb	2.6	2.2	18.1	58.1	7.1	26.3	8.8	13.8	6.1	7.7	19.0	9.0
Dy	12.7	11.5	92.8	311.8	7.3	27.0	8.9	13.6	5.3	-	-	8.3
Ho	2.2	2.0	15.8	54.0	7.3	26.5	9.0	13.8	4.6	6.6	16.8	7.0
Er	5.1	5.2	37.6	131.2	7.3	25.1	8.8	13.1	4.0	-	-	6.0
Tm	0.6	0.6	4.2	15.6	7.1	24.6	8.4	12.4	3.4	-	-	5.0
Yb	3.2	3.9	23.0	85.7	7.2	22.0	8.3	11.1	2.7	4	13.0	4.0
Lu	0.5	0.6	3.1	11.2	6.6	19.7	8.4	10.3	2.2	3.25	10.0	4.0

a Calculated partition coefficients between apatite and melt from sample MX-114-1. b Calculated partition coefficients between apatite and melt from sample 20PM19B. c Calculated partition coefficients between apatite and melt from sample LO-06. d Partition coefficients between apatite and melt from Charlier et al.(2005). e Partition coefficients between apatite and melt from Roelandts & Duchesne (1979). f Partition coefficients between apatite and melt from Vander Auwera et al.(1998). g Partition coefficients between apatite and melt from Bedard (2001), Watson & Green (1981) and Powatke & Klemme (2006).

3.6.7 Calculation of oxygen fugacity

The probable fO_2 conditions of the ferrodiorite magma, in equilibrium with the mineralization at Lac Mirepoix, were estimated by applying the mineral compositions of magnetite-hemo-ilmenite pairs from the fine-grained dykes in the QUILF program of Andersen et al. (1993). Previous work in the nearby Lac à l'Orignal Fe-Ti-P mineralization (Miloski et al. 2023) revealed that due to subsolidus (inter- and intra-oxides) re-equilibration of the OAN cumulates, only fine-grained dykes that cooled relatively quickly are suitable for this calculation. The fO_2 values at equilibrium between oxides were obtained by fixing the liquidus temperatures between 1100 and 1200^{o}C (Vander Auwera & Longhi, 1994; Vander Auwera et al. 1998), and pressures of 5kbar (Charlier et al. 2008; Lin & Sawyer, 2018). The calculations give values of Δ log fO_2 (relative to FMQ) between -0.5 and +1.52 for the more primitive ferrodiorite dykes and a higher value (+1.40 to +1.70) for the evolved jotunite dyke 20PM19-B (Fig.3.15, Appendix 3.1). Plotting of the calculated fO_2 values relative to the Fe content of orthopyroxene, in Figure 3.15, shows that the more primitive ferrodiorite dykes at Lac Mirepoix falls throughout the ilm – hm + mt + opx field (T = 1100 C), in agreement with the mineralogy present in the cumulates of Lac Mirepoix. Furthermore, it illustrates that the initial crystallization conditions of the more primitive composition (dyke MX-114) at Lac Mirepoix was not as oxidizing as ferrodiorite dykes (+0.96 to +1.31) associated with the hemo-ilmenite-orthopyroxene-bearing Lac à l'Orignal Fe-Ti-P mineralization (Miloski et al. 2023). However, the most evolved jotunite dyke (20PM19-B) plots over the silica-saturation line (qtz-K-feldspar normative), even more oxidized (+1.5) than the other occurrences previously mentioned, denoting a possible increase in the fO_2 conditions with increasing fractional crystallization (Snyder et al. 1993). The fO_2 determined from the jotunite dyke is most similar to that determined for hemo-ilmenite mineralization of the Labrieville Anorthosite (Frost et al. 2010).

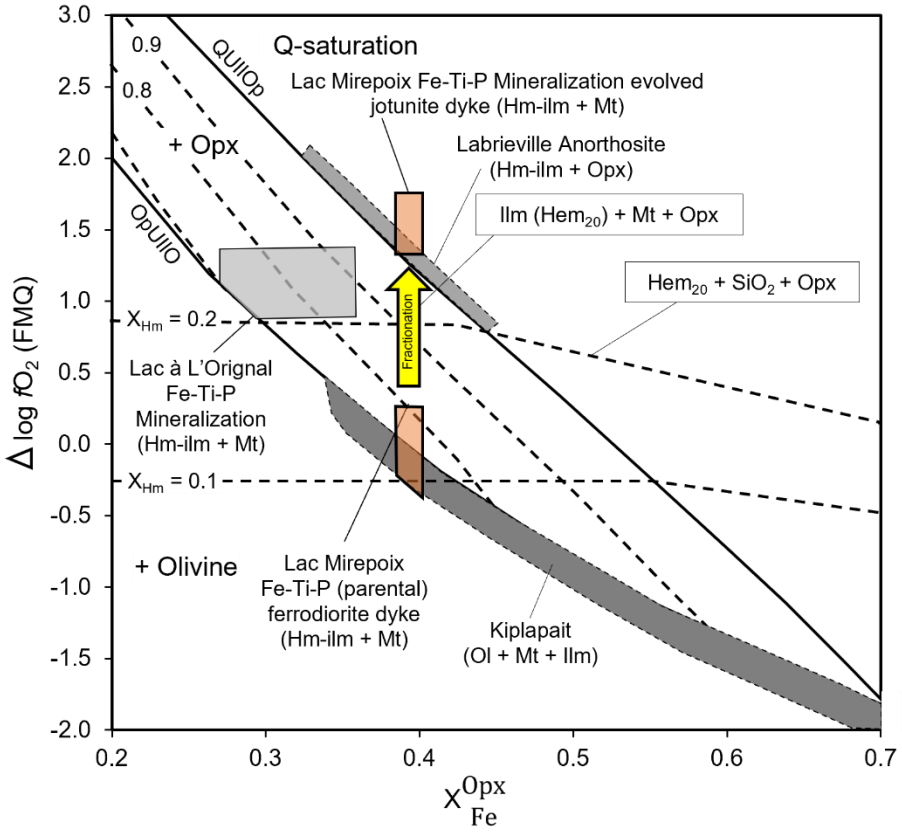

Figure 3.15. Δ log fO2 (relative to FMQ) versus X$Opx\ Fe$ diagram (modified from Frost et al. 2010) for fine-grained dykes from Lac Mirepoix representing the parental (primitive: MX-114-1) and residual (evolved: 20PM19B) magma of Fe-Ti-P mineralization. Comparison with fine-grained OAN dykes of the nearby Lac à l'Orignal Fe-Ti-P mineralization (grey field: Miloski et al. 2023a) and results from two anorthosite plutons of different silicate/oxide assemblages: the olivine-magnetite-bearing Kiglapait Intrusion (Nain Plutonic Suite, Emslie, 1980) and the hemo-ilmenite-orthopyroxene-bearing Labrieville Anorthosite (Owens & Dymek, 2001). Calculations from the QUILF program of Andersen et al. (1993). X$Opx\ Fe$ determined from microprobe. Modified from Frost et al. (2010) with the permission of © Mineralogical Association of Canada.

3.7 Discussion

3.7.1 The relationship between massive oxides, nelsonite and oxide-apatite-norite: fractional crystallization

Oxide (Fe-Ti) and oxide-apatite (Fe-Ti-P) mineralization can form at various stages in the evolution of a particular massif anorthosite complex (Charlier et al. 2015). Mineralized systems dominated by massive hemo-ilmenite cumulates (e.g., Lac Tio,

Charlier et al. 2010; Saint-Urbain Anorthosite, Morisset et al. 2009) have more primitive compositions (higher Ni-Cr-V concentrations of oxides and lower REE in apatite) than systems where apatite-bearing mineralization is present (e.g. Grader Intrusion, Charlier et al. 2008; Lac à l'Orignal Fe-Ti-P mineralization, Miloski et al. 2023). In the Grenville Province, younger AMCG suites are characterized by mineralization dominated by hemo-ilmenite (± apatite) hosted in andesine-type anorthosites.

Massive oxide cumulates reflect primary segregation of Fe-Ti oxides thorough fractional crystallization (with ilmenite) prior to the appearance of apatite as a cumulus phase. This has been demonstrated at Grader Intrusion (Charlier et al. 2008), where massive hemo-ilmenite is overlain by a nelsonite layer and subsequently by OAN. Mafic magmas dominated by the fractional crystallization of Fe-Ti oxides would present high concentration of compatible elements as Cr, Ni and V in the most primitive magnetite and ilmenite crystallized (associated with Fe-Ti-V deposits), coupled with labradorite plagioclase (An >50) and absence of cumulus apatite. Subsequent fractionation continuously decreases the concentration of Cr, Ni and V in oxides, generating more evolved magmas, leading to the saturation of P_2O_5 and the crystallization of apatite as a cumulus phase (generating Fe-Ti-P deposits), mostly coupled with andesine-type plagioclase (An < 50) (Barnes et al. 2004; Klemme et al 2006; Tegner et al. 2006; Namur et al. 2010; Dare et al. 2014; Grant, 2020; Miloski et al. 2023). At the Grader intrusion, both nelsonite and oxide-apatite gabbronorite layers have similar REE patterns indicating that they are a co-genetic (Charlier et al. 2008). Oxide-apatite (gabbro)norite would represent more evolved mineral compositions than anorthosites and massive nelsonite/oxide layers, i.e., formed during latter-stage fractionation after massive oxide/plagioclase crystallization, from which

ferrodiorite/jotunite liquids would form (Vander Auwera & Longhi, 1994; Vander Auwera et al. 1998).

The Lac Mirepoix Fe-Ti-P mineralization exhibits a variety of different oxide and oxide-apatite cumulates: Zone I is dominated by hemo-ilmenite (± magnetite)-bearing massive oxide injections in the host anorthosite, whereas the other zones are characterized by the appearance of apatite-rich cumulates: ilmenite + magnetite-bearing nelsonite (zone II) and hemo-ilmenite + magnetite bearing oxide-apatite norite (zone III). The rock types observed in zone I are similar to the hemo-ilmenite cumulates of Lac Tio Fe-Ti deposit (Charlier et al. 2010), and at the base of the Grader Layered Intrusion (Charlier et al. 2008). The Grader Intrusion, in particular, presents a similar cumulate succession between zones in relation to the Lac Mirepoix mineralization, with a higher proportion of massive hemo-ilmenite at the base of the intrusion (similar to zone I), followed by the presence of nelsonite horizons in the center (similar to zone II) and then layers of gabbronorite at the top (similar to zone III), being dominated by hemo-ilmenite + magnetite, presenting a lower ilmenite/magnetite ratio (Fig.3.13c) as well as lower Cr, Ni and V values in magnetite and ilmenite in relation to the younger dated OAN of zone I, denoting a more evolved character in the former. Similar to Grader Lake, in the Lac Mirepoix mineralization nelsonite and oxide-apatite-norite show similar REE-patterns in apatite (Fig.3.11a) indicating that they are cogenetic, with a relative REE-enrichment on OAN compared with nelsonite, reflecting the latter's more evolved character.

3.7.2 Origin of Fe-Ti-P mineralization in anorthosite: liquid immiscibility?

The origin of massive oxides/nelsonite is currently highly debated, with liquid immiscibility and fractional crystallization as the main debated mechanisms. Liquid

immiscibility between two silicate melts (Fe-Ti-P-rich ferrobasalt/Si-rich rhyolite) has been tested through experimental studies, demonstrating it has the potential to play an important role in the formation of Fe-Ti-P mineralization, especially for nelsonites (Roedder, 1978; Philpotts, 1967; 1982; Kolker 1982; Charlier & Grove, 2012; Charlier et al. 2011, 2013; Zhou et al. 2013; Hou et al. 2018; Naslund et al. 1996; Coint et al. 2020). Immiscibility is supported by the presence of contrasting Fe-rich and Si-rich melt inclusions trapped in cumulus apatite, which is common in the evolved parts of slowly cooled tholeiitic intrusions, such as Skaergaard, Greenland (e.g. Jakobsen et al. 2011), Bushveld, South Africa (e.g. Fischer et al. 2016), Sept Iles, Canada (Charlier et al. 2011; Namur et al. 2012) and Damiao (Wang et al. 2017). Phase diagrams and well-documented occurrences of small-scale immiscibility confirm that liquid-liquid unmixing and the separation of Fe-rich and Si-rich liquids may contribute significantly to the absence of some intermediary mafic compositions along the tholeiitic liquid line of descent (e.g. Sept Iles, Namur et al. 2010). Although, immiscibility may help enrich the evolved magma in Fe-Ti-P, another mechanism (crystal settling of oxide-apatite cumulates by density difference from the co-crystallizing silicates) is still required to form the mineralization (Duchesne, 1999; Dymek & Owens 2001; Tollari et al. 2008).

However, Fe-oxide melt (absent of silicates) has been proposed for the formation of V-rich ores in Panzhihua, China (Zhou et al. 2005; Wang et al. 2017) and for the Fe-Ti-P ores of Damiao Anorthosite Complex, China (Chen et al. 2013; He et al. 2016). Hou et al. (2018) have recently shown that increasing pH_2O and fO_2 enlarges the “two-liquid field” thus allowing a Fe–Ca–P melt (absent of silicates) to separate easily from host silicic magmas and produce Fe- oxide-apatite ores. However, such

water-rich conditions do not commonly occur in most mafic intrusions hosting nelsonites.

According to Veksler et al. (2007), the most iron-rich immiscible liquids produced experimentally do not exceed 28 w.t.% FeO and 5 w.t.% TiO_2, which is not enough to generate massive oxide layers (which normally contains upwards of 95 w.t.% FeO and TiO_2, Charlier et al. 2015). Furthermore, Fe-Ti immiscible liquids strongly partition P (Toplis & Carroll, 1995); the absence of apatite in many massive bodies therefore suggests they were not formed from an Fe-Ti-P oxide liquid. Besides that, according to Charlier & Groove (2012), immiscibility in evolved ferrobasalts do not produce melts saturated with a single-phase. A liquid of ilmenite composition would melt at 1360°, while magnetite melts at 1590°C, both unrealistically high temperatures for crustal conditions. Therefore, according to Charlier et al. (2006), pure massive ores, such as that in Lac Tio (Charlier et al. 2010), cannot be produced by immiscibility, favoring the fractional crystallizing model (section 5.1).

At Lac Mirepoix, no melt inclusions occur in apatite. Furthermore, bulk whole-rock compositions of fine-grained lithologies, interpreted as liquidus compositions of Fe-Ti-P mineralization, were projected into ternary diagrams for liquid immiscibility evaluation, previously applied to the Sept Iles Layered Intrusion (Appendix 3.2, modified from Tollari et al. 2008; Charlier & Grove, 2012). Overall, the composition of ferrodiorite dykes associated with Fe-Ti-P mineralization in the Grenville Province, Quebec, and the Rogaland Province, Norway precludes the occurrence of liquid immiscibility (Appendix 3.2), supporting the occurrence of fractional crystallization as the main process in the petrogenesis of these cumulates.

3.7.3 Relationship between the Fe-Ti-P mineralization and host anorthosite: a small, layered intrusion or a multi-injection model?

The Fe-Ti-P cumulates of the Lac Mirepoix mineralization are interlayered with thick-horizons of anorthosite (>5m-thick) free of apatite. In the nearby Lac a l'Orignal Fe-Ti-P mineralization, layered OAN cumulates contain thin (<30cm thick) apatite-bearing anorthosite interlayered with the mineralization, which is interpreted as local accumulations of plagioclase from Fe-Ti-P magmas where OAN crystallized (Miloski et al. 2023). However, thick massive anorthosite layers are absent.

Although the 'layering' observed throughout the different cumulates/zones in the Lac Mirepoix intrusion could suggest the occurrence of a layered intrusion in the area, our dating of the different OAN cumulates of zones I and III reveals that the intrusion has a much more complex configuration. The Lac Mirepoix is a multi-phase intrusion, with at least two episodes of Fe-Ti-P-rich magma injection into the host anorthosite over a period of 80 Mys. The magma also did not evolve by in-situ evolution of a single batch of magma from zone I (more primitive) towards zone III (more evolved), as demonstrated for Grader Lake (Charlier et al. 2008). The Grader Intrusion in Quebec presents a vertical appearance of the different cumulate phases and displays continuous fractionation trends, clearly denoting the occurrence of a layered intrusion. Moreover, there is an absence of large anorthosite layers within the mineralized cumulates of the Grader Intrusion. At Lac Mirepoix, the fact that the most evolved OAN cumulate (20PM08B, zone III) has an older age (1048 ± 8Ma) compared to the more primitive OAN (20PM06B, zone I: 964 ± 9 Ma) precludes an in-situ fractional crystallization from zone I up to zone III. Furthermore, multiple injections of Fe-Ti-P-rich melts into a host anorthosite rather than residual plagioclase

accumulations within an OAN layered intrusion would explain observed the field relationships.

3.7.4 Petrogenetic model for the Fe-Ti-P mineralization in the Central Grenville Province

Miloski et al. (2023) point to the occurrence of high- and low-Ti/Fe systems in the Central Grenville Province, where the Ti/Fe content of the magma coupled to the variation of compatible elements into ilmenite could be used to track fractionation. Using Cr in ilmenite (Fig.3.16b), it is clear that the Ti/Fe ratio decreases from high-Ti/Fe systems (dominated by hemo-ilmenite only) to low-Ti/Fe systems (hemo-ilmenite and magnetite) due to fractional crystallization, i.e., that Ti behaves as a compatible element due to the extensive crystallization of hemo-ilmenite from the Ti-rich melt. The low-Ti/Fe trend of the OAN cumulates of the Lac Mirepoix and Lac à l'Orignal could therefore be due to lower proportions of ilmenite and more abundant magnetite, whereas Lac Tio, the Grader Intrusion as well as the massive oxides of zone I in the Lac Mirepoix would form a high-Ti/Fe trend with hemo-ilmenite-rich cumulates containing much lower proportions of magnetite (Fig.3.16).

The Grader intrusion and the zone II (nelsonite + OAN) of the Lac Mirepoix would correspond to a transition from the high-Ti /Feto the low-Ti/Fe system during continued fractional crystallization in response to decreasing Ti/Fe ratio, with the appearance of cumulus apatite forming massive nelsonite layers (Charlier et al. 2009). Zone III of Lac Mirepoix would be then similar to the evolved Lac à l'Orignal mineralization, part of a low-Ti/Fe system with the lowest Ti/Fe ratios, representing the most evolved, oxide-apatite norite cumulates, due to the presence of hemo-ilmenite + magnetite + apatite as first liquidus phases, in the late stages of differentiation of ferrodiorite/jotunite magmas. Similar features were also observed in the uppermost

megacyclic units of the Bjerkreim-Sokndal Layered Intrusion (Duchesne & Charlier, 2005), where a progressive upward evolution is described from ilmenite-leuconorite cumulates (phi-C, similar to Lac Tio), to magnetite-leuconorite cumulates (phim-C) and then gabbronorite Fe-Ti-P cumulates (phimca-C, similar to Grader and Lac à l'Orignal).

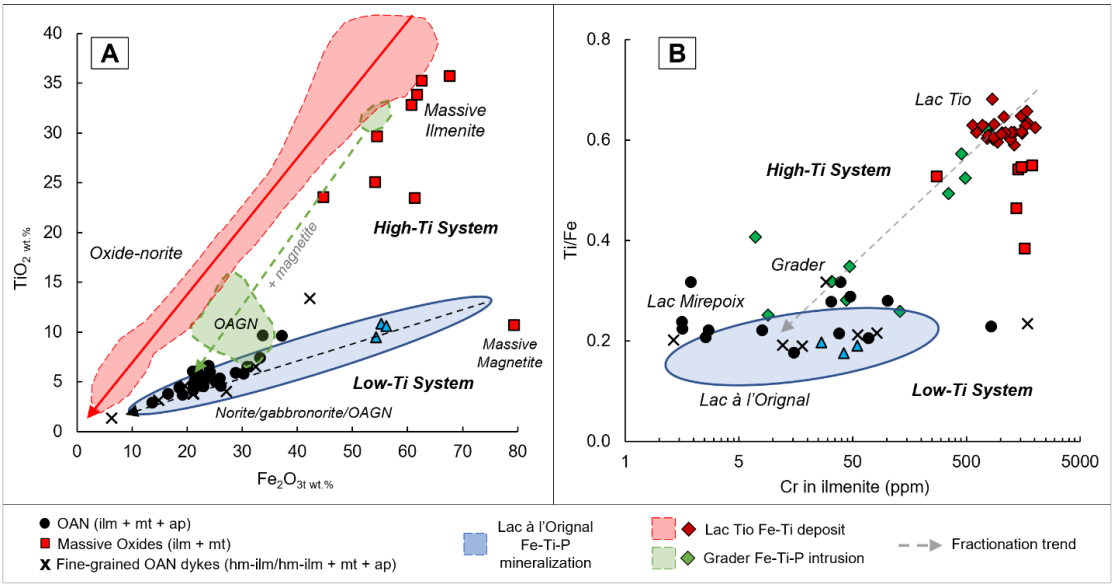

Figure 3.16. Geochemical comparison of the Lac Mirepoix Fe-Ti-P mineralization (this study) with the nearby Lac à l'Orignal Fe-Ti-P mineralization (blue field, Miloski et al. 2023a), the Lac Tio Ti deposit (red field) and the Fe-Ti-P mineralization at Grader Intrusion (green field), in the Havre-Saint-Pierre Anorthositic Suite, Quebec (data from Charlier at al. 2010; 2008). a. Whole-rock Fe_2O_{3t} vs. TiO_2. b. Ti/Fe whole rock ratio vs. Cr content of ilmenite (in ppm).

Chondrite normalized REE compositions (of whole rock and apatite) present similar patterns between the two dated OAN for Lac Mirepoix, indicating that multiple injections of Fe-Ti-P- rich magma with similar compositions formed the mineralization over a period of 80 Ma, as previously indicated in the nearby Lac à l'Orignal intrusion: 1069 ± 13 Ma border; 993 ± 13 Ma core of the intrusion (Miloski et al. 2023). The Lac Mirepoix and the Lac à l'Orignal Fe-Ti-P mineralization are located near the boundary of two massif-type anorthosites: Vanel (1080 ± 2 Ma) and Mattawa (1016 ± 2 Ma), whose ages are similar to those obtained for both mineralization.

First, due to extensive plagioclase crystallization/removal that generated massifs such as the Vanel Anorthosite host rocks (Fig.3.17a), there was also an accumulation of a high-Fe-Ti ferrodiorite residual magma that was likely squeezed/filter-pressed or drained to lower-pressure areas (I, Fig.3.17b) in the plagioclase-rich diapirs, mainly at the border of the anorthosite-massif (Scoates et al. 1996; Owens & Dymek, 2001) or into fractures (Charlier et al. 2007). The presence of different ages in the mineralization of Lac Mirepoix and Lac à l'Orignal, as well as the occurrence of coeval, younger anorthosite-massifs near Vanel (e.g., Mattawa Anorthosite) could account for multi-diapiric influence also in the formation of Fe-Ti-P mineralization (I, Fig.3.17b). Although there is indication of long-lived magmatism (>80Ma) in the petrogenesis of Fe-Ti-P mineralization (Miloski et al. 2023a), it is unlikely that a single batch of magma would remain molten over 80 Myr. Rather than that, we propose that different plagioclase-rich diapirs were injected into the crust between 1080-950Ma into the same region, favoured by the SFDZ (Saint Fulgence Detachment Zone). These different aged diapirs segregated residual Fe-Ti-P ferrodiorite liquids of similar composition but different ages (I-III, Fig.3.17b) that generate Fe-Ti-P mineralization in the Central Grenville. Therefore, different intrusions of similar residual melt composition, that follow similar fractional crystallisation histories, might have occurred over long periods of time (>80 Myr).

Due to the more primitive character and the absence of cumulus apatite, massive oxides crystallised first with plagioclase from the residual melt and likely accumulated by oxide sinking and lateral removal of plagioclase (II, Fig.3.17b), prior to the crystallization of the apatite-bearing cumulates. This type of mechanism has previously been suggested for similar cumulates at the Lac Tio deposit (Charlier et al. 2010) and at the base of the Grader Intrusion (Charlier et al. 2008). Nelsonites as well

as oxide-apatite-(gabbro) norites have more evolved compositions, which are likely to have been generated through fractional crystallization of a residual high-Ti-P magma (III, Fig.3.17b), after massive hemo-ilmenite + initial plagioclase removal. The lack of plagioclase in the massive-nelsonites in relation to the OAN cumulates could suggest local accumulation of oxide-apatite phases due to settling during plagioclase flotation (Charlier et al. 2008; 2010). Subsequently, OAN cumulates would be then formed by more fractionated residual mushes enriched in silicates, apatite and magnetite.

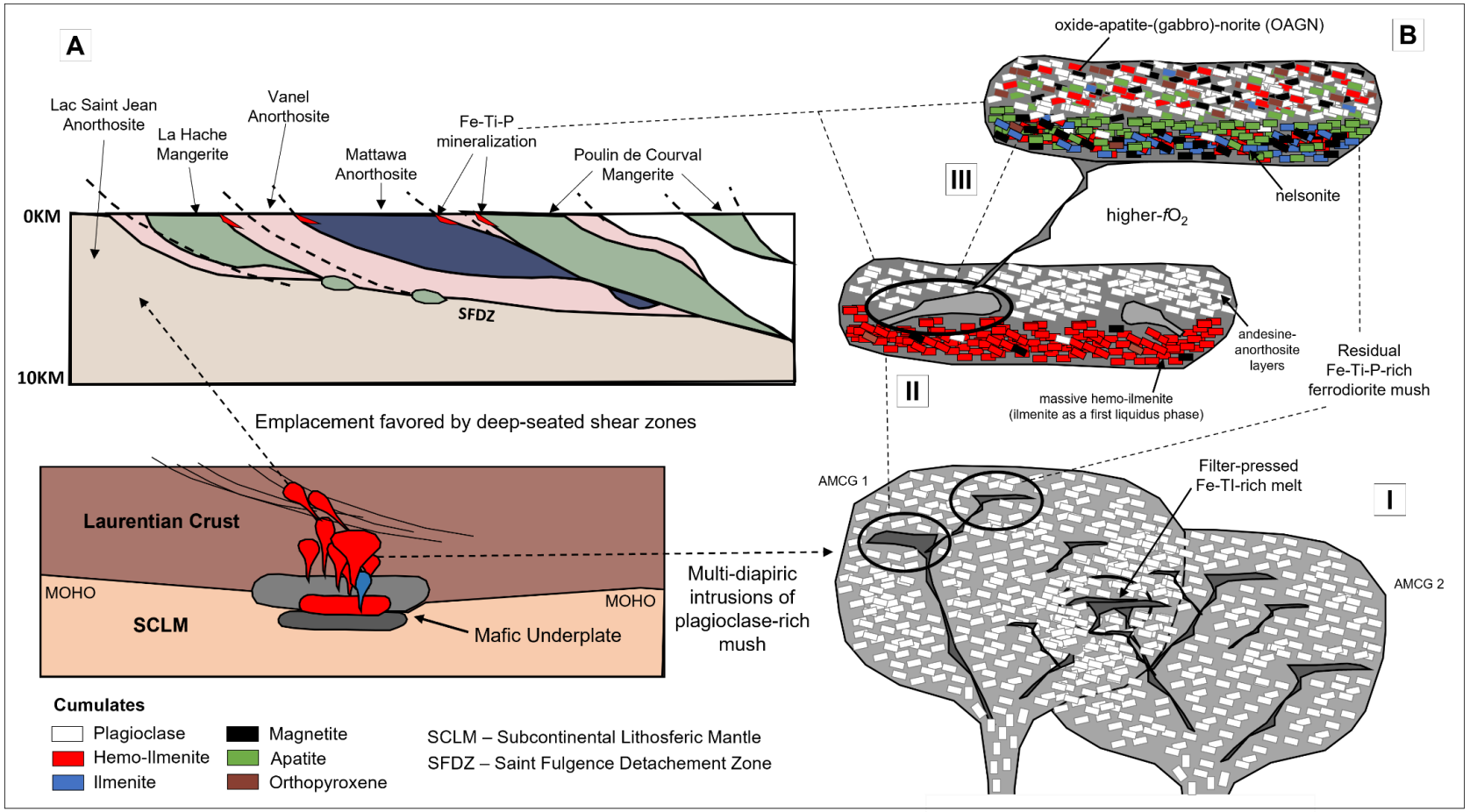

Figure 3.17. Schematic model for the formation of Fe-Ti-P mineralization in the Central Grenville Province, associated with residual injections of Fe-Ti rich ferrodiorite melts generated after anorthosite crystallization. a. Diapiric emplacement of mafic magmas and generation of the main AMCG in the Central Grenville Province favored by lower crust-type shear zones like the SFDZ. b. Simplified fractional crystallization model of residual Fe-Ti-P melts in three steps: I. initial segregation of Fe-Ti ferrodiorite melts from a plagioclase-rich mush by filter-pressing (after Charlier et al. 2015). II. migration of ferrodiorite liquids and initial fractionation dominated by hemo-ilmenite (sinking) and plagioclase (floating) as first-liquids phases. Generation of residual evolved Fe-Ti-P melts. III. fractionation of evolved Fe-Ti-P melts dominated by (hemo)-ilmenite + magnetite + apatite. Formation of oxide-apatite-rich layers (nelsonite) and residual oxide-apatite-norite (apatite + apatite + silicates)

3.8 Conclusions

The Lac Mirepoix Fe-Ti-P mineralization is a multi-stage intrusion formed by multiple injections of similar Fe-Ti-P-rich magma compositions, over at least 80 Myr (zone I: 964 ± 9 Ma and zone III: 1048 ± 8 Ma) where different zones containing mainly primitive hemo-ilmenite-rich lenses in anorthosite (zone I), nelsonite (zone II) and evolved oxide-apatite-norite (OAN) cumulates are present. Although the OAN in the different zones have different ages, they are (roughly) coeval to the youngest AMCG magmatic activity in the region. The cumulates were generated under similar high-fO_2 conditions from similar high-Ti-P evolved ferrodiorite magmas, with similar REE compositions, which evolved by fractional crystallization of hemo-ilmenite and plagioclase followed by the addition of orthopyroxene, magnetite and apatite.

The variation of trace element in oxides and apatite as well as new U-Pb dating for Fe-Ti-rich rocks forming the Lac Mirepoix Fe-Ti-P mineralization confirms that the petrogenesis of oxide-apatite mineralization related to anorthosite-massifs on the Central Grenville Province was a complex process. The similarity in composition/mineralogy between the OAN cumulates and the fine-grained ferrodiorite dykes of the Lac Mirepoix and the Lac à l'Orignal Fe-Ti-P mineralization, the overlap on the range of ages obtained as well as the proximity between the two sites corroborates that they formed in a similar way at similar times. This involved multiple injections of residual Fe-Ti-P melts, that were drained or filter-pressed from different aged anorthosite diapirs over a period of 80 Mys.

3.9 Acknowledgments

This work was funded by a research grant to support new academics from the Fonds de recherche du Québec – Nature and Technologie (FRQNT) to Sarah Dare

and the Canada Research Chair of Sarah Dare in Geochemistry Applied to Ore Deposits. The authors thank Christian Tremblay (TRCM-UQAC) and Leopold Tremblay for their assistance with field work; to Frank Guillemette (MRBoreal) for access and sampling of drillcore; Audrey Lavoie and Pape Doudou Tague for helping with LA-ICP-MS analytical procedures at LabMaTer, UQAC; Marc Choquette and Suzie Côté for their SEM, microprobe and uXRF work at Université Laval and André Poirier who helped with LA-ICP-MS data acquisition on zircons at GEOTOP, UQAM. The authors also thank the reviewers that revised the original version of the manuscript for their suggestions that helped to improve the paper.

3.10 References

Andersen, D.J., Lindsley, D.H., Davidson, P.M., 1993. QUILF: a PASCAL program to assess equilibria among Fe–Mg–Ti oxides, pyroxenes, olivine, and quartz. Computers & Geosciences 19, 1333–1350.

Arguin J-P, Pagé P, Barnes S-J, Girard R, Duran C. An Integrated Model for Ilmenite, Al-Spinel, and Corundum Exsolutions in Titanomagnetite from Oxide-Rich Layers of the Lac Doré Complex (Québec, Canada). *Minerals*. 2018; 8(11):476.

Ashwal, LD., 1993. Anorthosites. Springer, Heidelberg.

Ashwal, L. D. 2010. The temporality of anorthosites. The Canadian Mineralogist, 48(4), 711-728.

Ashwal, L. D., & Bybee, G. M. (2017). Crustal evolution and the temporality of anorthosites. *Earth-Science Reviews*, *173*, 307-330.

Barnes, S. J., Maier, W. D., & Ashwal, L. D. 2004. Platinum-group element distribution in the main zone and upper zone of the Bushveld Complex, South Africa. Chemical Geology, 208(1-4), 293-317.

Barnichon, J. D., Havenith, H., Hoffer, B., Charlier, R., Jongmans, D., & Duchesne, J. C. 1999. The deformation of the Egersund–Ogna anorthosite massif, south Norway: finite-element modelling of diapirism. *Tectonophysics*, *303*(1-4), 109-130.

Bouldreault, A. 2000. Rapport de la campagne d'exploration 2000-2001, propriete Mirepoix Titane et Phosphore, Projet 252. Les Ressources D'Arianne.

Boulianne, D. 2001. Rapport de Reconnaissance geologique 2001, Propriete Mirepoix II. Les Ressources D'Arianne.

Barnes, S. J., Mansur, E. T., Pagé, P., Meric, J., & Arguin, J. P. 2020. Major and trace element compositions of chromites from the Stillwater, Bushveld and Great Dyke intrusions compared with chromites from komatiites, boninites and large igneous provinces.

Bédard, J. H. 2023. Trace element partitioning coefficients between terrestrial silicate melts and plagioclase feldspar: Improved and simplified parameters. *Geochimica et Cosmochimica Acta*, *350*, 69-86.

Bybee, G. M., & Ashwal, L. D. 2015. Isotopic disequilibrium and lower crustal contamination in slowly ascending magmas: Insights from Proterozoic anorthosites. Geochimica et Cosmochimica Acta, 167, 286-300.

Charlier, B., Grove, T.L., 2012. Experiments on liquid immiscibility along tholeiitic liquid lines ofdescent Contrib. Mineral. Petrol. 164 (1), 27-44

Charlier, B., Vander Auwera, J., & Duchesne, J. C. 2005. Geochemistry of cumulates from the Bjerkreim–Sokndal layered intrusion (S. Norway): Part II. REE and the trapped liquid fraction. Lithos, 83(3-4), 255-276.

Charlier, B., Duchesne, J.-C., Vander Auwera, J. 2006. Magma chamber processes in the Tellnes ilmenite deposit (Rogaland Anorthosite Province, SW Norway) and the formation of Fe–Ti ores in massif-type anorthosites. Chemical Geology 234, 264–290.

Charlier, B., Skar, O., Korneliussen, A., Duchesne, J.-C., Vander Auwera, J., 2007. Ilmenite composition in the Tellnes Fe–Ti deposit, SW Norway: fractional crystallization, postcumulus evolution and ilmenite–zircon relation. Contributions to Mineralogy and Petrology 154, 119–134.

Charlier, B., Sakoma, E., Sauve, M., Stanaway, K., Vander Auwera, J., Duchesne, J.-C., 2008. The Grader layered intrusion (Havre-Saint-Pierre Anorthosite, Quebec) and genesis of nelsonite and other Fe–Ti–P ores. Lithos 101, 359–378.

Charlier, B., Namur, O., Duchesne, J.-C., Wiszniewska, J., Parecki, A., Vander Auwera, J., 2009. Cumulate origin and polybaric crystallization of Fe–Ti oxide ores in the Suwalki anorthosite, Northeastern Poland. Economic Geology 104, 205–221.

Charlier, B., Namur, O., Malpas, S., de Marneffe, C., Duchesne, J.C., Vander Auwera, J., Bolle, O, 2010b. Origin ofthe giant Allard Lake ilmenite ore deposit (Canada) by fractional crystallization, multiple magma pulses and mixing. Lithos 117, 119-134.

Charlier, B., Namur, O., Toplis, M. J., Schiano, P., Cluzel, N., Higgins, M. D., & Auwera, J. V. 2011. Large-scale silicate liquid immiscibility during differentiation of tholeiitic basalt to granite and the origin of the Daly gap. *Geology*, *39*(10), 907-910.

Charlier B, Namur O, Bolle O, et al 2015. Fe-Ti-V-P ore deposits associated with Proterozoic massif type anorthosites and related rocks. Earth Science Reviews, 141:56–81. doi: 10.1016/j.earscirev.2014.11.005.

Chen, W., Zhou, M.-F., Zhao, T.-P., 2013. Differentiation of nelsonitic magmas in the formation of the - 1.74 Ga Damiao Fe-Ti-P ore deposit, North China. Contrib. Mineral. Petrol. 165, 1341-1362.

Coint, N., Keiding, J. K., & Ihlen, P. M. 2020. Evidence for silicate–liquid immiscibility in monzonites and petrogenesis of associated Fe–Ti–P-rich rocks: example from the Raftsund intrusion, Lofoten, Northern Norway. Journal of Petrology, 61(4).

Corrigan, D., & Hanmer, S. 1997. Anorthosites and related granitoids in the Grenville orogen: a product of convective thinning of the lithosphere?. *Geology*, *25*(1), 61-64.

Corriveau, L., Perreault, S., Davidson, A., 2007. Prospective metallogenic settings of the Grenville Province. In: Goodfellow, W.D. (Ed.), Mineral Deposits of Canada: a Synthesis of Major Deposit-types, District Metallogeny, the Evolution of Geological Provinces, and Exploration Methods: Geological Survey of Canada, Mineral Deposits Division, Special Publication, pp. 819–847.

Dare S.A, Barnes S-J, Beaudoin G, et al 2014. Trace element in magnetite as petrogenetic indicators. Mineralium Deposita, 49:785–796.

Dare, S., Bethell, E., & Barnes, S. J. 2019. Constraining the formation of Fe-Ti-VP deposits using trace element in Fe-Ti oxides: insights from the chemostratigraphic variation of magnetite and ilmenite in the Upper Zone of the Bushveld Igneous Complex. GAC-MAC-IAH Québec 2019.

Duchesne, J. C. 1999. Fe-Ti deposits in Rogaland anorthosites (South Norway): geochemical characteristics and problems of interpretation. *Mineralium Deposita*, *34*, 182-198.

Duchesne, J.C., Charlier, B., 2005. Geochemistry of cumulares from the Bjerkreim-Sokndal layered intrusion (S. Norway). Part 1: constraints from major elements on the mechanism of cumulate formation and on the jotunite liquid line of descent. Lithos, 83, 229-254.

Duchesne, J.C., Shumlyanskyy , L, Charlier, B., 2006. The Fedorivka layered intrusion (Korosten Pluton, Ukraine) : an example ofhighly differentiated ferrobasaltic evolution. Lithos 89, 353-376.

Dymek, R.F., Owens, B.E., 2001. Petrogenesis of apatite-rich rocks (nelsonites and oxide apatite gabbronorites) associated with massif anorthosites. Economic Geology 96, 797–815.

Emslie, R.F., 1985. Proterozoic anorthosite massifs. In: Tobi, A.C., Touret, J.L.R. (Eds.), The Deep Proterozoic Crust in the North Atlantic Provinces. Reidel, Dordrecht, pp. 39–60.

Fischer, L. A., & Yuan, Q. (2016). Fe-Ti-V-(P) resources in the upper zone of the Bushveld complex, South Africa. In *Papers and Proceedings of the Royal Society of Tasmania* (Vol. 150, No. 1, pp. 15-22).

Frost, C. D., Frost, B. R., Lindsley, D. H., Chamberlain, K. R., Swapp, S. M., & Scoates, J. S. 2010. Chemical and isotopic evolution of the anorthositic plutons of the Laramie Anorthosite Complex: Explanations for variations in silica activity and oxygen fugacity of massif anorthosites. The Canadian Mineralogist, 48(4), 925-946.

Gobeil, A., Brisebois, D., Clark, T., Verpaelst, P., Madore, L., Wodicka, N., Cheve, S., 200. Geologie de la moyenne Cote-Nord. In: Brisebois, D., Clark, T. (Eds.), Geologie et ressources minerales de la partie est de la Province de Grenville. Ministere des Ressources naturelles, de la Faune et des Parcs, Quebec, pp. 9–58. DV 2002-03.

Grant, M. 2020. Formation of magmatic Fe-Ti-V-P deposits within the Lac St. Jean area Saguenay, Québec, Canada: Insights from trace element composition of Fe-oxides and apatite. (Unpublished masters thesis). University of Ottawa, Ontario, Canada, pp. 343.

He, H. L., Yu, S. Y., Song, X. Y., Du, Z. S., Dai, Z. H., Zhou, T., & Xie, W. 2016. Origin of nelsonite and Fe–Ti oxides ore of the Damiao anorthosite complex, NE China: Evidence from trace element geochemistry of apatite, plagioclase, magnetite and ilmenite. *Ore Geology Reviews*, *79*, 367-381.

Hébert, C., Cadieux, A.-M., Van Breemen, O., 2005. Temporal evolution and nature of Ti– Fe–P mineralization in the anorthosite–mangerite–charnockite–granite (AMCG) suites of the South–central Grenville Province, Saguenay – Lac St. Jean area, Quebec, Canada. Canadian Journal of Earth Sciences 42, 1865–1880.

Hébert, C., Van Breemen, O., & Cadieux, A. 2009. Région du reservoir Pipmuacan, (SNRC 22E): Synthese Geologique. RG 2009-01. Ministère des ressources naturelles et de la faune, Gouvernement du Québec.

Higgins, M. D., & Van Breemen, O. 1992. The age of the Lac-Saint-Jean anorthosite complex and associated mafic rocks, Grenville Province, Canada. Canadian Journal of Earth Sciences, 29(7), 1412-1423.

Higgins, M.D., Van Breemen, O., 1996. Three generations of Anorthosite–Mangerite–Charnockite–Granite magmatism, contact metamorphism and tectonism in the Saguenay – Lac–St-Jean region, Grenville Province, Canada. Precambrian Research 79, 347–362.

Higgins, M. D., Ider, M., & Breemen, O. V. 2002. U-Pb ages of plutonism, wollastonite formation, and deformation in the central part of the Lac-Saint-Jean anorthosite suite. Canadian Journal of Earth Sciences, 39(7), 1093-1105.

Hou, T., Charlier, B., Holtz, F., Veksler, I., Zhang, Z., Thomas, R., & Namur, O. 2018. Immiscible hydrous Fe–Ca–P melt and the origin of iron oxide-apatite ore deposits. Nature communications, 9(1), 1-8.

Irvine, T.N., 1982. Terminology for layered intrusions. Journal of Petrology 23 (2), 127–162.

Jakobsen, J. K., Veksler, I. V., Tegner, C., & Brooks, C. K. 2005. Immiscible iron-and silica-rich melts in basalt petrogenesis documented in the Skaergaard intrusion. *Geology*, *33*(11), 885-888.

Klemme, S., Gunther, D., Hametner, K., Prowatke, S., Zack, T., 2006. The partitioning of trace element between ilmenite, ulvospinel, armalcolite and silicate melts with implications for the early differentiation of the moon. Chemical Geology 234, 251–263.

Kolker, A. 1982. Mineralogy and geochemistry of Fe-Ti oxide and apatite (nelsonite) deposits and evaluation of the liquid immiscibility hypothesis. *Economic Geology*, *77*(5), 1146-1158.

Lin, L & Sawyer, E. 2019. Microstructure and compsotional changes across biotite-rich reaction selvedges around mafic schollen in a semppelitic diatexite migmatite. Journal of Metamorphic Geology, 37:539-566.

Miloski, P., Dare, S., Morisset, C.E., Davies, J., Perrot, M., Savard, D. 2023. Petrogenesis of the Fe-Ti-P mineral deposits associated with Proterozoic anorthosite massifs at Lac à l'Orignal, Quebec, Canada: insights from oxide and apatite trace element geochemistry. Mineralium Deposita, accepted.

Mitchell, J.N., Scoates, J.S., Frost, C.D., Kolker, A., 1996. The geochemical evolution of anorthosite residual magmas in the Laramie Anorthosite Complex, Wyoming.j. Petrol. 37, 637-660.

Morisset C.E. 2001. Mineralization in iron–titanium oxide minerals and apatite of the Lac Mirepoix ore deposit, Lac St-Jean Anorthosite Complex Québec, Canada. in Abstracts – GEODE field workshop 8-12th July 2001 on ilmenite deposits in the Rogaland anorthosite province, S. Norway.

Morisset, C.E. 2000. Cartohraphie geologique de la Propriete du Lac Mirepoix. IOS Services Scientifiques.

Morisset, C.-E., Scoates, J.S., Weis, D., Friedman, R.M., 2009. U–Pb and 40Ar/39Ar geochronology of the Saint-Urbain and Lac Allard (Havre-Saint-Pierre) anorthosites and their associated Fe–Ti oxide ores, Quebec: evidence for emplacement and slow cooling during the collisional Ottawan orogeny in the Grenville Province. Precambrian Research 174, 95–116.

Morisset, C.-E., Scoates,J.S., Weis, D., Sauve, M., Stanaway, K.J., 2010. Rutile-bearing ilmenite deposits associated with the Proterozoic Saint-Urbain and Lac Allard anorthosite massifs, Grenville Province, Québec. Can. Mineral. 48, 821-849.

Morisset, C. E., Williamson, M. C., & Hipkin, V. 2013. Investigation of three Fe–Ti oxide deposits associated with Grenvillian anorthosite massifs as potential source for lunar analogue ilmenite. *Canadian Journal of Earth Sciences*, *50*(1), 64-77.

Namur, O., Charlier, B., Toplis, M. J., Higgins, M. D., Liégeois, J. P., & Vander Auwera, J. 2010. Crystallization sequence and magma chamber processes in the ferrobasaltic Sept Iles layered intrusion, Canada. Journal of Petrology, 51(6), 1203-1236.

Namur, O., Charlier, B., Holness, M.B., 2012. Dual origin ofFe-Ti-P gabbros by immiscibility and fractional crystallization of evolved tholeiitic basalts in the Sept Iles layered intrusion. Lithos 154, 100-114.

Naslund, H. R., McBirney, A. R., & Cawthorn, R. G. 1996. Developments in Petrology.

Owens, B.E., Dymek, R.F., 1992. Fe-Ti-P-rich rocks and massif anorthosite: problems of interpretation illustrated from the Labrieville and St-Urbain plutons, Quebec. Can. Mineral. 30, 163-190

Owens, B.E., Rockow, M.W., Dymek, R.F., 1993. Jotunites from the Grenville Province, Quebec: petrological characteristics and implications for massif anorthosite petrogenesis. Lithos 30, 57–80.

Owens, B.E., Dymek, R.F., 2005. Rediscovery of the Mattawa anorthosite massif, Grenville Province, Quebec. Canadian Journal of Earth Sciences 42, 1699–1718.

Perrot, M., Tremblay, A., & David, J. 2017. Detrital zircon U-Pb geochronology of the Magog Group, southern Quebec–stratigraphic and tectonic implications for the Quebec Appalachians. American Journal of Science, 317(10), 1049-1094.

Philpotts, A.R., 1967. Origin of certain iron-titanium oxide and apatite rocks. Econ. Geol. 62, 303-315.

Philpotts, A.R., 1982. Compositions of immiscible liquids in volcanic roeks. Contrib. Mineral. Petrol. 80, 201-218.

Roedder, E. 1978. Silicate liquid immiscibility in magmas and in the system K2O-FeO-Al2O3-SiO2: an example of serendipity. *Geochimica et Cosmochimica Acta*, *42*(11), 1597-1617.

Rivers, T., 1997. Lithotectonic elements of the Grenville Province: review and tectonic implications. Precambrian Research 86, 117–154.

Ryan, B. 2000. The Nain-Churchill boundary and the Nain Plutonic Suite: A regional perspective on the geologic setting of the Voisey's Bay Ni-Cu-Co deposit. *Economic Geology*, *95*(4), 703-724.

Scoates, J. S., Frost, C. D., Mitchell, J. N., Lindsley, D. H., & Frost, B. R. 1996. Residual-liquid origin for a monzonitic intrusion in a mid-Proterozoic anorthosite complex: the Sybille intrusion, Laramie anorthosite complex, Wyoming. *Geological Society of America Bulletin*, *108*(11), 1357-1371.

Scoates, J.S., Lindsley, D.H., Frost, B.R., 2010. Magmatic and structural evolution of an anorthositic magma chamber: the Poe Mountain intrusion, Laramie Anorthosite complex, Wyoming. Can. Mineral. 48, 851-885.

Snyder, D., Carmichael, I.S.E., Wiebe, RA., 1993. Experimental study of liquid evolu-tion in an Fe-rich, layered mafic intrusion: constrains of Fe-Ti oxide precipitation on the T-}02 and T-p paths of tholeiitic magmas. Contrib. Mineral. Petrol. 113, 73-86.

Tegner, C., Cawthorn, R. G., & Kruger, F. J. 2006. Cyclicity in the Main and Upper Zones of the Bushveld Complex, South Africa: crystallization from a zoned magma sheet. Journal of Petrology, 47(11), 2257-2279.

Tollari, N., Barnes, S. J., Cox, R. A., & Nabil, H. 2008. Trace element concentrations in apatites from the Sept-Îles Intrusive Suite, Canada—implications for the genesis of nelsonites. Chemical Geology, 252(3-4), 180-190.

Toplis, MJ., Dingwell, D., Libourel, G., 1994a. The effect of phosphorous on the iron redox ratio, viscosity, and density of an evolved ferrobasalt. Contrib. Mineral. Petrol. 117, 293-304 .

Toplis, M. J., Libourel, G., & Carroll, M. R. 1994b. The role of phosphorus in crystallisation processes of basalt: an experimental study. Geochimica et Cosmochimica Acta, 58(2), 797-810.

Toplis, MJ, Carroll, M.R., 1995. An experimental study of the influence of oxygen fugacity on Fe-Ti oxide stability, phase relations, and mineral-melt equilibria in ferro-basaltic systems. J. Petrol. 36, 1137-1170.

Vander Auwera, J., Longhi, J. 1994. Experimental study of a jotunite (hypersthene monzodiorite): constraints on the parent magma composition and crystallization conditions (P, T,JO,) ofthe Bjerkreim-Sokndal layered intrusion (Norway) . Contrib. Mineral. Petrol. 118, 60-78.

Vander Auwera, J., Longhi, J, Duchesne, J.C., 1998. A liquid line of descent of the jotunite (hypersthene monzodiorite) suite. J. Petrol. 39, 439-468.

Vander Auwera, J., Weis, D., Duchesne,j.C., 2006. Marginal mafic intrusions as indicators of downslope draining of dense residual melts in anorthositic diapirs? Lithos 89, 329-352.

Veksler, I. V., Dorfman, A. M., Borisov, A. A., Wirth, R., & Dingwell, D. B. 2007. Liquid immiscibility and the evolution of basaltic magma. *Journal of Petrology*, *48*(11), 2187-2210.

Wang, M., Veksler, I., Zhang, Z., Hou, T., & Keiding, J. K. 2017. The origin of nelsonite constrained by melting experiment and melt inclusions in apatite: The Damiao anorthosite complex, North China Craton. *Gondwana Research*, *42*, 163-176.

Wilmart, E., Demaiffe, D., & Duchesne, J. C. 1989. Geochemical constraints on the genesis of the Tellnes ilmenite deposit, Southwest Norway. *Economic Geology*, *84*(5), 1047-1056.

Woodruff, L. G., Nicholson, S. W., & Fey, D. L. 2013. *A Deposit Model for Magmatic Iron-titanium-oxide Deposits Related to Proterozoic Massif Anorthosite Plutonic Suites*. US Department of the Interior, US Geological Survey.

Zhou, M. F., Robinson, P. T., Lesher, C. M., Keays, R. R., Zhang, C. J., & Malpas, J. 2005. Geochemistry, petrogenesis and metallogenesis of the Panzhihua gabbroic layered intrusion and associated Fe–Ti–V oxide deposits, Sichuan Province, SW China. *Journal of Petrology*, *46*(11), 2253-2280.

Zhou, M. F., Chen, W. T., Wang, C. Y., Prevec, S. A., Liu, P. P., & Howarth, G. H. 2013. Two stages of immiscible liquid separation in the formation of Panzhihua-type Fe-Ti-V oxide deposits, SW China. *Geoscience Frontiers*, *4*(5), 481-502.

CHAPTER 4

GEOCHEMICAL VARIATION OF FE-TI-(P) MINERALIZATION ASSOCIATED WITH THE YOUNGER GREENVILLIAN AMCG-SUITES (1080 – 950 Ma): NEW EVIDENCE FOR MANTLE SOURCE AND CRUSTAL CONTAMINATION CONSTRAINED FROM ZIRCON AND APATITE CHEMISTRY

Pedro Miloski[1], Sarah Dare[1], Morgann G. Perrot[2] , Joshua H.F.L. Davies[2]

1. Département des Sciences Appliquées, Université du Québec à Chicoutimi (UQAC), 555 Boulevard de l'Université, Chicoutimi, Québec, Canada, G7H 2B1

2. Département des Sciences de la Terre et de l'Atmosphère/GEOTOP, Université du Québec à Montréal (UQAM), 405 Rue Sainte-Catherine Est, Montréal, Québec, Canada, H2L 2C4

Precambrian Research (2023)
In preparation

Résumé

La Province Centrale du Grenville au Québec, Canada, abrite plusieurs occurrences de minéralisation Fe – Ti – P hébergées dans des suites AMCG (Anorthosite – Mangerite – Charnockite – Granite) protérozoïques, avec des occurrences majeures dans la région du Saguenay-Lac-Saint-Jean, Québec. Les deux suites AMCG plus jeunes de la province centrale de Grenville (suites AMCG Pipmuacan 1082-1045 Ma et Valin 1020-1008 Ma) ont une évolution pétrogénétique complexe, présentant une variation géochimique de la minéralisation en oxyde-apatite à partir d'oxydes massifs à haute teneur en Ti/Fe (hémo-ilménite ± magnétite) vers des nelsonites (oxydes et apatites) à faible teneur en Ti/Fe ((hémo)-ilménite + magnétite + apatite), des norites à oxydes-apatites ((hémo)-ilménite + magnétite + apatite + silicates) jusqu'aux mangérites minéralisées en Fe-Ti-P (ilménite + magnétite + apatite + oligoclase + K-feldspath + quartz). La géochimie minérale in situ des éléments traces du plagioclase et des oxydes indique une similitude entre les différentes minéralisations Fe-Ti-P dans les suites AMCG de Pipmuacan et Valin, corroborant une évolution par cristallisation fractionnée à partir d'oxydes massifs plus primitifs vers des liquides résiduels (évolués) cristallisent des mangérites riches en apatite. Les isotopes U-Pb-Hf in situ dans les zircons provenant de la minéralisation Fe-Ti-P associée spatialement aux suites AMCG de Pipmuacan et Valin ont principalement des valeurs εHf chondritiques à légèrement positives et négatives, dans lesquelles la minéralisation des anorthosites de Labrieville et Mattawa présente des valeurs plus suprachondritiques (εHf: +3,0 à +7,0; datation U-Pb : 1065 (± 5Ma) à 990 (± 7Ma)), reflétant possiblement une contamination par une croûte juvénile, similaire à la minéralisation de l'anorthosite de Saint Urbain. Les minéralisations associées à l'anorthosite Vanel et aux mangérites de La Hache et Poulin de Courval présentent une signature Hf plus enrichie (εHf: -5,0 à +7,4; datation U-Pb : 964 (± 9Ma) à 1115 (± 11Ma)), soit étant relativement plus contaminés et/ou associés à des

sources mantelliques plus enrichies par rapport à la minéralisation de Labrieville et de Mattawa. Les patrons d'éléments traces de l'apatite de toutes les minéralisations Fe-Ti-P dans cette étude présentent des patrons enrichis en LREE très similaires à l'apatite provenant d'intrusions litées, associées aux panaches du manteau, avec une contamination crustale négligeable. Cela indique l'implication d'une source de manteau asthénosphérique enrichi dans la formation des magmas riches en Fe-Ti-P pour les différentes minéralisations en Fe-Ti-P dans cette étude, plutôt qu'une source de manteau appauvrie ou un manteau lithosphérique sous-continental enrichi comme communément proposé dans les études précédentes des modèles tectoniques pour le magmatisme AMCG du Grenville. De plus, les données Lu-Hf révèlent que la minéralisation Fe-Ti-P dans l'anorthosite de Vanel et les mangérites de La Hache et Poulin de Courval ont probablement subi une contamination crustale inférieure faible à modérée. La datation U-Pb des roches minéralisés dans cette étude a donné des âges assez différents (> 50 Ma) par rapport aux publications précédentes sur chaque AMCG hôte respectif, indiquant l'implication de multi-injections complexes de diapirs riches en plagioclase et de magmas résiduels riche en Fe-Ti-P sur une période de 80 Mys dans la génération d'anorthosites et des minéralisations Fe-Ti-P associées. Ainsi, la géochimie de l'apatite et du zircon semble mieux contraindre la source mantellique et le rôle de la contamination dans la pétrogenèse des suites AMCG au Grenville.

Abstract

The Central Grenville Province in Quebec, Canada, hosts several occurrences of Fe–Ti–P mineralization hosted in Proterozoic AMCG (Anorthosite–Mangerite–Charnockite–Granite) suites, with major occurrences in the region of Saguenay-Lac-Saint-Jean, Quebec. The two younger AMCG suites in the Central Grenville Province (1082-1045 Ma Pipmuacan and 1020-1008 Ma Valin AMCG suites) have a complex petrogenetic evolution, presenting a geochemical variation of oxide-apatite mineralization from high Ti/Fe massive oxides (hemo-ilmenite ± magnetite) cumulates towards low-Ti/Fe apatite-bearing nelsonites ((hemo)-ilmenite + magnetite + apatite), oxide apatite norite ((hemo)-ilmenite + magnetite + apatite + silicates) up to mineralized mangerites (ilmenite + magnetite + apatite + oligoclase + K-feldspar + quartz). In-situ mineral trace-element geochemistry of plagioclase and oxides indicate a similarity between the different Fe-Ti-P mineralization in the Pipmuacan and Valin AMCG Suites, corroborating an evolution by fractional crystallization from more primitive massive oxides towards residual (evolved) oxide-apatite-rich mangerites. In-situ U-Pb-Hf isotopes in zircon from Fe-Ti-P mineralization spatially associated with the Pipmuacan and Valin AMCG Suites have mainly chondritic to slightly positive and negative εHf values, in which mineralization in the Labrieville and Mattawa anorthosites present more suprachondritic Hf signature (εHf: +3.0 to +7.0; U-Pb dating: 1065 (± 5Ma) to 990 (± 7Ma)), possibly reflecting contamination from juvenile crust, similar to mineralization in the Saint Urbain Anorthosite. Mineralization associated with the Vanel Anorthosite and the mangerites of La Hache and Poulin de Courval present a more enriched Hf signature (εHf: -5.0 to +7.4; U-Pb dating: 964 (± 9Ma) to 1115 (± 11Ma)), either being relatively more contaminated, and/or associated with more enriched mantle source(s) in relation to the mineralization at Labrieville and Mattawa. The trace element patterns of apatite from all of the Fe-Ti-P mineralization in this study have LREE enriched patterns very similar to apatite

from mafic layered intrusions, associated with mantle plumes, with negligible crustal contamination. This indicates the involvement of an asthenospheric enriched mantle source in forming the Fe-Ti-P rich melts for the different Fe-Ti-P mineralization in this study, rather than a depleted mantle source or enriched subcontinental lithospheric mantle as commonly proposed in previous tectonic models for the Grenville AMCG magmatism. Moreover, the Lu-Hf data reveal that Fe-Ti-P mineralization in Vanel Anorthosite and the mangerites of La Hache and Poulin de Courval probably underwent low- to moderate lower crustal contamination. U-Pb dating of the mineralized cumulates in this study resulted in quite different ages (>50Ma) from previous publications on each respective host-AMCG, indicating the involvement of complex multi-injections of plagioclase-rich diapirs and residual Fe-Ti-P magmas over a period of 80 Mys in the generation of anorthosites and related Fe-Ti-P mineralization. Therefore, apatite and zircon geochemistry seem to better constrain the mantle source and role of contamination in the petrogenesis of AMCG suites in the Grenville Province.

4.1 Introduction

The Grenville Province, Canada, hosts several occurrences of Fe–Ti–P mineral deposits as part of Proterozoic AMCG (Anorthosite–Mangerite–Charnockite–(rapakivi) Granite) suites (Owens & Dymek, 1992; 2001; 2005; Owens et al. 1993; 1994; Morisset et al. 2009; 2010; 2013; 2014; Charlier et al. 2008; 2010; Miloski et al. 2023a,b; Fig.4.1). Considerable debate exists regarding the petrogenesis of anorthosites, i.e., whether their parental melts were generated within the crust or mantle, the nature of the mantle source (depleted, enriched, asthenospheric or lithospheric), the influence of crustal contamination, the relationship between anorthosite, Fe-Ti-P rocks and coeval felsic rocks, and also the origin of AMCG generation in collisional tectonic settings (Ashwal, 1993; Corrigan & Hamner, 1997; Duchesne, 1999; Owens & Tomascak, 2002; Bickford et al. 2010; Regan et

al. 2011). Proterozoic massif-type anorthosites are thought to have a complex evolution, being generated from multiple diapiric intrusions of plagioclase-rich mushes into the mid-crust with strong effects of crustal assimilation (Bybee & Ashwal, 2015). Just before their emplacement, these intrusions of plagioclase-rich mushes require an extensive history of voluminous plagioclase crystallization from magmas ponded at the crust-mantle interface (MOHO); (Ashwal, 1993; Woodruff et al. 2013), of mantle-derived origin (Emslie, 1985; Ashwal, 1993; 2010) or mafic lower-crustal derived origin (Duchesne et al. 1999; Vander Auwera et al. 2011). Several lines of isotopic evidence support both crustal or mantle source models, in addition to other petrologic, geochemical and tectonic arguments (Bybee & Ashwal, 2015). Anorthosite parental magmas are thought to evolve through polybaric crystallization (Bybee & Ashwal, 2015; Charlier et al. 2015) during ascent, crystallizing plagioclase, orthopyroxene and/or olivine and oxides. Most of the oxide-apatite mineralization is then generated by further fractional crystallization of the residual Fe-Ti-V-P liquid, of jotunite/ferrodiorite composition (Vander Auwera et al. 1998; Owens et al. 1993; Charlier et al. 2008; Miloski et al. 2023a,b), from the host anorthosite diapirs, which are dominated by plagioclase, Fe-Ti oxides, and Fe-Mg silicates. The residual liquid can be drained through fractures/margins or zones of lower pressure (Owens et al. 1994; Scoates et al. 2010; Charlier et al. 2015) into the anorthosite massif, generating oxide-apatite ores (Miloski et al. 2023a). The residual/evolved character of Fe-Ti-P cumulates in relation to other AMCG lithologies can explain the higher concentration of evolved mineral phases as cumulus apatite and intercumulus zircon in these rocks. The presence of zircon crystals in oxide-apatite rocks as nelsonite and oxide-apatite norites allows U-Pb dating of the mineralization itself (Miloski et al. 2023a,b), so that the timing of mineralization can be compared with that of the previously dated host AMCG suite (Fig.4.2, e.g., Higgins & Van Breemen, 1996).

Due to extensive periods of magma ascending and polybaric crystallization, several publications suggest that contamination of mantle-derived magmas by the lower crust is an important process in AMCG petrogenesis (see Bybee & Ashwal, 2015, and references therein). In the Grenvillian anorthosites, Peck et al. (2010) suggested that AMCG suites in the Adirondack mountains (South Grenville) were formed by the result of contamination of mantle-derived magmas by crustal material (for example the detrital sediments studied by Papapavlou et al. 2022). However, due to proximal timing of the AMCG magmatism in the Grenville Province (1.3 – 1.0 Ga) in relation to the host-crustal lithologies (1.3-1.8 Ga), in many cases, Sm–Nd isotopes signatures in the upper mantle and contemporary juvenile crustal source reservoirs have not developed detectable compositional contrast in any of the AMCG suites during the relative short time elapsed since crust formation (Heinonen et al. 2014). In situ Hf isotope studies of zircon provide additional information to resolve these issues since the half life of ^{176}Lu is approximately half as long as that of ^{147}Sm leading to much faster generation of the daughter ^{176}Hf (e.g., Kemp et al. 2007; Heinonen et al. 2010a).

The Central Grenville Province in Quebec, Canada, has the largest area of AMCG exposure in the world (Ashwal, 1993; Hébert et al. 2005), with a general alignment along two north-northeast-trending anorthosite “corridors” (Indares & Moukhsil, 2013), in which the emplacement was probably favored by zones of weakness such as major deep-seated shear zones (Corrigan & Hanmer, 1997; Scoates & Chamberlain, 1997; Duchesne et al. 1999; Ryan, 2000; Bogdanova et al. 2004; Hébert et al. 2005; 2009) present in the region. A single anorthosite suite may be composed of multiple anorthosite lobes with varying ages/different plagioclase compositions and host differing styles of Fe-Ti-oxide mineralization (Charlier et al. 2015; Miloski et al. 2023 a,b), in which several mechanisms can concentrate ilmenite ± magnetite ± apatite during cooling of the parental magma (Charlier et al. 2015). AMCG suites and associated Fe–Ti–P mineralization in the Central

Grenville Province result from at least four different pulses of magmatism (Hébert et al. 2005; 2009), over a period of 300 million years (1327 – 1000 Ma). The two older suites (1327 ± 16 Ma De La Blache Mafic Suite and the 1160-1135 Ma Lac-Saint-Jean Anorthosite Suite) are dominated by labradorite (and minor andesine) plagioclase compositions (associated with olivine and minor orthopyroxene), whereas oxide mineralization is magnetite-dominated (more primitive Fe-Ti-V-P oxide mineralization). Plagioclase in the younger AMCGs (1082-1045 Ma Pipmuacan and 1020-1008 Ma Valin AMCG suites) are exclusively andesine in composition, associated with orthopyroxene and hemo-ilmenite bearing Fe-Ti-P mineralization such as nelsonites (massive oxides-apatite) and oxide–apatite (gabbro)norites (OAGN) (Dymek & Owens, 2001; Grant, 2020; Miloski et al. 2023a,b), with major occurrences in the region of Saguenay-Lac-Saint-Jean, Quebec.

Moreover, Fe-Ti-P mineralization associated with more silicic members of AMCG suites, such as mangerites and charnockites, is rare in anorthosite provinces worldwide, except for a few locations (e.g., the Raftsund Intrusion, Norway; Coint et al. 2020). However, in the Central Grenville, some sites such as the La Hache Mangerite (1010 ± 3Ma) presents extensive concentration of Fe-Ti-P mineralization associated with K-rich plagioclase (Hébert et al. 2005). Mangerites and charnockites would represent the most-evolved (and more contaminated) cumulates after extensive fractional crystallization that would have previously formed anorthosites and related orthopyroxene-bearing lithologies (Duchesne et al. 1999, Vander Auwera et al. 1998, 2000, 2003, Longhi et al. 1999). An alternative model however holds that the anorthosites and Si-rich members of the suite are broadly coeval (Longhi & Ashwal, 1985; McLelland et al. 1996; Frost & Frost, 1997) but not cogenetically correlated, whereas the granitoids result from melting of lower crustal rocks caused by intrusion of hot gabbroic magma.

Recent contributions on the petrogenesis of Fe-Ti-P mineralization in the Central Grenville (Miloski et al. 2023a,b) demonstrated, through direct dating of the mineralisation itself using U-Pb of zircon, the high complexity of these systems, with multi-stage injections of Fe-Ti-P magmas even in a single ore-deposit-scale, presenting a large range of ages (spanning up to 80Ma), but with similar apatite trace element compositions. These Fe-Ti-P mineralizations present a geochemical variation from high Ti/Fe systems (forming massive ilmenite cumulates) into low-Ti/Fe systems (forming nelsonites and oxide-apatite-norites), due to evolution through fractional crystallization of (hemo-ilmenite), magnetite and apatite, suggesting an order of crystallization. Comparison with worldwide ferrodiorite/jotunite dyke compositions, generally interpreted as the parental magmas of these intrusions, confirms their cogenetic relationship and oxide-apatite trace-element patterns to nelsonites and oxide-apatite-norite of the mineralization (Miloski et al. 2023a,b).

The long-lived AMCG magmatism in the Grenville Province was generated during different tectonic settings from an Andean-type margin (1.71-1.23Ga) to continental collision (1.19-0.98Ga) and even post-collisional collapse/lithospheric thinning (Rivers, 1997; Indares & Moukhsil, 2013; Groulier et al. 2018) that can allow for considerable changes in the petrogenetic factors, such as the sources of magma, crustal contamination and subsequent processes of evolution/differentiation between the different AMCG suites and associated Fe-Ti-P mineralization. The exclusive concentration of massive hemo-ilmenite apatite-rich mineralization within the younger syn/post-collisional AMCG suites (1082-1045 Ma Pipmuacan and 1020-1008 Ma Valin) suggests some changes in the magma composition in relation to older AMCG occurrences, whose causes are not yet understood. Owens et al. (1994), through the study of host anorthosites, refer to the younger massifs, such as Labrieville, as more alkaline in nature. They proposed that they were generated from an enriched SCLM source. A comparison between the composition of Fe-Ti-P

mineralization at Labrieville and other nearby coeval AMCG-suites could provide new information on the mantle source of magmatism in the Central Grenville. To evaluate the factors causing the geochemical variation of oxide-apatite mineralization among different anorthosite massifs, the role of crustal contamination, the nature of the mantle source and the implications for AMCG petrogenesis, we present here new Hf isotopes in zircon for Fe-Ti-P mineralization coupled U-Pb dating in zircon and trace-element geochemistry of apatite, oxides and plagioclase, in the Central Grenville Province. These data also have significant implications for our understanding of the emplacement of Anorthosite Suites in the Grenville and the construction of a tectonic model associated with it.

4.2 Regional geological setting

The Grenville Province in Eastern Canada (Fig.4.1a) is a Mesoproterozoic orogenic belt that represents the remnants of a large hot orogen built on the southeastern margin of the Paleocontinent Laurentia (Corriveau et al. 2007; Rivers, 2012) by a major collision between Laurentia and Amazonia. It comprises two major lithotectonic elements: (1) a Parautochthonous Polycyclic Belt formed of Archean and Paleoproterozoic to Mesoproterozoic rocks from the foreland that were reworked during the Grenvillian orogeny, and an (2) Allochthonous Polycyclic Belt (also known as the Central Granulite Terrain or the Core Zone) formed by terranes tectonically accreted onto the parautochthonous belt and separated from the latter by the southeast-dipping allochthon boundary thrust (Woussen et al. 1986; Rivers et al. 1989; Corrigan & Hamner, 1997; Owens & Dymek, 2005).

The Paleo to Late Mesoproterozoic rocks of the Grenville Province represent an active continental margin with more than 400Ma of tectonic activity and extensive episodes of subduction-accretion and arc formation (1710 – 1230Ma, Rivers, 1997). Specifically, in the Central Grenville, younger ages are reported related to more juvenile crust formation (e.g., 1.5Ga Quebecia Terrane; Dickin, 2000). Subsequent stages of continent-continent

collision (Shawinigan, 1190 – 1140Ma; Ottawan, 1080 – 1020Ma and Rigolet, 1000 – 850Ma) took place during the Grenvillian Orogeny, separated by periods of crustal extension and several occurrences of within-plate magmatism and AMCG generation. During the collisional phase, crustal thickening and tectonic extrusion led to widespread high-grade metamorphism (Ludden & Hynes, 2000b) and reactivation of deep-level shear zones (Fig.4.1b) (Corriveau et al. 2007).

The Allochthonous Polycyclic Belt (Fig.4.1), which host most of the AMCG suites in the Central Grenville Province, is a series of metamorphosed basement lithologies mainly in the granulite facies (Hébert et al. 2005): 1) paragneiss and mafic-intermediate orthogneiss of the 1506 ± 13 Ma (Hébert & Van Breemen, 2004) Saguenay gneiss complex, representing supracrustal rocks and plutonic rocks respectively; 2) tonalitic to dioritic orthogneiss of the 1434 +64/-28 Ma (Gobeil et al. 2002) Hulot complex; and 3) widespread felsic with some charnockitic orthogneiss of the 1393-1383 Ma (Hébert et al. 2004) Cap à l'Est gneiss complex (Hébert et al. 2005). The emplacement of most of the AMCG-suites in the Central Grenville Province are coeval to periods of either crustal shortening or crustal extension during the Grenvillian Orogeny (Fig.4.2, Corrigan & Hamner, 1997; Indares & Moukhsil, 2013).

AMCG suites are a prominent feature of the Grenville Orogeny in Quebec, representing one of the world's largest occurrences. The majority of AMCG magmatism ranges in age from 1160 to 1000 Ma (Shawinigan and Ottawan phases, Fig.4.1 & 4.2) in a broadly orogenic environment (Morisset 2008; McLelland et al. 2010), being attributed to episodic lithospheric-scale extension by removal of mantle lithosphere in an overall convergence setting (McLelland et al. 1996; Corrigan & Hanmer 1997). Anorthositic magmas may have formed in and (or) been channeled into long-lived zones of lithospheric weakness, with their ascent being controlled by intermittent activation of major fault systems

(Higgins & Van Breemen 1996; Indares & Moukhsil, 2013), such as the Saint Fulgence and Pipmuacan Deformation Zone in the Central Grenville Province (Higgins & Van Breemen, 1996; Gobeil et al. 2002; Hébert et al. 2005; 2009; Corriveau et al. 2007), aligned along two north-northeast-trending anorthosite “corridors” (Indares & Moukhsil, 2013) (Fig.4.1).

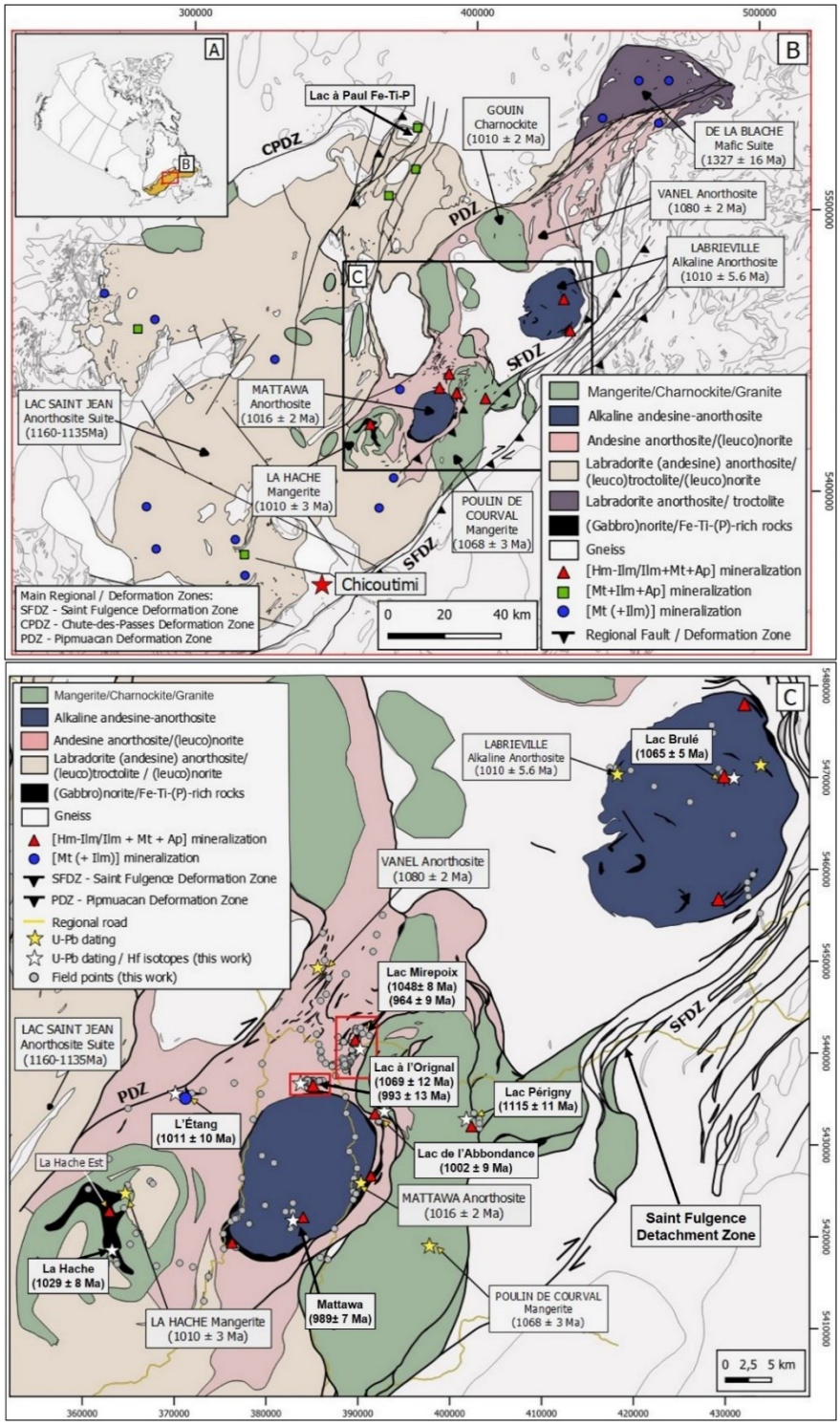

Figure 4.1. a. Location of the Grenville Province in Quebec, Canada. Red square locates the Central Grenville shown in Figure b. b. Detailed map of the AMCG-suites in the Central Grenville Province, Quebec with the location of the main Fe-Ti-(P) mineralization and regional deformation zones. c. Detailed map of study area where most of the lenses/sill-like Fe-Ti-(P) (gabbro)norite intrusions occur. Location of the field points (grey circles) within and nearby the eight Fe-Ti-(P) mineralization here analyzed. New-U-Pb/Hf-isotope data (white stars) were performed on eight of the mineralization. Geological maps modified from SIGEOM (Quebec System of Geomining Information; Gobeil et al. 2002; Hébert & Cadieux, 2003; Gobeil et al. 2002; Hébert & Cadieux, 2003).

4.3 AMCG suites and Fe-Ti-P mineralization in the Central Grenville Province

The oldest AMCG activity in the Central Grenville Province (Fig.4.2) is represented by the pre-Grenvillian 1327 ± 16 Ma (Gobeil et al. 2002) De La Blache Anorthosite Suite (Fig.4.1) composed of anorthosite and olivine-bearing leucotroctolite, with minor occurrences of gabbronorite and felsic rocks (Hébert et al. 2005). The second phase of AMCG activity (1160-1140Ma), largest in the area and in the world (Ashwal, 1993; Hébert et al. 2005), is represented by the Lac-Saint-Jean Anorthosite Suite (Fig.4.1) and minor occurrences of mangerite and charnockite (1155-1135 Ma, Higgins & Van Breemen 1996; Gobeil et al. 2002; Hébert et al. 2005), consisting of mainly massive anorthosite and leuconorite and minor olivine-bearing lithologies as troctolites. Labradorite-type plagioclase dominates Lac-Saint-Jean Anorthosite Suite but, in the northern and eastern sections, andesine-type is present (Hébert et al. 2005; Woussen et al. 1986). A few previous publications have dated and individualized the different intrusions that compose the Lac-Saint-Jean Anorthositic Suite (e.g., Higgins & Van Breemen 1996; Higgins et al. 2002; Gobeil et al. 2002), using U-Pb dating of zircons recovered from evolved pegmatite pockets within the massive anorthosites. Fe-Ti-V-P oxide mineralization, including massive Fe-Ti oxides and massive nelsonites, are mainly concentrated in the northern portion of the Lac-Saint-Jean anorthosite suite, in particular the region of Lac à Paul (Fig.4.1b; Hébert et al. 2005; Fredette, 2006), although the western (Lac Perron) and southern portions (St. Charles de Bourget) also contain significant mineralization, typically characterized by magnetite with minor ilmenite and olivine (Fredette, 2006; Grant 2020).

The two younger magmatic episodes (Fig.4.2) comprise several smaller AMCG plutons, associated with orthopyroxene-lithologies (e.g., leuconorite) that were emplaced along the eastern margin of the Lac-Saint-Jean Anorthositic Suite (Fig.4.1b), associated with the Saint Fulgence Detachment Zone (Hébert et al. 2005; 2009). They comprise

(Fig.4.1 and 2): I) the 1082-1045 Ma Pipmuacan AMCG Suite, consisting of the 1080 ± 2 Ma (Hébert et al. 2009) Vanel Anorthosite, and the 1068 ± 3 (Hébert et al. 2009) Poulin de Courval Mangerite; II) the 1020-1008 Ma Valin AMCG Suite, including the 1016 ± 2 (Hébert et al. 2005) Mattawa Anorthosite (Owens & Dymek, 2005), the 1010 ± 6 (Hébert et al. 2005) Labrieville Alkalic Anorthosite Massif (Owens & Dymek, 1992; Owens et al. 1993; 1994), the 1010 ± 2 (Hébert et al. 2005) Gouin Charnockite and the 1010 ± 3 (Hébert et al. 2005) La Hache Mangerite.

Anorthosite members of the Pipmuacan and Valin AMCG suites present variable plagioclase composition. The older Vanel Anorthosite presents the highest An contents from labradorite (An 60 – 50) through to andesine (An 50 – 40) in composition (Hébert et al. 2005; 2009; Miloski et al. 2023a,b). In contrast, the smaller and younger anorthosites of Mattawa and the Labrieville Alkalic Anorthosite have plagioclase compositions varying from andesine to oligoclase (An 40 to 30), with absence of extensive labradorite compositions (Owens & Dymek, 2005). Fe-Ti-P mineralization in these AMCGs are hemo-ilmenite-bearing (e.g., massive ilmenite, nelsonite, oxide-apatite-(gabbro)norite) associated with anorthosites but also mangerite.

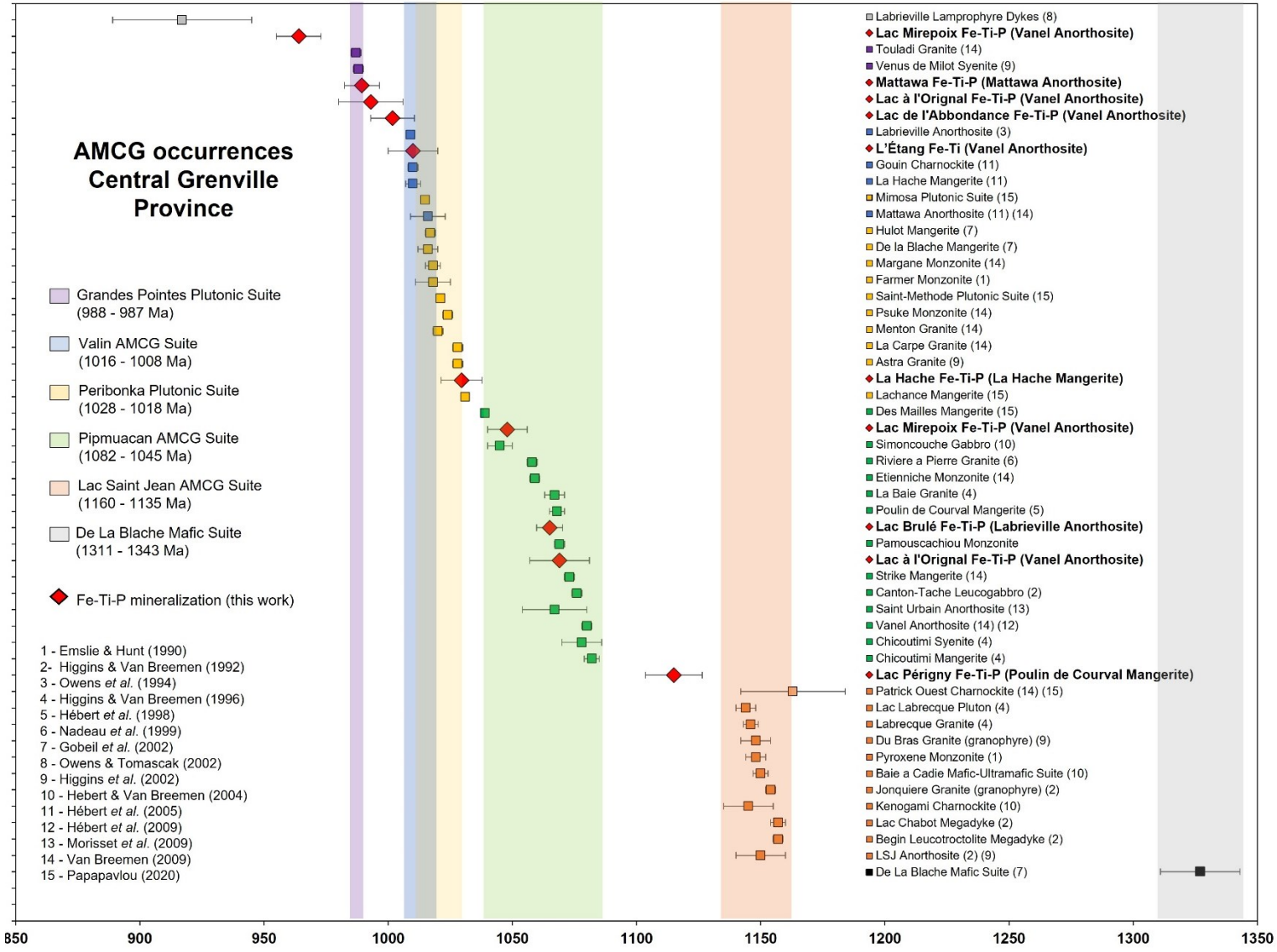

Figure 4.2. Geochronological data compiled for the main AMCG suites in the Central Grenville Province, Quebec, including the new U-Pb dating of Fe-Ti-P mineralization (red symbols) of this study and that of Lac à l'Orignal Fe-Ti-P deposit (Miloski et al. 2023a) and Lac Mirepoix Fe-Ti-P mineralization (Miloski et al.2023b). Host-AMCG of mineralization is respectively given in brackets afterwards. AMCG suites and subdivisions after Hébert et al. (2005); (2009).

4.4 Local geology: Fe-Ti-P mineralization and host-AMCG suite

Most of the Fe-Ti-P mineralization in the Central Grenville Province are associated with the younger Pipmuacan and Valin AMCG suites (Hébert et al. 2005; 2009), where several lenticular and/or layered tabular accumulations enriched in (hemo)-ilmenite, magnetite and apatite (e.g., massive oxides, leuconorite, oxide-apatite-(gabbro)-norite, nelsonite) occur mainly within orthopyroxene-bearing anorthosites and related lithologies (Fig.4.1b; Table 4.1). This study focus on Fe-Ti-P mineralization associated with five different AMCG intrusions in the Central Grenville Province (Fig.4.1c): 1) Vanel Anorthosite hosting Fe-Ti-P mineralization at the Lac à l'Orignal deposit (Miloski et al. 2023a), Lac Mirepoix (Miloski et al. 2023b) and Lac de l'Abbondance, and Fe-Ti mineralization at L'Étang; 2) Poulin de Courval Mangerite hosting the Lac Périgny Fe-Ti-P mineralization; 3) Mattawa Anorthosite hosting Fe-Ti-P mineralization within; 4) Labrieville Alkaline Anorthosite hosting the Lac Brûlé Fe-Ti-P deposit and the 5) La Hache Mangerite hosting Fe-Ti-P occurrences within. Representative photos are shown in Figure 4.3a-f & 4.3g-i.

Previous U-Pb dating in zircon (Owens et al. 1994; Hébert et al. 2005; 2009) have been carried out to determine the ages of the Pipmuacan and Valin AMCG Suites (Figs.4.1 & 4.2), using associated leuconorite/gabbronorite lenses and jotunite/ferrodiorite dykes that occur around the contacts or within these massifs. However, the anorthosites were not directly dated from evolved pegmatitic pockets. Recently, in-situ U-Pb dating in zircon of the Fe-Ti-P mineralization associated with those AMCG suites have been realized by Miloski et al. (2023a,b) at Lac à l'Orignal and Lac Mirepoix. However, no Lu-Hf isotope data has been published so far.

Several Fe-Ti-P mineralization occur in the Vanel Anorthosite near the northern boarder of the younger Mattawa Anorthosite massif (Fig.4.1, Table 4.1), where two multi-

stage intrusions have been previously studied in detail: the Lac à l'Orignal Fe-Ti-P deposit (1069 ± 12 Ma / 993 ± 13 Ma, U-Pb in zircon for OAN cumulates; Miloski et al. 2023a) and Lac Mirepoix Fe-Ti-P mineralization (1048 ± 8 Ma / 964 ± 9 Ma, Miloski et al. 2023b). The Lac à l'Orignal Fe-Ti-P deposit (Fig.4.1b) has a lenticular structure and contains resources estimates of 15.8 Mt at 5.18% P_2O_5, 4.23% TiO_2 and 23.90% Fe_2O_3, in ilmenite and apatite (Yassa, 2022). The Lac à l'Orignal Fe-Ti-P deposit has been studied in detail by Miloski et al. (2023a) who described the occurrence of a main oxide apatite norite (OAN, Fig.4.3a) mineralization, with thin apatite-bearing anorthosite layers, and minor amounts of massive nelsonite. The mineralization is (hemo)-ilmenite-dominated, accompanied by magnetite and apatite. The border of the intrusion is older (1069 ± 12 Ma) and dominated by OAN cumulates with hemo-ilmenite (± magnetite) + apatite (Fig.4.3j). The core, however, is younger (993 ± 13 Ma) and contains ilmenite (free of hematite exsolutions) + magnetite + apatite (Miloski et al. 2023a).

The nearby Lac Mirepoix Fe-Ti-P mineralization (Fig.4.1b) presents a larger variety of Fe-Ti-P lithologies (OAN, nelsonite and massive oxides) in relation to the Lac à l'Orignal one and shares more similarities to the Grader Intrusion (Charlier et al. 2008), Northeastern Grenville (Havre-Saint-Pierre Anorthositic Suite, Quebec). The Lac Mirepoix area has been studied in detail by Miloski et al. (2023b) who subdivided the mineralization into three different zones according to the appearance of different cumulate phases: zone I (964 ± 9 Ma) comprises mainly massive oxide (>70% hemo-ilmenite ± magnetite) lenses hosted in anorthosite (Fig.4.3b). Towards the center (zone II) of the Mirepoix area (Figs.4.3c & 4.3h), massive oxide layers are less common whereas apatite-bearing cumulates appear, forming massive nelsonite (50-70% magnetite ± ilmenite and 25-30% apatite) and oxide apatite norite (OAN, 15-25% hemo-ilmenite ± magnetite and 8-20% apatite. Finally, zone III (1048 ± 8 Ma) is marked by the alternance of OAN lenses (10-25m), richer in magnetite, in addition

to (hemo)-ilmenite and apatite, as well as the absence of massive oxide and nelsonite (Miloski et al. 2023b).

The Lac de l'Abbondance Fe-Ti-P mineralization outcrops on the southeastern limit of the Vanel Anorthosite (Fig.4.1), wrapping around the southeastern border of the Mattawa Anorthosite. The mineralization contains massive nelsonites and minor oxide-apatite-norite layers, similar to the features observed in zone II of the Lac Mirepoix mineralization (Miloski et al. 2023b). Also, in the Vanel Anorthosite at the L'Étang area (northwest of Mattawa Anorthosite near the Pipmuacan Detachment Zone, Fig.4.1c), Fe-Ti mineralized lenses of oxide-rich leuconorite (Fig.4.3f) occur with high concentration of magnetite + ilmenite (hematite exsolution free), but no apatite. Few publications have given basic descriptions of these smaller mineralization zones in the Vanel Anorthosite (e.g., Hébert & Cadieux, 2003; Hébert et al. 2009).

The Poulin de Courval Mangerite outcrops along the eastern border of the Vanel Anorthosite and hosts the Lac Périgny Fe-Ti-P mineralization (Fig.4.1). The mineralization is poorly exposed, and only briefly described during exploration in the area (Hébert & Cadieux, 2003), as containing levels of oxide-apatite-norite dominated by ilmenite + magnetite (Fig.4.3g), within a massive anorthosite/leuconorite. This latter mineral association can be also observed in other Fe-Ti-P mineralization related to the nearby Vanel Anorthosite, similar to zone II of the Lac Mirepoix mineralization (Miloski et al. 2023b) and the core of the Lac à l'Orignal intrusion (Miloski et al. 2023a). Regional mapping and data in the SIGEOM (Quebec Georeference Data System) attribute the host lithologies at Lac Périgny as part of the Poulin de Courval Mangerite (Hébert & Cadieux, 2003), although local sampling in this study points to the occurrence of massive grey anorthosite rocks in the area, similar to the Vanel Anorthosite. In the center of the study area (Fig.4.1) outcrops the pink, andesine-type dome-shaped Mattawa Anorthosite (Owens & Dymek, 2005), where

lenses of Fe-Ti-P mineralization (used for determining the age of the massif) occur at the interface of the Vanel Anorthosite. Alternatively, this border was interpreted as the interface between the core and border of the Mattawa Anorthosite massif by Owens & Dymek (2005) as the Vanel anorthosite was not known at that time. In this study, we found Fe-Ti-P mineralization within the Mattawa Anorthosite itself. It contains hemo-ilmenite + magnetite + apatite as lenses of oxide-apatite-norite (Table 4.1), similar to the cumulates observed at zone III of the Lac Mirepoix mineralization (Miloski et al. 2023b) and the border of the Lac à l'Orignal deposit (Miloski et al. 2023a), in the nearby Vanel Anorthosite.

The Labrieville Alkaline Anorthosite is another andesine-type dome-shaped intrusion, which occurs at the northeastern portion of the Central Grenville (Fig.4.1). It contains Fe-Ti-P mineralization comprising hemo-ilmenite + magnetite + apatite in the form of massive nelsonite layers, and massive hemo-ilmenite absent of magnetite and apatite, hosted in a massive pink anorthosite (Owens et al. 1994; Owens & Dymek, 2001). Both host anorthosite and mineralization shares similarities with those from Mattawa. The Lac Brûlé Fe-Ti-P mineralization (Lavalle & Rioux, 2017) occurs at the core of the Labrieville Anorthosite massif, containing abundant hemo-ilmenite-bearing massive nelsonite layers (Figs.4.3d & 4.3k), with coarse-grained apatite crystals and almost an absence of magnetite. Other mineralized occurrences are present at the north and south margins of the dome-shaped intrusion, as disseminated oxides in anorthosite or small lenses of oxide-apatite norite, containing the association hemo-ilmenite + magnetite + apatite (Table 4.1).

The La Hache Mangerite outcrops at the southwestern portion of the studied area (Fig.4.1c), intruding the Vanel and Lac-Saint-Jean Anorthositic Suites. Its mineralization (Boulianne, 2003) is concentrated in the form of lenses of oxide-apatite-rich mangerite (orthopyroxene-bearing monzonite, Figs.4.3e, 4.3i & 4.3l), dominated by the association ilmenite + magnetite + apatite, in a matrix containing normative K-feldspar and quartz (Table 4.1).

Table 4.1. Overview on the main Fe-Ti-P mineralization and associated host-AMCG-massif in the Central Grenville Province, Quebec

Location		Coordinates		AMCG Age (Ma)	Ore Age (Ma) "This work"	Anorthosite Type	Cumulate Types	Ore Paragenesis	Deposit Type
Deposit / Mineralization	AMCG Suite	UTM-E	UTM-N						
Lac à l'Original	Pipmuacan AMCG Suite Vanel Anorthosite	384535	5437021	1080 ± 2[A]	1069 ± 12[E] 993 ± 13[E]	Andesine	Oxide-apatite-norite Ferrodiorite dykes Apatite-bearing anorthosite	I) Hemo-ilmenite + Magnetite + Apatite (border-OAN, Ferrodiorite dykes) II) Ilmenite + Magnetite + Apatite (core-OAN)	Layered tabular/sill-like intrusion in anorthosite
Lac Mirepoix	Pipmuacan AMCG Suite Vanel Anorthosite	388808	5438818	1080 ± 2[A]	1048 ± 8[F] 964 ± 9[F]	Andesine	Oxide-apatite-norite Massive nelsonite Massive oxides Leuconorite Ferrodiorite dykes Jotunite dykes	I) Hemo-ilmenite (Massive) II) Hemo-ilmenite + Magnetite + Apatite (OAN, Leuconorite, Ferrodiorite/Jotunite dykes) III) Ilmenite + Magnetite + Apatite (Nelsonite)	Layered tabular/lenses of massive ore in anorthosite
Lac de l'Abbondance	Pipmuacan AMCG Suite Vanel Anorthosite	392299	5432637	1080 ± 2[A]	1002 ± 9 **	Andesine	Oxide-apatite-norite Massive nelsonite	I) Hemo-ilmenite + Magnetite + Apatite (OAN) II) Ilmenite + Magnetite + Apatite (Nelsonite)	Layered tabular/lenses of massive ore in anorthosite
L'Étang	Pipmuacan AMCG Suite Vanel Anorthosite	371910	5435680	1080 ± 2[A]	1011 ± 10 **	Labradorite	Leuconorite Massive oxides	Magnetite + Ilmenite	Lenses and disseminated oxides in leuconorite
Lac Périgny	Pipmuacan AMCG Suite Poulin de Courval Mangerite	403226	5432881	1068 ± 3[B]	1115 ± 11 **	Andesine	Oxide-apatite-norite Leuconorite	Ilmenite + Magnetite + Apatite	Lenses and disseminated oxides in anorthosite
Lac Brulé	Valin AMCG Suite Labrieville Alkaline Anorthosite	429698	5470593	1010 ± 2[C] 1016 ± 2[C]	1065 ± 5 **	Andesine	Massive nelsonite Massive oxides	I) Hemo-ilmenite (Massive) II) Hemo-ilmenite + Magnetite + Apatite (Nelsonite)	Massive lenses in anorthosite
Mattawa	Valin AMCG Suite Mattawa Anorthosite	376707	5418903	1016 ± 2[D]	989 ± 7 **	Andesine	Oxide-apatite-norite Leuco-OAN	I) Hemo-ilmenite + Magnetite + Apatite	Lenses and disseminated oxides in anorthosite
La Hache	Valin AMCG Suite La Hache Mangerite	360627	5425240	1010 ± 3[D]	1030 ± 8 **	Andesine / Oligoclase	Oxide-apatite mangerite	Magnetite + Ilmenite + Apatite	Lenses and disseminated oxides in mangerite

A. Hébert et al.(2009). B. Hébert et al.(1998). C. Owens et al.(1994). D. Hébert et al (2005). E. Miloski et al.(2023a). F. Miloski et al.(2023b). ** This work. Abbreviations: OAN - oxide-apatite-norite.

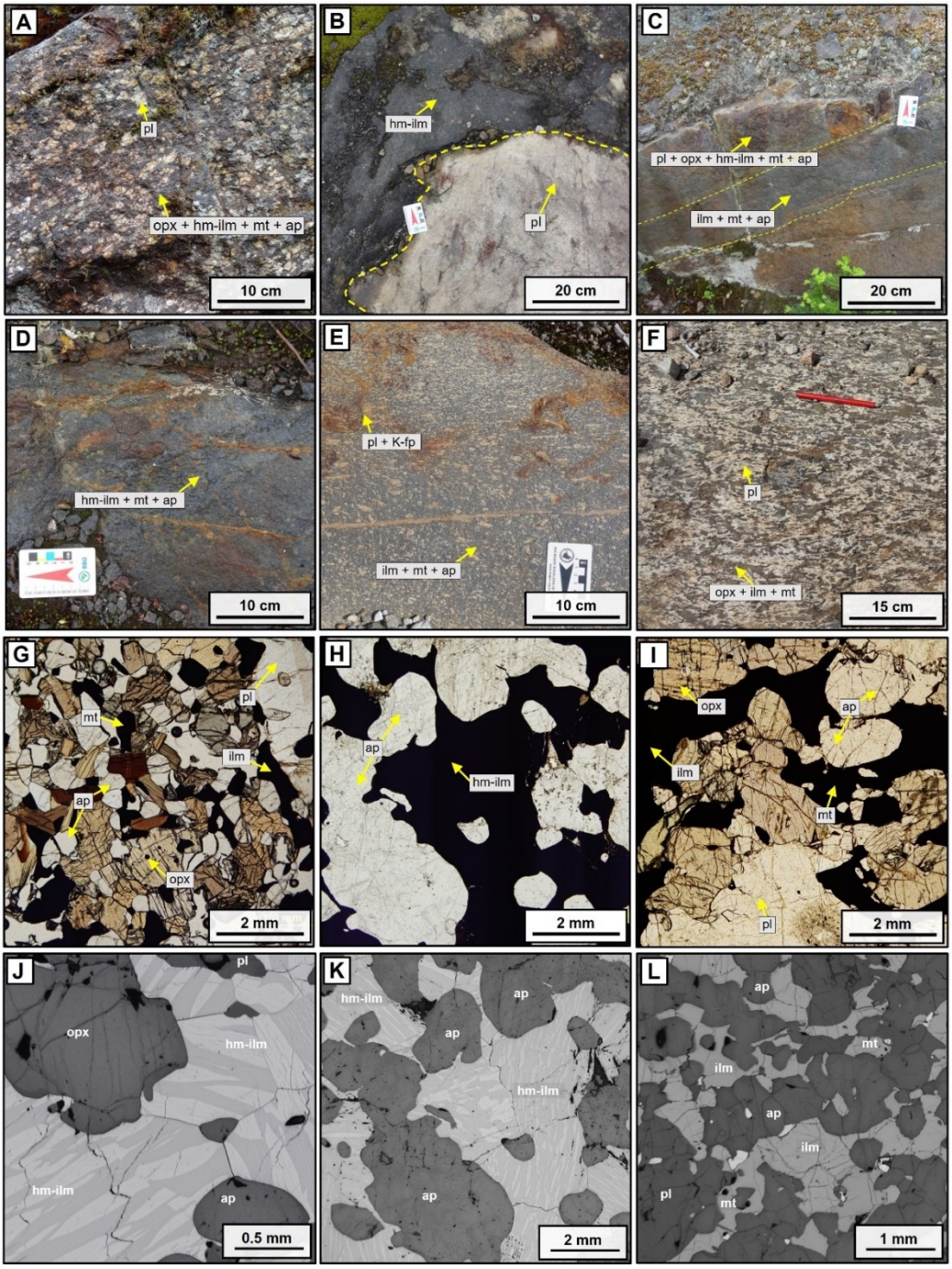

Figure 4.3. a-f. Photographs of representative outcrops and mineralized lithologies used for U-Pb dating in zircon. G-l. Photomicrographs (g-i transmitted light/ j-l reflected light) of the main cumulate types of Fe-Ti-P mineralization in the Central Grenville Province, Quebec. a. Coarse-grained oxide-apatite-norite (OAN) mineralization showing a matrix formed by pyroxene, oxides and apatite surrounding coarser plagioclase (20PM02, Lac à l'Orignal). b. Contact between massive oxide (hemo-ilmenite) lens and the host-andesine anorthosite (20PM05A, Lac Mirepoix). c. Contact between layered oxide-apatite-norite (OAN) and massive-nelsonite (20PM07, Lac Mirepoix). d. Massive nelsonite layer in anorthosite (20PM38, Lac Brûlé). e. Layered coarse-grained oxide-apatite-rich mangerite (21PM07, La Hache Mangerite). f. Coarse-grained leuconorite, dominated by large-OPX and a matrix of plagioclase, magnetite and ilmenite; absence of apatite (21PM55, L'Étang). Mineral abbreviations: pl = plagioclase; ox = oxides; opx = orthopyroxene. g. Medium-grained apatite-rich oxide-apatite-norite (OAN) (20PM25, Lac Périgny). h. Coarse-grained massive nelsonite (20PM07, Lac Mirepoix). i. Coarse-grained oxide-apatite-rich mangerite (21PM07, La Hache). j. Medium grained oxide-apatite norite (OAN) dominated by hemo-ilmenite containing coarse exsolution lamellae of hematite (pale) and ilmenite (dark) and minor magnetite (LO-10, Lac à l'Orignal). k. Coarse-grained apatite-rich nelsonite dominated by hemo-ilmenite and absence of magnetite (20PM38A, Lac Brûlé). l. Oxide-apatite-rich mangerite dominated by ilmenite (hematite exsolution-free), magnetite and apatite (21PM09, La Hache). Mineral abbreviations: opx – orthpopyroxene; pl – plagioclase; hm-ilm – hemo-ilmenite; mt – magnetite; ap – apatite; ilm – ilmenite; K-fp – K-feldspar.

4.5 Sampling and analytical methods

Eighty-two samples covering the different mineralization and host-lithologies (Fig.4.1b), including outcrops and boreholes, were selected for detailed lithological description of the massive oxides (n = 11), nelsonite (n = 10), leuconorite (n = 7), oxide-apatite norite (OAN) (n = 22), anorthosite (n = 20) and mangerite (n = 12) units. A subset of a hundred and fourty-six samples have been incorporated from previous work at the Lac à l'Orignal deposit and the Lac Mirepoix mineralisation (Miloski et al 2023a,b). Thirty-two samples have been selected for petrographic descriptions and modal mineral abundance estimates from polished thin sections using an optical microscope. A subset of ten samples, covering the different Fe-Ti-P mineralization, were selected for element mapping using the Bruker - Tornado M4 micro-X-Ray fluorescence (μXRF) analysis at Université Laval, Quebec. Thirty-four samples were selected for the determination of major and trace elements by whole rock, following the protocol, and carried out at the same time as those described in Miloski et al. (2023a,b) after Barnes & Mansur (2020). The major and trace element geochemistry of plagioclase, apatite, ilmenite and magnetite were determined in-situ by LA-ICP-MS at LabMaTer, UQAC on polished thin sections, following the same protocol (and at the same time) as that of Miloski et al. (2023a,b). A subset of a hundred and twenty-eight samples were analyzed by portable XRF for major and minor element geochemistry of plagioclase, following the method described in Miloski et al. (2023b). Six mineralized samples from Lac Périgny, Lac de l'Abbondance, L'Étang, Lac Brûlé, Mattawa and La Hache locations were selected for zircon U-Pb dating, following the methods described by Miloski et al. (2023 a,b). Zircon Lu-Hf isotopic data were acquired on the same ten mineralized samples analyzed for U-Pb dating. Zircon separation, preparation and U-Pb analysis, by LA-high resolution-ICP-MS followed the protocol of Perrot et al. (2017), and was conducted at the GEOTOP labs in the Université du Québec à Montréal (UQAM). Hf

isotopic analyses were carried out on the same zircon grains used for the dating, by LA-MC-ICP-MS at the University of Geneva, Switzerland. Details of the analytical methods, instrumentation and evaluation of the data quality are discussed in detail in Appendix 4.1.

4.6 Results

4.6.1 Characterization of the Fe-Ti-P mineralization

The characterization of the Fe-Ti-P mineralization, from the different localities in the Central Grenville Province, including cumulate type and ore paragenesis are summarized in Table 4.1. This is based on field and petrographic observations (both macro and microscale, Appendix 4.2), μXRF mineral maps and whole rock data (Appendix 4.3). Overall, the mineralization is (hemo)-ilmenite-apatite-bearing, containing significant amounts of each of these mineral phases (>5-10%), with variable modal proportions of plagioclase, orthopyroxene, magnetite, and minor amounts of primary biotite, hornblende ± K-feldspar (Fig.4.3, Appendix 4.3). Representative whole-rock data is presented in Table 4.4 and the complete dataset is in Appendix 4.2.

The whole rock compositions of Fe_2O_3, TiO_2 and P_2O (Appendix 4.3) reflect the mineral proportions of the main cumulus phases between the different Fe-Ti-P mineralization (Table 4.1). Whole rock Ti and Fe contents, plotted in Figure 4.4a, show that overall massive oxides mostly have a higher Ti/Fe ratio in relation to apatite-bearing cumulates, which plot on a low Ti/Fe trend. Miloski et al. (2023a,b) characterized the presence of different oxide in the Lac à l'Orignal and Lac Mirepoix intrusions, in which an evolutionary trend can be traced from high-Ti/Fe towards low-Ti/Fe cumulates, due to fractionation of ferrodiorite magmas through crystallization of prior (hemo)-ilmenite and plagioclase, followed by magnetite and apatite. Samples plotting on the high Ti/Fe trend are massive hemo- ilmenite cumulates containing lower proportions of magnetite, such as

massive oxides from Lac Tio Ti mine (Charlier et al. 2010), the base of the Grader Intrusion (Charlier et al. 2008), and zone I of Lac Mirepoix (Miloski et al. 2023b) (Fig.4.4a). Cumulates that plot on the low-Ti/Fe trend are apatite-bearing cumulates, such as nelsonites and oxide-apatite-(gabbro)-norites (OAN) containing higher proportions of magnetite (Fig.4.4a), from Lac à l'Orignal Fe-Ti-P deposit (Miloski et al. 2023a), zones II and III of Lac Mirepoix (Miloski et al. 2023b) and the top part of the Grader Intrusion (Charlier et al. 2008). Moreover, Miloski et al. (2023a,b) have noticed that a few massive oxides from Lac à l'Orignal and Lac Mirepoix also have low Ti/Fe ratios (Fig.4.4a), due to higher-amounts of magnetite and presence of Fe-poor ilmenite instead of hemo-ilmenite. The presence or absence of hematite exsolutions in ilmenite depends on the amount of magnetite present (Miloski et al. 2023a). When magnetite occurs in higher amounts (as in oxide-apatite-norites), a decrease in the amount of hematite exsolutions is clearly observed at the border of the ilmenite in contact with the magnetite (Fig.4.3k; Appendix 4.3) due to inter-oxide reequilibration (Miloski et al. 2023a).

The majority of massive oxides from this study are hemo-ilmenite-bearing (with thick hematite exsolutions, Appendix 4.3), due to the lower amount of magnetite in comparison to that in apatite-bearing lithologies (OAN and nelsonite cumulates). Massive oxides at Lac Brûlé have high Fe_2O_{3t} (54.6 – 81.3%), TiO_2 (31.2 – 34.1%) and V (1723 - 2014 ppm) contents and lowest CaO (4.2 – 17.1%) and P_2O_5 (0.1 – 0.4%) values among all of the mineralized samples due to a much higher proportion of oxides and very low proportions of plagioclase and apatite, respectively. These cumulates are predominantly hemo-ilmenite (>70%)-dominated with minor (<5%) Fe-poor ilmenite, Ti-poor magnetite (absent of ilmenite exsolutions), Al-spinel, plagioclase, orthopyroxene and biotite (Fig.4.3b). They plot on the low Ti/Fe trend, similar to zone I of the Lac Mirepoix Fe-Ti-P mineralization (Appendix 4.2 & Fig.4.4a; Miloski et al. 2023b).

The presence of abundant cumulus apatite generates massive nelsonite layers, (piam-C, Figs.4.3d, 4.3h & 4.3k) with the highest P_2O_5 (2.1 – 17.1%) and CaO values (2.9 – 20.5%), as at Lac de l'Abbondance and Lac Brûlé, dominated by cumulus (hematite-free) ilmenite (25-40%), magnetite (25-30%), apatite (20-40%) and minor plagioclase (5-10%), orthopyroxene (10-15%) and Al-spinel (1-3%). Massive nelsonites at Lac de l'Abbondance occur within medium to coarse-grained apatite-bearing oxide-apatite-norite (OAN) layers/lenses (phiam-C, Fig.4.3c-d, 4.3g & 4.3j); a similar association occurs at Lac Mirepoix (Miloski et al. 2023b). Nelsonites associated with the younger AMCGs in the Central Grenville (e.g., Vanel Anorthosite: Lac de l'Abbondance, Lac à l'Orignal and Lac Mirepoix), plot on the low-Ti/Fe trend (Fig.4.4a). As such, ilmenite is overall hematite-exsolution free, reflecting its higher magnetite/ilmenite ratio, containing the association ilmenite + magnetite + apatite (Miloski et al. 2023a,b). An exception is the coarse-grained nelsonites from Lac Brûlé (Labrieville Anorthosite) which are unusually poor in magnetite, and more enriched in apatite, having the association hemo-ilmenite + apatite ± magnetite (Table 4.1). At Lac Brûlé, nelsonites part of the high-Ti/Fe system similar to its associated hemo-ilmenite-bearing massive oxides (Fig.4.4a).

Oxide-apatite-norite (OAN) cumulates are the most frequently apatite-bearing cumulates observed in Fe-Ti-P mineralization associated with the Pipmuacan and Valin AMCG suites, which have been described in detailed by Miloski et al. (2023a,b) at Lac à l'Orignal, and Lac Mirepoix (Vanel Anorthosite). The oxide-apatite-norite cumulates, including those from the mineralized mangerite at La Hache, have lower Fe_2O_{3t} (11.8 – 47.2%), TiO_2 (1.8 – 14.7%), V (11– 1050 ppm), and higher SiO_2 (12.5– 50.6%), MgO (2.8 – 10.9%) and K_2O (0.02– 2.1%) contents in relation to massive oxides and nelsonites, reflecting lower proportions of Fe-Ti oxides and higher concentrations of plagioclase and orthopyroxene. The OAN contain the association (hemo)-ilmenite + plagioclase +

orthopyroxene + magnetite + apatite (Figs.4.3c-d, 4.3g & 4.3j). Overall, OAN from Lac Périgny, Lac de l'abbondance, Lac Brûlé and Mattawa plot along the low-Ti/Fe (Fig.4.4a). Exceptionally, a few hemo-ilmenite-rich OAN samples from the Mattawa Anorthosite plot on the high-Ti/Fe (Fig.4.4a) trend, between the fields of massive oxides and OAGN from Grader Lake, due to lower amounts of apatite and magnetite in relation to hemo-ilmenite compared to the other OAN mineralization. The La Hache Fe-Ti-P mineralization contains OAN layers hosted in mangerite instead of anorthosite, having higher amounts of apatite (10-20%), (hemo)-ilmenite (10-15%) and magnetite (10-15%) in association with normative orthopyroxene, quartz and K-feldspar phases (<10%) (Appendix 4.3), if compared to OAN in anorthosite. These mangerite-hosted OAN also plot on the low-Ti/Fe trend (Fig.4.4a), similar to OAN cumulates hosted in anorthosites.

Leuconorites at L'Étang (Vanel Anorthosite) are absent of apatite, containing high amounts of orthopyroxene and plagioclase (25-55%) and low ilmenite and Ti-magnetite (5-10%). They plot near the OAN cumulates on the low-Ti/Fe trend (Fig.4.4a), containing high SiO_2 (35.9 – 53%), MgO (2.2 – 16.2%) and K_2O (0.4 – 2.6%), as well as relatively low Fe_2O_{3t} (8.7 – 27.5%), TiO_2 (0.8 – 7.6%) and V (45 – 785 ppm) contents.

Fine-grained dykes (Miloski et al. 2023a,b) have the same mineralogy of OAN cumulates, being enriched in Fe_2O_3 (6.4 – 32.4%), TiO_2 (1.3 -7.0%) and P_2O_5 (0.8 – 7.0%) whereas their SiO_2 contents vary from 28.0 – 58.0%, characteristic of other ferrodiorite/jotunite dykes associated with anorthosite massifs elsewhere (Charlier et al. 2008).

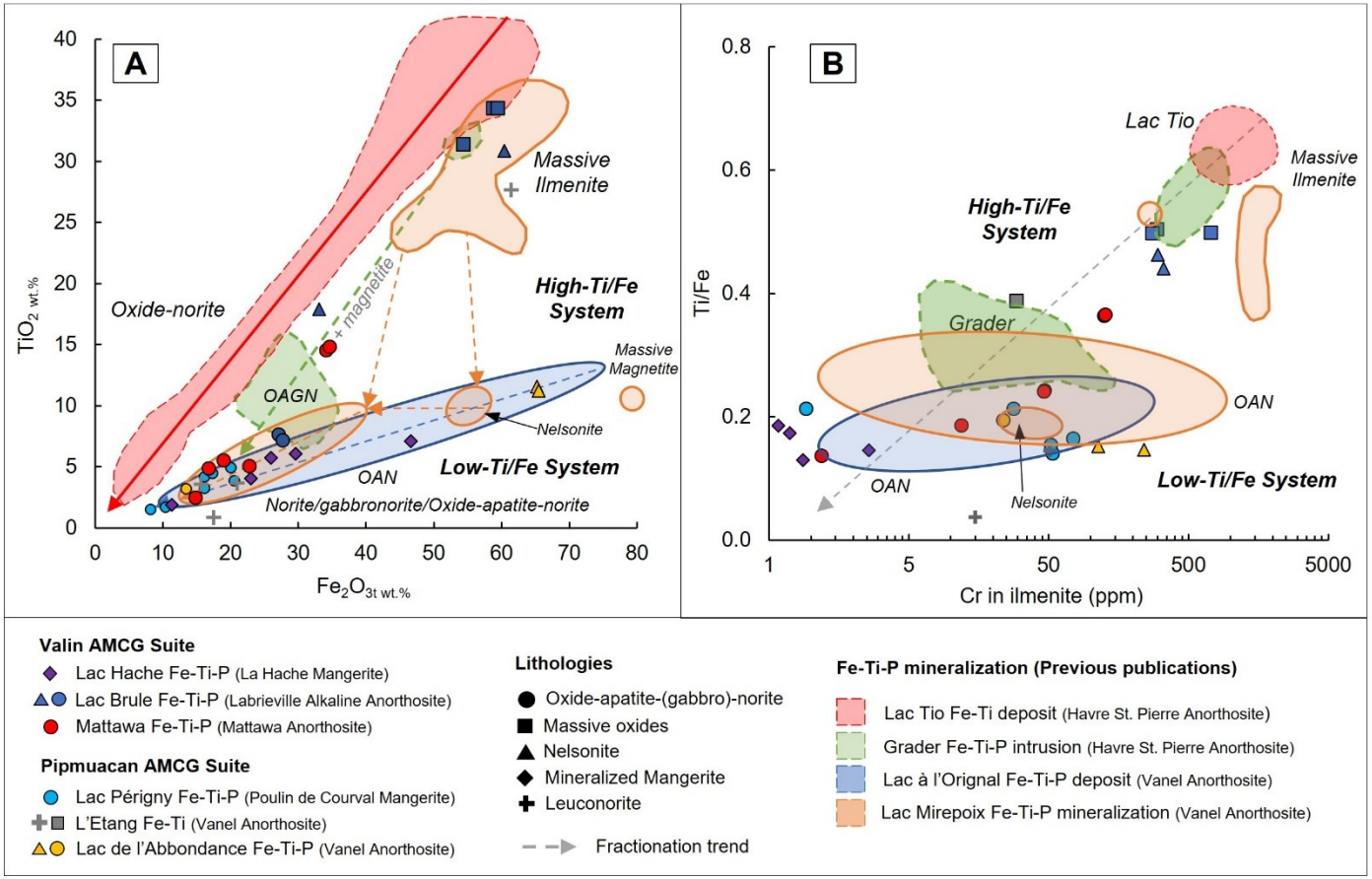

Figure 4.4. Geochemical comparison of Fe-Ti-(P) mineralization in the Central Grenville Province, Quebec (this study) with previous published data of nearby locations: Lac à l'Orignal Fe-Ti-P deposit (blue field, Miloski et al. 2023a), the Lac Mirepoix Fe-Ti-P mineralization(orange field, Miloski et al. 2023b), the Lac Tio Ti deposit (red field) and the Fe-Ti-P mineralization at Grader Intrusion (green field), in the Havre-Saint-Pierre Anorthositic Suite, Quebec (data from Charlier at al. 2010; 2008). A. Whole-rock Fe_2O_{3t} vs. TiO_2. B. Ti/Fe whole rock ratio vs. Cr content of ilmenite (in ppm).

4.6.2 U-Pb Zircon ages of Fe-Ti-P mineralization

U–Pb results for zircon analyzed from Fe-Ti-P mineralization at Lac Brûlé and Lac de l'Abbondance (massive nelsonite), L'Étang (leuconorite), Lac Périgny and Mattawa (oxide-apatite-norite), and La Hache (oxide-apatite-mangerite) are presented in Table 4.2, and are compared to oxide-apatite-norite mineralization from Lac à l'Orignal and Lac Mirepoix (Miloski et al. 2023a,b). Concordia diagrams are presented in Figure 4.5a, where all ages are calculated with 2σ uncertainty. These samples comprise subhedral prismatic to anhedral igneous zircons, and their cathodoluminescence photomicrographs (see some examples on Fig.4.5b; Appendix 4.2) show that they do not contain obvious cores or metamorphic recristallization but sector zoning can be observed in some of them. However, the samples from Lac Brûlé, L'Étang, La Hache and Mattawa Fe-Ti-P mineralization presented two populations of zircons, with several inherited older zircon ages that have been excluded from the Concordia ages calculation (Fig.4.5a and Appendix 4.3). Weighted mean diagrams with concordant ages for each sample are shown in Appendix 4.3. In general, the obtained U-Pb ages for Fe-Ti-P mineralization are within the range of previous ages of the Pipmuacan, Grande Pointes, Peribonka and Valin AMCG suites (1080-960Ma, Fig.4.2). An exception is observed at the Lac Périgny mineralization, which presents an older age (1115 ± 11 Ma, MSWD = 2.5, n=20/25) for the area, closer to the age of the Lac-Saint-Jean Anorthositic Suite (1160-1140Ma, Higgins & Van Breemen, 1992; 1996).

Pipmuacan AMCG type ages (1080 – 1040 Ma) were obtained for oxide-apatite-norite in the La Hache Mangerite (concordia age of 1029 ± 8 Ma (MSWD = 1.3, n=22/24) (Fig.4.5a) and the massive nelsonite at Lac Brûlé (Labrieville Anorthosite; concordia age of 1065 ± 5 Ma; MSWD = 1.2, n=12/25). However, nelsonite analyzed at Lac Brûlé contained a few zircons excluded from the concordia age calculation, as they represent inherited older cores (> 1200Ma, Fig.4.5a), or younger analyses scattering down the concordia curve

considered to be affected by Pb loss, with the latter grains closer to the host Labrieville Anorthosite massif and Rigolet metamorphic ages (1010Ma-850Ma). Younger ages, considered as Valin AMCG type ages (around 1000Ma) were obtained for Fe-Ti leuconorite mineralization at L'Étang (1011 ± 10 Ma, MSWD = 6.8, n=8/16) and OAN from Lac de l'Abbondance (1002 ± 9 Ma, MSWD = 1.4, n=13/15) associated with the Vanel Anorthosite and OAN from the core of Mattawa Anorthosite (989 ± 7 Ma, MSWD = 13, n=16/25) (Fig.4.5).

Table 4.2. Zircon U–Pb LA-ICP-MS analytical data of Fe-Ti-P mineralization in the Central Grenville Province, Quebec

LPR-01 - Lac Périgny Fe-Ti-P mineralization: sample 20PM23 - oxide-apatite norite. Concordia age: 1114 ± 11 Ma											
#Grain	U_{ppm}	Pb_{ppm}	Th/U	$^{206}Pb/^{204}Pb$	Isotopic ratios ±1se (%)			Apparent ages ±2se (abs)			Rho
					$^{206}Pb/^{238}U$	$^{207}Pb/^{235}U$	$^{207}Pb/^{206}Pb$	$^{206}Pb/^{238}U$	$^{207}Pb/^{235}U$	$^{207}Pb/^{206}Pb$	
GC-LPR-01_1	116	6606	1.0	-208.2	0.17073 ± 3.1	1.78757 ± 4.4	0.07428 ± 4.1	1,012.7 ± 57.0	1,032.3 ± 58.2	968.1 ± 173.4	0.41495
GC-LPR-01_2	43	2591	0.6	-93.6	0.18508 ± 3.3	1.91029 ± 5.7	0.07571 ± 5.5	1,088.0 ± 64.4	1,044.6 ± 71.5	930.5 ± 206.0	0.21350
GC-LPR-01_3	107	6077	0.2	-248.2	0.17406 ± 2.5	1.72285 ± 4.1	0.06747 ± 3.2	1,030.7 ± 48.1	990.6 ± 50.8	787.8 ± 147.7	0.54221
GC-LPR-01_4	32	1906	0.5	-63.2	0.18743 ± 3.2	2.1727 ± 6.3	0.08404 ± 6.1	1,139.5 ± 77.3	1,131.9 ± 84.8	925.6 ± 263.8	0.36176
GC-LPR-01_5	18	1030	0.3	-53.5	0.18180 ± 3.2	1.91552 ± 8.9	0.07049 ± 7.8	1,070.6 ± 62.0	963.2 ± 118.4	640.2 ± 338.6	0.34054
GC-LPR-01_6	47	2685	0.5	-157.5	0.19089 ± 2.9	2.06083 ± 5.0	0.07662 ± 4.5	1,120.5 ± 60.1	1,098.1 ± 70.1	943.0 ± 221.9	0.26199
GC-LPR-01_7	55	3048	0.7	-153.7	0.19256 ± 3.2	1.96282 ± 5.3	0.07454 ± 5.0	1,128.2 ± 66.1	1,079.8 ± 64.5	941.4 ± 188.9	0.21969
GC-LPR-01_8	46	2464	0.7	-152.1	0.19010 ± 3.4	1.7971 ± 5.5	0.06919 ± 5.0	1,115.3 ± 68.9	1,023.8 ± 76.5	1,023.8 ± 77.5	0.39039
GC-LPR-01_9	52	2811	0.5	-447.4	0.19211 ± 2.9	2.05264 ± 4.7	0.07650 ± 3.9	1,127.1 ± 60.0	1,114.7 ± 66.5	978.4 ± 181.6	0.46033
GC-LPR-01_10	40	2323	0.5	-832.2	0.19584 ± 2.7	2.01701 ± 5.0	0.07196 ± 5.2	1,147.9 ± 56.3	1,083.5 ± 70.0	772.8 ± 229.3	0.27829
GC-LPR-01_11	40	2090	0.5	381.7	0.19603 ± 3.2	2.17298 ± 5.5	0.08043 ± 5.6	1,147.0 ± 65.6	1,115.5 ± 75.1	906.6 ± 252.2	0.32062
GC-LPR-01_12	67	3376	0.7	172.0	0.18864 ± 3.0	1.91871 ± 4.5	0.07552 ± 4.4	1,108.1 ± 60.9	1,063.4 ± 60.3	922.7 ± 180.3	0.51163
GC-LPR-01_13	158	7745	1.0	245.7	0.18502 ± 2.8	1.85651 ± 3.4	0.07418 ± 3.2	1,099.0 ± 58.2	1,062.2 ± 47.4	940.1 ± 142.6	0.47110
GC-LPR-01_14	190	9831	0.2	158.1	0.19280 ± 2.8	2.02384 ± 3.8	0.07433 ± 3.2	1,131.0 ± 58.6	1,100.0 ± 46.9	941.5 ± 130.2	0.37261
GC-LPR-01_15	61	2773	0.6	-0.4	0.17654 ± 3.1	1.84033 ± 4.7	0.07620 ± 4.3	1,042.4 ± 58.8	1,031.1 ± 62.8	982.2 ± 196.9	0.20918
GC-LPR-01_16	61	2814	0.7	31.6	0.17840 ± 2.5	1.93710 ± 4.0	0.07861 ± 3.9	1,154.5 ± 48.6	1,063.5 ± 55.8	1,063.5 ± 55.8	0.50969
GC-LPR-01_17	42	2050	0.5	14.8	0.18994 ± 2.8	1.93510 ± 5.6	0.08595 ± 5.6	1,115.9 ± 56.5	1,039.0 ± 75.2	1,139.0 ± 75.2	0.02906
GC-LPR-01_18	51	2448	0.6	-7.4	0.19438 ± 2.7	1.79710 ± 5.2	0.07132 ± 5.0	1,140.2 ± 55.3	1,066.3 ± 64.5	1,066.3 ± 71.7	0.30863
GC-LPR-01_19	60	2702	0.6	-3.3	0.19206 ± 3.0	1.99981 ± 5.0	0.07497 ± 4.8	1,126.7 ± 61.3	1,080.4 ± 71.3	876.3 ± 224.0	0.32599
GC-LPR-01_20	70	3174	0.8	30.9	0.18865 ± 2.3	1.93073 ± 4.5	0.07541 ± 4.6	1,110.5 ± 46.9	1,080.5 ± 59.4	929.6 ± 197.2	0.11061
GC-LPR-01_21	96	3631	0.7	-44.4	0.17112 ± 2.7	1.69483 ± 4.9	0.07263 ± 4.7	1,014.9 ± 50.8	987.1 ± 64.9	888.8 ± 199.8	0.28347
GC-LPR-01_22	49	1997	0.7	12.4	0.19378 ± 3.1	2.27354 ± 5.9	0.08718 ± 6.1	1,135.3 ± 63.6	1,140.8 ± 78.2	983.7 ± 265.8	0.00459
GC-LPR-01_23	73	2904	0.4	-48.5	0.20764 ± 3.9	2.08085 ± 5.9	0.07631 ± 4.8	1,219.2 ± 87.6	1,119.2 ± 84.0	909.0 ± 214.6	0.54428
GC-LPR-01_24	27	1106	0.4	-12.5	0.20308 ± 4.2	2.28851 ± 6.8	0.08715 ± 7.2	1,179.3 ± 87.9	1,140.2 ± 102.1	839.1 ± 368.4	0.16559
GC-LPR-01_25	67	2492	0.6	-68.9	0.18500 ± 3.2	1.82458 ± 5.1	0.07151 ± 4.7	1,087.8 ± 63.1	1,012.3 ± 64.2	855.4 ± 231.3	0.32758

Table 4.2. (cont.) Zircon U–Pb LA-ICP-MS analytical data of Fe-Ti-P mineralization in the Central Grenville Province, Quebec

LAB-01 - Lac de l'Abbondance Fe-Ti-P mineralization: sample 20PM47 - nelsonite. Concordia age: 1001 ± 9 Ma											
#Grain	U_{ppm}	Pb_{ppm}	Th/U	$^{206}Pb/^{204}Pb$	Isotopic ratios ±1se (%)			Apparent ages ±2se (abs)			Rho
					$^{206}Pb/^{238}U$	$^{207}Pb/^{235}U$	$^{207}Pb/^{206}Pb$	$^{206}Pb/^{238}U$	$^{207}Pb/^{235}U$	$^{207}Pb/^{206}Pb$	
GC-LAB-01_6	137	21790	0.9	243.4	0.17298 ± 1.5	1.73562 ± 2.2	0.07286 ± 2.0	1,027.2 ± 28.9	1,019.2 ± 29.0	991.0 ± 86.7	0.40595
GC-LAB-01_7	1464	227530	0.6	131.5	0.17298 ± 2.1	1.66542 ± 1.9	0.07311 ± 1.5	1,003.9 ± 39.4	992.1 ± 22.8	1,001.5 ± 60.7	0.75213
GC-LAB-01_8	262	40483	0.2	-18.7	0.16700 ± 1.6	1.66542 ± 2.1	0.06948 ± 1.7	1,000.3 ± 32.1	968.5 ± 25.3	902.2 ± 71.7	0.65254
GC-LAB-01_9	114	17206	0.7	-335.1	0.16508 ± 1.9	1.66344 ± 2.4	0.07416 ± 2.2	983.2 ± 35.4	992.7 ± 31.8	999.6 ± 90.4	0.64387
GC-LAB-01_10	31	4891	1.2	-72.6	0.17352 ± 2.1	1.65456 ± 4.0	0.06969 ± 3.9	1,039.3 ± 44.4	983.2 ± 53.4	803.0 ± 184.9	0.30786
GC-LAB-01_11	16	2490	0.3	-129.3	0.17574 ± 2.8	1.74618 ± 6.0	0.07315 ± 5.9	1,039.3 ± 53.6	994.1 ± 79.0	899.7 ± 227.5	0.25309
GC-LAB-01_12	34	5416	0.7	772.0	0.17359 ± 1.9	1.62838 ± 3.8	0.07035 ± 3.8	1,029.8 ± 35.6	966.3 ± 50.4	770.6 ± 182.3	0.45526
GC-LAB-01_13	31	4673	0.4	249.7	0.16660 ± 2.3	1.65572 ± 5.3	0.07641 ± 5.4	991.2 ± 41.3	981.5 ± 66.0	880.3 ± 236.1	0.32572
GC-LAB-01_14	314	44835	0.1	1095.1	0.15791 ± 1.9	1.57314 ± 2.2	0.07131 ± 1.6	943.5 ± 32.5	952.8 ± 26.2	972.3 ± 71.4	0.62938
GC-LAB-01_15	26	3809	2.1	60.5	0.16613 ± 2.0	1.72920 ± 5.5	0.07478 ± 4.5	996.9 ± 39.7	969.0 ± 72.1	932.7 ± 188.2	0.47896
GC-LAB-01_16	15	2173	0.9	-1.4	0.16365 ± 3.1	1.76083 ± 7.4	0.08034 ± 7.7	974.8 ± 55.4	988.3 ± 96.8	953.9 ± 345.8	0.15701
GC-LAB-01_17	85	12299	0.4	-89.5	0.16572 ± 1.8	1.75829 ± 3.1	0.07765 ± 2.9	986.9 ± 32.0	1,020.3 ± 41.6	1,058.9 ± 126.9	0.35648
GC-LAB-01_18	1537	205510	0.8	-2871.7	0.15162 ± 1.4	1.54168 ± 1.6	0.07406 ± 1.2	909.2 ± 23.3	942.9 ± 20.6	1028.1 ± 46.7	0.83594
GC-LAB-01_19	141	20227	0.3	-503.0	0.16613 ± 2.0	1.68534 ± 3.2	0.07257 ± 2.4	988.6 ± 36.7	986.4 ± 40.4	936.8 ± 100.7	0.72424
GC-LAB-01_20	38	5522	1.1	-334.4	0.16879 ± 2.0	1.65370 ± 4.4	0.07212 ± 4.4	1,003.2 ± 37.1	960.6 ± 54.2	838.9 ± 186.9	0.25402

Table 4.2. (cont.) Zircon U–Pb LA-ICP-MS analytical data of Fe-Ti-P mineralization in the Central Grenville Province, Quebec

LHC-1 - La Hache Fe-Ti-P mineralization: sample 20PM07 - oxide-apatite-rich mangerite. Concordia age: 1029 ± 8 Ma											
#Grain	U_{ppm}	Pb_{ppm}	Th/U	$^{206}Pb/^{204}Pb$	Isotopic ratios ±1se (%)			Apparent ages ±2se (abs)			Rho
					$^{206}Pb/^{238}U$	$^{207}Pb/^{235}U$	$^{207}Pb/^{206}Pb$	$^{206}Pb/^{238}U$	$^{207}Pb/^{235}U$	$^{207}Pb/^{206}Pb$	
GC-LHC-01_1	22	3148	0.6	-134.0	0.16710 ± 1.8	1.68293 ± 5.6	0.07345 ± 5.2	994.3 ± 33.7	986.4 ± 69.6	929.9 ± 218.4	0.20236
GC-LHC-01_2	23	3420	0.7	132.5	0.17658 ± 2.2	1.64559 ± 5.8	0.07029 ± 5.7	1,045.8 ± 41.9	969.0 ± 74.6	610.9 ± 248.7	0.46671
GC-LHC-01_3	32	4664	0.4	83.1	0.17092 ± 2.2	1.76740 ± 4.0	0.07914 ± 4.3	1,014.4 ± 41.7	1,025.2 ± 53.2	1,063.6 ± 169.7	0.36862
GC-LHC-01_4	53	7494	1.3	158.8	0.16700 ± 1.9	1.67888 ± 3.5	0.07528 ± 3.2	1,000.6 ± 37.2	997.3 ± 44.8	1,032.4 ± 123.3	0.41644
GC-LHC-01_5	25	3667	0.9	66.2	0.17660 ± 2.1	1.73425 ± 5.0	0.07372 ± 4.8	1,054.0 ± 42.5	987.7 ± 65.8	823.6 ± 232.7	0.27176
GC-LHC-01_6	23	3318	0.7	42.5	0.16915 ± 2.1	1.65983 ± 6.2	0.07271 ± 5.8	1,005.0 ± 38.7	941.6 ± 79.6	914.6 ± 215.5	0.25818
GC-LHC-01_7	14	2013	0.6	46.3	0.17051 ± 2.5	1.90472 ± 5.7	0.08630 ± 6.3	1,011.8 ± 46.5	1065.3 ± 89.3	1,207.6 ± 259.4	0.08619
GC-LHC-01_8	13	1863	0.7	3.8	0.17456 ± 2.2	1.74472 ± 6.0	0.07525 ± 6.2	1,034.2 ± 42.8	987.6 ± 89.5	843.8 ± 294.9	-0.00145
GC-LHC-01_9	15	2175	0.5	24.1	0.17507 ± 2.1	1.72520 ± 5.2	0.07605 ± 5.5	1,037.5 ± 39.2	978.8 ± 71.5	1,003.5 ± 216.8	0.11410
GC-LHC-01_10	31	4761	0.7	60.7	0.17690 ± 2.1	1.68798 ± 4.4	0.06854 ± 4.1	1,047.3 ± 40.9	973.0 ± 55.7	725.1 ± 191.6	0.31715
GC-LHC-01_11	16	2407	0.5	34.5	0.17638 ± 2.1	1.80778 ± 5.5	0.07831 ± 5.5	1,044.5 ± 40.6	1,016.3 ± 78.3	1,039.9 ± 197.2	0.29262
GC-LHC-01_12	27	4142	0.7	24.5	0.18357 ± 2.4	1.82312 ± 4.3	0.07475 ± 4.0	1,083.0 ± 46.5	1,042.8 ± 55.8	871.4 ± 198.2	0.43155
GC-LHC-01_13	34	4898	1.0	68.3	0.16569 ± 2.0	1.74408 ± 4.3	0.07710 ± 4.1	992.7 ± 34.6	993.7 ± 56.5	1,083.6 ± 150.5	0.38828
GC-LHC-01_14	18	2557	0.6	41.6	0.17669 ± 2.8	1.68866 ± 6.9	0.07309 ± 6.7	1,044.4 ± 53.0	944.2 ± 97.3	880.0 ± 285.6	0.10280
GC-LHC-01_15	18	2775	0.4	120.9	0.17819 ± 2.2	1.86835 ± 6.2	0.07700 ± 5.7	1,054.2 ± 42.4	1,011.8 ± 85.3	1,084.2 ± 203.4	0.22628
GC-LHC-01_16	15	2328	0.6	1343.3	0.18120 ± 2.4	1.76098 ± 7.0	0.07002 ± 6.0	1,070.1 ± 46.5	979.8 ± 92.3	788.0 ± 264.0	0.39965
GC-LHC-01_17	13	2192	0.4	-166.8	0.19189 ± 2.6	1.78337 ± 7.2	0.07177 ± 7.3	1,127.0 ± 53.8	974.2 ± 92.9	831.7 ± 279.8	0.32819
GC-LHC-01_19	18	2886	0.4	-39.4	0.18697 ± 2.8	1.89430 ± 5.7	0.07663 ± 5.5	1,100.1 ± 54.8	1,029.2 ± 80.8	1,038.4 ± 197.8	0.27147
GC-LHC-01_20	33	5254	0.9	-34.1	0.17405 ± 2.2	1.76133 ± 3.8	0.07441 ± 3.8	1,040.4 ± 45.3	1,015.3 ± 50.9	984.4 ± 146.7	0.33616
GC-LHC-01_21	31	4916	1.0	-22.9	0.17653 ± 2.5	1.76561 ± 4.2	0.07644 ± 3.9	1,044.4 ± 46.6	1,030.3 ± 54.9	952.7 ± 170.1	0.43052
GC-LHC-01_22	16	2589	0.4	-27.6	0.16966 ± 2.3	1.81273 ± 6.0	0.08389 ± 6.0	1,008.2 ± 42.5	1033.6 ± 91.3	1,048.6 ± 251.8	0.53069
GC-LHC-01_23	16	2659	0.4	-21.4	0.17884 ± 2.5	1.68033 ± 6.2	0.06937 ± 5.9	1,057.0 ± 47.9	979.2 ± 75.9	795.6 ± 247.4	0.15312
GC-LHC-01_24	21	3543	0.7	-42.4	0.17947 ± 2.1	1.77955 ± 4.3	0.07348 ± 4.2	1,061.4 ± 40.9	1,015.7 ± 60.5	868.9 ± 188.4	0.33509
GC-LHC-01_25	20	3302	0.6	-71.5	0.16979 ± 1.8	1.66832 ± 4.7	0.07253 ± 4.6	1,009.3 ± 32.6	969.3 ± 64.8	778.9 ± 220.4	0.28682

Table 4.2. (cont.) Zircon U–Pb LA-ICP-MS analytical data of Fe-Ti-P mineralization in the Central Grenville Province, Quebec

LET-01 - L'Étang Fe-Ti mineralization: sample 21PM53 - leuconorite. Concordia ages: 1010 ± 10 Ma											
#Grain	U_{ppm}	Pb_{ppm}	Th/U	$^{206}Pb/^{204}Pb$	Isotopic ratios ±1se (%)			Apparent ages ±2se (abs)			Rho
					$^{206}Pb/^{238}U$	$^{207}Pb/^{235}U$	$^{207}Pb/^{206}Pb$	$^{206}Pb/^{238}U$	$^{207}Pb/^{235}U$	$^{207}Pb/^{206}Pb$	
GC-LET-01_1	95	16107	0.1	-104.7	0.16783 ± 1.9	1.60786 ± 3.2	0.06963 ± 2.9	998.7 ± 35.2	960.8 ± 40.4	863.5 ± 123.2	0.42795
GC-LET-01_2	48	8427	0.1	-5.0	0.17335 ± 1.8	1.87731 ± 3.8	0.07921 ± 3.4	1,029 ± 34.3	1,068.9 ± 49.3	1,072.7 ± 145.7	0.45212
GC-LET-01_3	397	69687	0.1	-88.7	0.17718 ± 1.7	1.76261 ± 2.3	0.07227 ± 1.8	1,049.9 ± 32.5	1,022.9 ± 29.6	968.8 ± 72.4	0.69969
GC-LET-01_4	116	20957	0.5	155.0	0.17450 ± 1.6	1.70067 ± 2.3	0.07071 ± 2.2	1,035.6 ± 31.4	1,000.9 ± 30.8	921.9 ± 85.3	0.48978
GC-LET-01_6	109	19200	0.3	800.0	0.16868 ± 1.6	1.64802 ± 2.7	0.07099 ± 2.3	1,003.8 ± 29.6	986.8 ± 34.3	912.6 ± 95.1	0.51915
GC-LET-01_7	41	8270	0.6	2685.0	0.19239 ± 1.9	1.96848 ± 3.3	0.07505 ± 3.4	1,132.2 ± 38.2	1,094.5 ± 47.6	997.6 ± 141.0	0.18691
GC-LET-01_8	80	14601	0.3	-438.8	0.17267 ± 1.9	1.72577 ± 3.2	0.07239 ± 3.0	1,025.8 ± 35.7	1,009.3 ± 42.3	944.8 ± 127.3	0.43087
GC-LET-01_9	92	15509	0.1	-67.3	0.16262 ± 2.0	1.55567 ± 2.7	0.07145 ± 2.7	969.8 ± 35.6	953.7 ± 36.7	910.8 ± 112.4	0.73261
GC-LET-01_10	129	21771	0.1	42.3	0.16056 ± 2.0	1.53414 ± 2.9	0.06939 ± 2.8	958.5 ± 35.2	935.4 ± 35.4	850.2 ± 115.1	0.57092
GC-LET-01_11	65	12171	0.2	43.5	0.17719 ± 2.6	1.74840 ± 3.4	0.07240 ± 3.3	1,048.8 ± 50.6	1,022.3 ± 41.7	955.7 ± 123.9	0.48232
GC-LET-01_12	146	26318	0.2	-54.9	0.16353 ± 1.7	1.57129 ± 2.5	0.06911 ± 2.2	975.1 ± 30.1	950.6 ± 30.7	853.2 ± 92.8	0.49424
GC-LET-01_13	153	27556	0.2	222.4	0.16721 ± 1.6	1.59961 ± 2.4	0.06917 ± 2.4	995.2 ± 30.3	960.6 ± 30.7	841.1 ± 98.4	-0.03443
GC-LET-01_14	173	30399	0.3	209.0	0.16307 ± 2.2	1.57088 ± 2.4	0.07031 ± 2.0	971.7 ± 39.9	951.7 ± 29.1	900.2 ± 82.0	0.63240
GC-LET-01_15	91	16146	0.1	58.6	0.16395 ± 1.8	1.56426 ± 2.5	0.06927 ± 2.2	976.9 ± 33.0	946.5 ± 30.6	869.8 ± 85.4	0.65425

Table 4.2. (cont.) Zircon U–Pb LA-ICP-MS analytical data of Fe-Ti-P mineralization in the Central Grenville Province, Quebec

MAT-01 - Mattawa Fe-Ti-(P) mineralization: sample 21PM18 - oxide-apatite norite. Concordia age: 989 ± 9 Ma											
#Grain	U_{ppm}	Pb_{ppm}	Th/U	$^{206}Pb/^{204}Pb$	Isotopic ratios ±1se (%)			Apparent ages ±2se (abs)			Rho
					$^{206}Pb/^{238}U$	$^{207}Pb/^{235}U$	$^{207}Pb/^{206}Pb$	$^{206}Pb/^{238}U$	$^{207}Pb/^{235}U$	$^{207}Pb/^{206}Pb$	
GC-MAT-01_1	27	5060	0.2	50.5	0.16454 ± 1.5	1.61265 ± 4.1	0.07170 ± 4.2	980.9 ± 26.4	948.6 ± 51.5	802.5 ± 179.7	0.12439
GC-MAT-01_2	69	12698	0.3	60.0	0.16482 ± 1.6	1.56596 ± 2.7	0.07010 ± 2.7	982.4 ± 29.4	954.2 ± 36.4	905.0 ± 108.1	0.52930
GC-MAT-01_3	22	3991	0.2	17.3	0.16632 ± 2.6	1.55006 ± 7.3	0.06756 ± 6.5	990.4 ± 47.1	913.0 ± 90.4	752.6 ± 277.0	0.38239
GC-MAT-01_4	57	10714	0.2	-10.8	0.16593 ± 1.4	1.51783 ± 3.8	0.06694 ± 3.5	988.8 ± 25.5	920.3 ± 44.9	734.6 ± 157.6	0.30771
GC-MAT-01_5	24	4387	0.1	-53.1	0.16451 ± 1.8	1.53832 ± 5.2	0.06849 ± 5.2	980.7 ± 32.9	920.4 ± 64.9	720.5 ± 235.5	0.15401
GC-MAT-01_6	45	8582	0.3	-34.8	0.16854 ± 1.4	1.65783 ± 3.2	0.07202 ± 3.2	1,003.0 ± 25.8	982.0 ± 41.9	914.7 ± 134.1	0.19170
GC-MAT-01_7	46	8943	0.2	-74.6	0.17054 ± 1.5	1.69134 ± 2.9	0.07203 ± 3.2	1,013.9 ± 27.9	991.2 ± 37.2	938.1 ± 122.8	0.07254
GC-MAT-01_8	89	16858	0.2	-268.7	0.16971 ± 2.2	1.57435 ± 2.6	0.06860 ± 2.9	1008.9 ± 40.3	953.6 ± 32.5	822.8 ± 130.4	0.19804
GC-MAT-01_9	84	15318	0.2	-146.5	0.16368 ± 2.2	1.53198 ± 2.9	0.06898 ± 2.8	975.6 ± 39.9	945.1 ± 41.7	858.5 ± 134.5	0.56526
GC-MAT-01_10	39	7433	0.2	-91.7	0.17006 ± 1.9	1.607269 ± 4.1	0.07152 ± 3.8	1,010.5 ± 34.4	965.6 ± 48.4	824.7 ± 163.2	0.36328
GC-MAT-01_11	64	12216	0.2	-184.1	0.16909 ± 2.2	1.61940 ± 3.7	0.07006 ± 3.2	1,005.4 ± 40.9	965.4 ± 43.8	856.3 ± 136.5	0.57053
GC-MAT-01_12	39	7638	0.2	-185.4	0.17483 ± 1.9	1.67363 ± 3.5	0.07150 ± 3.8	1,036.5 ± 36.1	986.7 ± 45.4	832.1 ± 152.8	0.35650
GC-MAT-01_13	69	12903	0.2	-651.4	0.16368 ± 1.4	1.57796 ± 3.4	0.07157 ± 2.9	976.4 ± 26.2	960.8 ± 37.4	961.5 ± 118.6	0.36623
GC-MAT-01_14	52	9742	0.2	-367.7	0.16619 ± 1.5	1.73050 ± 2.9	0.07170 ± 2.7	989.9 ± 26.9	1,006.1 ± 36.9	1,033.0 ± 103.3	0.43113
GC-MAT-01_15	83	16273	0.1	-648.2	0.17324 ± 1.6	1.68103 ± 2.3	0.07170 ± 2.2	1,028.5 ± 29.6	992.6 ± 29.4	916.5 ± 96.6	0.41982
GC-MAT-01_16	34	6593	0.2	253.8	0.17452 ± 1.6	1.74159 ± 3.7	0.07449 ± 3.1	1,041.9 ± 32.8	1,027.2 ± 49.6	1,012.9 ± 133.8	0.47854
GC-MAT-01_17	36	6715	0.2	282.1	0.16462 ± 1.1	1.60980 ± 3.8	0.07192 ± 3.9	981.7 ± 20.8	961.1 ± 45.1	907.7 ± 148.4	-0.05766
GC-MAT-01_18	28	5278	0.2	85.0	0.16979 ± 1.6	1.84503 ± 4.4	0.07939 ± 4.2	1,009.8 ± 30.0	1,036.6 ± 58.1	1,026.9 ± 185.2	0.28605
GC-MAT-01_19	66	12541	0.4	114.5	0.17313 ± 1.4	1.79974 ± 2.6	0.07514 ± 2.1	1,028.2 ± 26.4	1,034.7 ± 32.0	1,035.3 ± 90.3	0.55617
GC-MAT-01_20	147	27513	0.2	269.7	0.17443 ± 1.6	1.79922 ± 2.0	0.07548 ± 1.8	1,034.9 ± 30.8	1,043.3 ± 27.3	1,055.9 ± 72.7	0.66992
GC-MAT-01_21	57	11270	0.2	51.0	0.18333 ± 1.5	1.91149 ± 2.8	0.07556 ± 2.5	1,083.7 ± 29.6	1,071.3 ± 36.8	1,011.8 ± 105.4	0.41271
GC-MAT-01_22	43	8295	0.2	-21.8	0.17993 ± 1.3	1.82478 ± 3.2	0.07417 ± 3.4	1,065.5 ± 26.0	1,036.2 ± 42.8	930.5 ± 147.6	0.00240
GC-MAT-01_23	29	5319	0.3	-19.2	0.17461 ± 1.5	1.87219 ± 4.2	0.07839 ± 4.1	1,036.2 ± 28.4	1,047.5 ± 58.7	1,023.8 ± 175.7	0.32362
GC-MAT-01_24	32	6001	0.2	-79.5	0.18648 ± 2.1	1.86996 ± 4.2	0.07478 ± 3.5	1,099.3 ± 42.6	1,061.3 ± 55.8	986.6 ± 160.9	0.53732
GC-MAT-01_25	88	16128	0.3	-949.3	0.17572 ± 1.1	1.88236 ± 2.4	0.07785 ± 2.4	1,043.0 ± 21.3	1,067.8 ± 31.2	1,099.7 ± 96.5	0.01012

Table 4.2. (cont.) Zircon U–Pb LA-ICP-MS analytical data of Fe-Ti-P mineralization in the Central Grenville Province, Quebec

LBR-01 - Labrieville Anorthosite Fe-Ti-P mineralization: sample 20PM37 - nelsonite. Concordia age: 1065 ± 5 Ma											
#Grain	U_{ppm}	Pb_{ppm}	Th/U	$^{206}Pb/^{204}Pb$	Isotopic ratios ±1se (%)			Apparent ages ±2se (abs)			Rho
					$^{206}Pb/^{238}U$	$^{207}Pb/^{235}U$	$^{207}Pb/^{206}Pb$	$^{206}Pb/^{238}U$	$^{207}Pb/^{235}U$	$^{207}Pb/^{206}Pb$	
GC-LBR-01_1	4	1759	0.2	-3.2	0.16440 ± 2.0	1.72800 ± 7.1	0.07786 ± 7.3	979.1 ± 35.4	928.7 ± 97.2	785.6 ± 362.4	-0.01956
GC-LBR-01_2	112	79510	0.3	665.6	0.23060 ± 0.7	2.69662 ± 1.0	0.08503 ± 1.0	1,337.2 ± 17.1	1,325.2 ± 14.9	1,312.0 ± 40.3	0.41033
GC-LBR-01_3	37	20162	0.3	85.4	0.17916 ± 1.0	1.85688 ± 1.9	0.07537 ± 1.9	1,065.0 ± 18.6	1,059.3 ± 25.5	1,050.9 ± 75.0	0.30920
GC-LBR-01_4	37	20563	0.3	48.6	0.18385 ± 0.8	1.94611 ± 1.8	0.07670 ± 1.8	1,087.6 ± 15.6	1,090.9 ± 24.8	1,074.1 ± 77.9	0.16526
GC-LBR-01_5	45	23822	0.3	530.8	0.17967 ± 1.0	1.87511 ± 1.8	0.07586 ± 1.8	1,064.5 ± 19.9	1,070.6 ± 25.5	1,066.6 ± 77.8	0.23353
GC-LBR-01_6	46	24946	0.2	225.5	0.18424 ± 0.8	1.90518 ± 1.7	0.07554 ± 1.7	1,089.7 ± 15.2	1,081.6 ± 23.1	1,048.2 ± 72.9	0.18681
GC-LBR-01_7	8	4020	2.4	20.6	0.17323 ± 2.0	1.71551 ± 5.6	0.07301 ± 6.0	1,028.7 ± 37.7	983.4 ± 78.9	896.0 ± 257.5	-0.10805
GC-LBR-01_8	32	16104	0.3	80.1	0.18254 ± 1.0	1.83354 ± 3.0	0.07353 ± 3.3	1,080.5 ± 20.7	1,049.8 ± 39.1	968.5 ± 135.9	-0.08443
GC-LBR-01_9	190	105587	0.4	203.5	0.21204 ± 1.4	2.41822 ± 1.7	0.08333 ± 1.5	1,239.0 ± 30.9	1,245.2 ± 24.3	1,265.7 ± 58.9	0.55346
GC-LBR-01_10	61	27692	0.4	4.5	0.18977 ± 0.7	1.96221 ± 1.6	0.07479 ± 1.4	1,119.8 ± 14.3	1,098.1 ± 21.1	1,049.0 ± 59.2	0.40444
GC-LBR-01_11	115	49117	0.5	-507.4	0.18426 ± 0.8	1.92571 ± 1.7	0.07549 ± 1.8	1,090.0 ± 15.8	1,086.8 ± 23.1	1,060.6 ± 71.8	0.20009
GC-LBR-01_12	52	19997	0.4	-312.5	0.18212 ± 0.9	1.87979 ± 1.9	0.07487 ± 1.9	1,078.1 ± 17.4	1,067.5 ± 25.5	1,024.2 ± 78.6	0.22703
GC-LBR-01_13	406	277904	0.4	-2373.1	0.34482 ± 0.7	5.43888 ± 0.8	0.11460 ± 0.7	1,908.9 ± 23.2	1,891.5 ± 14.1	1,868.2 ± 25.9	0.57088
GC-LBR-01_14	79	25776	0.3	-659.9	0.17863 ± 1.2	1.80465 ± 2.3	0.07302 ± 2.2	1,058.9 ± 23.8	1,048.2 ± 27.2	1,004.9 ± 82.0	0.27321
GC-LBR-01_15	89	24542	0.4	-924.1	0.17580 ± 1.8	1.92773 ± 2.7	0.07973 ± 3.2	1,043.1 ± 34.7	1,084.7 ± 36.1	1,145.5 ± 118.4	0.10432
GC-LBR-01_16	78	22536	0.4	-497.6	0.18331 ± 1.2	1.89761 ± 2.5	0.07485 ± 2.3	1,084.5 ± 24.4	1,073.8 ± 33.2	1,052.2 ± 87.1	0.42315
GC-LBR-01_17	84	24062	0.4	-437.0	0.18339 ± 0.9	1.93416 ± 1.5	0.07621 ± 1.5	1,085.0 ± 17.0	1,088.7 ± 20.6	1,084.4 ± 63.7	0.18490
GC-LBR-01_18	31	8088	0.2	-422.7	0.16700 ± 0.9	1.76954 ± 2.7	0.07673 ± 2.7	995.1 ± 16.4	1,022.5 ± 35.3	1,062.4 ± 104.4	0.15171
GC-LBR-01_19	75	21108	0.6	159.6	0.17712 ± 1.1	1.78470 ± 2.1	0.07327 ± 2.1	1,050.7 ± 21.7	1,034.3 ± 27.7	986.2 ± 87.7	-0.06949
GC-LBR-01_20	76	21266	0.5	347.8	0.17843 ± 1.1	1.79847 ± 1.7	0.07388 ± 1.7	1,057.7 ± 21.1	1,043.8 ± 23.2	1,003.5 ± 72.6	0.32389
GC-LBR-01_21	75	21889	0.4	290.8	0.18194 ± 1.0	1.85387 ± 1.8	0.07378 ± 1.8	1,076.9 ± 20.0	1,063.0 ± 23.2	1,036.8 ± 69.5	0.24096
GC-LBR-01_22	9	2421	2.9	191.6	0.17214 ± 1.6	1.60744 ± 6.6	0.07294 ± 6.7	1,022.4 ± 30.9	926.4 ± 90.5	715.8 ± 331.4	-0.17528
GC-LBR-01_23	105	31935	0.4	-1333.1	0.18237 ± 1.2	1.84685 ± 1.7	0.07388 ± 1.88	1,079.3 ± 22.8	1,058.6 ± 22.7	1,007.6 ± 81.1	0.30305
GC-LBR-01_24	69	21607	0.4	-204.7	0.17793 ± 1.0	1.86177 ± 2.1	0.07596 ± 2.2	1,055.1 ± 19.1	1,059.8 ± 27.8	1,046.7 ± 82.8	0.17518
GC-LBR-01_25	73	23119	0.5	-262.7	0.17661 ± 0.9	1.80717 ± 1.6	0.07473 ± 1.8	1,048.0 ± 17.4	1,043.5 ± 21.4	1,022.7 ± 77.9	0.04579

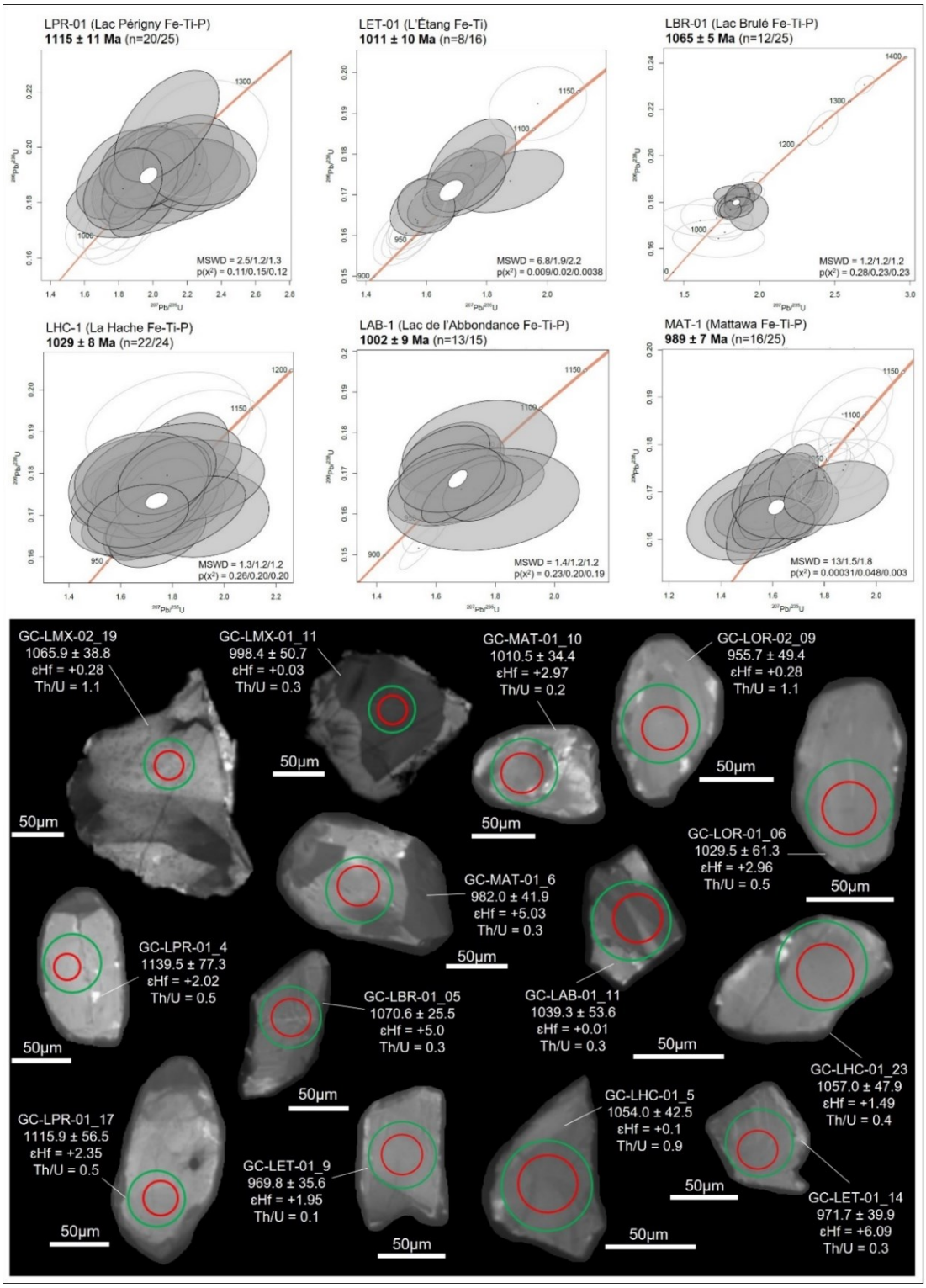

Figure 4.5. LA-ICP-MS U–Pb analysis in zircon of Fe-Ti-(P) mineralization in the Central Grenville Province, Quebec. a. Concordia diagrams. Each ellipse represents the result of the analysis of a single zircon crystal. Grey ellipses represent the zircon grains selected for the Concordia age calculation while opened ellipses represent excluded grains with discordant ages. b. Representative cathodoluminescence images of analyzed zircons. Red and green circles show the location of the 25 µm and 50 µm beam for U–Pb and Lu–Hf microanalysis, respectively.

4.6.3 Zircon Hf isotopes of Fe-Ti-P mineralization

The Lu/Hf analysis were conducted on zircon that produced concordant U-Pb analyses from our ten dated samples of Fe-Ti-P mineralization, these data are presented in Table 4.3. The calculated εHf values are plotted against their sample age date in Figure 4.6. A compilation with previous εHf values for zircon from AMCG bedrock and detrital grains from metasedimentary rocks of the Grenville Province (e.g., Dickin, 2000; Papapavlou et al. 2022; Bickford et al. 2010) is also presented in Figure 4.6b. The obtained εHf results for this study have mainly supra-chondritic to negative εHf values, varying from -5.0 to +7.4 (Fig.4.6a). Fe-Ti-P mineralization hosted in the Labrieville Alkaline Anorthosite (Lac Brûlé, εHf: +5.0 to +7.0) and the Mattawa Anorthosite (εHf: +3.0 to +5.2) present slightly more supra-chondritic signatures (Fig.4.6a), with higher εHf for the same age range, in relation to the other Fe-Ti-P mineralization located in the Vanel Anorthosite (e.g Lac à l'Orignal, Lac Mirepoix and Lac de l'Abbondance) and La Hache Mangerite (εHf < +4).

In detail, two oxide-apatite-norite samples that were previously dated from the Lac à l'Orignal Fe-Ti-P deposit (Miloski et al. 2023a), were analyzed from the older border (1069 ± 12 Ma) and younger core (993 ± 13 Ma) of the deposit for their initial Hf isotopic composition, and the samples produced different εHf values (Fig.4.6a). Zircons from the younger core of the intrusion have lower εHf values (εHf: -5.0 to +0.3) in comparison to the older border (εHf: -1.7 to +3.0). Similarly, oxide-apatite-norite from nearby Lac Mirepoix reveal slightly different εHf values between the two analyzed samples, with lower εHf values in the younger OAN (zone I: 964 ± 9 Ma; εHf: -1.0 to +2.2) compared with the more juvenile older OAN lens (zone III: 1048 ± 8 Ma; εHf: +1.3 to +4.6) (Fig.4.6a). Other Fe-Ti-P occurrences in the Vanel Anorthosite, such as the massive nelsonite at Lac de l'Abbondance (εHf: -2.7 to 0), also have subchondrititic Hf values. OAN mineralization hosted in the mangerite at La Hache, in contrast to those from Vanel, contain exclusively suprachondritic

εHf values (εHf: +0.1 to +4.7) (Fig.4.6a). Finally, the zircon grains from the mineralization at Lac Périgny contain exclusively supra-chondritic εHf values (εHf: +2.2 to +7.4) while L'Étang present supra-chondritic εHf values but also slight negative values (εHf: -1.0 to +6.3).

Table 4.3. Zircon Lu-Hf LA-ICP-MS analytical data of Fe-Ti-P mineralization in the Central Grenville Province, Quebec

.	Age (Ma)	$^{176}Lu/^{177}Hf$	$^{176}Hf/^{177}Hf$	2σ	Hf_i	εHf(T)	εHf(T) cor.
LPR-01 - Lac Périgny Fe-Ti-P mineralization: sample 20PM23 - oxide-apatite norite							
GC-LPR-01_2	1088.0	0.0013819	0.282142	0.000041	0.282112	1.21	2.21
GC-LPR-01_4	1139.5	0.0018705	0.282147	0.000039	0.282107	1.03	2.03
GC-LPR-01_5	1070.6	0.0004498	0.282269	0.000034	0.282260	6.44	7.44
GC-LPR-01_6	1120.5	0.0014862	0.282238	0.000058	0.282207	4.56	5.56
GC-LPR-01_7	1128.2	0.0014067	0.282188	0.000031	0.282158	2.84	3.84
GC-LPR-01_8	1115.3	0.0013505	0.282160	0.000047	0.282132	1.89	2.89
GC-LPR-01_9	1127.1	0.0018413	0.282157	0.000034	0.282118	1.42	2.42
GC-LPR-01_11	1147.0	0.0016445	0.282142	0.000033	0.282107	1.02	2.02
GC-LPR-01_13	1099.0	0.0016689	0.282145	0.000042	0.282110	1.14	2.14
GC-LPR-01_14	1131.0	0.0010915	0.282216	0.000030	0.282194	4.09	5.09
GC-LPR-01_15	1042.4	0.0014115	0.282203	0.000030	0.282173	3.38	4.38
GC-LPR-01_16	1154.5	0.0015299	0.282163	0.000047	0.282131	1.86	2.86
GC-LPR-01_17	1115.9	0.0023211	0.282165	0.000036	0.282116	1.35	2.35
GC-LPR-01_18	1140.2	0.0023384	0.282232	0.000034	0.282183	3.72	4.72
LAB-01 - Lac de l'Abbondance Fe-Ti-P mineralization: sample 20PM47 - nelsonite							
GC-LAB-01_9	983.2	0.0012998	0.282093	0.000099	0.282069	-2.90	-1.90
GC-LAB-01_11	1039.3	0.0002198	0.282127	0.000110	0.282123	-0.99	0.01
GC-LAB-01_17	986.9	0.0004606	0.282056	0.000127	0.282047	-3.67	-2.67

^{176}Lu decay constant $\lambda=1.865\times10-11$ $year^{-1}$; chondritic values: $^{176}Lu/^{177}Hf=0.0332\pm0.002$, $^{176}Hf/^{177}Hf=0.282772\pm0.000029$; depleted mantle values: $(^{176}Lu/^{177}Hf)_{DM}=0.0384$, $(^{176}Hf/^{177}Hf)_{DM}=0.28325$; Hf_i: initial Hf isotopic composition for U–Pb age.

Table 4.3. (cont.) Zircon Lu-Hf LA-ICP-MS analytical data of Fe-Ti-P mineralization in the Central Grenville Province, Quebec

#Grain	Age (Ma)	$^{176}Lu/^{177}Hf$	$^{176}Hf/^{177}Hf$	2σ	Hf_i	εHf(T)	εHf(T) cor.
LHC-1 - La Hache Fe-Ti-P mineralization: sample 20PM07 - oxide-apatite-rich mangerite							
GC-LHC-01_2	1045.8	0.0007480	0.282192	0.000061	0.282178	1.59	2.59
GC-LHC-01_4	1000.6	0.0004390	0.282157	0.000068	0.282148	0.54	1.54
GC-LHC-01_5	1054.0	0.0006349	0.282120	0.000067	0.282108	-0.90	0.10
GC-LHC-01_11	1044.5	0.0004238	0.282199	0.000058	0.282190	2.04	3.04
GC-LHC-01_12	1083.0	0.0006855	0.282209	0.000064	0.282195	2.22	3.22
GC-LHC-01_13	992.7	0.0005135	0.282117	0.000073	0.282107	-0.91	0.09
GC-LHC-01_14	1044.4	0.0004753	0.282237	0.000071	0.282228	3.36	4.36
GC-LHC-01_19	1100.1	0.0006353	0.282144	0.000093	0.282132	-0.05	0.95
GC-LHC-01_23	1057.0	0.0004858	0.282156	0.000063	0.282147	0.49	1.49
GC-LHC-01_24	1061.4	0.0004872	0.282147	0.000082	0.282138	0.17	1.17
GC-LHC-01_25	1009.3	0.0005427	0.282248	0.000117	0.282237	3.69	4.69
LET-01 - L'Étang Fe-Ti mineralization: sample 21PM53 - leuconorite							
GC-LET-01_1	998.7	0.0016072	0.282160	0.000082	0.282129	-0.55	0.45
GC-LET-01_2	1029.0	0.0004473	0.282212	0.000077	0.282204	2.08	3.08
GC-LET-01_6	1003.8	0.0008418	0.282307	0.000053	0.282290	5.16	6.16
GC-LET-01_8	1025.8	0.0010376	0.282183	0.000104	0.282163	0.65	1.65
GC-LET-01_9	969.8	0.0011365	0.282194	0.000088	0.282172	0.95	1.95
GC-LET-01_10	958.5	0.0008602	0.282104	0.000078	0.282088	-2.03	-1.03
GC-LET-01_11	1048.8	0.0017472	0.282328	0.000063	0.282295	5.30	6.30
GC-LET-01_14	971.7	0.0007641	0.282303	0.000048	0.282288	5.09	6.09
GC-LET-01_15	976.9	0.0002226	0.282284	0.000058	0.282280	4.79	5.79

Table 4.3. (cont.) Zircon Lu-Hf LA-ICP-MS analytical data of Fe-Ti-P mineralization in the Central Grenville Province, Quebec

#Grain	Age (Ma)	$^{176}Lu/^{177}Hf$	$^{176}Hf/^{177}Hf$	2σ	Hf_i	εHf(T)	εHf(T) cor.
LOR-01 - Lac à l'Orignal Fe-Ti-P mineralization: sample 14.0 - 16.0m depth - oxide-apatite norite							
GC-LOR-01_05	1083.5	0.0004256	0.282135	0.000044	0.282126	0.66	1.66
GC-LOR-01_06	1029.5	0.0004932	0.282173	0.000053	0.282163	1.96	2.96
GC-LOR-01_07	1101.7	0.0003835	0.282081	0.000054	0.282073	-1.24	-0.24
GC-LOR-01_09	971.6	0.0002733	0.282153	0.000057	0.282147	1.40	2.40
GC-LOR-01_12	1019.3	0.0006080	0.282160	0.000050	0.282148	1.43	2.43
GC-LOR-01_13	992.5	0.0005983	0.282147	0.000045	0.282135	0.98	1.98
GC-LOR-01_15	1021.3	0.0006518	0.282129	0.000064	0.282116	0.29	1.29
GC-LOR-01_19	990.3	0.0004169	0.282123	0.000060	0.282115	0.26	1.26
GC-LOR-01_20	1044.6	0.0006984	0.282045	0.000063	0.282031	-2.73	-1.73
LOR-02 - Lac à l'Orignal Fe-Ti-P mineralization: sample 41.0 - 43.0m depth - oxide-apatite norite							
GC-LOR-02_07	1017.6	0.0006249	0.282133	0.000047	0.282121	-1.25	-0.25
GC-LOR-02_08	1020.2	0.0026761	0.282038	0.000064	0.281988	-5.97	-4.97
GC-LOR-02_09	955.7	0.0006065	0.282147	0.000068	0.282136	-0.72	0.28
GC-LOR-02_12	1028.5	0.0021176	0.282025	0.000065	0.281985	-6.06	-5.06

^{176}Lu decay constant $\lambda=1.865\times10-11$ $year^{-1}$; chondritic values: $^{176}Lu/^{177}Hf=0.0332\pm0.002$, $^{176}Hf/^{177}Hf=0.282772\pm0.000029$; depleted mantle values: $(^{176}Lu/^{177}Hf)_{DM}=0.0384$, $(^{176}Hf/^{177}Hf)_{DM}=0.28325$; Hf_i: initial Hf isotopic composition for U–Pb age.

Table 4.3. (cont.) Zircon Lu-Hf LA-ICP-MS analytical data of Fe-Ti-P mineralization in the Central Grenville Province, Quebec

#Grain	Age (Ma)	$^{176}Lu/^{177}Hf$	$^{176}Hf/^{177}Hf$	2σ	Hf_i	εHf(T)	εHf(T) cor.
LMX-01 - Lac Mirepoix Fe-Ti-P mineralization: sample 20PM06 - oxide-apatite norite							
GC-LMX-01_02	960.0	0.0010020	0.282205	0.000031	0.282186	0.41	1.41
GC-LMX-01_03	971.8	0.0010640	0.282207	0.000031	0.282188	0.46	1.46
GC-LMX-01_04	980.9	0.0007589	0.282184	0.000031	0.282171	-0.15	0.85
GC-LMX-01_05	1044.6	0.0008216	0.282223	0.000034	0.282209	1.20	2.20
GC-LMX-01_06	956.1	0.0037893	0.282196	0.000059	0.282128	-1.67	-0.67
GC-LMX-01_07	967.3	0.0005195	0.282192	0.000026	0.282182	0.26	1.26
GC-LMX-01_08	985.8	0.0005212	0.282198	0.000030	0.282188	0.47	1.47
GC-LMX-01_09	1026.4	0.0004551	0.282188	0.000034	0.282180	0.17	1.17
GC-LMX-01_10	972.0	0.0008568	0.282192	0.000029	0.282177	0.07	1.07
GC-LMX-01_11	998.4	0.0007306	0.282161	0.000034	0.282147	-0.97	0.03
GC-LMX-01_12	967.9	0.0006121	0.282201	0.000030	0.282190	0.54	1.54
GC-LMX-01_13	929.1	0.0028716	0.282171	0.000024	0.282119	-1.97	-0.97
GC-LMX-01_23	1002.4	0.0003155	0.282158	0.000028	0.282152	-0.80	0.20
GC-LMX-01_24	1021.2	0.0010214	0.282191	0.000046	0.282172	-0.09	0.91
LMX-02 - Lac Mirepoix Fe-Ti-P mineralization: sample 20PM08 - oxide-apatite norite							
GC-LMX-02_01	1083.3	0.0005346	0.282182	0.000041	0.282171	1.78	2.78
GC-LMX-02_04	1023.3	0.0005619	0.282172	0.000040	0.282161	1.40	2.40
GC-LMX-02_05	1076.3	0.0004661	0.282197	0.000030	0.282188	2.37	3.37
GC-LMX-02_06	1093.0	0.0004473	0.282138	0.000037	0.282129	0.28	1.28
GC-LMX-02_09	1064.9	0.0006482	0.282208	0.000036	0.282195	2.61	3.61
GC-LMX-02_13	1065.7	0.0004635	0.282201	0.000042	0.282192	2.50	3.50
GC-LMX-02_14	1038.6	0.0005975	0.282236	0.000037	0.282224	3.65	4.65
GC-LMX-02_16	1067.7	0.0004625	0.282190	0.000040	0.282181	2.12	3.12
GC-LMX-02_19	1065.9	0.0004356	0.282181	0.000044	0.282173	1.83	2.83
GC-LMX-02_25	1091.0	0.0015317	0.282179	0.000035	0.282149	0.98	1.98

^{176}Lu decay constant $\lambda=1.865\times10-11$ $year^{-1}$; chondritic values: $^{176}Lu/^{177}Hf=0.0332\pm0.002$, $^{176}Hf/^{177}Hf=0.282772\pm0.000029$; depleted mantle values: $(^{176}Lu/^{177}Hf)_{DM}=0.0384$, $(^{176}Hf/^{177}Hf)_{DM}=0.28325$; Hf_i: initial Hf isotopic composition for U–Pb age.

Table 4.3. (cont.) Zircon Lu-Hf LA-ICP-MS analytical data of Fe-Ti-P mineralization in the Central Grenville Province, Quebec

#Grain	Age (Ma)	$^{176}Lu/^{177}Hf$	$^{176}Hf/^{177}Hf$	2σ	Hf_i	εHf(T)	εHf(T) cor.
MAT-01 - Mattawa Fe-Ti-(P) mineralization: sample 21PM18 - oxide-apatite norite							
GC-MAT-01_01	980.9	0.0006510	0.282246	0.000048	0.282234	2.66	3.66
GC-MAT-01_02	982.4	0.0012854	0.282280	0.000038	0.282256	3.45	4.45
GC-MAT-01_04	988.8	0.0007601	0.282248	0.000049	0.282234	2.68	3.68
GC-MAT-01_05	980.7	0.0010176	0.282244	0.000047	0.282225	2.37	3.37
GC-MAT-01_06	1003.0	0.0005653	0.282283	0.000040	0.282272	4.03	5.03
GC-MAT-01_08	1008.9	0.0003277	0.282232	0.000058	0.282225	2.37	3.37
GC-MAT-01_10	1010.5	0.0007659	0.282228	0.000063	0.282214	1.97	2.97
GC-MAT-01_16	1041.9	0.0007098	0.282292	0.000041	0.282279	4.26	5.26
GC-MAT-01_17	981.7	0.0003569	0.282265	0.000024	0.282259	3.55	4.55
GC-MAT-01_19	1028.2	0.0008301	0.282279	0.000027	0.282264	3.74	4.74
GC-MAT-01_20	1034.9	0.0018725	0.282252	0.000038	0.282217	2.09	3.09
LBR-01 - Labrieville Anorthosite Fe-Ti-P mineralization: sample 20PM37 - nelsonite							
GC-LBR-01_3	1065.0	0.0002061	0.282285	0.000040	0.282281	6.04	7.04
GC-LBR-01_4	1087.6	0.0003516	0.282257	0.000028	0.282250	4.94	5.94
GC-LBR-01_5	1064.5	0.0006631	0.282236	0.000044	0.282223	4.00	5.00
GC-LBR-01_6	1089.7	0.0003389	0.282286	0.000034	0.282279	5.98	6.98
GC-LBR-01_8	1080.5	0.0005502	0.282263	0.000040	0.282252	5.01	6.01
GC-LBR-01_14	1058.9	0.0005803	0.282288	0.000047	0.282277	5.89	6.89
GC-LBR-01_17	1085.0	0.0005085	0.282237	0.000045	0.282227	4.13	5.13
GC-LBR-01_20	1057.7	0.0004047	0.282260	0.000050	0.282251	5.00	6.00
GC-LBR-01_23	1079.3	0.0003203	0.282249	0.000040	0.282242	4.67	5.67
GC-LBR-01_24	1055.1	0.0002911	0.282271	0.000040	0.282265	5.48	6.48

^{176}Lu decay constant $\lambda=1.865\times10-11$ $year^{-1}$; chondritic values: $^{176}Lu/^{177}Hf=0.0332\pm0.002$, $^{176}Hf/^{177}Hf=0.282772\pm0.000029$; depleted mantle values: $(^{176}Lu/^{177}Hf)_{DM}=0.0384$, $(^{176}Hf/^{177}Hf)_{DM}=0.28325$; Hf_i: initial Hf isotopic composition for U–Pb age.

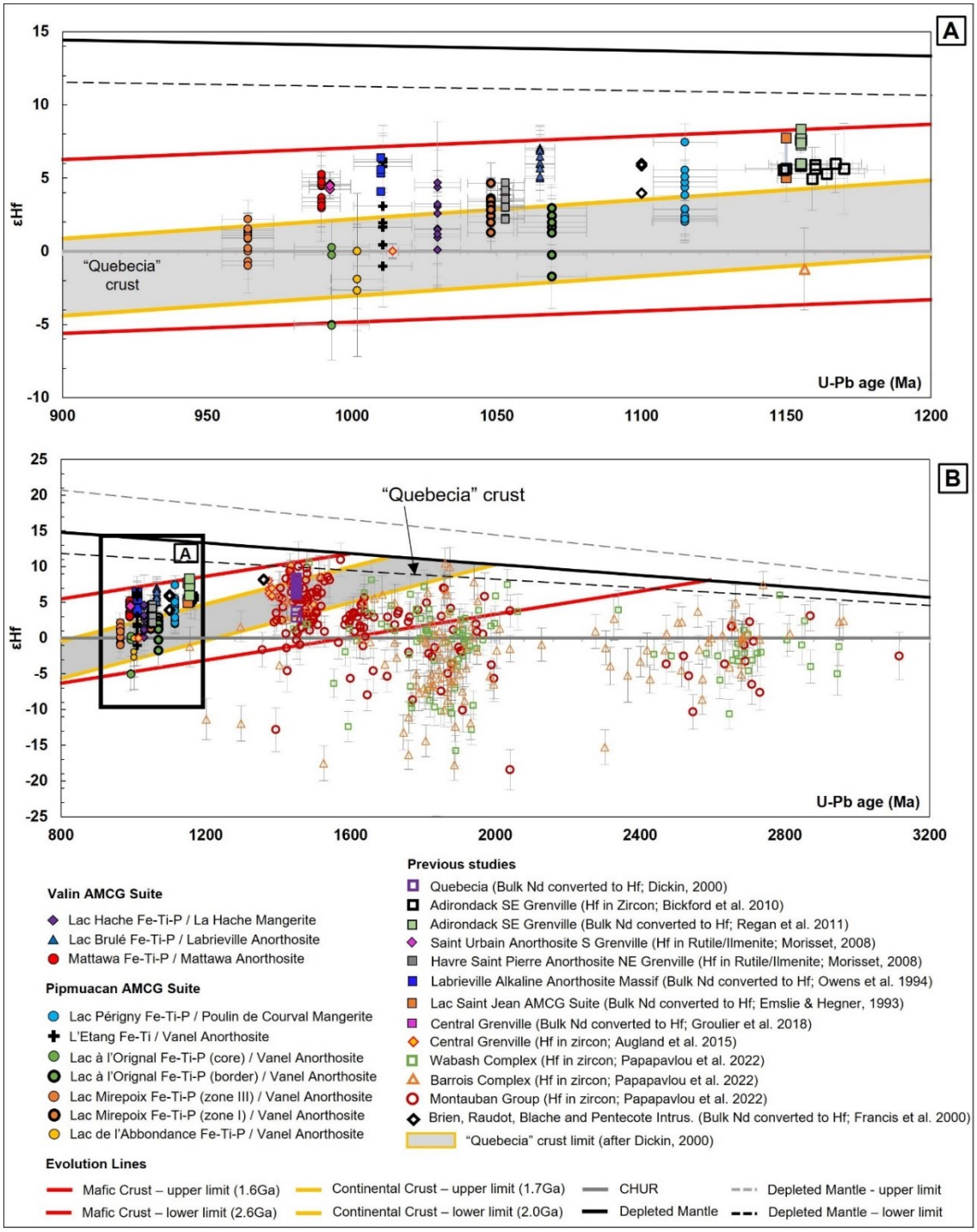

Figure 4.6. a. Epsilon Hf versus U-Pb Concordia ages from the zircon grains of Fe-Ti-P mineralization in the Central Grenville Province, Quebec. Error on the ƐHf calculated after Ickert (2013). b. Compilation of previous publications of Hf and Nd (converted) isotope data for the Grenville Province: Adirondack AMCG (Bickford et al. 2010; Regan et al. 2011); Fe-Ti mineralization in the Saint Urbain Anorthosite (Morisset 2008); Big Island Fe-Ti mineralization/ Havre-Saint-Pierre Anorthositic Suite, Morisset 2008); Labrieville Anorthosite Massif, Central Grenville (Owens et al. 1994); Lac Saint Jean AMCG Suite, Central Grenville (Emslie & Hegner, 1993); Magmatic rocks, Central Grenville (Augland et al. 2015); Meta-sedimentary rocks Montauban group, Wabash Complex and Barrois Complex (Papapavlou et al. 2022); Brien, Raudot, Blache and Riviere Pentecote Intrusions, Central Grenville (Francis et al. 2000). The lines with different slopes correspond to different Lu–Hf isotope evolution curves for the depleted mantle ($^{176}Lu/^{177}Hf$ = 0.0393; Blichert-Toft & Puchtel, 2010); mafic crust ($^{176}Lu/^{177}Hf$ = 0.022; Spencer et al. 2020); juvenile continental crust ("Quebecia", $^{176}Lu/^{177}Hf$ = 0.014; Spencer et al. 2020) reservoirs. The CHUR reference line (εHf = 0) involves an uncertainty of ±0.4 εHf units (Bouvier et al. 2008). U-Pb data of the Lac à l'Orignal Fe-Ti-P deposit after Miloski et al. (2023a) and for the Lac Mirepoix Fe-Ti-P mineralization after Miloski et al. (2023b).

Table 4.4. LA-ICP-MS Whole-rock major and trace element compositions for Fe-Ti-(P) mineralization in the Central Grenville Province

Sample	Lithology	Oxides	UTM-E	UTM-N	SiO_2	TiO_2	Al_2O_3	Fe_2O_{3t}	MnO	MgO	CaO	Na_2O	K_2O	P_2O_5	LOI	Total
Lac Périgny Fe-Ti-P mineralization - Poulin de Courval Mangerite																
20PM09A	Medium-grained OAN	Ilm + Mt	403222	5431875	40.1	4.1	15.8	16.6	0.2	4.9	9.9	3.1	1.1	3.8	0.3	100.0
20PM09B	Medium-grained OAN	Ilm + Mt	403222	5431875	38.5	4.8	11.1	20.5	0.3	8.9	8.1	1.6	2.1	4.0	0.1	100.0
20PM23C	Medium-grained OAN	Ilm + Mt	403226	5432881	37.1	4.4	15.2	17.8	0.2	4.5	11.8	2.8	0.5	5.7	0.0	100.0
20PM25	Medium-grained OAN	Ilm + Mt	403226	5432418	39.2	3.7	13.0	21.0	0.4	4.8	9.9	2.6	0.9	4.5	0.0	100.0
20PM26A	Medium-grained Leuco-OAN	Ilm + Mt	402636	5433515	45.0	3.2	15.8	16.6	0.2	4.2	8.9	3.2	0.5	2.2	0.1	100.0
20PM24	Medium-grained Leuco-OAN	Ilm + Mt	403214	5432851	49.0	1.4	22.1	8.7	0.1	2.9	9.2	4.0	0.9	1.3	0.4	100.0
20PM26B	Medium-grained Leuco-OAN	Ilm + Mt	402636	5433515	49.9	1.6	18.9	10.9	0.2	3.7	9.0	3.7	0.5	1.0	0.6	100.0
Lac de l'Abbondance Fe-Ti-P mineralization - Vanel Anorthosite																
20PM46E	Medium-grained OAN	Hm-ilm	392299	5432637	44.3	3.1	17.6	13.9	0.2	4.1	9.0	4.5	1.0	2.2	0.0	100.0
20PM46A	Medium-grained nelsonite	Ilm + Mt	392299	5432637	4.0	11.4	5.4	65.4	0.2	2.7	5.8	0.3	0.1	4.2	0.0	100.0
20PM47	Medium-grained nelsonite	Ilm + Mt	392270	5432656	3.0	11.1	4.8	65.7	0.2	2.4	6.8	0.2	0.1	5.2	0.0	100.0
Mattawa Fe-Ti-P mineralization - Mattawa Anorthosite																
20PM12-C2	Medium-grained Leuco-OAN	Hm-ilm + Mt	389480	5424110	42.2	5.4	12.7	19.4	0.2	3.1	8.8	3.3	1.1	3.3	0.5	100.0
20PM12B	Medium-grained Leuco-OAN	Hm-ilm + Mt	389480	5424110	37.1	5.0	11.8	23.2	0.2	5.2	9.6	2.3	0.6	4.1	0.9	100.0
20PM12D	Medium-grained Leuco-OAN	Hm-ilm + Mt	389480	5424110	44.9	4.8	12.9	17.2	0.2	3.7	8.3	3.3	1.1	2.6	1.0	100.0
21PM11-B	Medium-grained OAN	Ilm + Mt	376707	5418903	47.9	2.4	14.8	15.3	0.2	3.2	7.0	4.1	2.1	2.7	0.3	100.0
21PM18-B	Medium-grained OAN	Hm-ilm + Mt	382116	5422795	30.4	14.4	4.7	34.5	0.2	7.3	7.2	1.1	0.2	0.0	-0.2	100.0
21PM19	Medium-grained OAN	Hm-ilm + Mt	382889	5422795	30.1	14.7	4.3	35.0	0.2	7.6	7.0	0.9	0.1	0.0	-0.4	100.0
21PM12	Medium-grained Leuco-OAN	Hm-ilm + Mt	375331	5420378	53.0	2.7	13.6	13.9	0.2	2.2	5.7	3.6	2.6	1.8	0.6	100.0
21PM11-A	Medium-grained Leuco-OAN	Hm-ilm + Mt	376707	5418903	49.7	2.5	14.9	14.6	0.2	2.9	6.0	4.2	2.5	2.2	0.3	100.0
Labrieville Alkaline Anorthosite																
20PM32A	Medium-grained Leuco-OAN	Hm-ilm + Mt	433018	5459507	35.9	7.6	7.7	27.5	0.3	6.8	8.7	1.8	0.4	3.3	0.0	100.0
20PM42A	Medium-grained OAN	Hm-ilm + Mt	418253	5471028	35.3	7.1	7.4	28.0	0.3	6.5	9.6	1.8	0.4	3.5	0.0	100.0
20PM42B	Medium-grained Leuco-OAN	Hm-ilm	418253	5471028	55.9	2.2	13.7	12.6	0.2	2.2	5.4	3.3	3.1	1.6	0.0	100.0
20PM32B	Massive oxides	Hm-ilm	433018	5459507	1.0	34.1	2.0	59.0	0.1	2.5	0.5	0.0	0.0	0.1	0.0	100.0
20PM33B	Massive oxides	Hm-ilm	430892	5463836	6.7	31.2	3.3	54.6	0.1	1.5	1.2	0.7	0.2	0.1	0.0	100.0
20PM37	Massive oxides	Hm-ilm	429782	5470490	0.8	34.1	1.3	59.6	0.1	2.1	0.8	0.0	0.0	0.4	0.0	100.0
20PM38A	Medium-grained nelsonite	Hm-ilm	429698	5470593	0.8	30.7	1.0	60.7	0.1	1.3	2.9	0.0	0.0	2.1	0.0	100.0
20PM38C	Medium-grained nelsonite	Hm-ilm	429698	5470593	6.3	17.7	2.8	33.5	0.1	1.1	20.5	0.5	0.1	17.1	0.0	100.0
La Hache Fe-Ti-P mineralization - La Hache Mangerite																
21PM06	Oxide-apatite-rich mangerite	Ilm + Mt	363669	5417435	37.0	5.6	8.3	26.3	0.5	6.4	9.7	2.0	0.7	3.5	-0.1	100.0
21PM07	Oxide-apatite-rich mangerite	Ilm + Mt	363763	5417085	34.8	6.0	7.8	30.0	0.6	5.9	8.9	2.0	1.0	3.0	-0.6	100.0
21PM08	Oxide-apatite-rich mangerite	Ilm + Mt	360627	5425240	37.9	3.9	11.6	23.4	0.3	5.2	9.7	2.7	0.6	4.7	0.0	100.0
21PM09	Oxide-apatite-rich mangerite	Ilm + Mt	360627	5425240	12.5	7.0	4.9	46.9	0.3	2.9	13.2	0.8	0.3	11.1	-0.2	100.0
21PM57	Oxide-apatite-rich mangerite	Ilm + Mt	364912	5425682	50.6	1.8	16.7	11.8	0.3	3.1	6.9	4.6	2.1	1.9	0.2	100.0
L'Étang Fe-Ti mineralization - Vanel Anorthosite																
21PM53-A	Massive oxides	Ilm + Mt	371910	5435680	3.3	27.5	3.6	61.6	0.4	3.0	0.5	0.1	0.0	0.0	-3.1	100.0
21PM53-B	Medium-grained leuconorite	Ilm + Mt	371910	5435680	41.2	3.6	17.9	21.4	0.2	5.2	6.9	3.0	0.5	0.0	0.2	100.0
21PM55	Medium-grained leuconorite	Ilm + Mt	364953	5434038	43.9	0.8	12.9	17.9	0.2	16.2	5.1	1.9	0.4	0.2	0.5	100.0

Table 4.4. (cont.) LA-ICP-MS Whole-rock major and trace element compositions for sFe-Ti-(P) mineralization in the Central Grenville Province, Quebec

Sample	Lithology	Oxides	UTM-E	UTM-N	^{51}V	^{53}Cr	^{60}Ni	^{88}Sr	^{89}Y	^{90}Zr	^{93}Nb	^{137}Ba	^{139}La	^{140}Ce	^{153}Eu	^{172}Yb	^{175}Lu
Lac Périgny Fe-Ti-P mineralization - Poulin de Courval Mangerite																	
20PM09A	Medium-grained OAN	Ilm + Mt	403222	5431875	174.1	25.1	24.9	547.7	47.8	63.9	10.2	271.0	29.2	75.7	4.3	2.8	0.4
20PM09B	Medium-grained OAN	Ilm + Mt	403222	5431875	178.4	24.9	29.4	320.9	69.2	75.5	24.5	237.7	44.5	114.6	4.0	4.4	0.6
20PM23C	Medium-grained OAN	Ilm + Mt	403226	5432881	179.2	16.0	26.7	592.3	76.2	53.0	9.9	229.2	42.1	117.4	5.5	4.1	0.5
20PM25	Medium-grained OAN	Ilm + Mt	403226	5432418	101.8	12.3	11.9	441.9	81.0	370.3	15.5	384.0	48.2	123.8	5.9	5.3	0.8
20PM26A	Medium-grained Leuco-OAN	Ilm + Mt	402636	5433515	226.0	82.4	37.7	490.5	41.2	72.4	14.0	221.6	32.3	80.8	3.0	3.0	0.4
20PM24	Medium-grained Leuco-OAN	Ilm + Mt	403214	5432851	102.1	44.7	22.9	721.2	16.0	47.1	2.6	321.9	12.1	30.9	2.6	1.0	0.1
20PM26B	Medium-grained Leuco-OAN	Ilm + Mt	402636	5433515	60.1	39.9	12.0	553.8	33.3	49.7	11.1	273.3	20.8	51.6	3.1	3.0	0.4
Lac de l'Abbondance Fe-Ti-P mineralization - Vanel Anorthosite																	
20PM46E	Medium-grained OAN	Hm-ilm	392299	5432637	206.1	47.9	56.8	1288.0	22.4	60.7	5.4	801.3	25.4	63.1	3.1	1.3	0.2
20PM46A	Medium-grained nelsonite	Ilm + Mt	392299	5432637	###	784.0	443.1	232.5	20.2	53.0	2.7	64.1	20.8	56.4	2.4	0.9	0.1
20PM47	Medium-grained nelsonite	Ilm + Mt	392270	5432656	###	851.6	341.4	218.6	23.6	30.7	2.6	60.7	24.0	65.0	2.7	1.0	0.1
Mattawa Fe-Ti-P mineralization - Mattawa Anorthosite																	
20PM12-C2	Medium-grained Leuco-OAN	Hm-ilm + Mt	389480	5424110	282.3	42.9	36.8	889.6	66.0	218.4	35.7	835.3	60.7	156.3	6.0	4.4	0.6
20PM12B	Medium-grained Leuco-OAN	Hm-ilm + Mt	389480	5424110	351.5	24.7	30.0	959.6	56.8	206.3	15.2	755.4	67.0	166.5	6.4	3.4	0.5
20PM12D	Medium-grained Leuco-OAN	Hm-ilm + Mt	389480	5424110	249.0	34.9	31.9	893.1	59.1	207.4	29.0	832.1	52.4	132.3	4.8	4.0	0.6
21PM11-B	Medium-grained OAN	Ilm + Mt	376707	5418903	80.7	4.0	23.2	1467.3	41.3	39.7	16.7	####	42.5	107.2	7.2	2.4	0.3
21PM18-B	Medium-grained OAN	Hm-ilm + Mt	382116	5422795	###	63.1	35.5	183.5	11.9	73.2	17.8	108.2	2.0	7.2	0.9	1.0	0.1
21PM19	Medium-grained OAN	Hm-ilm + Mt	382889	5422795	###	63.1	47.7	144.4	11.5	128.7	17.9	77.7	1.8	6.4	0.8	1.0	0.1
21PM12	Medium-grained Leuco-OAN	Hm-ilm + Mt	375331	5420378	108.5	4.5	13.5	787.6	46.5	819.8	25.8	2104.5	55.8	131.0	6.7	3.3	0.5
21PM11-A	Medium-grained Leuco-OAN	Hm-ilm + Mt	376707	5418903	57.9	3.0	4.7	1380.8	45.2	62.8	20.6	####	45.8	116.4	8.7	2.7	0.4
Labrieville Alkaline Anorthosite																	
20PM32A	Medium-grained Leuco-OAN	Hm-ilm + Mt	433018	5459507	394.4	26.8	18.0	589.5	37.7	97.1	12.4	294.5	24.2	66.7	3.7	2.2	0.3
20PM42A	Medium-grained OAN	Hm-ilm + Mt	418253	5471028	450.7	13.5	10.2	568.1	48.1	169.5	13.9	292.5	34.9	90.8	4.6	3.1	0.4
20PM42B	Medium-grained Leuco-OAN	Hm-ilm	418253	5471028	100.5	36.5	18.8	743.2	47.5	1204.9	19.1	####	66.7	156.7	6.8	3.5	0.5
20PM32B	Massive oxides	Hm-ilm	433018	5459507	###	369.3	128.1	11.7	1.1	131.4	24.2	21.3	1.1	2.7	0.1	0.1	0.0
20PM33B	Massive oxides	Hm-ilm	430892	5463836	###	314.9	75.1	234.3	1.3	198.7	26.6	112.0	1.1	2.5	0.2	0.2	0.0
20PM37	Massive oxides	Hm-ilm	429782	5470490	###	651.4	72.0	17.0	2.8	163.6	31.5	19.1	2.1	6.0	0.3	0.2	0.0
20PM38A	Medium-grained nelsonite	Hm-ilm	429698	5470593	###	351.7	164.9	63.4	12.0	140.4	38.5	10.2	9.4	26.6	1.5	0.6	0.1
20PM38C	Medium-grained nelsonite	Hm-ilm	429698	5470593	988.1	201.7	60.6	576.8	93.9	87.9	22.3	110.7	76.6	214.5	12.2	4.2	0.5
La Hache Fe-Ti-P mineralization - La Hache Mangerite																	
21PM06	Oxide-apatite-rich mangerite	Ilm + Mt	363669	5417435	156.3	7.2	8.6	770.7	60.4	95.3	11.6	960.9	65.3	174.1	8.6	3.3	0.4
21PM07	Oxide-apatite-rich mangerite	Ilm + Mt	363763	5417085	85.5	6.2	24.4	541.5	57.3	65.9	9.5	1395.0	50.5	143.0	8.9	3.0	0.4
21PM08	Oxide-apatite-rich mangerite	Ilm + Mt	360627	5425240	193.2	7.2	11.7	1029.2	55.3	133.8	11.1	766.9	62.8	164.2	7.8	3.0	0.4
21PM09	Oxide-apatite-rich mangerite	Ilm + Mt	360627	5425240	621.8	4.2	12.9	621.5	97.6	79.3	14.9	305.5	119.1	349.1	13.0	4.7	0.6
21PM57	Oxide-apatite-rich mangerite	Ilm + Mt	364912	5425682	10.6	13.0	4.5	1473.4	49.8	147.2	12.4	4040.1	73.1	176.3	13.6	2.8	0.4
L'Étang Fe-Ti mineralization - Vanel Anorthosite																	
21PM53-A	Massive oxides	Ilm + Mt	371910	5435680	###	269.4	127.5	3.7	1.2	153.1	25.6	15.5	0.1	0.5	0.1	0.2	0.0
21PM53-B	Medium-grained leuconorite	Ilm + Mt	371910	5435680	784.8	112.7	95.5	470.2	2.0	17.3	1.8	174.0	1.5	2.8	0.9	0.3	0.0
21PM55	Medium-grained leuconorite	Ilm + Mt	364953	5434038	45.4	28.6	430.1	377.8	4.3	32.8	3.0	152.7	5.0	11.0	0.9	0.5	0.1

4.6.4 Geochemical variation of ore minerals

4.6.4.1 Fe-Ti oxides

Ilmenite and hemo-ilmenite compositions, determined by LA-ICP-MS, are presented in Table 4.5 and Appendix 4.1. Magnetite compositions, determined by LA-ICP-MS, are presented in Table 4.6 and Appendix 4.1. Magnetite in Fe-Ti-P mineralization from the Central Grenville is unusually poor in Ti (< 0.5wt%) and HFSE (Nb, Ta, Sc, Zr, Hf) compared to Ti-rich magnetite from layered intrusions and Fe-Ti-V mineralization in anorthosite (Fig.4.8), where higher magnetite/ilmenite ratios are normally observed. Fe-Ti-P mineralization contain larger proportions of ilmenite (Miloski et al. 2023a,b) than those normally observed on mafic layered intrusions associated with Fe-Ti-V and Fe-Ti-P mineralization (e.g. Dare et al. 2014, Fig.4.8). Moreover, similar to other studies (Dare et al. 2014; Arguin et al. 2018), the High Field Strength Elements (Zr, Hf, Nb, Ta, Ti) are preferentially enriched in ilmenite over co-existing magnetite whereas magnetite is enriched in Ga, Zn, Co, V, Ni and Cr relatively to ilmenite.

The trace elements concentrations of (hemo)-ilmenite from the different Fe-Ti-(P) mineralization are plotted on multi-element diagrams (Fig.4.7) and shows that overall, ilmenite has similar trace-element patterns among the different localities of Fe-Ti-P mineralization, but different concentrations according to lithology. In particular, Cr, Ni, V, Co and Pb decrease in ilmenite from the apatite-free lithologies (massive oxides and Fe-Ti leuconorite) towards the apatite-bearing nelsonite, OAN and oxide-apatite-mangerite, whereas Zn, W, Y, Ta and Nb increase as previously observed at Lac Mirepoix (Miloski et al. 2023b) and Lac à l'Orignal (Miloski et al. 2023a) mineralization. At these locations, Miloski et al. (2023a,b) pointed for the correlation between X_{Hem} in ilmenite and the distribution of V, whereas higher presence of hematite exsolutions would concentrate more V instead of in nearby magnetite crystals, in which V is usually more compatible. This is

corroborated by the dataset observed in the hematite-rich massive cumulates of Lac Brûlé, where highest V contents (> 3000ppm) are observed, instead of lower (<2000ppm) V values in ilmenite of L'Étang, Lac de L'Abbondance or La Hache, where it coexists with magnetite and ilmenite, and has consequently lower Xhem.

Oxide-apatite-norite in the different localities also have quite similar patterns, except for ilmenite from Lac Périgny that has positive-W anomalies that are absent in the other samples. Ilmenite in nelsonites at Lac Brûlé and Lac de l'Abbondance have similar patterns (Fig.4.7) to those in nelsonites from Lac Mirepoix and Lac à l'Orignal (Miloski et al. 2023a,b), although Lac de l'Abbondance contains ilmenite with slightly lower concentrations of Sc, Ta and Nb in relation to the other areas. Leuco-OAN in the Mattawa Anorthosite present lower Cr, Ni, V and Co and higher W, Sc, Ta, Nb, Sn and Ga values in relation to apatite-free leuconorites at L'Étang, being the latter more similar to massive oxides, as previously mentioned. Mineralization at La Hache, hosted in mangerite, have broadly the lowest Cr, Ni, V and Co and higher concentrations of Pb, Zr, Hf, W, Ta, Nb in relation to the other cumulates. Fine-grained ferrodiorite samples in the different Fe-Ti-P mineralization have similar patterns, displaying concentrations in the same range of OAN cumulates, except for Ta and Nb, that are higher in the former.

Magnetite trace element concentrations from the different localities of Fe-Ti-(P) mineralization are plotted on multi-element diagrams (Fig.4.8). Overall, magnetite in this study has similar trace-element patterns (Fig.4.8) in comparison to those from Lac Mirepoix and Lac à l'Orignal (Miloski et al. 2023a,b), but again different concentrations according to lithology, as observed in ilmenite. Cr, Ni, V, Co and Mn decrease in magnetite from massive oxides cumulates towards apatite-bearing nelsonite, OAN and oxide-apatite-mangerites. Moreover, magnetite at the La Hache Mangerite contains higher Pb, Ge, Sc, Ta Nb, Mo, Sn, Ga, Mn and Zn in relation to the other analyzed cumulates. Overall, magnetite in the

leuconorites (e.g., L'Étang) have similar trace-element patterns and concentrations to OAN cumulates (e.g., Lac Mirepoix and Lac à l'Orignal and Mattawa; Fig.4.8).

Table 4.5. LA-ICP-MS major and trace element analyses of ilmenite for Fe-Ti-P mineralization in the Central Grenville Province

Detection Limits (33-55µm)													0.205-1.345	0.035-0.296	0.252-3.179	0.251-1.198
Sample	Lithology	Oxide Mineralogy	# analysis	SiO_2	TiO2	Al_2O_3	FeO_t	Fe_2O_3	FeO	MnO	MgO	Total	^{45}Sc	^{51}V	^{53}Cr	^{60}Ni
20PM09	Medium-grained OAN	Ilm + Mt	n=8	0.0	50.2	0.0	48.0	4.9	43.7	0.8	0.4	100.1	13.8	254.5	0.9	3.8
20PM24	Medium-grained Leuco-OAN	Ilm + Mt	n=3	0.7	47.3	0.1	49.5	8.3	42.1	0.7	0.2	99.2	17.0	455.4	53.7	9.8
20PM23C	Medium-grained OAN	Ilm + Mt	n=3	0.6	50.2	0.0	49.5	6.9	43.3	0.3	1.1	102.4	9.3	455.1	28.1	6.0
20PM25	Medium-grained OAN	Ilm + Mt	n=3	0.5	49.1	0.1	49.5	7.8	42.5	1.0	0.4	101.4	29.8	154.8	51.9	2.2
20PM26A	Medium-grained Leuco-OAN	Ilm + Mt	n=3	0.4	45.0	0.1	52.7	14.5	39.7	0.6	0.5	101.0	45.5	974.7	75.5	4.6
20PM46A	Medium-grained nelsonite	Ilm + Mt	n=3	0.0	44.5	0.0	50.2	14.5	37.1	0.8	1.3	98.4	33.1	1136.8	113.4	26.2
20PM47	Medium-grained nelsonite	Ilm + Mt	n=3	0.1	43.5	0.1	51.0	16.9	35.8	0.9	1.5	98.9	39.5	991.7	242.1	67.3
20PM46E	Medium-grained OAN	Hm-ilm	n=3	0.2	41.0	0.1	56.6	23.5	35.5	1.5	0.1	101.9	19.3	1010.5	23.8	21.2
20PM12B	Medium-grained Leuco-OAN	Hm-ilm + Mt		0.4	36.3	0.1	62.3	34.2	31.5	0.4	0.7	103.6	54.1	1422.4	11.9	3.9
20PM12C	Medium-grained Leuco-OAN	Hm-ilm + Mt	n=3	0.1	34.8	0.1	63.5	36.3	30.9	0.4	0.2	102.9	67.9	1343.3	47.0	4.6
20PM12D	Medium-grained Leuco-OAN	Hm-ilm + Mt	n=3	0.1	35.9	0.1	62.8	34.5	31.7	0.4	0.2	103.1	68.8	1330.3	46.5	6.7
21PM50	Medium-grained OAN	Hm-ilm + Mt	n=3	0.0	41.5	0.1	55.4	5.1	50.9	0.2	2.0	100.0	26.3	1956.3	67.4	35.4
21PM13B	Medium-grained OAN	Hm-ilm + Mt	n=3	0.0	44.6	0.0	54.4	3.9	50.8	0.3	0.1	99.9	41.7	782.2	9.0	4.2
21PM17A	Medium-grained OAN	Hm-ilm + Mt	n=3	0.1	38.2	0.1	59.2	5.7	54.1	0.3	1.4	100.1	31.4	2005.1	521.0	53.5
21PM16D	Medium-grained OAN	Hm-ilm + Mt	n=3	0.1	38.6	0.1	58.4	5.6	53.4	0.2	1.6	100.0	27.0	2154.1	211.0	60.5
21PM18B	Medium-grained OAN	Hm-ilm + Mt	n=3	0.0	38.7	0.1	59.3	5.7	54.2	0.2	0.9	100.1	31.1	1910.6	125.5	14.5
21PM19	Medium-grained OAN	Hm-ilm + Mt	n=3	0.0	38.5	0.1	59.4	5.5	54.5	0.2	0.9	100.0	30.2	2121.1	127.9	14.4
21PM11B	Medium-grained Leuco-OAN	Ilm + Mt	n=3	0.1	48.6	0.1	49.6	2.5	47.3	0.7	0.4	99.7	62.6	211.6	1.2	0.2
20PM32B	Massive oxides	Hm-ilm	n=3	0.2	36.9	0.1	56.3	29.7	29.6	0.1	2.2	99.1	26.0	2156.1	300.1	90.3
20PM33A	Massive oxides	Hm-ilm + Mt	n=3	-	37.6	0.1	58.9	31.1	31.0	0.2	1.7	101.9	28.0	2116.7	277.0	44.3
20PM34	Massive oxides	Hm-ilm	n=3	0.1	37.5	0.1	59.8	31.8	31.2	0.2	1.5	102.7	29.9	1846.0	232.3	40.8
20PM37A	Massive oxides	Hm-ilm	n=3	0.0	37.4	0.1	60.2	32.8	30.6	0.2	1.8	103.4	30.0	2311.2	724.9	149.9
20PM38A	Medium-grained nelsonite	Hm-ilm	n=3	0.1	37.0	0.1	62.4	33.3	32.5	0.1	0.5	103.8	32.5	2022.6	335.5	34.0
20PM38C	Medium-grained nelsonite	Hm-ilm	n=3	0.8	37.7	0.1	61.9	33.1	32.1	0.1	1.2	105.0	33.1	1932.0	305.8	9.0
20PM32A	Medium-grained leuconorite	Hm-ilm	n=3	0.4	37.2	0.1	62.8	33.7	32.4	0.3	0.7	104.9	36.1	2206.4	42.9	18.2
20PM42A	Medium-grained OAN	Hm-ilm + Mt	n=3	-	39.2	0.1	59.1	28.9	33.0	0.4	1.1	103.0	51.9	1334.3	6.7	3.0
20PM42B	Medium-grained Leuco-OAN	Hm-ilm	n=3	0.1	41.5	0.1	55.8	23.6	34.5	1.0	1.1	102.0	96.0	535.4	5.2	0.4
21PM08	Oxide-apatite-rich mangerite	Ilm + Mt	n=3	0.0	49.0	0.1	50.0	6.3	44.3	0.8	0.7	101.3	68.8	382.0	2.6	0.6
21PM09	Oxide-apatite-rich mangerite	Ilm + Mt	n=3	0.0	49.2	0.1	49.9	6.3	44.2	0.7	0.7	101.3	71.0	410.4	0.9	1.0
21PM57	Oxide-apatite-rich mangerite	Ilm + Mt	n=3	0.1	50.5	0.1	47.4	4.6	43.3	1.5	0.7	100.8	73.2	17.6	0.3	0.0
21PM06	Oxide-apatite-rich mangerite	Ilm + Mt	n=3	0.0	52.2	0.0	45.3	1.3	44.1	1.1	0.8	99.6	50.2	51.8	0.6	0.6
21PM07	Oxide-apatite-rich mangerite	Ilm + Mt	n=3	0.1	50.3	0.0	48.8	8.2	41.4	1.3	0.9	102.2	73.3	31.4	0.7	0.4
21PM59	Oxide-apatite-rich mangerite	Ilm + Mt	n=3	0.3	47.4	0.1	51.4	8.3	44.0	1.3	0.5	102.0	52.0	60.3	0.8	0.1
21PM56	Oxide-apatite-rich charnockite	Ilm + Mt	n=3	0.3	48.9	0.0	50.5	7.0	44.3	1.1	0.1	101.6	12.4	6.1	0.9	0.1
21PM53A	Massive oxides	Ilm + Mt	n=3	0.0	49.7	0.1	47.3	2.7	44.9	0.5	1.7	99.9	42.0	987.6	29.5	39.2
21PM52A	Medium-grained leuconorite	Ilm + Mt	n=3	0.1	47.0	0.1	50.4	3.4	47.4	0.4	1.3	100.0	15.4	1442.8	345.1	43.9
21PM53B	Medium-grained leuconorite	Ilm + Mt	n=3	0.2	50.4	0.1	47.2	2.8	44.7	0.6	1.2	99.9	27.6	735.8	51.5	30.6
21PM55	Medium-grained leuconorite	Ilm + Mt	n=3	0.1	51.1	0.0	46.1	2.9	43.4	0.6	1.8	100.0	6.0	70.8	15.0	191.0

Table 4.6. LA-ICP-MS major and trace element analyses of magnetite for Fe-Ti-P mineralization in the Central Grenville Province

Detection Limits (33-55µm)												0.047-0.242	1.527-9.987	0.719-2.736
Sample	Lithology	Oxide Mineralogy	# analysis	SiO_2	TiO_2	Al_2O_3	Fe_2O_3	FeO	MnO	MgO	Total	^{51}V	^{53}Cr	^{60}Ni
Lac Périgny Fe-Ti-P mineralization - Poulin de Courval Mangerite														
20PM09	Medium-grained OAN	Ilm + Mt	n=8	0.60	0.41	0.54	69.91	29.48	0.03	0.11	101.2	990.9	5.7	14.8
20PM24	Medium-grained Leuco-OAN	Ilm + Mt	n=3	1.07	0.16	0.79	72.48	26.76	0.02	0.23	102.3	3345.4	1064.3	61.1
20PM23C	Medium-grained OAN	Ilm + Mt	n=3	0.65	0.63	1.14	72.57	26.69	0.01	0.17	102.5	3859.7	50.6	35.3
20PM25	Medium-grained OAN	Ilm + Mt	n=3	0.84	2.92	2.40	80.30	19.72	0.11	0.14	106.7	1359.6	37.8	14.0
20PM26A	Medium-grained Leuco-OAN	Ilm + Mt	n=3	0.84	0.08	0.63	70.52	28.53	0.01	0.12	101.4	3789.1	790.4	22.9
Lac de l'Abbondance Fe-Ti-P mineralization - Vanel Anorthosite														
20PM46A	Medium-grained nelsonite	Ilm + Mt	n=3	0.04	0.08	0.47	67.67	31.09	0.02	0.09	100.1	3220.8	1451.3	213.2
20PM47	Medium-grained nelsonite	Ilm + Mt	n=3	0.07	0.05	0.40	67.52	31.22	0.02	0.11	100.1	3200.9	1348.9	245.6
20PM46E	Medium-grained OAN	Hm-ilm	n=3	0.18	0.08	0.42	67.12	31.59	0.02	0.09	99.81	1920.3	92.4	53.6
Mattawa Fe-Ti-P mineralization - Mattawa Anorthosite														
20PM12B	Medium-grained Leuco-OAN	Hm-ilm + Mt	n=3	0.48	0.09	0.50	68.18	30.63	0.01	0.08	100.3	2096.3	78.4	22.6
20PM12C	Medium-grained Leuco-OAN	Hm-ilm + Mt	n=3	0.13	0.10	0.43	66.93	31.76	0.01	0.04	99.76	2274.0	130.9	28.6
20PM12D	Medium-grained Leuco-OAN	Hm-ilm + Mt	n=3	0.24	0.06	0.35	66.79	31.88	0	0.03	99.7	2055.8	193.5	29.3
21PM13B	Medium-grained OAN	Hm-ilm + Mt	n=3	0.21	0.09	0.01	65.45	33.09	0.01	0.06	99.2	1965.8	44.9	14.9
21PM11B	Medium-grained OAN	Ilm + Mt	n=3	0.30	0.57	0.00	66.63	32.02	0.03	0.12	99.83	1110.1	0.6	1.4
Labrieville Alkaline Anorthosite														
20PM33A	Massive oxides	Hm-ilm + Mt	n=3	0.31	0.05	0.46	68.61	30.25	0	0.17	100.5	3143.9	1358.3	301.9
20PM42A	Medium-grained OAN	Hm-ilm + Mt	n=3	1.70	0.09	0.47	72.89	26.40	0.01	0.08	102.6	2554.1	92.8	11.1
20PM42B	Medium-grained Leuco-OAN	Hm-ilm	n=3	0.28	0.07	0.41	67.18	31.53	0.02	0.13	99.8	1059.3	8.0	4.8
La Hache Fe-Ti-P mineralization - La Hache Mangerite														
21PM08	Oxide-apatite-rich mangerite	Ilm + Mt	n=3	0.68	0.28	0.00	67.36	31.37	0.02	0.15	100.1	1457.5	25.3	6.2
21PM09	Oxide-apatite-rich mangerite	Ilm + Mt	n=3	0.34	0.70	0.00	69.59	29.37	0.03	0.15	101.2	1684.8	3.3	3.3
21PM57	Oxide-apatite-rich mangerite	Ilm + Mt	n=3	0.32	2.32	0.00	70.55	28.50	0.12	0.23	102.1	164.2	2.0	0.2
21PM06	Oxide-apatite-rich mangerite	Ilm + Mt	n=3	0.25	9.07	0.01	72.20	21.28	0.43	0.26	103.7	1079.1	31.7	6.7
21PM07	Oxide-apatite-rich mangerite	Ilm + Mt	n=3	0.28	9.84	0.01	74.79	14.85	0.62	0.36	104.2	676.3	31.4	2.7
21PM59	Oxide-apatite-rich mangerite	Ilm + Mt	n=3	0.68	0.89	0.00	68.46	30.38	0.06	0.17	100.7	276.9	4.7	1.0
21PM56	Oxide-apatite-rich charnockite	Ilm + Mt	n=3	0.66	1.59	0.00	69.23	29.69	0.07	0.04	101.3	54.9	2.9	0.6
L'Étang Fe-Ti mineralization - Vanel Anorthosite														
21PM53A	Massive oxides	Ilm + Mt	n=3	0.06	1.03	0.13	70.22	28.80	0.04	0.3	101.7	7585.3	720.0	234.7
21PM52A	Medium-grained leuconorite	Ilm + Mt	n=3	0.54	0.40	0.78	72.58	26.67	0.02	0.21	102.8	6674.7	4289.7	322.2
21PM53B	Medium-grained leuconorite	Ilm + Mt	n=3	0.18	0.98	0.20	70.27	28.75	0.04	0.27	101.7	6289.9	1085.6	202.4
21PM55	Medium-grained leuconorite	Ilm + Mt	n=3	0.15	1.52	0.04	69.94	29.05	0.04	0.42	101.5	527.7	222.2	1325.6

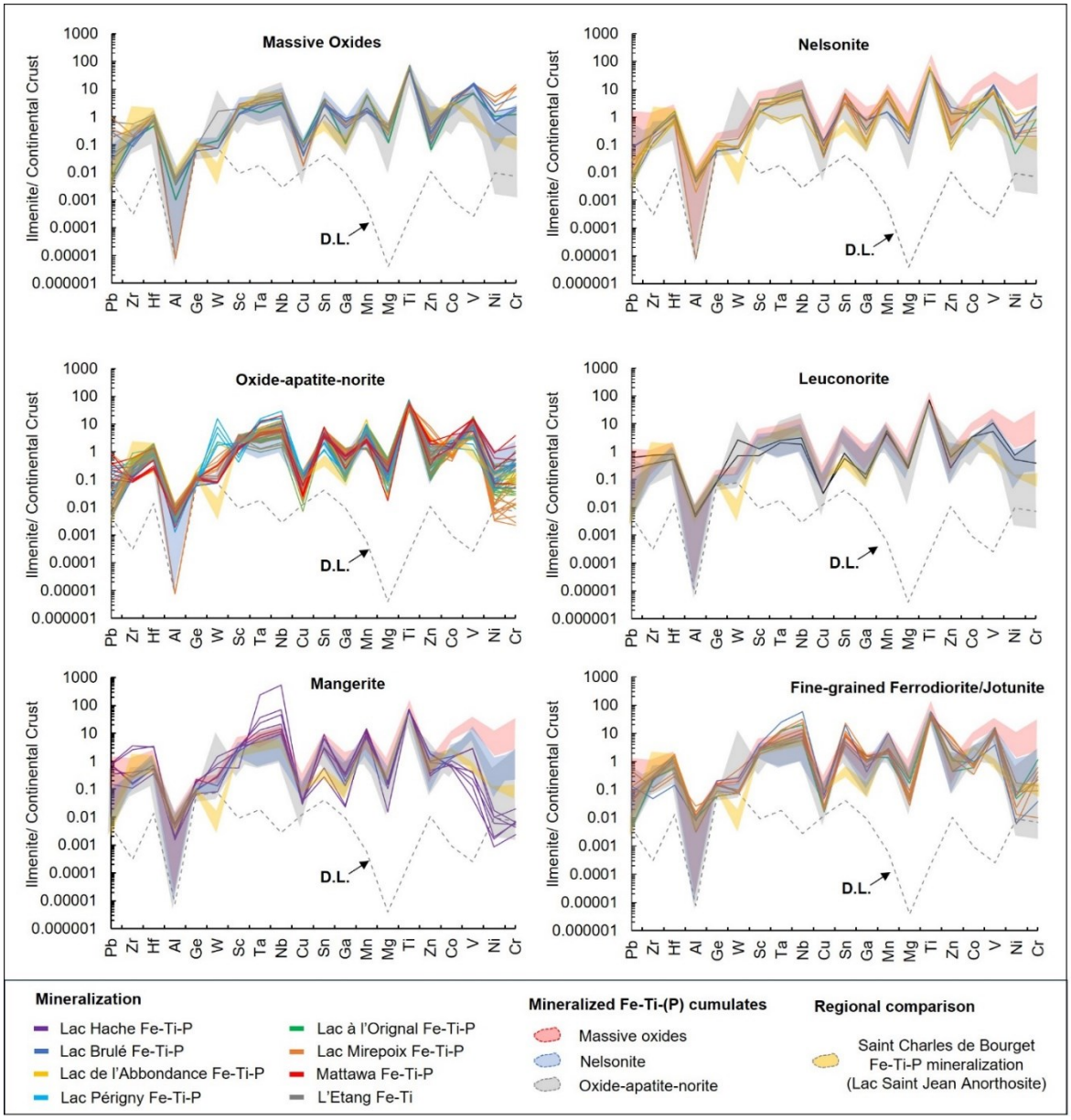

Figure 4.7. Continental-crust-normalized trace element compositions of ilmenite (after Rudnick & Gao, 2003) from the different analyzed Fe-Ti-P mineralization in the Central Grenville Province, Quebec. Comparison with Fe-Ti-P mineralization at St. Charles de Bourget of the Lac-Saint-Jean Anorthositic Suite (yellow fields, Dare et al. 2014). Previously published data: Lac à l'Orignal Fe-Ti-P deposit (Miloski et al. 2023a) and the Lac Mirepoix Fe-Ti-P mineralization (Miloski et al. 2023b).

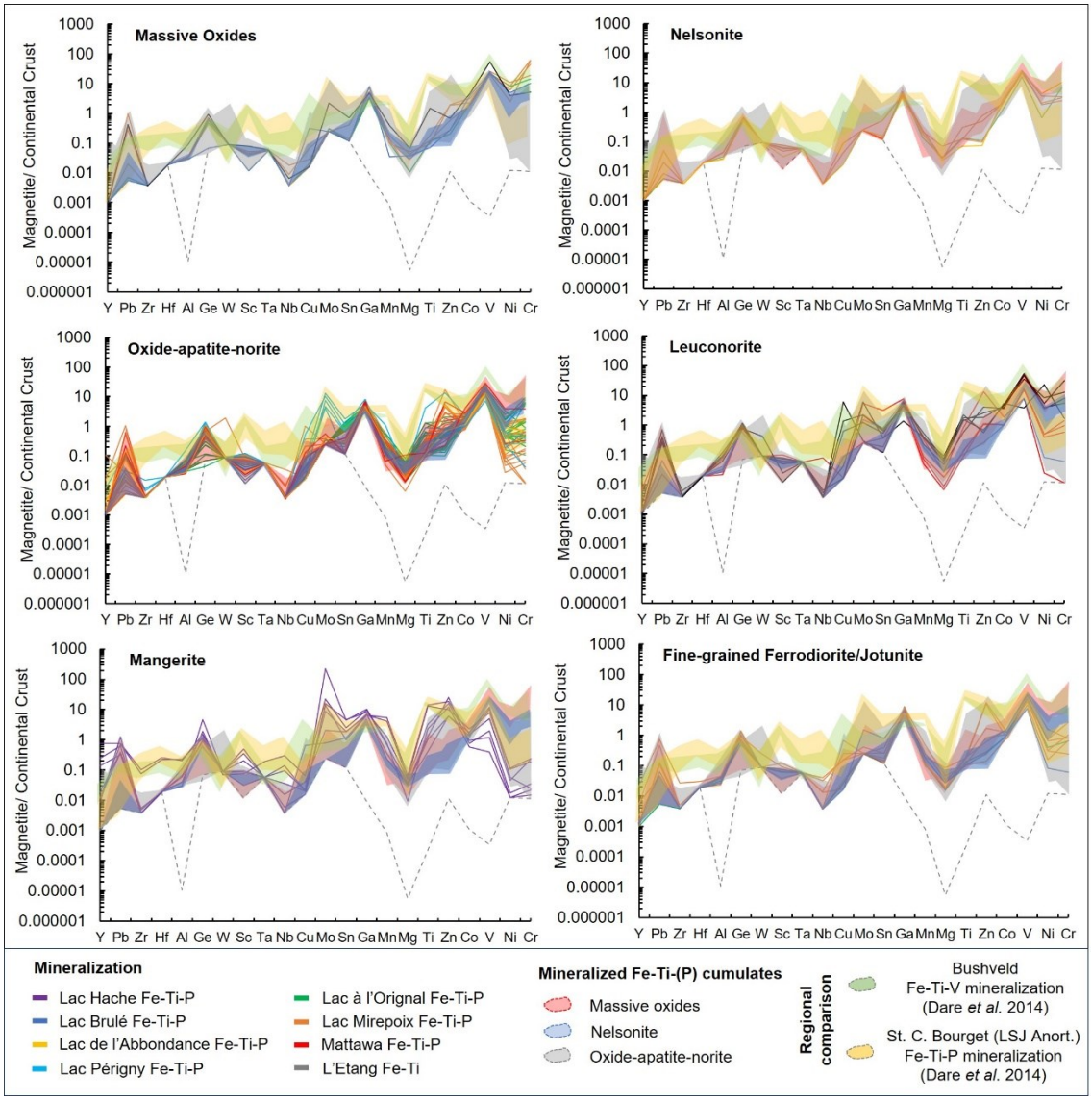

Figure 4.8. Continental-crust-normalized trace element compositions of magnetite (after Rudnick & Gao, 2003) from the different analyzed Fe-Ti-P mineralization in the Central Grenville Province, Quebec. Comparison with Fe-Ti-V mineralization at the Bushveld (green fields) and Fe-Ti-P mineralization at St. Charles-de-Bourget of the Lac-Saint-Jean Anorthositic Suite (yellow fields, Dare et al. 2014). Previously published data: Lac à l'Orignal Fe-Ti-P deposit (Miloski et al. 2023a) and the Lac Mirepoix Fe-Ti-P mineralization (Miloski et al. 2023b).

4.6.4.2 Apatite

Apatite compositions of mineralized cumulates, determined by LA-ICP-MS, are presented in Table 4.7 and displayed in Figure 4.9 and Appendix 4.3. The trace element concentrations of apatite (including REE) from the different localities of Fe-Ti-(P) mineralization are plotted on multi-element diagrams (Fig.4.9) and shows that overall, as observed in the oxide phases, apatite has similar trace element patterns in the different localities of Fe-Ti-(P) mineralization (Fig.4.9), including those from Lac Mirepoix and Lac à l'Orignal (Miloski et al. 2023a,b). Trace element REE, Th, U concentrations in apatite generally increase from massive nelsonites towards oxide-apatite norite and oxide-apatite mangerite (Fig.4.9). Slightly positive Th-U anomalies are present in samples associated to the Vanel Anorthosite and the La Hache Mangerite, whereas negative anomalies are observed for mineralization in the anorthosites of Labrieville (Lac Brûlé mineralization) and Mattawa. Trace element concentrations of apatite of Fe-Ti-(P) mineralization in the Central Grenville Province show similar pattern, in particular a LREE enrichment relative to HREE, in relation to apatite from Fe-Ti-P mineralization from the Saint Urbain Anorthosite (Morisset, 2008), southern Quebec, the Grader intrusion, Havre-Saint-Pierre Anorthositic Suite (Charlier et al. 2008) and the Sept-Iles (Kieffer et al. 2022) layered intrusion, northeastern Quebec.

However, the Sr content of apatite (Appendix 4.3) varies with location, with the highest values (Sr_{Ap}: 600 – 1500 ppm) in the Fe-Ti-P mineralization related to the Vanel Anorthosite (Lac à l'Orignal, Lac Mirepoix, Lac de l'Abbondance). Mineralization in the La Hache Mangerite (Sr_{Ap}: 700 – 1200 ppm) and the anorthosite massifs of Labrieville (Sr_{Ap}: 800 – 1100 ppm) and Mattawa (Sr_{Ap}: 550 – 950 ppm) have intermediate Sr values in apatite, whereas Lac Périgny has clearly lower Sr contents in apatite (350 -750 ppm), similar to that in the Grader Intrusion (Sr_{Ap}: 450 – 550 ppm, Charlier et al. 2008).

Table 4.7. LA-ICP-MS major and trace element analysis of apatite for Fe-Ti-P mineralization in the Central Grenville Province, Quebec

Detection Limits (33-55µm bean size)												0.01-0.07	0.01-0.02	0.003-0.014	0.003-0.012
Sample	Lithology	Oxide Mineralogy	# analysis	La_2O_3	Ce_2O_3	Pr_2O_3	Nd_2O_3	CaO	P_2O_5	FeO_t	Total	Sr	Y	La	Ce
Lac Périgny Fe-Ti-P mineralization - Poulin de Courval Mangerite															
20PM23C	Medium-grained OAN	Ilm + Mt	n=5	0.0	0.1	0.0	0.1	54.4	48.8	0.1	103.6	654.3	227.7	296.0	829.6
20PM24	Medium-grained Leuco-OAN	Ilm + Mt	n=5	0.0	0.1	0.0	0.1	54.4	49.3	0.1	104.0	436.1	378.4	255.1	712.8
20PM25	Medium-grained OAN	Ilm + Mt	n=5	0.1	0.1	0.0	0.1	54.4	48.8	0.1	103.6	430.7	623.8	467.8	1248.0
20PM26A	Medium-grained Leuco-OAN	Ilm + Mt	n=5	0.0	0.1	0.0	0.1	54.4	50.5	0.1	105.3	353.5	599.7	377.4	1019.0
20PM09A	Medium-grained OAN	Ilm + Mt	n=5	0.0	0.1	0.0	0.1	54.1	45.2	0.3	99.8	503.0	320.1	290.8	767.6
Lac de l'Abbondance Fe-Ti-P mineralization - Vanel Anorthosite															
20PM46A	Medium-grained nelsonite	Ilm + Mt	n=5	0.0	0.1	0.0	0.1	54.4	51.0	0.1	105.7	2113.9	191.2	222.3	604.7
20PM47A	Medium-grained nelsonite	Ilm + Mt	n=5	0.0	0.1	0.0	0.1	54.4	51.5	0.3	106.4	1839.1	182.1	202.9	562.6
20PM46E	Medium-grained OAN	Hm-ilm	n=5	0.0	0.1	0.0	0.1	54.4	50.5	0.0	105.2	988.6	207.3	322.6	834.4
Mattawa Fe-Ti-P mineralization - Mattawa Anorthosite															
20PM11B	Medium-grained OAN	Ilm + Mt	n=5	0.1	0.2	0.0	0.1	54.4	47.9	0.2	102.9	975.7	621.6	623.7	1643.3
Labrieville Alkaline Anorthosite															
20PM38A	Medium-grained nelsonite	Hm-ilm	n=5	0.0	0.1	0.0	0.1	54.4	65.8	0.6	121.0	1305.1	267.9	222.0	609.6
20PM38C	Medium-grained nelsonite	Hm-ilm	n=5	0.0	0.1	0.0	0.1	54.4	53.9	0.5	109.0	1295.8	265.0	214.7	593.7
20PM42A	Medium-grained OAN	Hm-ilm + Mt	n=5	0.1	0.1	0.0	0.1	54.4	50.9	0.1	105.8	940.2	554.8	460.1	1195.9
20PM42B	Medium-grained Leuco-OAN	Hm-ilm	n=5	0.2	0.4	0.1	0.3	54.4	45.4	0.3	101.1	440.9	1115.9	1498.8	3674.8
La Hache Fe-Ti-P mineralization - La Hache Mangerite															
21PM06	Oxide-apatite-rich mangerite	Ilm + Mt	n=5	0.1	0.2	0.0	0.2	54.4	46.8	0.3	102.0	1020.1	572.2	789.2	2066.2
21PM07	Oxide-apatite-rich mangerite	Ilm + Mt	n=5	0.1	0.2	0.0	0.2	54.4	47.0	0.5	102.4	794.4	628.3	710.7	1979.5
21PM08	Oxide-apatite-rich mangerite	Ilm + Mt	n=5	0.1	0.2	0.0	0.1	54.4	46.1	0.4	101.3	851.3	464.8	498.3	1351.9
21PM09	Oxide-apatite-rich mangerite	Ilm + Mt	n=5	0.1	0.2	0.0	0.1	54.4	46.7	0.3	101.8	761.2	436.8	534.5	1396.2
21PM57	Oxide-apatite-rich mangerite	Ilm + Mt	n=5	0.2	0.4	0.1	0.3	54.4	48.0	0.2	103.6	1049.5	834.8	1331.1	3375.3
21PM59	Oxide-apatite-rich mangerite	Ilm + Mt	n=5	0.1	0.2	0.0	0.2	54.4	46.1	0.2	101.2	1053.5	1445.8	448.5	1656.7

Table 4.7. (cont.) LA-ICP-MS major and trace element analysis of apatite for Fe-Ti-P mineralization in the Central Grenville Province

Detection Limits (33-55µm bean size)				0.002-0.008	0.012-0.030	0.013-0.021	0.003-0.009	0.015-0.057	0.002-0.004	0.008-0.014	0.002-0.003	0.006-0.015	0.002-0.004	0.009-0.027	0.002-0.003
Sample	Lithology	Oxide Mineralogy	# analysis	Pr	Nd	Sm	Eu	Gd	Tb	Dy	Ho	Er	Tm	Yb	Lu
Lac Périgny Fe-Ti-P mineralization - Poulin de Courval Mangerite															
20PM23C	Medium-grained OAN	Ilm + Mt	n=5	128.7	667.3	147.2	28.4	137.9	14.4	64.6	8.7	14.6	1.0	3.5	0.3
20PM24	Medium-grained Leuco-OAN	Ilm + Mt	n=5	108.2	556.0	126.9	26.2	128.8	15.2	81.1	14.3	33.3	3.5	18.3	2.5
20PM25	Medium-grained OAN	Ilm + Mt	n=5	183.1	897.8	199.8	37.5	194.6	23.9	131.5	23.5	55.4	6.1	32.3	4.4
20PM26A	Medium-grained Leuco-OAN	Ilm + Mt	n=5	151.4	762.1	174.8	31.4	175.9	21.7	119.6	22.0	54.0	6.1	33.4	4.6
20PM09A	Medium-grained OAN	Ilm + Mt	n=5	114.4	573.0	123.6	27.1	126.9	13.7	68.4	11.8	27.6	3.0	15.6	2.2
Lac de l'Abbondance Fe-Ti-P mineralization - Vanel Anorthosite															
20PM46A	Medium-grained nelsonite	Ilm + Mt	n=5	94.4	483.8	97.3	24.1	86.3	9.0	44.5	7.3	15.7	1.6	7.6	0.9
20PM47A	Medium-grained nelsonite	Ilm + Mt	n=5	87.4	449.7	90.8	23.0	81.0	8.6	41.5	7.0	14.9	1.5	7.6	1.0
20PM46E	Medium-grained OAN	Hm-ilm	n=5	120.9	593.6	110.2	26.9	93.8	9.6	47.3	7.8	17.2	1.8	9.4	1.3
Mattawa Fe-Ti-P mineralization - Mattawa Anorthosite															
20PM11B	Medium-grained OAN	Ilm + Mt	n=5	249.6	1251.5	274.8	58.8	248.0	28.4	143.8	23.7	54.2	5.8	30.3	3.8
Labrieville Alkaline Anorthosite															
20PM38A	Medium-grained nelsonite	Hm-ilm	n=5	100.3	527.3	121.8	34.9	112.0	12.0	60.6	10.0	21.9	2.3	11.8	1.5
20PM38C	Medium-grained nelsonite	Hm-ilm	n=5	97.9	516.0	120.2	34.2	109.8	12.1	60.9	10.1	22.4	2.3	12.4	1.6
20PM42A	Medium-grained OAN	Hm-ilm + Mt	n=5	184.1	924.1	210.6	49.3	197.7	22.9	123.3	21.2	50.7	5.5	29.7	3.8
20PM42B	Medium-grained Leuco-OAN	Hm-ilm	n=5	557.3	2641.1	529.8	93.3	424.9	50.7	257.6	43.7	102.7	11.1	64.7	8.0
La Hache Fe-Ti-P mineralization - La Hache Mangerite															
21PM06	Oxide-apatite-rich mangerite	Ilm + Mt	n=5	312.9	1548.2	316.6	60.8	266.5	28.4	135.0	21.2	46.1	4.6	23.5	2.9
21PM07	Oxide-apatite-rich mangerite	Ilm + Mt	n=5	318.3	1672.3	351.0	70.2	303.9	31.8	150.3	23.5	50.1	4.9	24.3	3.1
21PM08	Oxide-apatite-rich mangerite	Ilm + Mt	n=5	209.6	1072.8	231.2	53.8	202.0	22.2	109.2	17.5	39.7	4.2	22.4	2.9
21PM09	Oxide-apatite-rich mangerite	Ilm + Mt	n=5	209.3	1046.5	221.6	51.6	191.5	20.9	102.4	16.3	36.7	3.9	21.4	2.8
21PM57	Oxide-apatite-rich mangerite	Ilm + Mt	n=5	512.7	2488.3	482.4	98.3	395.7	42.5	205.0	32.2	70.8	7.3	37.5	4.7
21PM59	Oxide-apatite-rich mangerite	Ilm + Mt	n=5	346.4	2141.4	596.5	180.8	568.8	67.2	339.6	55.4	127.1	13.7	73.9	9.6

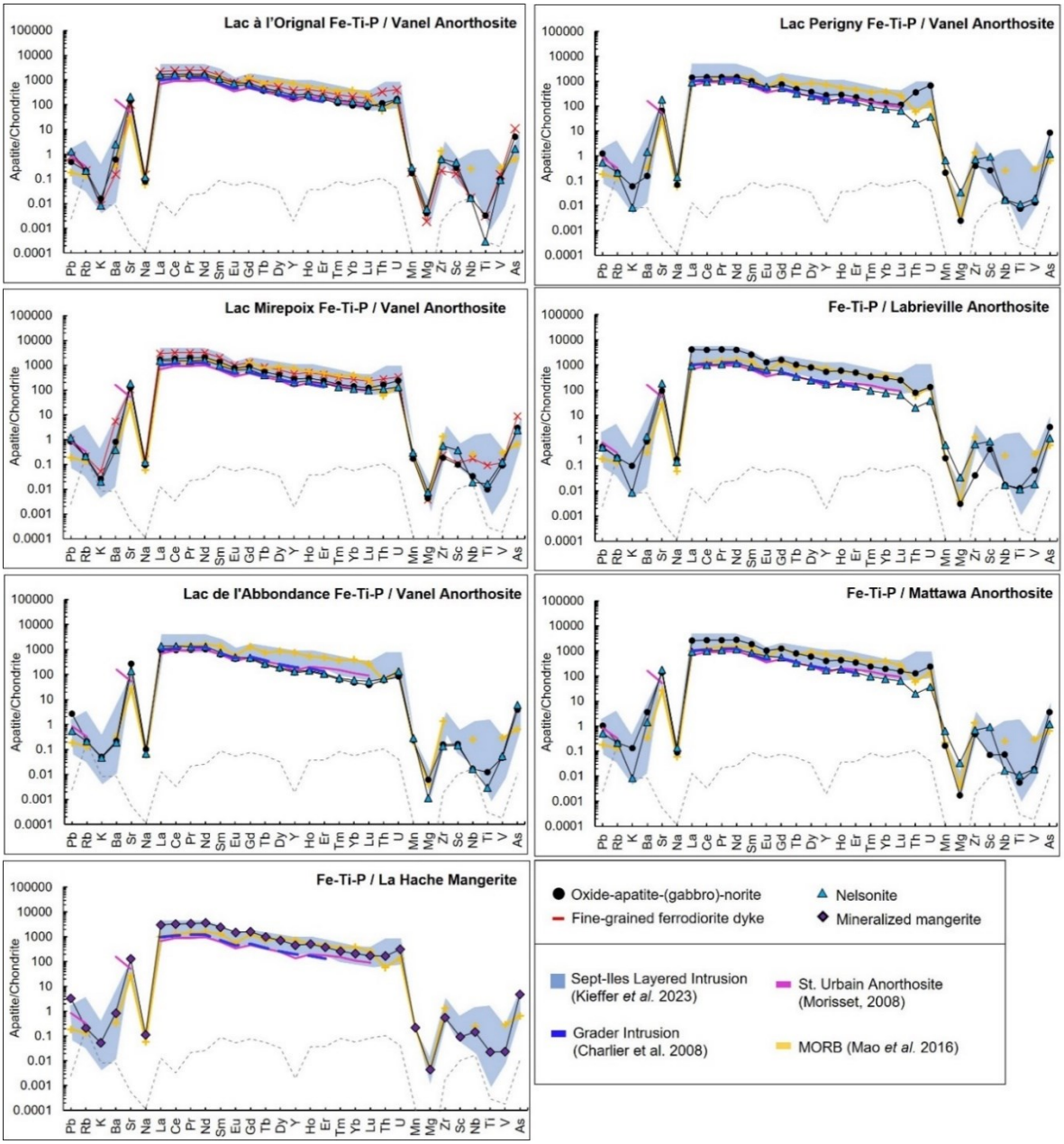

Figure 4.9. Chondrite-normalized trace element compositions of apatite (after Sun & McDonough, 1989) in the different analyzed Fe-Ti-P mineralization of the Central Grenville Province, Quebec. Comparison with reference cumulus apatite data of the Sept Iles Layered Mafic Intrusion, Quebec (Kieffer et al. 2022), MORB (Mao et al. 2016), Fe-Ti-P mineralization: Lac à l'Orignal Fe-Ti-P deposit (Miloski et al. 2023a) and Lac Mirepoix Fe-Ti-P mineralization (Miloski et al. 2023b).

4.6.4.3 Plagioclase

Plagioclase compositions of mineralized cumulates and host anorthosite/mangerite, determined by LA-ICP-MS (Table 4.8) and pXRF (Table 4.9), are presented in Figure 4.10. Plagioclase from Fe-Ti-P mineralization display different An and Sr concentrations according to the different types of cumulates and locality. Overall, plagioclase compositions of nelsonites have slightly higher An and Sr contents compared to those in OAN cumulates in the same mineralized locality (e.g., Lac de l'Abbondance and Lac Brûlé; Fig.4.10), which has been previously observed at Lac Mirepoix (Miloski et al. 2023b). Although minor differences in the plagioclase composition are observed in relation to lithology (nelsonite higher than OAN), the main variation in An and Sr contents seem to be associated with the regional locality of the Fe-Ti-(P) mineralization and its respective host-AMCG. Overall, plagioclase of Fe-Ti-P cumulates and its respective host-AMCG have similar An compositions, but mineralized cumulates contain higher Sr values in relation to the host (Fig. 4.10).

The Vanel Anorthosite and related Fe-Ti-(P) mineralization varies between the eastern (OAN of Lac à l'Orignal, Lac Mirepoix, Lac de l'Abbondance) and western portions (Fe-Ti norite of L'Étang). Eastern Vanel Anorthosite contains andesine plagioclase (An_{40-50}) with higher Sr contents (OAN mineralization: > 1700 ppm; host anorthosite: >1500ppm), in relation to the western portion, which has major labradorite composition (An > 50) with lower Sr values (500 - 1200ppm). Plagioclase from the western portion of Vanel also is similar to that of Lac Périgny Fe-Ti-P mineralization (An_{35-50}; Sr: 700-1200ppm), and the Grader Intrusion (An_{45-50}; Sr: 1200-1300ppm) of NE Grenville (Charlier et al. 2008). Moreover, the labradorite-type plagioclase of the western Vanel Anorthosite (up to An_{65}) is more similar to the older, Lac-Saint-Jean Anorthositic Suite (Gueye, 2023) which also has low Sr (450-1300ppm), but for varying An content (An_{36-68}) (Fig.4.9).

Mineralization associated to the anorthosite-massifs of Labrieville and Mattawa have similar high Sr contents (1500 – 2400ppm), but different An contents. Nelsonites at Lac Brûlé (Labrieville Anorthosite) have relatively higher An contents (An_{30-42}) in relation to the host Labrieville Anorthosite (An_{28-35}), and mineralization (An_{16-40})/host anorthosite (An_{25-36}) from Mattawa. Overall, both Fe-Ti-P mineralization and host anorthosites of Labrieville and Mattawa have higher-Sr and lower An contents if compared to that of the nearby massifs of Vanel and Lac-Saint-Jean (Fig.4.10).

The La Hache Mangerite has the most sodic plagioclase compositions among all the analyzed AMCG, albite-oligoclase (An_{5-35}) in composition in both the host mangerite and its Fe-Ti-P mineralization. Their Sr values are highly variable (179-2243ppm), decreasing with lower An contents (Fig.4.10).

Table 4.8. LA-ICP-MS major and trace element analyses of plagioclase for selected Fe-Ti-P mineralization in the Central Grenville Province, Quebec

Sample	Lithology	Oxide Mineralogy	# analysis	SiO_2	Al_2O_3	CaO	Na_2O	K_2O	Total	An	Ab	Or
Lac Périgny Fe-Ti-P mineralization - Poulin de Courval Mangerite												
20PM09A	Medium-grained OAN	Ilm + Mt	n=5	57.5	29.0	8.5	6.2	0.1	101.3	42.9	56.3	0.8
20PM23C	Medium-grained OAN	Ilm + Mt	n=5	59.5	26.3	7.3	6.1	0.1	99.3	39.3	59.7	0.9
20PM24	Medium-grained Leuco-OAN	Ilm + Mt	n=5	56.4	28.5	9.5	5.0	0.1	99.6	50.7	48.7	0.6
20PM25	Medium-grained OAN	Ilm + Mt	n=5	58.8	26.5	7.8	5.7	0.2	99.1	42.5	56.4	1.1
20PM26A	Medium-grained Leuco-OAN	Ilm + Mt	n=5	57.7	27.4	8.6	5.0	0.2	99.1	47.8	50.5	1.7
Lac de l'Abbondance Fe-Ti-P mineralization - Vanel Anorthosite												
20PM46E	Medium-grained OAN	Hm-ilm	n=5	58.1	27.4	8.0	5.7	0.0	99.2	43.5	56.2	0.3
Mattawa Fe-Ti-P mineralization - Mattawa Anorthosite												
20PM13B	Medium-grained OAN	Hm-ilm + Mt	n=5	58.4	24.9	5.7	6.5	2.6	98.6	27.9	57.0	15.1
21PM18B	Medium-grained OAN	Hm-ilm + Mt	n=5	58.0	25.5	5.9	6.1	2.7	98.5	29.2	54.9	16.0
21PM19	Medium-grained OAN	Hm-ilm + Mt	n=5	55.8	27.6	7.9	6.7	0.3	98.5	38.9	59.5	1.6
21PM11B	Medium-grained OAN	Ilm + Mt	n=5	59.7	23.9	4.0	5.5	5.1	98.9	19.7	49.9	30.3
Labrieville Alkaline Anorthosite												
20PM32A	Medium-grained Leuco-OAN	Hm-ilm + Mt	n=5	60.4	25.5	6.8	5.8	0.4	99.0	38.4	59.1	2.5
20PM42A	Medium-grained OAN	Hm-ilm + Mt	n=5	60.5	25.7	6.6	5.9	0.3	99.1	37.7	60.5	1.8
20PM42B	Medium-grained Leuco-OAN	Hm-ilm	n=5	63.0	24.2	5.0	6.9	0.3	99.5	28.2	70.1	1.8
La Hache Fe-Ti-P mineralization - La Hache Mangerite												
21PM06	Oxide-apatite-rich mangerite	Ilm + Mt	n=5	58.4	25.2	5.5	7.0	2.1	98.7	26.7	60.9	12.5
21PM07	Oxide-apatite-rich mangerite	Ilm + Mt	n=5	59.5	24.0	4.4	6.1	4.1	99.0	21.5	54.3	24.2
21PM08	Oxide-apatite-rich mangerite	Ilm + Mt	n=5	56.3	27.2	7.5	6.8	0.6	98.5	36.7	59.7	3.6
21PM09	Oxide-apatite-rich mangerite	Ilm + Mt	n=5	56.8	26.7	7.2	6.6	1.0	98.5	35.4	58.5	6.1
21PM57	Oxide-apatite-rich mangerite	Ilm + Mt	n=5	59.1	24.5	4.4	5.9	4.3	99.2	21.7	53.1	25.3
21PM59	Oxide-apatite-rich mangerite	Ilm + Mt	n=5	59.0	25.2	5.6	8.1	0.3	98.4	27.1	71.5	1.4
21PM56	Oxide-apatite-rich mangerite	Ilm + Mt	n=5	63.4	20.0	0.5	3.9	10.4	98.4	2.7	35.2	62.0
L'Étang Fe-Ti mineralization - Vanel Anorthosite												
21PM52A	Medium-grained leuconorite	Ilm + Mt	n=5	49.7	32.2	12.3	4.1	0.1	98.6	61.9	37.6	0.5
21PM53B	Medium-grained leuconorite	Ilm + Mt	n=5	53.0	29.8	10.0	5.6	0.1	98.5	49.3	50.0	0.8
21PM55	Medium-grained leuconorite	Ilm + Mt	n=5	53.6	29.4	9.5	5.9	0.1	98.5	46.7	52.6	0.6

Table 4.8. LA-ICP-MS major and trace element analyses of plagioclase for selected Fe-Ti-P mineralization in the Central Grenville Province, Quebec

Detection Limits (33-55µm)				0.058-0.245	0.515-0.809	0.005-0.013	0.003-1.838	0.008-0.476	0.010-0.057	0.005-0.058	0.001-0.023	
Sample	Lithology	Oxide Mineralogy	# analysis	^{88}Sr	^{137}Ba	^{139}La	^{140}Ce	^{141}Pr	^{146}Nd	^{147}Sm	^{153}Eu	Total REE
Lac Périgny Fe-Ti-P mineralization - Poulin de Courval Mangerite												
20PM09A	Medium-grained OAN	Ilm + Mt	n=5	1108.7	36.2	3.4	5.0	0.5	1.3	0.0	1.5	11.7
20PM23C	Medium-grained OAN	Ilm + Mt	n=5	1210.5	127.0	3.8	6.2	0.3	0.7	0.0	1.1	12.1
20PM24	Medium-grained Leuco-OAN	Ilm + Mt	n=5	901.6	68.0	3.8	6.3	0.6	1.5	0.0	1.6	13.9
20PM25	Medium-grained OAN	Ilm + Mt	n=5	860.5	271.8	5.7	8.6	0.6	2.2	0.0	3.4	20.5
20PM26A	Medium-grained Leuco-OAN	Ilm + Mt	n=5	790.7	176.4	4.4	6.7	0.5	0.8	0.0	1.6	14.0
Lac de l'Abbondance Fe-Ti-P mineralization - Vanel Anorthosite												
20PM46E	Medium-grained OAN	Hm-ilm	n=5	1953.8	352.4	5.3	7.2	0.6	0.7	0.0	0.9	14.7
Mattawa Fe-Ti-P mineralization - Mattawa Anorthosite												
20PM13B	Medium-grained OAN	Hm-ilm + Mt	n=5	2080.1	-	6.6	10.1	0.9	3.0	0.3	2.3	23.6
21PM18B	Medium-grained OAN	Hm-ilm + Mt	n=5	1573.7	-	2.2	3.3	0.3	1.2	0.1	1.2	8.4
21PM19	Medium-grained OAN	Hm-ilm + Mt	n=5	876.5	385.3	4.0	5.7	0.5	1.8	0.2	1.4	13.8
21PM11B	Medium-grained OAN	Ilm + Mt	n=5	2223.1	-	5.4	6.3	0.5	1.8	0.2	4.8	19.3
Labrieville Alkaline Anorthosite												
20PM32A	Medium-grained Leuco-OAN	Hm-ilm + Mt	n=5	1560.2	233.7	3.2	4.8	0.4	0.0	0.0	1.1	9.4
20PM42A	Medium-grained OAN	Hm-ilm + Mt	n=5	1790.4	861.8	4.2	6.2	0.5	1.0	0.0	2.0	14.0
20PM42B	Medium-grained Leuco-OAN	Hm-ilm	n=5	1064.4	852.9	16.8	20.9	1.6	4.1	0.0	3.9	47.3
La Hache Fe-Ti-P mineralization - La Hache Mangerite												
21PM06	Oxide-apatite-rich mangerite	Ilm + Mt	n=5	2171.9	-	9.7	12.9	1.2	3.9	0.4	6.7	31.9
21PM07	Oxide-apatite-rich mangerite	Ilm + Mt	n=5	1582.4	-	7.7	10.8	1.0	3.4	0.3	8.3	31.8
21PM08	Oxide-apatite-rich mangerite	Ilm + Mt	n=5	2242.9	590.4	6.7	9.7	0.9	3.3	0.3	3.4	24.7
21PM09	Oxide-apatite-rich mangerite	Ilm + Mt	n=5	1877.3	782.3	6.3	8.4	0.7	2.5	0.2	3.1	21.5
21PM57	Oxide-apatite-rich mangerite	Ilm + Mt	n=5	2063.6	-	18.8	23.5	2.1	6.6	0.7	10.3	62.6
21PM59	Oxide-apatite-rich mangerite	Ilm + Mt	n=5	2135.3	554.6	23.6	29.8	2.6	7.9	0.6	11.6	76.5
21PM56	Oxide-apatite-rich mangerite	Ilm + Mt	n=5	178.7	-	17.5	17.9	1.1	2.8	0.1	3.7	43.1
L'Étang Fe-Ti mineralization - Vanel Anorthosite												
21PM52A	Medium-grained leuconorite	Ilm + Mt	n=5	880.3	136.3	1.7	2.2	0.2	0.6	0.1	0.5	5.4
21PM53B	Medium-grained leuconorite	Ilm + Mt	n=5	821.5	152.4	2.0	2.6	0.2	0.6	0.1	0.9	6.6
21PM55	Medium-grained leuconorite	Ilm + Mt	n=5	1286.3	323.7	9.1	9.9	0.7	1.5	0.1	0.8	22.2

Table 4.9. pXRF analysis of plagioclase for selected Fe-Ti-P mineralization and its respective AMCG-suite in the Central Grenville Province, Quebec

Sample	Lithology	Oxide Mineralogy	UTM-E	UTM-N	# analysis	Si	Al	Ca	K	Sr	Ba	**An**
Lac Périgny Fe-Ti-P mineralization - Poulin de Courval Mangerite												
20PM09B	Medium-grained OAN	Ilm + Mt	403222	5431875	n = 5	29.2	14.4	5.4	0.4	0.1	0.0	34.1
20PM23A	Medium-grained OAN	Ilm + Mt	403226	5432881	n = 5	27.0	14.5	6.3	0.3	0.1	0.0	41.4
20PM23B	Medium-grained OAN	Ilm + Mt	403226	5432881	n = 5	28.8	16.2	7.0	0.2	0.1	0.0	42.9
20PM25	Medium-grained OAN	Ilm + Mt	403226	5432418	n = 5	28.1	15.1	6.5	0.5	0.1	0.1	41.2
20PM26B	Medium-grained Leuco-OAN	Ilm + Mt	402636	5433515	n = 5	26.6	14.1	6.9	0.5	0.1	0.1	45.7
Lac de l'Abbondance Fe-Ti-P mineralization - Vanel Anorthosite												
20PM48A	Medium-grained OAN	-	389788	5424741	n = 5	30.2	14.5	5.1	0.6	0.2	0.1	31.7
20PM45	Anorthoite	-	392199	5432529	n = 5	27.7	14.1	6.1	0.7	0.2	0.1	39.7
20PM46D	Anorthosite	-	392299	5432637	n = 5	26.6	13.5	6.1	0.7	0.2	0.2	41.1
Mattawa Fe-Ti-P mineralization - Mattawa Anorthosite												
20PM12A	Medium-grained OAN	Hm-ilm + Mt	389480	5424110	n = 5	28.1	13.2	4.8	1.3	0.2	0.1	31.6
20PM12C1	Medium-grained OAN	Hm-ilm + Mt	389480	5424110	n = 5	28.0	13.4	4.8	0.9	0.2	0.1	32.0
20PM12D	Medium-grained OAN	Hm-ilm + Mt	389480	5424110	n = 5	30.7	13.0	4.7	1.6	0.2	0.2	29.0
21PM13B	Medium-grained OAN	Hm-ilm + Mt	389462	5424979	n = 5	27.3	11.2	4.0	2.0	0.2	0.2	27.8
21PM18B	Medium-grained OAN	Hm-ilm + Mt	382116	5422795	n = 5	27.8	12.3	4.0	2.2	0.2	0.2	27.2
21PM19	Medium-grained OAN	Hm-ilm + Mt	382889	5422795	n = 5	27.5	11.4	4.2	1.6	0.1	0.1	28.8
20PM13A	Anorthosite	-	389462	5424979	n = 5	31.6	14.6	5.1	1.1	0.2	0.1	30.2
20PM14	Anorthosite	-	389559	5426399	n = 5	28.3	13.7	4.7	1.0	0.2	0.1	31.0
20PM15A	Anorthosite	-	389915	5427523	n = 5	27.8	14.0	5.1	0.9	0.2	0.1	33.6
20PM15B	Anorthosite	-	389915	5427523	n = 5	25.6	17.9	9.4	0.1	0.1	0.1	60.0
20PM16A	Anorthosite	-	388648	5435283	n = 5	30.6	14.1	4.7	1.3	0.2	0.1	29.0
20PM16B	Anorthosite	-	388648	5435283	n = 5	29.9	14.5	5.1	1.2	0.2	0.1	32.0
21PM14	Anorthosite	-	376843	5422068	n = 5	27.1	13.1	5.4	0.6	0.2	0.1	36.7
21PM15	Anorthosite	-	377390	5422917	n = 5	28.0	12.9	4.7	1.2	0.2	0.1	31.4
21PM16A	Anorthosite	-	378144	542147	n = 5	27.8	13.1	4.8	1.2	0.2	0.1	32.0
21PM16D	Anorthosite	-	378144	542147	n = 5	27.1	12.1	4.5	1.2	0.2	0.1	31.4
21PM17A	Anorthosite	-	379884	5423471	n = 5	27.7	12.8	4.6	1.1	0.2	0.1	30.9
21PM17B	Anorthosite	-	379884	5423471	n = 5	26.9	12.5	4.7	1.0	0.2	0.1	32.4
21PM18	Anorthosite	-	382116	5422795	n = 5	29.1	11.7	3.7	3.0	0.2	0.3	24.2
21PM18A	Anorthosite	-	382116	5422795	n = 5	28.4	13.4	4.9	1.1	0.2	0.1	31.9
21PM20	Anorthosite	-	382918	5423725	n = 5	28.2	13.1	4.7	1.2	0.2	0.1	30.9
21PM20B	Anorthosite	-	382918	5423725	n = 5	27.6	12.5	4.7	1.1	0.2	0.1	31.9
21PM21	Anorthosite	-	382654	5420957	n = 5	27.5	11.8	3.9	1.4	0.2	0.1	26.7
21PM22	Anorthosite	-	384277	5419897	n = 5	27.8	12.3	4.6	1.2	0.2	0.1	31.0
21PM23	Anorthosite	-	389048	5429351	n = 5	29.2	13.2	4.7	0.8	0.2	0.1	30.4
21PM24	Anorthosite	-	389690	5430937	n = 5	28.0	13.0	4.5	1.2	0.2	0.1	30.2
21PM25	Anorthosite	-	388741	5433509	n = 5	27.8	13.0	4.8	0.9	0.2	0.1	31.9
21PM46	Anorthosite	-	376625	5422007	n = 5	27.1	12.9	4.9	0.9	0.2	0.1	33.7
21PM49	Anorthosite	-	380857	5428097	n = 5	28.5	12.7	4.3	1.4	0.2	0.1	28.7
21PM50	Anorthosite	-	379552	5428885	n = 5	27.9	13.3	5.2	0.9	0.2	0.1	34.3

Table 4.9. (cont.) pXRF analysis of plagioclase for selected Fe-Ti-P mineralization and its respective AMCG-suite in the Central Grenville Province, Quebec

Sample	Lithology	Oxide Mineralogy	UTM-E	UTM-N	# analysis	Si	Al	Ca	K	Sr	Ba	**An**
Labrieville Alkaline Anorthosite												
20PM42A	Medium-grained OAN	Hm-ilm + Mt	418253	5471028	n = 5	30.8	15.3	5.6	1.0	0.2	0.1	33.5
20PM42C	Medium-grained OAN	Hm-ilm + Mt	418253	5471028	n = 5	28.6	13.6	5.2	1.1	0.2	0.1	33.6
20PM32A	Medium-grained OAN	Hm-ilm	433018	5459507	n = 5	31.4	15.7	5.7	1.7	0.2	0.1	33.4
20PM29	Anorthosite	-	432543	5457096	n = 5	29.4	13.8	5.4	1.0	0.2	0.1	34.0
20PM30	Anorthosite	-	432407	5457928	n = 5	28.3	12.5	5.3	1.0	0.2	0.1	34.5
20PM31	Anorthosite	-	432409	5458675	n = 5	28.0	13.1	5.1	1.2	0.2	0.1	33.8
20PM36	Anorthosite	-	428530	5475767	n = 5	29.6	15.2	5.1	1.1	0.2	0.1	32.2
20PM37B	Anorthosite	-	429782	5470490	n = 5	30.7	15.4	5.1	1.2	0.2	0.2	30.9
20PM38B	Anorthosite	-	429698	5470593	n = 5	29.7	13.9	4.9	1.9	0.2	0.2	31.1
20PM39	Anorthosite	-	426164	5467412	n = 5	31.0	15.6	4.7	1.6	0.2	0.2	28.9
20PM40	Anorthosite	-	422255	5469097	n = 5	29.1	13.7	5.1	1.2	0.2	0.1	32.6
20PM41	Anorthosite	-	419713	5470839	n = 5	29.9	15.6	5.3	1.0	0.2	0.1	32.9
20PM43	Anorthosite	-	418089	5471125	n = 5	27.3	13.1	5.3	1.4	0.2	0.1	35.7
La Hache Fe-Ti-P mineralization - La Hache Mangerite												
21PM02	Mangerite	-	368048	5416875	n = 5	31.2	9.5	0.8	4.5	0.0	0.2	4.2
21PM03	Mangerite	-	364517	5423194	n = 5	31.4	13.8	2.9	2.7	0.1	0.8	18.2
21PM05	Mangerite	-	365188	5419244	n = 5	28.5	10.5	2.5	4.4	0.2	0.7	17.3
21PM56	Charnockite	-	362879	5428524	n = 5	32.6	10.6	0.9	5.7	0.0	0.2	4.8
21PM57	Oxide-apatite-rich mangerite	Ilm + Mt	364912	5425682	n = 5	29.2	12.9	3.7	2.7	0.2	0.6	24.3
21PM59	Oxide-apatite-rich mangerite	Ilm + Mt	367651	5425849	n = 5	29.6	12.5	3.5	2.7	0.2	1.0	22.8
21PM07	Oxide-apatite-rich mangerite	Ilm + Mt	363763	5417085	n = 5	28.9	11.9	3.2	3.1	0.2	0.5	21.5
21PM08	Oxide-apatite-rich mangerite	Ilm + Mt	360627	5425240	n = 5	28.3	14.4	6.1	0.7	0.2	0.2	38.6
21PM09	Oxide-apatite-rich mangerite	Ilm + Mt	360627	5425240	n = 5	29.5	13.3	4.7	1.1	0.3	0.1	30.2
L'Étang Fe-Ti mineralization - Vanel Anorthosite												
21PM52	Medium-grained leuconorite	Ilm + Mt	373129	5435965	n = 5	25.4	14.7	7.6	0.2	0.1	0.0	51.1
21PM53	Medium-grained leuconorite	Ilm + Mt	371910	5435680	n = 5	25.3	15.2	7.2	0.2	0.1	0.0	49.0
21PM54	Medium-grained leuconorite	Ilm + Mt	371448	5435310	n = 5	25.4	15.4	7.7	0.3	0.1	0.0	51.5
21PM55	Medium-grained leuconorite	Ilm + Mt	364953	5434038	n = 5	26.3	14.9	6.4	0.2	0.1	0.0	43.1
Lac à l'Orignal Fe-Ti-P mineralization - Vanel Anorthosite												
20PM02	Medium-grained OAN	Hm-ilm + Mt	384943	5436888	n = 5	27.2	15.8	6.8	0.3	0.2	0.1	44.3
LO-21-01	Medium-grained OAN	Hm-ilm + Mt	384535	5437021	n = 5	27.8	15.1	6.9	0.6	0.2	0.2	43.8
LO-21-05	Medium-grained OAN	Hm-ilm + Mt	384535	5437021	n = 5	28.5	15.7	6.8	0.7	0.2	0.1	42.3
LO-21-07	Medium-grained OAN	Hm-ilm + Mt	384535	5437021	n = 5	28.5	15.1	6.3	0.7	0.2	0.2	39.9
LO-21-22	Medium-grained OAN	Hm-ilm + Mt	384535	5437021	n = 5	28.5	14.1	5.9	1.0	0.2	0.1	37.7
LO-21-24-1	Medium-grained OAN	Hm-ilm + Mt	384535	5437021	n = 5	27.6	14.6	7.5	0.5	0.2	0.1	47.3
LO-21-41B	Medium-grained OAN	Ilm + Mt	384535	5437021	n = 5	28.3	14.5	6.8	0.8	0.3	0.1	42.7
LO-21-51-1	Medium-grained OAN	Hm-ilm + Mt	384535	5437021	n = 5	27.9	15.7	6.9	0.2	0.2	0.1	43.7
20PM03	Anorthosite	-	384535	5437021	n = 5	26.2	16.3	8.0	0.3	0.1	0.1	52.0
LO-21-47	Anorthosite	-	384535	5437021	n = 5	26.7	16.0	7.3	0.4	0.2	0.1	47.5

Table 4.9. (cont.) pXRF analysis of plagioclase for selected Fe-Ti-P mineralization and its respective AMCG-suite in the Central Grenville Province, Quebec

Sample	Lithology	Oxide Mineralogy	UTM-E	UTM-N	# analysis	Si	Al	Ca	K	Sr	Ba	**An**
Lac Mirepoix Fe-Ti-P mineralization - Vanel Anorthosite												
20PM04A	Medium-grained OAN	Ilm + Mt	387222	5438777	n = 5	30.11	17.28	7.58	0.20	0.22	0.06	44.3
20PM05B	Semi-massive Oxides	Hm-ilm	388808	5438818	n = 5	27.57	14.55	6.17	0.14	0.19	0.04	40.2
20PM08A	Medium-grained leuconorite	Hm-ilm + Mt	389447	5439789	n = 5	26.42	16.32	8.38	0.28	0.09	0.04	53.5
20PM08B2	Medium-grained OAN	Hm-ilm + Mt	389447	5439789	n = 5	27.60	15.08	6.71	0.31	0.28	0.19	43.1
MX-102-1	Medium-grained OAN	Hm-ilm + Mt	389229	5439206	n = 5	26.17	13.83	6.42	0.85	0.25	0.27	43.3
MX-102-2	Medium-grained OAN	Hm-ilm + Mt	389229	5439206	n = 5	27.16	14.18	6.15	0.33	0.26	0.14	40.6
MX-102-4	Medium-grained OAN	Hm-ilm + Mt	389229	5439206	n = 5	25.77	13.76	6.28	0.35	0.25	0.17	43.2
MX-102-6	Medium-grained OAN	Hm-ilm + Mt	389229	5439206	n = 5	27.87	15.18	7.53	0.31	0.26	0.15	47.0
MX-105-3	Medium-grained OAN	Hm-ilm + Mt	389685	5439902	n = 5	26.23	13.30	6.96	0.35	0.24	0.09	46.2
20PM05C	Anorthosite	-	388808	5438818	n = 5	28.16	15.14	5.68	0.63	0.17	0.08	36.8
20PM18A	Anorthosite	-	388631	5438801	n = 5	29.17	14.44	5.39	0.37	0.10	0.03	34.1
20PM17	Anorthosite	-	387724	5438757	n = 5	27.36	15.19	6.97	0.64	0.21	0.11	44.8
MX-108-1	Anorthosite	-	388813	5438656	n = 5	26.41	14.19	6.53	0.75	0.17	0.10	43.7
MX-108-5	Anorthosite	-	388813	5438656	n = 5	28.23	14.92	6.71	0.88	0.20	0.16	42.2
MX-108-8	Anorthosite	-	388813	5438656	n = 5	28.50	14.69	5.41	0.68	0.15	0.15	34.9
MX-109-6	Anorthosite	-	388516	5438567	n = 5	27.06	14.12	5.80	0.85	0.20	0.13	38.7
MX-109-7	Anorthosite	-	388516	5438567	n = 5	27.36	14.65	6.20	0.86	0.20	0.15	40.6
Vanel Anorthosite												
20PM22	Anorthosite	-	403174	5432901	n = 5	27.08	15.61	7.18	0.38	0.10	0.03	46.2
21PM26	Anorthosite	-	402636	5433515	n = 5	27.47	14.39	5.63	1.11	0.19	0.18	37.3
21PM27	Anorthosite	-	399362	5435472	n = 5	27.27	14.47	7.28	0.65	0.21	0.11	46.6
21PM28	Anorthosite	-	433814	5455284	n = 5	24.78	13.47	6.76	0.64	0.19	0.11	47.4
21PM29	Anorthosite	-	432543	5457096	n = 5	26.53	15.47	7.03	0.50	0.17	0.12	46.2
21PM33	Anorthosite	-	430892	5463836	n = 5	25.89	14.76	6.99	0.39	0.10	0.04	47.0
21PM37	Anorthosite	-	429782	5470490	n = 5	22.52	12.35	7.02	0.14	0.08	0.03	52.6
21PM38	Anorthosite	-	429698	5470593	n = 5	24.89	15.35	7.90	0.21	0.09	0.02	53.5
21PM39	Anorthosite	-	426164	5467412	n = 5	25.46	15.69	8.30	0.26	0.08	0.04	54.7
21PM40	Anorthosite	-	422255	5469097	n = 5	26.35	16.00	8.03	0.43	0.09	0.04	51.8
21PM41	Anorthosite	-	419713	5470839	n = 5	23.69	15.88	8.57	0.11	0.11	0.03	59.3
21PM42	Anorthosite	-	418253	5471028	n = 5	24.65	16.37	8.14	0.12	0.08	0.03	55.3
21PM43	Anorthosite	-	418089	5471125	n = 5	23.57	11.89	6.06	0.78	0.19	0.17	45.1
21PM60	Anorthosite	-	370593	5417194	n = 5	23.39	14.28	7.83	0.36	0.06	0.04	55.9
21PM44	Anorthosite	-	378597	5432830	n = 5	25.25	15.58	7.51	0.38	0.06	0.03	50.8
21PM45	Anorthosite	-	377386	5426449	n = 5	24.94	16.14	7.94	0.37	0.13	0.03	53.7
Lac-Saint-Jean Anorthositic Suite												
21PM47	Anorthosite	-	373719	5415727	n = 5	25.54	15.36	7.11	0.30	0.07	0.03	48.1
21PM48	Anorthosite	-	373222	5413054	n = 5	25.60	15.21	7.02	0.19	0.09	0.04	47.6
21PM58	Anorthosite	-	367385	5426092	n = 5	25.25	16.98	8.62	0.22	0.06	0.03	56.7
21PM10	Anorthosite	-	375391	5418742	n = 5	23.82	14.62	8.84	0.22	0.08	0.01	60.6

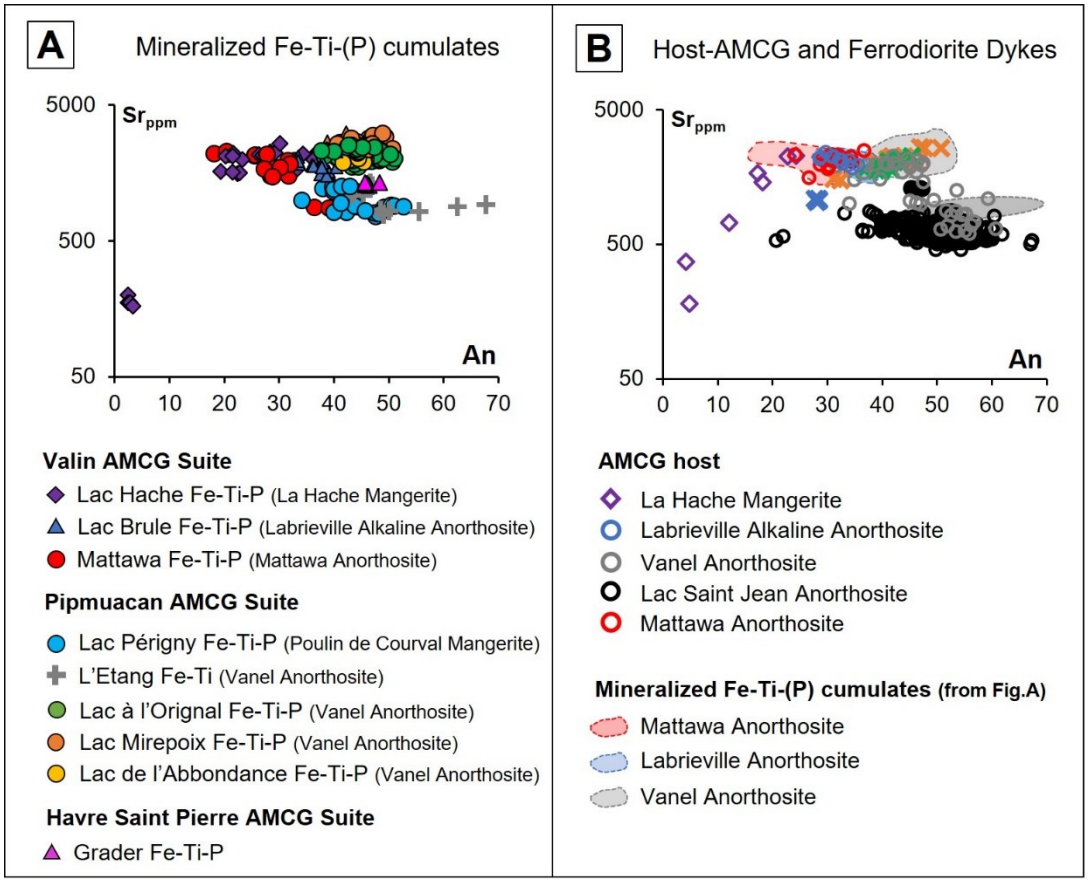

Figure 4.10. Geochemical variation diagrams of plagioclase of Fe-Ti-P mineralization and associated AMCG-host in the Central Grenville Province. LA-ICP-MS analysis of plagioclase from mineralized samples. B. pXRF analysis of plagioclase from mineralized and host-samples. Comparison with data of the Lac à l'Orignal Fe-Ti-P deposit (Miloski et al. 2023a), Lac Mirepoix Fe-Ti-P mineralization (Miloski et al. 2023b), Lac-Saint-Jean Anorthositic Suite (Gueye, 2023) and the Grader Fe-Ti-P Intrusion by XRF (Charlier et al. 2008).

4.7 Discussion

4.7.1 Insights on the petrogenesis of AMCG suites and related Fe-Ti-P mineralization in the Central Grenville Province: the role of magmas sources and crustal contamination

The petrogenesis of the Proterozoic AMCG suites and related Fe-Ti-P mineralization, and most notably, the role and nature of the mantle and crust components involved in their petrogenesis have been debated by petrologists for decades. The two sources model (mantle for the anorthosite members and crust for the felsic rocks; e.g. Emslie, 1985; Scoates & Mitchell (2000); McLelland et al. (2010)) has been challenged by two competing single-source hypotheses that advocate either the mantle (Turner et al. 1992; Frost et al. 2002) or the continental crust (Duchesne & Wilmart 1997; Duchesne et al. 1999; Schiellerup et al. 2000) as the only source for the rock types in these suites. In addition, the type of mantle source is also debated, with models ranging from depleted mantle (Ashwal & Wooden, 1985; Ashwal et al. 1986; Francis et al. 2000; Morisset, 2008; Morisset et al. 2013; Owens et al. 1994) to enriched metasomatized subcontinental lithospheric mantle (SCLM, Owens & Tomascak, 2002; Bickford et al. 2010; Groulier et al. 2018) and even to an enriched asthenospheric mantle for the origin of Fe-rich melts (Francis et al. 2000; Regan et al. 2011), including Fe-Ti rich jotunites (Icehower et al. 1998) which have geochemical similarities to continental flood basalts. Also, according to Bybee & Ashwal, (2015), contamination of mantle-derived magmas by lower crust is an important process in AMCG petrogenesis. However, due to the proximal timing of AMCG magmatism in the Grenville Province with respect to the formation ages of the host-crustal lithologies, the Sm–Nd signatures in the upper mantle and contemporary juvenile crustal source reservoirs have not developed detectable compositional contrast between the formation of the host rocks and the emplacement of any one AMCG suite (Bickford et al. 2010; Frost et al. 2010;

Heinonen et al. 2014). In situ Hf isotope studies of zircon provide additional information to resolve these issues (e.g., Kemp et al. 2007; Heinonen et al. 2010; Bickford et al. 2010). The much shorter half-life of ^{176}Lu compared with ^{147}Sm results in much quicker evolution in the initial $^{176}Hf/^{177}Hf$ values compared with initial $^{143}Nd/^{144}Nd$ values between potential juvenile source-reservoirs (Bickford et al. 2023). Here we apply new Hf isotopes measurements in zircon associated with Fe-Ti-P mineralization, coupled with mineral chemistry, apatite in particular (e.g., Kieffer et al. *in review*), to try to constrain the magma source and role of crustal contamination in the petrogenesis of Fe-Ti-P mineralization and host AMCGs in the Central Grenville Province.

4.7.1.1 Hf isotopes

In general, samples with younger ages present lower εHf values than older samples which could be simply explained by the melts being extracted from the same source over time (see trend in Fig.4.6). This trend is shown by the evolution lines for mafic and continental crust calculated at 1.7 Ga and 1.98 Ga and envelope the range of Hf values of the juvenile crust (1.3 – 1.5Ga) of Quebecia (Dickin, 2000; Papapavlou et al. 2022; Groulier et al. 2020; Fig.4.6b). Regionally, the Hf isotope composition of metamorphosed detrital zircon grains (Fig.4.6b) suggests three peaks of crustal generation in the Central Grenville Province (Papapavlou et al. 2022; Augland et al. 2015): 1) a 1.3-1.7 Ga juvenile (Quebecia) crust, which is consistent with the Nd isotope work of Dickin (2000) for Quebecia crustal gneisses (converted to Hf using the equation εHf = εNd*1.36 + 3; White, 2020); 2) a 1.8–1.9 Ga source, which is interpreted as a product of reworking of 3) older archean (2.7 Ga) continental crust derived from a near-chondritic mantle reservoir (Papapavlou et al. 2022). A compilation of previous isotope data from the AMCG suites of the Grenville Province, comprising Hf in ilmenite/rutile in mineralization from Saint Urbain and Havre-Saint-Pierre anorthosites (Morisset, 2008), Hf in zircon from the Adirondack Anorthosite (Bickford et al.

2010) and Hf calculated from whole rock Nd of metagabbros from Adirondack AMCG (Regan et al. 2011); of troctolite and gabbro intrusions from Brien, Raudot, Blache and Pentecote AMCG (Francis et al. 2000), of the Labrieville Anorthosite (Owens et al. 1994);of troctolite and leuconorite from the Lac-Saint-Jean Anorthositic Suite and related granitoids (Emslie & Hegner, 1993), are plotted for comparison with this study in Figure 4.6b.

Individual εHf values of zircon plotted against the weighted mean U-Pb ages from the samples they come from (Fig.4.6a) reveal evolution trends among the mineralized samples. One striking feature of the whole dataset is that the upper limit of the data (at the highest εHf values) follows a line that represents mafic crust extracted from the depleted mantle at 1.6 Ga (a time in the middle of the youngest period of crust formation in the central Grenville; Papapvlou et al. 2022; Augland et al. 2015). This upper limit is defined by mineralization from Labrieville and Mattawa anorthosites (studied here) and also the published data from the Saint Urbain Anorthosite (ilmenite/rutile data: Morisset, 2008; Morisset et al. 2013), ferrodiorite/jotunite from Labrieville Anorthosite (calculated from Nd whole rock: Owens et al. 1994) and metagabbros from the Adirondack AMCG (calculated from Nd whole rock; Regan et al. 2011;Fig.4.6a). These all have more juvenile Hafnium isotopic compositions than the other samples studied here. The samples with more evolved εHf values, the Vanel Anorthosite and the mangerites of La Hache and Poulin de Courval (Lac Périgny) seem to have isotopic compositions that follow the evolution of Quebecia continental crust (Fig.4.6a). The Hf isotope compositions from Fe-Ti mineralization at the Big Island deposit, Havre-Saint-Pierre Anorthositic Suite (ilmenite/rutile: Morisset, 2008; Morisset et al. 2013), of the Adirondacks AMCG (zircon: Bickford et al. 2010) and for AMCG intrusions in the Manicouagan corridor (Francis et al. 2000) and Lac-Saint-Jean Anorthositic Suite (Emslie & Hegner, 2003), converted from whole rock Nd data, plot in between these limits. Although the Hf data of AMCG-related rocks from the Grenville are mostly

suprachondritic they overlap with Quebecia crustal compositions (Dickin, 2000), although it should be remembered that these trends represent how felsic crust extracted from the depleted mantle would evolve, which is not likely to be a widespread process. All previous works argued for mantle-derived melts with crustal contamination rather than melting of the lower crust. However, they do not agree on the nature of the mantle source.

The more depleted samples (Labrieville and Mattawa anorthosites) possibly reflect magma from a depleted mantle source contaminated by lower crustal rocks, or partial melting of mafic lower crust, which has been previously proposed by Owens et al. (1994) for the Labrieville Alkaline Anorthosite. However, according to Owens & Dymek (2001), the Sr, Nd, and Pb isotopic compositions of rocks from the Labrieville massif are consistent with a mantle derivation, suggesting that high K, Sr, and Ba must be features of the mantle source. Bybee & Ashwal (2015) also argue that the decoupling between the Nd–Pb-Sr mineral systematics in both the Nain and Mealy Mountains anorthosites (εNd between -10 to +4), supports the role of lower crustal contamination into mantle-derived magmas rather than the melting of the lower crust as the source of Proterozoic anorthosites. Lower crustal sources could be potential contaminants for the samples studied here, and if this contaminant was Quebecia mafic crust formed it would be difficult to tease apart the contributions from the contaminant and the mantle source using our Hf isotopic dataset alone.

Morisset (2008) proposed that the Hf isotope data from the Fe-Ti-(P) mineralization at Saint Urbain and Havre-Saint-Pierre anorthosites suggested that the melts derived from 1) juvenile lower crust extracted from juvenile depleted mantle at 1.52 Ga and 1.64 Ga respectively (i.e., Quebecia crust) or 2) from a mantle source with Lu/Hf > MORB (more “enriched” than depleted mantle). However, based on the combined Hf, Pb and Sr isotopic systematics of the Fe-Ti deposits and anorthosites, the source of magma for both oxide

mineralization and anorthosites would most likely have been an upper mantle reservoir with slightly higher Sm/Nd than depleted mantle, and a Sr isotopic composition close to depleted mantle with 3-8% contamination of middle crust (Morisset, 2008). Icehower et al. (1998) propose a correlation between ferrodiorite magmas from Saint Urbain and continental flood basalts where the parental magmas of these Fe-Ti-P melts would be derived from an enriched asthenospheric (plume-like) mantle source with further lower crustal contamination. According to Bickford et al. (2010), Hf data from the Adirondacks Anorthosite massif indicates fractionation of mantle-derived magmas extracted between 1.35-1.40Ga, derived from juvenile, enriched mantle lithosphere (SCLM), with moderate contamination of lower mafic crust. For Francis et al. (2000), based on the Al, Ti and Fe contents of dykes and chilled margins associated with the anorthosite-troctolite intrusions in the Manicouagan corridor of the Grenville, they proposed that there were two types of parental magmas: an Al-rich melt similar MORB-picrites (i.e., depleted mantle) and an Fe-rich melt similar to hotspot picrites (ferropicrites) (i.e., enriched asthenospheric mantle). However, Sr and Nd data suggested an interaction of mantle-derived parental magmas with juvenile feldspathic crust. Finally, Regan et al. (2011) studied metagabbros associated with the Adirondack AMCG and proposed an enriched (OIB-like) asthenospheric mantle source. The slightly positive Nd values (εNd between +2.2 to +4) observed in gabbros (clinopyroxene-bearing, absent of orthopyroxene) were interpreted as derived from an uncontaminated enriched mantle source. The associated host anorthosites in the Adirondacks would therefore be derived from the same source but contain a higher degree of contamination.

The more evolved samples in our dataset (Fe-Ti-P mineralization in the Vanel Anorthosites and mangerites of La Hache and Poulin de Courval), could have formed from same mantle source(s) as the more juvenile ones but with more crustal contamination, and/or have formed from a more enriched mantle source(s). The slightly negative εHf values

from mineralization associated with the Vanel Anorthosite suggest some additional crustal assimilation although the assimilant could alternatively be represented by Archean mafic crust rather than Quebecia (see lower red line on Fig.4.6a which represents the evolution of mafic crust extracted from the depleted mantle at 2.6 Ga). These potential sources and contaminants are difficult to disentangle from the Hf data alone. However, as a whole it seems that the data suggest that an isotopically similar source has been continually tapped over time for all of the samples with the potential for cryptic mafic crustal contamination which is difficult to precisely identify. The individual analyzed zircons in some samples (e.g, L'Étang, La Hache, Lac Périgny) present within-sample variations of εHf >3. According to Bickford et al. (2010), variations of this scale are either a consequence of rock–magma interactions during ascent and emplacement of the magma (i.e., crustal contamination), and or a consequence of magma mixing with distinct initial εHf values that were derived from non-zircon-bearing sources (e.g., the mantle or lower crust), supporting the crustal contamination model.

4.7.1.2 Trace element geochemistry of apatite/ plagioclase

The obtained Hf isotopes reveal a range of εHf values among the analyzed zircon grains, mostly indicating the presence of either a depleted mantle source with a moderate amount of crustal contamination or an enriched mantle source with less crustal contamination. Therefore, we use apatite trace element concentrations to constrain the nature of the mantle source of the magma and the influence of lower/upper crust assimilation in order to better interpret the Lu-Hf zircon data. Multielement diagrams of apatite (Fig.4.9) display a comparison of apatite compositions between Fe-Ti-P mineralization from this study and data from other Fe-Ti-P mineralisation locations in Quebec, where the magma source and crustal contamination have been constrained, for the 1.05Ga Saint Urbain Anorthosite (Morisset, 2008) and 565 Ma Sept Iles Layered Intrusion (Namur et al. 2010; Kieffer et al.

2022). Kieffer et al. (2022) characterised apatite from Fe-Ti-P (nelsonite) layers in the layered mafic part of the Sept Iles Intrusive Suite, whose magma is mantle plume-related and thus represents an enriched-mantle source with minor influence of upper crustal contamination (Higgins & Doig, 1981; Higgins, 2005; Namur et al. 2010). Apatite from Fe-Ti mineralization in the Saint Urbain Anorthosite has been characterized by Morisset (2008), where its petrogenesis is interpreted as either derivation from juvenile depleted mantle with 3-8 % crustal contamination or from a mantle source with Lu/Hf> MORB (more “enriched” than depleted mantle). However, previous work has proposed an enriched asthenospheric mantle source (with lower crustal contamination) as the source of Fe-Ti-P rich dykes from Saint Urbain parental melts (Icehower et al. (1998)) and Adirondack metagabbros (Regan et al. 2011).

Overall, apatite of the different Fe-Ti-P mineralization analyzed in this study (Fig.4.9) have similar patterns (LREE enriched relative to HREE) not only to those from other Grenvillian ACMG-related Fe-Ti-P mineralization (e.g., Saint Urbain Anorthosite and Grader Intrusion, Morisset, 2008; Charlier et al. 2008) but also to Fe-Ti-P mineralization from the mantle-plume related Sept Iles Intrusive Suite (Kieffer et al. 2022). Apatite data from MORB (Mao et al. 2016), widely accepted as generated from a depleted mantle source, are also plotted on Figure 4.9, and show much flatter REE patterns, i.e., no enrichment in LREE relative to HREE, which is distinctively different from apatite from mineralization associated with all AMCG- and mantle-plume related intrusions. Therefore, the near identical pattern of apatite from AMCG-hosted Fe-Ti-P mineralization and those hosted in mantle-plume related layered intrusions strongly indicates an enriched mantle source, rather than a depleted mantle source, for the AMCG suites hosting Fe-Ti-P mineralization in the Central Grenville. Moreover, apatite data from Fe-Ti-P mineralization plots far from the field of alkaline melts (higher LREE enrichment: Fig 4.11), precluding the involvement of a metasomatized SCLM

source (Owens & Tomascak, 2002; Bickford et al. 2010). Instead, the apatite data of Fe-Ti-P mineralization in the Central Grenville suggests the involvement of an enriched mantle source (plume-like) for the generation of Fe-Ti-P rich melts in AMCG suites, as proposed for jotunite dikes, with similarity to continental flood basalts, from the Saint Urbain Anorthosite (Icehower et al. 1998) and Fe-rich melts from Manicougan (Francis et al. 2000). According to Icehower et al. (1998), enrichment of the mantle may have occurred via fluids from subduction processes or by close proximity to a mantle plume just prior to anatexis. However, the long-lived magmatism (>80Ma) involved in the petrogenesis of Fe-Ti-P mineralization (Miloski et al. 2023a,b) precludes the enrolment of a mantle plume, as large igneous provinces, associated with the initiation of a mantle plume head do not last more than 5-8Ma (Peate & Hawkesworth, 1996). However, some mantle plume systems (trails) can last 80 to 120 Mys (Koppers et al. 2021). Moreover, Regan et al. (2011) proposed an enriched (OIB-like) asthenospheric mantle source for gabbros from the nearby Adirondack AMCG (εHf similar to mineralization at the Mattawa and Labrieville anorthosites, Fig.4.6b), with absence to low-degree of crustal contamination. If an enriched (OIB like) asthenospheric source is considered as the main source of magma of the Fe-Ti-P mineralization associated to Mattawa and Labrieville (supported by the trace-element geochemistry of apatite), then the remaining samples on the Vanel Anorthosite and the mangerites of La Hache and Poulin de Courval could be related to the same source but with slightly higher amounts of crustal contamination in relation to Mattawa and Labrieville samples. Therefore, the possible role of enriched asthenospheric source should be considered in tectonic models for the Grenville in the future (e.g., Regan et al. 2011). Although, subduction-related processes during accretion that formed the juvenile Quebecia crust (e.g., accretion of older arc terranes) could have produced rocks in the lower crust and subjacent mantle that were “enriched” in both Hf and Nd isotopic compositions in relation to the “depleted” mantle (Bickford et al. 2010), although this is not reflected in the apatite trace

element data.

According to Kieffer et al. *in review*, trace-element ratios of apatite can be used to evaluate the occurrence of upper crustal contamination of magmas involved in forming mafic layered intrusions and their apatite-rich cumulates. This was based on a comparison of apatite data from a number of layered intrusions with different amounts of contamination of upper crust (Figure 4.11). Mafic magmas with significant crustal contamination (associated with opx-bearing mafic lithologies, e.g., Bushveld and Sudbury intrusions) have significantly higher La/Nd and Th/Lu ratios than magmas where contamination with upper crust is negligible (associated with olivine/clinopyroxene-bearing mafic lithologies, such as Sept Iles, Skaergaard intrusions). Applying these petrogenetic diagrams to our dataset, the occurrence of crustal contamination as a major factor in the petrogenesis of Fe-Ti-P-rich cumulates in the Central Grenville Province is not supported, as apatite from Fe-Ti-P mineralization does not show high La/Nd and Th/Lu ratios and is most similar to uncontaminated layered intrusions. However, the zircon Hf data clearly shows evidence for some crustal contamination in this study. However, contamination occurs in the lower crust rather than the upper crust in AMCG (e.g., Emslie, 1985; Peck and Valley, 2000; Peck et al. 2010; Bybee & Ashwal, 2015). AMCG suites have a complex petrogenesis, and are considered to be formed through multiple pulses/phases of magmatism from the mantle through the lower crust (e.g. Emslie, 1985, Ashwal, 1993, Miloski et al. 2023a,b) during long periods of time, with further ascending and magma crystallization into deep to intermediary crustal levels. The unusual long-lived magmatism associated with AMCG suites in the Central Grenville Province and its related Fe-Ti-P mineralization (>80Ma, e.g. Lac à l'Orignal and Lac Mirepoix, Miloski et al. (2023a,b)) corroborates the occurrence of high interaction between hot-mantle derived magmas and cooler mafic lower crustal lithologies (Bybee & Ashwal, 2015), where crustal assimilation might have occurred leading to increased Si activity and generation of orthopyroxene-bearing cumulates (Frost et al. 2010). So why does

apatite in this case not record contamination with the lower crust? Lower crust has a different composition in relation to upper crust, being the formed more mafic, depleted in Th, La and enriched in Nd in relation to the latter (Rudnick & Gao, 2003).

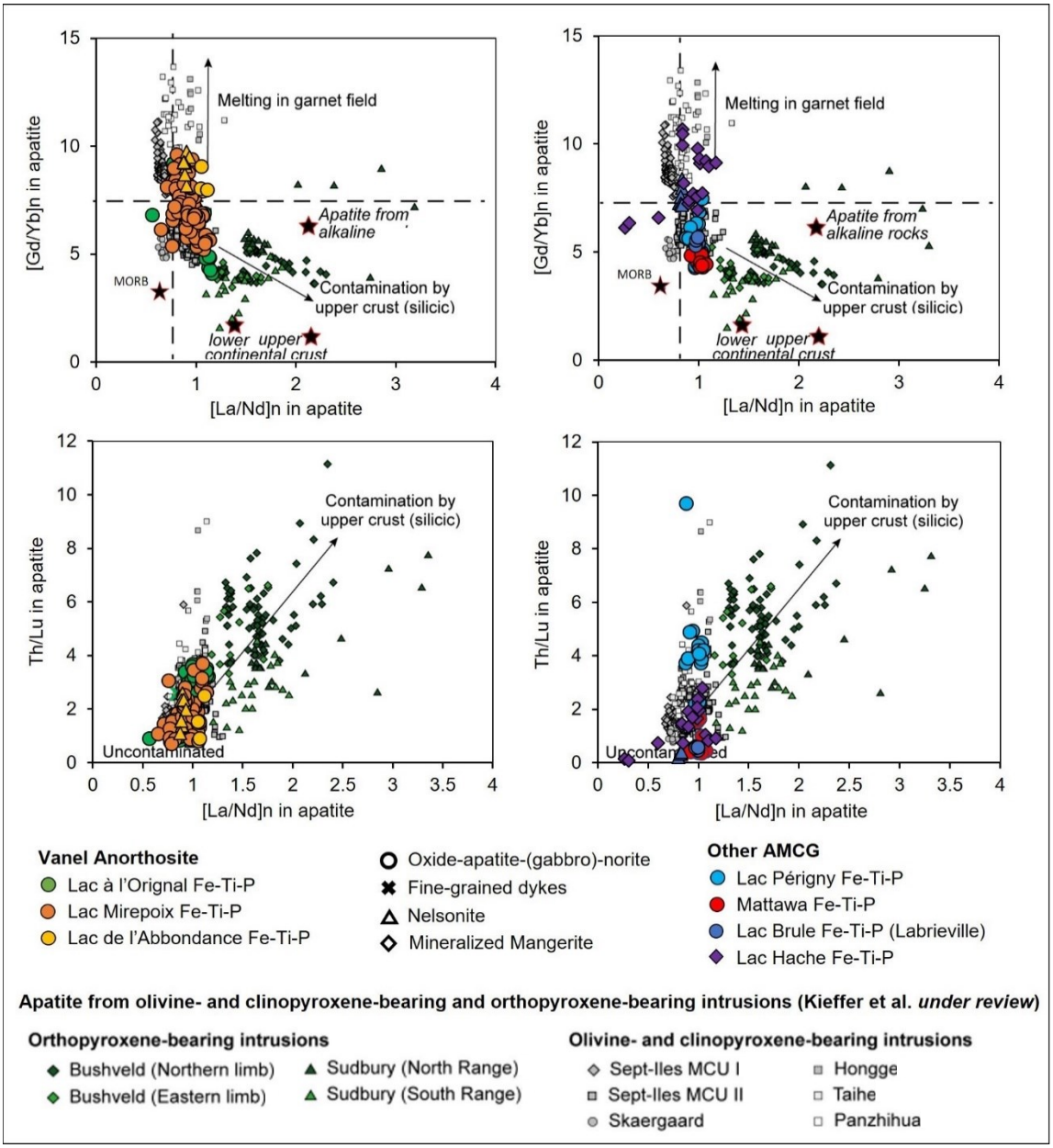

Figure 4.11. Trace element composition of cumulus apatite from olivine- clinopyroxene- and orthopyroxene-bearing intrusions through (La/Nd)n, (Gd/Yb)n and Th/Lu ratios, as indicator of crustal contamination (after Kieffer et al. *in review*). Values for lower and upper continental crust from Rudnick & Gao (2014). Apatite from alkaline rocks from Li et al. (2023). Fe-Ti-P mineralization data from AMCG of the Central Grenville Province form this work.

4.7.2 Insights on magmas evolution: fractional crystallization and the occurrence of Fe-Ti-P mineralization in the Si-rich mangerites

Trace-element variation in magnetite and ilmenite corroborate the fractionation model between the different types of cumulates (e.g., OAN more evolved than nelsonites), as previously described for apatite compositions. The oxide chemistry (Cr, Ni and V contents) of Fe-Ti-(P) mineralization in the Central Grenville Province, displayed in variation diagrams (Figs.4.4b & 4.12), is compared with previously described mineralization in Quebec: the Lac Tio Fe-Ti deposit (Charlier et al. 2010), the Grader Intrusion (Charlier et al. 2008), the Lac à l'Orignal Fe-Ti-P deposit (Miloski et al. 2023a) and the Lac Mirepoix Fe-Ti-P mineralization (Miloski et al. 2023b). Magnetite and ilmenite from massive oxides (e.g., Lac Mirepoix, Lac Brûlé; high-Ti/Fe trend, Fig.4.4a) and leuconorites (L'Étang) have more primitive compositions with the highest Cr, Ni and V contents, similar to the massive hemo-ilmenite cumulates of Lac Tio, and the base of the Grader Intrusion (Figs.4.4b & 4.12). This confirms a more primitive composition of the massive oxides in relation to apatite-bearing cumulates, as previously noted by Owens & Dymek (1992), Charlier et al. (2008) and Miloski et al. (2023a,b). According to these authors, apatite-bearing mineralization (e.g., nelsonites and OAN) is formed from further stages of fractionation in relation to massive oxides, in which an evolutionary trend can be traced from high- Ti/Fe towards low-Ti/Fe cumulates, due to fractionation of ferrodiorite magmas through crystallization of prior (hemo)-ilmenite and plagioclase, followed by magnetite and apatite (Figs.4.4b & 4.12).

The increasing abundance in REE, Th and U content of apatite in Figure 4.9 is related to fractional crystallization of the magma (Kieffer et al. 2022). Apatite from nelsonites (at Lac de l'Abbondance, Lac Brûlé and Saint Urbain) consistently have the lowest abundance of REE whereas oxide-apatite-norites at Lac à l'Orignal and Lac Mirepoix, as well as oxide-apatite-mangerite at La Hache, have the highest abundance of REE similar to

the most fractionated nelsonitic troctolites/gabbros at Sept Iles (Fig.4.9), reflecting as expected, its more evolved character. The L'Étang Fe-Ti mineralization, for example, is absent of cumulus apatite, which corroborates its more primitive character observed in the oxide chemistry. Massive nelsonites at Lac Mirepoix, Lac de l'Abbondance and Lac Brûlé have intermediate Cr, Ni and V compositions, similar to those described at the Grader Intrusion (Charlier et al. 2008). In contrast, the content of Cr, Ni and V of oxides from the oxide-apatite-norites (low Ti/Fe system) are in general lower than those from massive oxides and nelsonites, reflecting the more evolved composition (higher magnetite to ilmenite) of the former (Owens & Dymek, 1992; Charlier et al. 2008; Miloski et al. 2023a,b).This reflects that Ti is behaving compatibly with fractionation. Fe-Ti-P mineralized mangerites at La Hache contain the lowest Cr, Ni and V concentrations in oxides among all the analyzed cumulates (evolved Low-Ti/Fe trend), evidence of its more evolved character, as previously indicated by the lowest An contents in plagioclase for both host and mineralized samples (Fig.4.10).

The Pipmuacan and Valin AMCG suites in the Central Grenville have widespread occurrences of Si-rich lithologies associated with Fe-Ti-P mineralization (e.g., La Hache and Poulin de Courval mangerites) in which the petrogenesis is still highly debated. A first model proposes that most, if not all, members of the AMCG suite are comagmatic and related by fractional crystallization of a parental magma, commonly considered to be of intermediate composition and possibly derived in the lower crust (Duchesne et al. 1999, Vander Auwera et al. 1998, 2000, 2003, Longhi et al. 1999). In this way, mangerites and charnockites would represent the most-evolved (and more contaminated) cumulates after extensive fractional crystallization that would have previously formed anorthosites and related OPX-bearing lithologies. An alternative model however holds that the anorthosites and Si-rich members of the suite are broadly coeval (Longhi & Ashwal 1985, McLelland et al. 1996, Frost & Frost

1997). In this model, the anorthosites are considered to be mantle-derived, although crustally contaminated, whereas the granitoids result from melting of lower crustal rocks caused by intrusion of hot gabbroic magma. According to Zhang et al. (2007), high degrees of fractional crystallization of these mafic melts could also have formed mangerites and charnockites. In this study we present new data on Fe-Ti-P mineralized cumulates hosted in the La Hache Mangerite (Hébert et al. 2005). Si-rich cumulates in AMCG systems, as the ones presented at La Hache, if genetically correlated to coeval Fe-Ti-P mineralization in anorthosites, should contain the most evolved compositions among different AMCG lithologies. As expected, mineralization at La Hache contains lower-An and higher Sr- K in plagioclase (Fig.4.10); higher-REE in apatite (Fig.4.9) as well as lower Cr, Ni, Co and V in oxides in relation to the other mineralization associated with the Vanel, Labrieville, Mattawa and Lac-Saint-Jean anorthosites (Figs.4.7 & 4.8), corroborating the more evolved character of the former. As previously discussed, Hf isotope data (Fig.6) precludes higher degree of assimilation as the main cause of the more evolved character observed at La Hache (Figs.4.7-4.9). Therefore, both the mangerite and the Fe-Ti-P mineralization at La Hache represent the most evolved part of the anorthosite system, forming by extensive fractional crystallization, from a high-Ti/Fe system towards a Low-Ti/Fe system in the Grenville Province (Figs.4.4 & 4.12).

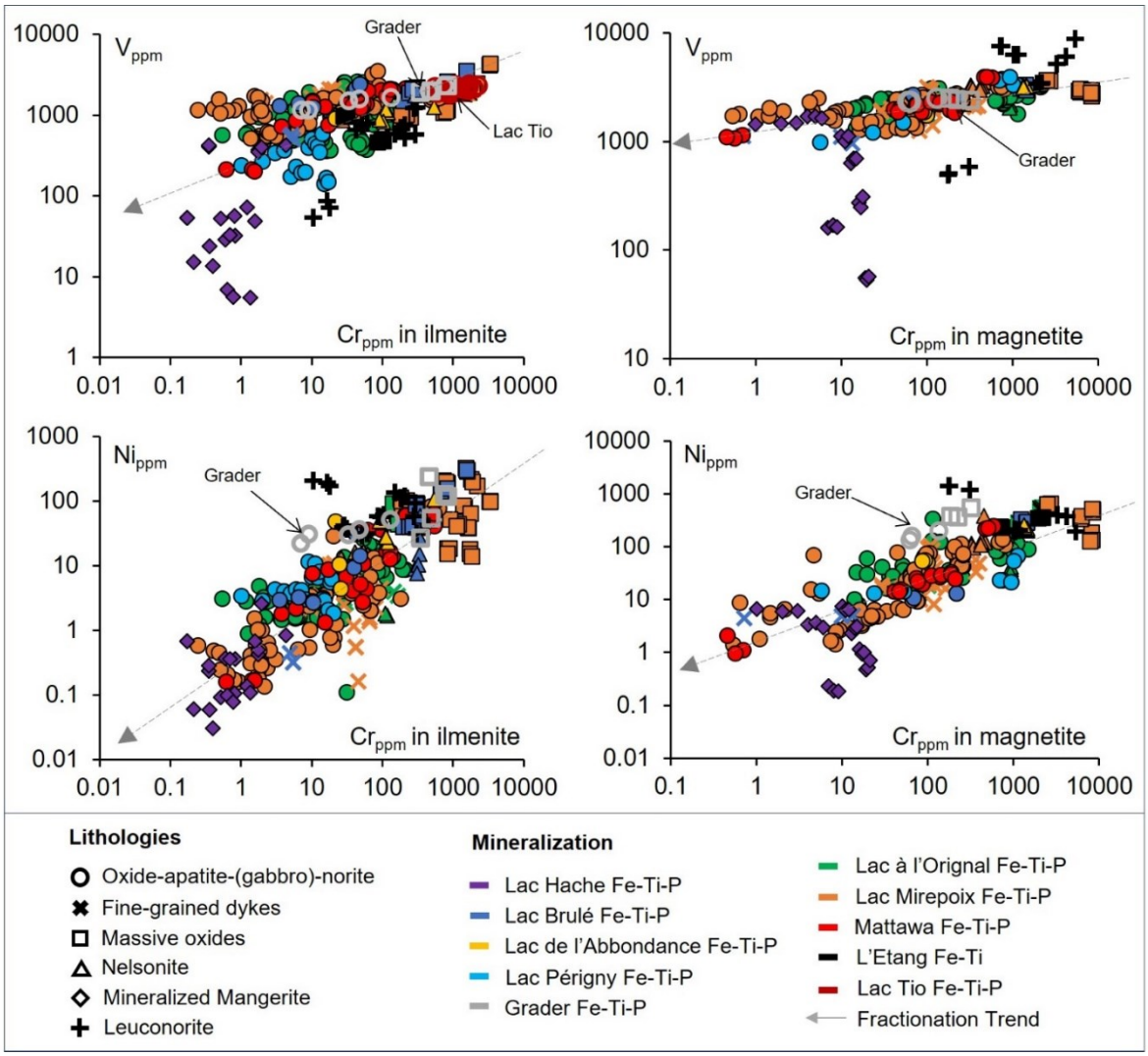

Figure 4.12. Binary diagrams displaying concentrations of compatible elements in magnetite (a) and ilmenite (b), using Cr, V and Ni as a proxy for fractional crystallization. Comparison with the Grader Intrusion Fe-Ti-P, Quebec (Charlier et al. 2008), the world-class ilmenite deposit of Lac Tio Fe-Ti, Quebec (Charlier et al. 2010), the Lac à l'Orignal Fe-Ti-P deposit (Miloski et al. 2023a) and the Lac Mirepoix Fe-Ti-P mineralization (Miloski et al. 2023b).

4.7.3 A mismatch in the U-Pb ages in zircon between Fe-Ti-P mineralization and host-AMCG: the high-complexity of anorthosite systems

The U-Pb ages for each mineralization event obtained in this study is displayed in comparison with a compilation of published geochronological data of the main AMCG suites in the Central Grenville Province (Figs.4.2 & 4.13). However, dating of the mineralization has resulted in quite different ages from previously published ages for each respective host-AMCG (Fig.4.13). For example, the massive nelsonite of the Lac Brûlé Fe-Ti-P mineralization (1065 ± 5 Ma) is hosted in the core of the Labrieville Alkaline Anorthosite (1010 ± 6 Ma, Owens et al. 1994), has a 50Ma older age in relation to the host anorthosite. However, this anorthosite was previously dated from marginal dykes in the area, thus giving a minimal age, rather than dating pegmatitic pockets of trapped, residual liquid from the anorthosite itself. Therefore, the Fe-Ti-P mineralization probably better represents that actual age of Labrieville Anorthosite. If we use the 1065 (± 5) Ma age of the Lac Brûlé Fe-Ti-P mineralization as the best estimate for the age of the host Labrieville Anorthosite, this becomes coeval to the magmatism of the nearby Vanel Anorthosite (1080 ± 2 Ma, Hébert et al. 2009) and Pipmuacan AMCG suite (1082-1045 Ma, Hébert et al. 2005; 2009). Mineralization at the La Hache Mangerite (1030 ± 8 Ma) also has an older obtained age in relation to the host-mangerite (1010 ± 3 Ma, Hébert et al. 2009), being instead coeval to the Peribonka AMCG suite (1028-1028Ma, Moukhsil et al. 2009) rather than the Valin age of unmineralized mangerite at La Hache (1010 ± 3Ma).

On the other side, mineralized Fe-Ti leuconorite lenses at L'Étang (1011 ± 10 Ma) and nelsonite layers at Lac de l'Abbondance (1002 ± 9 Ma), hosted in the 1080 ± 2 Ma Vanel Anorthosite, have much younger ages (< 70Ma) in relation to the host anorthosite, and are instead coeval to the Valin AMCG suite (1016-1008 Ma; Hébert et al. 2005; 2009). In the same way, mineralized oxide-apatite-norite from the centre of the Mattawa

Anorthosite (990 ± 7 Ma) are slightly younger than the andesine-anorthosite host (1016 ± 2, Hébert et al. 2005), and similar in age to the youngest AMCG suite dated at the Central Grenville Province: the nearby Grandes Pointes Plutonic Suite (988 – 987 Ma, Higgins et al. 2002; Moukhsil et al. 2009). However, as observed at Labrieville, both Vanel and Mattawa Anorthosites were previously dated from leuconorite lenses rather than using pegmatitic pockets of trapped, residual liquid from the anorthosite itself.

As previously mentioned, overall plagioclase of Fe-Ti-P cumulates and its respective host-AMCG have similar An compositions, whereas mineralized cumulates contain slightly higher Sr values in relation to the host. Although most of the host-AMCG and respective Fe-Ti-P cumulates have had considerable differences in their crystallization ages, they seem to be co-genetically related according to their plagioclase composition. Bybee & Ashwal (2015) have shown that the ascent of plagioclase-rich mushes into the lower and middle crust levels occurred over long-time scales, on the order of 80–100Ma, suggesting that the ascent of these magmas was particularly slow. Miloski et al. (2023a,b) pointed out the high complexity of mineralized systems associated with AMCG suites, with the occurrence of multi-stage injections of different ages into Fe-Ti-P mineralization in the Central Grenville Province (Lac à l'Orignal, 1069 ± 12 Ma / 993 ± 13 Ma; Lac Mirepoix, 1048 ± 8 Ma / 964 ± 9 Ma). A mismatch into the ages of the mineralization and the host-rocks that have been dated so far, together with the available previous U-Pb dating for the host-AMCG using lenses of orthopyroxene-bearing lithologies, corroborate the hypothesis of long-lived (> 70Ma) multi-diapiric intrusions in the petrogenesis of both mineralization and AMCG rocks (Miloski et al. 2023b). A single AMCG-massif in the Central Grenville can therefore contain a wide range of ages due to its complex petrogenetic context of emplacement and further evolution (Miloski et al. 2023a,b). Previous geochronological data of the main AMCG suites in the Central Grenville Province have been performed using marginal/residual

lithologies/dykes as well as pegmatitic pockets in massive anorthosite massifs due to the almost absence of abundant zircons crystals in plagioclase-rich cumulates as anorthosites (e.g., Higgins & Van Breemen 1992; 1996; Owens et al. 1994; Hébert et al. 2005; 2009). Moreover, the use of pegmatitic pockets should be preferred for dating of anorthosites instead of using random lenses/mafic-related lithologies that could not be coeval to the host-AMCG. Moreover, the huge time interval of magmatism, their similarities in petrography and field exposure, coupled with the large area of occurrence in Quebec, evidence the high complexity of these systems in the Central Grenville Province.

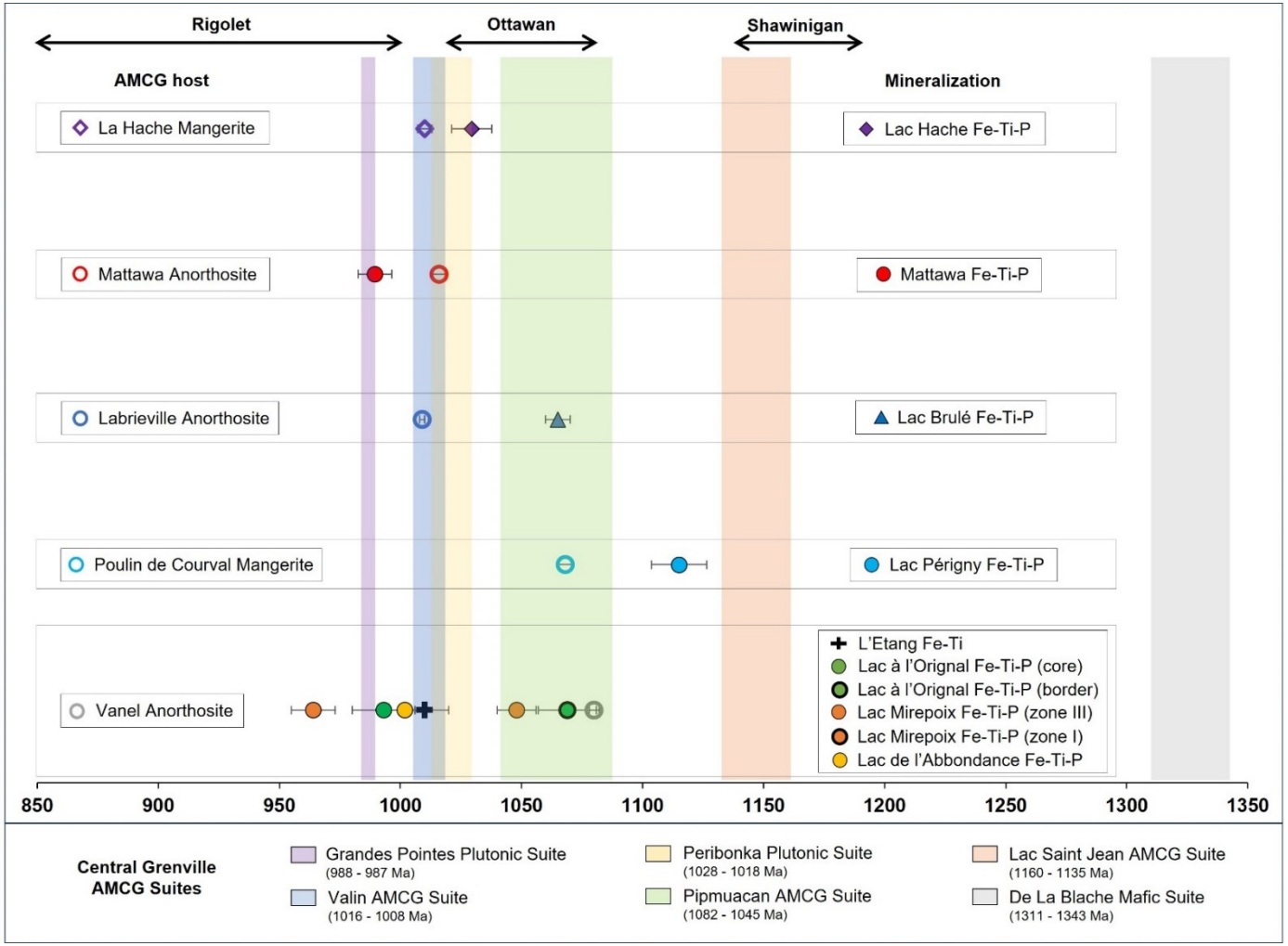

Figure 4.13. Geochronological data compilation of the main AMCG suites in the Central Grenville Province, Quebec and the U-Pb analysis of Fe-Ti-P mineralization from this work. U-Pb data of the Lac à l'Orignal Fe-Ti-P deposit after Miloski et al. (2023a) and for the Lac Mirepoix Fe-Ti-P mineralization after Miloski et al. (2023b).

4.8 Conclusions

Fe-Ti-P mineralization in the Central Grenville Province Proterozoic have a complex petrogenetic evolution, presenting a geochemical variation of oxide-apatite mineralization (massive oxides, nelsonite, oxide-apatite-norite, leuconorite and oxide-apatite-mangerite) with age among different anorthosite-massifs. The two younger AMCG suites in the Central Grenville Province (1082-1045 Ma Pipmuacan and 1020-1008 Ma Valin AMCG suites) present a geochemical variation of oxide-apatite mineralization from high Ti/Fe massive oxides (hemo-ilmenite ± magnetite) cumulates towards low-Ti/Fe apatite-bearing nelsonites ((hemo)-ilmenite + magnetite + apatite), oxide apatite norite ((hemo)-ilmenite + magnetite + apatite + silicates) up to mineralized mangerites (ilmenite + magnetite + apatite + oligoclase + K-feldspar + quartz). In-situ mineral trace-element geochemistry of plagioclase and oxides indicate a similarity between the different Fe-Ti-P mineralization in the Pipmuacan and Valin AMCG Suites, corroborating an evolution by fractional crystallization from more primitive massive oxides towards residual (evolved) oxide-apatite-rich mangerites. In-situ U-Pb-Hf isotopes in zircon from Fe-Ti-P mineralization spatially associated with the Pipmuacan and Valin AMCG Suites have mainly suprachondritic to slightly positive and negative εHf values, in which mineralization in the Labrieville and Mattawa anorthosites present more suprachondritic Hf signature (εHf: +3.0 to +7.0; U-Pb dating: 1065 (± 5Ma) to 990 (± 7Ma)), possibly reflecting contamination from juvenile crust, similar to mineralization in the Saint Urbain Anorthosite. Mineralization associated with the Vanel Anorthosite and the mangerites of La Hache and Poulin de Courval present a more enriched Hf signature (εHf: -5.0 to +7.4; U-Pb dating: 964 (± 9Ma) to 1115 (± 11Ma)), either being relatively more contaminated, and/or associated with more enriched mantle source(s) in relation to the mineralization at Labrieville and Mattawa. However, trace element patterns of apatite from all of the Fe-Ti-P mineralization indicate the involvement of an asthenospheric enriched

mantle source in forming the Fe-Ti-P rich melts for the different Fe-Ti-P mineralization in this study, rather than a depleted mantle source or enriched subcontinental lithospheric mantle as commonly proposed in previous tectonic models for the Grenville AMCG magmatism. Moreover, the Lu-Hf data reveal that Fe-Ti-P mineralization in Vanel Anorthosite and the mangerites of La Hache and Poulin de Courval probably underwent low- to moderate lower crustal contamination. Therefore, apatite and zircon geochemistry seem to better constrain the mantle source and role of contamination in the petrogenesis of AMCG suites in the Grenville Province.

U-Pb dating of the mineralized cumulates in this study resulted in quite different ages (>50Ma) from previously published ages from each respective host-AMCG, evidencing the high complexity of these systems and corroborating the occurrence of multiple injections of magmas as a main aspect in the generation of anorthosites and related Fe-Ti-P mineralization. Further detailed U-Pb dating and Hf isotopes, as well trace-element geochemistry in apatite in the different AMCG and associated Fe-Ti-P mineralization in the Central Grenville Province are necessary to better constrain the role of magma sources/crustal contamination in the region, the geographical distribution of each respective AMCG, and the relationship between the different massif anorthosite and mineralization occurrences.

4.9 Acknowledgments

This research was supported financially from the Fonds de recherche du Québec – Nature and Technologie (FRQNT) grant for new academics No 2020-NC-271033 & 2021-NC-309329 and the Canada Research Chair in Geochemistry Applied to Ore Deposits No CRC-2017-0286 of Sarah Dare. The authors thank Christian Tremblay (TRCM-UQAC), Leopold Tremblay and Randolph Maier for their assistance with field work; to Frank

Guillemette (MRBoreal) for access and sampling of drillcore; Audrey Lavoie and Pape Doudou Tague for helping with LA-ICP-MS analytical procedures at LabMaTer, UQAC; Marc Choquette and Suzie Côté for their SEM, microprobe and uXRF work at Université Laval and André Poirier who helped with LA-ICP-MS data acquisition on zircons at GEOTOP, UQAM. The authors also thank the reviewers that revised the original version of the manuscript for their suggestions that helped to improve the paper.

4.10 References

Arguin J-P, Pagé P, Barnes S-J, Girard R, Duran C. An Integrated Model for Ilmenite, Al-Spinel, and Corundum Exsolutions in Titanomagnetite from Oxide-Rich Layers of the Lac Doré Complex (Québec, Canada). Minerals. 2018; 8(11):476.

Ashwal, LD., 1993. Anorthosites. Springer, Heidelberg.

Ashwal, L. D. 2010. The temporality of anorthosites. The Canadian Mineralogist, 48(4), 711-728.

Ashwal, L. D., & Bybee, G. M. 2017. Crustal evolution and the temporality of anorthosites. Earth-Science Reviews, 173, 307-330.

Ashwal, L. D., & Wooden, J. L. 1985. Sm-Nd isotopic studies of Proterozoic anorthosites: systematics and implications. In The Deep Proterozoic Crust in the North Atlantic Provinces (pp. 61-73). Dordrecht: Springer Netherlands.

Ashwal, L. D., Wooden, J. L., & Emslie, R. F. 1986. Sr, Nd and Pb isotopes in Proterozoic intrusives astride the Grenville Front in Labrador: Implications for crustal contamination and basement mapping. Geochimica et Cosmochimica Acta, 50(12), 2571-2585.

Augland, L. E., Moukhsil, A., Solgadi, F., & Indares, A. 2015. Pinwarian to Grenvillian magmatic evolution in the central Grenville Province: new constraints from ID–TIMS U–Pb ages and coupled Lu–Hf S–MC–ICP–MS data. Canadian Journal of Earth Sciences, 52(9), 701-721.

Boulianne, D. 2003. Rapport des travaux de 2002-2003, Projet Titane 2002. Chimitec Ltee. Les Ressources d'Arianne. Quebec.

Barnes, S. J., Mansur, E. T., Pagé, P., Meric, J., & Arguin, J. P. 2020. Major and trace element compositions of chromites from the Stillwater, Bushveld and Great Dyke intrusions compared with chromites from komatiites, boninites and large igneous provinces.

Bickford, M. E., McLelland, J. M., Mueller, P. A., Kamenov, G. D., & Neadle, M. 2010. Hafnium isotopic compositions of zircon from Adirondack AMCG suites: Implications for the petrogenesis of anorthosites, gabbros, and granitic members of the suites. The Canadian Mineralogist, 48(4), 751-761.

Blichert-Toft, J., & Puchtel, I. S. 2010. Depleted mantle sources through time: evidence from Lu–Hf and Sm–Nd isotope systematics of Archean komatiites. Earth and Planetary Science Letters, 297(3-4), 598-606.

Bogdanova, S. V., Pashkevich, I. K., Buryanov, V. B., Makarenko, I. B., Orlyuk, M. I., Skobelev, V. M., ... & Legostaeva, O. V. 2004. The 1.80–1.74-Ga gabbro–anorthosite–rapakivi Korosten Pluton in the Ukrainian Shield: a 3-D geophysical reconstruction of deep structure. Tectonophysics, 381(1-4), 5-27.

Bybee, G. M., & Ashwal, L. D. 2015. Isotopic disequilibrium and lower crustal contamination in slowly ascending magmas: Insights from Proterozoic anorthosites. Geochimica et Cosmochimica Acta, 167, 286-300.

Charlier, B., Sakoma, E., Sauve, M., Stanaway, K., Vander Auwera, J., Duchesne, J.-C., 2008. The Grader layered intrusion (Havre-Saint-Pierre Anorthosite, Quebec) and genesis of nelsonite and other Fe–Ti–P ores. Lithos 101, 359–378.

Charlier, B., Namur, O., Malpas, S., de Marneffe, C., Duchesne, j.C., Vander Auwera, J., Bolle, O, 2010. Origin ofthe giant Allard Lake ilmenite ore deposit (Canada) by fractional crystallization, multiple magma pulses and mixing. Lithos 117, 119-134.

Charlier B, Namur O, Bolle O, et al 2015. Fe-Ti-V-P ore deposits associated with Proterozoic massif type anorthosites and related rocks. Earth Science Reviews, 141:56–81. doi: 10.1016/j.earscirev.2014.11.005.

Coint, N., Keiding, J. K., & Ihlen, P. M. 2020. Evidence for silicate–liquid immiscibility in monzonites and petrogenesis of associated Fe–Ti–P-rich rocks: example from the Raftsund intrusion, Lofoten, Northern Norway. Journal of Petrology, 61(4).

Corrigan, D., & Hanmer, S. 1997. Anorthosites and related granitoids in the Grenville orogen: a product of convective thinning of the lithosphere?. Geology, 25(1), 61-64.

Corriveau, L., Perreault, S., Davidson, A., 2007. Prospective metallogenic settings of the Grenville Province. In: Goodfellow, W.D. (Ed.), Mineral Deposits of Canada: a Synthesis of Major Deposit-types, District Metallogeny, the Evolution of Geological Provinces, and Exploration Methods: Geological Survey of Canada, Mineral Deposits Division, Special Publication, pp. 819–847.

Dare S.A, Barnes S-J, Beaudoin G, et al 2014. Trace element in magnetite as petrogenetic indicators. Mineralium Deposita, 49:785–796.

Dickin, A. P. 2000. Crustal formation in the Grenville Province: Nd-isotope evidence. Canadian Journal of Earth Sciences, 37(2-3), 165-181.

Duchesne, J. C., & Wilmart, E. 1997. Igneous charnockites and related rocks from the Bjerkreim–Sokndal layered intrusion (Southwest Norway): a jotunite (hypersthene monzodiorite)-derived A-type granitoid suite. Journal of petrology, 38(3), 337-369.

Duchesne, J. C. 1999. Fe-Ti deposits in Rogaland anorthosites (South Norway): geochemical characteristics and problems of interpretation. Mineralium Deposita, 34, 182-198.

Duchesne, J. C., Liégeois, J. P., Vander Auwera, J., & Longhi, J. 1999. The crustal tongue melting model and the origin of massive anorthosites. Terra Nova, 11(2-3), 100-105.

Dymek, R.F., Owens, B.E., 2001. Petrogenesis of apatite-rich rocks (nelsonites and oxide apatite gabbronorites) associated with massif anorthosites. Economic Geology 96, 797–815.

Emslie, R.F., 1985. Proterozoic anorthosite massifs. In: Tobi, A.C., Touret, J.L.R. (Eds.), The Deep Proterozoic Crust in the North Atlantic Provinces. Reidel, Dordrecht, pp. 39–60.

Emslie, R. F., & Hegner, E. 1993. Reconnaissance isotopic geochemistry of anorthosite mangerite-charnockite-granite (AMCG) complexes, Grenville Province, Canada. Chemical Geology, 106(3-4), 279-298.

Francis, D., Scowen, P., Panneton, G., & Doig, R. 2000. Contrasting Si-saturation in troctolite–anorthosite intrusions along the Manicouagan corridor of the Abitibi–Grenville transect. Canadian Journal of Earth Sciences, 37(2-3), 271-289.

Fredette, J. 2006. Pétrographie, géochimie et potentiel économique en Fe-Ti-P du secteur du Lac à Paul, partie nord de la suite anorthositique de Lac-Saint-Jean, province de Grenville, Québec. Université du Québec à Chicoutimi.

Frost, C. D., & Ronald Frost, B. 1997. Reduced rapakivi-type granites: the tholeiite connection. Geology, 25(7), 647-650.

Frost, C. D., Frost, B. R., Bell, J. M., & Chamberlain, K. R. 2002. The relationship between A-type granites and residual magmas from anorthosite: evidence from the northern Sherman batholith, Laramie Mountains, Wyoming, USA. Precambrian Research, 119(1-4), 45-71.

Frost, C. D., Frost, B. R., Lindsley, D. H., Chamberlain, K. R., Swapp, S. M., & Scoates, J. S. 2010. Chemical and isotopic evolution of the anorthositic plutons of the Laramie Anorthosite Complex: Explanations for variations in silica activity and oxygen fugacity of massif anorthosites. The Canadian Mineralogist, 48(4), 925-946.

Gobeil, A., Brisebois, D., Clark, T., Verpaelst, P., Madore, L., Wodicka, N., Cheve, S., 2002. Geologie de la moyenne Cote-Nord. In: Brisebois, D., Clark, T. (Eds.), Geologie et ressources minerales de la partie est de la Province de Grenville. Ministere des Ressources naturelles, de la Faune et des Parcs, Quebec, pp. 9–58. DV 2002-03.

Grant, M. 2020. Formation of magmatic Fe-Ti-V-P deposits within the Lac St. Jean area Saguenay, Québec, Canada: Insights from trace element composition of Fe-oxides and apatite. (Unpublished masters thesis). University of Ottawa, Ontario, Canada, pp. 343.

Groulier, P. A., Indares, A., Dunning, G., Moukhsil, A., & Jenner, G. 2018. Syn-orogenic magmatism over 100 my in high crustal levels of the central Grenville Province: characteristics, age and tectonic significance. Lithos, 312, 128-152.

Groulier, P. A., Indares, A., Dunning, G., & Moukhsil, A. 2020. Andean style 1.50–1.35 Ga arc dynamics in the Southeastern Laurentian margin: The rifting and reassembly of Quebecia. Terra Nova, 32(6), 450-457.

Gueye, B. 2023 Répartition spatiale de la composition de plagioclase de la Suite anorthositique de Lac-Saint-Jean, secteur Nord-Ouest du Lac-Saint-Jean : implications pour exploration minérale. Undergraduate thesis (UQAC), 55 pp.

Hébert, C., & Cadieux, A. M. 2003. Géologie de la région des lacs Portneuf et Maria-Chapdelaine (22E/01 et 22E/02). Géologie Québec [Ressources naturelles].

Hébert, C., van Breemen, O., Tollo, R. P., Corriveau, L., McLelland, J., & Bartholomew, M. 2004. Mesoproterozoic basement of the Lac St. Jean Anorthosite Suite and younger Grenvillian intrusions in the Saguenay region, Québec: structural relationships and U-Pb geochronology. MEMOIRS-GEOLOGICAL SOCIETY OF AMERICA, 65-80.

Hébert, C., van Breemen, O., Tollo, R. P., Corriveau, L., McLelland, J., & Bartholomew, M. 2004. Mesoproterozoic basement of the Lac St. Jean Anorthosite Suite and younger Grenvillian intrusions in the Saguenay region, Québec: structural relationships and U-Pb geochronology. MEMOIRS-GEOLOGICAL SOCIETY OF AMERICA, 65-80.

Hébert, C., Cadieux, A.-M., Van Breemen, O., 2005. Temporal evolution and nature of Ti–Fe–P mineralization in the anorthosite–mangerite–charnockite–granite (AMCG) suites of the South–central Grenville Province, Saguenay – Lac St. Jean area, Quebec, Canada. Canadian Journal of Earth Sciences 42, 1865–1880.

Hébert, C., Van Breemen, O., & Cadieux, A. 2009. Région du reservoir Pipmuacan, (SNRC 22E): Synthese Geologique. RG 2009-01. Ministère des ressources naturelles et de la faune, Gouvernement du Québec.

Heinonen, A. P., T. Andersen, and O. T. Rämö. 2010. Re-evaluation of rapakivi petrogenesis: Source constraints from the Hf isotope composition of zircon in the rapakivi granites and associated mafic rocks of southern Finland. Journal of Petrology 51.8: 1687-1709.

Heinonen, A., Andersen, T., Rämö, O. T., & Whitehouse, M. 2014. The source of Proterozoic anorthosite and rapakivi granite magmatism: evidence from combined in situ Hf–O isotopes of zircon in the Ahvenisto complex, southeastern Finland. Journal of the Geological Society, 172(1), 103-112.

Higgins, M. D., & Doig, R. 1981. The Sept Iles anorthosite complex: field relationships, geochronology, and petrology. Canadian Journal of Earth Sciences, 18(3), 561-573.

Higgins, M. D. 2005. A new interpretation of the structure of the Sept Iles Intrusive suite, Canada. Lithos, 83(3-4), 199-213.

Higgins, M. D., & Van Breemen, O. 1992. The age of the Lac-Saint-Jean anorthosite complex and associated mafic rocks, Grenville Province, Canada. Canadian Journal of Earth Sciences, 29(7), 1412-1423.

Higgins, M.D., Van Breemen, O., 1996. Three generations of Anorthosite–Mangerite–Charnockite–Granite magmatism, contact metamorphism and tectonism in the Saguenay – Lac–St-Jean region, Grenville Province, Canada. Precambrian Research 79, 347–362.

Higgins, M. D., Ider, M., & Breemen, O. V. 2002. U-Pb ages of plutonism, wollastonite formation, and deformation in the central part of the Lac-Saint-Jean anorthosite suite. Canadian Journal of Earth Sciences, 39(7), 1093-1105.

Icenhower, J. P., Dymek, R. F., & Weaver, B. L. 1998. Evidence for an enriched mantle source for jøtunite (orthopyroxene monzodiorite) associated with the St. Urbain anorthosite, Quebec. Lithos, 42(3-4), 191-212.

Ickert, R. B. 2013. Algorithms for estimating uncertainties in initial radiogenic isotope ratios and model ages. Chemical Geology, 340, 131-138.

Indares, A., & Moukhsil, A. 2013. Geon 12 crustal extension in the central Grenville Province, implications for the orogenic architecture, and potential influence on the emplacement of anorthosites. Canadian Journal of Earth Sciences, 50(9), 955-966.

Kemp, A. I. S., Shimura, T., & Hawkesworth, C. J. 2007. Linking granulites, silicic magmatism, and crustal growth in arcs: Ion microprobe (zircon) U-Pb ages from the Hidaka metamorphic belt, Japan. Geology, 35(9), 807-810.

Kieffer, M. A., Dare, S. A., & Namur, O. 2022. The use of trace element in apatite to trace differentiation of a ferrobasaltic melt in the Sept-Iles Intrusive Suite, Quebec, Canada: Implications for provenance discrimination. Geochimica et Cosmochimica Acta.

Kieffer, M. A., Dare, S. A., & Namur, O., Mansur, E. 2023. Apatite chemistry as a petrogenetic indicator for mafic layered intrusions. Journal of Petrology (in review).

Kieffer, M. A., Dare, S. A., & Namur, O. 2023. Discrimination of apatite from I-, S- and A-type granites using trace element: implications for mineral exploration and provenance studies. Lithos.).

Koppers, A. A., Becker, T. W., Jackson, M. G., Konrad, K., Müller, R. D., Romanowicz, B., ... & Whittaker, J. M. 2021. Mantle plumes and their role in Earth processes. Nature Reviews Earth & Environment, 2(6), 382-401.

Lavelle, J-S. & Rioux, P. 2017. Rapport de forage sur la propriete Lac Brule. Argex Titane inc. Lavel, Quebec.

Li, W., Costa, F., Oppenheimer, Nagashima, K. 2023. Volatile and trace element partitioning between apatite and alkaline melts. Contributions to Mineralogy and Petrology 178.

Longhi, J., & Ashwal, L. D. 1985. Two-stage models for lunar and terrestrial anorthosites: Petrogenesis without a magma ocean. Journal of Geophysical Research: Solid Earth, 90(S02), C571-C584.

Longhi, J., Auwera, J. V., Fram, M. S., & Duchesne, J. C. 1999. Some phase equilibrium constraints on the origin of Proterozoic (massif) anorthosites and related rocks. Journal of Petrology, 40(2), 339-362.

Ludden, J., & Hynes, A. 2000. The Lithoprobe Abitibi-Grenville transect: two billion years of crust formation and recycling in the Precambrian Shield of Canada. Canadian Journal of Earth Sciences, 37(2-3), 459-476.

Mao, M., Rukhlov, A. S., Rowins, S. M., Spence, J. & Coogan, L. A. 2016. Apatite Trace Element Compositions: A Robust New Tool for Mineral Exploration. Economic Geology 111, 1187-1222.

McLelland, J., Daly, J. S., & McLelland, J. M. 1996. The Grenville orogenic cycle (ca. 1350-1000 Ma): an Adirondack perspective. Tectonophysics, 265(1-2), 1-28.

McLelland, J. M., Selleck, B. W., Bickford, M. E., Tollo, R. P., Bartholomew, M. J., Hibbard, J. P., & Karabinos, P. M. 2010. Review of the Proterozoic evolution of the Grenville Province, its Adirondack outlier, and the Mesoproterozoic inliers of the Appalachians. From Rodinia to Pangea: The Lithotectonic Record of the Appalachian Region: Geological Society of America Memoir, 206, 21-49.

Miloski, P., Dare, S., Morisset, C-E., Davies, J., Perrot., Savard, D. 2023a. Petrogenesis of Fe-Ti-P mineral deposits associated with Proterozoic anorthosite massifs in the Grenville Province: insights from oxide and apatite trace element geochemistry at Lac à l'Orignal, Quebec, Canada. Mineralium Deposita (accepted).

Miloski, P., Dare, S., Morisset, C-E., Davies, J., Perrot. 2023b. Petrogenesis of oxide-apatite mineralization associated with Proterozoic anorthosite massifs at Lac Mirepoix, Quebec, Canada: a multi-stage model of evolution for Fe-Ti-P mineralization in the Central Grenville Province. Ore Geology Reviews.

Morisset, C. E. 2008. Origin of rutile-bearing ilmenite Fe-Ti deposits in Proterozoic anorthosite massifs of the Grenville Province (Doctoral dissertation, University of British Columbia).

Morisset, C.-E., Scoates, J.S., Weis, D., Friedman, R.M., 2009. U–Pb and 40Ar/39Ar geochronology of the Saint-Urbain and Lac Allard (Havre-Saint-Pierre) anorthosites and their associated Fe–Ti oxide ores, Quebec: evidence for emplacement and slow cooling during the collisional Ottawan orogeny in the Grenville Province. Precambrian Research 174, 95–116.

Morisset, C.-E., Scoates,J.S., Weis, D., Sauve, M., Stanaway, K.J., 2010. Rutile-bearing ilmenite deposits associated with the Proterozoic Saint-Urbain and Lac Allard anorthosite massifs, Grenville Province, Québec. Can. Mineral. 48, 821-849.

Morisset, C. E., Williamson, M. C., & Hipkin, V. 2013. Investigation of three Fe–Ti oxide deposits associated with Grenvillian anorthosite massifs as potential source for lunar analogue ilmenite. Canadian Journal of Earth Sciences, 50(1), 64-77.

Morisset, C. E., Scoates, J. S., Weis, D., & Rahier, A. 2014. Methodology and Application of Hafnium Isotopes in Ilmenite and Rutile by MC-ICP-MS. Geostandards and Geoanalytical Research, 38(2), 159-176.

Moukhsil, A., Clark, T., Hébert, C., & Labbé, J. Y. 2009. Géologie de la région de Baie-Comeau–Labrieville (feuillets SNRC 22F/01, 22F/02, 22F/03, 22 F/04, 22 F/05 et 22 F/06). Ministère des Ressources naturelles et de la Faune, Québec, 2009-01.

Namur, O., Charlier, B., Toplis, M. J., Higgins, M. D., Liégeois, J. P., & Vander Auwera, J. 2010. Crystallization sequence and magma chamber processes in the ferrobasaltic Sept Iles layered intrusion, Canada. Journal of Petrology, 51(6), 1203-1236.

Nebel, O., Nebel-Jacobsen, Y., Mezger, K., & Berndt, J. 2007. Initial Hf isotope compositions in magmatic zircon from early Proterozoic rocks from the Gawler Craton, Australia: a test for zircon model ages. Chemical Geology, 241(1-2), 23-37.

Owens, B.E., Dymek, R.F., 1992. Fe-Ti-P-rich rocks and massif anorthosite: problems of interpretation illustrated from the Labrieville and St-Urbain plutons, Quebec. Can. Mineral. 30, 163-190.

Owens, B.E., Rockow, M.W., Dymek, R.F., 1993. Jotunites from the Grenville Province, Quebec: petrological characteristics and implications for massif anorthosite petrogenesis. Lithos 30, 57–80.
Owens, B. E., Dymek, R. F., Tucker, R. D., Brannon, J. C., & Podosek, F. A. 1994. Age and radiogenic isotopic composition of a late-to post-tectonic anorthosite in the Grenville Province: the Labrieville massif, Quebec. Lithos, 31(3-4), 189-206.
Owens, B.E., Dymek, R.F., 2005. Rediscovery of the Mattawa anorthosite massif, Grenville Province, Quebec. Canadian Journal of Earth Sciences 42, 1699–1718.
Owens, B. E., & Tomascak, P. B. 2002. Mesoproterozoic lamprophyres in the Labrieville Massif, Quebec: clues to the origin of alkalic anorthosites?. Canadian Journal of Earth Sciences, 39(6), 983-997.
Papapavlou, K., Moukhsil, A., Poirier, A., & Davies, J. H. F. L. 2022. The Pre-Grenvillian assembly of the southeastern Laurentian margin through the U–Pb–Hf detrital zircon record of Mesoproterozoic supracrustal sequences (Central Grenville Province, Quebec, Canada). Geological Magazine, 159(2), 199-211.
Peate, D. W., & Hawkesworth, C. J. 1996. Lithospheric to asthenospheric transition in low-Ti flood basalts from southern Parana, Brazil. Chemical Geology, 127(1-3), 1-24.
Peck, W. H., & Valley, J. W. 2000. Large crustal input to high δ 18 O anorthosite massifs of the southern Grenville Province: new evidence from the Morin Complex, Quebec. Contributions to Mineralogy and Petrology, 139, 402-417.
Peck, W. H., Clechenko, C. C., Hamilton, M. A., & Valley, J. W. 2010. Oxygen isotopes in the Grenville and Nain AMCG suites: Regional aspects of the crustal component in massif anorthosites. The Canadian Mineralogist, 48(4), 763-786.
Perrot, M., Tremblay, A., & David, J. 2017. Detrital zircon U-Pb geochronology of the Magog Group, southern Quebec–stratigraphic and tectonic implications for the Quebec Appalachians. American Journal of Science, 317(10), 1049-1094.
Regan, S. P., Chiarenzelli, J. R., McLelland, J. M., & Cousens, B. L. 2011. Evidence for an enriched asthenospheric source for coronitic metagabbros in the Adirondack Highlands. *Geosphere*, *7*(3), 694-709.
Rivers, T., 1997. Lithotectonic elements of the Grenville Province: review and tectonic implications. Precambrian Research 86, 117–154.
Rivers, T. 2012. Upper-crustal orogenic lid and mid-crustal core complexes: signature of a collapsed orogenic plateau in the hinterland of the Grenville Province. Canadian Journal of Earth Sciences, 49(1), 1-42.
Rivers, T., Martignole, J., Gower, C. F., & Davidson, A. 1989. New tectonic divisions of the Grenville Province, southeast Canadian Shield. Tectonics, 8(1), 63-84.
Rudnick, R., & Gao, S. 2003. The role of lower crustal recycling in continent formation. Geochimica et Cosmochimica Acta Supplement, 67(18), 403.
Rudnick, R. L., Gaschnig, R. M., Li, S., Tang, M., Qiu, L., Valley, J. W., ... & McDonough, W. F. 2014. Temporal Evolution of the Upper Continental Crust: Implications for the Mode of Crustal Growth and the Evolution of the Hydrosphere. In AGU Fall Meeting Abstracts (Vol. 2014, pp. V41E-08).
Ryan, B. 2000. The Nain-Churchill boundary and the Nain Plutonic Suite: A regional perspective on the geologic setting of the Voisey's Bay Ni-Cu-Co deposit. Economic Geology, 95(4), 703-724.
Schiellerup, H., Lambert, D. D., Prestvik, T., Robins, B., McBride, J. S., & Larsen, R. B. 2000. Re–Os isotopic evidence for a lower crustal origin of massif-type anorthosites. Nature, 405(6788), 781-784.
Scoates, J.S., Lindsley, D.H., Frost, B.R., 2010. Magmatic and structural evolution of an anorthositic magma chamber: the Poe Mountain intrusion, Laramie Anorthosite complex, Wyoming. Can. Mineral. 48, 851-885.

Scoates, J. S., & Chamberlain, K. R. 1997. Orogenic to post-orogenic origin for the 1.76 Ga Horse Creek anorthosite complex, Wyoming, USA. The Journal of Geology, 105(3), 331-344.

Scoates, J. S., & Mitchell, J. N. 2000. The evolution of troctolitic and high Al basaltic magmas in Proterozoic anorthosite plutonic suites and implications for the Voisey's Bay massive Ni-Cu sulfide deposit. Economic Geology, 95(4), 677-701.

Spencer, C. J., Kirkland, C. L., Roberts, N. M. W., Evans, N. J., & Liebmann, J. 2020. Strategies towards robust interpretations of in situ zircon Lu–Hf isotope analyses. Geoscience Frontiers, 11(3), 843-853.

Sun, S. S., & McDonough, W. F. 1989. Chemical and isotopic systematics of oceanic basalts: implications for mantle composition and processes. Geological Society, London, Special Publications, 42(1), 313-345.

Turner, S., Sandiford, M., & Foden, J. 1992. Some geodynamic and compositional constraints on" postorogenic" magmatism. Geology, 20(10), 931-934.

Vander Auwera, J., Longhi, J, Duchesne, J.C., 1998. A liquid line of descent of the jotunite (hypersthene monzodiorite) suite. J. Petrol. 39, 439-468.

Vander Auwera, J., Longhi, J., & Duchesne, J. C. 2000. The effect of pressure on DSr (plag/melt) and DCr (opx/melt): implications for anorthosite petrogenesis. Earth and Planetary Science Letters, 178(3-4), 303-314.

Vander Auwera, J., Bogaerts, M., Liégeois, J. P., Demaiffe, D., Wilmart, E., Bolle, O., & Duchesne, J. C. 2003. Derivation of the 1.0–0.9 Ga ferro-potassic A-type granitoids of southern Norway by extreme differentiation from basic magmas. Precambrian Research, 124(2-4), 107-148.

Vander Auwera, J., Bolle, O., Bingen, B., Liégeois, J. P., Bogaerts, M., Duchesne, J. C., ... & Longhi, J. 2011. Sveconorwegian massif-type anorthosites and related granitoids result from post-collisional melting of a continental arc root. Earth-Science Reviews, 107(3-4), 375-397.

White, W. M. 2020. Geochemistry. John Wiley & Sons.

Woodruff, L. G., Nicholson, S. W., & Fey, D. L. 2013. A Deposit Model for Magmatic Iron-titanium-oxide Deposits Related to Proterozoic Massif Anothosite Plutonic Suites. US Department of the Interior, US Geological Survey.

Woussen, G., Roy, D. W., Dimroth, E., & Chown, E. H. 1986. Mid-Proterozoic extensional tectonics in the core zone of the Grenville Province. Geol Assoc Can Spec Pap, 31, 297-311.

Yassa, A. 2022. Technical report and initial mineral resource estimate of the Lac Orignal phosphate property, Saguenay-Lac-Saint-Jean region, Northern Québec. First Phosphate Corp.

Zhang, S.-H., Liu, S.-W., Zhao, Y., Yang, J.H., Song, B., Liu, X.-M., 2007. The 1.75–1.68 Ga anorthosite mangerite-alkali granitoid-rapakivi granite suite from the northern North China Craton: Magmatism related to a Paleoproterozoic orogen. Precambrian Research 155, 287-312. doi.org/10.1016/j.precamres.2007.02.008.

CHAPTER 5

CONCLUSIONS

CONCLUSIONS

Fe-Ti-P mineralization in the Central Grenville Province Proterozoic have a complex petrogenetic evolution, presenting a geochemical variation of oxide-apatite mineralization (massive oxides, nelsonite, oxide-apatite-norite, leuconorite and oxide-apatite-mangerite) with age among different anorthosite-massifs. Detailed study of Fe-Ti-P mineralization in the 1080 ± 2 Ma Vanel Anorthosite indicate the occurrence of multiple injections of residual Fe-Ti-P-rich liquids at Lac à l'Orignal and Lac Mirepoix. Both intrusions were derived from residual high-Ti-P magmas after anorthosite crystallization, with similar REE compositions, that evolved through extensive crystallization of hemo-ilmenite, magnetite and apatite, in the late stages of differentiation of ferrodiorite/jotunite magmas.

The Lac à l'Orignal deposit, dominated by oxide-apatite norite cumulates, presents a change in the oxide mineralogy from hemo-ilmenite (+ minor magnetite) at the older border (1069 ± 12 Ma) to Fe-poor ilmenite + magnetite towards the younger core (993 ± 12 Ma). Although core and border have different ages, their range of ages are coeval with those previously described for the two youngest AMCG magmatic events in the region, and both cumulates have been generated under similar high-fO_2 conditions. The variation and spatial distribution of hemo-ilmenite (Xhem) between the border and core of Lac à l'Orignal must account for higher amounts of magnetite at the core of the intrusion (more evolved) in relation to border (more primitive). Border and core have had variable degrees of subsolidus inter-oxide re-equilibration, which had influence on the compositional evolution of the analyzed cumulates, especially within the core portion, modifying its original composition.

The Lac Mirepoix Fe-Ti-P mineralization was formed by multiple injections of similar magma compositions, over at least 80 Ma (zone I: 964 ± 9 Ma and zone III: 1048 ± 8 Ma) where different zones containing mainly primitive hemo-ilmenite-rich lenses in anorthosite

(zone I), nelsonite (zone II) and evolved oxide-apatite-norite cumulates are present. Although the dated OAN in the different zones have different ages, they are (roughly) coeval to the youngest AMCG magmatic activity in the region. Similar to Lac à l'Orignal, the cumulates were generated under similar high-fO_2 conditions from a high-Ti-P evolved ferrodiorite magma, with similar REE compositions, evolving by fractional crystallization of hemo-ilmenite, plagioclase, orthopyroxene, magnetite and apatite.

The similarity in composition/mineralogy between the OAN cumulates and the parental fine-grained ferrodiorite dykes of the Lac Mirepoix and the Lac à l'Orignal Fe-Ti-P mineralization, the overlap on the range of ages obtained as well as the proximity between the two sites corroborates the cogenetic hypothesis. As previously suggested, the different Fe-Ti-P mineralization in the Central Grenville Province could be related to accumulation of magmas with a similar parental composition at intermediary/shallow levels, which then produced several magma injections at higher crustal levels after different amounts of differentiation. We propose a complex model of evolution multiple injections of residual Fe-Ti-P melts, that were drained or filter-pressed from different aged anorthosite diapirs over a period of 80 Mys, further evolving by fractional crystallization forming oxide-apatite cumulates.

Residual ferrodiorite magmas that formed the several Fe-Ti-P mineralization in the two younger AMCG suites in the Central Grenville Province (1082-1045 Ma Pipmuacan and 1020-1008 Ma Valin AMCG suites) evolved from a high Ti/Fe system represented by massive oxides (hemo-ilmenite ± magnetite, similar to Lac Tio, the base of Grader Intrusion and zone I of Lac Mirepoix) cumulates towards low-Ti/Fe system of apatite-bearing nelsonites ((hemo)-ilmenite + magnetite + apatite, similar to Grader and zone II of Lac Mirepoix), oxide apatite norite ((hemo)-ilmenite + magnetite + apatite + silicates, similar to evolved zone III of Lac Mirepoix and to Lac à l'Orignal) up to mineralized mangerites

(ilmenite + magnetite + apatite + oligoclase + K-feldspar + quartz, similar to La Hache). Therefore, mineralized mangerites (Si-rich cumulates) would represent the most evolved (fractionated) part of a low-Ti/Fe system in the Grenville Province, rather than the product of anatexis of crustal rocks.

In-situ U-Pb-Hf isotopes in zircon from Fe-Ti-P mineralization in this study have mainly chondritic to slightly positive and negative εHf values, in which mineralization in the Labrieville and Mattawa anorthosites present more suprachondritic Hf signature (εHf: +3.0 to +7.0; U-Pb dating: 1065 (± 5Ma) to 990 (± 7Ma)), possibly reflecting contamination from juvenile crust, similar to mineralization in the Saint Urbain Anorthosite. Mineralization associated with the Vanel Anorthosite and the mangerites of La Hache and Poulin de Courval present a more enriched Hf signature (εHf: -5.0 to +7.4; U-Pb dating: 964 (± 9Ma) to 1115 (± 11Ma)), either being relatively more contaminated, and/or associated with more enriched mantle source(s) in relation to the mineralization at Labrieville and Mattawa. The trace element patterns of apatite from all of the Fe-Ti-P mineralization have LREE enriched patterns very similar to apatite from mafic layered intrusions, associated with mantle plumes, with negligible crustal contamination. This indicates the involvement of an asthenospheric enriched mantle source in forming the Fe-Ti-P rich melts for the different Fe-Ti-P mineralization in this study, rather than a depleted mantle source or enriched subcontinental lithospheric mantle as commonly proposed in previous tectonic models for the Grenville AMCG magmatism. Moreover, the Lu-Hf data reveal that Fe-Ti-P mineralization in Vanel Anorthosite and the mangerites of La Hache and Poulin de Courval probably underwent low- to moderate lower crustal contamination. Therefore, we show for the first time that apatite and zircon geochemistry provide important constraints on the mantle source and role of contamination in the petrogenesis of AMCG suites in the Grenville Province, which should be taken into account for the tectonic model of the Grenville.

U-Pb dating of the mineralized cumulates in this study resulted in quite different ages (>50Ma) from previously published ages from each respective host-AMCG, evidencing the high complexity of these systems and corroborating the occurrence of multiple injections of magmas as a main aspect in the generation of anorthosites and related Fe-Ti-P mineralization. The variation of trace element in oxides and apatite as well as new U-Pb ages for Fe-Ti-rich mineralized rocks at Lac à l'Orignal and Lac Mirepoix, indicate the complex petrogenesis of oxide-apatite mineralization related to anorthosite-massifs in the Central Grenville Province. Understanding the petrogenesis of Fe-Ti-P mineralization and their relationship to the host AMCG suite is essential for helping to predict the occurrence of similar deposits in nearby locations, which can guide exploration efforts, saving time and resources. Future work on detailed U-Pb dating, Hf isotopes as well as trace element geochemistry of apatite in the different AMCG and associated Fe-Ti-P mineralization in the Central Grenville Province (both eastern and western portions) are necessary to better constrain the role of magma sources/crustal contamination in the region, the geographical distribution of each respective AMCG, and the relationship between the different massif anorthosite and mineralization occurrences.

APPENDICES

APPENDIX 2.1 SUPPLEMENTARY TABLES (CHAPTER 2)

Appendix 2.1.1 Whole-rock reference materials (separate excel sheet)

Appendix 2.1.2 Mineral chemistry reference materials (separate excel sheet)

Appendix 2.1.3 Petrographic modal proportions

Sample	Depth (m)	Location	Lithology	Modal Proportions (%)										µxrf Maps	Ilmenite/Magnetite ratio
				Plagioclase	OPX	Hemo-ilmenite	Ilmenite	Magnetite	Al-spinel	Apatite	Biotite	Hornblende	Sulphides		
LO-01	3.70	Borehole LO-14-21	Medium-grained OAN	65	15	7	-	3	-	5	5	-	<1	x	2.3
LO-02	4.60	Borehole LO-14-21	Massive apatite	-	-	-	-	-	-	85	-	-	15	-	-
LO-05	6.40	Borehole LO-14-21	Coarse-grained OAN	60	25	5	-	3	-	7	-	-	<1	-	1.7
LO-06	6.80	Borehole LO-14-21	Fine-grained OAN dyke	45	20	15	-	3	-	7	10	-	<1	-	5.0
LO-07	8.50	Borehole LO-14-21	Medium-grained OAN	70	15	4	-	1	-	10	-	-	<1	-	4.0
LO-08	8.60	Borehole LO-14-21	Fine-grained OAN dyke	54	23	10	-	1	-	10	2	-	<1	-	10.0
LO-09	9.90	Borehole LO-14-21	Medium-grained OAN	30	35	8	-	12	-	7	5	3	<1	x	0.7
LO-15	14.20	Borehole LO-14-21	Medium-grained OAN	43	15	13	-	12	-	15	2	-	<1	-	1.1
LO-16	16.40	Borehole LO-14-21	Coarse-grained-OAN	45	28	8		7	1	10	1	-	<1	-	1.1
LO-21	20.80	Borehole LO-14-21	Nelsonite	5	10	25		20		40	-	-	-	-	1.3
LO-22	21.50	Borehole LO-14-21	Coarse-grained-OAN	52	28	4	1	5	<1	7	2	-	<1	x	0.8
LO-24	28.20	Borehole LO-14-21	Medium-grained OAN	60	23	5	2	3	<1	5	2	-	<1	-	1.0
LO-26	36.30	Borehole LO-14-21	Medium-grained OAN	55	25	-	5	5	1	10	-	-	<1	-	1.0

LO-29	42.40	Borehole LO-14-21	Medium-grained OAN	35	42	-	3	7	<1	12	-	-	<1	-	1.0
LO-32	48.70	Borehole LO-14-21	Medium-grained OAN	30	40	-	8	7	2	12	-	-	<1	x	0.4
LO-35	57.30	Borehole LO-14-21	Medium-grained OAN	10	50	-	13	12	<1	15	-	-	<1	-	1.1
LO-38	62.20	Borehole LO-14-21	Apatite-bearing anorthosite	85	1	-	1	1	<1	12	-	-	<1	-	1.1
LO-39	63.40	Borehole LO-14-21	Medium-grained OAN	10	47	-	12	12	2	15	2	-	<1	x	1.0
LO-40	67.50	Borehole LO-14-21	Medium-grained OAN	18	54	-	8	7	2	10	1	-	<1	-	1.0
LO-41	70.10	Borehole LO-14-21	Coarse-grained-OAN	15	60	-	8	7	2	7	1	-	<1	-	1.1

Appendix 2.1.3 Petrographic modal proportions (Cont.)

Sample	Depth (m)	Location	Lithology	Modal Proportions (%)										µxrf Maps	Ilmenite/Magnetite ratio
				Plagioclase	OPX	Hemo-ilmenite	Ilmenite	Magnetite	Al-spinel	Apatite	Biotite	Hornblende	Sulphides		
LO-43	75.70	Borehole LO-14-21	Medium-grained OAN	27	45	-	12	10	1	5	<1	-	<1	x	1.1
LO-44-2	77.00	Borehole LO-14-21	Apatite-bearing anorthosite	85	1	-	1	1	-	12	-	-	<1	-	1.2
LO-46	79.00	Borehole LO-14-21	Medium-grained OAN	40	30	-	12	5	2	10	-	-	<1	-	1.0
LO-47	84.20	Borehole LO-14-21	Medium-grained OAN	40	30	-	6	9	1	12	-	-	2	-	2.4
LO-49	87.80	Borehole LO-14-21	Medium-grained OAN	30	40	-	7	7	<1	15	-	-	<1	x	0.7
LO-50	91.20	Borehole LO-14-21	Medium-grained OAN	30	35	-	10	12	<1	12	-	-	1	-	1.0
LO-51	95.80	Borehole LO-14-21	Medium-grained OAN	35	35	7	2	10	<1	10	-	-	<1	x	0.9
LO-55	99.70	Borehole LO-14-21	Medium-grained OAN	50	35	6	-	3	-	8	-	-	<1	-	2.0
LO-57	102.10	Borehole LO-14-21	Medium-grained OAN	40	34	9	-	6	-	10	1	-	<1	x	1.5
LO-58	105.40	Borehole LO-14-21	Anorthosite	98	-	1	-	-	-	-	1	-	<1	-	-
LO-59	108.50	Borehole LO-14-21	Anorthosite	99	-	-	-	-	-	-	1	-	<1	-	-
20PM02	-	Surface outcrop	Medium-grained OAN	40	30	12	-	5	1	10	2	-	<1	-	2.4
20PM03-A	-	Surface outcrop	Massive oxides in Anorthosite	10	20	-	35	35	-	-	-	-	<1	-	1.0

20PM03-B	-	Surface outcrop	Anorthosite	95	3	2	-	-	-	-	-	-	-	-	-
MG-LO-01[a]	51.30	Borehole LO-12-10	Medium-grained OAN	40	40	5	-	5	-	5	5	-	<1	-	1.0
MG-LO-02[a]	3.90	Borehole LO-12-25	Anorthosite	98	-	2	-	-	-	-	-	-	-	-	-
MG-LO-03[a]	93.00	Borehole LO-12-31	Medium-grained OAN	50	30	5	-	5	-	10	3	-	<1	-	1.0
MG-LO-04[a]	90.60	Borehole LO-12-13	Massive oxides in Anorthosite	10	15	-	40	35	-	-	-	-	-	-	1.1

Appendix 2.1.3 Petrographic modal proportions (cont.)

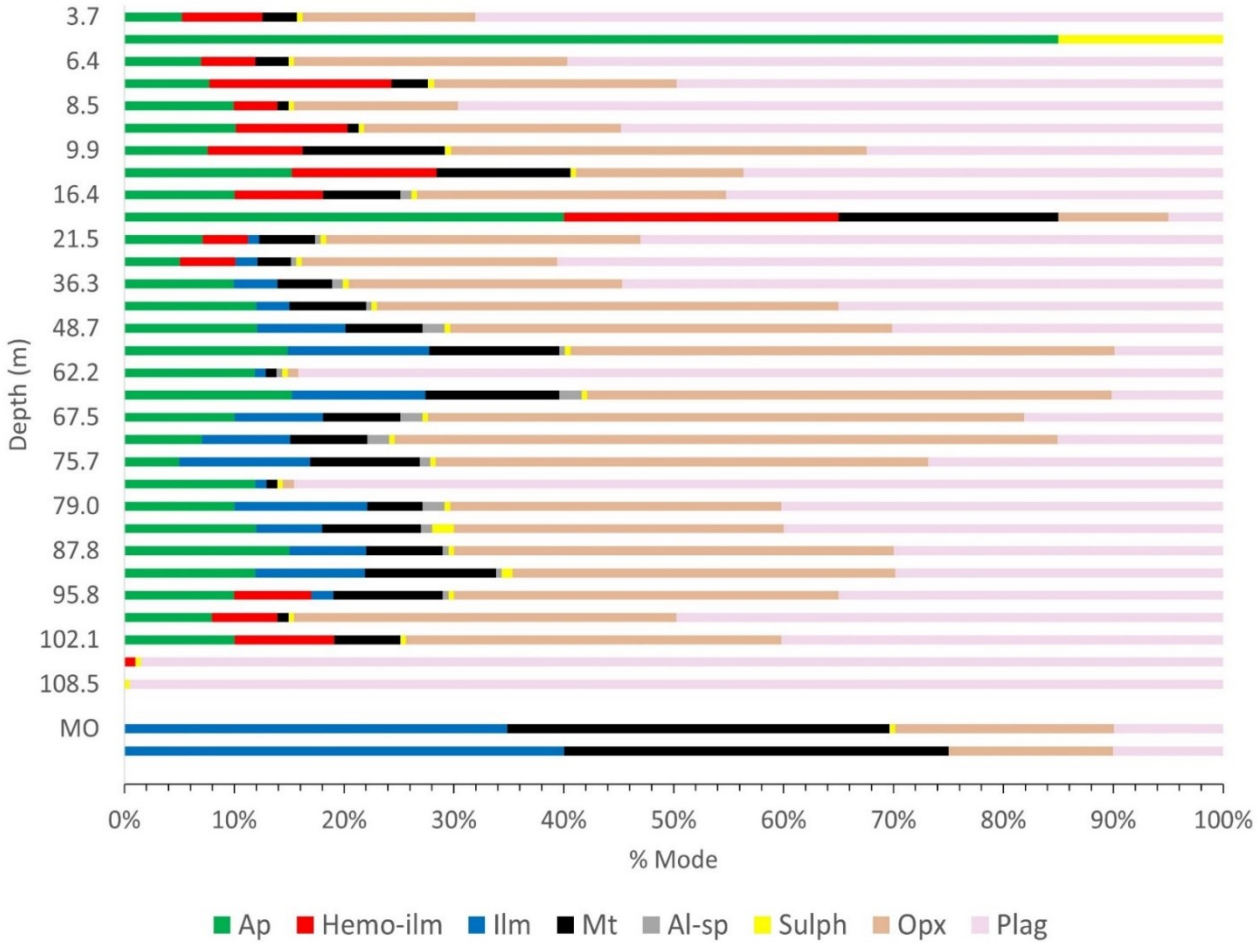

Appendix 2.1.4 Complete LA-ICP-MS whole-rock results

Sample	Location	Lithology	Oxide Mineralogy	SiO_2	TiO_2	Al_2O_3	Fe_2O_{3t}	MnO	MgO	CaO	Na_2O	K_2O	P_2O_5	LOI	Total
LO-01	Borehole LO-14-21	Medium-grained OAN	Hm-ilm + Mt	42.59	3.43	15.77	16.96	0.17	4.86	9.06	3.07	0.65	3.14	0.31	100.00
LO-05	Borehole LO-14-21	Coarse-grained OAN	Hm-ilm + Mt	39.19	3.98	15.20	18.22	0.15	4.33	10.36	2.94	0.72	4.50	0.41	100.00
LO-06	Borehole LO-14-21	Fine-grained-OAN dyke	Hm-ilm + Mt	34.63	5.05	10.88	23.67	0.25	6.34	10.15	2.18	0.43	5.27	1.09	100.00
LO-07	Borehole LO-14-21	Medium-grained OAN	Hm-ilm + Mt	39.57	2.81	16.77	14.23	0.10	2.82	12.84	3.49	0.84	6.09	0.44	100.00
LO-08	Borehole LO-14-21	Fine-grained-OAN dyke	Hm-ilm	41.83	5.20	13.49	19.26	0.20	4.58	8.78	3.24	0.70	2.66	0.00	100.00
LO-10	Borehole LO-14-21	Medium-grained OAN	Hm-ilm + Mt	30.57	4.70	7.11	33.06	0.33	9.12	8.70	1.15	0.26	5.00	0.00	100.00
LO-16	Borehole LO-14-21	Coarse-grained OAN	Hm-ilm + Mt	33.72	5.49	9.81	25.17	0.23	7.34	10.04	1.84	0.49	5.67	0.21	100.00
LO-18	Borehole LO-14-21	Medium-grained OAN	Hm-ilm + Mt	37.20	3.77	12.37	22.62	0.21	6.25	10.11	2.37	0.58	4.21	0.31	100.00
LO-22	Borehole LO-14-21	Coarse-grained-OAN	Hm-ilm + Mt	37.43	4.44	9.78	22.18	0.26	8.51	9.29	1.92	0.64	5.10	0.46	100.00
LO-23	Borehole LO-14-21	Medium-grained OAN	Hm-ilm + Mt	34.07	5.00	10.20	23.93	0.23	6.86	10.63	2.05	0.52	6.06	0.46	100.00
LO-24	Borehole LO-14-21	Medium-grained OAN	Hm-ilm + Mt	37.92	4.64	12.62	20.99	0.19	6.20	9.31	2.57	0.68	4.44	0.43	100.00
LO-25	Borehole LO-14-21	Medium-grained OAN	Ilm + Mt	35.19	3.30	10.94	23.42	0.22	7.30	11.12	1.99	0.45	6.03	0.05	100.00
LO-26	Borehole LO-14-21	Medium-grained OAN	Ilm + Mt	35.15	3.80	11.09	26.04	0.23	7.20	9.46	2.01	0.47	4.49	0.07	100.00
LO-29	Borehole LO-14-21	Medium-grained OAN	Ilm + Mt	31.69	3.75	8.25	27.62	0.26	8.59	11.29	1.45	0.31	6.78	0.00	100.00
LO-32	Borehole LO-14-21	Medium-grained OAN	Ilm + Mt	29.09	5.02	7.16	33.25	0.30	8.87	9.45	1.13	0.28	5.45	0.00	100.00
LO-34	Borehole LO-14-21	Medium-grained OAN	Ilm + Mt	29.35	6.27	6.08	33.84	0.30	9.03	9.78	0.95	0.19	4.21	0.00	100.00
LO-37	Borehole LO-14-21	Medium-grained OAN	Ilm + Mt	32.37	5.71	8.14	28.74	0.26	8.08	10.27	1.45	0.32	4.66	0.00	100.00
LO-38	Borehole LO-14-21	Apatite-bearing Anorthosite	-	44.05	0.92	19.24	6.54	0.07	1.65	14.97	3.98	0.90	7.06	0.61	100.00
LO-39	Borehole LO-14-21	Medium-grained OAN	Ilm + Mt	20.20	7.77	3.26	47.15	0.36	10.13	6.43	0.10	0.02	4.58	0.00	100.00
LO-40	Borehole LO-14-21	Medium-grained OAN	Ilm + Mt	28.13	5.81	6.49	36.34	0.30	9.33	7.82	0.95	0.20	4.63	0.00	100.00
LO-41B	Borehole LO-14-21	Coarse-grained-OAN	Ilm + Mt	35.56	4.01	11.01	26.90	0.23	6.17	9.14	2.26	0.57	3.74	0.42	100.00

LO-43	Borehole LO-14-21	Medium-grained OAN	Ilm + Mt	24.61	6.96	3.93	42.47	0.34	10.89	6.23	0.34	0.07	4.16	0.00	100.00
LO-44-2	Borehole LO-14-21	Apatite-bearing Anorthosite	-	45.37	1.30	19.88	7.38	0.07	1.71	13.46	4.06	0.91	5.63	0.22	100.00
LO-46	Borehole LO-14-21	Medium-grained OAN	Ilm + Mt	24.83	6.16	5.01	39.95	0.30	9.74	7.92	0.60	0.13	5.35	0.00	100.00
LO-49	Borehole LO-14-21	Medium-grained OAN	Ilm + Mt	29.09	5.66	8.30	31.21	0.24	7.78	9.96	1.38	0.32	6.06	0.00	100.00
LO-50	Borehole LO-14-21	Medium-grained OAN	Ilm + Mt	29.25	5.62	8.43	31.21	0.24	8.09	9.62	1.43	0.31	5.79	0.00	100.00
LO-51	Borehole LO-14-21	Medium-grained OAN	Hm-ilm + Mt	29.39	4.81	8.85	28.22	0.22	7.03	12.04	1.53	0.37	7.54	0.00	100.00
LO-55	Borehole LO-14-21	Medium-grained OAN	Hm-ilm + Mt	42.17	2.45	15.79	14.83	0.15	4.85	10.83	3.19	0.73	4.41	0.59	100.00
LO-57	Borehole LO-14-21	Medium-grained OAN	Hm-ilm + Mt	29.29	4.49	8.06	27.47	0.26	7.73	12.38	1.38	0.39	8.16	0.40	100.00
LO-58	Borehole LO-14-21	Anorthosite	-	53.04	0.18	28.15	1.27	0.01	0.66	11.09	4.20	0.36	0.08	0.95	100.00
LO-59	Borehole LO-14-21	Anorthosite	-	54.25	0.09	28.02	0.89	0.01	0.33	10.86	4.44	0.46	0.03	0.63	100.00
20PM02	Surface outcrop	Medium-grained OAN	Hm-ilm + Mt	34.69	4.88	9.78	26.58	0.21	7.68	8.83	2.00	0.79	4.48	0.06	100.00
20PM03	Surface outcrop	Massive oxides in anorthosite	Ilm + Mt	18.70	9.53	7.62	54.52	0.20	5.51	1.92	0.89	0.41	0.28	0.36	100.00
20PM03B	Surface outcrop	Anorthosite hosting massive oxides	-	53.31	0.67	22.74	4.85	0.06	2.62	8.49	4.61	1.54	0.40	0.69	100.00

Appendix 2.1.4 Complete LA-ICP-MS whole-rock results (cont.)

Sample	Location	Lithology	Oxide Mineralogy	^{45}Sc	^{51}V	^{53}Cr	^{59}Co	^{60}Ni	^{63}Cu	^{66}Zn	^{69}Ga	^{85}Rb	^{88}Sr	^{89}Y	^{90}Zr	^{93}Nb	^{137}Ba	^{139}La
LO-01	Borehole LO-14-21	Medium-grained OAN	Hm-ilm + Mt	17.2	195.0	29.7	44.7	29.4	53.6	214.4	24.5	3.5	1296.1	28.1	75.0	5.5	889.5	32.9
LO-05	Borehole LO-14-21	Coarse-grained OAN	Hm-ilm + Mt	16.7	233.6	31.0	46.5	49.9	61.4	205.0	24.6	2.9	1319.7	37.5	100.5	5.4	1020.8	42.1
LO-06	Borehole LO-14-21	Fine-grained-OAN dyke	Hm-ilm + Mt	25.3	342.0	31.5	59.1	52.6	47.5	296.0	25.4	2.4	890.7	48.1	110.2	10.7	466.7	55.8
LO-07	Borehole LO-14-21	Medium-grained OAN	Hm-ilm + Mt	12.4	180.9	18.4	39.8	41.9	58.3	164.1	26.9	2.7	1513.6	54.8	52.9	4.3	1255.8	62.3
LO-08	Borehole LO-14-21	Fine-grained-OAN dyke	Hm-ilm	23.2	307.2	44.4	48.7	41.2	92.6	216.0	25.2	3.6	1126.0	56.3	411.9	23.5	970.6	73.1
LO-10	Borehole LO-14-21	Medium-grained OAN	Hm-ilm + Mt	24.1	522.4	180.0	89.4	238.8	87.8	459.3	27.6	1.6	541.5	47.1	124.3	8.8	261.9	37.2
LO-16	Borehole LO-14-21	Coarse-grained OAN	Hm-ilm + Mt	24.1	337.9	23.2	67.8	38.7	36.3	270.5	23.1	1.4	898.7	42.6	72.3	7.5	704.2	45.1
LO-18	Borehole LO-14-21	Medium-grained OAN	Hm-ilm + Mt	22.9	332.9	80.1	68.9	168.0	86.7	246.1	25.9	2.2	1023.0	36.5	22.5	4.2	749.1	35.5
LO-22	Borehole LO-14-21	Coarse-grained-OAN	Hm-ilm + Mt	25.0	258.7	17.1	61.5	25.3	25.5	270.2	21.9	6.3	811.3	49.1	369.7	9.8	726.3	58.1
LO-23	Borehole LO-14-21	Medium-grained OAN	Hm-ilm + Mt	22.9	292.5	15.0	68.7	44.5	41.9	265.4	23.6	1.7	959.0	46.1	117.5	7.2	711.2	48.7
LO-24	Borehole LO-14-21	Medium-grained OAN	Hm-ilm + Mt	20.5	272.3	16.0	57.2	41.1	27.9	219.1	23.4	2.7	1163.8	34.9	160.6	6.0	1037.3	38.1
LO-25	Borehole LO-14-21	Medium-grained OAN	Ilm + Mt	19.4	350.4	137.2	70.5	140.8	49.7	271.0	24.5	1.5	912.2	41.0	39.3	1.8	510.8	38.8
LO-26	Borehole LO-14-21	Medium-grained OAN	Ilm + Mt	21.1	394.7	125.1	73.0	115.0	40.3	291.5	26.8	1.7	870.5	36.2	89.8	3.0	575.3	35.0
LO-29	Borehole LO-14-21	Medium-grained OAN	Ilm + Mt	23.0	405.1	152.2	78.1	134.2	44.2	313.9	24.6	1.2	721.2	47.7	52.7	2.2	345.2	42.7

LO-32	Borehole LO-14-21	Medium-grained OAN	Ilm + Mt	26.1	492.7	161.4	87.3	114.1	41.4	378.8	26.9	1.5	554.8	38.1	40.0	2.5	307.4	32.8
LO-34	Borehole LO-14-21	Medium-grained OAN	Ilm + Mt	41.9	454.9	36.4	90.4	41.8	36.5	356.3	25.3	0.8	436.8	38.3	65.7	4.3	223.5	28.3
LO-37	Borehole LO-14-21	Medium-grained OAN	Ilm + Mt	33.8	441.0	30.2	78.0	45.6	35.3	288.1	23.3	4.5	620.5	37.6	163.2	5.1	299.6	30.8
LO-38	Borehole LO-14-21	Apatite-bearing Anorthosite	-	6.2	91.2	37.6	16.2	16.0	10.4	78.4	23.2	4.0	1617.1	46.7	27.9	1.5	1002.8	49.6
LO-39	Borehole LO-14-21	Medium-grained OAN	Ilm + Mt	25.5	721.8	145.8	134.0	102.5	60.2	533.9	32.3	0.3	162.3	30.6	127.9	2.9	31.7	26.7
LO-40	Borehole LO-14-21	Medium-grained OAN	Ilm + Mt	26.0	532.5	66.4	93.9	58.2	36.7	393.7	27.5	0.7	471.4	30.4	70.5	4.0	221.5	26.9
LO-41B	Borehole LO-14-21	Coarse-grained-OAN	Ilm + Mt	27.3	350.4	23.4	59.3	20.0	17.2	342.4	30.4	2.3	947.3	41.9	26.5	6.9	750.1	43.6
LO-43	Borehole LO-14-21	Medium-grained OAN	Ilm + Mt	25.5	631.7	70.5	113.5	76.6	49.8	442.3	28.6	BelowLOD	241.3	28.1	69.2	3.7	85.3	24.6
LO-44-2	Borehole LO-14-21	Apatite-bearing Anorthosite	-	6.9	107.2	32.4	19.1	23.0	12.8	107.6	24.0	6.2	1626.5	36.7	77.4	1.8	1000.6	38.9
LO-46	Borehole LO-14-21	Medium-grained OAN	Ilm + Mt	24.3	604.0	33.5	112.7	52.9	46.2	420.9	28.4	0.5	364.7	34.4	113.2	3.5	141.4	31.2
LO-49	Borehole LO-14-21	Medium-grained OAN	Ilm + Mt	21.5	460.0	50.1	90.2	61.0	41.6	329.5	26.0	1.3	677.9	38.1	95.2	3.7	353.3	35.9
LO-50	Borehole LO-14-21	Medium-grained OAN	Ilm + Mt	20.8	478.2	30.4	93.2	52.2	44.9	319.5	25.6	1.2	688.1	36.9	128.3	3.2	353.8	35.1
LO-51	Borehole LO-14-21	Medium-grained OAN	Hm-ilm + Mt	18.4	434.5	35.2	81.3	51.4	40.4	292.6	25.3	1.8	781.8	46.7	64.4	3.3	398.7	44.5
LO-55	Borehole LO-14-21	Medium-grained OAN	Hm-ilm + Mt	14.6	255.5	69.7	51.2	71.9	31.7	179.3	24.4	3.7	1230.8	34.6	101.9	4.4	865.1	40.7
LO-57	Borehole LO-14-21	Medium-grained OAN	Hm-ilm + Mt	17.7	466.2	30.0	82.9	92.3	75.4	404.8	24.9	3.2	696.5	40.4	65.1	3.1	340.9	37.7

LO-58	Borehole LO-14-21	Anorthosite	-	3.0	14.1	22.1	4.7	18.7	6.2	11.5	17.2	2.8	639.3	1.8	10.1	0.6	117.1	3.2
LO-59	Borehole LO-14-21	Anorthosite	-	2.0	6.3	15.7	2.1	13.5	20.4	87.7	18.0	1.5	663.3	0.7	3.3	0.4	132.1	2.3
20PM02	Surface outcrop	Medium-grained OAN	Hm-ilm + Mt	19.6	441.8	24.5	36.0	21.2	41.0	878.8	27.2	4.9	697.5	28.4	109.9	4.5	336.7	29.2
20PM03	Surface outcrop	Massive oxides in anorthosite	Ilm + Mt	16.6	1768.5	943.3	143.3	336.9	72.4	630.8	52.6	3.2	247.0	3.9	59.4	5.3	156.1	19.2
20PM03B	Surface outcrop	Anorthosite hosting massive oxides	-	9.7	57.9	86.8	15.0	55.6	23.8	590.1	18.6	11.7	509.9	10.7	134.4	3.2	318.1	19.3

Appendix 2.1.4 Complete LA-ICP-MS whole-rock results (cont.)

Sample	Depth (m)	Location	Lithology	Oxide Mineralogy	^{140}Ce	^{141}Pr	^{146}Nd	^{147}Sm	^{153}Eu	^{157}Gd	^{159}Tb	^{163}Dy	^{165}Ho	^{166}Er	^{169}Tm	^{172}Yb	^{175}Lu	^{174}Hf	^{208}Pb
LO-01	3.7	Borehole LO-14-21	Medium-grained OAN	Hm-ilm + Mt	83.7	12.5	62.2	12.5	4.0	10.9	1.2	6.4	1.0	2.4	0.3	1.5	0.2	2.1	4.3
LO-05	6.4	Borehole LO-14-21	Coarse-grained OAN	Hm-ilm + Mt	108.9	16.5	83.8	17.4	5.4	15.2	1.7	8.5	1.4	3.3	0.4	1.9	0.2	2.7	3.5
LO-06	6.8	Borehole LO-14-21	Fine-grained-OAN dyke	Hm-ilm + Mt	141.9	21.3	103.5	20.9	5.7	18.3	2.1	10.7	1.8	4.3	0.5	2.7	0.4	3.3	3.6
LO-07	8.5	Borehole LO-14-21	Medium-grained OAN	Hm-ilm + Mt	161.0	24.5	122.4	25.2	7.7	21.8	2.4	12.2	2.0	4.9	0.5	2.8	0.4	1.6	4.1
LO-08	8.6	Borehole LO-14-21	Fine-grained-OAN dyke	Hm-ilm	176.4	24.4	108.6	21.9	5.6	17.9	2.2	12.0	2.1	5.5	0.7	4.1	0.6	10.3	9.9
LO-10	10.5	Borehole LO-14-21	Medium-grained OAN	Hm-ilm + Mt	102.5	15.8	79.9	17.8	4.2	15.9	1.8	10.2	1.8	4.6	0.6	3.7	0.5	3.7	1.9
LO-16	16.4	Borehole LO-14-21	Coarse-grained OAN	Hm-ilm + Mt	117.7	18.2	91.0	19.3	5.6	17.1	1.9	9.5	1.6	3.7	0.4	2.3	0.3	2.5	2.5
LO-18	19.5	Borehole LO-14-21	Medium-grained OAN	Hm-ilm + Mt	93.1	14.6	74.2	16.4	4.9	14.3	1.7	8.1	1.4	3.2	0.4	2.0	0.3	1.3	2.6
LO-22	21.5	Borehole LO-14-21	Coarse-grained-OAN	Hm-ilm + Mt	147.9	22.1	107.8	22.2	5.5	18.9	2.2	11.1	1.9	4.4	0.5	2.8	0.4	10.4	3.7
LO-23	22.7	Borehole LO-14-21	Medium-grained OAN	Hm-ilm + Mt	128.3	19.8	99.0	21.0	6.2	18.4	2.0	10.3	1.7	4.2	0.5	2.5	0.3	3.3	2.8
LO-24	28.2	Borehole LO-14-21	Medium-grained OAN	Hm-ilm + Mt	98.2	15.0	75.6	16.0	5.0	13.7	1.6	7.8	1.3	3.1	0.3	1.8	0.2	4.2	3.2
LO-25	32.2	Borehole LO-14-21	Medium-grained OAN	Ilm + Mt	104.6	16.6	87.3	18.8	5.4	17.1	1.9	9.2	1.6	3.6	0.4	2.1	0.3	1.2	1.7
LO-26	36.3	Borehole LO-14-21	Medium-grained OAN	Ilm + Mt	92.4	14.5	74.3	16.2	4.8	14.5	1.6	8.1	1.3	3.3	0.4	2.0	0.2	2.5	2.1

LO-29	42.4	Borehole LO-14-21	Medium-grained OAN	Ilm + Mt	117.7	19.0	99.4	21.9	6.1	19.5	2.1	10.8	1.8	4.3	0.5	2.5	0.3	1.6	1.4
LO-32	48.7	Borehole LO-14-21	Medium-grained OAN	Ilm + Mt	89.6	14.5	77.0	17.2	4.7	15.8	1.7	8.5	1.5	3.3	0.4	2.0	0.3	1.5	1.2
LO-34	56.7	Borehole LO-14-21	Medium-grained OAN	Ilm + Mt	78.1	12.8	68.6	16.0	4.3	14.5	1.7	8.8	1.5	3.6	0.4	2.2	0.3	2.5	1.9
LO-37	61.2	Borehole LO-14-21	Medium-grained OAN	Ilm + Mt	83.5	13.3	70.9	15.7	4.5	14.4	1.7	8.5	1.5	3.5	0.4	2.2	0.3	4.5	2.3
LO-38	62.2	Borehole LO-14-21	Apatite-bearing Anorthosite	-	131.5	20.6	107.2	22.7	7.0	20.6	2.2	11.2	1.8	4.1	0.4	2.3	0.3	0.7	3.5
LO-39	63.4	Borehole LO-14-21	Medium-grained OAN	Ilm + Mt	73.3	11.8	63.4	13.7	3.6	12.7	1.4	6.9	1.2	2.6	0.3	1.6	0.2	3.3	0.3
LO-40	67.5	Borehole LO-14-21	Medium-grained OAN	Ilm + Mt	73.3	11.8	62.7	13.5	3.8	12.4	1.4	7.0	1.2	2.7	0.3	1.6	0.2	2.0	0.8
LO-41B	70.1	Borehole LO-14-21	Coarse-grained-OAN	Ilm + Mt	112.2	17.2	85.9	18.1	5.2	16.1	1.8	9.4	1.6	3.9	0.4	2.4	0.3	1.5	3.1
LO-43	75.7	Borehole LO-14-21	Medium-grained OAN	Ilm + Mt	67.6	10.9	57.2	12.4	3.4	11.7	1.2	6.3	1.1	2.4	0.3	1.5	0.2	2.2	0.4
LO-44-2	77.0	Borehole LO-14-21	Apatite-bearing Anorthosite	-	102.0	15.9	82.7	17.4	5.6	15.6	1.6	8.4	1.4	3.1	0.3	1.7	0.2	1.9	3.9
LO-46	79.0	Borehole LO-14-21	Medium-grained OAN	Ilm + Mt	85.0	13.7	72.1	15.9	4.3	14.2	1.6	7.8	1.3	3.0	0.3	1.8	0.2	3.1	0.6
LO-49	87.8	Borehole LO-14-21	Medium-grained OAN	Ilm + Mt	97.3	15.6	81.4	17.7	5.0	15.7	1.8	8.7	1.5	3.2	0.4	1.8	0.3	2.6	1.2
LO-50	91.2	Borehole LO-14-21	Medium-grained OAN	Ilm + Mt	95.1	15.0	79.2	17.2	4.8	15.3	1.6	8.5	1.4	3.2	0.3	1.8	0.3	3.3	1.3
LO-51	95.8	Borehole LO-14-21	Medium-grained OAN	Hm-ilm + Mt	120.8	19.2	101.9	22.1	6.0	19.6	2.1	10.6	1.7	3.9	0.4	2.2	0.3	1.8	1.5
LO-55	99.7	Borehole LO-14-21	Medium-grained OAN	Hm-ilm + Mt	101.5	15.0	74.1	15.0	4.7	13.3	1.5	7.8	1.3	3.0	0.4	2.0	0.3	2.4	4.8

LO-57	102.1	Borehole LO-14-21	Medium-grained OAN	Hm-ilm + Mt	102.2	16.4	86.4	18.9	5.1	17.2	1.8	9.1	1.5	3.4	0.4	2.0	0.3	1.8	3.1
LO-58	105.4	Borehole LO-14-21	Anorthosite	-	6.8	0.9	3.7	0.7	0.8	0.6	0.1	0.4	0.1	0.2	0.0	0.1	0.0	0.3	3.3
LO-59	108.5	Borehole LO-14-21	Anorthosite	-	4.7	0.5	2.3	0.4	0.7	0.3	0.0	0.2	0.0	0.1	0.0	0.1	0.0	0.1	4.2
20PM02	0.0	Surface outcrop	Medium-grained OAN	Hm-ilm + Mt	75.8	11.6	60.2	12.6	3.6	10.9	1.2	6.2	1.0	2.4	0.3	1.4	0.2	2.7	0.2
20PM03	0.0	Surface outcrop	Massive oxides in anorthosite	Ilm + Mt	32.5	3.1	11.8	1.7	0.5	1.3	0.1	0.8	0.2	0.3	0.1	0.3	0.0	1.9	0.5
20PM03B	0.0	Surface outcrop	Anorthosite hosting massive oxides	-	40.6	5.2	22.3	4.2	1.7	3.2	0.4	2.3	0.4	1.0	0.1	0.7	0.1	3.2	15.7

Eu/Eu* = 2(Eu)n/[(Sm)n+(Gd)n] calculated with Chondrite normalization values of Sun & McDonough (1989).

Appendix 2.1.4 CIPW norm from LA-ICP-MS whole-rock results

Sample	Depth (m)	Location	Lithology	Oxide Mineralogy	Or	Ab	An	An*	Or*	Ap
LO-01	3.70	Borehole LO-14-21	Medium-grained OAN	Hm-ilm + Mt	3.86	25.98	24.40	44.99	7.11	7.44
LO-05	6.40	Borehole LO-14-21	Coarse-grained OAN	Hm-ilm + Mt	4.25	24.89	21.99	43.02	8.30	10.67
LO-06	6.80	Borehole LO-14-21	Fine-grained OAN dyke	Hm-ilm + Mt	2.56	18.46	15.92	43.11	6.92	12.48
LO-07	8.50	Borehole LO-14-21	Medium-grained OAN	Hm-ilm + Mt	4.97	29.51	23.95	40.98	8.51	14.41
LO-08	8.60	Borehole LO-14-21	Fine-grained OAN dyke	Hm-ilm + Mt	4.15	27.40	20.20	39.04	8.02	6.30
LO-10	10.50	Borehole LO-14-21	Medium-grained OAN	Hm-ilm + Mt	1.54	9.69	10.49	48.29	7.10	11.84
LO-16	16.40	Borehole LO-14-21	Coarse-grained-OAN	Hm-ilm + Mt	2.87	15.54	12.75	40.92	9.22	13.44
LO-18	19.50	Borehole LO-14-21	Medium-grained OAN	Hm-ilm + Mt	3.44	20.09	21.39	47.63	7.65	9.96
LO-22	21.50	Borehole LO-14-21	Coarse-grained OAN	Hm-ilm + Mt	3.77	16.22	12.78	38.99	11.51	12.08
LO-23	22.70	Borehole LO-14-21	Medium-grained OAN	Hm-ilm + Mt	3.06	17.33	13.13	39.16	9.12	14.36
LO-24	28.20	Borehole LO-14-21	Medium-grained OAN	Hm-ilm + Mt	4.05	21.73	17.17	39.98	9.42	10.52
LO-25	32.20	Borehole LO-14-21	Medium-grained OAN	Ilm + Mt	2.65	16.81	15.78	44.77	7.53	14.28
LO-26	36.30	Borehole LO-14-21	Medium-grained OAN	Ilm + Mt	2.75	16.99	17.61	47.15	7.37	10.63
LO-29	42.40	Borehole LO-14-21	Medium-grained OAN	Ilm + Mt	1.85	12.29	11.67	45.21	7.17	16.07
LO-32	48.70	Borehole LO-14-21	Medium-grained OAN	Ilm + Mt	1.64	9.53	11.29	50.26	7.31	12.91
LO-34	56.70	Borehole LO-14-21	Medium-grained OAN	Ilm + Mt	1.11	8.03	11.77	56.29	5.32	9.98
LO-37	61.20	Borehole LO-14-21	Medium-grained OAN	Ilm + Mt	1.88	12.24	14.79	51.16	6.49	11.04
LO-38	62.20	Borehole LO-14-21	Apatite-bearing Anorthosite	-	5.34	33.72	28.19	41.92	7.94	16.71
LO-40	67.50	Borehole LO-14-21	Medium-grained OAN	Ilm + Mt	1.19	8.02	8.51	48.04	6.69	10.97
LO-41B	70.10	Borehole LO-14-21	Coarse-grained-OAN	Ilm + Mt	3.36	19.09	18.23	44.82	8.26	8.85
LO-43	75.70	Borehole LO-14-21	Medium-grained OAN	Ilm + Mt	0.43	2.91	3.70	52.50	6.14	9.86
LO-44-2	77.00	Borehole LO-14-21	Apatite-bearing Anorthosite	-	5.39	34.34	29.99	43.01	7.73	13.35
LO-46	79.00	Borehole LO-14-21	Medium-grained OAN	Ilm + Mt	0.80	5.09	4.34	42.44	7.78	12.67
LO-49	87.80	Borehole LO-14-21	Medium-grained OAN	Ilm + Mt	1.90	11.64	9.79	41.95	8.16	14.36
LO-50	91.20	Borehole LO-14-21	Medium-grained OAN	Ilm + Mt	1.83	12.09	9.88	41.50	7.70	13.72
LO-51	95.80	Borehole LO-14-21	Medium-grained OAN	Hm-ilm + Mt	2.19	12.92	10.46	40.93	8.56	17.86
LO-55	99.70	Borehole LO-14-21	Medium-grained OAN	Hm-ilm + Mt	4.34	27.02	24.91	44.27	7.71	10.45
LO-57	102.10	Borehole LO-14-21	Medium-grained OAN	Hm-ilm + Mt	2.28	11.69	8.13	36.79	10.33	19.32
LO-58	105.40	Borehole LO-14-21	Anorthosite	-	2.15	35.55	54.49	59.11	2.33	0.19
LO-59	108.50	Borehole LO-14-21	Anorthosite	-	2.72	37.57	53.69	57.13	2.89	0.07

20PM02	0.00	Surface outcrop	Medium-grained OAN	Hm-ilm + Mt	4.67	16.91	14.55	40.28	12.92	10.61
20PM03	0.00	Surface outcrop	Massive oxides in anorthosite	Ilm + Mt	2.43	7.50	7.65	43.52	13.80	0.68
20PM03B	0.00	Surface outcrop	Anorthosite hosting massive oxides	-	9.09	39.04	36.80	43.33	10.70	0.96

Appendix 2.1.5 Complete LA-ICP-MS results of plagioclase

Detection Limits (33-55µm)														24.21-318.92	0.107 - 3.216	1.642-22.856	18.53-1033.89
Sample	Depth (m)	Lithology	Oxide Mineralogy	# analysis	SiO_2	Al_2O_3	CaO	Na_2O	K_2O	Total	An	Ab	Or	^{23}Na	^{25}Mg	^{27}Al	^{31}P
LO-01	3.7	Medium-grained OAN	Hm-ilm + Mt	n=5	56.08	28.13	8.66	5.73	0.28	99.03	44.7	53.6	1.7	42530.2	102.8	148871.3	2343.3
LO-02	4.7	Anorthosite	-	n=5	54.79	29.19	9.38	5.16	0.32	99.11	49.1	48.9	2.0	38313.6	359.5	154476.2	2645.5
LO-05	6.4	Coarse-grained OAN	Hm-ilm + Mt	n=5	56.22	28.09	8.85	5.52	0.36	99.18	45.9	51.8	2.3	40929.9	87.6	148653.3	3020.8
LO-06	6.8	Fine-grained OAN dyke	Hm-ilm + Mt	n=5	56.57	27.96	8.34	6.00	0.27	99.30	42.7	55.6	1.7	44507.1	148.1	147993.3	2261.0
LO-07	8.5	Medium-grained OAN	Hm-ilm + Mt	n=5	56.70	27.77	8.38	5.78	0.42	99.21	43.3	54.1	2.6	42888.5	72.8	146981.6	3484.7
LO-08	8.6	Fine-grained-OAN dyke	Hm-ilm	n=5	57.73	27.02	7.55	5.90	0.78	99.15	39.4	55.7	4.8	43761.2	206.6	142981.5	6453.3
LO-09	9.9	Medium-grained OAN	Hm-ilm + Mt	n=5	54.63	29.31	9.65	5.16	0.21	99.15	50.1	48.5	1.3	38273.6	261.2	155130.8	1772.9
LO-15-1	14.2	Medium-grained OAN	Hm-ilm + Mt	n=4	54.98	29.04	9.36	5.34	0.25	99.14	48.5	50.0	1.5	39585.9	98.2	153667.5	2083.8
LO-15-2	14.4	Medium-grained OAN	Hm-ilm + Mt	n=5	55.65	28.52	8.84	5.53	0.40	99.11	45.7	51.8	2.4	41056.0	164.2	150954.2	3296.4
LO-16	16.4	Coarse-grained-OAN	Hm-ilm + Mt	n=5	56.78	27.73	8.28	5.79	0.39	99.25	43.1	54.5	2.4	42941.9	517.0	146771.7	3251.5
LO-22	21.5	Coarse-grained OAN	Hm-ilm + Mt	n=5	57.08	27.52	7.96	5.91	0.56	99.21	41.2	55.4	3.5	43878.8	160.2	145654.1	4667.1
LO-24	28.2	Medium-grained OAN	Hm-ilm + Mt	n=4	56.89	27.78	8.02	5.89	0.59	99.33	41.4	55.0	3.6	43685.8	45.9	147036.1	4899.7
LO-26	36.3	Medium-grained OAN	Ilm + Mt	n=5	56.26	28.14	8.49	5.54	0.56	99.16	44.3	52.2	3.5	41064.0	93.1	148923.6	4643.8

LO-29	42.4	Medium-grained OAN	Ilm + Mt	n=5	56.41	28.09	8.37	5.68	0.51	99.24	43.5	53.4	3.2	42137.3	50.1	148677.5	4270.6
LO-32	48.7	Medium-grained OAN	Ilm + Mt	n=6	56.21	28.15	8.47	5.62	0.48	99.17	44.1	52.9	3.0	41653.7	235.9	148997.1	4024.4
LO-38	62.2	Apatite-bearing Anorthosite	-	n=5	56.18	28.39	8.63	5.39	0.55	99.33	45.3	51.3	3.4	40016.2	125.0	150278.1	4578.3
LO-39	63.4	Medium-grained OAN	Ilm + Mt	n=5	56.33	28.13	8.26	5.87	0.34	99.15	42.8	55.1	2.1	43511.1	243.7	148868.4	2845.9
LO-40	67.5	Medium-grained OAN	Ilm + Mt	n=6	56.10	28.29	8.48	5.72	0.43	99.24	43.8	53.5	2.6	42427.5	100.1	149749.0	3529.6
LO-41B	70.1	Coarse-grained OAN	Ilm + Mt	n=6	57.24	27.59	7.81	6.07	0.42	99.36	40.5	56.9	2.6	45065.5	279.7	146022.5	3479.0
LO-43	75.7	Medium-grained OAN	Ilm + Mt	n=4	56.33	28.15	8.32	5.76	0.31	99.12	43.5	54.5	1.9	42727.8	240.2	148990.6	2558.5
LO-44-2	77.0	Apatite-bearing Anorthosite	-	n=5	56.59	28.11	8.49	5.45	0.52	99.31	44.7	52.0	3.2	40457.5	80.6	148752.1	4293.9
LO-46	79.0	Medium-grained OAN	Ilm + Mt	n=5	56.47	28.19	8.49	5.68	0.34	99.37	44.3	53.6	2.1	42158.6	110.2	149186.4	2857.1
LO-47-1	84.2	Medium-grained OAN	Ilm + Mt	n=5	55.62	28.72	8.95	5.33	0.38	99.23	47.0	50.6	2.4	39569.3	244.4	152014.9	3173.5
LO-47-2	84.3	Anorthosite	-	n=5	55.98	28.66	8.77	5.27	0.50	99.36	46.4	50.5	3.1	39106.6	98.5	151677.4	4110.5
LO-49	87.8	Medium-grained OAN	Ilm + Mt	n=5	56.19	28.41	8.61	5.56	0.34	99.29	45.2	52.7	2.1	41214.0	78.1	150381.0	2831.7
LO-50	91.2	Medium-grained OAN	Ilm + Mt	n=4	56.54	27.80	8.49	5.66	1.38	99.95	41.8	50.3	7.9	41999.7	39.9	145795.6	3545.2
LO-51	95.8	Medium-grained OAN	Hm-ilm + Mt	n=6	56.36	28.22	8.64	5.68	0.25	99.29	45.0	53.5	1.5	42112.3	116.7	149332.2	2038.2
LO-55	99.7	Medium-grained OAN	Hm-ilm + Mt	n=4	56.47	27.69	8.39	5.63	1.01	99.31	42.4	51.6	6.1	41800.9	41.6	146546.0	8390.1

LO-57	102.1	Medium-grained OAN	Hm-ilm + Mt	n=6	55.44	28.87	9.08	5.56	0.11	99.22	47.1	52.2	0.7	41233.4	222.7	152796.6	877.7
LO-58	105.4	Anorthosite	-	n=6	52.30	31.23	11.04	4.24	0.21	99.21	58.2	40.5	1.3	31448.5	56.7	165294.9	1716.2
LO-59	108.5	Anorthosite	-	n=4	53.37	30.21	11.53	4.32	0.48	100.10	57.9	39.2	2.9	32077.4	56.4	166505.3	9213.7
20PM02	0.0	Medium-grained OAN	Hm-ilm + Mt	n=5	56.43	29.25	9.46	5.63	0.37	101.27	47.1	50.7	2.2	41731.3	86.6	154806.3	3078.2
20PM03B	0.0	Anorthosite	Ilm + Mt	n=5	55.57	30.66	10.56	5.37	0.12	102.36	51.7	47.6	0.7	39869.4	46.8	162258.5	956.2

Appendix 2.1.5 Complete LA-ICP-MS results of plagioclase (Cont.)

Detection Limits (33-55μm)					132.83-2630.29	1.009-15.39	0.060-0.697	1.295-5.303	0.516-2.963	1.278-6.950	0.165-2.006	0.191-1.473	19.622-216.80
Sample	Depth (m)	Lithology	Oxide Mineralogy	# analysis	^{44}Ca	^{49}Ti	^{51}V	^{55}Mn	^{63}Cu	^{66}Zn	^{69}Ga	^{72}Ge	^{85}Rb
LO-01	3.7	Medium-grained OAN	Hm-ilm + Mt	n=5	61861.8	92.1	0.2	12.0	0.7	7.5	25.7	1.0	0.4
LO-02	4.7	Anorthosite	-	n=5	67051.0	101.2	0.2	26.0	0.5	6.2	22.7	1.0	0.5
LO-05	6.4	Coarse-grained OAN	Hm-ilm + Mt	n=5	63229.7	97.5	0.1	13.3	0.2	6.7	25.2	0.8	0.1
LO-06	6.8	Fine-grained OAN dyke	Hm-ilm + Mt	n=5	59602.1	90.2	0.2	11.8	0.8	7.1	28.0	1.0	0.1
LO-07	8.5	Medium-grained OAN	Hm-ilm + Mt	n=5	59904.1	118.0	0.2	13.8	0.2	7.1	26.3	1.1	0.8
LO-08	8.6	Fine-grained-OAN dyke	Hm-ilm	n=5	53966.4	96.2	0.3	10.7	0.3	5.8	27.9	1.0	3.4
LO-09	9.9	Medium-grained OAN	Hm-ilm + Mt	n=5	68948.4	62.7	0.3	17.4	0.2	3.9	24.3	0.7	0.3
LO-15-1	14.2	Medium-grained OAN	Hm-ilm + Mt	n=4	66929.4	90.3	0.2	14.2	0.1	3.6	23.7	0.6	0.5
LO-15-2	14.4	Medium-grained OAN	Hm-ilm + Mt	n=5	63146.4	122.7	0.2	12.5	0.4	4.8	23.3	0.6	0.0
LO-16	16.4	Coarse-grained-OAN	Hm-ilm + Mt	n=5	59200.9	116.2	0.2	18.5	0.1	3.7	24.7	1.0	0.4
LO-22	21.5	Coarse-grained OAN	Hm-ilm + Mt	n=5	56856.8	117.6	0.1	11.1	0.2	3.7	23.5	0.9	1.1
LO-24	28.2	Medium-grained OAN	Hm-ilm + Mt	n=4	57302.1	157.6	0.2	10.2	0.4	3.8	23.6	1.0	0.1
LO-26	36.3	Medium-grained OAN	Ilm + Mt	n=5	60702.8	107.8	0.2	12.4	0.4	4.1	22.9	1.1	0.3
LO-29	42.4	Medium-grained OAN	Ilm + Mt	n=5	59810.5	100.1	0.2	8.5	0.3	3.7	23.0	1.0	0.2
LO-32	48.7	Medium-grained OAN	Ilm + Mt	n=6	60548.1	111.0	0.3	11.6	0.2	3.0	21.5	0.7	0.1
LO-38	62.2	Apatite-bearing Anorthosite	-	n=5	61643.6	120.5	0.2	15.7	0.6	4.8	23.3	0.9	1.9
LO-39	63.4	Medium-grained OAN	Ilm + Mt	n=5	59006.8	125.5	0.2	13.5	0.6	3.6	21.9	0.7	0.6
LO-40	67.5	Medium-grained OAN	Ilm + Mt	n=6	60581.6	146.4	0.3	10.8	0.5	3.8	20.9	0.7	0.4
LO-41B	70.1	Coarse-grained OAN	Ilm + Mt	n=6	55833.6	133.6	0.2	12.9	0.3	4.2	23.2	0.8	0.4
LO-43	75.7	Medium-grained OAN	Ilm + Mt	n=4	59464.4	120.9	0.2	10.9	0.4	3.0	20.4	0.7	0.1

LO-44-2	77.0	Apatite-bearing Anorthosite	-	n=5	60650.8	127.8	0.3	15.5	0.1	3.3	23.4	1.1	Below DL
LO-46	79.0	Medium-grained OAN	Ilm + Mt	n=5	60669.1	114.6	0.2	12.6	0.2	3.1	22.2	0.8	Below DL
LO-47-1	84.2	Medium-grained OAN	Ilm + Mt	n=5	63968.9	115.3	0.2	15.0	0.4	3.9	21.1	0.8	Below DL
LO-47-2	84.3	Anorthosite	-	n=5	62691.8	144.0	0.3	16.1	0.7	4.5	20.2	0.9	0.8
LO-49	87.8	Medium-grained OAN	Ilm + Mt	n=5	61537.7	92.8	0.2	9.8	0.5	3.2	22.1	0.8	0.0
LO-50	91.2	Medium-grained OAN	Ilm + Mt	n=4	60685.4	112.8	0.5	8.9	1.4	1.9	47.7	Below DL	109.8
LO-51	95.8	Medium-grained OAN	Hm-ilm + Mt	n=6	61725.1	100.3	0.2	12.5	0.3	2.9	22.2	0.8	Below DL
LO-55	99.7	Medium-grained OAN	Hm-ilm + Mt	n=4	59928.8	110.9	0.0	11.8	Below DL	8.9	53.2	Below DL	178.1
LO-57	102.1	Medium-grained OAN	Hm-ilm + Mt	n=6	64928.1	59.8	0.3	17.3	0.3	2.3	23.6	0.8	Below DL
LO-58	105.4	Anorthosite	-	n=6	78934.7	98.4	0.2	20.2	0.5	2.1	15.5	0.9	0.3
LO-59	108.5	Anorthosite	-	n=4	82378.2	76.9	0.0	16.1	1.0	2.2	20.4	Below DL	Below DL
20PM 02	0.0	Medium-grained OAN	Hm-ilm + Mt	n=5	67627.1	137.2	0.3	9.6	1.1	3.6	22.8	0.8	-
20PM 03B	0.0	Anorthosite	Ilm + Mt	n=5	75435.2	92.0	0.2	19.3	4.7	5.0	21.1	0.8	2.4

Appendix 2.1.5 Complete LA-ICP-MS results of plagioclase (Cont.)

Detection Limits (33-55μm)					0.058-0.245	0.042-0.243	0.515-0.809	0.005-0.013	0.003-1.838	0.008-0.476	0.010-0.057	0.005-0.058	0.001-0.023	
Sample	Depth (m)	Lithology	Oxide Mineralogy	# analysis	^{88}Sr	^{89}Y	^{137}Ba	^{139}La	^{140}Ce	^{141}Pr	^{146}Nd	^{147}Sm	^{153}Eu	Total REE
LO-01	3.7	Medium-grained OAN	Hm-ilm + Mt	n=5	2208.8	0.1	365.3	6.1	9.2	0.9	3.0	0.3	2.0	21.5
LO-02	4.7	Anorthosite	-	n=5	1500.9	0.2	192.6	7.1	11.4	1.1	3.8	0.4	1.2	25.0
LO-05	6.4	Coarse-grained OAN	Hm-ilm + Mt	n=5	2232.9	0.2	303.2	7.6	11.4	1.1	3.9	0.4	2.2	26.6
LO-06	6.8	Fine-grained OAN dyke	Hm-ilm + Mt	n=5	2106.3	0.2	450.5	7.9	11.2	1.0	3.4	0.2	2.0	25.7
LO-07	8.5	Medium-grained OAN	Hm-ilm + Mt	n=5	2077.8	0.3	393.1	10.8	16.2	1.5	4.8	0.5	2.2	36.1
LO-08	8.6	Fine-grained-OAN dyke	Hm-ilm	n=5	1803.4	0.3	474.6	15.5	20.7	1.8	5.1	0.5	2.4	46.0
LO-09	9.9	Medium-grained OAN	Hm-ilm + Mt	n=5	2186.8	0.2	423.8	7.1	10.4	1.0	3.3	0.1	1.4	23.2
LO-15-1	14.2	Medium-grained OAN	Hm-ilm + Mt	n=4	2040.3	0.1	679.5	6.3	9.5	0.9	2.9	0.2	1.2	21.1
LO-15-2	14.4	Medium-grained OAN	Hm-ilm + Mt	n=5	1985.2	0.2	412.0	7.3	11.0	1.0	3.5	0.0	1.4	24.2
LO-16	16.4	Coarse-grained-OAN	Hm-ilm + Mt	n=5	2321.6	0.1	566.0	5.7	8.5	0.8	2.6	0.1	1.6	19.3
LO-22	21.5	Coarse-grained OAN	Hm-ilm + Mt	n=5	2170.6	0.2	315.3	5.9	8.9	0.8	2.8	0.1	1.8	20.3
LO-24	28.2	Medium-grained OAN	Hm-ilm + Mt	n=4	2337.3	0.1	599.8	5.2	7.8	0.7	2.6	0.0	1.9	18.2
LO-26	36.3	Medium-grained OAN	Ilm + Mt	n=5	2034.6	0.2	468.3	4.8	7.4	0.8	2.8	0.0	1.6	17.4
LO-29	42.4	Medium-grained OAN	Ilm + Mt	n=5	2158.1	0.2	715.3	4.9	8.1	0.9	3.1	0.1	1.4	18.5
LO-32	48.7	Medium-grained OAN	Ilm + Mt	n=6	2159.1	0.2	776.4	4.2	6.9	0.7	2.6	0.0	1.4	15.7
LO-38	62.2	Apatite-bearing Anorthosite	-	n=5	2005.5	0.1	322.2	4.1	6.4	0.6	2.3	0.0	1.6	15.0
LO-39	63.4	Medium-grained OAN	Ilm + Mt	n=5	2308.8	0.1	1008.3	4.3	6.6	0.7	2.4	0.0	1.1	15.0
LO-40	67.5	Medium-grained OAN	Ilm + Mt	n=6	2218.1	0.2	863.0	4.1	6.6	0.7	2.4	0.0	1.3	15.0
LO-41B	70.1	Coarse-grained OAN	Ilm + Mt	n=6	2279.4	0.2	366.5	7.6	11.0	1.0	3.5	0.0	2.4	25.7
LO-43	75.7	Medium-grained OAN	Ilm + Mt	n=4	2290.4	0.2	1016.1	4.3	6.8	0.7	2.4	0.0	1.2	15.3

LO-44-2	77.0	Apatite-bearing Anorthosite	-	n=5	2153.9	0.1	343.2	4.3	6.6	0.7	2.3	0.0	1.6	12.4
LO-46	79.0	Medium-grained OAN	Ilm + Mt	n=5	2224.4	0.2	753.3	4.4	7.2	0.7	2.5	0.0	1.3	16.0
LO-47-1	84.2	Medium-grained OAN	Ilm + Mt	n=5	1907.2	0.2	402.0	4.8	7.4	0.8	2.7	0.0	1.3	17.0
LO-47-2	84.3	Anorthosite	-	n=5	1661.4	0.2	401.0	6.7	10.2	1.0	3.3	0.0	1.6	22.8
LO-49	87.8	Medium-grained OAN	Ilm + Mt	n=5	2150.0	0.1	679.3	4.2	6.5	0.7	2.4	0.0	1.3	15.0
LO-50	91.2	Medium-grained OAN	Ilm + Mt	n=4	2126.7	Below DL	435.9	4.0	6.2	0.5	0.0	0.0	1.4	12.0
LO-51	95.8	Medium-grained OAN	Hm-ilm + Mt	n=6	2095.7	0.2	351.1	4.2	6.5	0.6	2.4	0.0	1.3	15.1
LO-55	99.7	Medium-grained OAN	Hm-ilm + Mt	n=4	2005.6	Below DL	467.3	6.7	9.8	0.9	2.2	0.0	1.6	21.2
LO-57	102.1	Medium-grained OAN	Hm-ilm + Mt	n=6	2052.6	0.1	197.3	3.5	5.7	0.6	2.0	0.0	1.0	12.8
LO-58	105.4	Anorthosite	-	n=6	631.3	0.3	90.0	1.4	2.7	0.3	1.1	0.0	0.6	6.1
LO-59	108.5	Anorthosite	-	n=4	644.7	Below DL	93.0	1.1	2.6	Below DL	Below DL	Below DL	Below DL	3.7
20PM 02	0.0	Medium-grained OAN	Hm-ilm + Mt	n=5	2274.5	0.1	414.4	5.3	7.9	0.8	2.7	0.0	1.8	18.5
20PM 03B	0.0	Anorthosite	Ilm + Mt	n=5	2128.8	0.5	188.6	12.9	21.3	2.1	7.0	0.7	2.0	46.0

Appendix 2.1.6 Complete LA-ICP-MS results of ilmenite

Sample	Depth (m)	Lithology	Oxide Mineralogy	# analysis	SiO_2	TiO_2	Al_2O_3	FeO_t	Fe_2O_3	FeO	MnO	MgO	Total	X_{geik}	X_{pyr}	X_{hem}	X_{ilm}
LO-01	3.7	Medium-grained OAN	Hm-ilm + Mt	n=4	0.15	28.22	0.12	70.41	50.27	25.17	0.12	0.24	99.27	0.009	0.003	0.472	0.522
LO-05	6.4	Coarse-grained OAN	Hm-ilm + Mt	n=3	0.19	21.53	0.19	77.05	64.50	19.00	0.20	0.36	99.52	0.013	0.004	0.600	0.389
LO-06	6.8	Fine-grained OAN dyke	Hm-ilm + Mt	n=4	0.11	24.37	0.14	75.02	59.09	21.85	0.13	0.22	100.00	0.008	0.003	0.549	0.445
LO-08	8.6	Fine-grained-OAN dyke	Hm-ilm	n=4	0.05	31.09	0.14	67.12	45.06	26.57	0.24	0.79	99.43	0.029	0.005	0.421	0.564
LO-09	9.9	Medium-grained OAN	Hm-ilm + Mt	n=3	1.60	46.15	0.04	50.40	12.71	38.97	0.75	1.59	100.52	0.059	0.016	0.131	0.859
LO-15-1	14.2	Medium-grained OAN	Hm-ilm + Mt	n=4	0.35	42.38	0.08	55.06	22.23	35.06	0.58	1.64	100.10	0.060	0.012	0.211	0.772
LO-21	20.7	Medium-grained Nelsonite	Hm-ilm + Mt	n=3	0.01	41.60	0.07	55.35	23.22	34.45	0.46	1.49	98.98	0.055	0.010	0.219	0.765
LO-22	21.5	Coarse-grained OAN	Hm-ilm + Mt	n=3	0.09	40.55	0.10	57.31	24.70	35.09	0.28	0.75	99.08	0.028	0.006	0.235	0.757
LO-24	28.2	Medium-grained OAN	Hm-ilm + Mt	n=4	0.14	43.72	0.08	54.45	19.58	36.83	0.51	1.24	100.13	0.046	0.011	0.185	0.804
LO-26	36.3	Medium-grained OAN	Ilm + Mt	n=4	0.19	47.26	0.07	49.53	12.35	38.42	0.87	1.91	99.83	0.071	0.018	0.117	0.871
LO-29	42.4	Medium-grained OAN	Ilm + Mt	n=3	0.22	50.97	0.07	49.53	9.35	41.11	1.00	2.22	104.01	0.079	0.020	0.086	0.904
LO-32	48.7	Medium-grained OAN	Ilm + Mt	n=3	0.22	49.36	0.12	49.53	10.95	39.68	0.98	2.22	102.43	0.080	0.020	0.102	0.887
LO-35	57.3	Medium-grained OAN	Ilm + Mt	n=3	0.16	47.17	0.06	49.53	12.44	38.33	0.78	2.01	99.70	0.074	0.016	0.119	0.869
LO-39	63.4	Medium-grained OAN	Ilm + Mt	n=4	0.19	53.34	0.06	49.53	8.05	42.28	0.99	2.79	106.90	0.096	0.019	0.073	0.918
LO-40	67.5	Medium-grained OAN	Ilm + Mt	n=3	0.04	50.08	0.06	49.53	10.54	40.04	0.87	2.35	102.92	0.084	0.018	0.096	0.893
LO-41B	70.1	Coarse-grained-OAN	Ilm + Mt	n=3	0.09	43.15	0.05	49.53	14.83	36.19	0.64	1.20	94.66	0.047	0.014	0.148	0.842
LO-43	75.7	Medium-grained OAN	Ilm + Mt	n=4	0.09	48.02	0.07	49.53	11.47	39.21	0.83	1.86	100.41	0.068	0.017	0.108	0.882
LO-44-1	77.1	Medium-grained OAN	Ilm + Mt	n=3	0.05	48.95	0.06	49.53	11.37	39.29	1.02	2.15	101.75	0.078	0.021	0.105	0.883
LO-46	79.0	Medium-grained OAN	Ilm + Mt	n=3	0.17	50.49	0.06	49.53	9.76	40.75	0.81	2.27	103.33	0.081	0.016	0.090	0.900
LO-47	84.2	Medium-grained OAN	Ilm + Mt	n=3	0.09	47.83	0.06	49.53	10.96	39.66	0.80	1.50	99.82	0.056	0.017	0.104	0.888

LO-49	87.8	Medium-grained OAN	Ilm + Mt	n=3	0.36	48.25	0.06	49.53	0.00	49.53	0.70	2.08	100.99	0.076	0.015	0.108	0.881
LO-50	91.2	Medium-grained OAN	Ilm + Mt	n=3	0.52	49.98	0.06	49.53	2.19	47.56	0.81	2.19	103.09	0.079	0.017	0.094	0.896
LO-51	95.8	Medium-grained OAN	Hm-ilm + Mt	n=4	0.12	41.77	0.07	55.95	23.34	34.94	0.51	1.29	99.71	0.048	0.011	0.220	0.767
LO-55	99.7	Medium-grained OAN	Hm-ilm + Mt	n=5	0.26	28.94	0.16	70.23	49.41	25.76	0.12	0.40	100.12	0.015	0.003	0.463	0.529
LO-57	102.1	Medium-grained OAN	Hm-ilm + Mt	n=5	0.10	25.87	0.15	72.41	55.35	22.61	0.13	0.53	99.19	0.020	0.003	0.518	0.470
20PM02	0.0	Medium-grained OAN	Hm-ilm + Mt	n=5	0.02	44.60	0.05	50.22	14.99	36.73	0.60	1.62	98.75	0.062	0.013	0.145	0.843
20PM03	0.0	Massive oxides in anorthosite	Ilm + Mt	n=5	0.01	46.70	0.04	50.21	10.72	40.57	0.61	0.55	99.36	0.021	0.013	0.105	0.892
MG-LO-01	51.3	Medium-grained OAN	Hm-ilm + Mt	n=12	0.07	44.87	0.05	51.69	15.76	37.51	0.57	1.29	100.26	0.048	0.012	0.150	0.841
MG-LO-03	93.0	Medium-grained OAN	Hm-ilm + Mt	n=9	0.02	44.30	0.05	52.99	16.31	38.31	0.29	0.69	100.01	0.026	0.006	0.155	0.839
MG-LO-04	90.6	Massive oxides in anorthosite	Ilm + Mt	n=12	0.04	49.05	0.04	48.63	8.01	41.05	0.70	1.13	100.08	0.042	0.015	0.072	0.923

Major elements in wt.%, FeO and Fe_2O_3 recalculated from FeOt by charge balance equations; molar fractions of geikielite, pyrophanite, hematite and ilmenite (Xgeik, Xpyr, Xhem, Xilm) calculated following QUILF algorithm (Andersen et al.1993); trace element in ppm. OAN = Oxide-apatite norite; Hm-ilm = hemo-ilmenite; Ilm = ilmenite; Mt = magnetite.

Appendix 2.1.6 Complete LA-ICP-MS results of ilmenite (Cont.)

Detection Limits (33-55μm)					0.111-0.411	0.947-10.27	0.648-4.274	280.87-1450.82	66.62-124.50	0.205-1.345	0.035-0.296	0.952-3.179	0.463-1.920	0.025-0.220	0.551-1.198	0.335-0.745
Sample	Depth (m)	Lithology	Oxide Mineralogy	# analysis	^{25}Mg	^{49}Ti	^{27}Al	^{29}Si	^{44}Ca	^{45}Sc	^{51}V	^{53}Cr	^{55}Mn	^{59}Co	^{60}Ni	^{63}Cu
LO-01	3.7	Medium-grained OAN	Hm-ilm + Mt	n=4	1660.7	132170.5	720.2	511.6	44.7	48.0	1781.3	7.1	1033.8	18.1	1.7	0.9
LO-05	6.4	Coarse-grained OAN	Hm-ilm + Mt	n=3	2192.9	129073.4	1009.5	908.8	89.1	49.5	1683.2	29.0	1512.8	19.7	0.8	0.7
LO-06	6.8	Fine-grained OAN dyke	Hm-ilm + Mt	n=4	1404.8	129186.6	793.0	548.5	31.7	52.4	2179.9	29.6	1068.1	16.6	2.9	0.4
LO-08	8.6	Fine-grained-OAN dyke	Hm-ilm	n=4	4832.4	187781.5	755.2	229.4	Below DL	61.8	1428.3	154.8	1863.7	23.2	3.7	0.5
LO-09	9.9	Medium-grained OAN	Hm-ilm + Mt	n=3	9949.8	267124.6	238.9	7470.2	623.2	72.5	931.9	68.8	6002.2	41.7	20.7	2.0
LO-15-1	14.2	Medium-grained OAN	Hm-ilm + Mt	n=4	9897.5	253087.4	436.2	1363.1	459.9	66.5	1188.2	144.9	4503.7	39.9	8.8	0.9
LO-21	20.7	Medium-grained Nelsonite	Hm-ilm + Mt	n=3	9154.8	247828.0	405.8	19.2	104.6	90.8	1030.4	111.9	3677.0	26.7	2.8	1.2
LO-22	21.5	Coarse-grained OAN	Hm-ilm + Mt	n=3	6770.0	244699.7	538.9	282.7	56.3	83.6	1061.8	5.0	3222.0	40.3	2.0	0.7
LO-24	28.2	Medium-grained OAN	Hm-ilm + Mt	n=4	7574.3	258594.7	412.4	562.6	135.7	87.3	937.0	4.2	4021.1	35.3	3.4	0.7
LO-26	36.3	Medium-grained OAN	Ilm + Mt	n=4	11493.4	283339.9	354.9	885.7	71.2	93.5	503.7	42.2	6734.8	51.0	10.4	3.6
LO-29	42.4	Medium-grained OAN	Ilm + Mt	n=3	13390.5	305572.3	382.0	603.3	22.6	72.1	399.3	52.5	7734.0	53.2	10.9	3.5
LO-32	48.7	Medium-grained OAN	Ilm + Mt	n=3	13412.6	295885.3	608.7	1037.6	197.9	71.3	463.2	45.1	7582.6	48.3	8.6	3.2
LO-35	57.3	Medium-grained OAN	Ilm + Mt	n=3	12122.5	282751.4	307.6	692.3	29.9	72.6	562.2	3.7	6003.2	41.3	1.6	3.7
LO-39	63.4	Medium-grained OAN	Ilm + Mt	n=4	16816.7	319771.1	327.6	887.4	72.6	68.6	384.2	15.5	7628.7	56.8	5.2	3.4
LO-40	67.5	Medium-grained OAN	Ilm + Mt	n=3	14200.2	300202.8	296.7	165.8	66.6	75.2	438.6	10.8	6737.8	50.7	3.6	2.3
LO-41B	70.1	Coarse-grained-OAN	Ilm + Mt	n=3	7225.9	258694.4	254.4	405.2	9.5	86.7	578.3	1.2	4985.0	45.0	1.7	3.0
LO-43	75.7	Medium-grained OAN	Ilm + Mt	n=4	11224.5	287902.2	389.8	397.8	0.3	66.1	478.1	11.4	6459.8	46.3	3.7	3.1
LO-44-1	77.1	Medium-grained OAN	Ilm + Mt	n=3	12961.0	293450.6	323.9	217.4	9.0	73.4	446.2	13.5	7861.6	46.0	2.7	2.4
LO-46	79.0	Medium-grained OAN	Ilm + Mt	n=3	13714.3	305206.1	303.4	801.3	41.4	70.0	483.9	3.8	6275.1	49.4	2.4	3.5

LO-47	84.2	Medium-grained OAN	Ilm + Mt	n=3	9029.5	286748.8	323.1	433.5	Below DL	82.1	548.6	13.4	6227.7	39.6	2.6	3.1
LO-49	87.8	Medium-grained OAN	Ilm + Mt	n=3	12516.2	289257.3	327.5	1692.2	83.5	69.6	530.1	6.3	5456.0	50.8	2.9	3.0
LO-50	91.2	Medium-grained OAN	Ilm + Mt	n=3	13211.8	299632.7	318.1	2424.7	150.8	67.0	556.7	5.0	6295.1	51.4	2.9	2.9
LO-51	95.8	Medium-grained OAN	Hm-ilm + Mt	n=4	7957.6	244572.1	375.8	548.0	90.5	62.5	1206.0	9.0	4065.7	40.1	2.4	0.4
LO-55	99.7	Medium-grained OAN	Hm-ilm + Mt	n=5	2504.4	141499.1	925.6	1213.4	87.4	44.3	2603.0	41.7	989.9	23.1	16.4	0.6
LO-57	102.1	Medium-grained OAN	Hm-ilm + Mt	n=5	3435.4	125158.8	879.2	700.3	41.8	34.3	2437.6	28.6	1078.9	22.4	3.7	0.2
20PM02	0.0	Medium-grained OAN	Hm-ilm + Mt	n=5	9760.2	285100.0	167.3	139.4	Below DL	71.4	772.5	5.6	4675.5	41.9	2.6	3.9
20PM03	0.0	Massive oxides in anorthosite	Ilm + Mt	n=5	3339.4	280200.0	85.7	163.4	9.1	47.1	937.6	166.9	4684.0	69.1	60.1	3.2
MG-LO-01	51.3	Medium-grained OAN	Hm-ilm + Mt	n=12	7287.6	193453.0	260.9	331.7	55.3	49.7	800.0	1.8	4274.8	30.5	1.2	4.8
MG-LO-03	93.0	Medium-grained OAN	Hm-ilm + Mt	n=9	3115.6	158799.0	450.9	169.8	14.5	34.7	1523.4	15.9	1543.6	27.6	6.3	3.2
MG-LO-04	90.6	Massive oxides in anorthosite	Ilm + Mt	n=12	7110.7	262884.0	117.4	161.7	16.4	26.0	859.0	180.2	5558.3	59.7	50.2	6.4

Major elements in wt.%, FeO and Fe_2O_3 recalculated from FeOt by charge balance equations; molar fractions of geikielite, pyrophanite, hematite and ilmenite (Xgeik, Xpyr, Xhem, Xilm) calculated following QUILF algorithm (Andersen et al.1993); trace element in ppm. OAN = Oxide-apatite norite; Hm-ilm = hemo-ilmenite; Ilm = ilmenite; Mt = magnetite.

Appendix 2.1.6 Complete LA-ICP-MS results of ilmenite (Cont.)

Detection Limits (33-55µm)					0.761-1.438	0.151-0.365	0.079-0.309	0.038-0.056	0.022-0.027	0.074-0.345	0.034--?	0.073-0.089	0.051-0.062	0.013-0.015	0.075-0.095
Sample	Depth (m)	Lithology	Oxide Mineralogy	# analysis	^{66}Zn	^{69}Ga	^{72}Ge	^{90}Zr	^{93}Nb	Sn	^{139}La	^{172}Yb	^{178}Hf	^{181}Ta	^{182}W
LO-01	3.7	Medium-grained OAN	Hm-ilm + Mt	n=4	75.7	20.4	Below DL	21.9	28.2	10.0	Below DL	Below DL	3.5	2.0	Below DL
LO-05	6.4	Coarse-grained OAN	Hm-ilm + Mt	n=3	50.8	21.4	Below DL	38.9	24.3	8.6	0.2	Below DL	7.3	1.6	Below DL
LO-06	6.8	Fine-grained OAN dyke	Hm-ilm + Mt	n=4	32.4	23.8	Below DL	26.8	44.2	12.7	Below DL	Below DL	5.5	2.7	Below DL
LO-08	8.6	Fine-grained-OAN dyke	Hm-ilm	n=4	78.1	17.8	Below DL	31.8	155.6	16.0	Below DL	Below DL	2.1	8.7	Below DL
LO-09	9.9	Medium-grained OAN	Hm-ilm + Mt	n=3	10.7	3.8	Below DL	22.9	50.2	13.4	Below DL	Below DL	2.7	1.8	Below DL
LO-15-1	14.2	Medium-grained OAN	Hm-ilm + Mt	n=4	20.5	5.5	Below DL	33.3	42.1	10.2	Below DL	Below DL	6.5	2.0	Below DL
LO-21	20.7	Medium-grained Nelsonite	Hm-ilm + Mt	n=3	12.8	5.5	Below DL	40.1	75.7	12.0	Below DL	Below DL	5.9	3.8	Below DL
LO-22	21.5	Coarse-grained OAN	Hm-ilm + Mt	n=3	34.9	6.7	Below DL	33.5	88.9	11.8	Below DL	Below DL	3.1	4.5	Below DL
LO-24	28.2	Medium-grained OAN	Hm-ilm + Mt	n=4	17.6	4.9	Below DL	38.7	55.7	10.1	Below DL	Below DL	4.4	3.1	Below DL
LO-26	36.3	Medium-grained OAN	Ilm + Mt	n=4	9.8	2.3	Below DL	58.9	44.0	7.8	0.1	Below DL	6.0	2.2	Below DL
LO-29	42.4	Medium-grained OAN	Ilm + Mt	n=3	22.6	1.7	Below DL	60.9	28.6	5.7	Below DL	Below DL	6.9	1.4	Below DL
LO-32	48.7	Medium-grained OAN	Ilm + Mt	n=3	18.5	2.3	Below DL	48.6	26.6	6.2	Below DL	Below DL	4.9	1.5	Below DL
LO-35	57.3	Medium-grained OAN	Ilm + Mt	n=3	12.6	2.2	Below DL	36.2	46.6	9.5	0.1	Below DL	5.7	2.9	Below DL
LO-39	63.4	Medium-grained OAN	Ilm + Mt	n=4	12.8	1.8	Below DL	68.2	26.7	5.4	Below DL	Below DL	6.6	1.5	Below DL
LO-40	67.5	Medium-grained OAN	Ilm + Mt	n=3	8.2	1.6	Below DL	55.7	31.6	6.3	Below DL	Below DL	5.7	1.6	Below DL
LO-41B	70.1	Coarse-grained-OAN	Ilm + Mt	n=3	29.4	3.3	Below DL	21.4	95.2	11.2	Below DL	Below DL	4.6	4.7	Below DL
LO-43	75.7	Medium-grained OAN	Ilm + Mt	n=4	8.7	1.7	Below DL	61.8	28.5	5.8	Below DL	Below DL	6.6	1.7	Below DL
LO-44-1	77.1	Medium-grained OAN	Ilm + Mt	n=3	6.9	1.5	Below DL	48.7	17.0	6.1	Below DL	Below DL	4.3	0.9	Below DL

LO-46	79.0	Medium-grained OAN	Ilm + Mt	n=3	7.0	1.6	Below DL	64.9	27.2	6.4	Below DL	Below DL	7.3	1.5	Below DL
LO-47	84.2	Medium-grained OAN	Ilm + Mt	n=3	6.5	1.9	Below DL	34.8	32.6	6.9	Below DL	Below DL	4.7	1.7	Below DL
LO-49	87.8	Medium-grained OAN	Ilm + Mt	n=3	8.2	1.8	Below DL	40.7	38.8	7.0	Below DL	Below DL	4.5	2.0	Below DL
LO-50	91.2	Medium-grained OAN	Ilm + Mt	n=3	10.3	1.9	Below DL	39.3	28.7	6.6	Below DL	Below DL	4.6	1.5	Below DL
LO-51	95.8	Medium-grained OAN	Hm-ilm + Mt	n=4	7.5	5.4	Below DL	28.4	27.9	8.5	Below DL	Below DL	4.6	1.5	Below DL
LO-55	99.7	Medium-grained OAN	Hm-ilm + Mt	n=5	40.3	19.7	Below DL	17.8	48.9	8.0	Below DL	Below DL	2.2	2.8	Below DL
LO-57	102.1	Medium-grained OAN	Hm-ilm + Mt	n=5	12.7	18.6	Below DL	38.3	11.5	6.9	0.1	Below DL	3.5	0.7	Below DL
20PM02	0.0	Medium-grained OAN	Hm-ilm + Mt	n=5	17.0	3.2	0.1	37.8	44.1	9.6	0.0	0.0	6.0	1.8	0.2
20PM03	0.0	Massive oxides in anorthosite	Ilm + Mt	n=5	4.8	1.8	0.1	20.0	25.5	7.2	0.0	0.0	1.8	1.0	0.1
MG-LO-01	51.3	Medium-grained OAN	Hm-ilm + Mt	n=12	37.0	4.7	0.2	19.3	47.0	11.9	Below DL	Below DL	3.1	1.9	0.1
MG-LO-03	93.0	Medium-grained OAN	Hm-ilm + Mt	n=9	75.9	9.5	0.1	26.6	50.1	8.2	Below DL	Below DL	4.9	2.1	0.1
MG-LO-04	90.6	Massive oxides in anorthosite	Ilm + Mt	n=12	31.0	1.5	0.1	19.7	11.0	5.9	Below DL	Below DL	2.2	0.4	0.1

Appendix 2.1.7 Complete LA-ICP-MS results of magnetite

Detection Limits (33-55µm)														0.157-0.672	0.904-4.484	298.61-2397.08
Sample	Depth (m)	Lithology	Oxide Mineralogy	# analysis	SiO_2	TiO_2	Al_2O_3	FeO_t	Fe_2O_3	FeO	MnO	MgO	Total	^{25}Mg	^{27}Al	^{29}Si
LO-01	3.7	Medium-grained OAN	Hm-ilm + Mt	n=3	0.40	0.06	0.40	91.98	67.47	31.27	0.01	0.06	99.98	360.2	2121.6	1882.8
LO-05	6.4	Coarse-grained OAN	Hm-ilm + Mt	n=3	0.64	0.08	0.50	91.98	68.69	30.17	0.03	0.11	100.52	686.1	2660.1	2988.6
LO-06	6.8	Fine-grained OAN dyke	Hm-ilm + Mt	n=3	0.20	0.09	0.49	91.98	67.30	31.42	0.01	0.07	99.89	442.0	2597.7	705.0
LO-09	9.9	Medium-grained OAN	Hm-ilm + Mt	n=3	0.41	0.10	0.62	91.98	68.97	29.92	0.02	0.16	100.66	957.3	3258.4	1926.0
LO-15-1	14.2	Medium-grained OAN	Hm-ilm + Mt	n=3	0.04	0.09	0.47	91.98	67.70	31.06	0.02	0.14	100.11	831.7	2513.8	n.a
LO-15-2	14.4	Medium-grained OAN	Hm-ilm + Mt	n=3	0.15	0.09	0.51	91.98	68.12	30.68	0.02	0.20	100.26	1179.0	2693.7	110.2
LO-21	20.7	Medium-grained Nelsonite	Hm-ilm + Mt	n=3	0.00	0.09	0.49	91.98	67.39	31.35	0.01	0.14	99.94	821.3	2578.7	n.a
LO-22	21.5	Coarse-grained-OAN	Hm-ilm + Mt	n=4	0.35	0.09	0.58	91.98	68.26	30.56	0.02	0.13	100.31	773.2	3074.2	1613.5
LO-24	28.2	Medium-grained OAN	Hm-ilm + Mt	n=4	0.53	0.09	0.54	91.98	68.66	30.20	0.02	0.11	100.52	673.7	2880.2	2477.2
LO-26	36.3	Medium-grained OAN	Ilm + Mt	n=3	0.04	0.60	1.03	91.98	70.97	28.12	0.05	0.30	101.61	1802.0	5453.4	n.a
LO-29	42.4	Medium-grained OAN	Ilm + Mt	n=3	0.26	0.90	1.19	91.98	73.00	26.29	0.06	0.39	102.61	2329.0	6300.7	435.9
LO-32	48.7	Medium-grained OAN	Ilm + Mt	n=3	0.16	0.24	0.64	91.98	68.80	30.08	0.03	0.20	100.59	1180.9	3392.0	731.4
LO-35	57.3	Medium-grained OAN	Ilm + Mt	n=3	0.23	0.26	0.56	91.98	68.55	30.30	0.02	0.19	100.47	1165.6	2973.0	824.2
LO-39	63.4	Medium-grained OAN	Ilm + Mt	n=4	0.27	0.90	1.02	91.98	72.18	27.04	0.06	0.36	102.23	2187.4	5378.8	1275.6
LO-40	67.5	Medium-grained OAN	Ilm + Mt	n=3	0.08	0.37	0.72	91.98	69.11	29.80	0.04	0.23	100.72	1389.2	3812.3	90.3
LO-41B	70.1	Coarse-grained OAN	Ilm + Mt	n=3	0.18	0.11	0.58	91.98	67.78	30.99	0.02	0.12	100.09	747.0	3055.7	856.3
LO-43	77	Medium-grained OAN	Ilm + Mt	n=3	0.09	0.46	0.76	91.98	69.49	29.45	0.04	0.24	100.91	1449.1	4044.6	n.a
LO-44-1	77.1	Medium-grained OAN	Ilm + Mt	n=3	0.13	0.37	0.83	91.98	69.72	29.25	0.04	0.27	100.97	1613.7	4389.1	592.8
LO-46	79	Medium-grained OAN	Ilm + Mt	n=3	0.14	0.43	0.86	91.98	70.08	28.92	0.03	0.30	101.14	1803.3	4526.8	675.2

LO-47	84.2	Medium-grained OAN	Ilm + Mt	n=3	0.26	0.35	0.82	91.98	69.83	29.15	0.02	0.21	101.06	1243.4	4363.8	1232.4
LO-49	87.8	Medium-grained OAN	Ilm + Mt	n=3	0.46	0.34	0.88	91.98	70.83	28.25	0.03	0.30	101.48	1798.3	4638.9	2147.9
LO-50	91.2	Medium-grained OAN	Ilm + Mt	n=3	0.27	0.17	0.81	91.98	70.50	28.54	0.02	0.29	101.39	1724.3	4273.6	1278.9
LO-51	95.8	Medium-grained OAN	Hm-ilm + Mt	n=3	0.15	0.08	0.48	91.98	67.48	31.26	0.02	0.12	99.97	743.5	2519.6	709.5
LO-55	99.7	Medium-grained OAN	Hm-ilm + Mt	n=3	0.29	0.10	0.49	91.98	68.20	30.61	0.03	0.12	100.33	725.3	2584.3	1371.8
LO-57	102.1	Medium-grained OAN	Hm-ilm + Mt	n=3	0.15	0.08	0.51	91.98	67.73	31.03	0.02	0.16	100.06	963.0	2711.8	701.6
20PM02	0.0	Medium-grained OAN	Hm-ilm + Mt	n=5	0.15	0.09	0.46	92.38	68.18	31.04	0.01	0.12	100.04	629.3	2363.8	565.5
20PM03	0.0	Massive oxides in anorthosite	Ilm + Mt	n=5	0.09	0.08	0.49	92.09	68.05	30.85	0.01	0.05	99.63	305.6	2613.0	485.5
MG-LO-01	51.3	Medium-grained OAN	Hm-ilm + Mt	n=5	0.19	0.08	0.58	91.42	67.12	31.02	0.01	0.15	99.44	909.4	1843.1	816.9
MG-LO-03	93.0	Medium-grained OAN	Hm-ilm + Mt	n=5	0.04	0.08	0.52	92.12	67.93	31.00	0.01	0.12	100.12	480.0	1695.7	348.3
MG-LO-04	90.6	Massive oxides in anorthosite	Ilm + Mt	n=5	0.07	0.08	0.50	91.40	67.10	0.08	0.02	0.07	99.76	675.5	2547.7	534.6

Major elements in wt.%, FeO and Fe2O3 recalculated from FeOt by charge balance equations; trace element in ppm; OAN = Oxide-apatite norite; Hm-ilm = hemo-ilmenite; Ilm = ilmenite; Mt = magnetite. aXRF data published on Grant (2020).

Appendix 2.1.7 Complete LA-ICP-MS results of magnetite (Cont.)

Detection Limits (33-55µm)					40.36-195.38	76.13-368.87	0.260 - 1.343	0.947 - 10.27	0.047 - 0.242	1.527 - 9.987	0.637 - 2.315	0.029 - 0.208	0.719 - 2.736	0.447 - 1.605	0.816 - 3.891	0.147 - 0.608	0.096 - 0.545
Sample	Depth (m)	Lithology	Oxide Mineralogy	# analysis	^{31}P	^{44}Ca	^{45}Sc	^{49}Ti	^{51}V	^{53}Cr	^{55}Mn	^{59}Co	^{60}Ni	^{63}Cu	^{66}Zn	^{69}Ga	^{72}Ge
LO-01	3.7	Medium-grained OAN	Hm-ilm + Mt	n=3	139.4	239.1	1.6	387.9	1732.9	29.0	72.5	28.9	26.9	0.4	14.3	108.8	0.7
LO-05	6.4	Coarse-grained OAN	Hm-ilm + Mt	n=3	69.3	###	2.0	454.5	1596.8	54.6	222.1	54.0	14.6	0.8	16.6	121.5	1.8
LO-06	6.8	Fine-grained OAN dyke	Hm-ilm + Mt	n=3	n.a	123.5	1.3	563.4	1781.4	86.8	86.7	26.9	23.0	0.7	20.3	139.3	0.6
LO-09	9.9	Medium-grained OAN	Hm-ilm + Mt	n=3	91.6	68.8	0.9	588.6	2307.9	769.6	146.1	39.0	146.5	0.2	30.7	79.3	n.a
LO-15-1	14.2	Medium-grained OAN	Hm-ilm + Mt	n=3	n.a	n.a	1.3	527.7	2662.0	1243.9	148.3	44.0	105.4	0.1	13.1	80.6	0.1
LO-15-2	14.4	Medium-grained OAN	Hm-ilm + Mt	n=3	n.a	n.a	0.7	514.6	2499.7	842.8	158.1	36.5	95.8	0.7	15.3	78.9	n.a
LO-21	20.7	Medium-grained Nelsonite	Hm-ilm + Mt	n=3	n.a	81.7	1.3	539.4	2142.9	930.9	104.1	27.8	37.1	0.3	7.6	80.4	0.8
LO-22	21.5	Coarse-grained-OAN	Hm-ilm + Mt	n=4	10.8	70.3	1.8	545.1	2133.3	28.1	155.4	27.8	31.8	n.a	56.6	92.1	0.8
LO-24	28.2	Medium-grained OAN	Hm-ilm + Mt	n=4	35.9	139.5	1.6	557.9	2313.0	39.5	122.3	36.5	35.4	0.6	9.5	86.3	0.9
LO-26	36.3	Medium-grained OAN	Ilm + Mt	n=3	n.a	n.a	2.1	3612.1	2604.2	735.8	358.6	57.5	98.5	0.1	145.8	80.0	0.9
LO-29	42.4	Medium-grained OAN	Ilm + Mt	n=3	n.a	42.9	2.7	5417.4	2568.4	886.3	458.6	54.4	98.6	0.4	107.1	74.7	0.8
LO-32	48.7	Medium-grained OAN	Ilm + Mt	n=3	9.1	29.0	1.9	1417.4	2395.2	657.3	232.4	40.8	75.4	0.4	28.7	64.6	0.5
LO-35	57.3	Medium-grained OAN	Ilm + Mt	n=3	n.a	107.3	1.4	1569.8	2206.2	43.9	165.3	36.1	15.7	n.a	29.2	63.2	0.4
LO-39	63.4	Medium-grained OAN	Ilm + Mt	n=4	17.7	48.1	2.1	5396.1	2492.7	232.5	441.9	50.3	39.4	0.3	51.5	63.9	0.2
LO-40	67.5	Medium-grained OAN	Ilm + Mt	n=3	1.8	n.a	2.1	####	2426.5	194.7	273.1	45.2	33.8	n.a	35.6	67.4	0.4
LO-41B	70.1	Coarse-grained OAN	Ilm + Mt	n=3	28.3	n.a	1.1	663.5	1999.2	14.5	118.2	42.8	9.3	0.2	42.0	83.8	0.3
LO-43	77	Medium-grained OAN	Ilm + Mt	n=3	n.a	n.a	1.6	####	2394.6	179.1	277.5	42.6	32.7	0.2	26.8	60.0	0.9
LO-44-1	77.1	Medium-grained OAN	Ilm + Mt	n=3	n.a	20.7	1.7	####	2219.5	200.3	333.3	43.9	26.7	0.1	34.2	63.0	n.a

LO-46	79	Medium-grained OAN	Ilm + Mt	n=3	6.3	83.9	1.7	####	2394.9	69.4	245.8	46.1	22.3	0.1	54.6	65.0	0.3
LO-47	84.2	Medium-grained OAN	Ilm + Mt	n=3	49.4	160.0	2.3	####	2444.8	232.1	172.1	41.6	26.8	0.3	91.0	70.4	0.7
LO-49	87.8	Medium-grained OAN	Ilm + Mt	n=3	15.4	127.5	1.6	####	2508.3	110.0	222.4	42.4	27.1	0.5	38.9	69.5	0.7
LO-50	91.2	Medium-grained OAN	Ilm + Mt	n=3	3.9	n.a	1.5	1002.5	2575.6	64.1	176.9	46.6	29.2	n.a	34.6	65.7	1.0
LO-51	95.8	Medium-grained OAN	Hm-ilm + Mt	n=3	n.a	23.1	1.4	451.0	2510.4	71.3	160.9	45.3	35.4	n.a	7.2	81.7	0.1
LO-55	99.7	Medium-grained OAN	Hm-ilm + Mt	n=3	17.1	164.0	1.1	575.9	3080.4	121.2	207.3	32.3	197.9	0.2	22.4	130.0	0.7
LO-57	102.1	Medium-grained OAN	Hm-ilm + Mt	n=3	n.a	120.7	1.4	489.7	2318.5	90.5	146.5	46.1	61.1	0.9	12.0	105.8	0.7
20PM02	0.0	Medium-grained OAN	Hm-ilm + Mt	n=5	101.4	16.7	1.2	475.6	2254.3	64.1	77.6	37.1	26.2	1.0	6.0	69.2	0.8
20PM03	0.0	Massive oxides in anorthosite	Ilm + Mt	n=5	n.a	11.4	0.8	492.8	3041.1	1960.8	80.7	58.8	470.2	0.5	14.9	52.7	0.7
MG-LO-01	51.3	Medium-grained OAN	Hm-ilm + Mt	n=5	12.1	29.2	1.2	493.2	1872.3	13.4	241.8	34.7	13.2	0.1	39.0	79.1	0.7
MG-LO-03	93.0	Medium-grained OAN	Hm-ilm + Mt	n=5	5.8	11.4	0.8	337.1	2116.9	76.0	82.2	35.3	27.5	0.1	10.6	78.1	0.7
MG-LO-04	90.6	Massive oxides in anorthosite	Ilm + Mt	n=5	12.8	70.7	0.7	1170.8	3536.2	####	136.3	60.2	507.6	0.1	15.3	54.8	0.6

Major elements in wt.%, FeO and Fe2O3 recalculated from FeOt by charge balance equations; trace element in ppm; OAN = Oxide-apatite norite; Hm-ilm = hemo-ilmenite; Ilm = ilmenite; Mt = magnetite. aXRF data published on Grant (2020).

Appendix 2.1.8 Complete LA-ICP-MS results of apatite

Detection Limits (33-55μm bean size)													0.93-2.40	0.05-0.28	0.10-0.28	156.10-494.82
Sample	Depth (m)	Lithology	Oxide Mineralogy	# analysis	La_2O_3	Ce_2O_3	Pr_2O_3	Nd_2O_3	CaO	P_2O_5	FeO_t	Total	^{23}Na	^{25}Mg	^{27}Al	^{29}Si
LO-01	3.7	Medium-grained OAN	Hm-ilm + Mt	n=4	0.04	0.11	0.02	0.09	53.23	46.09	0.07	99.65	288.4	166.0	15.9	1145.5
LO-02	4.7	Massive Apatite	-	n=4	0.04	0.11	0.02	0.08	52.99	46.57	0.10	99.91	427.1	323.7	2.0	395.6
LO-05	6.4	Coarse-grained OAN	Hm-ilm + Mt	n=4	0.05	0.13	0.02	0.10	52.27	46.74	0.15	99.45	335.1	460.6	174.4	1507.3
LO-06	6.8	Fine-grained OAN dyke	Hm-ilm + Mt	n=4	0.05	0.13	0.02	0.10	52.40	46.82	0.07	99.59	530.9	177.9	4.3	1446.6
LO-07	8.5	Medium-grained OAN	Hm-ilm + Mt	n=6	0.08	0.21	0.03	0.14	52.72	46.54	0.07	99.80	470.8	216.4	3.2	1032.1
LO-08	8.6	Fine-grained OAN dyke	Hm-ilm	n=3	0.07	0.21	0.03	0.16	53.64	45.53	0.08	99.73	891.0	184.6	5.4	1830.1
LO-09	9.9	Medium-grained OAN	Hm-ilm + Mt	n=4	0.04	0.11	0.02	0.08	52.02	47.46	0.07	99.79	412.3	266.5	6.2	375.0
LO-15-1	14.2	Medium-grained OAN	Hm-ilm + Mt	n=4	0.04	0.11	0.02	0.08	52.11	47.16	0.07	99.59	459.8	239.8	4.6	992.5
LO-21	20.7	Medium-grained Nelsonite	Hm-ilm + Mt	n=4	0.05	0.12	0.02	0.09	51.31	47.92	0.15	99.66	591.1	579.0	27.6	918.4
LO-22	21.5	Coarse-grained OAN	Hm-ilm + Mt	n=4	0.05	0.12	0.02	0.09	52.43	46.96	0.09	99.75	355.7	262.0	43.8	1026.0
LO-24	28.2	Medium-grained OAN	Hm-ilm + Mt	n=4	0.04	0.10	0.02	0.08	52.53	46.95	0.08	99.79	382.1	322.5	10.4	917.5
LO-26	36.3	Medium-grained OAN	Ilm + Mt	n=4	0.03	0.08	0.01	0.07	52.20	46.98	0.17	99.55	286.2	308.0	9.4	877.3
LO-29	42.4	Medium-grained OAN	Ilm + Mt	n=4	0.03	0.08	0.01	0.07	52.49	47.06	0.06	99.80	260.5	264.8	3.7	545.4
LO-32	48.7	Medium-grained OAN	Ilm + Mt	n=4	0.03	0.07	0.01	0.06	51.77	47.54	0.08	99.56	284.4	316.4	19.8	960.1
LO-38	62.2	Apatite-bearing Anorthosite	-	n=4	0.03	0.08	0.01	0.07	52.05	47.21	0.10	99.56	221.3	345.7	52.3	1068.0
LO-39	63.4	Medium-grained OAN	Ilm + Mt	n=4	0.03	0.07	0.01	0.06	51.38	47.57	0.12	99.24	315.2	627.0	80.1	1075.9
LO-40	67.5	Medium-grained OAN	Ilm + Mt	n=4	0.03	0.07	0.01	0.06	52.09	47.26	0.07	99.60	270.6	319.5	5.0	585.1
LO-41B	70.1	Coarse-grained OAN	Ilm + Mt	n=4	0.05	0.14	0.02	0.11	51.97	47.42	0.07	99.79	368.4	213.5	3.3	799.5
LO-43	75.7	Medium-grained OAN	Ilm + Mt	n=4	0.03	0.09	0.01	0.08	56.95	42.86	0.20	100.23	385.1	456.7	62.8	-988.4
LO-44-2	77.0	Apatite-bearing anorthosite	-	n=4	0.03	0.08	0.01	0.06	52.35	47.00	0.08	99.60	299.9	370.8	7.7	840.5
LO-46	79.0	Medium-grained OAN	Ilm + Mt	n=4	0.03	0.08	0.01	0.07	56.15	42.59	0.22	99.16	433.4	591.6	172.9	1381.4
LO-47	84.2	Medium-grained OAN	Ilm + Mt	n=4	0.03	0.09	0.01	0.07	56.77	42.65	0.28	99.92	389.9	830.0	256.3	245.6
LO-49	87.8	Medium-grained OAN	Ilm + Mt	n=4	0.03	0.07	0.01	0.06	52.23	47.20	0.09	99.69	305.3	355.2	19.0	549.3
LO-50	91.2	Medium-grained OAN	Ilm + Mt	n=3	0.03	0.09	0.01	0.07	55.84	43.58	0.14	99.76	432.5	616.3	95.6	873.2
LO-51	95.8	Medium-grained OAN	Hm-ilm + Mt	n=4	0.03	0.08	0.01	0.07	52.24	47.14	0.09	99.66	380.2	325.6	14.3	669.4
LO-55	99.7	Medium-grained OAN	Hm-ilm + Mt	n=4	0.05	0.14	0.02	0.10	56.93	41.99	0.38	99.61	716.4	355.9	85.6	291.2
LO-57	102.1	Medium-grained OAN	Hm-ilm + Mt	n=4	0.02	0.05	0.01	0.05	52.13	46.74	0.44	99.45	404.8	925.5	177.1	1089.6
20PM02	0.0	Medium-grained OAN	Hm-ilm + Mt	n=13	0.03	0.09	0.01	0.08	54.69	43.68	0.25	98.82	417.5	306.6	86.9	1167.7

Appendix 2.1.8 Complete LA-ICP-MS results of apatite (Cont.)

Detection Limits (33-55µm bean size)					0.11-0.32	0.23-0.63	0.02-0.05	0.48-1.47	0.32-0.72	0.49-1.07	0.01-0.04	0.17-0.31	0.12-0.27	0.10-0.26	0.03-0.07	0.19-0.34	0.11-0.25
Sample	Depth (m)	Lithology	Oxide Mineralogy	# analysis	^{45}Sc	^{49}Ti	^{51}V	^{53}Cr	^{55}Mn	^{56}Fe	^{59}Co	^{60}Ni	^{63}Cu	^{66}Zn	^{69}Ga	^{72}Ge	As
LO-01	3.7	Medium-grained OAN	Hm-ilm + Mt	n=4	1.3	0.9	3.1	0.1	336.0	522.9	0.3	0.2	0.1	1.2	0.8	48.6	14.6
LO-02	4.7	Massive Apatite	-	n=4	1.5	0.8	4.7	0.2	680.4	814.7	0.2	0.1	0.1	1.3	0.7	39.3	11.6
LO-05	6.4	Coarse-grained OAN	Hm-ilm + Mt	n=4	1.1	1.1	3.8	0.0	324.6	1154.4	0.2	0.1	0.1	0.7	1.0	47.6	14.6
LO-06	6.8	Fine-grained OAN dyke	Hm-ilm + Mt	n=4	1.2	0.0	5.9	Below DL	352.4	539.2	0.1	0.2	0.2	1.4	1.0	50.7	15.5
LO-07	8.5	Medium-grained OAN	Hm-ilm + Mt	n=6	1.1	1.5	4.9	0.1	383.4	565.3	0.2	0.1	0.1	0.9	1.3	66.4	19.8
LO-08	8.6	Fine-grained OAN dyke	Hm-ilm	n=3	0.7	2.6	10.3	0.2	341.7	594.1	0.1	0.0	0.2	1.1	1.3	80.1	24.4
LO-09	9.9	Medium-grained OAN	Hm-ilm + Mt	n=4	1.1	0.0	4.3	0.0	387.8	568.4	0.1	0.0	0.1	0.9	0.8	37.6	11.4
LO-15-1	14.2	Medium-grained OAN	Hm-ilm + Mt	n=4	0.9	2.3	7.3	0.0	322.6	520.0	0.2	0.0	0.1	1.1	0.7	40.2	11.9
LO-21	20.7	Medium-grained Nelsonite	Hm-ilm + Mt	n=4	2.7	0.0	5.0	0.9	546.5	1162.1	0.1	0.0	0.2	2.9	0.7	2.9	3.0
LO-22	21.5	Coarse-grained OAN	Hm-ilm + Mt	n=4	1.0	0.9	3.3	0.2	289.8	663.1	0.2	0.1	0.0	0.6	0.8	41.2	12.6
LO-24	28.2	Medium-grained OAN	Hm-ilm + Mt	n=4	1.0	1.5	4.8	0.0	307.6	648.6	0.2	0.1	0.1	0.7	0.7	34.5	10.4
LO-26	36.3	Medium-grained OAN	Ilm + Mt	n=4	0.9	1.4	5.1	0.3	277.2	1343.7	0.2	0.2	0.1	0.5	0.7	31.9	9.7
LO-29	42.4	Medium-grained OAN	Ilm + Mt	n=4	1.0	1.1	4.0	0.2	255.0	493.1	0.3	0.2	0.1	0.6	0.7	35.5	11.5
LO-32	48.7	Medium-grained OAN	Ilm + Mt	n=4	0.9	0.9	5.0	0.1	249.9	585.8	0.2	0.3	0.0	0.4	0.8	30.7	9.9
LO-38	62.2	Apatite-bearing Anorthosite	-	n=4	1.0	0.6	5.5	0.3	345.4	803.8	0.3	0.3	0.2	0.9	0.7	33.7	11.5
LO-39	63.4	Medium-grained OAN	Ilm + Mt	n=4	0.9	1.0	4.9	Below DL	255.1	920.2	0.2	0.2	0.2	1.8	0.9	29.1	9.3
LO-40	67.5	Medium-grained OAN	Ilm + Mt	n=4	0.9	1.2	4.5	0.1	259.6	559.8	0.2	0.3	0.1	0.5	0.7	28.6	8.9
LO-41B	70.1	Coarse-grained OAN	Ilm + Mt	n=4	0.9	0.7	3.3	0.1	280.2	543.8	0.2	0.2	0.2	1.0	0.9	51.3	16.0
LO-43	75.7	Medium-grained OAN	Ilm + Mt	n=4	3.3	0.0	6.5	Below DL	313.9	1535.1	0.2	0.3	Below DL	0.6	0.6	2.2	2.0
LO-44-2	77.0	Apatite-bearing anorthosite	-	n=4	1.0	1.4	6.1	Below DL	281.8	588.8	0.3	0.3	0.1	0.4	1.1	29.7	9.2
LO-46	79.0	Medium-grained OAN	Ilm + Mt	n=4	3.2	0.0	5.5	Below DL	318.9	1699.0	0.2	0.2	Below DL	0.9	0.8	2.4	1.8

LO-47	84.2	Medium-grained OAN	Ilm + Mt	n=4	3.1	0.0	5.7	Below DL	360.0	2210.3	0.1	0.3	0.2	1.3	0.8	1.7	1.9
LO-49	87.8	Medium-grained OAN	Ilm + Mt	n=4	0.9	2.7	5.5	0.2	274.6	668.9	0.2	0.2	0.1	0.7	0.7	27.7	9.1
LO-50	91.2	Medium-grained OAN	Ilm + Mt	n=3	3.7	0.0	6.4	1.1	304.1	1093.6	0.1	Below DL	0.0	0.7	0.5	1.9	1.5
LO-51	95.8	Medium-grained OAN	Hm-ilm + Mt	n=4	0.8	1.8	5.8	0.3	327.8	695.3	0.2	0.3	0.1	0.7	0.7	29.6	8.9
LO-55	99.7	Medium-grained OAN	Hm-ilm + Mt	n=4	4.5	0.0	10.5	Below DL	309.3	2975.7	0.2	1.5	0.3	1.3	0.4	2.7	2.2
LO-57	102.1	Medium-grained OAN	Hm-ilm + Mt	n=4	0.9	0.9	3.2	0.1	422.6	3457.2	0.2	1.3	0.0	2.2	0.7	21.5	6.6
20PM02	0.0	Medium-grained OAN	Hm-ilm + Mt	n=13	4.5	12.0	8.0	0.0	259.3	1904.9	3.1	3.2	0.9	1.0	0.4	11.9	4.1
MG-LO-01	51.3	Medium-grained OAN	Hm-ilm + Mt	n=12	0.2	4.9	4.4	0.4	315.2	927.2	0.3	0.2	0.1	1.1	0.2	Below DL	5.5
MG-LO-03	93.0	Medium-grained OAN	Hm-ilm + Mt	n=9	0.2	0.9	6.7	0.1	253.4	950.3	0.1	0.3	0.1	0.7	0.1	Below DL	4.4

[La/Yb]n and Eu/Eu* = 2(Eu)n/[(Sm)n+(Gd)n] calculated with Chondrite normalization values of Sun & McDonough (1989). OAN = Oxide-apatite norite; Hm-ilm = hemo-ilmenite; Ilm = ilmenite; Mt = magnetite. aXRF data published on Grant (2020).

Appendix 2.1.8 Complete LA-ICP-MS results of apatite (Cont.)

Detection Limits (33-55μm bean size)					0.01-0.07	0.01-0.02	0.01-0.02	0.004-0.007	0.02-0.06	0.003-0.014	0.003-0.012	0.002-0.008	0.012-0.030	0.013-0.021	0.003-0.009	0.015-0.057
Sample	Depth (m)	Lithology	Oxide Mineralogy	# analysis	^{88}Sr	^{89}Y	^{90}Zr	^{93}Nb	^{137}Ba	^{139}La	^{140}Ce	^{141}Pr	^{146}Nd	^{147}Sm	^{153}Eu	^{157}Gd
LO-01	3.7	Medium-grained OAN	Hm-ilm + Mt	n=4	997.1	368.5	1.0	0.0	0.9	325.8	957.2	155.2	799.2	168.1	42.2	150.9
LO-02	4.7	Massive Apatite	-	n=4	987.2	268.3	3.2	0.0	0.8	356.5	952.4	140.2	655.2	126.4	25.5	109.1
LO-05	6.4	Coarse-grained OAN	Hm-ilm + Mt	n=4	862.2	379.2	2.3	0.0	0.6	387.8	1094.9	171.4	851.8	175.5	43.6	154.7
LO-06	6.8	Fine-grained OAN dyke	Hm-ilm + Mt	n=4	831.2	413.8	0.9	0.0	0.7	408.0	1139.6	178.5	888.8	182.6	44.4	161.2
LO-07	8.5	Medium-grained OAN	Hm-ilm + Mt	n=6	863.8	608.8	2.2	0.0	0.6	689.7	1825.5	263.5	1210.1	237.2	45.3	201.3
LO-08	8.6	Fine-grained OAN dyke	Hm-ilm	n=3	679.3	762.9	0.7	0.0	0.0	637.3	1794.3	280.9	1350.7	282.7	44.8	247.2
LO-09	9.9	Medium-grained OAN	Hm-ilm + Mt	n=4	927.6	336.3	1.1	0.0	1.2	344.2	910.5	139.9	687.3	142.9	32.4	128.6
LO-15-1	14.2	Medium-grained OAN	Hm-ilm + Mt	n=4	796.2	332.7	2.3	0.0	0.7	353.3	955.3	146.2	712.8	148.0	29.3	129.8
LO-21	20.7	Medium-grained Nelsonite	Hm-ilm + Mt	n=4	1501.1	381.2	2.4	0.0	5.9	403.9	1051.8	160.8	793.9	169.6	43.2	149.9
LO-22	21.5	Coarse-grained OAN	Hm-ilm + Mt	n=4	932.8	349.2	2.8	0.0	0.5	394.1	1030.8	159.8	771.4	158.9	35.9	138.7
LO-24	28.2	Medium-grained OAN	Hm-ilm + Mt	n=4	952.8	289.3	1.8	0.0	1.0	306.6	826.0	129.1	655.0	137.5	36.1	121.7
LO-26	36.3	Medium-grained OAN	Ilm + Mt	n=4	917.1	285.6	2.1	0.0	1.5	265.5	720.2	117.4	620.0	132.3	34.2	119.4
LO-29	42.4	Medium-grained OAN	Ilm + Mt	n=4	1047.3	250.5	2.2	0.0	2.2	240.7	662.3	107.7	566.4	120.7	31.4	108.8
LO-32	48.7	Medium-grained OAN	Ilm + Mt	n=4	1091.9	234.0	2.0	0.0	2.9	227.3	620.1	100.2	532.2	114.2	29.4	102.4
LO-38	62.2	Apatite-bearing Anorthosite	-	n=4	880.8	262.7	5.5	0.0	1.0	260.4	708.4	113.2	597.0	127.9	32.7	113.9
LO-39	63.4	Medium-grained OAN	Ilm + Mt	n=4	1123.3	229.2	2.6	0.0	3.7	232.3	630.1	101.4	531.7	112.3	28.9	101.1
LO-40	67.5	Medium-grained OAN	Ilm + Mt	n=4	1126.3	227.0	1.8	0.0	2.6	220.9	609.4	98.9	522.4	111.5	28.8	99.5
LO-41B	70.1	Coarse-grained OAN	Ilm + Mt	n=4	1140.7	418.7	3.0	0.0	1.1	458.4	1202.6	186.0	924.9	190.6	45.6	167.7
LO-43	75.7	Medium-grained OAN	Ilm + Mt	n=4	1376.7	281.4	2.7	0.0	2.9	289.5	784.8	125.4	663.6	141.8	36.4	127.3
LO-44-2	77.0	Apatite-bearing anorthosite	-	n=4	1414.1	238.2	2.1	0.0	5.5	235.5	647.4	104.0	546.9	115.1	30.0	103.4
LO-46	79.0	Medium-grained OAN	Ilm + Mt	n=4	1363.8	253.8	1.5	0.0	2.3	264.0	714.5	115.4	605.3	129.1	33.0	117.0
LO-47	84.2	Medium-grained OAN	Ilm + Mt	n=4	1104.6	284.8	1.4	0.0	0.9	297.7	786.1	124.0	641.5	139.9	35.8	126.7

LO-49	87.8	Medium-grained OAN	Ilm + Mt	n=4	1040.0	228.5	1.8	0.0	2.0	226.5	624.7	100.5	523.9	111.2	28.6	99.2
LO-50	91.2	Medium-grained OAN	Ilm + Mt	n=3	1196.1	259.2	2.1	0.0	0.0	270.8	734.4	116.1	616.1	130.6	33.7	118.9
LO-51	95.8	Medium-grained OAN	Hm-ilm + Mt	n=4	985.7	248.9	1.6	0.0	0.7	244.2	671.0	108.0	562.2	119.9	30.9	107.4
LO-55	99.7	Medium-grained OAN	Hm-ilm + Mt	n=4	923.7	382.2	3.1	0.0	0.0	447.1	1159.5	175.4	872.1	180.4	41.9	158.2
LO-57	102.1	Medium-grained OAN	Hm-ilm + Mt	n=4	1012.8	186.7	0.8	0.0	0.5	163.5	463.5	77.2	422.8	90.9	23.3	82.0
20PM02	0.0	Medium-grained OAN	Hm-ilm + Mt	n=13	871.6	281.5	2.2	0.0	1.2	277.0	765.5	120.2	643.2	136.0	33.6	132.0
MG-LO-01	51.3	Medium-grained OAN	Hm-ilm + Mt	n=12	1091.0	366.3	3.2	0.0	1.2	405.0	1182.5	166.6	815.7	161.7	42.1	145.5
MG-LO-03	93.0	Medium-grained OAN	Hm-ilm + Mt	n=9	855.3	241.5	1.5	0.0	0.6	311.5	1040.1	135.4	565.2	114.6	30.1	94.5

[La/Yb]n and Eu/Eu* = 2(Eu)n/[(Sm)n+(Gd)n] calculated with Chondrite normalization values of Sun & McDonough (1989). OAN = Oxide-apatite norite; Hm-ilm = hemo-ilmenite; Ilm = ilmenite; Mt = magnetite. aXRF data published on Grant (2020).

Appendix 2.1.9 Compilation of whole-rock analysis of ferrodiorite dykes

Sample	Rock Type	Location	SiO_2	TIO_2	Al_2O_3	Fe_2O_3	FeO	MnO	MgO	CaO	Na_2O	K_2O	P_2O_5	Total	Sc	V	Cr	Co	Ni	Cu	Zn	Ga	Rb	Sr	Y	Zr
LO-06[#]	Fine-grained OAGN	Lac a l'Original	41.1	5.2	13.3	19.5	—	0.2	4.7	8.9	3.0	0.7	2.3	100.0	22.7	297.6	49.2	48.5	52.7	98.3	353.8	24.4	4.5	1024.9	52.5	386.2
LO-08[#]	Fine-grained OAGN	Lac a l'Original	35.5	5.0	11.2	23.7	—	0.2	6.4	10.5	2.2	0.6	4.8	100.0	24.4	341.3	32.6	57.4	68.6	55.4	421.2	25.1	2.9	906.3	45.9	107.2
145–937[b]	Ferrodiorite dyke	Grader Intrusion	39.0	4.6	13.7	20.9	—	0.2	4.3	10.4	2.4	0.5	3.3	99.2	—	250.0	15.6	58.0	27.0	56.0	222.0	31.0	3.2	688.0	50.6	190.0
145–938[b]	Ferrodiorite dyke	Grader Intrusion	38.5	4.4	13.1	21.8	—	0.2	4.5	10.5	2.5	0.5	3.3	99.2	—	287.0	28.5	54.0	30.0	55.0	261.0	35.0	3.1	718.0	66.6	197.0
223–601[b]	Ferrodiorite dyke	Grader Intrusion	39.7	3.9	12.7	21.9	—	0.2	4.9	11.2	2.5	0.4	2.7	100.1	—	251.0	5.9	57.0	50.0	84.0	263.0	36.0	1.2	637.0	59.8	147.0
223–604[b]	Ferrodiorite dyke	Grader Intrusion	39.5	6.2	15.0	16.8	—	0.1	5.3	9.4	2.9	0.5	3.1	98.7	—	337.0	42.4	51.0	93.0	31.0	85.0	38.0	3.0	669.0	66.4	163.0
225–135[b]	Ferrodiorite dyke	Grader Intrusion	37.7	5.2	11.9	21.0	—	0.2	5.2	11.2	2.2	0.3	3.9	98.8	—	233.0	6.3	54.0	28.0	66.0	213.0	30.0	0.3	698.0	47.1	147.0
145–648[b]	Ferrodiorite dyke	Grader Intrusion	40.1	4.6	13.6	19.9	—	0.2	5.1	9.5	2.7	0.5	2.9	99.1	—	283.0	24.0	54.0	56.0	77.0	200.0	25.0	3.0	592.0	54.0	151.0
225–302[b]	Ferrodiorite dyke	Grader Intrusion	52.5	4.3	13.4	14.5	—	0.2	2.8	5.1	3.3	2.2	0.8	99.0	—	150.0	7.6	34.0	27.0	33.0	207.0	27.0	30.0	642.0	25.0	376.0

Sample	Rock Type	Location	Nb	Cs	Ba	La	Ce	Pr	Nd	Sm	Eu	Gd	Tb	Dy	Ho	Er	Tm	Yb	Lu	Hf	Ta	W	Pb	Th	U	
LO-06[#]	Fine-grained OAN	Lac a l'Original	23.3	0.0	765.6	69.3	165.2	22.8	101.6	19.6	5.2	16.2	2.1	11.1	1.9	5.1	0.6	3.7	0.5	9.5	1.1	—	10.8	1.1	0.6	
LO-08[#]	Fine-grained OAN	Lac a l'Original	10.7	-0.2	862.0	53.5	135.4	19.9	97.5	19.4	5.4	16.7	1.9	9.7	1.7	4.0	0.4	2.5	0.3	3.0	0.5	—	5.0	0.6	0.2	
145–937[b]	Ferrodiorite dyke	Grader Intrusion	17.3	—	305.0	51.1	134.0	20.9	82.5	18.4	4.2	14.9	2.2	11.6	2.1	4.4	0.5	2.9	0.4	4.6	1.2	—	6.5	1.1	0.2	
145–938[b]	Ferrodiorite dyke	Grader Intrusion	20.4	—	394.0	56.6	145.0	22.8	96.2	21.9	5.4	17.2	2.3	13.0	2.2	4.9	0.5	3.3	0.4	4.3	1.1	—	13.4	1.5	0.2	
223–601[b]	Ferrodiorite dyke	Grader Intrusion	17.2	—	309.0	40.6	108.0	16.0	74.1	16.1	4.3	15.4	2.2	11.7	2.1	4.7	0.5	3.1	0.4	4.3	0.9	—	2.3	0.6	0.1	
223–604[b]	Ferrodiorite dyke	Grader Intrusion	19.2	—	301.0	54.3	141.0	22.4	91.2	18.3	4.2	17.0	2.6	12.7	2.4	5.1	0.6	3.2	0.4	5.3	1.5	—	6.7	1.2	0.0	
225–135[b]	Ferrodiorite dyke	Grader Intrusion	17.6	—	235.0	49.9	122.0	19.0	90.8	18.7	5.2	15.1	2.0	10.0	1.9	4.0	0.5	2.6	0.4	4.3	1.1	—	2.2	0.8	0.1	
145–648[b]	Ferrodiorite dyke	Grader Intrusion	21.6	—	325.0	58.0	144.0	20.7	91.2	18.6	4.5	16.4	2.1	10.7	2.0	4.5	0.5	3.0	0.4	4.4	1.2	—	3.0	1.3	0.1	
225–302[b]	Ferrodiorite dyke	Grader Intrusion	19.2	—	945.0	34.2	81.0	11.8	50.8	13.2	4.1	9.5	1.3	6.5	1.1	2.3	0.3	1.4	0.2	9.5	1.4	—	11.2	1.3	0.3	

Appendix 2.1.10 fO_2 Calculations of fine-grained dykes

Sample	Temperature (C)	Pressure (bar)	Calculated fO_2 (FMQ)	
			QUILF (Anderson al. 1993)	Lattard *et al.* 2005
LO-06 Primitive ferrodiorite dyke	1100	1	1.71	1.4 - 2.0
	1100	1000	1.63	
	1100	5000	1.31	
	1200	1	1.34	2.2 - 2.9
	1200	1000	1.26	
	1200	5000	0.96	

* Calcultions applying mineral chemistry of magnetite and ilmenite (Tables 4 & 5)

** Note that applying the QUILF-equilibrium without fixing the temperature, for a pressure of 1Kbar, unrealistic FMQ values of fO_2 around – 20.95 and +7.78 are obtained. As expected, these calculated values reflect the modification of Fe-Ti oxides primary compositions (especially the loss of Ti content on magnetite) with exchange of elements between the oxides and silicates in subsolidus re-equilibration (Charlier *et al*. 2009), and do not reflect the parental magma conditions .

Appendix 2.1.11 Results of LA-TOF-Maps analysis

Sample	Area (µm²)	Points	Al_2O_3 (%)	CaO (%)	FeOt (%)	K_2O (%)	MgO (%)	MnO (%)	Na_2O (%)	P_2O_5 (%)	SiO_2 (%)	TiO_2	Na	Mg	Al	Si	P	S	K	Ca	Sc
Ilmenite_Core-1	56755	748	0.1	0.1	43.3	0.0	1.6	0.6	0.0	0.0	0.2	54.3	148.7	9821.1	407.3	703.8	163.7	2841.0	153.0	707.4	103.4
Ilmenite-Edge_1	13285	202	0.3	0.1	38.4	0.0	1.9	0.7	0.0	0.0	0.4	58.4	132.6	11257.3	1351.1	1971.3	114.0	2863.5	146.4	576.4	120.4
Relative Difference (%)			69.9	-22.7	-12.7	-4.5	12.8	14.8	-12.1	-43.6	64.3	6.9	-12.1	12.8	69.9	64.3	-43.6	0.8	-4.5	-22.7	14.1
Ilmenite_Core_2	16104	222	0.1	0.1	43.4	0.0	1.6	0.6	0.0	0.0	0.3	54.1	117.3	9741.1	590.3	1198.9	151.1	1982.5	105.9	733.9	110.1
Ilmenite_Edge_2	8459	133	0.3	0.1	38.3	0.0	1.8	0.8	0.0	0.0	0.3	58.5	135.4	11150.8	1750.2	1508.8	216.1	3131.2	117.2	827.5	132.5
Relative Difference (%)			66.3	11.3	-13.2	9.7	12.6	16.6	13.4	30.1	20.5	7.6	13.4	12.6	66.3	20.5	30.1	36.7	9.7	11.3	16.9
Magnetite_Core	47314	620	1.6	0.4	89.6	0.0	0.5	0.0	0.0	0.1	1.1	0.3	201.9	3005.0	8618.3	5194.1	251.2	4201.7	167.5	3020.4	5.2
Magnetite_Edge	7078	113	1.9	0.1	89.3	0.0	0.5	0.0	0.0	0.1	1.0	0.8	219.2	3023.6	10100.9	4455.2	223.8	4588.7	238.0	829.4	4.8
Relative Difference (%)			14.7	-264.2	-0.3	29.6	0.6	-27.6	7.9	-12.2	-16.6	67.5	7.9	0.6	14.7	-16.6	-12.2	8.4	29.6	-264.2	-8.1
Sample	Area (µm²)	Points	Ti	V	Cr	Mn	Fe	Co	Ni	Cu	Zn	Ga	Ge	As	Se	Rb	Sr	Y	Zr	Nb	Mo
Ilmenite_Core-1	56755	748	325496.5	976.2	47.2	4726.1	336379.8	35.3	15.9	23.2	95.9	4.4	3.4	10.6	16.7	16.3	3.1	0.4	53.6	61.5	1.2
Ilmenite-Edge_1	13285	202	349786.2	781.4	39.7	5546.8	298597.5	36.8	15.9	23.1	311.1	4.8	3.0	11.1	14.2	19.7	4.6	0.4	41.2	48.3	0.8
Relative Difference (%)			6.9	-24.9	-18.9	14.8	-12.7	4.0	0.1	-0.5	69.2	8.1	-12.8	3.8	-17.2	17.3	33.9	-2.9	-30.2	-27.4	-46.7
Ilmenite_Core_2	16104	222	323890.6	979.9	54.7	4909.7	337198.2	37.3	14.1	25.0	85.4	4.2	3.3	8.7	14.5	16.1	3.6	0.4	49.4	60.5	1.0
Ilmenite_Edge_2	8459	133	350483.0	646.2	40.3	5890.4	297787.5	37.8	15.3	24.4	635.6	4.6	3.5	10.7	12.9	17.8	5.2	0.6	34.0	51.4	0.9
Relative Difference (%)			7.6	-51.6	-35.7	16.6	-13.2	1.5	7.4	-2.8	86.6	7.3	5.8	19.1	-12.3	9.8	30.9	35.9	-45.4	-17.5	-11.9
Magnetite_Core	47314	620	1616.6	3101.3	87.8	284.1	696084.0	56.6	59.3	5.8	62.3	123.6	6.7	16.6	24.3	20.9	10.2	0.6	2.8	0.2	0.8

Magnetite_ Edge	7078	113	4971.6	2656.3	94.5	222.6	693872.0	47.0	52.7	12.1	673.2	104.6	7.2	14.8	22.9	22.2	4.1	0.4	6.7	0.5	0.7
Relative Difference (%)			67.5	-16.8	7.1	-27.6	-0.3	-20.5	-12.5	52.3	90.7	-18.2	6.8	-12.6	-6.4	5.8	-147.4	-45.7	57.7	62.6	-12.6

Appendix 2.1.11 Results of LA-TOF-Maps analysis (Cont.)

Sample	Area (μm²)	Points	Ru	Rh	Pd	Ag	Pd	Ag	Cd	In	Sn	Sb	Te	Cs	Ba	La	Ce	Pr	Nd	Sm	Eu
Ilmenite_Core-1	56755	748	0.3	0.0	0.2	0.1	0.2	0.2	0.6	0.5	9.7	0.5	0.6	0.1	2.8	0.1	0.2	0.1	0.4	0.3	0.1
Ilmenite-Edge_1	13285	202	0.3	0.0	0.2	0.1	0.2	0.2	0.7	0.6	6.9	0.4	0.3	0.1	4.0	0.2	0.3	0.1	0.4	0.2	0.1
Relative Difference (%)			3.2	-31.8	11.1	15.0	23.1	-7.8	9.6	14.5	-40.5	-8.1	-87.1	8.3	29.8	59.0	48.0	-12.1	-17.9	-41.3	-24.1
Ilmenite_Core_2	16104	222	0.4	0.0	0.2	0.1	0.1	0.2	0.6	0.5	8.5	0.5	0.5	0.1	3.3	0.2	0.3	0.1	0.3	0.3	0.1
Ilmenite_Edge_2	8459	133	0.3	0.0	0.2	0.1	0.1	0.2	0.7	0.6	5.4	0.4	0.8	0.1	3.0	0.4	0.8	0.2	0.6	0.4	0.1
Relative Difference (%)			-37.6	17.2	21.8	28.0	0.3	6.2	4.5	15.7	-58.7	-21.0	31.5	24.2	-8.9	54.7	67.0	20.8	50.5	6.5	0.8
Magnetite_Core	47314	620	0.3	0.0	0.2	0.1	0.2	0.1	0.9	0.1	1.6	0.7	0.9	0.2	5.3	0.3	0.6	0.2	0.5	0.5	0.1
Magnetite_Edge	7078	113	0.3	0.1	0.1	0.1	0.1	0.1	0.9	0.1	1.2	0.6	0.7	0.1	3.1	0.3	0.5	0.1	0.6	0.4	0.1
Relative Difference (%)			-22.7	30.2	-15.2	-7.6	-20.2	22.1	3.7	20.8	-31.3	-3.8	-22.1	-72.4	-68.1	1.3	-5.4	-35.5	9.5	-25.9	-83.9
Sample	Area (μm²)	Points	Gd	Tb	Dy	Ho	Er	Tm	Yb	Lu	Hf	Ta	W	Re	Os	Ir	Pt	Hg	Pb	Th	U
Ilmenite_Core-1	56755	748	0.1	0.0	0.1	0.0	0.1	0.1	0.2	0.0	7.8	3.5	0.2	0.1	0.1	0.0	0.1	1.4	9.2	0.0	2.4
Ilmenite-Edge_1	13285	202	0.1	0.0	0.1	0.0	0.1	0.1	0.1	0.0	5.1	2.7	0.2	0.1	0.1	0.1	0.1	1.4	7.9	0.0	2.2
Relative Difference (%)			-10.3	-9.9	-0.2	24.8	1.8	-19.2	-26.0	41.7	-51.0	-30.0	-4.1	-34.2	-72.9	23.8	5.6	1.7	-17.3	2.3	-8.9
Ilmenite_Core_2	16104	222	0.1	0.0	0.2	0.0	0.0	0.1	0.1	0.0	7.5	3.6	0.2	0.0	0.1	0.0	0.0	1.4	8.5	0.0	2.0
Ilmenite_Edge_2	8459	133	0.2	0.1	0.2	0.0	0.1	0.1	0.2	0.0	4.7	3.0	0.2	0.1	0.1	0.1	0.0	1.5	8.8	0.0	3.2
Relative Difference (%)			26.1	44.0	-2.3	29.7	27.0	-22.8	10.0	7.4	-59.5	-21.6	-0.5	23.7	-46.8	33.6	-53.5	6.4	3.0	24.5	37.6
Magnetite_Core	47314	620	0.3	0.0	0.1	0.0	0.1	0.1	0.1	0.0	0.2	0.1	0.4	0.1	0.1	0.1	0.0	2.7	12.6	0.0	2.7
Magnetite_Edge	7078	113	0.3	0.0	0.1	0.0	0.0	0.1	0.2	0.0	0.3	0.0	0.2	0.1	0.0	0.1	0.1	3.4	15.5	0.0	2.5
Relative Difference (%)			16.2	15.5	8.5	6.7	-162.2	-15.7	24.5	43.9	36.3	-32.9	-88.8	36.0	-126.4	11.5	39.9	22.0	18.7	-147.6	-10.5

Appendix 2.1.12 EMPA analysis - plagioclase

Sample	Lithology	Analysis Code	SiO_2	Al_2O_3	CaO	Na_2O	K_2O	FeO	Total	Ab	An	Or
20PM02	Medium-grained OAN	20-PM-02 Plag1	56.88	27.26	9.43	6.18	0.47	0.09	100.38	44.56	52.83	2.62
20PM02	Medium-grained OAN	20-PM-02 Plag2	57.23	27.17	9.45	6.03	0.51	0.12	100.54	45.08	52.05	2.87
20PM02	Medium-grained OAN	20-PM-02 Plag3	56.36	27.43	9.65	5.90	0.48	0.06	99.88	46.18	51.08	2.74
20PM02	Medium-grained OAN	20-PM-02 Plag4	56.82	27.37	9.52	5.92	0.47	0.10	100.24	45.79	51.52	2.69
20PM02	Medium-grained OAN	20-PM-02 Plag6	55.19	27.64	10.48	5.49	0.46	0.15	99.48	50.00	47.39	2.61
20PM02	Medium-grained OAN	20-PM-02 Plag01r	56.79	27.38	9.56	5.97	0.48	0.11	100.34	45.65	51.61	2.74
20PM02	Medium-grained OAN	20-PM-02 Plag02r	57.42	27.06	9.30	6.10	0.51	0.11	100.53	44.39	52.70	2.91
20PM02	Medium-grained OAN	20-PM-02 Plag03r	56.27	27.45	10.01	5.77	0.46	0.09	100.06	47.68	49.74	2.58
20PM02	Medium-grained OAN	20-PM-02 Plag04r	56.29	27.00	9.63	5.26	1.39	0.09	99.94	46.26	45.76	7.98
20PM02	Medium-grained OAN	20-PM-02 Plag5r	55.76	28.57	10.86	5.40	0.41	0.12	101.15	51.42	46.29	2.29
20PM02	Medium-grained OAN	20-PM-02 Plag6r	56.28	28.09	10.34	5.50	0.42	0.25	100.99	49.75	47.87	2.38
Average			56.48	27.49	9.84	5.77	0.55	0.12	100.32	46.98	49.89	3.13
Standart Deviation			0.61	0.44	0.49	0.30	0.27	0.05	0.46	2.29	2.50	1.54
20PM03A	Oxide-rich Norite	20-PM-03A Plag1	55.81	28.17	10.41	5.63	0.11	0.07	100.19	50.23	49.14	0.63
20PM03A	Oxide-rich Norite	20-PM-03A Plag2	56.67	27.95	10.83	5.72	0.10	0.04	101.31	50.84	48.59	0.57
20PM03A	Oxide-rich Norite	20-PM-03A Plag3	55.66	28.60	10.61	5.54	0.13	0.08	100.61	51.04	48.20	0.76
20PM03A	Oxide-rich Norite	20-PM-03A Plag4	55.56	28.36	10.66	5.70	0.16	0.04	100.48	51.04	48.75	0.87
20PM03A	Oxide-rich Norite	20-PM-03A Plag5	55.82	28.06	10.52	5.74	0.16	0.06	100.37	51.04	49.26	0.89
20PM03A	Oxide-rich Norite	20-PM-03A Plag6	55.83	27.82	10.29	5.92	0.19	0.04	100.14	51.04	50.46	1.09
20PM03A	Oxide-rich Norite	20-PM-03A Plag1r	54.77	28.80	11.13	5.35	0.10	0.06	100.20	51.04	46.25	0.55
20PM03A	Oxide-rich Norite	20-PM-03A Plag2r	55.05	28.15	10.76	5.44	0.12	0.13	99.64	51.04	47.46	0.68
20PM03A	Oxide-rich Norite	20-PM-03A Plag3r	55.05	28.73	11.17	5.28	0.11	0.10	100.45	51.04	45.80	0.65
20PM03A	Oxide-rich Norite	20-PM-03A Plag4r	55.42	28.26	10.74	5.47	0.17	0.08	100.19	51.04	47.47	0.97
20PM03A	Oxide-rich Norite	20-PM-03A Plag5r	56.00	28.15	10.51	5.58	0.18	0.06	100.52	51.04	48.51	1.01
20PM03A	Oxide-rich Norite	20-PM-03A Plag6r	55.87	27.79	10.29	5.51	0.20	0.09	99.74	51.04	48.65	1.15
Average			55.63	28.24	10.66	5.57	0.14	0.07	100.32	50.96	48.21	0.82
Standart Deviation			0.49	0.32	0.28	0.17	0.03	0.02	0.41	0.22	1.24	0.20

Appendix 2.1.12 EMPA analysis - orthopyroxene

Sample	Lithology	Analysis Code	SiO_2	TiO_2	Al_2O_3	Cr_2O_3	FeO_t	MnO	MgO	CaO	Na_2O	K_2O	TOTAL
20PM02	Oxide-Apatite Norite	20-PM-02 Px1	52.82	0.10	2.17	0.07	19.20	0.57	24.09	0.45	0.03	0.00	99.98
20PM02	Oxide-Apatite Norite	20-PM-02 Px2	52.97	0.15	2.08	0.00	19.13	0.56	23.96	0.54	0.01	0.00	99.81
20PM02	Oxide-Apatite Norite	20-PM-02 Px5	52.14	0.18	2.20	0.02	19.78	0.59	23.91	0.55	0.02	0.01	99.76
20PM02	Oxide-Apatite Norite	20-PM-02 Px4	52.13	0.20	1.98	0.00	19.85	0.54	23.92	0.42	0.03	0.01	99.31
20PM02	Oxide-Apatite Norite	20-PM-02 Px6	52.37	0.15	2.36	0.00	19.50	0.57	23.63	0.52	0.02	0.00	99.36
20PM02	Oxide-Apatite Norite	20-PM-02 Px7	52.76	0.10	2.22	0.05	19.55	0.55	23.91	0.59	0.02	0.00	100.27
20PM02	Oxide-Apatite Norite	20-PM-02 Px01r	52.31	0.04	2.14	0.00	18.88	0.55	24.16	0.43	0.01	0.00	98.68
20PM02	Oxide-Apatite Norite	20-PM-02 Px02r	52.61	0.14	2.24	0.04	18.27	0.58	23.58	0.98	0.04	0.00	98.54
20PM02	Oxide-Apatite Norite	20-PM-02 Px5r	52.21	0.18	2.35	0.00	19.38	0.52	23.61	0.45	0.01	0.01	98.80
20PM02	Oxide-Apatite Norite	20-PM-02 Px4r	53.18	0.13	2.32	0.03	18.33	0.55	24.31	0.43	0.03	0.01	99.84
20PM02	Oxide-Apatite Norite	20-PM-02 Px6r	52.14	0.14	2.40	0.03	18.89	0.59	23.61	1.04	0.03	0.00	99.08
20PM02	Oxide-Apatite Norite	20-PM-02 Px7r	53.36	0.18	2.36	0.00	18.01	0.54	24.73	0.40	0.03	0.00	100.34
Average			52.58	0.14	2.24	0.02	19.06	0.56	23.95	0.57	0.02	0.00	99.48
Standart Deviation			0.41	0.04	0.12	0.02	0.58	0.02	0.33	0.21	0.01	0.00	0.59
20PM03	Oxide-rich Norite	20-PM-03A Ox3c (OPX)	51.28	0.09	3.61	0.00	21.03	0.47	22.51	0.24	0.01	0.01	99.32
20PM03	Oxide-rich Norite	20-PM-03A Ox3r (OPX)	51.56	0.00	3.83	0.00	20.54	0.52	22.49	0.17	0.02	0.01	99.23
20PM03	Oxide-rich Norite	20-PM-03A Px2	51.37	0.20	3.66	0.00	20.42	0.51	22.64	0.37	0.03	0.01	99.31
20PM03	Oxide-rich Norite	20-PM-03A Px3	50.99	0.11	3.72	0.09	20.65	0.45	22.40	0.18	0.03	0.00	98.61
20PM03	Oxide-rich Norite	20-PM-03A Px4	51.57	0.00	3.32	0.00	20.09	0.50	22.61	0.33	0.01	0.00	98.43
20PM03	Oxide-rich Norite	20-PM-03A Px5	51.64	0.13	3.26	0.00	20.60	0.49	22.76	0.35	0.03	0.00	99.38
20PM03	Oxide-rich Norite	20-PM-03A Px6	51.92	0.10	3.02	0.03	20.72	0.47	22.42	0.41	0.02	0.00	99.09
20PM03	Oxide-rich Norite	20-PM-03A Px8	51.23	0.07	3.19	0.08	20.79	0.46	22.75	0.33	0.02	0.00	98.91
20PM03	Oxide-rich Norite	20-PM-03A Px2r	51.35	0.10	3.45	0.00	21.11	0.49	22.71	0.29	0.03	0.00	99.73
20PM03	Oxide-rich Norite	20-PM-03A Px3r	51.24	0.04	4.16	0.00	20.36	0.47	22.55	0.19	0.07	0.02	99.20
20PM03	Oxide-rich Norite	20-PM-03A Px4r	50.78	0.05	3.39	0.00	20.57	0.50	22.40	0.22	0.03	0.00	97.95
20PM03	Oxide-rich Norite	20-PM-03A Px5r	51.58	0.09	3.26	0.05	20.71	0.51	22.53	0.34	0.01	0.00	99.07
20PM03	Oxide-rich Norite	20-PM-03A Px6r	51.40	0.13	3.32	0.00	20.56	0.48	22.39	0.37	0.00	0.01	98.66
20PM03	Oxide-rich Norite	20-PM-03A Px8r	51.57	0.04	3.19	0.00	21.41	0.48	22.72	0.35	0.01	0.01	100.05
Average			51.39	0.08	3.46	0.02	20.68	0.49	22.56	0.30	0.02	0.01	99.07
Standart Deviation			0.28	0.05	0.29	0.03	0.32	0.02	0.13	0.08	0.01	0.01	0.52

Appendix 2.1.12 EMPA analysis - ilmenite

Sample	Lithology	Analysis Code	SiO_2	TiO_2	Al_2O_3	FeO_t	Fe_2O_3	FeO	MnO	MgO	Cr_2O_3	Total
20PM02	Medium-grained OAN	20-PM-02 Ox2 EDX	0.00	48.01	0.09	49.56	2.52	47.29	0.68	1.53	0.04	99.87
20PM02	Medium-grained OAN	20-PM-02 Ox2 EDX	0.00	47.03	0.13	50.89	4.54	46.81	0.58	1.68	0.06	100.31
Average			0.00	47.52	0.11	50.23	3.53	47.05	0.63	1.61	0.05	100.09
Standart Deviation			0.00	0.49	0.02	0.66	1.01	0.24	0.05	0.08	0.01	0.22
20PM03A	Massive oxides in anorthosite	20-PM-03A Ox1c	0.01	45.93	0.03	51.11	0.00	51.11	0.61	0.53	0.02	98.22
20PM03A	Massive oxides in anorthosite	20-PM-03A Ox1r	0.01	49.19	0.02	49.19	0.00	49.19	0.64	0.57	0.00	99.61
20PM03A	Massive oxides in anorthosite	20-PM-03A Ox8c	0.03	47.56	0.01	50.50	0.00	50.50	0.53	0.42	0.00	99.06
20PM03A	Massive oxides in anorthosite	20-PM-03A Ox8r	0.02	49.75	0.01	48.56	0.00	48.56	0.56	0.40	0.03	99.30
20PM03A	Massive oxides in anorthosite	20-PM-03A Ox9c	0.02	46.56	0.01	51.32	0.00	51.32	0.53	0.52	0.02	98.95
20PM03A	Massive oxides in anorthosite	20-PM-03A Ox9r	0.02	47.28	0.00	50.73	0.00	50.73	0.57	0.52	0.00	99.13
Average			0.02	47.71	0.02	50.23	0.00	50.23	0.57	0.49	0.01	99.05
Standart Deviation			0.01	1.36	0.01	1.01	0.00	1.01	0.04	0.06	0.01	0.43
LO-01	Medium-grained OAN	LO-01-OX1 EDX	0.30	27.61	0.21	70.69	4.23	66.88	0.13	0.33	0.01	99.27
LO-01	Medium-grained OAN	LO-01-OX7 EDX	0.31	28.83	0.22	70.12	6.16	64.58	0.16	0.36	0.04	100.00
Average			0.31	28.22	0.22	70.41	5.19	65.73	0.15	0.35	0.03	99.64
Standart Deviation			0.01	0.61	0.01	0.28	0.96	1.15	0.01	0.02	0.02	0.37
LO-06	Fine-grained OAN dyke	LO-06-OX20 EDX	0.24	25.58	0.29	73.40	6.35	67.69	0.14	0.20	0.04	99.85
LO-06	Fine-grained OAN dyke	LO-06-OX22 EDX	0.05	26.74	0.24	73.14	7.64	66.27	0.15	0.17	0.05	100.49
LO-06	Fine-grained OAN dyke	LO-06-OX25 EDX	0.31	28.45	0.22	70.89	6.77	64.80	0.14	0.23	0.08	100.24
Average			0.20	26.92	0.25	72.48	6.92	66.25	0.14	0.20	0.06	100.19
Standart Deviation			0.11	1.18	0.03	1.13	0.54	1.18	0.00	0.02	0.02	0.26
LO-07	Medium-grained OAN	LO-07-OX28 EDX	0.34	33.44	0.18	65.24	5.56	60.24	0.17	0.64	0.08	100.01
LO-07	Medium-grained OAN	LO-07-OX29 EDX	0.28	32.01	0.26	65.95	4.07	62.29	0.21	0.65	0.04	99.36
Average			0.31	32.73	0.22	65.60	4.81	61.26	0.19	0.65	0.06	99.69
Standart Deviation			0.03	0.72	0.04	0.36	0.75	1.03	0.02	0.01	0.02	0.32
LO-09	Medium-grained OAN	LO-09-OX35 EDX	0.10	46.06	0.37	51.65	2.93	49.01	0.24	1.36	0.08	99.78
LO-09	Medium-grained OAN	LO-09-OX37 EDX	0.06	42.92	0.04	55.74	4.38	51.80	0.14	1.30	0.03	100.20
Average			0.08	44.49	0.21	53.70	3.66	50.41	0.19	1.33	0.06	99.99
Standart Deviation			0.02	1.57	0.17	2.05	0.73	1.39	0.05	0.03	0.03	0.21
LO-15	Medium-grained OAN	LO-15-OX40 EDX	0.19	43.07	0.15	55.70	5.38	50.86	0.20	1.22	0.05	100.53
LO-15	Medium-grained OAN	LO-15-OX44 EDX	0.08	41.92	0.09	56.43	4.87	52.05	0.20	1.43	0.02	100.15
LO-15	Medium-grained OAN	LO-15-OX49 EDX	0.25	40.79	0.11	53.31	0.00	53.31	0.12	1.57	0.04	96.15
Average			0.17	41.93	0.12	55.15	3.42	52.07	0.17	1.41	0.04	98.94
Standart Deviation			0.07	0.93	0.02	1.33	2.42	1.00	0.04	0.14	0.01	1.98

Appendix 2.1.12 EMPA analysis – ilmenite (Cont.)

Sample	Lithology	Analysis Code	SiO_2	TiO_2	Al_2O_3	FeO_t	Fe_2O_3	FeO	MnO	MgO	Cr_2O_3	Total
LO-21	Nelsonite	LO-21-OX50 EDX	0.18	42.57	0.12	56.14	5.46	51.23	0.32	1.22	0.02	100.55
LO-21	Nelsonite	LO-21-OX51 EDX	0.08	40.40	0.21	54.15	0.00	54.15	0.36	1.33	0.05	96.53
LO-21	Nelsonite	LO-21-OX55 EDX	0.08	43.86	0.15	55.05	6.03	49.63	0.36	1.29	0.06	100.79
Average			0.11	42.28	0.16	55.11	3.83	51.67	0.35	1.28	0.04	99.29
Standart Deviation			0.05	1.43	0.04	0.81	2.72	1.87	0.02	0.05	0.02	1.95
LO-22	Coarse-grained OAN	LO-22-OX58 EDX	0.08	43.76	1.79	54.67	11.75	44.10	0.32	1.43	0.04	102.05
LO-22	Coarse-grained OAN	LO-22-OX60 EDX	0.27	40.26	0.21	59.11	6.92	52.88	0.24	0.93	0.00	101.02
Average			0.18	42.01	1.00	56.89	9.34	48.49	0.28	1.18	0.02	101.54
Standart Deviation			0.10	1.75	0.79	2.22	2.41	4.39	0.04	0.25	0.02	0.52
LO-24	Medium-grained OAN	LO-24-OX65 EDX	0.26	43.75	0.08	54.83	4.10	51.14	0.39	1.03	0.03	100.34
LO-24	Medium-grained OAN	LO-24-OX68 EDX	0.25	43.50	0.09	55.13	4.25	51.31	0.37	1.02	0.04	100.36
Average			0.26	43.63	0.09	54.98	4.17	51.22	0.38	1.03	0.04	100.35
Standart Deviation			0.01	0.13	0.01	0.15	0.07	0.09	0.01	0.01	0.01	0.01
LO-44	Medium-grained OAN	LO-44-OX111 EDX	0.10	51.14	0.06	48.88	9.45	40.37	0.48	1.76	0.03	102.42
LO-44	Medium-grained OAN	LO-44-OX113 EDX	0.06	49.47	0.06	47.87	2.05	46.02	0.48	1.75	0.04	99.69
Average			0.08	50.31	0.06	48.38	5.75	43.20	0.48	1.76	0.04	101.06
Standart Deviation			0.02	0.84	0.00	0.51	3.70	2.82	0.00	0.01	0.01	1.37
LO-46	Medium-grained OAN	LO-46-OX116 EDX	0.05	49.54	0.07	48.06	2.41	45.89	0.26	1.81	0.02	99.79
LO-46	Medium-grained OAN	LO-46-OX121 EDX	0.03	49.74	0.06	48.28	3.41	45.21	0.31	1.77	0.02	100.19
Average			0.04	49.64	0.07	48.17	2.91	45.55	0.29	1.79	0.02	99.99
Standart Deviation			0.01	0.10	0.01	0.11	0.50	0.34	0.03	0.02	0.00	0.20
LO-51	Medium-grained OAN	LO-51-OX142 EDX	0.26	43.05	1.56	53.94	8.32	46.45	0.18	1.65	0.04	100.64
LO-51	Medium-grained OAN	LO-51-OX143 EDX	0.17	41.80	0.14	56.59	4.03	52.96	0.19	1.14	0.03	100.03
Average			0.22	42.43	0.85	55.27	6.18	49.71	0.19	1.40	0.04	100.34
Standart Deviation			0.05	0.63	0.71	1.33	2.14	3.25	0.01	0.26	0.01	0.31
LO-55	Medium-grained OAN	LO-55-OX148 EDX	0.29	26.80	0.24	71.27	4.26	67.44	0.14	0.37	0.06	99.11
LO-55	Medium-grained OAN	LO-55-OX149 EDX	0.10	28.47	0.23	71.35	7.91	64.23	0.09	0.37	0.04	100.61
LO-55	Medium-grained OAN	LO-55-OX153 EDX	0.30	31.56	0.18	68.06	6.90	61.85	0.11	0.34	0.06	100.55
Average			0.23	28.94	0.22	70.23	6.36	64.51	0.11	0.36	0.05	100.09
Standart Deviation			0.09	1.97	0.03	1.53	1.54	2.29	0.02	0.01	0.01	0.69
LO-57	Medium-grained OAN	LO-57-OX155 EDX	0.22	30.61	0.22	67.01	3.15	64.17	0.19	0.68	0.02	98.93
LO-57	Medium-grained OAN	LO-57-OX160 EDX	0.25	29.13	0.31	69.61	7.42	62.93	0.17	0.69	0.07	100.16
Average			0.24	29.87	0.27	68.31	5.28	63.55	0.18	0.69	0.05	99.55
Standart Deviation			0.02	0.74	0.05	1.30	2.13	0.62	0.01	0.00	0.03	0.61

Appendix 2.1.12 EMPA analysis – magnetite

Sample	Lithology	Analysis Code	SiO_2	TiO2	Al_2O_3	Cr_2O_3	V_2O_3	FeO_t	Fe_2O_3	FeO	Total
20PM02	Oxide-Apatite Norite	20-PM-02 Ox4c	0.02	0.05	0.38	0.00	0.34	92.53	68.09	31.26	100.13
20PM02	Oxide-Apatite Norite	20-PM-02 Ox4r	0.03	0.27	0.29	0.01	0.33	92.49	68.31	31.03	100.27
20PM02	Oxide-Apatite Norite	20-PM-02 Ox1c	0.03	0.06	0.26	0.00	0.32	92.43	67.62	31.58	99.87
20PM02	Oxide-Apatite Norite	20-PM-02 Ox1r	0.54	0.05	0.45	0.01	0.48	90.98	66.91	30.77	99.22
20PM02	Oxide-Apatite Norite	20-PM-02 Ox8c	0.01	0.06	0.28	0.01	0.27	91.57	65.47	32.66	98.76
20PM02	Oxide-Apatite Norite	20-PM-02 Ox8r	0.04	0.04	0.35	0.00	0.42	92.87	69.25	30.55	100.65
20PM02	Oxide-Apatite Norite	20-PM-02 Ox5c	0.05	0.06	0.38	0.05	0.18	92.28	67.44	31.60	99.74
20PM02	Oxide-Apatite Norite	20-PM-02 Ox5r	0.04	0.09	0.35	0.01	0.28	91.85	66.63	31.89	99.28
Average			0.09	0.08	0.34	0.01	0.33	92.12	67.46	31.42	99.74
Standart Deviation			0.17	0.07	0.06	0.02	0.09	0.58	1.08	0.63	0.58
20PM03A	Oxide-rich Norite	20-PM-03A Ox4c	0.12	0.07	0.33	0.30	0.51	91.97	67.77	30.98	100.08
20PM03A	Oxide-rich Norite	20-PM-03A Ox4r	0.06	0.07	0.28	0.35	0.61	90.90	65.42	32.03	98.81
20PM03A	Oxide-rich Norite	20-PM-03A Ox6c	0.04	0.06	0.35	0.30	0.59	92.10	68.06	30.86	100.25
20PM03A	Oxide-rich Norite	20-PM-03A Ox6r	0.21	0.09	0.54	0.32	0.61	90.03	64.85	31.67	98.29
20PM03A	Oxide-rich Norite	20-PM-03A Ox10c	0.04	0.07	0.34	0.34	0.57	91.16	66.02	31.75	99.13
20PM03A	Oxide-rich Norite	20-PM-03A Ox10r	0.01	0.04	0.38	0.35	0.44	92.36	68.38	30.82	100.42
20PM03A	Oxide-rich Norite	20-PM-03A Ox14c	0.03	0.07	0.34	0.34	0.76	91.51	67.18	31.06	99.77
20PM03A	Oxide-rich Norite	20-PM-03A Ox14r	0.07	0.08	0.32	0.33	0.81	90.72	65.59	31.70	98.89
20PM03A	Oxide-rich Norite	20-PM-03A Ox17c	0.03	0.06	0.36	0.28	0.76	91.54	67.19	31.08	99.77
20PM03A	Oxide-rich Norite	20-PM-03A Ox17r	0.03	0.04	0.32	0.32	0.54	91.99	67.54	31.21	100.01
Average			0.06	0.06	0.36	0.32	0.62	91.43	66.80	31.32	99.54
Standart Deviation			0.06	0.01	0.07	0.02	0.12	0.69	1.17	0.41	0.68

Appendix 2.1.12 EMPA analysis – apatite

Sample	Lithology	Analysis code	CaO	SO_3	F	P_2O_5	SiO_2	Cl	FeO	La_2O_3	Ca_2O_3	Total
20PM02	Medium-grained OAN	20-PM-02 Apt 6c	55.27	0.08	3.24	43.05	0.12	0.07	0.03	0.07	0.11	101.06
20PM02	Medium-grained OAN	20-PM-02 Apt 6r	55.25	0.09	3.39	43.02	0.15	0.10	0.00	0.07	0.03	100.85
20PM02	Medium-grained OAN	20-PM-02 Apt 8c	55.09	0.12	3.33	42.99	0.12	0.09	0.11	0.05	0.11	100.69
20PM02	Medium-grained OAN	20-PM-02 Apt 8r	55.44	0.04	3.33	42.68	0.07	0.10	0.29	0.00	0.04	100.58
20PM02	Medium-grained OAN	20-PM-02 Apt 10c	54.83	0.01	3.42	42.42	0.17	0.08	0.12	0.02	0.16	100.05
20PM02	Medium-grained OAN	20-PM-02 Apt 10r	55.37	0.05	3.45	42.82	0.11	0.09	0.00	0.07	0.08	100.74
20PM02	Medium-grained OAN	20-PM-02 Apt 13c	55.32	0.11	3.31	42.87	0.16	0.10	0.00	0.00	0.11	100.60
20PM02	Medium-grained OAN	20-PM-02 Apt 13r	52.20	0.07	3.15	40.33	1.93	0.11	0.81	0.01	0.09	97.37
20PM02	Medium-grained OAN	20-PM-02 Apt 14c	55.29	0.05	3.29	42.94	0.11	0.10	0.13	0.00	0.00	100.50
20PM02	Medium-grained OAN	20-PM-02 Apt 14r	55.44	0.05	3.29	42.80	0.15	0.09	0.18	0.05	0.17	100.83
20PM02	Medium-grained OAN	20-PM-02 Apt 1c	55.04	0.09	3.29	42.35	0.11	0.08	0.05	0.11	0.03	99.81
20PM02	Medium-grained OAN	20-PM-02 Apt 1r	55.09	0.12	3.39	42.47	0.13	0.09	0.14	0.02	0.00	100.09
20PM02	Medium-grained OAN	20-PM-02 Apt 2c	55.26	0.12	3.63	42.33	0.10	0.09	0.06	0.00	0.10	100.22
20PM02	Medium-grained OAN	20-PM-02 Apt 2r	55.49	0.13	3.54	42.38	0.08	0.08	0.00	0.01	0.09	100.35
20PM02	Medium-grained OAN	20-PM-02 Apt 4c	55.26	0.06	3.54	42.46	0.10	0.08	0.00	0.00	0.07	100.28
20PM02	Medium-grained OAN	20-PM-02 Apt 4r	55.15	0.08	3.47	42.78	0.14	0.12	0.00	0.00	0.06	100.34
Average			55.05	0.08	3.38	42.54	0.23	0.09	0.12	0.03	0.08	100.27
Standart Deviation			0.75	0.03	0.12	0.62	0.44	0.01	0.20	0.03	0.05	0.82
20PM03A	Oxide-rich Norite	20-PM-03A Apt 1c	54.36	0.06	3.45	42.01	0.16	0.15	0.19	0.08	0.16	99.44
20PM03A	Oxide-rich Norite	20-PM-03A Apt 1r	54.78	0.05	3.43	42.63	0.06	0.15	0.21	0.08	0.12	100.14
20PM03A	Oxide-rich Norite	20-PM-03A Apt 2c	54.86	0.08	3.33	42.12	0.19	0.17	0.17	0.01	0.12	99.64
20PM03A	Oxide-rich Norite	20-PM-03A Apt 2r	54.54	0.07	3.29	42.52	0.20	0.15	0.27	0.08	0.19	100.14
20PM03A	Oxide-rich Norite	20-PM-03A Apt 3c	54.69	0.14	3.34	42.18	0.24	0.15	0.07	0.08	0.24	99.76
20PM03A	Oxide-rich Norite	20-PM-03A Apt 3r	54.64	0.10	3.17	41.88	0.25	0.17	0.28	0.16	0.15	99.51
20PM03A	Oxide-rich Norite	20-PM-03A Apt 5c	54.72	0.10	3.30	42.38	0.13	0.15	0.21	0.14	0.08	99.97
20PM03A	Oxide-rich Norite	20-PM-03A Apt 5r	54.85	0.00	3.23	42.30	0.14	0.14	0.14	0.07	0.02	99.69
20PM03A	Oxide-rich Norite	20-PM-03A Apt 9c	54.79	0.04	3.36	42.55	0.11	0.14	0.09	0.09	0.25	100.01
20PM03A	Oxide-rich Norite	20-PM-03A Apt 9r	54.38	0.02	3.33	42.48	0.15	0.20	0.15	0.12	0.09	99.66
20PM03A	Oxide-rich Norite	20-PM-03A Apt 8c	54.70	0.04	3.24	42.40	0.11	0.14	0.07	0.07	0.36	100.20
20PM03A	Oxide-rich Norite	20-PM-03A Apt 8r	55.01	0.04	3.45	42.37	0.15	0.16	0.14	0.12	0.08	100.22
20PM03A	Oxide-rich Norite	20-PM-03A Apt 6c	54.40	0.18	3.33	42.09	0.27	0.14	0.15	0.07	0.21	99.69
20PM03A	Oxide-rich Norite	20-PM-03A Apt 6r	54.78	0.14	3.33	41.98	0.24	0.17	0.17	0.09	0.27	99.92
20PM03A	Oxide-rich Norite	20-PM-03A Apt 7c	54.69	0.08	3.34	42.35	0.13	0.16	0.30	0.00	0.23	100.18
20PM03A	Oxide-rich Norite	20-PM-03A Apt 7r	55.02	0.00	3.54	42.03	0.12	0.16	0.18	0.06	0.06	99.73

Average	54.70	0.07	3.34	42.27	0.17	0.16	0.17	0.08	0.16	99.87
Standart Deviation	0.20	0.05	0.09	0.22	0.06	0.02	0.07	0.04	0.09	0.25

APPENDIX 2.2 METHODOLOGY (CHAPTER 2)

Appendix 2.2.1 Whole rock lithogeochemistry by fusion-LA-ICP-MS

Whole-rock major and trace element analyses were carried out by fusion – LA-ICP-MS at LabMaTer, UQAC, following the protocol of Barnes & Mansur (2020). First, the sample powder was fused into glass disks following a conventional XRF major element fusing technique, using a lithium borate mix as a flux (e.g., Perkins *et al*. 1993; Norman *et al*. 2003). The glass disks of silicate rocks were made in a 1:4 ratio by mixing 0.5g of each sample powder with 2g of pre-mixed LiB flux (49.75% $Li_2B_4O_7$ + 49.75% $LiBO_2$ + 0.5% LiBr) provided by CLAISS and 0.5g of ammonium nitrate (NH_4NO_3) in a 1'' platinum crucible mould. For oxide-rich samples, the sample:flux ratio increased from 1:4 to 1:10 to ensure complete fusion. The platinum crucible was then placed in a CLAISSE (LeNeo -Beta Version) and the fusion carried out in four distinctive stages, taking 15 minutes before the glass disks was generated. First, the instrument was preheated to 850˚C for 3 minutes, before adjusting the temperature to 1050˚C for the next 4 minutes and 20 rotation per minute (rpm). Following an increase to 40 rpm the crucible was tilted at 20˚ to promote homogenization for 3 minutes. The temperature increased to 1100 ˚C and 35 rpm for the final 3 minutes. Upon complete fusion, the melting product cooled down for 2 minutes before producing the glass disk. The glass disks were mounted in epoxy mounts and polished for analysis by LA-ICP-MS using an Excimer 193nm Resolution M-50 laser ablation system equipped with a double volume cell S-155 and coupled with an Agilent 7900 mass spectrometer. The LA-ICP-MS analyses of the glass disks were determined using a laser frequency of 10 Hz, a power of 4.5 to 5 mJ/pulse, a dwell time of 7.5 to 10 ms, a rastering speed of 5 to 10 µm/s, and a fluence of 3 J/cm^2. Line scans ablating the surface of each polished glass disk were made with a beam size of 75µm. The gas blank was measured for 25 to 30s before switching on the laser for at least 40s. The ablated material was carried into the ICP-MS by an Ar–He gas mix at a

rate of 0.8–1 L/min for Ar and 350 mL/min for He, and 2mL/min of nitrogen was also added to the mixture. Data reduction was carried out using the Iolite software based on semi-quantitative data reduction scheme normalized to 100% oxides for major elements and including loss on ignition (LOI) (Paton *et al.* 2011). A series of reference materials, international and in-house, (listed in Table A.1) were prepared using the same fusion method to 1) us for calibration (an in-house MIX-KPT-610) and 2) monitor the quality of the results for silicate rocks and glasses (KPT-1, OKUM, LK-NIP, GEOPT-23, GEOPT-25, GEOPT-34, AN-G, GSE, NIST 610), Fe-Ti oxides (BC-28, AMIS-0454, NIST27f) and 3 Fe-Ti-P mineralised rocks, from the study of Grant (2020) previously analysed in commercial labs by XRF, INAA and ICP-MS. A glass disk of NIST-616 was prepared and analysed as an approximation of a procedural blank as this synthetic glass contains sub ppm levels of most trace element. The results are within the accepted range of working values and the reference materials data and limits of detection (LOD) are reported below.

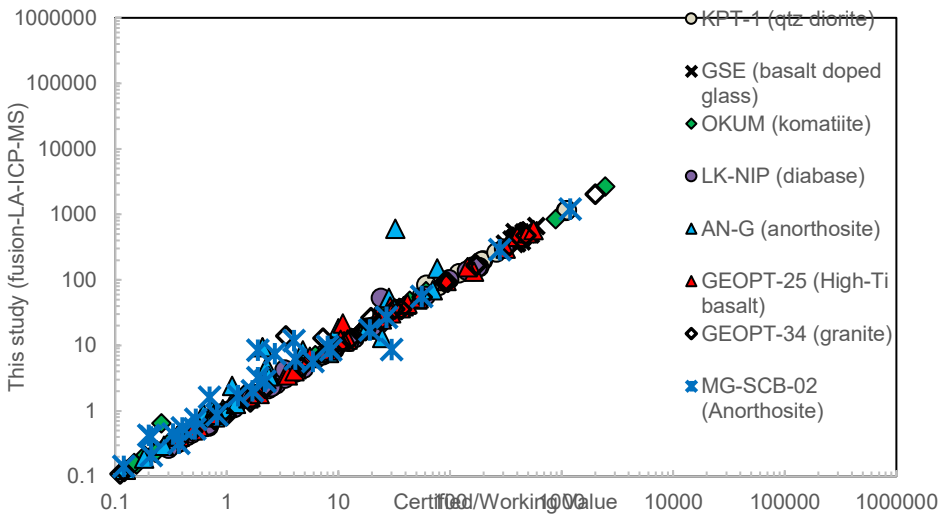

Figure 1. Comparison between certified/working values and the respective values obtained for LA-ICP-MS analysis of reference materials in this study.

Appendix 2.2.2 Mineral Chemistry by LA-ICP-MS

Forty-eight trace element concentrations [Li, Na, Mg, Al, Si, P, Cl, K, Ca, Sc, Ti, V, Cr, Mn, Fe, Co, Ni, Cu, Zn, Ga, Ge, Rb, Sr, Y, Zr, Nb, Cs, Ba, La, Ce, Pr, Nd, Sm, Eu, Gd, Tb, Dy, Ho, Er, Tm, Yb, Lu, Hf, Ta, W, Pb, Th and U] in plagioclase (n=168), magnetite (n=88), ilmenite (n=108) and apatite (n=132) were determined in-situ for 38 samples using an Excimer 193nm Resolution M-50 laser ablation system, equipped with a double volume cell S-155, and coupled with an Agilent 7900 mass spectrometer at LabMaTer, UQAC. The LA-ICP-MS tuning parameters were a laser frequency of 10 Hz, a power of 4.5 to 5 mJ/pulse, a dwell time of 7.5 to 10 ms, a rastering speed of 5 to 10 µm/s, and a fluence of 3 J/cm^2. Line scans across the surface of 3-5 grains (per mineral) per polished thinsection were made with beam sizes ranging from 33-55µm according to the size of the grain. The gas blank was measured for 25 to 30s before switching on the laser for at least 40s. The ablated material was carried into the ICP-MS by an Ar–He gas mix at a rate of 0.8–1 L/min for Ar and 350 mL/min for He, and 2mL/min of nitrogen was also added to the mixture.

Data reduction was carried out using Iolite 4 (Iolite Software, The University of Melbourne), based on semi-quantitative data reduction scheme, normalized to 100% oxides (Paton *et al.* 2011) for plagioclase and ilmenite. Magnetite data was treated using the traditional normalization using a fixed Fe value, close to stoichiometry, obtained by microprobe for a few samples. Due to the low-Ti concentration of magnetite in all samples (< 0.5 wt.%), there is no substantial change in the Fe content which is close to stoichiometry (72 wt.%). In the same way, apatite data was normalized using a fixed Ca value (give value, close to stoichiometry) obtained by microprobe for a few samples. In contrast, a semi-quantitative data reduction scheme (i.e. normalising to 100% of the major elements without fixing an internal standard) was carried out for minerals (plagioclase and ilmenite) that show

extensive solid-solution and exsolution lamellae. Due to the difference in beam size and area that sampled between LA-ICP-MS (line of 50um x 300um) and EPMA (5-10 um beam) techniques, exsolutions of K-rich anti-perthite in plagioclase and hematite exsolutions in (hemo)-ilmenite are not similarly sampled during analysis, therefore leading to inaccurate values for internal standardization of LA-ICP-MS data using EMPA results. For the oxide minerals the recalculation of Fe total to FeO and Fe_2O_3 contents, required to balance the total to 100%, was carried out using charge balance spreadsheet. The Xhem content in ilmenite was calculated using the QUILF program (Anderson et al. 1993). For plagioclase, the molar proportions of An-Ab-Or was calculated using the EPMA spreadsheet for charge balance. Comparison between LA-ICP-MS results and SEM-EMPA results is given below in Section A.4.

International reference materials used for calibration and to monitor the data quality for each mineral protocol are presented in Table A.1. NIST-610 glass was used to calibrate plagioclase and apatite whereas the Fe-rich GSE glass was used to calibrate ilmenite and magnetite. NIST-612, NIST-614, NIST-616, G-PROBE-6 and GSD were used as monitors for plagioclase. NIST-612, NIST-614, NIST-616, G-PROBE-6, GSD, MAPS-4 as well as in-house reference material UQAC-APA (apatite concentrate) were used as monitors for apatite. NIST-612, NIST-614, NIST-616, G-PROBE-6, GSD as well as in-house reference materials BC-28 (massive magnetite), AMIS-0454 (massive ilmenite) were used as monitors for oxides (Appendix – Table A.2). The results are within an accepted range of working values (<10% Relative difference; <10% RSD) as shown below.

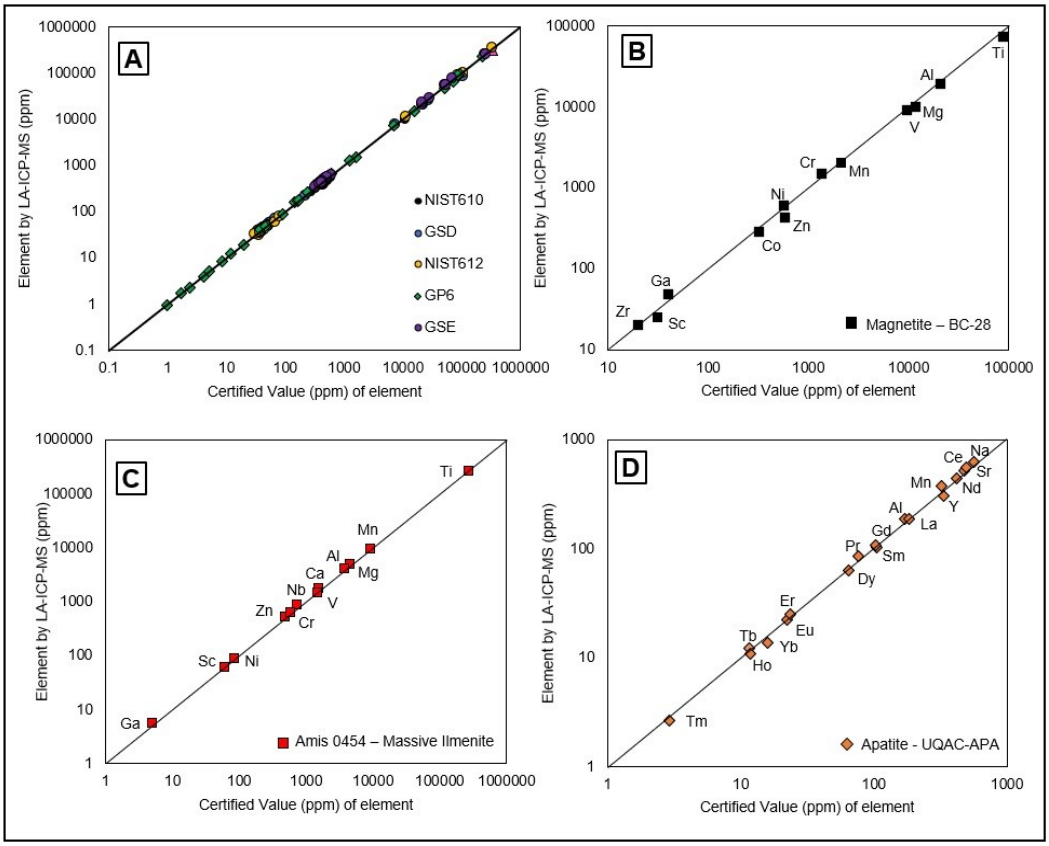

Figure 2. Comparison between LA-ICP-MS results obtained for different reference materials (RM)and their respective certified values. A. International glass reference materials. B. In-house magnetite RM (BC28). C. International ilmenite RM (Amis 0454). D. In-house apatite RM (UQAC-APA). Values are accurate and precise (<10% relative standard deviation and relative difference).

Appendix 2.2.3 Trace element mapping of oxides by LA-(TOF) ICP-MS

One mineralized sample was selected for detailed trace element mapping of Fe-Ti-oxides using a 193nm laser (Applied Spectra, California), equipped with a large double-volume cell (Laurin Technic, Australia), coupled with a time of flight (TOF) ICP-MS (TOFWERK, Switzerland) at LabMaTer, UQAC. The LA-TOF-ICP-MS, developed at LabMaTer, allows a fast and high- resolution mapping (Savard et al. accepted). The LA-ICP-TOF-MS tuning parameters were a laser frequency of 60Hz, a fluence of 6 J/cm^2 and a displacement speed of 100um/s. A beam size of 9 um was used to make a high-resolution

map size of 1.3mm x 1.3mm, with 145 lines of analysis of 13 seconds each, for a total acquisition time of 55 minutes. Calibration was done using a mix of different standards: GSD-1g, GSE-1g, UQAC-FeS-1 (sulfide RM) and UQAC-APA-1 (apatite RM), following the protocol of Savard et al. (accepted). 2970 extractions were co-added which produce extraction cycle of 90ms. Oxides and double-charged interference formation were monitored from $^{248}ThO^{+}/^{232}Th^{+}$ and $^{137}Ba^{+2}/^{137}Ba^{+}$ respectively, and both were <1%. The baseline was subtracted using Tofware software (TOFWERK), and data reduction was completed using IOLITE v4, applying a semi-quantitative scheme with normalization to 100% (Savard et al. accepted).

Appendix 2.2.4 Electron microprobe and scanning electron microscope

Analyses of major and minor elements were determined in plagioclase, orthopyroxene, biotite, magnetite, ilmenite, spinel and apatite of 15 samples by electron microprobe analysis at Université Laval (ULaval), Quebec, using a CAMECA SX-100 EPMA, equipped with five wavelength-dispersive spectrometers (WDS). Beam size was 10 µm with a voltage of 15 kV and a current of 20 nA. The defocussed beam was chosen to ensure that any fine grained exsolutions were incorporated into the analysis and also to limit the affect of volatile diffusion during the analysis of apatite. The background was measured for 15–20 s on both sides and a peak counting time of 10 s was carried out. The mix of synthetic and natural materials were used for calibration: Apatite (P, Ca, F), quartz (Si), tugvz (Cl), hematite (Fe), $LaPO_4$ (La), $CePO_4$ (Ce), rut (Ti), $PrPO_4$ (Pr), $NdPO_4$ (Nd) and chalcopyrite (S). The calculated cationic proportion, the recalculation of Fe^{+2}/Fe^{+3} ratios, and molar proportions of An-Ab-Or contents in plagioclase were done using charge balance spreadsheets provided by the probe operator.

Thirteen samples covering the entire borehole stratigraphy were selected for energy-dispersive micro-X-Ray spectrometry (EDX) analysis at Université Laval (ULaval). Beam size was 10 µm with a voltage of 15 kV and a current of 20 nA, for an acquisition time of 120s. EDX analysis of areas of 500 x 500µm in ilmenite and hemo-ilmenite grains (n=44) were made instead of punctual analysis (used for the other minerals) in a way to obtain an average major composition due to the presence of high-hematite exsolutions, for direct comparison with the LA-ICP-MS data (Fig. A.3).

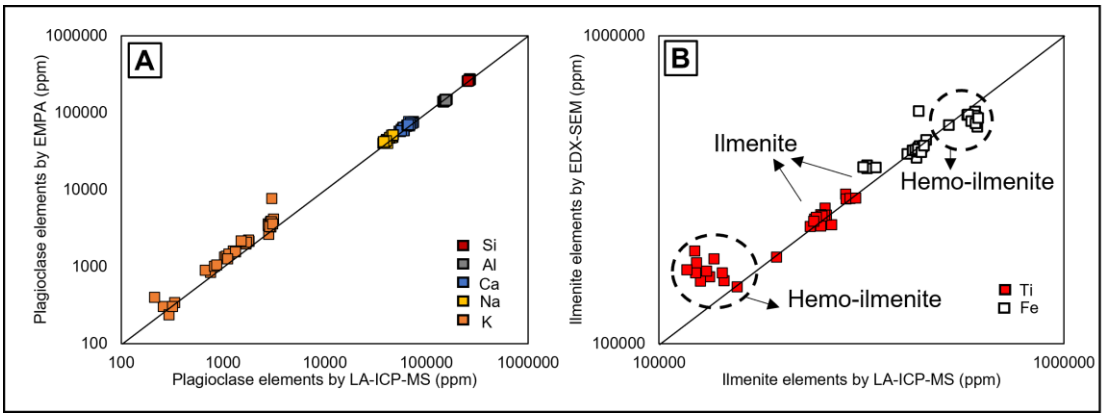

Figure 3. Semi-quantitative LA-ICP-MS results, normalized to 100%, analyses of (A) plagioclase compared to results of electron microprobe (EMPA) and (B) (hemo)-ilmenite compared to results from EDX-SEM for the Lac a L'Orignal samples. Plagioclase and ilmenite are in good agreement (<10% relative standard deviation) with their analysis by EMPA and EDX-SEM, respectively. However, hemo-ilmenite grains with large hematite lamellae are very heterogeneous and there is a lower agreement between SEM and LA-ICP-MS results
compared to the other ilmenite grains (<25% relative standard deviation).

Appendix 2.2.5 U-Pb geochronology

Zircon separation, preparation and U-Pb analysis were conducted in GEOTOP labs at the Université du Québec à Montréal. About 2kg per sample was cleaned and then crushed in a jaw crusher before being sieved to under 250 microns. The resulting rock powder was passed over a Wilfley table using a similar approach to Rocha *et al.* (2020), where the sample is introduced to the Wilfley table one spoonful at a time to ensure that all heavy

minerals of all sizes are collected. The zircons were further concentrated using heavy liquids and a Franz isodynamic separator using a current up to 1 ampere. Zircon was then separated from the dense and non-magnetic fraction by hand under a binocular microscope. The selected grains were then annealed in a muffle furnace at 1000 degrees for 48 hours.

Annealed grains were mounted in epoxy and polished before being imaged on a Hitachi S-3400 Variable Pressure SEM at an accelerating voltage of 20 kV using a Centaurus Cathodoluminescence (CL) detector. The acquired CL images were used to guide spot selection for the in-situ analysis. CL images were used to highlight growth zoning, rims overgrowth and inherited cores within individual grains. Most of the samples show zircons with very homogenous textures with oscillatory and sector zoning, however zircons of sample LOR-1, show a bit more complexity with the presence of inherited cores and rims overgrowth. Most of the time, the homogeneous areas of the selected zircons were analysed. We were particularly careful to avoid fractures and inclusions-rich domains within zircon grains. Laser ablation U-Pb analysis was performed using a Nu Attom single collector mass spectrometer attached to a photon machines G2 193nm excimer laser following a procedure adapted from Perrot *et al*. (2017), for details, see table below where metadata are included as recommended by Horstwood *et al.* 2016). Data processing, and down-hole fractionation correction were done using Iolite 4 software, using 91500 (Wiedenbeck *et al*. 1995) as a primary reference material for calibration assuming that the reference material and samples behave identically for laser-induced elemental fractionation correction. Two secondary reference material were analysed: Plešovice and OG1 for quality control and validation purposes. The age obtained for Plešovice was 340 ± 1 (2σ) Ma and of OG1 was 3476 ± 9(2σ), which are respectively in good agreement with their known age (Sláma et al., 2008; Bodorkos et al, 2009). Once the raw data were processed, Concordia diagrams and

weighted mean ages were plotted and treated through Isoplot R (Vermeesch, 2018) software.

Data reporting table for LA-ICP-MS U-Pb analyses

Laboratory & Sample Preparation	
Laboratory name	Geotop, University of Quebec in Montreal
Sample type/mineral	Detrital zircons
Sample preparation	Conventional mineral separation, 1 inch resin mount, 1µm polish to finish
Imaging	Centaurus, Hitachi S-3400N SEM
Laser ablation system	
Make, Model & type	Photon-machines G2
Ablation cell & volume	Helex, 2-volume cells
Laser wavelength (nm)	193 nm
Pulse width (ns)	4 ns
Fluence ($J.cm^{-2}$)	3.18 $J.cm^{-2}$
Repetition rate (Hz)	6 Hz
Ablation duration (secs)	30 secs
Ablation pit depth / ablation rate	Not available
Spot diameter (µm)	30 µm
Sampling mode / pattern	Static spot ablation
Carrier gas	100% He in the cell,
Cell carrier gas flow (l/min)	0.7 l/min He in the 1st volume cell 0.5/min He in the 2nd volume cell
ICP-MS Instrument	
Make, Model & type	ICP-MS (Attom, Nu Instruments)
Sample introduction	Ablation aerosol from laser to torch
RF power (W)	1300W
Make-up gas flow (l/min)	0.3 L/min Ar mixed along the sample transport line to the torch 3 ml/min N2 also added before torch
Detection system	single ion counter
Masses measured	202, 204, 206, 207, 208, 232, 235, 238.
Integration time per peak/dwell times (ms)	500ms for each isotope
Total integration time per output datapoint (secs)	~0.9secs
'Sensitivity' as useful yield (%, element)	0.4% U (NIST610 = 500ppm, #atoms sampled: 500ppm*85um*3Hz*3J/cm^2, #ions detected: >25 mcps)
IC Dead time (ns)	25 ns
Data Processing	
Gas blank	15 second on-peak zero subtracted
Calibration strategy	91500 used as primary reference material,

Reference Material info	91500 (Wiedenbeck et al. 1995)
Data processing package used / Correction for LIEF	Iolite4 and IsoplotR softwares. laser-induced elemental fractionation correction assumes reference material and samples behave identically.
Mass discrimination	N/A - Down-hole effect with iolite.
Common-Pb correction, composition and uncertainty	No common-Pb correction applied to the data.
Uncertainty level & propagation	Ages are quoted at 1*s* absolute, propagation is by quadratic addition. Reproducibility and age uncertainty of reference material are propagated where appropriate.
Quality control / Validation	Plesovice, R33, OG1

References

Bodorkos S, Stern R.A, Kamo S, Corfu F, Hickman AH. 2009. OG1: a natural reference material for quantifying SIMS instrumental mass fractionation of Pb Isotopes during zircon dating. InAGU Fall Meeting Abstracts 2009 Dec (Vol. 2009, pp. V33B-2044).

Barnes, S. J., Mansur, E. T., Pagé, P., Meric, J., & Arguin, J. P. 2020. Major and trace element compositions of chromites from the Stillwater, Bushveld and Great Dyke intrusions compared with chromites from komatiites, boninites and large igneous provinces.

Norman, M., Robinson, P., & Clark, D. 2003. Major-and trace element analysis of sulfide ores by laser-ablation ICP–MS, solution ICP–MS, and XRF: new data on international reference materials. The Canadian Mineralogist, 41(2), 293-305.

Paton, C., Hellstrom, J., Paul, B., Woodhead, J., & Hergt, J. (2011). Iolite: Freeware for the visualisation and processing of mass spectrometric data. Journal of Analytical Atomic Spectrometry, 26(12), 2508-2518.

Perkins, W. T., Pearce, N. J. G., & Jeffries, T. E. 1993. Laser ablation inductively coupled plasma mass spectrometry: a new technique for the determination of trace and ultra-trace element in silicates. Geochimica et Cosmochimica Acta, 57(2), 475-482.

Perrot, M., Tremblay, A., David, J., 2017. Detrital zircon U-Pb geochronology of the Magog Group, southern Quebec–stratigraphic and tectonic implications for the Quebec Appalachians. Am. J. Sci. 317 (10), 1049–1094

Rocha, B.C, Davies J.H.F.L., Janasi V.A., Schaltegger U, Nardy A.J.R., Greber N.D, Lucchetti A.C.F,. Polo L.A. 2020. Rapid eruption of silicic magmas from the Paraná magmatic province (Brazil) did not trigger the Valanginian event. Geology; 48 (12): 1174–1178. doi: https://doi.org/10.1130/G47766.1

Sláma J, Košler J, Condon DJ, Crowley JL, Gerdes A, Hanchar JM, Horstwood MS, Morris GA, Nasdala L, Norberg N, Schaltegger U. 2008. Plešovice zircon—a new natural reference material for U–Pb and Hf isotopic microanalysis. Chemical Geology. Mar 30;249(1-2):1-35.

Vermeesch, P., 2018, IsoplotR: a free and open toolbox for geochronology. Geoscience Frontiers, v.9, p.1479-1493, doi:10.1016/j.gsf.2018.04.001.

APPENDIX 2.3 SUPPLEMENTARY FIGURES (CHAPTER 2)

Appendix 2.3.1 CL Images of selected analyzed zircons

GC-LOR-01

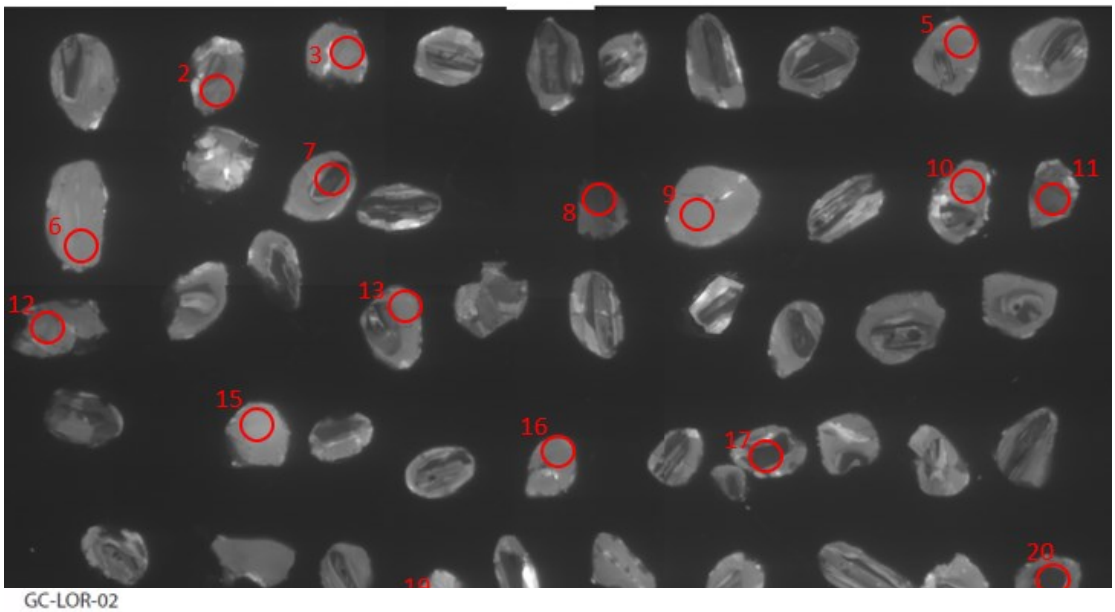

GC-LOR-02

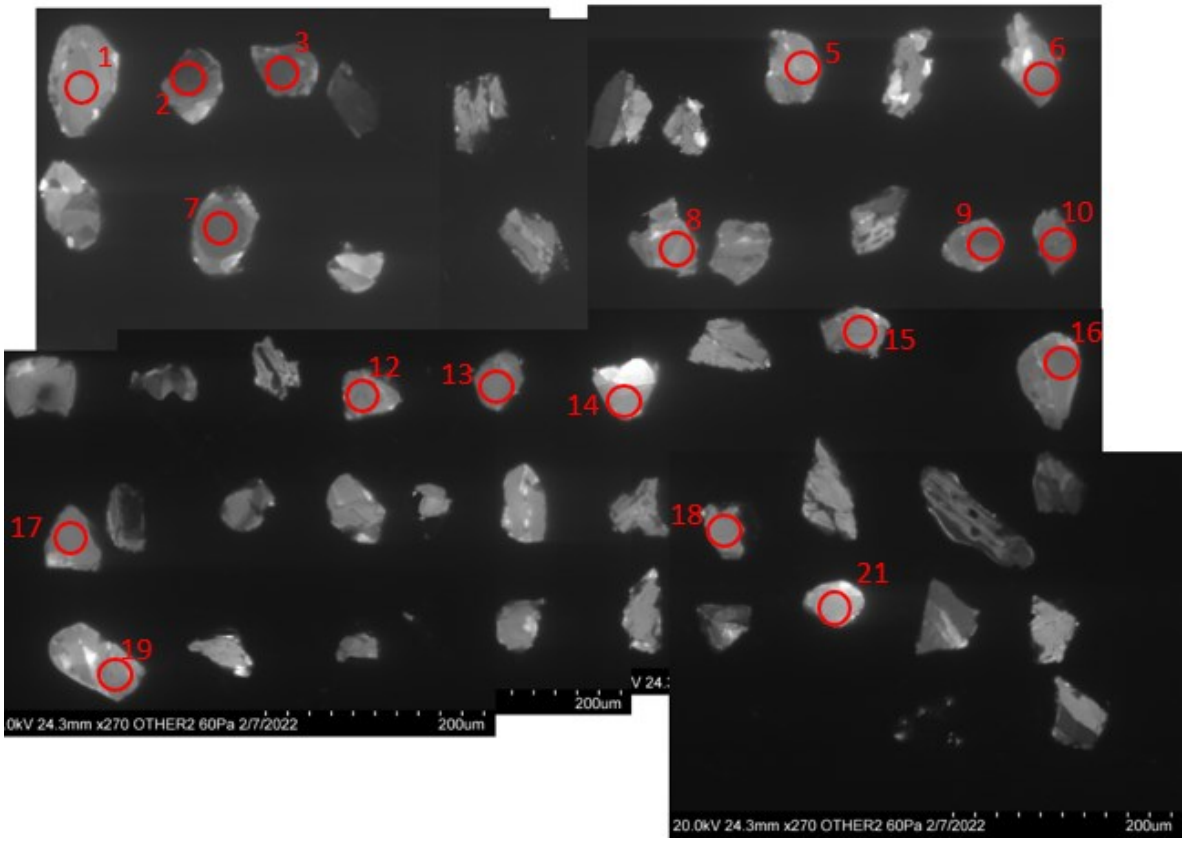

Appendix 2.3.2 Weighted mean diagrams for LA-ICP-MS U–Pb analysis in zircon Each bar represents the result of the analysis of a single grain

LOR01

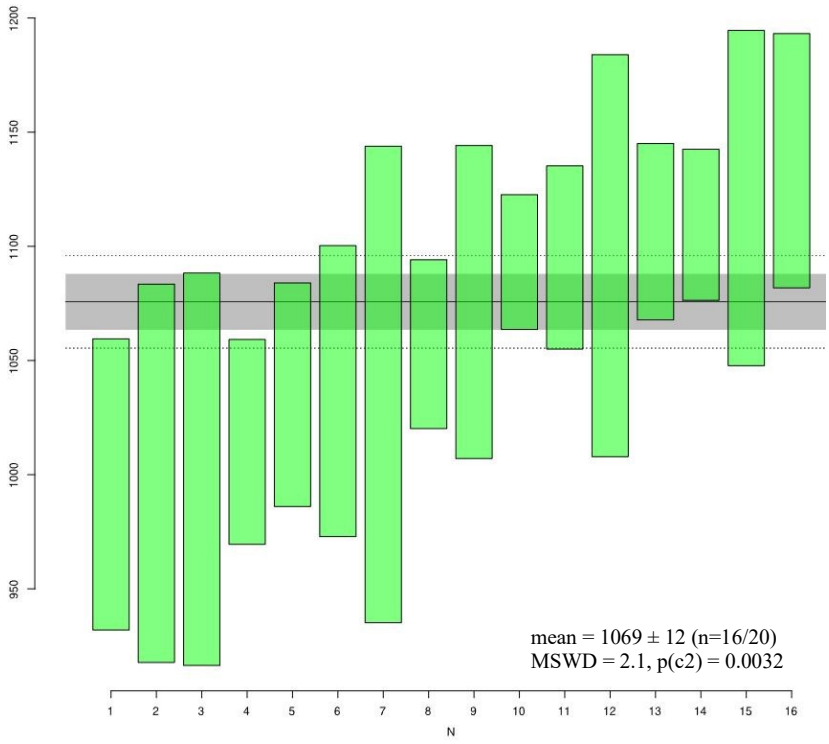

LOR02

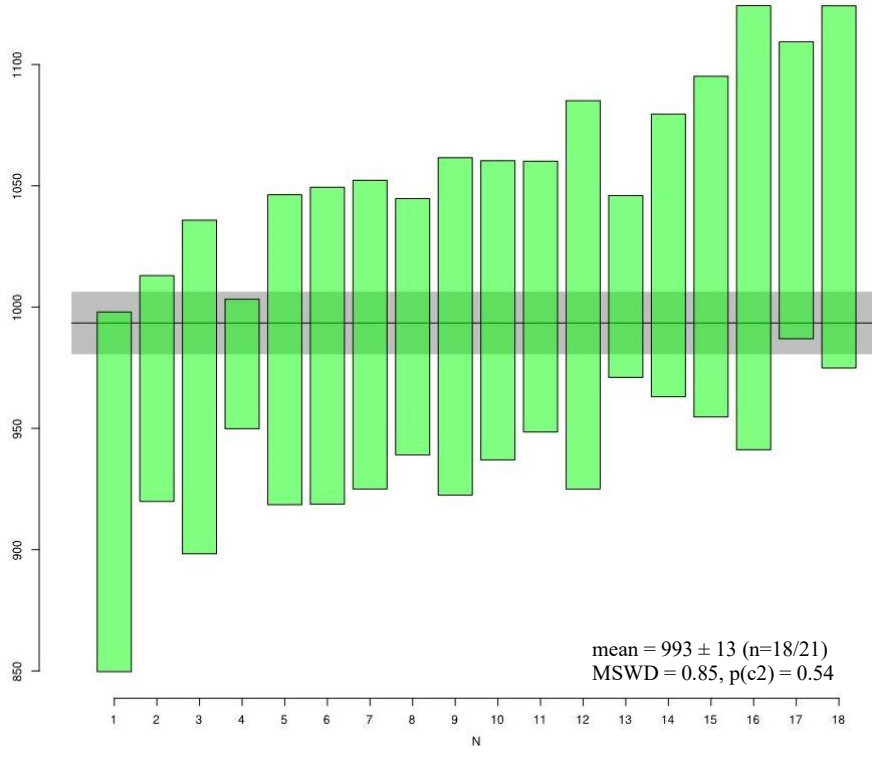

\\

Appendix 2.3.3 µXRF-maps, combining P (white), Ti (blue) and Fe (green), showing the different proportions of oxides and apatite from the Lac à l'Orignal Fe-Ti-P mineralized zone. Ilmenite is blue, where as hematite-rich part of ilmenite is cyan. Magnetite is bright green. Orthopyroxene/biotite is dark green

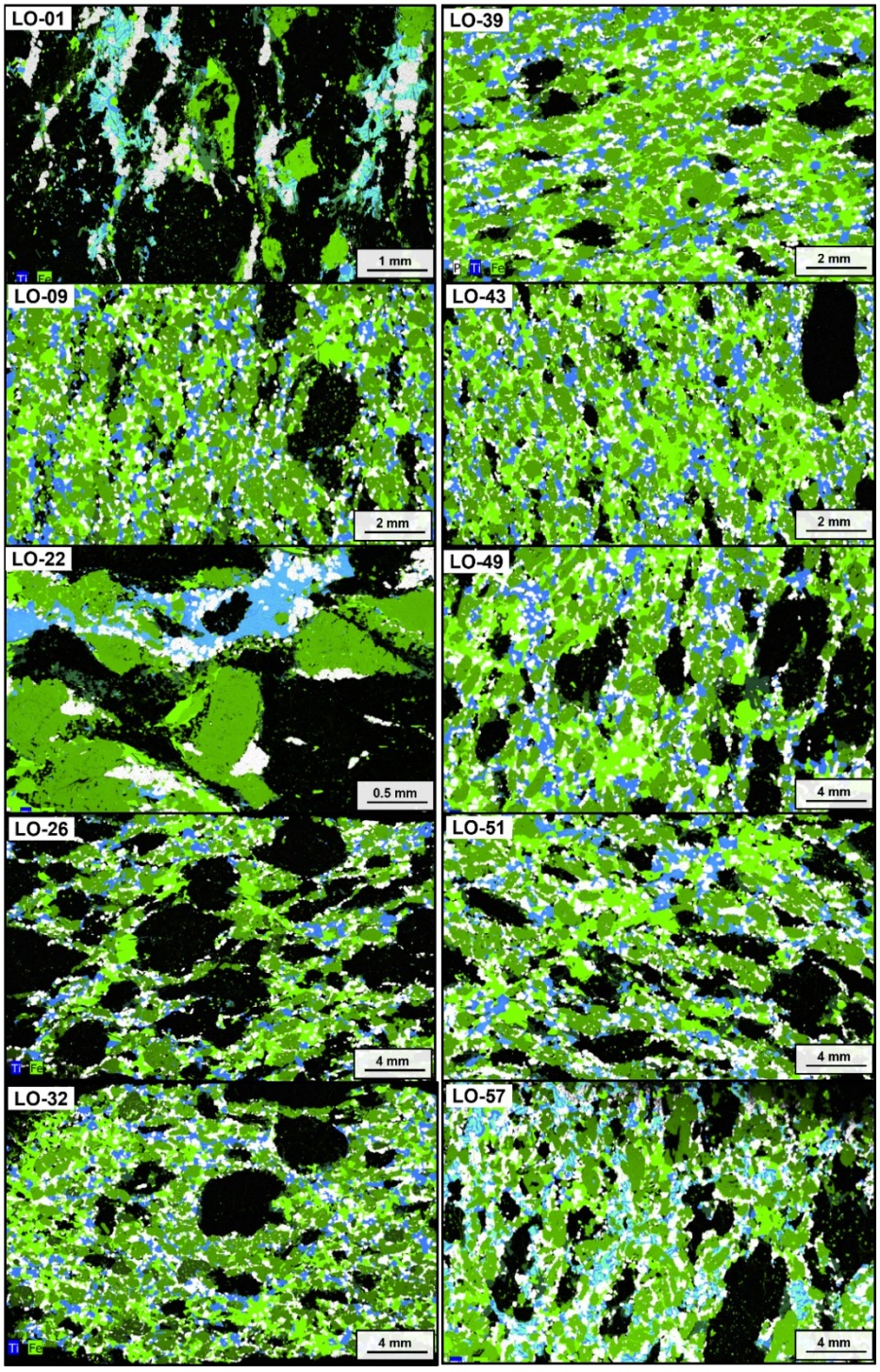

Appendix 2.3.4 Stratigraphic variation for selected whole-rock major element compositions in hole LO-14-21. The brownish horizon represents the host-anorthosite. Red lines indicating the oxide changing from Hm-ilmenite to Fe-poor ilmenite towards the core of the intrusion. Mineral abbreviations: ap = apatite

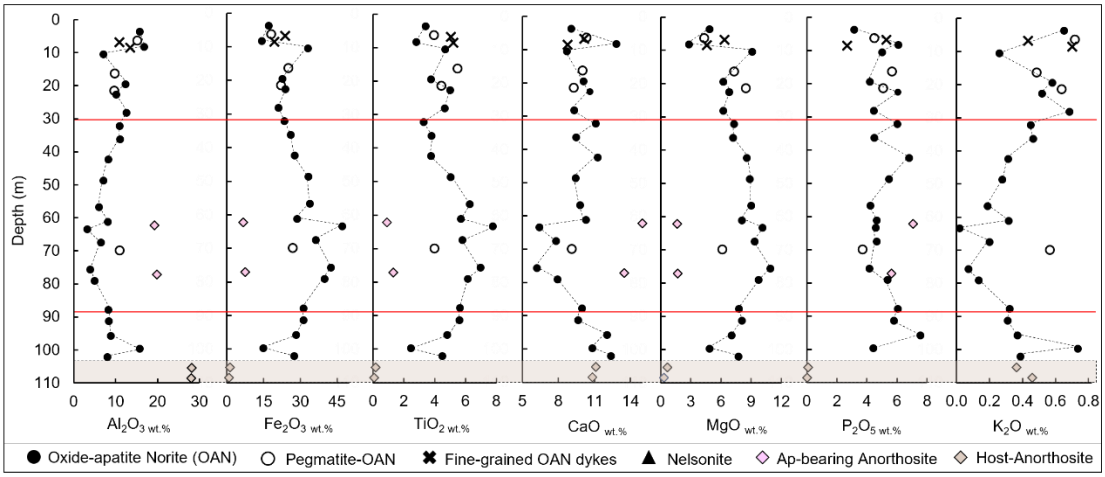

Appendix 2.3.5 Stratigraphic variation of plagioclase compositions in hole LO-14-21. The pink horizons represent the apatite-bearing anorthosite (pa-C) layers and the brownish horizon the host-anorthosite. Red lines indicating the oxide changing from Hm-ilmenite to Fe-poor ilmenite towards the core of the intrusion. Error bars=1 standard deviation and represents the natural variation within the thin section

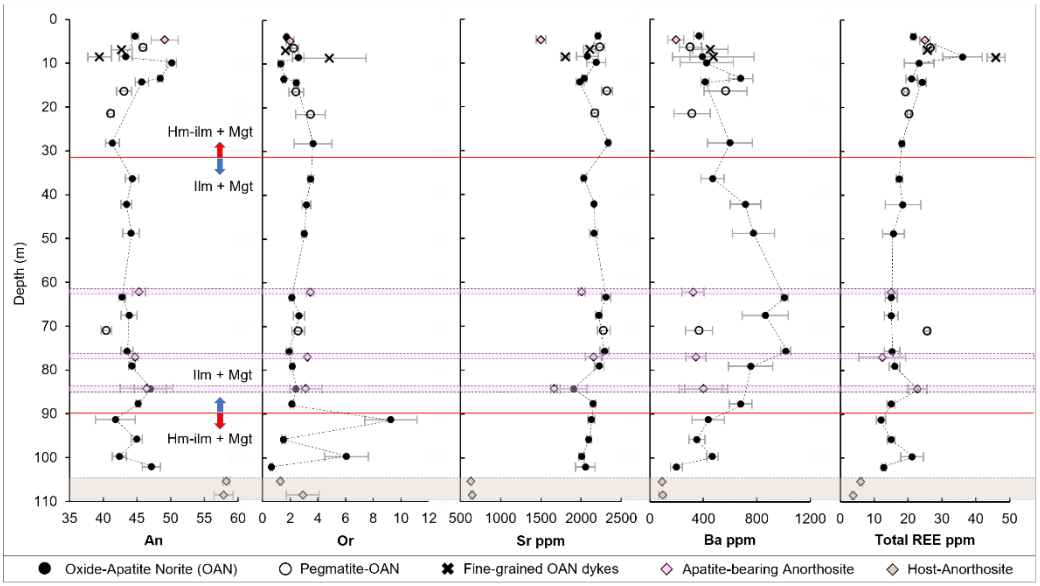

Appendix 2.3.6 Stratigraphic variation of ilmenite compositions in hole LO-14-21. The grey horizon represents the nelsonite (iap-C) layer. Red lines indicating the oxide changing from Hm-ilmenite to Fe-poor ilmenite towards the core of the intrusion. Error bars = 1 standard deviation and represents the natural variation within the thin section. Mineral abbreviations: ilm = ilmenite; mt = magnetite

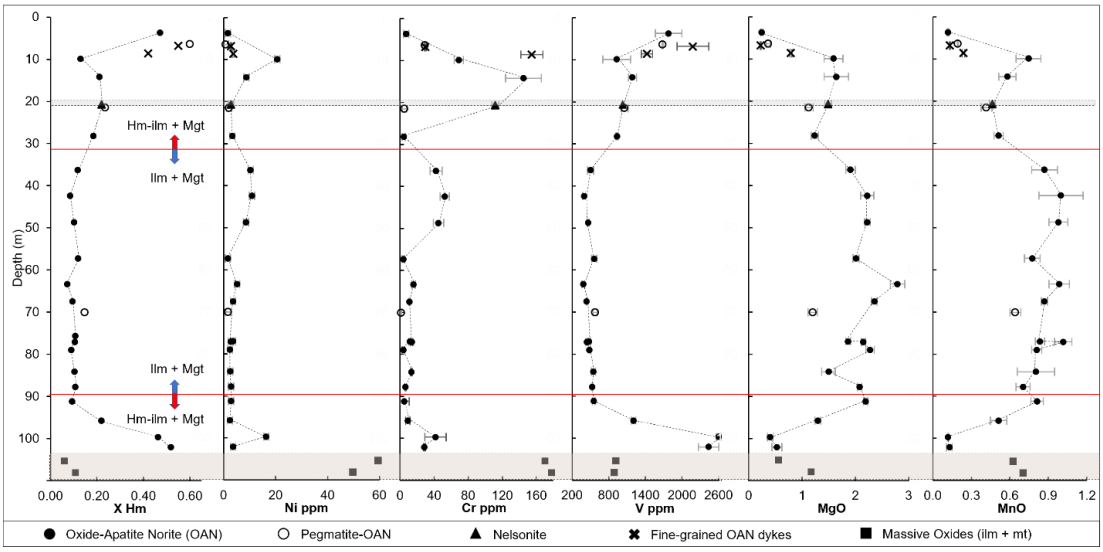

Appendix 2.3.7 Stratigraphic variation of magnetite compositions in hole LO-14-21. The grey horizon represents the nelsonite (iap-C) layer. Red lines indicating the oxide changing from Hm-ilmenite to Fe-poor ilmenite towards the core of the intrusion. Error bars = 1 standard deviation and represents the natural variation within the thin section. Mineral abbreviations: ilm = ilmenite; mt = magnetite

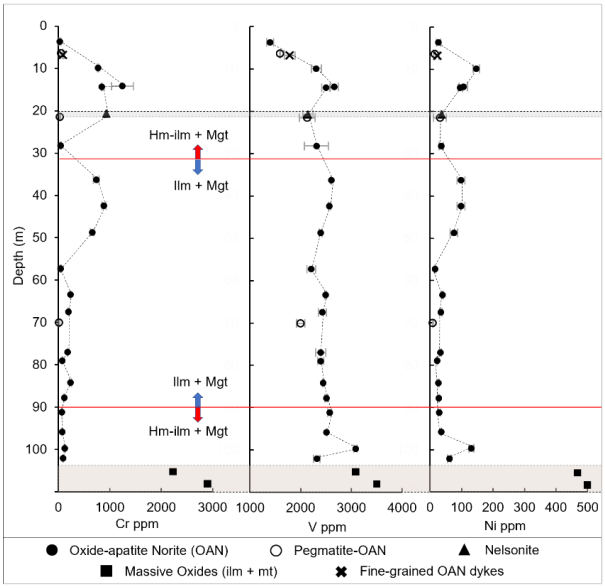

Appendix 2.3.8 Stratigraphic variation of apatite trace element compositions in hole LO-14-21. The grey horizon represents the nelsonite (iap-C) layer, the pink horizons represent the apatite-bearing anorthosite (pa-C) layers and the brownish horizon the host-anorthosite (apatite-free). Red lines indicating the oxide changing from Hm-ilmenite to Fe-poor ilmenite towards the core of the intrusion. Error bars = 1 standard deviation and represents the natural variation within the thin section. Mineral abbreviations: ap = apatite

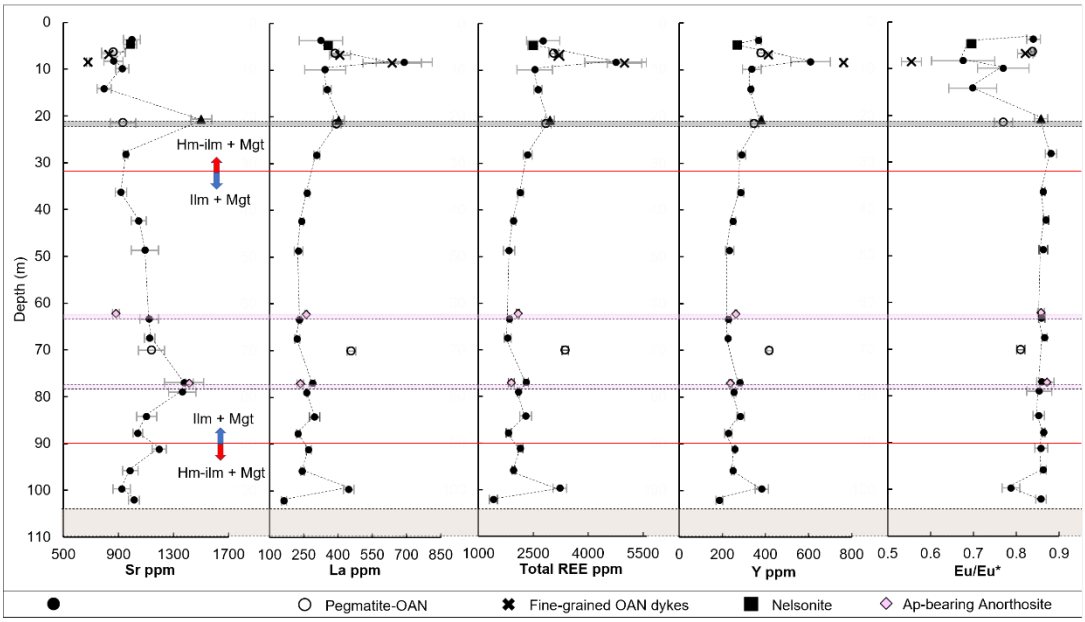

Appendix 2.3.9 Chondrite-normalized REE patterns (Sun and McDonough,1989) for fine-grained OAN dykes (samples LO-06 and LO-08) compared to calculated liquids from the inversion of apatite compositions of border (orange lines) and core (blue lines) samples. A. Calculated liquids applying partition coefficients for REE between apatite and melt (D_{REE}^{Ap}) from Charlier *et al*. (2005). B. Calculated liquids applying D_{REE}^{Ap} values obtained from the dyke sample LO-08

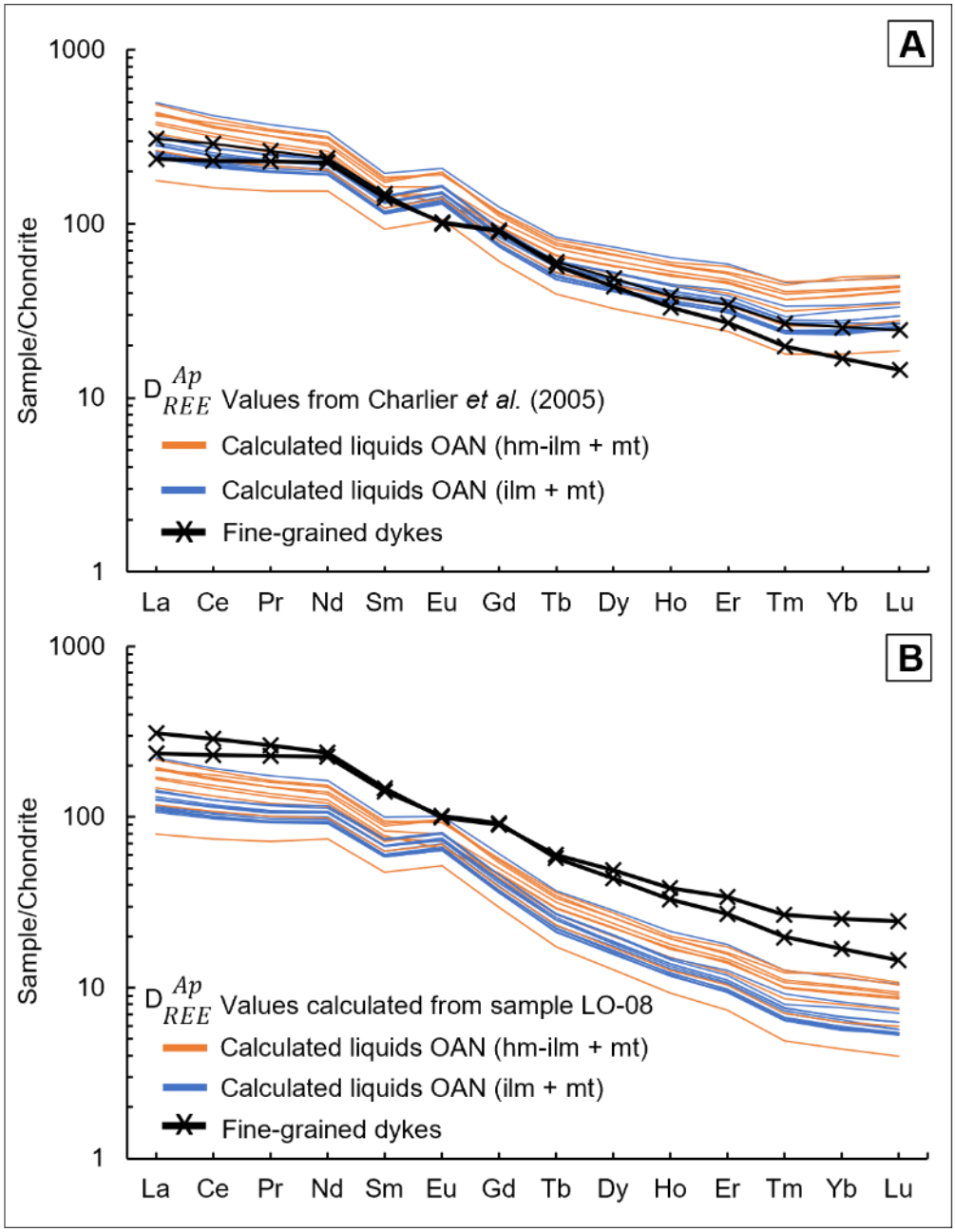

Appendix 2.3.10 Chondrite-normalized REE compositions of apatites (after Sun and McDonough, 1989) presenting a comparison between the Lac à l'Orignal Fe-Ti-P mineralization (this work) and the Grader Intrusion Fe-Ti-P (grey field) in the Havre Saint Pierre Anorthosite (after Charlier *et al.* 2008)

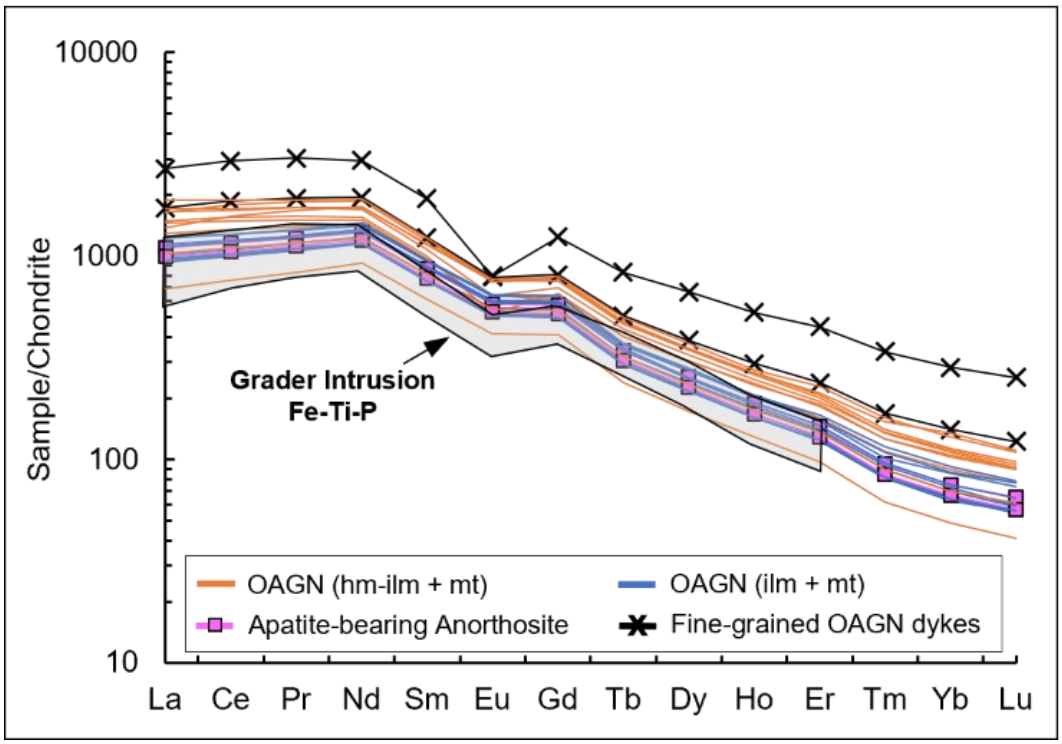

Appendix 2.3.11 Δ log fO_2 (relative to FMQ) versus X^{Opx}_{Fe} diagram (after Frost et al. 2010) showing the crystallization conditions of the fine-grained OAN dykes (probable parental melt) of the Lac à l'Orignal mineralization in comparison with two anorthosite plutons of different silicate/oxide assemblages: the olivine-magnetite-bearing Kiglapait Intrusion (Nain Plutonic Suite, Emslie, 1985) and the hemo-ilmenite-orthopyroxene-bearing Labrieville Anorthosite (Owens & Dymek, 2005). Calculations from the QUILF program of Anderson et al. (1993)

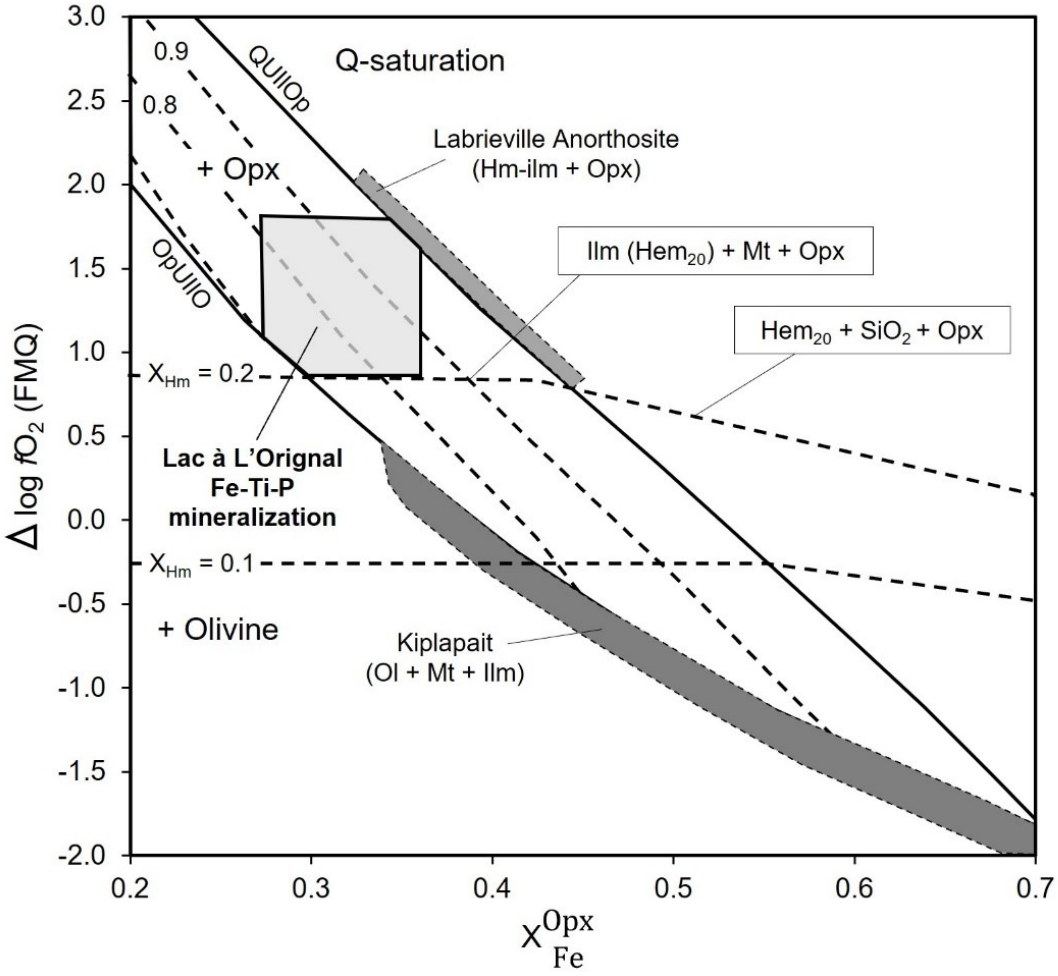

Appendix 2.3.12 Binary diagrams displaying the An content of plagioclase (as a proxy of fractional crystallization) versus the concentration of major and compatible elements (ppm) in (A) plagioclase, (B) apatite, (C) ilmenite and (D) magnetite from Lac à l'Orignal Fe-Ti-P mineralization (this work). Data from the Grader Intrusion Fe-Ti-P, Quebec (Charlier et al. 2008) plotted for comparison. An (mol.%) = 100 [Ca/(Ca+Na+K)] and Or (mol.%) = 100 [K/(Ca+Na+K)]. Mineral abbreviations: hm-ilm = hemo-ilmenite; ilm = ilmenite; mt = magnetite

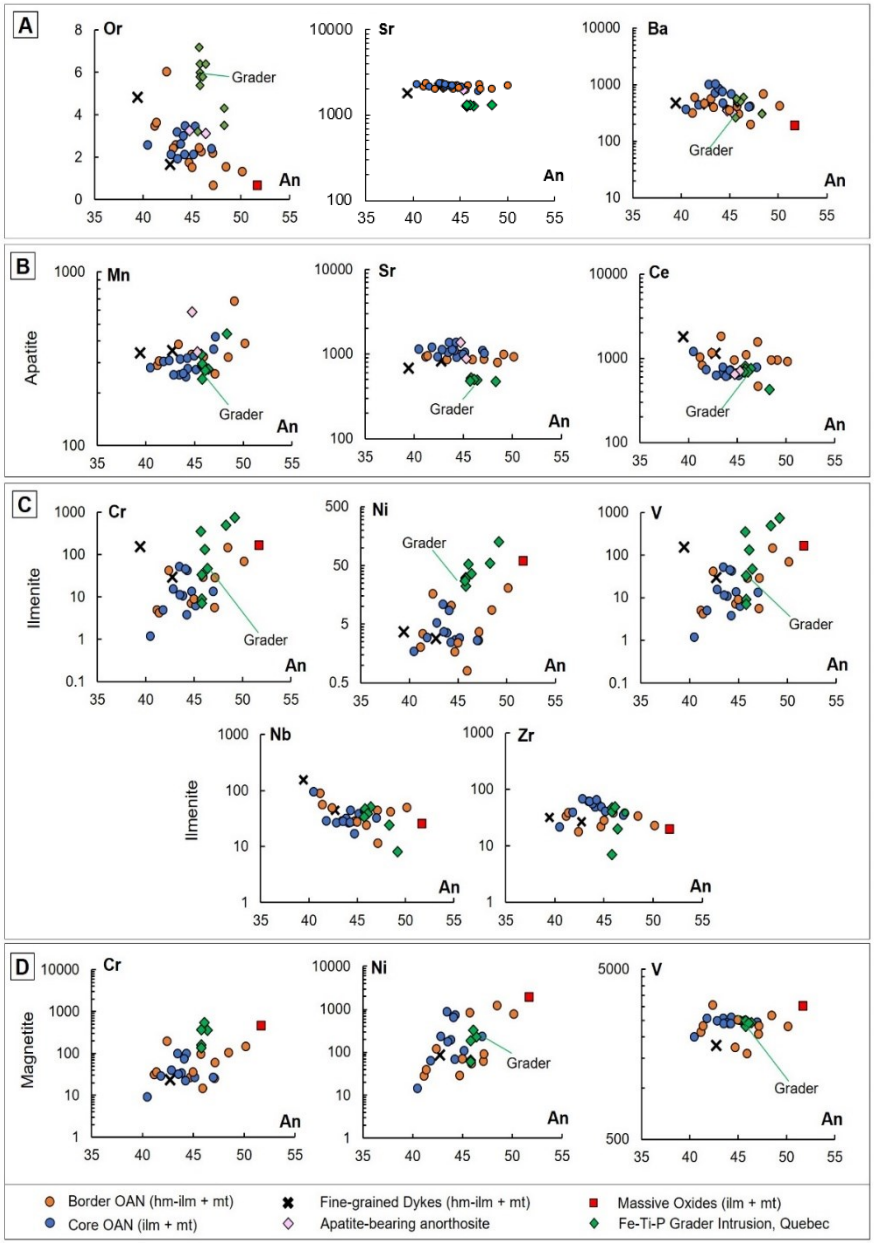

Appendix 2.3.13. Bulk whole-rock compositions of fine-grained lithologies projected into ternary diagrams for liquid immiscibility evaluation in the Sept Iles Layered Intrusion. A. Composition of the proposed liquid line of descent (after Charlier & Grove, 2012). B-E. Tie lines for various conjugate immiscible melt pairs (after Charlier *et al.* 2011). Grey fields of low-temperature immiscibility field in system leucite-fayalite-SiO2 (Roedder, 1978). B: Immiscible ferrobasalts and granitic liquids obtained from melt inclusion compositions in the Sept Iles layered intrusion (Namur et al. 2010). C: Experimental immiscible pairs in lunar basalts (Longhi, 1990). D: Natural immiscible pairs of glassy globules in tholeiitic basalts (Philpotts,1982). E: Experimental immiscible ferrobasalt and granitic liquids (Dixon and Rutherford, 1979). Grey projection of low-temperature immiscibility field in system leucite-fayalite-SiO2 (Roedder, 1978)

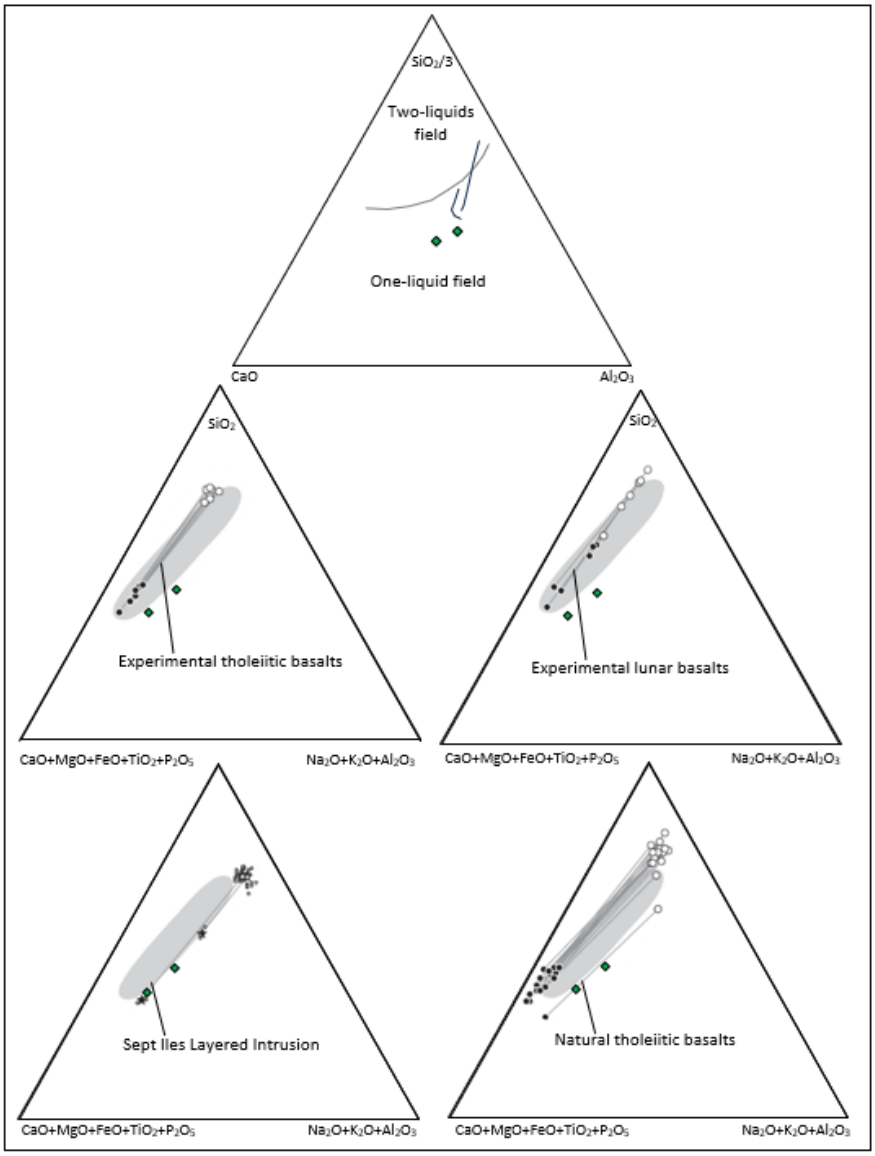

APPENDIX 3.1 SUPPLEMENTARY TABLES (CHAPTER 3)

Appendix 3.1.1 Whole-rock reference materials (separate excel sheet)

Appendix 3.1.2 Mineral chemistry reference materials (separate excel sheet)

Appendix 3.1.3 Petrographic modal proportions

Sample	Depth (m)	Location	UTM Coordinates		Lithology	Modal Proportions (%)										Ilmenite/Magnetite ratio
			E	N		Plagioclase	OPX	Hemo-ilmenite	Ilmenite	Magnetite	Al-spinel	Apatite	K-Feldspar	Quartz	Biotite	
20PM04A	-	Outcrop	387222	5438777	Medium-grained OAN	30	27	15	-	15	1	10			2	1.0
20PM04B	-	Outcrop	387222	5438777	Massive Oxides	-	-	-	40	55	5	-			-	-
20PM05A	-	Outcrop	388808	5438818	Massive Oxides	-	-	95			5	-			-	-
20PM05B	-	Outcrop	388808	5438818	Semi-massive Oxides	45	-	50			2	-			3	-
20PM05C	-	Outcrop	388808	5438818	Anorthosite	99	-	<1			-	-			-	-
20PM06A	-	Outcrop	388751	5438533	Medium-grained OAN	25	35	25		5	-	10			<1	5.0
20PM06B	-	Outcrop	388751	5438533	Medium-grained OAN	35	35	20		5	-	10			<1	4.0
20PM07	-	Outcrop	388943	5438922	Nelsonite	5	15	-	25	25	<1	30			-	-
20PM08A	-	Outcrop	389447	5439789	Anorthosite	80	10	-			<1	1			-	-
20PM08B1	-	Outcrop	389447	5439789	Medium-grained OAN	20	30	15		15	-	10			<1	1.0
20PM08B2	-	Outcrop	389447	5439789	Medium-grained OAN	25	25	15		15	-	10			<1	1.0
20PM17	-	Outcrop	387724	5438757	Anorthosite	99	-	<1			-				-	-
20PM18A	-	Outcrop	388631	5438801	Anorthosite	95	2	3			-				-	-
20PM18B	-	Outcrop	388631	5438801	Medium-grained OAN	45	35	10		5	-	5			<1	2.0
20PM19A	-	Outcrop	387838	5441789	Fine-grained ferrodiorite	80	10	5		2	-	3			<1	2.5
20PM19B	-	Outcrop	387838	5441789	Fine-grained jotunite	55	15	5		5	-	5	10	5	<1	1.0
MX102-3	13.5	Borehole MX-102	389229	5439206	Fine-grained ferrodiorite	50	30	8		2	-	10			<1	4.0
MX102-5	21.0	Borehole MX-102	389229	5439206	Medium-grained OAN	50	30	8		5	-	7			<1	1.6
MX105-1	0.5	Borehole MX-105	389685	5439902	Medium-grained OAN	40	35	8		2	-	15			<1	4.0
MX106-1	5.0	Borehole MX-106	389564	5439722	Medium-grained OAN	65	10	8		5	-	12			<1	1.6
MX108-6		Borehole MX-108	388813	5438656	Semi-massive Oxides	30	5	60		5	-				-	12.0

MX108-4	12.0	Borehole MX-108	388813	5438656	Fine-grained OAN	20	35	27		3	-	15			<1	9.0
MX-109-2		Borehole MX-109	388516	5438567	Semi-massive Oxides	30	-	35	2	28	2	3			-	1.3

Appendix 3.1.3 (Cont.) Petrographic modal proportions

Sample	Depth (m)	Location	UTM Coordinates		Lithology	Modal Proportions (%)										Ilmenite/Magnetite ratio
			E	N		Plagioclase	OPX	Hemo-ilmenite	Ilmenite	Magnetite	Al-spinel	Apatite	K-Feldspar	Quartz	Biotite	
MX114-1	8.5	Borehole MX-114	388920	5438795	Fine-grained ferrodiorite	40	30	15		5	-	10			<1	3.0
MX115	16.5	Borehole MX-115	388860	5438790	Semi-massive Oxides	17	5	60	3	15	-				-	4.0
MX118	4.0	Borehole MX-118	388705	5438323	Massive Oxides	2	-	95	3		-				-	-
MX123-1	0.5	Borehole MX-123	388748	5438622	Massive Oxides	3	-	95	2		-				-	-
CM1001A	-	Outcrop	389880	5442740	Fine-grained ferrodiorite	50	30	10			-	10			<1	-
CM1007	-	Outcrop	390250	5442660	Medium-grained OAN	55	30	5		3	-	7			<1	1.7
CM1013	-	Outcrop	390292	5442830	Medium-grained OAN	65	20	5		2	-	8			<1	2.5
CM1036	-	Outcrop	389499	5441083	Medium-grained OAN		-	100			-				<1	-
CM1038	-	Outcrop	389712	5441016	Medium-grained OAN	30	40	15			-	15			<1	-
CM1045	-	Outcrop	389678	5439869	Medium-grained OAN	50	35	8		2	-	5			<1	4.0
CM1047	-	Outcrop	389679	5439870	Medium-grained OAN	45	30	2		8	-	15			<1	0.3
CM1050	-	Outcrop	389607	5439789	Medium-grained OAN	25	30	15		10	-	20			<1	1.5
CM1051	-	Outcrop	387305	5438687	Medium-grained OAN	60	20	7		3	-	10			<1	2.3
CM1052	-	Outcrop	389536	5439689	Medium-grained OAN	50	30	5		5	-	10			<1	1.0
CM1053B	-	Outcrop	389391	5439579	Medium-grained OAN	30	50	3		7	-	10			<1	0.4
CM1060	-	Outcrop	389030	5439320	Fine-grained ferrodiorite	55	25	5		5	-	10			<1	1.0
CM1062	-	Outcrop	389085	5438894	Anorthosite	99	-	1			-	<1			-	-
CM1063A	-	Outcrop	389132	5439027	Medium-grained OAN	60	30	5			-	5			-	-
CM1064	-	Outcrop	388970	5438870	Nelsonite	5	5	-	35	30	-	25			-	-
CM1067	-	Outcrop	388900	5438700	Nelsonite	5	5	-	35	35	-	20			-	-
CM1071	-	Outcrop	388845	5438647	Anorthosite	95	3	2	-	-	-	<1			-	-
CM1074	-	Outcrop	388659	5438196	Anorthosite	95	3	2	-	-	-	<1			-	-

CM1075	-	Outcrop	388707	5438593	Anorthosite	90	5	1	-	1	-	3			-	1.0
CM1076B	-	Outcrop	388579	5438578	Fine-grained ferrodiorite	55	25	5	-	5	-	10			<1	1.0
CM1110	-	Outcrop	389340	5440421	Fine-grained ferrodiorite	60	25	4	-	4	-	7			<1	1.0

"CM" samples from Morisset (2001) by XRF

Appendix 3.1.4 Complete LA-ICP-MS whole-rock results

Sample	Depth (m)	Location	UTM-E	UTM-N	Lithology	Oxide Mineralogy	SiO_2	TiO_2	Al_2O_3	Fe_2O_{3t}	MnO	MgO	CaO	Na_2O	K_2O	P_2O_5	LOI	Total	^{45}Sc	^{51}V
20PM04A	-	Surface outcrop	387222	5438777	Medium-grained OAN	Ilm + Mt	33.2	4.9	11.6	24.9	0.2	5.9	10.6	2.2	0.5	5.9	0.0	100.0	14.6	526.2
20PM04B	-	Surface outcrop	387222	5438777	Massive Oxides	Ilm + Mt	0.6	10.7	5.0	81.3	0.2	0.9	0.4	0.0	0.0	0.1	0.0	100.0	11.6	2541.2
20PM05A	-	Surface outcrop	388790	5438625	Massive Oxides	Hm-Ilm	0.6	33.2	1.1	61.2	0.1	2.2	0.6	0.0	0.1	0.2	0.0	100.0	46.2	1962.2
20PM05B	-	Surface outcrop	388790	5438625	Semi-massive Oxides	Hm-Ilm + Mt	32.9	13.5	15.8	25.9	0.1	2.4	5.2	3.1	0.8	0.1	0.0	100.0	19.5	777.2
20PM05C	-	Surface outcrop	388790	5438625	Anorthosite	-	56.0	0.3	24.9	1.8	0.0	1.1	7.2	4.8	1.2	0.1	2.6	100.0	2.5	11.9
20PM06A		Surface outcrop	388751	5438533	Medium-grained OAN	Hm-Ilm + Mt	24.7	10.4	3.2	40.7	0.2	10.4	5.7	0.3	0.1	4.1	0.0	100.0	26.7	870.9
20PM06B	-	Surface outcrop	388751	5438533	Medium-grained OAN	Hm-Ilm + Mt	26.4	10.3	4.6	36.6	0.2	9.1	6.5	0.7	0.1	4.3	1.1	100.0	29.8	722.7
20PM07	-	Surface outcrop	388943	5438922	Nelsonite	Ilm + Mt	4.9	11.2	4.0	56.4	0.2	2.4	11.2	0.3	0.1	8.8	0.0	100.0	17.9	1411.8
20PM08A	-	Surface outcrop	389447	5439789	Anorthosite	-	54.1	0.4	20.8	5.2	0.1	4.2	8.2	4.5	0.8	0.2	1.4	100.0	13.5	44.5
20PM08B1	-	Surface outcrop	389447	5439789	Medium-grained OAN	Hm-Ilm + Mt	29.9	7.4	4.2	33.2	0.4	9.4	10.5	0.9	0.5	3.7	-0.4	100.0	62.5	340.6
20PM08B2	-	Surface outcrop	389447	5439789	Medium-grained OAN	Hm-Ilm + Mt	37.6	5.1	10.3	23.0	0.3	7.4	10.5	2.0	0.7	3.0	-1.5	100.0	49.3	227.9
20PM17	-	Surface outcrop	387724	5438757	Anorthosite	-	56.0	0.3	26.3	1.3	0.0	0.2	9.4	5.1	1.0	0.4	0.0	100.0	2.5	19.2
20PM18A	-	Surface outcrop	388631	5438801	Anorthosite	-	55.1	0.8	23.5	3.2	0.0	0.8	8.0	5.0	1.3	0.5	1.6	100.0	5.8	47.5
20PM18B	-	Surface outcrop	388631	5438801	Medium-grained OAN	Hm-Ilm + Mt	39.8	6.5	10.5	23.5	0.2	4.7	8.3	2.6	0.8	2.9	0.1	100.0	27.8	349.6
20PM19A	-	Surface outcrop	387838	5441789	Fine-grained ferrodiorite	Hm-Ilm + Mt	51.8	1.3	21.7	6.4	0.1	1.5	8.5	4.7	1.3	0.8	1.9	100.0	9.9	71.3
20PM19B	-	Surface outcrop	387838	5441789	Fine-grained jotunite	Hm-Ilm + Mt	58.0	2.0	14.8	9.4	0.1	2.1	5.5	3.1	3.5	1.4	0.0	100.0	19.1	99.5
MX102-3	13.5	Borehole MX-102	389229	5439206	Fine-grained ferrodiorite	Hm-Ilm + Mt	40.4	4.6	12.5	19.6	0.2	5.5	9.1	2.9	0.8	3.7	0.7	100.0	35.0	337.2
MX102-5	21.0	Borehole MX-102	389229	5439206	Medium-grained OAN	Hm-Ilm + Mt	38.0	4.7	12.1	21.2	0.3	6.4	10.7	2.3	0.6	3.7	0.1	100.0	46.2	182.8
MX105-1	0.5	Borehole MX-105	389685	5439902	Medium-grained OAN	Hm-Ilm + Mt	36.0	6.0	9.9	24.2	0.3	6.1	10.8	2.0	0.4	4.0	0.4	100.0	48.9	313.7
MX106-1	5.0	Borehole MX-106	389564	5439722	Medium-grained OAN	Hm-Ilm + Mt	38.1	4.4	15.1	18.6	0.1	4.2	10.5	3.0	0.6	4.5	0.9	100.0	24.2	394.6
MX108-4	12.0	Borehole MX-108	388813	5438656	Fine-grained-OAN	Hm-Ilm + Mt	22.9	13.4	2.2	42.2	0.3	11.3	4.3	0.1	0.0	2.3	1.1	100.0	35.0	1118.7
MX108-6	20.0	Borehole MX-108	388813	5438656	Semi-massive Oxides	Hm-Ilm + Mt	15.3	23.6	6.8	44.8	0.2	3.6	3.8	1.0	0.3	0.5	-0.4	100.0	32.1	1601.6

MX-108-8	31.0	Borehole MX-108	388813	5438656	Anorthosite	-	54.8	0.3	26.1	1.7	0.0	0.4	8.3	5.0	1.2	0.1	2.1	100.0	19.6	14.1

Appendix 3.1.4. (Cont.) Complete LA-ICP-MS whole-rock results

Sample	Depth (m)	Location	Lithology	Oxide Mineralogy	^{53}Cr	^{59}Co	^{60}Ni	^{63}Cu	^{66}Zn	^{69}Ga	^{85}Rb	^{88}Sr	^{89}Y	^{90}Zr	^{93}Nb	^{137}Ba	^{139}La	^{140}Ce
20PM04 A	-	Surface outcrop	Medium-grained OAN	Ilm + Mt	110.9	57.7	47.6	31.7	189.0	24.8	3.7	882.1	30.4	56.5	3.3	464.8	32.4	83.3
20PM04 B	-	Surface outcrop	Massive Oxides	Ilm + Mt	1877.9	165.8	524.6	15.7	873.6	74.8	BelowLOD	13.6	0.8	21.6	4.9	17.6	0.7	1.5
20PM05 A	-	Surface outcrop	Massive Oxides	Hm-Ilm	1488.6	114.5	184.9	12.4	218.7	18.3	0.7	13.1	2.0	337.5	30.9	26.6	2.3	5.1
20PM05 B	-	Surface outcrop	Semi-massive Oxides	Hm-Ilm + Mt	653.9	109.1	272.4	95.1	100.8	21.5	5.1	941.9	2.6	208.0	12.1	587.5	6.7	13.9
20PM05 C	-	Surface outcrop	Anorthosite	-	26.6	4.3	33.5	13.4	54.6	19.0	7.3	1379.0	3.1	17.5	0.9	606.3	12.6	23.8
20PM06 A		Surface outcrop	Medium-grained OAN	Hm-Ilm + Mt	58.8	127.7	41.3	44.1	347.0	22.6	0.6	168.0	19.1	154.6	6.1	48.1	16.4	44.8
20PM06 B	-	Surface outcrop	Medium-grained OAN	Hm-Ilm + Mt	50.8	46.2	34.0	37.3	266.2	19.5	3.1	298.9	20.7	82.2	5.9	102.0	17.4	47.4
20PM07	-	Surface outcrop	Nelsonite	Ilm + Mt	208.7	189.4	319.9	136.6	594.4	43.9	1.2	339.8	59.7	237.7	9.7	121.6	65.0	167.3
20PM08 A	-	Surface outcrop	Anorthosite	-	86.7	19.2	32.0	2.9	77.7	21.4	6.2	762.8	14.3	75.3	3.6	413.0	31.4	61.9
20PM08 B1	-	Surface outcrop	Medium-grained OAN	Hm-Ilm + Mt	23.2	57.3	26.6	25.8	605.0	26.5	3.5	294.6	52.5	212.8	6.4	171.3	33.4	94.9
20PM08 B2	-	Surface outcrop	Medium-grained OAN	Hm-Ilm + Mt	20.2	41.2	24.4	19.5	314.9	27.2	8.4	774.7	46.6	138.0	5.0	703.5	161.6	268.3
20PM17	-	Surface outcrop	Anorthosite	-	88.0	3.9	25.9	8.1	16.7	24.1	5.1	1975.5	7.2	31.5	1.3	811.5	13.2	28.5
20PM18 A	-	Surface outcrop	Anorthosite	-	20.1	8.9	20.0	9.1	35.5	23.3	9.7	1588.7	10.1	92.9	4.9	1016.0	20.5	43.1
20PM18 B	-	Surface outcrop	Medium-grained OAN	Hm-Ilm + Mt	16.6	30.7	21.0	28.1	228.2	21.9	4.9	720.9	47.9	208.5	29.7	594.4	43.0	108.6
20PM19 A	-	Surface outcrop	Fine-grained ferrodiorite	Hm-Ilm + Mt	23.0	12.1	13.1	5.1	101.2	25.4	10.2	1637.0	17.6	70.7	7.0	1364.9	28.1	62.5
20PM19 B	-	Surface outcrop	Fine-grained jotunite	Hm-Ilm + Mt	19.2	15.6	11.8	10.7	140.9	29.3	46.0	1034.2	61.9	1173.1	25.3	3074.9	101.6	235.0
MX102-3	13.5	Borehole MX-102	Fine-grained ferrodiorite	Hm-Ilm + Mt	22.1	53.7	55.8	34.2	285.5	25.2	7.1	1001.1	59.6	255.5	18.0	1047.4	73.6	179.8
MX102-5	21.0	Borehole MX-102	Medium-grained OAN	Hm-Ilm + Mt	6.4	40.5	10.4	12.1	272.4	24.2	2.3	1071.3	50.5	175.2	5.4	1042.3	39.8	108.8
MX105-1	0.5	Borehole MX-105	Medium-grained OAN	Hm-Ilm + Mt	2.6	46.6	5.5	13.3	247.0	24.6	2.1	971.9	51.6	243.8	11.3	616.8	45.7	120.9
MX106-1	5.0	Borehole MX-106	Medium-grained OAN	Hm-Ilm + Mt	14.5	58.7	64.7	60.0	177.3	25.5	4.3	1244.9	35.5	206.0	8.2	806.0	44.1	108.0
MX108-4	12.0	Borehole MX-108	Fine-grained-OAN	Hm-Ilm + Mt	142.2	200.0	318.5	138.7	278.2	17.1	0.2	77.6	12.5	206.3	10.0	31.6	9.1	25.3
MX108-6	20.0	Borehole MX-108	Semi-massive Oxides	Hm-Ilm + Mt	887.8	128.8	377.9	108.3	154.5	17.8	2.7	354.7	8.8	297.1	20.7	302.7	11.2	27.2
MX-108-8	31.0	Borehole MX-108	Anorthosite	-	4.0	3.4	18.1	14.7	21.8	24.6	6.1	1518.9	2.9	13.4	1.3	1054.9	11.8	22.2

Appendix 3.1.4 (Cont.) Complete LA-ICP-MS whole-rock results

Sample	Depth (m)	Location	Lithology	Oxide Mineralogy	^{141}Pr	^{146}Nd	^{147}Sm	^{153}Eu	^{157}Gd	^{159}Tb	^{163}Dy	^{165}Ho	^{166}Er	^{169}Tm	^{172}Yb	^{175}Lu	^{174}Hf	^{208}Pb	Eu/Eu*
20PM04A	-	Surface outcrop	Medium-grained OAN	Ilm + Mt	12.9	64.8	14.1	4.0	12.2	1.3	6.6	1.1	2.5	0.3	1.5	0.2	1.7	3.3	0.9
20PM04B	-	Surface outcrop	Massive Oxides	Ilm + Mt	0.6	1.0	0.2	0.0	0.2	0.0	0.1	0.0	0.1	0.0	0.1	0.0	1.0	0.2	0.6
20PM05A	-	Surface outcrop	Massive Oxides	Hm-Ilm	0.8	4.0	0.9	0.2	0.8	0.1	0.4	0.1	0.3	0.0	0.2	0.0	11.6	0.4	0.6
20PM05B	-	Surface outcrop	Semi-massive Oxides	Hm-Ilm + Mt	1.7	7.1	1.2	1.0	1.0	0.1	0.7	0.1	0.2	0.0	0.3	0.0	5.6	3.0	2.5
20PM05C	-	Surface outcrop	Anorthosite	-	2.8	11.0	1.7	1.4	1.2	0.1	0.7	0.1	0.3	0.0	0.2	0.0	0.4	9.9	2.9
20PM06A		Surface outcrop	Medium-grained OAN	Hm-Ilm + Mt	7.1	37.7	8.2	2.1	7.6	0.8	4.2	0.7	1.6	0.2	1.1	0.1	3.8	0.5	0.8
20PM06B	-	Surface outcrop	Medium-grained OAN	Hm-Ilm + Mt	7.6	40.7	9.1	2.4	8.1	0.9	4.5	0.8	1.8	0.2	1.1	0.1	2.4	0.8	0.8
20PM07	-	Surface outcrop	Nelsonite	Ilm + Mt	25.2	126.5	26.5	6.4	22.6	2.6	13.0	2.3	5.3	0.6	3.2	0.4	6.4	1.7	0.8
20PM08A	-	Surface outcrop	Anorthosite	-	7.5	29.6	5.4	2.5	4.1	0.5	3.0	0.6	1.5	0.2	1.3	0.2	2.1	11.6	1.6
20PM08B1	-	Surface outcrop	Medium-grained OAN	Hm-Ilm + Mt	15.7	86.9	20.2	5.8	18.5	2.2	11.9	2.0	4.7	0.5	3.0	0.4	5.9	6.0	0.9
20PM08B2	-	Surface outcrop	Medium-grained OAN	Hm-Ilm + Mt	30.0	118.0	21.2	6.0	17.6	2.0	10.7	1.8	4.2	0.5	2.6	0.4	3.9	19.2	1.0
20PM17	-	Surface outcrop	Anorthosite	-	3.8	17.0	3.1	1.5	2.5	0.3	1.6	0.3	0.7	0.1	0.4	0.0	0.7	4.6	1.6
20PM18A	-	Surface outcrop	Anorthosite	-	5.5	23.5	4.3	2.3	3.5	0.4	2.2	0.4	1.0	0.1	0.7	0.1	2.5	7.1	1.7
20PM18B	-	Surface outcrop	Medium-grained OAN	Hm-Ilm + Mt	16.0	75.6	16.8	4.6	14.7	1.8	10.2	1.8	4.7	0.6	3.5	0.5	6.0	5.7	0.9
20PM19A	-	Surface outcrop	Fine-grained ferrodiorite	Hm-Ilm + Mt	8.5	38.2	7.5	3.3	6.1	0.7	3.8	0.7	1.7	0.2	1.2	0.2	2.2	9.6	1.4
20PM19B	-	Surface outcrop	Fine-grained jotunite	Hm-Ilm + Mt	32.3	140.3	27.0	6.0	20.7	2.5	13.8	2.4	6.2	0.8	4.7	0.7	28.6	28.0	0.7
MX102-3	13.5	Borehole MX-102	Fine-grained ferrodiorite	Hm-Ilm + Mt	25.8	120.3	23.9	6.9	22.9	2.5	13.0	2.3	5.8	0.7	4.1	0.6	7.3	7.8	0.9
MX102-5	21.0	Borehole MX-102	Medium-grained OAN	Hm-Ilm + Mt	17.7	94.9	21.1	7.3	20.9	2.3	11.9	2.0	4.7	0.5	3.1	0.4	5.4	2.6	1.0
MX105-1	0.5	Borehole MX-105	Medium-grained OAN	Hm-Ilm + Mt	18.9	97.5	21.4	6.6	20.7	2.4	11.9	2.0	4.8	0.6	3.2	0.4	6.6	3.4	0.9
MX106-1	5.0	Borehole MX-106	Medium-grained OAN	Hm-Ilm + Mt	15.9	77.2	15.9	5.1	15.1	1.6	8.0	1.4	3.2	0.4	2.1	0.3	5.2	5.0	1.0
MX108-4	12.0	Borehole MX-108	Fine-grained-OAN	Hm-Ilm + Mt	4.2	22.1	5.1	1.3	4.9	0.5	2.5	0.5	1.2	0.1	0.7	0.1	5.6	0.4	0.8
MX108-6	20.0	Borehole MX-108	Semi-massive Oxides	Hm-Ilm + Mt	4.0	18.6	3.9	1.2	3.6	0.4	1.9	0.4	0.9	0.1	0.6	0.1	8.8	2.2	1.0
MX-108-8	31.0	Borehole MX-108	Anorthosite	-	2.6	10.2	1.6	2.5	1.7	0.1	0.7	0.1	0.3	0.0	0.2	0.0	0.4	6.8	4.7

Appendix 3.1.4 (Cont.) Complete LA-ICP-MS whole-rock results

Sample	Depth (m)	Location	UTM-E	UTM-N	Lithology	Oxide Mineralogy	SiO_2	TiO_2	Al_2O_3	Fe_2O_3 t	MnO	MgO	CaO	Na_2O	K_2O	P_2O_5	LOI	Total	^{45}Sc	^{51}V
MX-109-3	9.0	Borehole MX-109	388516	5438567	Massive Oxides	Hm-Ilm + Mt	6.0	23.5	4.0	61.3	0.2	3.0	1.3	0.4	0.1	0.1	-1.2	100.0	28.1	2098.3
MX109-7	35.0	Borehole MX-109	388516	5438567	Anorthosite	-	55.3	0.3	25.0	2.2	0.0	0.8	8.3	5.3	1.3	0.4	1.1	100.0	20.2	19.7
MX114-1	8.5	Borehole MX-114	388920	5438795	Fine-grained ferrodiorite	Hm-Ilm + Mt	28.0	6.5	8.8	32.4	0.3	5.4	9.8	1.6	0.4	6.0	0.8	100.0	29.7	661.9
MX-115	16.5	Borehole MX-115	388860	5438790	Semi-massive Oxides	Hm-Ilm + Mt	7.0	21.4	4.9	61.3	0.2	1.9	2.2	0.6	0.2	0.3	-1.1	100.0	28.3	2105.5
MX-117	13.5	Borehole MX-117	388833	5438709	Massive Oxides	Hm-Ilm + Mt	9.5	25.1	4.6	54.1	0.2	1.8	2.8	0.9	0.2	0.7	-1.3	100.0	40.7	1730.0
MX-118	4.0	Borehole MX-118	388705	5438323	Massive Oxides	Hm-ilm	7.1	29.7	4.2	54.5	0.2	2.4	1.3	0.6	0.1	0.0	-0.9	100.0	36.3	2013.8
MX-123	0.5	Borehole MX-123	388748	5438622	Massive Oxides	Hm-ilm	0.2	33.8	1.1	61.7	0.2	2.0	1.0	0.0	0.0	0.0	-1.9	100.0	39.3	2348.9
CM1001A	-	Surface outcrop	389880	5442740	Fine-grained ferrodiorite	Hm-ilm	46.8	3.1	13.5	14.9	0.2	4.3	7.7	3.2	2.0	2.4	0.2	98.1	-	113.1
CM1007	-	Surface outcrop	390250	5442660	Medium-grained OAN	Hm-Ilm + Mt	37.8	5.3	9.3	23.2	0.3	7.1	10.7	1.6	0.5	3.3	0.6	99.2	-	143.6
CM1013	-	Surface outcrop	390292	5442830	Medium-grained OAN	Hm-Ilm + Mt	36.3	5.1	10.0	21.3	0.3	6.5	11.2	1.8	0.5	3.8	0.4	96.8	-	141.4
CM1036	-	Surface outcrop	389499	5441083	Medium-grained OAN	Hm-ilm	46.7	2.9	16.7	13.6	0.2	5.4	8.3	3.2	0.7	1.7	0.5	99.3	-	168.4
CM1038	-	Surface outcrop	389712	5441016	Semi-massive Oxides	Hm-Ilm + Mt	25.6	18.0	3.9	40.6	0.3	8.7	1.5	0.2	0.1	0.1	0.7	99.0	-	703.8
CM1045	-	Surface outcrop	389678	5439869	Medium-grained OAN	Hm-Ilm + Mt	34.7	6.6	8.9	23.9	0.3	6.6	12.0	1.6	0.3	4.7	0.1	99.7	-	179.1
CM1047	-	Surface outcrop	389679	5439870	Medium-grained OAN	Hm-Ilm + Mt	32.9	4.6	11.0	26.1	0.2	5.5	10.9	1.7	0.6	5.4	1.0	99.1	-	354.2
CM1050	-	Surface outcrop	389607	5439789	Medium-grained OAN	Hm-Ilm + Mt	31.5	5.4	11.5	25.9	0.2	5.2	11.8	1.6	0.4	5.3	0.9	98.8	-	303.5
CM1052	-	Surface outcrop	389536	5439689	Medium-grained OAN	Hm-Ilm + Mt	33.0	5.9	8.9	28.8	0.3	8.3	9.0	1.1	0.3	4.0	0.0	99.6	-	366.2
CM1053A	-	Surface outcrop	389391	5439579	Medium-grained OAN	Hm-Ilm + Mt	35.6	5.5	10.0	23.3	0.3	7.0	11.6	1.6	0.4	3.4	0.2	98.8	-	77.2
CM1053	-	Surface outcrop	389391	5439579	Anorthosite	-	52.5	0.7	23.4	5.0	0.1	1.3	10.2	4.5	1.0	1.2	2.2	99.7	-	55.2

CM1053 B	-	Surface outcrop	389391	5439579	Medium-grained OAN	Hm-Ilm + Mt	40.4	3.7	13.0	19.2	0.3	5.2	10.7	2.9	0.7	3.4	1.3	99.4	-	148.0
CM1053 C	-	Surface outcrop	389391	5439579	Medium-grained OAN	Hm-Ilm + Mt	30.3	5.8	7.0	30.2	0.4	7.8	11.8	1.0	0.3	4.5	0.4	99.1	-	217.0
CM1056	-	Surface outcrop	389220	5439220	Medium-grained OAN	Hm-Ilm + Mt	41.0	3.8	14.1	16.5	0.2	5.2	11.5	2.6	0.7	3.3	0.2	98.9	-	45.6
CM1060	-	Surface outcrop	389030	5439320	Fine-grained ferrodiorite	Hm-Ilm + Mt	39.1	4.0	12.3	21.2	0.2	5.4	10.3	2.2	0.5	3.6	0.4	98.9	-	210.2

Appendix 3.1.4 (Cont.) Complete LA-ICP-MS whole-rock results

Sample	Depth (m)	Location	Lithology	Oxide Mineralogy	^{53}Cr	^{59}Co	^{60}Ni	^{63}Cu	^{66}Zn	^{69}Ga	^{85}Rb	^{88}Sr	^{89}Y	^{90}Zr	^{93}Nb	^{137}Ba	^{139}La	^{140}Ce
MX-109-3	9.0	Borehole MX-109	Massive Oxides	Hm-Ilm + Mt	1015.2	199.3	469.7	172.4	416.7	32.7	1.0	121.3	1.4	427.7	18.8	95.2	1.6	3.9
MX109-7	35.0	Borehole MX-109	Anorthosite	-	5.4	5.0	8.3	9.1	38.2	24.3	10.1	####	7.7	17.5	1.8	1084.5	16.0	33.7
MX114-1	8.5	Borehole MX-114	Fine-grained ferrodiorite	Hm-Ilm + Mt	40.1	83.2	70.7	47.1	398.9	30.5	1.7	779.6	56.5	360.9	12.7	486.9	64.6	164.2
MX-115	16.5	Borehole MX-115	Semi-massive Oxides	Hm-Ilm + Mt	1692.6	156.5	334.5	75.8	545.5	40.7	2.2	181.7	4.1	386.1	23.2	126.9	4.9	11.4
MX-117	13.5	Borehole MX-117	Massive Oxides	Hm-Ilm + Mt	1261.2	94.1	126.6	41.9	289.4	21.6	2.1	289.8	8.8	620.3	45.9	208.8	10.5	26.1
MX-118	4.0	Borehole MX-118	Massive Oxides	Hm-ilm	1555.7	121.5	240.5	35.5	268.9	19.9	0.9	160.4	1.5	476.0	29.8	103.0	1.9	4.1
MX-123	0.5	Borehole MX-123	Massive Oxides	Hm-ilm	1630.4	147.5	309.3	55.7	234.2	19.1	0.3	12.2	1.2	918.4	33.6	28.5	0.3	0.8
CM1001A	-	Surface outcrop	Fine-grained ferrodiorite	Hm-ilm	-	21.9	31.5	3.9	219.9	24.5	21.4	909.5	78.5	437.9	25.9	1991.6	-	170.6
CM1007	-	Surface outcrop	Medium-grained OAN	Hm-Ilm + Mt	-	16.2	35.2	23.3	251.4	13.7	14.9	881.2	60.3	193.8	18.0	634.8	-	101.3
CM1013	-	Surface outcrop	Medium-grained OAN	Hm-Ilm + Mt	-	12.9	37.7	-1.2	199.3	14.0	13.2	903.5	59.4	210.6	16.3	659.2	-	100.2
CM1036	-	Surface outcrop	Medium-grained OAN	Hm-ilm	19.6	28.3	55.7	13.8	136.9	17.4	12.9	1170.9	23.4	136.8	12.1	736.2	24.4	56.5
CM1038	-	Surface outcrop	Semi-massive Oxides	Hm-Ilm + Mt	403.7	10.7	40.8	18.8	251.1	14.4	13.2	872.7	58.7	246.5	16.9	303.8	-	10.0
CM1045	-	Surface outcrop	Medium-grained OAN	Hm-Ilm + Mt	-	26.2	41.8	6.5	212.0	11.5	10.4	826.8	59.0	209.9	21.3	531.2	-	100.3
CM1047	-	Surface outcrop	Medium-grained OAN	Hm-Ilm + Mt	61.9	27.8	83.9	79.5	274.4	15.1	11.8	890.0	57.2	173.5	14.6	822.3	-	127.4
CM1050	-	Surface outcrop	Medium-grained OAN	Hm-Ilm + Mt	36.6	24.8	61.0	29.1	214.9	15.9	10.9	928.9	46.2	91.6	12.4	487.7	-	94.8
CM1052	-	Surface outcrop	Medium-grained OAN	Hm-Ilm + Mt	17.4	25.7	66.3	25.4	282.9	14.4	11.7	717.8	38.1	150.2	14.5	461.4	-	94.6
CM1053A	-	Surface outcrop	Medium-grained OAN	Hm-Ilm + Mt	-	-	-	-	-	-	-	-	-	-	-	1033.3	-	84.6
CM1053	-	Surface outcrop	Anorthosite	-	10.3	1.9	15.5	2.6	39.3	20.2	10.7	####	12.4	80.3	4.7	1194.0	18.6	36.1
CM1053B	-	Surface outcrop	Medium-grained OAN	Hm-Ilm + Mt	-	21.2	42.4	11.9	172.6	15.0	10.4	989.9	81.9	233.5	23.8	874.7	-	192.8
CM1053C	-	Surface outcrop	Medium-grained OAN	Hm-Ilm + Mt	-	24.4	57.7	12.4	346.5	9.4	11.4	622.8	59.8	150.7	12.9	550.8	-	84.1
CM1056	-	Surface outcrop	Medium-grained OAN	Hm-Ilm + Mt	-	16.0	36.6	5.1	193.9	17.3	9.8	####	52.5	285.6	10.2	1377.2	-	89.0
CM1060	-	Surface outcrop	Fine-grained ferrodiorite	Hm-Ilm + Mt	-	20.5	44.3	12.4	244.5	16.6	9.7	1013.5	63.7	194.8	19.7	870.3	-	132.0

Appendix 3.1.4 (Cont.) Complete LA-ICP-MS whole-rock results

Sample	Depth (m)	Location	Lithology	Oxide Mineralogy	^{141}Pr	^{146}Nd	^{147}Sm	^{153}Eu	^{157}Gd	^{159}Tb	^{163}Dy	^{165}Ho	^{166}Er	^{169}Tm	^{172}Yb	^{175}Lu	^{174}Hf	^{208}Pb	Eu/Eu*
MX-109-3	9.0	Borehole MX-109	Massive Oxides	Hm-Ilm + Mt	0.5	2.3	0.4	0.2	0.4	0.1	0.3	0.1	0.2	0.0	0.2	0.0	12.0	0.9	1.7
MX109-7	35.0	Borehole MX-109	Anorthosite	-	4.4	18.6	3.3	2.7	3.1	0.3	1.6	0.3	0.7	0.1	0.6	0.1	0.5	6.8	2.5
MX114-1	8.5	Borehole MX-114	Fine-grained ferrodiorite	Hm-Ilm + Mt	24.3	121.1	24.4	6.4	23.7	2.6	12.7	2.2	5.1	0.6	3.2	0.5	8.5	3.1	0.8
MX-115	16.5	Borehole MX-115	Semi-massive Oxides	Hm-Ilm + Mt	1.6	7.7	1.5	0.6	1.4	0.2	0.9	0.2	0.4	0.0	0.3	0.1	10.3	1.2	1.2
MX-117	13.5	Borehole MX-117	Massive Oxides	Hm-Ilm + Mt	3.7	18.0	3.7	1.1	3.4	0.4	2.0	0.3	0.9	0.1	0.7	0.1	16.9	2.1	0.9
MX-118	4.0	Borehole MX-118	Massive Oxides	Hm-ilm	0.5	2.2	0.4	0.3	0.4	0.0	0.3	0.1	0.2	0.0	0.3	0.0	13.8	0.9	2.0
MX-123	0.5	Borehole MX-123	Massive Oxides	Hm-ilm	0.1	0.6	0.1	0.0	0.1	0.0	0.2	0.1	0.2	0.0	0.3	0.0	21.6	0.3	1.1
CM1001A	-	Surface outcrop	Fine-grained ferrodiorite	Hm-ilm	-	-	-	-	-	-	-	-	-	-	-	-	-	35.1	-
CM1007	-	Surface outcrop	Medium-grained OAN	Hm-Ilm + Mt	-	-	-	-	-	-	-	-	-	-	-	-	-	30.6	-
CM1013	-	Surface outcrop	Medium-grained OAN	Hm-Ilm + Mt	-	-	-	-	-	-	-	-	-	-	-	-	-	27.7	-
CM1036	-	Surface outcrop	Medium-grained OAN	Hm-ilm	7.0	37.0	7.2	2.3	6.5	0.8	4.0	0.7	1.5	0.2	1.2	0.2	-	23.1	1.0
CM1038	-	Surface outcrop	Semi-massive Oxides	Hm-Ilm + Mt	-	-	-	-	-	-	-	-	-	-	-	-	-	26.6	-
CM1045	-	Surface outcrop	Medium-grained OAN	Hm-Ilm + Mt	-	-	-	-	-	-	-	-	-	-	-	-	-	28.6	-
CM1047	-	Surface outcrop	Medium-grained OAN	Hm-Ilm + Mt	-	-	-	-	-	-	-	-	-	-	-	-	-	32.7	-
CM1050	-	Surface outcrop	Medium-grained OAN	Hm-Ilm + Mt	-	-	-	-	-	-	-	-	-	-	-	-	-	25.3	-
CM1052	-	Surface outcrop	Medium-grained OAN	Hm-Ilm + Mt	-	-	-	-	-	-	-	-	-	-	-	-	-	31.4	-
CM1053A	-	Surface outcrop	Medium-grained OAN	Hm-Ilm + Mt	-	-	-	-	-	-	-	-	-	-	-	-	-	-	1.5
CM1053	-	Surface outcrop	Anorthosite	-	4.4	20.4	4.9	2.3	4.1	0.5	2.4	0.4	0.8	0.1	0.5	0.1	-	15.5	-
CM1053B	-	Surface outcrop	Medium-grained OAN	Hm-Ilm + Mt	-	-	-	-	-	-	-	-	-	-	-	-	-	27.2	-
CM1053C	-	Surface outcrop	Medium-grained OAN	Hm-Ilm + Mt	-	-	-	-	-	-	-	-	-	-	-	-	-	30.4	-
CM1056	-	Surface outcrop	Medium-grained OAN	Hm-Ilm + Mt	-	-	-	-	-	-	-	-	-	-	-	-	-	22.7	-
CM1060	-	Surface outcrop	Fine-grained ferrodiorite	Hm-Ilm + Mt	-	-	-	-	-	-	-	-	-	-	-	-	-	28.5	-

Sample	Depth (m)	Location	UTM-E	UTM-N	Lithology	Oxide Mineralogy	SiO_2	TiO_2	Al_2O_3	Fe_2O_{3t}	MnO	MgO	CaO	Na_2O	K_2O	P_2O_5	LOI	Total	^{51}V
CM1062	-	Surface outcrop	389085	5438894	Anorthosite	-	56.0	0.3	25.6	1.4	0.0	0.2	9.4	5.1	1.1	0.1	1.9	99.3	22.9
CM1063A	-	Surface outcrop	389132	5439027	Medium-grained OAN	Hm-ilm	38.3	4.8	10.6	22.2	0.3	6.6	10.5	1.8	0.6	3.2	0.0	99.0	110.1
CM1064	-	Surface outcrop	388970	5438870	Nelsonite	Ilm + Mt	4.7	10.6	3.3	56.2	0.3	1.5	13.2	0.1	0.0	8.4	0.0	98.3	1219.4
CM1067	-	Surface outcrop	388900	5438700	Nelsonite	Ilm + Mt	7.7	9.5	4.7	54.3	0.2	2.4	10.7	0.5	0.1	6.6	-1.4	96.7	1252.8
CM1067-2	-	Surface outcrop	388900	5438700	Nelsonite	Ilm + Mt	7.8	9.5	4.7	54.3	0.2	2.4	10.8	0.5	0.1	6.7	1.0	96.9	1264.6
CM1071	-	Surface outcrop	388845	5438647	Anorthosite	-	54.6	0.4	24.2	2.5	0.0	0.5	9.4	5.1	1.3	1.0	2.6	99.1	43.1
CM1072C	-	Surface outcrop	388808	5438818	Massive Oxides	Hm-Ilm + Mt	0.2	35.7	0.5	62.6	0.2	1.5	0.1	0.0	0.0	0.0	0.0	100.8	1411.0
CM1074	-	Surface outcrop	388659	5438196	Anorthosite	-	56.2	0.2	25.5	1.3	0.0	0.3	8.7	5.1	1.4	0.1	2.1	99.0	34.7
CM1074B	-	Surface outcrop	388659	5438196	Massive Oxides	Hm-Ilm + Mt	0.2	35.2	0.4	67.7	0.2	1.0	0.1	0.3	0.0	0.0	-0.1	105.0	1316.4
CM1075	-	Surface outcrop	388707	5438593	Anorthosite	-	53.4	1.3	22.8	5.5	0.0	1.2	7.9	5.0	0.9	0.8	4.0	98.9	54.4
CM1076B	-	Surface outcrop	388579	5438578	Fine-grained ferrodiorite	Hm-Ilm + Mt	39.0	4.0	12.6	21.1	0.2	5.1	10.7	2.0	0.5	3.5	1.4	98.8	197.5
CM1077A	-	Surface outcrop	388513	5438563	Semi-massive Oxides	Hm-Ilm + Mt	17.6	18.5	4.8	46.5	0.2	6.7	2.2	0.4	0.1	0.8	-0.1	97.9	901.4
CM1077B	-	Surface outcrop	388513	5438563	Semi-massive Oxides	Hm-Ilm + Mt	17.9	18.6	4.7	46.8	0.2	6.7	2.2	0.4	0.1	0.8	-0.5	98.5	907.5
CM1081	-	Surface outcrop	387762	5438580	Anorthosite	-	53.9	0.5	24.1	4.2	0.0	1.5	9.2	4.7	1.0	0.3	0.9	99.4	63.1
CM1081-2	-	Surface outcrop	387762	5438580	Anorthosite	-	54.4	0.5	24.2	4.2	0.0	1.5	9.2	4.7	1.1	0.3	0.1	99.9	70.5
CM1089D	-	Surface outcrop	388588	5438823	Medium-grained OAN	Hm-Ilm + Mt	38.9	4.2	11.9	21.1	0.3	5.5	10.2	2.1	0.6	3.9	0.5	98.7	211.3
CM1092A	-	Surface outcrop	388123	5438867	Medium-grained OAN	Hm-Ilm + Mt	35.1	5.0	10.9	25.2	0.2	5.1	10.6	1.9	0.5	4.6	0.9	99.1	304.3
CM1095	-	Surface outcrop	387715	5439012	Anorthosite	-	56.4	0.1	26.0	1.1	0.0	0.3	9.0	5.1	1.3	0.1	0.4	99.3	32.6
CM1099	-	Surface outcrop	387305	5438687	Anorthosite	-	55.5	0.1	26.1	1.2	0.0	0.3	10.0	4.9	1.1	0.1	2.9	99.4	33.7
CM1104	-	Surface outcrop	387190	5438630	Medium-grained OAN	Hm-Ilm + Mt	32.5	6.5	7.3	30.9	0.3	9.1	7.7	0.8	0.3	3.8	0.0	99.3	543.2
CM1110	-	Surface outcrop	389340	5440421	Fine-grained ferrodiorite	Hm-Ilm + Mt	29.7	7.0	6.6	27.1	0.3	8.9	11.4	0.9	0.2	7.0	-0.1	99.0	421.1
CM1121	-	Surface outcrop	387924	5440708	Medium-grained OAN	Hm-Ilm + Mt	37.1	6.1	10.2	21.0	0.2	7.7	9.9	1.8	0.4	4.6	0.0	99.0	252.3

Appendix 3.1.4 (Cont.) Complete LA-ICP-MS whole-rock results

Sample	Depth (m)	Location	Lithology	Oxide Mineralogy	^{53}Cr	^{59}Co	^{60}Ni	^{63}Cu	^{66}Zn	^{69}Ga	^{85}Rb	^{88}Sr	^{89}Y	^{90}Zr	^{93}Nb	^{137}Ba	^{139}La	^{140}Ce
CM1062	-	Surface outcrop	Anorthosite	-	-	-9.7	9.5	2.2	14.9	20.1	8.6	1659.9	1.5	25.4	4.8	1049.3	-	32.2
CM1063A	-	Surface outcrop	Medium-grained OAN	Hm-ilm	-	34.2	327.9	40.9	318.6	-1.5	14.0	201.6	6.6	286.6	24.5	1507.8	-	115.3
CM1064	-	Surface outcrop	Nelsonite	Ilm + Mt	145.7	39.1	345.9	153.3	773.4	26.8	15.4	518.9	101.9	98.2	27.3	218.8	-	149.8
CM1067	-	Surface outcrop	Nelsonite	Ilm + Mt	131.6	27.6	151.0	41.1	647.6	28.7	16.1	437.5	68.7	194.0	21.1	256.9	-	107.9
CM1067-2	-	Surface outcrop	Nelsonite	Ilm + Mt	131.4	-	-	-	-	-	-	-	-	-	-	229.4	-	112.1
CM1071	-	Surface outcrop	Anorthosite	-	-	-6.4	16.1	6.3	24.2	18.7	9.4	1475.8	13.2	49.6	5.0	1044.9	-	85.6
CM1072C	-	Surface outcrop	Massive Oxides	Hm-Ilm + Mt	1083.4	-	-	-	-	-	-	-	-	-	-	323.0	-	10.0
CM1074	-	Surface outcrop	Anorthosite	-	7.9	-17.4	10.0	5.6	14.6	20.1	11.8	1523	2.1	27.7	4.1	852.2	8.1	14.8
CM1074B	-	Surface outcrop	Massive Oxides	Hm-Ilm + Mt	1199.6	37.3	256.6	1.0	373.9	-13.3	16.5	21.5	8.5	524.6	47.6	216.9	-	10.0
CM1075	-	Surface outcrop	Anorthosite	-	-	3.9	19.2	6.1	52.5	18.0	10.9	1249.1	14.0	74.3	8.7	988.0	-	72.4
CM1076B	-	Surface outcrop	Fine-grained ferrodiorite	Hm-Ilm + Mt	-	21.9	44.7	19.3	244.9	16.5	9.5	902.9	51.4	133.6	13.7	607.5	-	124.7
CM1077A	-	Surface outcrop	Semi-massive Oxides	Hm-Ilm + Mt	542.1	43.7	736.0	267.2	229.9	2.7	15.1	227.9	14.7	299.8	27.0	217.6	-	10.0
CM1077B	-	Surface outcrop	Semi-massive Oxides	Hm-Ilm + Mt	527.9	-	-	-	-	-	-	-	-	-	-	232.2	-	10.0
CM1081	-	Surface outcrop	Anorthosite	-	234.1	4.4	37.7	6.1	43.1	20.7	9.4	1786	5.8	47.4	5.2	808.5	-	18.4
CM1081-2	-	Surface outcrop	Anorthosite	-	224.3	-	-	-	-	-	-	-	-	-	-	730.8	-	56.8
CM1089D	-	Surface outcrop	Medium-grained OAN	Hm-Ilm + Mt	-	14.0	39.5	5.5	242.6	16.3	10.0	970.8	67.5	273.2	20.6	1012.2	-	147.2
CM1092A	-	Surface outcrop	Medium-grained OAN	Hm-Ilm + Mt	24.3	16.1	50.3	37.2	261.3	13.6	11.1	838.4	70.4	245.7	20.9	786.2	-	131.4
CM1095	-	Surface outcrop	Anorthosite	-	-	-13.6	12.9	10.5	12.9	20.5	10.0	1877	0.9	24.9	3.4	877.1	-	41.9
CM1099	-	Surface outcrop	Anorthosite	-	13.1	-7.3	8.0	13.1	16.3	18.0	10.3	1622	1.7	35.1	4.3	717.5	7.4	11.9
CM1104	-	Surface outcrop	Medium-grained OAN	Hm-Ilm + Mt	69.8	32.1	90.9	50.0	278.0	11.9	11.0	526.8	30.0	131.2	14.9	304.5	-	62.0
CM1110	-	Surface outcrop	Fine-grained ferrodiorite	Hm-Ilm + Mt	18.7	17.6	57.1	4.1	224.6	6.0	10.8	587.7	51.2	159.9	19.2	234.1	51.8	134.0
CM1121	-	Surface outcrop	Medium-grained OAN	Hm-Ilm + Mt	55.7	23.4	67.5	27.8	200.1	9.3	8.9	819.6	69.7	333.5	25.2	627.4	-	139.6

Sample	Depth (m)	Location	Lithology	Oxide Mineralogy	^{141}Pr	^{146}Nd	^{147}Sm	^{153}Eu	^{157}Gd	^{159}Tb	^{163}Dy	^{165}Ho	^{166}Er	^{169}Tm	^{172}Yb	^{175}Lu	^{174}Hf	^{208}Pb	Eu/Eu*
CM1062	-	Surface outcrop	Anorthosite	-	-	-	-	-	-	-	-	-	-	-	-	-	-	12.4	-
CM1063A	-	Surface outcrop	Medium-grained OAN	Hm-ilm	-	-	-	-	-	-	-	-	-	-	-	-	-	34.9	-
CM1064	-	Surface outcrop	Nelsonite	Ilm + Mt	-	-	-	-	-	-	-	-	-	-	-	-	-	50.5	-
CM1067	-	Surface outcrop	Nelsonite	Ilm + Mt	-	-	-	-	-	-	-	-	-	-	-	-	-	46.0	-
CM1067-2	-	Surface outcrop	Nelsonite	Ilm + Mt	-	-	-	-	-	-	-	-	-	-	-	-	-	-	-
CM1071	-	Surface outcrop	Anorthosite	-	-	-	-	-	-	-	-	-	-	-	-	-	-	13.8	-
CM1072C	-	Surface outcrop	Massive Oxides	Hm-Ilm + Mt	-	-	-	-	-	-	-	-	-	-	-	-	-	-	-
CM1074	-	Surface outcrop	Anorthosite	-	1.4	6.1	1.0	1.3	0.7	0.1	0.4	0.1	0.1	0.0	0.1	0.0	-	14.2	4.6
CM1074B	-	Surface outcrop	Massive Oxides	Hm-Ilm + Mt	-	-	-	-	-	-	-	-	-	-	-	-	-	59.8	-
CM1075	-	Surface outcrop	Anorthosite	-	-	-	-	-	-	-	-	-	-	-	-	-	-	15.3	-
CM1076B	-	Surface outcrop	Fine-grained ferrodiorite	Hm-Ilm + Mt	-	-	-	-	-	-	-	-	-	-	-	-	-	29.4	-
CM1077A	-	Surface outcrop	Semi-massive Oxides	Hm-Ilm + Mt	-	-	-	-	-	-	-	-	-	-	-	-	-	43.3	-
CM1077B	-	Surface outcrop	Semi-massive Oxides	Hm-Ilm + Mt	-	-	-	-	-	-	-	-	-	-	-	-	-	-	-
CM1081	-	Surface outcrop	Anorthosite	-	-	-	-	-	-	-	-	-	-	-	-	-	-	16.3	-
CM1081-2	-	Surface outcrop	Anorthosite	-	-	-	-	-	-	-	-	-	-	-	-	-	-	-	-
CM1089D	-	Surface outcrop	Medium-grained OAN	Hm-Ilm + Mt	-	-	-	-	-	-	-	-	-	-	-	-	-	27.4	-
CM1092A	-	Surface outcrop	Medium-grained OAN	Hm-Ilm + Mt	-	-	-	-	-	-	-	-	-	-	-	-	-	33.9	-
CM1095	-	Surface outcrop	Anorthosite	-	-	-	-	-	-	-	-	-	-	-	-	-	-	13.5	-
CM1099	-	Surface outcrop	Anorthosite	-	1.2	5.2	0.9	1.0	0.7	0.1	0.4	0.1	0.1	0.0	0.1	0.0	-	11.2	3.5
CM1104	-	Surface outcrop	Medium-grained OAN	Hm-Ilm + Mt	-	-	-	-	-	-	-	-	-	-	-	-	-	29.9	-
CM1110	-	Surface outcrop	Fine-grained ferrodiorite	Hm-Ilm + Mt	18.9	99.1	20.4	5.0	17.3	2.0	10.0	1.8	3.7	0.4	2.5	0.3	-	33.7	0.8
CM1121	-	Surface outcrop	Medium-grained OAN	Hm-Ilm + Mt	-	-	-	-	-	-	-	-	-	-	-	-	-	27.4	-

Appendix 3.1.5 CIPW norm from LA-ICP-MS whole-rock results

Sample	20PM04A	20PM04B	20PM05A	20PM05B	20PM05C	20PM06A	20PM06B	20PM07	20PM08A	20PM08B1	20PM08B2	20PM17
Depth (m)	-	-	-	-	-		-	-	-	-	-	-
Location	Surface Outcrop	Surface Outcrop	Surface Outcrop	Surface Outcrop	Surface Outcrop	Surface Outcrop	Surface Outcrop	Surface Outcrop	Surface Outcrop	Surface Outcrop	Surface Outcrop	Surface Outcrop
Lithology	Medium-grained OAN	Massive Oxides	Massive Oxides	Semi-massive Oxides	Anorthosite	Medium-grained OAN	Medium-grained OAN	Nelsonite	Anorthosite	Medium-grained OAN	Medium-grained OAN	Anorthosite
Oxide Mineralogy	Ilm + Mt	Ilm + Mt	Hm-Ilm	Hm-Ilm + Mt	-	Hm-ilm	Hm-Ilm	Ilm + Mt	-	Hm-Ilm + Mt	Hm-Ilm + Mt	-
Or	4.1	0.0	0.0	4.8	7.3	1.7	4.7	1.6	5.1	2.7	4.4	5.0
Ab	21.1	0.0	0.0	28.0	40.4	3.5	9.2	3.0	37.3	7.3	16.8	45.0
An	15.2	1.0	0.8	23.3	35.0	7.4	5.8	0.0	33.9	6.2	17.1	43.2
An*	37.5	100.0	100.0	41.6	42.3	58.6	29.3	0.0	44.4	38.3	44.6	46.4
Or*	10.2	0.0	0.0	8.6	8.8	13.8	23.8	34.3	6.7	16.6	11.4	5.4
Ap	13.5	0.3	0.7	0.4	0.3	8.4	10.3	20.6	0.5	8.8	7.2	0.9
Sample	MX-109-3	MX109-7	MX114-1	MX-115	MX-117	MX-118	MX-123	CM1001A	CM1007	CM1013	CM1036	CM1038
Depth (m)	9.0	35.0	8.5	16.5	13.5	4.0	0.5	-	-	-	-	-
Location	Borehole MX-109	Borehole MX-109	Borehole MX-114	Borehole MX-115	Borehole MX-117	Borehole MX-118	Borehole MX-123	Surface Outcrop	Surface Outcrop	Surface Outcrop	Surface Outcrop	Surface Outcrop
Lithology	Massive Oxides	Anorthosite	Fine-grained-OAN dyke	Semi-massive Oxides	Massive Oxides	Massive Oxides	Massive Oxides	Fine-grained-OAN dyke	Medium-grained OAN	Medium-grained OAN	Medium-grained OAN	Semi-massive Oxides
Oxide Mineralogy	Hm-Ilm + Mt	-	Hm-Ilm + Mt	Hm-Ilm + Mt	Hm-Ilm + Mt	Hm-ilm	Hm-ilm	Hm-ilm	Hm-Ilm + Mt	Hm-Ilm + Mt	Hm-ilm	Hm-Ilm + Mt
Or	0.2	7.7	2.5	1.0	1.5	0.8	0.0	11.5	3.1	3.0	4.4	0.8
Ab	0.0	45.0	13.7	0.1	4.6	2.4	0.0	27.2	13.6	15.4	27.3	1.7
An	6.1	38.9	9.5	8.9	8.0	6.1	2.8	16.7	16.7	17.7	28.8	6.6
An*	96.6	42.4	37.2	89.5	56.9	65.8	100.0	30.1	49.9	49.0	47.6	72.7
Or*	3.4	8.4	9.5	9.7	10.5	8.3	0.0	20.8	9.4	8.3	7.3	8.7
Ap	0.2	0.9	14.1	0.7	1.6	0.1	0.0	5.8	7.8	9.0	4.0	0.2
Sample	CM1063A	CM1064	CM1067	CM1067-2	CM1071	CM1072C	CM1074	CM1074B	CM1075	CM1076B	CM1077A	CM1077B
Depth (m)	-	-	-	-	-	-	-	-	-	-	-	-
Location	Surface Outcrop	Surface Outcrop	Surface Outcrop	Surface Outcrop	Surface Outcrop	Surface Outcrop	Surface Outcrop	Surface Outcrop	Surface Outcrop	Surface Outcrop	Surface Outcrop	Surface Outcrop
Lithology	Medium-grained OAN	Nelsonite	Nelsonite	Nelsonite	Anorthosite	Massive Oxides	Anorthosite	Massive Oxides	Anorthosite	Fine-grained-OAN dyke	Semi-massive Oxides	Semi-massive Oxides
Oxide Mineralogy	Hm-ilm	Ilm + Mt	Ilm + Mt	Ilm + Mt	-		-	Hm-Ilm + Mt	-	Hm-Ilm + Mt	Hm-Ilm + Mt	Hm-Ilm + Mt
Or	3.8	0.0	0.8	0.8	7.8	0.0	8.5	0.0	5.6	3.1	0.8	0.8
Ab	15.0	0.0	0.5	0.7	43.0	0.0	43.5	0.0	42.4	17.3	3.4	3.3
An	19.1	8.4	9.9	9.8	39.2	0.2	42.2	0.0	33.7	23.6	5.7	5.7
An*	50.4	100.0	88.4	86.8	43.5	100.0	44.8	-	41.3	53.7	57.7	57.9

Or*	10.1	0.0	7.3	7.3	8.7	0.0	9.0	-	6.8	7.0	7.9	8.2
Ap	7.7	19.8	15.7	15.8	2.5	0.1	0.3	0.1	1.9	8.4	1.9	1.9

Appendix 3.1.5 CIPW norm from LA-ICP-MS whole-rock results

Sample	20PM18A	20PM18B	20PM19A	20PM19B	MX102-3	MX102-5	MX105-1	MX106-1	MX108-4	MX108-6	MX-108-8
Depth (m)	-	-	-	-	13.5	21.0	0.5	5.0	12.0	20.0	31.0
Location	Surface Outcrop	Surface Outcrop	Surface Outcrop	Surface Outcrop	Borehole MX-102	Borehole MX-102	Borehole MX-105	Borehole MX-106	Borehole MX-108	Borehole MX-108	Borehole MX-108
Lithology	Anorthosite	Medium-grained OAN	Fine-grained-OAN dyke	Fine-grained-OAN dyke	Fine-grained-OAN dyke	Medium-grained OAN	Medium-grained OAN	Medium-grained OAN	Fine-grained-OAN	Massive Oxides	Anorthosite
Oxide Mineralogy	-	Hm-Ilm + Mt	Hm-Ilm + Mt	Hm-Ilm + Mt	Hm-Ilm + Mt	Hm-Ilm + Mt	Hm-Ilm + Mt	Hm-Ilm + Mt	Hm-Ilm + Mt	Hm-Ilm + Mt	-
Or	6.8	5.1	20.6	11.7	4.5	3.4	2.3	3.8	0.1	1.9	6.9
Ab	45.5	23.7	27.0	42.0	24.5	19.4	17.2	25.2	0.7	8.2	42.3
An	35.5	13.5	15.5	28.8	18.9	21.0	16.7	22.4	5.5	13.1	40.7
An*	40.4	31.9	24.5	34.9	39.5	48.0	46.2	43.6	87.3	56.5	45.3
Or*	7.7	12.0	32.7	14.2	9.3	7.7	6.3	7.4	1.3	8.2	7.7
Ap	1.1	6.7	3.1	1.8	8.7	8.9	9.4	10.7	5.4	1.2	0.3
Sample	CM1045	CM1047	CM1050	CM1052	CM1053A	CM1053	CM1053B	CM1053C	CM1056	CM1060	CM1062
Depth (m)	-	-	-	-	-	-	-	-	-	-	-
Location	Surface Outcrop	Surface Outcrop	Surface Outcrop	Surface Outcrop	Surface Outcrop	Surface Outcrop	Surface Outcrop	Surface Outcrop	Surface Outcrop	Surface Outcrop	Surface Outcrop
Lithology	Medium-grained OAN	Medium-grained OAN	Medium-grained OAN	Medium-grained OAN	Medium-grained OAN	Anorthosite	Medium-grained OAN	Medium-grained OAN	Medium-grained OAN	Fine-grained-OAN dyke	Anorthosite
Oxide Mineralogy	Hm-Ilm + Mt	Hm-Ilm + Mt	Hm-Ilm + Mt	Hm-Ilm + Mt	Hm-Ilm + Mt	-	Hm-Ilm + Mt	Hm-Ilm + Mt	Hm-Ilm + Mt	Hm-Ilm + Mt	-
Or	2.0	3.8	2.4	1.6	2.4	5.9	3.9	1.5	4.3	2.9	6.7
Ab	13.9	14.2	13.9	9.7	13.9	37.9	24.2	8.9	21.7	18.7	43.2
An	15.9	18.5	22.7	18.3	18.7	40.8	20.7	13.6	24.7	22.2	43.5
An*	50.0	50.7	58.3	61.8	53.5	48.2	42.4	56.7	48.7	50.7	46.6
Or*	6.4	10.4	6.1	5.5	6.8	7.0	8.0	6.2	8.5	6.6	7.1
Ap	11.0	12.9	12.5	9.5	8.0	2.7	8.1	10.7	7.9	8.6	0.3
Sample	CM1081	CM1081-2	CM1089D	CM1092A	CM1095	CM1099	CM1104	CM1110	CM1121		
Depth (m)	-	-	-	-	-	-	-	-	-		
Location	Surface Outcrop	Surface Outcrop	Surface Outcrop	Surface Outcrop	Surface Outcrop	Surface Outcrop	Surface Outcrop	Surface Outcrop	Surface Outcrop		
Lithology	Anorthosite	Anorthosite	Medium-grained OAN	Medium-grained OAN	Anorthosite	Anorthosite	Medium-grained OAN	Fine-grained-OAN dyke	Medium-grained OAN		
Oxide Mineralogy	-	-	Hm-Ilm + Mt	Hm-Ilm + Mt	-	-	Hm-Ilm + Mt	Hm-Ilm + Mt	Hm-Ilm + Mt		
Or	6.2	6.2	3.6	2.7	7.5	6.5	1.6	1.1	2.6		
Ab	40.1	39.5	17.6	15.7	43.4	41.2	6.8	7.6	15.3		
An	41.3	41.9	21.3	20.0	44.1	46.0	13.6	11.0	18.4		

An*	47.1	47.8	50.1	52.1	46.4	49.1	61.8	55.9	50.6
Or*	7.1	7.1	8.5	7.2	7.9	7.0	7.2	5.7	7.3
Ap	0.7	0.7	9.3	11.0	0.1	0.3	9.0	16.5	10.8

Appendix 3.1.6 Complete LA-ICP-MS results of plagioclase

Sample	Depth (m)	Location	Lithology	Oxide Mineralogy	# analysis	SiO_2	Al_2O_3	FeO_t	CaO	Na_2O	K_2O	Total	An	Ab	Or
20PM05C	-	Surface Outcrop	Anorthosite enclaves	-	n=6	56.7	28.1	0.1	8.4	5.9	0.3	99.6	43.2	54.8	2.1
20PM06B	-	Surface Outcrop	Medium-grained OAN	Hm-Ilm + Mt	n=6	56.7	29.1	0.2	8.9	5.7	0.1	100.7	45.8	53.6	0.6
20PM07	-	Surface Outcrop	Nelsonite	Ilm + Mt	n=6	58.5	28.2	0.2	8.1	6.5	0.0	101.5	40.7	59.1	0.2
20PM08B1	-	Surface Outcrop	Medium-grained OAN	Hm-Ilm + Mt	n=6	56.4	29.8	0.1	9.3	5.5	0.2	101.5	47.7	51.0	1.3
20PM08B2	-	Surface Outcrop	Medium-grained OAN	Hm-Ilm + Mt	n=6	57.4	27.9	0.1	8.3	5.4	0.2	99.2	45.4	53.4	1.2
20PM18B	-	Surface Outcrop	Medium-grained OAN	Hm-Ilm + Mt	n=6	58.7	26.6	0.1	8.0	5.2	0.1	98.7	45.7	53.6	0.7
20PM19B	-	Surface Outcrop	Fine-grained jotunite	Hm-Ilm + Mt	n=6	61.1	25.3	0.2	6.1	6.5	0.3	99.5	33.7	64.4	1.9
CM1001A	-	Surface Outcrop	Fine-grained ferrodiorite	Hm-Ilm	n=4	59.5	24.4	0.1	4.4	5.3	4.6	98.9	31.8	66.3	1.9
CM1007	-	Surface Outcrop	Medium-grained OAN	Hm-Ilm + Mt	n=4	55.3	28.0	0.2	8.4	6.3	0.4	98.5	41.4	56.1	2.5
CM1012	-	Surface Outcrop	Medium-grained Anort-OAN	Hm-Ilm + Mt	n=4	55.3	28.1	0.1	8.3	6.2	0.4	98.5	41.7	55.9	2.5
CM1013	-	Surface Outcrop	Medium-grained OAN	Hm-Ilm + Mt	n=4	55.0	28.1	0.2	8.6	6.2	0.4	98.5	42.3	55.1	2.6
CM1038	-	Surface Outcrop	Medium-grained OAN	Hm-Ilm + Mt	n=4	54.6	28.0	0.6	8.8	6.1	0.4	98.6	43.1	54.5	2.4
CM1045	-	Surface Outcrop	Medium-grained OAN	Hm-Ilm + Mt	n=4	54.6	28.5	0.1	9.0	5.9	0.3	98.5	44.9	53.3	1.8
CM1047	-	Surface Outcrop	Medium-grained OAN	Hm-Ilm + Mt	n=4	54.6	28.5	0.4	8.7	5.9	0.4	98.6	43.9	53.8	2.2
CM1050	-	Surface Outcrop	Medium-grained OAN	Hm-Ilm + Mt	n=4	53.0	29.6	0.1	10.2	5.4	0.2	98.6	50.5	48.6	0.9
CM1051	-	Surface Outcrop	Medium-grained OAN	Hm-Ilm + Mt	n=4	54.0	28.9	0.1	9.4	5.7	0.4	98.5	46.8	51.1	2.1
CM1052	-	Surface Outcrop	Medium-grained OAN	Hm-Ilm + Mt	n=4	53.6	29.3	0.1	9.6	5.6	0.2	98.6	47.9	50.7	1.4
CM1053	-	Surface Outcrop	Medium-grained OAN	Hm-Ilm + Mt	n=4	54.4	28.7	0.1	9.1	6.0	0.3	98.6	44.8	53.3	1.9
CM1060	-	Surface Outcrop	Fine-grained ferrodiorite	Hm-Ilm + Mt	n=4	55.1	28.1	0.1	8.5	6.3	0.4	98.5	41.8	55.9	2.3
CM1063B	-	Surface Outcrop	Medium-grained OAN	Hm-Ilm	n=4	53.9	28.9	0.2	9.2	5.9	0.3	98.5	45.1	52.9	2.0
CM1076B	-	Surface Outcrop	Fine-grained ferrodiorite	Hm-Ilm + Mt	n=4	54.7	28.4	0.2	8.9	6.0	0.3	98.5	44.2	54.2	1.6
CM1110	-	Surface Outcrop	Fine-grained ferrodiorite	Hm-Ilm + Mt	n=4	53.6	29.3	0.1	9.7	5.6	0.2	98.5	48.5	50.6	0.9
MX102-3	13.50	Boregole MX-102	Fine-grained ferrodiorite	Hm-Ilm + Mt	n=4	55.7	27.7	0.2	8.1	6.0	0.7	98.6	40.7	55.0	4.3
MX102-5	21.00	Boregole MX-102	Medium-grained OAN	Hm-Ilm + Mt	n=4	53.6	29.1	0.2	9.3	6.0	0.3	98.6	45.3	52.9	1.8
MX105-1	0.50	Boregole MX-105	Medium-grained OAN	Hm-Ilm + Mt	n=4	54.5	28.5	0.1	8.9	6.2	0.3	98.5	43.4	54.6	1.9
MX106-1	5.00	Boregole MX-106	Medium-grained OAN	Hm-Ilm + Mt	n=4	53.8	28.9	0.2	9.2	6.0	0.4	98.6	45.0	52.8	2.2
MX108-6	3.00	Boregole MX-108	Semi-massive Oxides	Hm-Ilm + Mt	n=4	54.3	28.5	0.3	9.0	6.1	0.3	98.6	44.0	54.5	1.5
MX109-2	4.50	Boregole MX-109	Semi-massive Oxides	Hm-Ilm	n=4	53.9	29.1	0.3	9.0	6.1	0.1	98.5	44.8	54.4	0.8
MX114-1	8.50	Boregole MX-114	Fine-grained ferrodiorite	Hm-Ilm + Mt	n=4	54.6	28.4	0.2	8.9	6.1	0.3	98.5	43.8	54.3	2.0
MX-115	16.50	Boregole MX-115	Semi-massive Oxides	Hm-Ilm + Mt	n=4	52.0	30.3	0.1	10.2	5.8	0.1	98.6	48.9	50.7	0.4

Appendix 3.1.6 (Cont.) Complete LA-ICP-MS results of plagioclase

Detection Limits (33-55µm)						8.57 - 91.86	24.21-318.92	0.107 - 3.216	1.642-22.856	26.84 - 129.84	132.83 - 2630.29	0.622- 4.295	1.009 - 15.39	0.060- 0.697	2.634 - 22.997
Sample	Depth (m)	Location	Lithology	Oxide Mineralogy	# analysis	^{7}Li	^{23}Na	^{25}Mg	^{27}Al	^{31}P	^{44}Ca	^{45}Sc	^{49}Ti	^{51}V	^{53}Cr
20PM05 C	-	Surface Outcrop	Anorthosite enclaves	-	n=6	n.a	43569.0	149.2	148942.4	70.7	59875.8	2.6	39.8	0.2	n.a
20PM06 B	-	Surface Outcrop	Medium-grained OAN	Hm-Ilm + Mt	n=6	n.a	42640.7	490.0	153774.0	98.7	63570.8	2.4	94.1	0.3	n.a
20PM07	-	Surface Outcrop	Nelsonite	Ilm + Mt	n=6	n.a	48226.0	283.2	149161.1	84.7	57878.1	2.4	118.1	1.1	n.a
20PM08 B1	-	Surface Outcrop	Medium-grained OAN	Hm-Ilm + Mt	n=6	n.a	40944.0	105.6	157645.5	58.1	66727.8	1.8	66.8	0.3	n.a
20PM08 B2	-	Surface Outcrop	Medium-grained OAN	Hm-Ilm + Mt	n=6	n.a	39990.5	26.2	147551.8	101.0	59281.3	5.5	80.4	n.a	10.6
20PM18 B	-	Surface Outcrop	Medium-grained OAN	Hm-Ilm + Mt	n=6	n.a	38382.4	215.7	140990.8	49.5	57101.8	3.4	45.3	n.a	n.a
20PM19 B	-	Surface Outcrop	Fine-grained jotunite	Hm-Ilm + Mt	n=6	n.a	48122.1	378.3	133748.0	84.4	43856.2	4.2	57.5	n.a	n.a
CM1001 A	-	Surface Outcrop	Fine-grained ferrodiorite	Hm-Ilm	n=4	n.a	39675.1	140.0	128964.6	n.a	31501.6	3.5	47.2	0.1	n.a
CM1007	-	Surface Outcrop	Medium-grained OAN	Hm-Ilm + Mt	n=4	n.a	46468.4	293.7	147959.0	120.2	59744.4	3.9	251.8	0.6	n.a
CM1012	-	Surface Outcrop	Medium-grained Anort-OAN	Hm-Ilm + Mt	n=4	n.a	45720.5	112.9	148638.9	66.5	59313.8	3.5	64.6	0.2	n.a
CM1013	-	Surface Outcrop	Medium-grained OAN	Hm-Ilm + Mt	n=4	n.a	45751.3	40.1	148844.3	167.5	61095.8	3.6	71.7	0.4	n.a
CM1038	-	Surface Outcrop	Medium-grained OAN	Hm-Ilm + Mt	n=4	n.a	45427.0	196.3	148202.9	1538.1	62576.5	3.9	239.4	1.5	n.a
CM1045	-	Surface Outcrop	Medium-grained OAN	Hm-Ilm + Mt	n=4	n.a	43887.0	61.9	150998.0	67.7	64253.9	3.7	67.7	0.3	n.a
CM1047	-	Surface Outcrop	Medium-grained OAN	Hm-Ilm + Mt	n=4	n.a	43922.4	126.5	150602.6	92.6	62344.4	3.8	1223.2	9.6	n.a
CM1050	-	Surface Outcrop	Medium-grained OAN	Hm-Ilm + Mt	n=4	n.a	40228.0	40.6	156851.2	31.4	72801.9	3.5	95.8	0.2	n.a
CM1051	-	Surface Outcrop	Medium-grained OAN	Hm-Ilm + Mt	n=4	9.0	42113.8	79.7	153114.4	28.2	67119.5	3.7	85.3	0.3	n.a
CM1052	-	Surface Outcrop	Medium-grained OAN	Hm-Ilm + Mt	n=4	n.a	41874.3	92.5	155274.4	40.2	68747.3	3.6	77.9	0.3	n.a
CM1053	-	Surface Outcrop	Medium-grained OAN	Hm-Ilm + Mt	n=4	n.a	44201.5	82.9	151866.0	56.5	64713.2	3.8	61.4	0.1	n.a
CM1060	-	Surface Outcrop	Fine-grained ferrodiorite	Hm-Ilm + Mt	n=4	10.2	46670.3	258.2	148478.7	46.0	60670.2	4.1	51.7	0.5	n.a
CM1063 B	-	Surface Outcrop	Medium-grained OAN	Hm-Ilm	n=4	13.4	44156.9	189.0	153164.0	28.2	65446.1	4.3	52.4	0.3	n.a
CM1076 B	-	Surface Outcrop	Fine-grained ferrodiorite	Hm-Ilm + Mt	n=4	n.a	44698.6	121.2	150239.9	34.3	63278.3	4.5	89.4	0.1	n.a
CM1110	-	Surface Outcrop	Fine-grained ferrodiorite	Hm-Ilm + Mt	n=4	n.a	41680.8	31.8	155030.7	53.5	69361.1	3.3	80.2	0.1	n.a

MX102-3	13.50	Boregole MX-102	Fine-grained ferrodiorite	Hm-Ilm + Mt	n=4	n.a	44830.0	507.2	146481.0	197.3	57710.7	3.7	36.0	0.5	n.a
MX102-5	21.00	Boregole MX-102	Medium-grained OAN	Hm-Ilm + Mt	n=4	n.a	44749.2	259.9	153812.4	43.2	66628.0	3.2	93.6	0.1	n.a
MX105-1	0.50	Boregole MX-105	Medium-grained OAN	Hm-Ilm + Mt	n=4	10.8	45747.8	69.9	150901.0	55.6	63254.5	3.3	66.6	0.3	n.a
MX106-1	5.00	Boregole MX-106	Medium-grained OAN	Hm-Ilm + Mt	n=4	9.4	44585.7	213.6	153124.1	49.4	65949.6	3.5	103.8	0.2	n.a
MX108-6	3.00	Boregole MX-108	Semi-massive Oxides	Hm-Ilm + Mt	n=4	8.7	45582.0	152.0	150845.3	124.7	64053.4	3.3	688.0	8.7	7.5
MX109-2	4.50	Boregole MX-109	Semi-massive Oxides	Hm-Ilm	n=4	n.a	45086.8	1028.4	153873.3	82.2	64423.2	3.3	128.0	0.6	n.a
MX114-1	8.50	Boregole MX-114	Fine-grained ferrodiorite	Hm-Ilm + Mt	n=4	n.a	45113.1	416.7	150105.6	54.9	63273.1	3.5	46.8	0.3	n.a
MX-115	16.50	Boregole MX-115	Semi-massive Oxides	Hm-Ilm + Mt	n=4	n.a	43393.3	315.5	160187.6	93.3	72796.7	3.5	112.8	0.6	n.a

Appendix 3.1.6 (Cont.) Complete LA-ICP-MS results of plagioclase

Detection Limits (33-55µm)						1.295-5.303	0.075-0.452	0.898-4.867	0.516-2.963	1.278-6.950	0.165-2.006	0.191-1.473	0.058-0.245	0.042-0.243
Sample	Depth (m)	Location	Lithology	Oxide Mineralogy	# analysis	^{55}Mn	^{59}Co	^{60}Ni	^{63}Cu	^{66}Zn	^{69}Ga	^{72}Ge	^{88}Sr	^{89}Y
20PM05C	-	Surface Outcrop	Anorthosite enclaves	-	n=6	8.2	0.2	1.0	0.5	4.7	22.6	0.7	1656.8	0.4
20PM06B	-	Surface Outcrop	Medium-grained OAN	Hm-Ilm + Mt	n=6	14.4	0.8	1.5	4.4	4.3	21.6	0.7	2026.6	0.2
20PM07	-	Surface Outcrop	Nelsonite	Ilm + Mt	n=6	18.2	0.4	2.4	0.7	2.7	18.0	0.9	2614.2	0.2
20PM08B 1	-	Surface Outcrop	Medium-grained OAN	Hm-Ilm + Mt	n=6	13.1	n.a	n.a	1.1	5.9	23.1	0.8	2964.9	0.2
20PM08B 2	-	Surface Outcrop	Medium-grained OAN	Hm-Ilm + Mt	n=6	13.3	n.a	n.a	n.a	3.2	123.2	0.0	2478.2	0.1
20PM18B	-	Surface Outcrop	Medium-grained OAN	Hm-Ilm + Mt	n=6	15.8	n.a	0.8	n.a	18.2	50.7	0.0	1975.3	n.a
20PM19B	-	Surface Outcrop	Fine-grained jotunite	Hm-Ilm + Mt	n=6	15.6	n.a	n.a	n.a	11.5	47.9	0.0	1433.9	0.4
CM1001A	-	Surface Outcrop	Fine-grained ferrodiorite	Hm-Ilm	n=4	4.1	0.6	0.2	0.6	7.4	587.7	0.8	1613.3	0.2
CM1007	-	Surface Outcrop	Medium-grained OAN	Hm-Ilm + Mt	n=4	9.8	0.9	0.3	1.4	6.1	52.6	0.9	2607.9	0.3
CM1012	-	Surface Outcrop	Medium-grained Anort-OAN	Hm-Ilm + Mt	n=4	9.0	0.2	0.2	1.4	7.2	42.9	0.8	2083.1	0.3
CM1013	-	Surface Outcrop	Medium-grained OAN	Hm-Ilm + Mt	n=4	10.1	0.4	0.1	1.1	4.8	56.5	0.8	2384.6	0.5
CM1038	-	Surface Outcrop	Medium-grained OAN	Hm-Ilm + Mt	n=4	14.7	0.3	0.4	2.6	9.4	84.1	0.9	2317.6	3.5
CM1045	-	Surface Outcrop	Medium-grained OAN	Hm-Ilm + Mt	n=4	8.7	0.2	0.1	0.8	7.6	60.6	0.7	2506.6	0.3
CM1047	-	Surface Outcrop	Medium-grained OAN	Hm-Ilm + Mt	n=4	38.4	0.4	1.9	4.8	6.2	49.6	0.7	2211.1	0.3
CM1050	-	Surface Outcrop	Medium-grained OAN	Hm-Ilm + Mt	n=4	15.1	0.1	0.2	0.6	2.3	45.6	0.7	2313.6	0.2
CM1051	-	Surface Outcrop	Medium-grained OAN	Hm-Ilm + Mt	n=4	8.4	0.2	0.8	1.3	4.7	52.6	0.7	2118.6	0.2
CM1052	-	Surface Outcrop	Medium-grained OAN	Hm-Ilm + Mt	n=4	9.2	0.2	9.4	2.4	2.8	58.2	0.7	2312.9	0.2
CM1053	-	Surface Outcrop	Medium-grained OAN	Hm-Ilm + Mt	n=4	12.3	0.1	0.1	0.8	3.8	67.0	0.8	2560.4	0.2
CM1060	-	Surface Outcrop	Fine-grained ferrodiorite	Hm-Ilm + Mt	n=4	9.4	0.4	1.0	2.1	6.1	63.9	0.8	2204.5	0.3
CM1063B	-	Surface Outcrop	Medium-grained OAN	Hm-Ilm	n=4	7.2	0.5	4.3	2.9	7.5	42.9	0.7	1988.3	0.3
CM1076B	-	Surface Outcrop	Fine-grained ferrodiorite	Hm-Ilm + Mt	n=4	19.6	0.6	0.3	1.1	8.9	53.9	0.8	2076.8	0.2
CM1110	-	Surface Outcrop	Fine-grained ferrodiorite	Hm-Ilm + Mt	n=4	9.2	0.1	0.2	0.6	1.5	42.0	0.6	2614.8	0.2
MX102-3	13.50	Boregole MX-102	Fine-grained ferrodiorite	Hm-Ilm + Mt	n=4	9.5	n.a	n.a	0.8	5.6	106.6	0.8	2091.5	0.5

MX102-5	21.00	Boregole MX-102	Medium-grained OAN	Hm-Ilm + Mt	n=4	17.0	0.1	n.a	0.7	6.2	59.9	0.8	2530.5	0.3
MX105-1	0.50	Boregole MX-105	Medium-grained OAN	Hm-Ilm + Mt	n=4	11.2	0.2	n.a	0.9	9.1	61.2	0.8	2697.2	0.2
MX106-1	5.00	Boregole MX-106	Medium-grained OAN	Hm-Ilm + Mt	n=4	12.9	2.0	0.3	0.8	8.5	62.0	0.8	2186.0	0.2
MX108-6	3.00	Boregole MX-108	Semi-massive Oxides	Hm-Ilm + Mt	n=4	26.7	0.5	6.2	1.3	8.0	46.5	0.8	1956.5	0.4
MX109-2	4.50	Boregole MX-109	Semi-massive Oxides	Hm-Ilm	n=4	23.1	0.3	7.3	n.a	3.6	35.9	0.8	1904.9	0.4
MX114-1	8.50	Boregole MX-114	Fine-grained ferrodiorite	Hm-Ilm + Mt	n=4	20.6	0.1	4.4	0.6	14.6	60.0	0.8	2213.2	0.2
MX-115	16.50	Boregole MX-115	Semi-massive Oxides	Hm-Ilm + Mt	n=4	26.6	0.1	2.4	1.1	3.1	29.2	0.8	1876.5	0.5

Appendix 3.1.6 (Cont.) Complete LA-ICP-MS results of plagioclase

Detection Limits (33-55µm)						0.091-0.218	0.515-0.809	0.005-0.013	0.003-1.838	0.008-0.476	0.010-0.057	0.005-0.058	0.001-0.023	
Sample	Depth (m)	Location	Lithology	Oxide Mineralogy	# analysis	^{90}Zr	^{137}Ba	^{139}La	^{140}Ce	^{141}Pr	^{146}Nd	^{147}Sm	^{153}Eu	Total REE
20PM05C	-	Surface Outcrop	Anorthosite enclaves	-	n=6	n.a	114.9	8.6	14.5	1.5	5.0	0.5	1.3	31.5
20PM06B	-	Surface Outcrop	Medium-grained OAN	Hm-Ilm + Mt	n=6	0.3	193.5	3.1	4.7	0.5	1.8	0.0	0.8	10.8
20PM07	-	Surface Outcrop	Nelsonite	Ilm + Mt	n=6	0.2	133.3	5.3	7.6	0.7	2.6	0.0	0.8	16.9
20PM08B1	-	Surface Outcrop	Medium-grained OAN	Hm-Ilm + Mt	n=6	n.a	1315.7	7.2	10.9	1.1	3.8	0.0	2.4	25.4
20PM08B2	-	Surface Outcrop	Medium-grained OAN	Hm-Ilm + Mt	n=6	n.a	947.5	6.2	9.9	1.0	3.4	0.0	2.0	22.5
20PM18B	-	Surface Outcrop	Medium-grained OAN	Hm-Ilm + Mt	n=6	n.a	251.4	8.5	12.2	0.9	0.0	0.0	2.4	24.1
20PM19B	-	Surface Outcrop	Fine-grained jotunite	Hm-Ilm + Mt	n=6	n.a	133.1	30.0	38.9	3.2	9.2	0.0	2.9	84.2
CM1001A	-	Surface Outcrop	Fine-grained ferrodiorite	Hm-Ilm	n=4	0.1	7842.0	12.8	12.8	0.9	2.6	0.2	3.5	33.1
CM1007	-	Surface Outcrop	Medium-grained OAN	Hm-Ilm + Mt	n=4	3.5	436.6	10.2	14.5	1.4	4.6	0.5	3.0	34.5
CM1012	-	Surface Outcrop	Medium-grained Anort-OAN	Hm-Ilm + Mt	n=4	0.2	242.1	12.4	16.5	1.5	4.8	0.4	2.5	38.6
CM1013	-	Surface Outcrop	Medium-grained OAN	Hm-Ilm + Mt	n=4	0.2	498.8	10.2	14.2	1.4	4.6	0.5	2.6	34.1
CM1038	-	Surface Outcrop	Medium-grained OAN	Hm-Ilm + Mt	n=4	0.5	603.0	14.3	24.5	3.0	12.7	2.2	3.7	38.1
CM1045	-	Surface Outcrop	Medium-grained OAN	Hm-Ilm + Mt	n=4	n.a	575.0	8.3	11.4	1.1	3.6	0.4	2.2	27.5
CM1047	-	Surface Outcrop	Medium-grained OAN	Hm-Ilm + Mt	n=4	10.9	405.4	8.8	11.9	1.1	3.6	0.4	2.1	28.2
CM1050	-	Surface Outcrop	Medium-grained OAN	Hm-Ilm + Mt	n=4	0.1	373.3	5.4	7.9	0.8	2.8	0.3	1.3	18.8
CM1051	-	Surface Outcrop	Medium-grained OAN	Hm-Ilm + Mt	n=4	n.a	422.6	7.0	10.0	1.0	3.3	0.3	1.8	23.7

CM1052	-	Surface Outcrop	Medium-grained OAN	Hm-Ilm + Mt	n=4	1.7	571.6	7.1	9.8	0.9	3.1	0.3	1.5	23.0
CM1053	-	Surface Outcrop	Medium-grained OAN	Hm-Ilm + Mt	n=4	0.1	667.0	8.0	11.8	1.2	4.3	0.4	3.1	29.1
CM1060	-	Surface Outcrop	Fine-grained ferrodiorite	Hm-Ilm + Mt	n=4	0.6	536.9	12.8	16.8	1.5	4.9	0.4	2.8	39.6
CM1063B	-	Surface Outcrop	Medium-grained OAN	Hm-Ilm	n=4	0.2	205.6	10.8	14.9	1.4	4.5	0.4	2.1	34.5
CM1076B	-	Surface Outcrop	Fine-grained ferrodiorite	Hm-Ilm + Mt	n=4	0.1	388.1	10.0	13.8	1.3	4.2	0.4	2.3	32.3
CM1110	-	Surface Outcrop	Fine-grained ferrodiorite	Hm-Ilm + Mt	n=4	0.2	307.7	6.3	8.9	0.9	2.9	0.3	1.3	20.8
MX102-3	13.50	Boregole MX-102	Fine-grained ferrodiorite	Hm-Ilm + Mt	n=4	0.1	1283.9	13.7	17.2	1.6	4.9	0.4	2.8	41.1
MX102-5	21.00	Boregole MX-102	Medium-grained OAN	Hm-Ilm + Mt	n=4	n.a	580.3	8.8	13.4	1.4	4.9	0.5	3.3	32.8
MX105-1	0.50	Boregole MX-105	Medium-grained OAN	Hm-Ilm + Mt	n=4	n.a	559.6	8.4	11.8	1.1	3.8	0.4	2.6	28.5
MX106-1	5.00	Boregole MX-106	Medium-grained OAN	Hm-Ilm + Mt	n=4	n.a	562.2	7.5	10.8	1.1	3.5	0.3	1.9	25.4
MX108-6	3.00	Boregole MX-108	Semi-massive Oxides	Hm-Ilm + Mt	n=4	0.2	359.7	8.8	13.5	1.4	4.6	0.5	1.8	30.9
MX109-2	4.50	Boregole MX-109	Semi-massive Oxides	Hm-Ilm	n=4	n.a	204.5	11.6	18.5	1.9	6.4	0.7	1.8	41.5
MX114-1	8.50	Boregole MX-114	Fine-grained ferrodiorite	Hm-Ilm + Mt	n=4	n.a	489.2	7.9	10.5	1.0	3.2	0.3	2.0	25.1
MX-115	16.50	Boregole MX-115	Semi-massive Oxides	Hm-Ilm + Mt	n=4	n.a	140.9	13.6	21.0	2.1	7.0	0.7	1.6	46.8

Major elements in wt.%, An=100 [Ca/(Ca+Na+K)]; Ab=100 [Na/(Ca+Na+K)]; Or=100 [K/(Ca+Na+K)]; trace element in ppm. OAN = Oxide-apatite norite; Hm-ilm = hemo-ilmenite; Ilm = ilmenite; Mt = magnetite.

Appendix 3.1.7 Complete LA-ICP-MS results of ilmenite

Sample	Depth (m)	Location	Lithology	Oxide Mineralogy	# analysis	SiO_2	TiO2	Al_2O_3	FeO_t	Fe_2O_3	FeO	MnO	MgO	Total	X_{hem}	X_{ilm}
20PM04B	-	Sample Outcrop	Massive Oxides	Ilm + Mt	n=6	0.02	48.19	0.09	50.43	10.34	41.12	0.83	0.87	101.63	0.1	0.9
20PM05A	-	Sample Outcrop	Massive Oxides	Hm-Ilm	n=6	0.04	47.42	0.08	64.67	29.43	38.19	0.21	2.59	118.47	0.26	0.74
20PM06B	-	Sample Outcrop	Medium-grained OAN	Hm-Ilm + Mt	n=6	0.05	28.46	0.11	63.90	42.64	25.53	0.20	0.15	97.46	0.43	0.57
20PM07	-	Sample Outcrop	Nelsonite	Ilm + Mt	n=6	0.02	47.62	0.05	47.81	9.71	39.07	0.83	1.73	99.17	0.10	0.90
20PM08B1	-	Sample Outcrop	Medium-grained OAN	Hm-Ilm + Mt	n=6	0.02	44.07	0.05	50.34	15.95	35.99	0.81	1.65	98.63	0.17	0.83
20PM08B2	-	Sample Outcrop	Medium-grained OAN	Hm-Ilm + Mt	n=6	0.16	42.06	0.07	55.18	23.05	34.44	0.76	1.59	102.16	0.23	0.77
20PM18B	-	Sample Outcrop	Medium-grained OAN	Hm-Ilm + Mt	n=6	1.78	23.79	0.30	71.67	55.79	21.47	0.48	0.19	104.01	0.55	0.45
20PM19B	-	Sample Outcrop	Fine-grained jotunite	Hm-Ilm + Mt	n=6	0.21	22.27	0.12	76.34	63.14	19.53	0.23	0.31	105.88	0.60	0.40
CM1001A	-	Sample Outcrop	Fine-grained ferrodiorite	Hm-ilm	n=4	0.16	26.82	0.24	71.99	10.89	62.19	0.19	0.18	100.91	0.50	0.50
CM1007	-	Sample Outcrop	Medium-grained OAN	Hm-Ilm + Mt	n=4	0.11	34.74	0.19	63.58	8.43	55.99	0.42	0.64	100.67	0.36	0.64
CM1012	-	Sample Outcrop	Medium-grained OAN	Hm-ilm	n=4	0.04	30.66	0.15	68.48	10.67	58.88	0.20	0.41	101.19	0.44	0.56
CM1013	-	Sample Outcrop	Medium-grained OAN	Hm-Ilm + Mt	n=4	0.07	38.64	0.14	59.69	7.18	53.23	0.38	0.69	100.57	0.29	0.71
CM1036	-	Sample Outcrop	Massive Oxides	Hm-ilm	n=4	0.05	37.40	0.12	60.70	7.42	54.02	0.22	1.09	100.77	0.32	0.68
CM1038	-	Sample Outcrop	Medium-grained OAN	Hm-Ilm + Mt	n=4	0.20	29.51	0.18	69.33	10.87	59.55	0.26	0.38	101.14	0.46	0.54
CM1045	-	Sample Outcrop	Medium-grained OAN	Hm-Ilm + Mt	n=4	0.07	34.87	0.10	64.03	9.29	55.68	0.31	0.58	101.09	0.36	0.64
CM1047	-	Sample Outcrop	Medium-grained OAN	Hm-Ilm + Mt	n=4	0.06	38.57	0.17	60.16	8.11	52.86	0.46	0.56	101.03	0.29	0.71
CM1050	-	Sample Outcrop	Medium-grained OAN	Hm-Ilm + Mt	n=4	0.08	40.25	0.14	58.84	9.79	50.03	0.54	0.83	101.83	0.26	0.74
CM1051	-	Sample Outcrop	Medium-grained OAN	Hm-Ilm + Mt	n=4	0.09	33.55	0.15	65.91	11.56	55.51	0.23	0.57	101.91	0.39	0.61
CM1052	-	Sample Outcrop	Medium-grained OAN	Hm-Ilm + Mt	n=4	0.06	36.53	0.10	62.67	10.74	53.01	0.35	0.86	101.89	0.34	0.66
CM1053	-	Sample Outcrop	Medium-grained OAN	Hm-Ilm + Mt	n=4	0.03	42.72	0.07	55.97	9.32	47.58	0.78	1.28	101.86	0.23	0.77
CM1060	-	Sample Outcrop	Fine-grained ferrodiorite	Hm-Ilm + Mt	n=4	0.23	24.75	0.23	74.50	13.54	62.31	0.19	0.28	101.86	0.55	0.45
CM1063B	-	Sample Outcrop	Medium-grained OAN	Hm-ilm	n=4	0.07	24.42	0.15	75.05	13.37	63.02	0.12	0.35	101.84	0.56	0.44
CM1064	-	Sample Outcrop	Nelsonite	Ilm + Mt	n=4	0.11	34.66	0.15	64.27	10.86	54.50	0.62	0.89	101.67	0.37	0.63

CM1067	-	Sample Outcrop	Nelsonite	Ilm + Mt	n=4	0.08	43.72	0.14	54.31	8.86	46.34	0.75	1.72	101.78	0.21	0.79
CM1076B	-	Sample Outcrop	Fine-grained ferrodiorite	Hm-Ilm + Mt	n=4	0.16	26.11	0.15	73.49	13.25	61.56	0.27	0.13	101.90	0.52	0.48
CM1110	-	Sample Outcrop	Fine-grained ferrodiorite	Hm-Ilm + Mt	n=4	0.06	37.87	0.10	60.48	8.27	53.04	0.30	1.10	101.04	0.31	0.69
MX102-3	13.50	Borehole MX-102	Fine-grained ferrodiorite	Hm-Ilm + Mt	n=4	0.29	32.18	0.17	66.03	8.57	58.32	0.27	0.43	100.56	0.41	0.60
MX102-5	21.00	Borehole MX-102	Medium-grained OAN	Hm-Ilm + Mt	n=4	0.06	34.53	0.29	61.76	3.71	58.42	0.57	0.96	98.68	0.36	0.64
MX105-1	0.50	Borehole MX-105	Medium-grained OAN	Hm-Ilm + Mt	n=4	0.23	30.22	0.26	66.45	4.85	62.09	0.34	0.55	98.72	0.44	0.56
MX106-1	5.00	Borehole MX-106	Medium-grained OAN	Hm-Ilm + Mt	n=4	0.09	30.50	0.22	67.89	9.13	59.67	0.20	0.50	100.58	0.44	0.56
MX108-6	3.00	Borehole MX-108	Semi-massive Oxides	Hm-Ilm + Mt	n=4	0.06	29.17	0.21	67.04	2.93	64.41	0.22	0.67	98.23	0.46	0.54
MX108-4	12.00	Borehole MX-108	Fine-grained OAN	Hm-ilm	n=4	0.04	31.57	0.18	65.21	3.17	62.36	0.18	0.53	98.36	0.41	0.59
MX109-2	4.50	Borehole MX-109	Semi-massive Oxides	Hm-ilm	n=4	0.13	31.81	0.15	64.30	1.32	63.11	0.24	0.58	97.89	0.40	0.60
MX114-1	8.50	Borehole MX-114	Fine-grained ferrodiorite	Hm-Ilm + Mt	n=4	0.21	31.01	0.19	67.55	8.89	59.55	0.22	0.22	100.53	0.42	0.58
MX-115	16.50	Borehole MX-115	Semi-massive Oxides	Hm-Ilm + Mt	n=4	0.06	33.04	0.10	63.96	4.77	59.67	0.24	0.95	99.29	0.39	0.61
MX-117	13.50	Borehole MX-117	Massive Oxides	Hm-Ilm + Mt	n=4	0.03	34.00	0.14	63.18	5.28	58.44	0.21	1.02	99.61	0.38	0.62
MX-118	4.00	Borehole MX-118	Massive Oxides	Hm-ilm	n=4	0.03	33.87	0.07	62.33	2.95	59.67	0.17	1.39	98.78	0.38	0.62
MX-123	0.50	Borehole MX-123	Massive Oxides	Hm-ilm	n=4	0.03	36.50	0.09	59.99	4.59	55.86	0.16	1.81	99.58	0.34	0.66

Appendix 3.1.7 (Cont.) Complete LA-ICP-MS results of ilmenite

Detection Limits (33-55µm)					0.111-0.411	280.87-1450.82	32.12-83.39	66.62-124.50	0.205 - 1.345	0.035-0.296	0.252-3.179	0.463-1.920	0.025 - 0.220	0.251 - 1.198	0.335 - 0.745	0.761 - 1.438
Sample	Depth (m)	Lithology	Oxide Mineralogy	# analysis	^{25}Mg	^{27}Al	^{29}Si	^{44}Ca	^{45}Sc	^{51}V	^{53}Cr	^{55}Mn	^{59}Co	^{60}Ni	^{63}Cu	^{66}Zn
20PM04B	-	Massive Oxides	Ilm + Mt	n=6	5264.56	519.34	268.25	45113.0	49.15	952.67	198.0	1652876.0	83.31	98.66	2.76	23.43
20PM05A	-	Massive Oxides	Hm-Ilm	n=6	15647.1	n.a	n.a	n.a	63.1	2037.3	1457.7	1587.4	132.1	216.8	2.0	7.9
20PM06B	-	Medium-grained OAN	Hm-Ilm + Mt	n=6	899.6	386.6	n.a	n.a	45.0	2189.7	48.8	1580.5	12.2	11.8	1.2	64.5
20PM07	-	Nelsonite	Ilm + Mt	n=6	10430.2	n.a	n.a	n.a	63.7	934.4	27.1	6453.4	48.6	11.7	2.7	10.9
20PM08B1	-	Medium-grained OAN	Hm-Ilm + Mt	n=6	9957.2	n.a	n.a	n.a	72.8	527.3	1.6	6294.0	21.2	0.5	2.2	11.5
20PM08B2	-	Medium-grained OAN	Hm-Ilm + Mt	n=6	9599.4	774.8	n.a	n.a	72.6	560.0	2.8	5868.8	21.4	0.4	5.6	33.0
20PM18B	-	Medium-grained OAN	Hm-Ilm + Mt	n=6	1135.8	7049.5	57.0	3568.5	55.5	2024.5	103.9	5272.1	9.1	4.0	2.8	186.2
20PM19B	-	Fine-grained jotunite	Hm-Ilm + Mt	n=6	1893.0	2201.1	n.a	104.4	65.1	1364.3	40.7	1768.6	9.1	0.4	2.5	96.4
CM1001A	-	Fine-grained ferrodiorite	Hm-ilm	n=4	1095.3	748.7	n.a	88.3	51.0	1544.9	1.4	1467.7	17.2	0.8	0.5	494.7
CM1007	-	Medium-grained OAN	Hm-Ilm + Mt	n=4	3859.2	496.8	n.a	n.a	67.2	1066.0	1.9	3222.8	20.9	0.2	0.8	217.3
CM1012	-	Medium-grained OAN	Hm-ilm	n=4	2502.3	195.0	62.6	n.a	59.6	1129.3	0.6	1541.2	17.4	0.2	0.5	281.7
CM1013	-	Medium-grained OAN	Hm-Ilm + Mt	n=4	4175.4	342.5	532.9	532.4	70.8	1095.6	1.6	2944.3	21.9	0.3	0.7	239.9
CM1036	-	Massive Oxides	Hm-ilm	n=4	6591.6	n.a	n.a	n.a	55.5	2140.3	842.7	1729.8	37.0	17.5	1.4	134.3
CM1038	-	Medium-grained OAN	Hm-Ilm + Mt	n=4	2278.9	955.0	n.a	n.a	62.4	1186.9	19.6	2028.9	15.0	0.7	1.1	210.3
CM1045	-	Medium-grained OAN	Hm-Ilm + Mt	n=4	3480.2	332.7	n.a	n.a	61.5	1320.9	0.4	2391.6	21.1	0.5	1.0	105.0
CM1047	-	Medium-grained OAN	Hm-Ilm + Mt	n=4	3394.5	n.a	n.a	n.a	75.7	1525.1	39.1	3539.4	32.5	6.3	1.4	150.2
CM1050	-	Medium-grained OAN	Hm-Ilm + Mt	n=4	4993.2	384.6	53.2	n.a	73.8	1133.4	33.1	4163.4	33.9	4.7	1.4	42.9
CM1051	-	Medium-grained OAN	Hm-Ilm + Mt	n=4	3451.0	443.3	n.a	n.a	63.7	1656.9	1.7	1785.5	30.3	1.2	2.5	142.8
CM1052	-	Medium-grained OAN	Hm-Ilm + Mt	n=4	5209.8	282.8	n.a	n.a	52.0	1581.0	15.5	2689.5	32.6	3.0	1.2	34.0
CM1053	-	Medium-grained OAN	Hm-Ilm + Mt	n=4	7689.4	n.a	n.a	n.a	87.8	594.4	2.6	6011.8	24.1	0.5	0.8	51.4
CM1060	-	Fine-grained ferrodiorite	Hm-Ilm + Mt	n=4	1713.3	1054.7	n.a	164.1	55.9	1974.1	56.7	1460.0	14.8	1.4	2.6	238.7
CM1063B	-	Medium-grained OAN	Hm-ilm	n=4	2101.2	347.8	n.a	n.a	49.3	2255.3	70.5	913.3	18.9	3.2	0.8	132.9

CM1064	-	Nelsonite	Ilm + Mt	n=4	4589.4	513.4	35.8	n.a	60.8	1543.9	56.4	3839.6	37.6	14.8	0.9	45.4
CM1067	-	Nelsonite	Ilm + Mt	n=4	10348.1	366.3	n.a	n.a	68.4	1113.8	42.9	5815.1	47.4	14.7	1.0	36.3
CM1076B	-	Fine-grained ferrodiorite	Hm-Ilm + Mt	n=4	771.1	726.4	n.a	84.9	70.5	1663.6	12.4	2099.3	18.8	5.0	0.7	302.5
CM1110	-	Fine-grained ferrodiorite	Hm-Ilm + Mt	n=4	6662.4	265.3	n.a	n.a	42.1	1979.4	18.5	2320.2	35.8	10.2	1.3	32.6
MX102-3	13.50	Fine-grained ferrodiorite	Hm-Ilm + Mt	n=4	2571.0	1363.9	n.a	254.0	61.7	1872.5	83.7	2066.2	19.6	3.5	0.6	204.6
MX102-5	21.00	Medium-grained OAN	Hm-Ilm + Mt	n=4	5785.8	286.3	n.a	n.a	92.1	824.7	8.2	4441.5	20.3	0.7	0.6	453.2
MX105-1	0.50	Medium-grained OAN	Hm-Ilm + Mt	n=4	3300.3	1080.0	100.1	n.a	68.9	1181.5	0.3	2660.6	22.6	0.2	3.1	588.7
MX106-1	5.00	Medium-grained OAN	Hm-Ilm + Mt	n=4	2984.9	440.1	n.a	n.a	58.9	1712.6	39.9	1537.2	31.4	6.4	0.6	173.3
MX108-6	3.00	Semi-massive Oxides	Hm-Ilm + Mt	n=4	4052.9	295.6	n.a	n.a	61.8	1943.3	1758.3	1710.7	36.7	16.0	0.6	80.1
MX108-4	12.00	Fine-grained OAN	Hm-ilm	n=4	3220.1	204.7	n.a	n.a	53.9	1900.5	280.2	1413.8	16.3	50.3	0.7	228.6
MX109-2	4.50	Semi-massive Oxides	Hm-ilm	n=4	3483.6	598.5	n.a	n.a	58.1	2099.9	1663.5	1851.2	27.3	47.9	0.5	139.2
MX114-1	8.50	Fine-grained ferrodiorite	Hm-Ilm + Mt	n=4	1316.7	998.7	n.a	n.a	65.1	1605.6	29.8	1708.1	20.9	3.9	0.6	428.9
MX-115	16.50	Semi-massive Oxides	Hm-Ilm + Mt	n=4	5754.5	269.8	n.a	n.a	50.4	2009.2	1070.9	1869.9	42.7	45.7	0.5	8.8
MX-117	13.50	Massive Oxides	Hm-Ilm + Mt	n=4	6133.2	n.a	n.a	n.a	63.7	1923.3	1412.0	1629.0	72.6	83.7	0.5	11.0
MX-118	4.00	Massive Oxides	Hm-ilm	n=4	8400.5	n.a	n.a	n.a	51.5	2272.7	1941.4	1289.6	106.8	197.0	0.5	27.5
MX-123	0.50	Massive Oxides	Hm-ilm	n=4	10933.7	n.a	n.a	n.a	53.5	2077.9	1557.6	1242.8	74.9	307.9	0.5	11.7

Appendix 3.1.7 (Cont.) Complete LA-ICP-MS results of ilmenite

Detection Limits (33-55µm)					0.151-0.365	0.079-0.309	0.019-0.055	0.038-0.056	0.022-0.027	0.074-0.345	0.034--?	0.073-0.089	0.051-0.062	0.013-0.015	0.075-0.095	0.051-0.078
Sample	Depth (m)	Lithology	Oxide Mineralogy	# analysis	^{69}Ga	^{72}Ge	^{89}Y	^{90}Zr	^{93}Nb	Sn	^{139}La	^{172}Yb	^{178}Hf	^{181}Ta	^{182}W	^{208}Pb
20PM04B	-	Massive Oxides	Ilm + Mt	n=6	2.51	0.12	n.a	29.96	20.96	7.14	0.0	0.0	3.19	0.69	0.1	0.28
20PM05A	-	Massive Oxides	Hm-Ilm	n=6	7.3	0.1	n.a	21.8	43.3	5.3	0.0	n.a	4.5	2.4	n.a	0.3
20PM06B	-	Medium-grained OAN	Hm-Ilm + Mt	n=6	10.5	0.2	0.1	14.9	14.0	7.2	0.0	n.a	2.2	0.9	n.a	0.1
20PM07	-	Nelsonite	Ilm + Mt	n=6	2.0	0.1	0.0	25.5	42.8	8.6	0.0	n.a	2.4	2.1	0.1	0.1
20PM08B1	-	Medium-grained OAN	Hm-Ilm + Mt	n=6	3.8	0.1	0.1	24.2	36.8	7.1	0.0	n.a	2.2	2.1	n.a	0.2
20PM08B2	-	Medium-grained OAN	Hm-Ilm + Mt	n=6	5.0	0.0	0.1	46.6	41.5	7.0	n.a	n.a	5.5	2.6	n.a	n.a
20PM18B	-	Medium-grained OAN	Hm-Ilm + Mt	n=6	19.1	0.0	0.6	31.2	66.6	15.7	0.6	n.a	3.1	3.3	n.a	1.4
20PM19B	-	Fine-grained jotunite	Hm-Ilm + Mt	n=6	25.9	0.0	0.2	11.5	255.1	38.4	0.2	n.a	1.1	9.3	n.a	0.9
CM1001A	-	Fine-grained ferrodiorite	Hm-ilm	n=4	24.6	0.2	0.2	32.6	189.1	20.7	0.2	n.a	2.3	7.8	0.5	0.4
CM1007	-	Medium-grained OAN	Hm-Ilm + Mt	n=4	15.2	0.2	0.2	39.0	68.0	9.0	0.2	n.a	3.4	3.6	0.3	0.2
CM1012	-	Medium-grained OAN	Hm-ilm	n=4	17.1	0.2	0.1	36.1	104.8	10.4	0.3	n.a	2.5	5.3	0.7	0.1
CM1013	-	Medium-grained OAN	Hm-Ilm + Mt	n=4	10.5	0.2	0.8	33.7	77.0	8.3	0.7	0.1	3.1	4.0	0.3	0.9
CM1036	-	Massive Oxides	Hm-ilm	n=4	12.1	0.1	0.1	22.0	33.1	5.4	0.0	0.1	1.4	1.8	0.1	0.3
CM1038	-	Medium-grained OAN	Hm-Ilm + Mt	n=4	17.8	0.2	0.2	45.9	55.3	9.4	0.3	n.a	3.8	2.9	0.2	0.2
CM1045	-	Medium-grained OAN	Hm-Ilm + Mt	n=4	12.5	0.2	0.1	50.0	58.8	9.0	0.2	n.a	5.8	3.0	0.3	n.a
CM1047	-	Medium-grained OAN	Hm-Ilm + Mt	n=4	8.6	0.1	0.1	33.1	69.2	11.0	0.1	n.a	3.0	3.2	0.2	0.2
CM1050	-	Medium-grained OAN	Hm-Ilm + Mt	n=4	7.0	0.2	0.0	35.6	29.1	9.2	0.1	n.a	3.3	1.4	n.a	0.4
CM1051	-	Medium-grained OAN	Hm-Ilm + Mt	n=4	13.1	0.2	0.1	24.9	68.9	8.6	0.1	n.a	1.8	3.4	0.4	0.3
CM1052	-	Medium-grained OAN	Hm-Ilm + Mt	n=4	8.6	0.1	0.1	41.1	40.4	7.9	0.1	n.a	4.0	2.2	0.1	0.5
CM1053	-	Medium-grained OAN	Hm-Ilm + Mt	n=4	4.6	0.1	0.1	42.1	46.4	8.0	0.0	n.a	4.7	2.7	0.2	0.1
CM1060	-	Fine-grained ferrodiorite	Hm-Ilm + Mt	n=4	19.6	0.2	0.1	35.0	81.5	17.0	0.3	n.a	3.6	3.8	0.1	0.4
CM1063B	-	Medium-grained OAN	Hm-ilm	n=4	21.4	0.2	0.1	77.6	59.2	10.7	0.3	n.a	6.0	2.9	0.3	0.2
CM1064	-	Nelsonite	Ilm + Mt	n=4	10.7	0.2	0.1	36.1	58.1	11.0	0.1	n.a	3.8	2.8	0.2	0.1
CM1067	-	Nelsonite	Ilm + Mt	n=4	3.8	0.1	0.0	24.6	52.2	10.0	0.0	n.a	2.7	2.6	n.a	0.1
CM1076B	-	Fine-grained ferrodiorite	Hm-Ilm + Mt	n=4	15.5	0.2	0.3	41.3	79.0	13.8	0.5	n.a	4.2	3.8	n.a	0.5

CM1110	-	Fine-grained ferrodiorite	Hm-Ilm + Mt	n=4	10.3	0.1	0.1	39.5	45.5	6.8	0.1	n.a	6.6	2.4	n.a	0.9
MX102-3	13.50	Fine-grained ferrodiorite	Hm-Ilm + Mt	n=4	15.1	0.2	0.6	15.6	109.8	15.7	2.3	0.1	1.4	5.1	0.2	5.2
MX102-5	21.00	Medium-grained OAN	Hm-Ilm + Mt	n=4	12.2	0.2	0.1	25.9	41.0	10.5	0.3	n.a	2.6	2.2	0.1	9.3
MX105-1	0.50	Medium-grained OAN	Hm-Ilm + Mt	n=4	14.3	0.2	0.3	33.7	57.6	9.9	0.3	n.a	2.9	2.8	0.1	3.8
MX106-1	5.00	Medium-grained OAN	Hm-Ilm + Mt	n=4	15.8	0.2	0.0	50.0	52.4	7.0	0.1	n.a	3.2	2.5	0.2	6.8
MX108-6	3.00	Semi-massive Oxides	Hm-Ilm + Mt	n=4	15.9	0.2	0.0	17.0	53.1	7.6	n.a	n.a	1.3	2.7	n.a	5.1
MX108-4	12.00	Fine-grained OAN	Hm-ilm	n=4	12.3	0.1	0.0	44.3	26.5	4.7	n.a	n.a	3.0	1.5	n.a	6.4
MX109-2	4.50	Semi-massive Oxides	Hm-ilm	n=4	11.8	0.2	0.0	28.3	35.1	5.8	0.2	n.a	2.0	1.9	n.a	5.1
MX114-1	8.50	Fine-grained ferrodiorite	Hm-Ilm + Mt	n=4	15.1	0.2	0.2	57.8	61.0	8.6	0.2	n.a	5.9	3.1	0.1	1.4
MX-115	16.50	Semi-massive Oxides	Hm-Ilm + Mt	n=4	8.3	0.2	0.0	20.4	34.8	5.2	n.a	n.a	1.5	1.9	n.a	10.2
MX-117	13.50	Massive Oxides	Hm-Ilm + Mt	n=4	11.0	0.1	n.a	46.3	58.8	8.0	n.a	n.a	4.0	3.0	n.a	2.1
MX-118	4.00	Massive Oxides	Hm-ilm	n=4	9.5	0.1	n.a	25.0	34.1	5.8	n.a	n.a	2.5	1.9	n.a	3.6
MX-123	0.50	Massive Oxides	Hm-ilm	n=4	7.7	0.1	0.0	28.0	34.6	5.4	n.a	n.a	4.4	2.0	n.a	10.2

Major elements in wt.%, FeO and Fe2O3 recalculated from FeOt by charge balance equations; molar fractions of geikielite, pyrophanite, hematite and ilmenite (Xhem, Xilm) calculated following QUILF algorithm (Andersen et al.1993); trace element in ppm. OAN = Oxide-apatite norite; Hm-ilm = hemo-ilmenite; Ilm = ilmenite; Mt = magnetite.

Appendix 3.1.8 Complete LA-ICP-MS results of magnetite

Sample	Depth (m)	Location	Lithology	Oxide Mineralogy	# analysis	SiO_2	TiO_2	Al_2O_3	FeO_t	Fe_2O_3	FeO	MnO	MgO	Total
20PM04B	-	Surface Outcrop	Massive Oxides	Ilm + Mt	n=6	0.05	0.08	0.51	91.91	67.98	30.73	0.01	0.05	100.39
20PM06B	-	Surface Outcrop	Medium-grained OAN	Hm-Ilm + Mt	n=6	0.0	0.1	0.4	92.0	66.3	32.2	0.0	0.0	99.5
20PM07	-	Surface Outcrop	Nelsonite	Ilm + Mt	n=6	0.0	0.1	0.4	92.0	67.7	31.2	0.0	0.1	100.1
20PM08B1	-	Surface Outcrop	Medium-grained OAN	Hm-Ilm + Mt	n=6	0.1	0.1	0.5	92.0	67.8	31.3	0.0	0.2	100.1
20PM08B2	-	Surface Outcrop	Medium-grained OAN	Hm-Ilm + Mt	n=6	0.4	0.1	0.4	92.0	67.8	31.0	0.0	0.4	100.4
20PM18B	-	Surface Outcrop	Medium-grained OAN	Hm-Ilm + Mt	n=6	0.6	0.1	0.4	92.0	68.4	30.4	0.0	0.1	100.4
20PM19B	-	Surface Outcrop	Fine-grained jotunite	Hm-Ilm + Mt	n=6	1.0	0.1	0.4	92.0	69.9	29.1	0.0	0.2	101.0
CM1007	-	Surface Outcrop	Medium-grained OAN	Hm-Ilm + Mt	n=4	0.1	0.1	0.0	92.0	65.2	33.3	0.0	0.1	99.1
CM1013	-	Surface Outcrop	Medium-grained OAN	Hm-Ilm + Mt	n=4	0.1	0.2	0.0	92.0	66.3	32.3	0.0	0.1	99.6
CM1038	-	Surface Outcrop	Medium-grained OAN	Hm-Ilm + Mt	n=4	0.7	0.2	0.0	92.0	67.2	31.5	0.0	0.1	100.0
CM1045	-	Surface Outcrop	Medium-grained OAN	Hm-Ilm + Mt	n=4	0.2	0.1	0.0	92.0	65.6	33.0	0.0	0.1	99.3
CM1047	-	Surface Outcrop	Medium-grained OAN	Hm-Ilm + Mt	n=4	0.1	0.1	0.0	92.0	65.6	33.0	0.0	0.1	99.3
CM1050	-	Surface Outcrop	Medium-grained OAN	Hm-Ilm + Mt	n=4	0.3	0.1	0.0	92.0	66.1	32.5	0.0	0.1	99.5
CM1051	-	Surface Outcrop	Medium-grained OAN	Hm-Ilm + Mt	n=4	0.4	0.2	0.0	92.0	66.3	32.3	0.0	0.1	99.6
CM1052	-	Surface Outcrop	Medium-grained OAN	Hm-Ilm + Mt	n=4	0.3	0.2	0.0	92.0	66.3	32.4	0.0	0.1	99.6
CM1053	-	Surface Outcrop	Medium-grained OAN	Hm-Ilm + Mt	n=4	0.3	0.2	0.0	92.0	66.4	32.2	0.0	0.2	99.6
CM1060	-	Surface Outcrop	Fine-grained ferrodiorite	Hm-Ilm + Mt	n=4	0.4	0.1	0.0	92.0	66.2	32.4	0.0	0.1	99.6
CM1064	-	Surface Outcrop	Nelsonite	Ilm + Mt	n=4	0.4	0.2	0.1	92.0	67.0	31.7	0.0	0.1	100.0
CM1067	-	Surface Outcrop	Nelsonite	Ilm + Mt	n=4	0.3	0.1	0.1	92.0	67.4	31.3	0.0	0.3	100.0
CM1076B	-	Surface Outcrop	Fine-grained ferrodiorite	Hm-Ilm + Mt	n=4	0.2	0.1	0.0	92.0	65.7	32.9	0.0	0.1	99.3
CM1110	-	Surface Outcrop	Fine-grained ferrodiorite	Hm-Ilm + Mt	n=4	0.2	0.1	0.0	92.0	66.3	32.4	0.0	0.1	99.6
MX102-3	13.50	Borehole MX-102	Fine-grained ferrodiorite	Hm-Ilm + Mt	n=4	0.4	0.1	0.1	92.0	66.8	31.8	0.0	0.2	99.8
MX102-5	21.00	Borehole MX-102	Medium-grained OAN	Hm-Ilm + Mt	n=4	0.4	0.1	0.0	92.0	66.4	32.3	0.0	0.2	99.6
MX105-1	0.50	Borehole MX-102	Medium-grained OAN	Hm-Ilm + Mt	n=4	0.6	0.2	0.0	92.0	66.9	31.8	0.0	0.1	99.9
MX106-1	5.00	Borehole MX-106	Medium-grained OAN	Hm-Ilm + Mt	n=4	0.6	0.2	0.0	92.0	67.3	31.4	0.0	0.2	100.1
MX108-6	3.00	Borehole MX-108	Semi-massive Oxides	Hm-Ilm + Mt	n=4	0.1	0.1	1.4	92.0	72.6	26.6	0.0	0.1	102.6
MX114-1	8.50	Borehole MX-114	Fine-grained ferrodiorite	Hm-Ilm + Mt	n=4	8.4	0.1	0.0	92.0	85.4	15.1	0.0	0.5	110.9
MX-115	16.50	Borehole MX-115	Semi-massive Oxides	Hm-Ilm + Mt	n=4	0.2	0.1	1.1	92.0	71.3	27.8	0.0	0.2	101.9
MX-117	13.50	Borehole MX-117	Massive Oxides	Hm-Ilm + Mt	n=4	0.1	0.1	1.5	92.0	73.1	26.2	0.0	0.2	102.8

Appendix 3.1.8 (Cont.) Complete LA-ICP-MS results of magnetite

Detection Limits (33-55µm)					0.157-0.672	0.904-4.484	298.61-2397.08	40.36-195.38	76.13-368.87	0.260-1.343	0.947-10.27	0.047-0.242	1.527-9.987	0.637-2.315
Sample	Depth (m)	Lithology	Oxide Mineralogy	# analysis	^{25}Mg	^{27}Al	^{29}Si	^{31}P	^{44}Ca	^{45}Sc	^{49}Ti	^{51}V	^{53}Cr	^{55}Mn
20PM04B	-	Massive Oxides	Ilm + Mt	n=6	308.9	2697.84	240.96	n.a	15.48	0.9	478.7	3662.0	2560.48	104.47
20PM06B	-	Medium-grained OAN	Hm-Ilm + Mt	n=6	181.2	2129.3	230.3	48.1	n.a	1.1	414.1	2366.8	219.4	38.5
20PM07	-	Nelsonite	Ilm + Mt	n=6	776.6	2156.2	306.8	15.3	n.a	1.0	512.5	3194.0	329.7	145.8
20PM08B1	-	Medium-grained OAN	Hm-Ilm + Mt	n=6	910.5	2397.8	574.9	18.9	n.a	1.3	559.1	1369.0	16.8	164.6
20PM08B2	-	Medium-grained OAN	Hm-Ilm + Mt	n=6	2478.2	2329.3	1988.7	40.3	n.a	1.3	412.3	1429.5	20.0	236.9
20PM18B	-	Medium-grained OAN	Hm-Ilm + Mt	n=6	576.3	2337.8	3035.9	29.3	n.a	1.6	508.0	1826.5	89.3	109.5
20PM19B	-	Fine-grained jotunite	Hm-Ilm + Mt	n=6	1311.5	2357.8	4657.4	86.9	436.6	2.6	428.5	1375.0	89.7	368.3
CM1007	-	Medium-grained OAN	Hm-Ilm + Mt	n=4	653.6	3243.3	551.7	25.0	n.a	1.3	552.6	1652.3	7.8	102.0
CM1013	-	Medium-grained OAN	Hm-Ilm + Mt	n=4	404.9	2587.3	521.3	2138.6	2100.7	1.3	1112.1	1911.7	9.6	75.6
CM1038	-	Medium-grained OAN	Hm-Ilm + Mt	n=4	898.3	4301.7	3267.2	600.6	361.1	1.8	1101.3	1408.2	72.1	82.4
CM1045	-	Medium-grained OAN	Hm-Ilm + Mt	n=4	416.3	2435.9	1199.1	43.0	n.a	1.4	915.8	1892.1	1.7	104.0
CM1047	-	Medium-grained OAN	Hm-Ilm + Mt	n=4	352.2	2851.6	612.5	111.1	n.a	1.6	768.1	2567.1	238.9	83.0
CM1050	-	Medium-grained OAN	Hm-Ilm + Mt	n=4	580.0	3366.8	1276.2	479.1	126.6	1.8	919.0	2360.0	250.0	101.7
CM1051	-	Medium-grained OAN	Hm-Ilm + Mt	n=4	611.2	3638.7	2041.3	44.5	n.a	1.7	1077.8	2257.6	4.7	90.8
CM1052	-	Medium-grained OAN	Hm-Ilm + Mt	n=4	733.5	3150.6	1274.6	69.1	n.a	1.3	1266.9	2638.7	81.4	104.7
CM1053	-	Medium-grained OAN	Hm-Ilm + Mt	n=4	1227.2	4080.4	1506.8	n.a	n.a	1.7	1484.6	1530.7	23.4	251.5
CM1060	-	Fine-grained ferrodiorite	Hm-Ilm + Mt	n=4	536.3	3588.1	1855.9	279.2	114.6	1.7	840.9	2122.8	141.1	101.3
CM1064	-	Nelsonite	Ilm + Mt	n=4	776.9	3447.4	1800.2	n.a	n.a	1.6	1269.2	3092.2	419.5	189.4
CM1067	-	Nelsonite	Ilm + Mt	n=4	1980.3	3663.3	1291.3	109.3	n.a	1.3	505.8	3413.3	457.4	172.1
CM1076B	-	Fine-grained ferrodiorite	Hm-Ilm + Mt	n=4	526.5	3486.3	1127.8	n.a	266.5	1.7	752.7	1940.0	32.3	80.5
CM1110	-	Fine-grained ferrodiorite	Hm-Ilm + Mt	n=4	781.4	3042.9	1218.3	136.6	131.8	0.8	811.3	3044.7	107.5	76.5
MX102-3	13.50	Fine-grained ferrodiorite	Hm-Ilm + Mt	n=4	999.1	1978.5	2184.7	156.7	190.2	1.4	491.9	2129.7	365.7	204.1

MX102-5	21.00	Medium-grained OAN	Hm-Ilm + Mt	n=4	1279.8	3274.5	1829.8	42.1	111.9	1.8	760.8	1300.0	43.0	275.2
MX105-1	0.50	Medium-grained OAN	Hm-Ilm + Mt	n=4	530.5	3821.1	2972.3	708.8	115.6	2.2	1501.6	1743.7	n.a	250.4
MX106-1	5.00	Medium-grained OAN	Hm-Ilm + Mt	n=4	986.1	3980.3	2803.3	n.a	74.1	2.5	1219.5	2532.7	81.3	403.0
MX108-6	3.00	Semi-massive Oxides	Hm-Ilm + Mt	n=4	789.5	3067.8	735.5	n.a	85.6	1.1	759.2	2805.1	8089.9	86.2
MX114-1	8.50	Fine-grained ferrodiorite	Hm-Ilm + Mt	n=4	2403.0	3727.0	28303.3	361.0	4761.4	2.0	743.9	1942.4	115.9	148.6
MX-115	16.50	Semi-massive Oxides	Hm-Ilm + Mt	n=4	1218.7	2896.6	883.6	n.a	n.a	0.9	523.2	2968.8	6106.9	138.1
MX-117	13.50	Massive Oxides	Hm-Ilm + Mt	n=4	1467.7	2712.3	715.4	n.a	110.9	1.0	383.1	2863.3	8321.2	76.3

.

Appendix 3.1.8 (Cont.) Complete LA-ICP-MS results of magnetite

Detection Limits (33-55µm)					0.029-0.208	0.719-2.736	0.447-1.605	0.816-3.891	0.147-0.608	0.096-0.545	0.024-0.095	0.05-0.06
Sample	Depth (m)	Lithology	Oxide Mineralogy	# analysis	^{59}Co	^{60}Ni	^{63}Cu	^{66}Zn	^{69}Ga	^{72}Ge	^{89}Y	^{90}Zr
20PM04B	-	Massive Oxides	Ilm + Mt	n=6	66.09	647.3	0.14	20.13	55.92	0.75	n.a	0.19
20PM06B	-	Medium-grained OAN	Hm-Ilm + Mt	n=6	20.5	62.0	0.5	29.0	84.0	0.5	n.a	0.0
20PM07	-	Nelsonite	Ilm + Mt	n=6	45.5	103.4	0.2	6.7	54.5	0.8	n.a	0.1
20PM08B 1	-	Medium-grained OAN	Hm-Ilm + Mt	n=6	21.6	3.8	n.a	29.9	77.2	0.8	n.a	0.1
20PM08B 2	-	Medium-grained OAN	Hm-Ilm + Mt	n=6	24.7	5.8	n.a	11.1	81.3	0.9	n.a	n.a
20PM18B	-	Medium-grained OAN	Hm-Ilm + Mt	n=6	23.1	27.1	0.6	138.8	75.5	1.1	n.a	n.a
20PM19B	-	Fine-grained jotunite	Hm-Ilm + Mt	n=6	21.6	9.1	0.9	10.2	135.2	1.6	n.a	0.7
CM1007	-	Medium-grained OAN	Hm-Ilm + Mt	n=4	27.6	1.6	1.0	320.5	122.9	0.8	n.a	0.3
CM1013	-	Medium-grained OAN	Hm-Ilm + Mt	n=4	22.8	2.7	0.5	53.4	116.2	0.8	2.2	0.4
CM1038	-	Medium-grained OAN	Hm-Ilm + Mt	n=4	23.1	9.7	9.8	322.8	121.3	0.9	0.4	0.6
CM1045	-	Medium-grained OAN	Hm-Ilm + Mt	n=4	29.2	5.6	2.6	203.8	119.3	1.0	0.1	0.2
CM1047	-	Medium-grained OAN	Hm-Ilm + Mt	n=4	38.4	82.5	5.7	80.2	95.2	0.8	0.1	n.a
CM1050	-	Medium-grained OAN	Hm-Ilm + Mt	n=4	28.6	66.4	3.2	65.2	93.5	0.8	0.1	0.1
CM1051	-	Medium-grained OAN	Hm-Ilm + Mt	n=4	30.8	32.7	2.5	345.1	116.6	1.1	0.1	0.2
CM1052	-	Medium-grained OAN	Hm-Ilm + Mt	n=4	42.9	35.1	1.4	61.4	99.2	0.7	n.a	0.4
CM1053	-	Medium-grained OAN	Hm-Ilm + Mt	n=4	26.6	4.9	0.7	401.3	94.7	0.9	0.0	0.4
CM1060	-	Fine-grained ferrodiorite	Hm-Ilm + Mt	n=4	33.4	18.3	18.4	861.4	118.5	1.8	0.1	0.4
CM1064	-	Nelsonite	Ilm + Mt	n=4	48.4	117.1	1.1	34.8	70.0	0.9	0.0	0.1
CM1067	-	Nelsonite	Ilm + Mt	n=4	49.8	139.5	2.3	52.8	61.1	0.8	n.a	0.2
CM1076B	-	Fine-grained ferrodiorite	Hm-Ilm + Mt	n=4	33.1	17.6	4.0	120.8	106.9	0.9	0.0	0.4
CM1110	-	Fine-grained ferrodiorite	Hm-Ilm + Mt	n=4	43.5	94.3	6.7	43.3	95.7	0.6	0.0	0.5
MX102-3	13.50	Fine-grained ferrodiorite	Hm-Ilm + Mt	n=4	28.3	42.9	0.5	60.4	124.8	1.0	0.1	0.4
MX102-5	21.00	Medium-grained OAN	Hm-Ilm + Mt	n=4	23.7	6.5	n.a	220.3	105.7	0.9	0.0	0.2

MX105-1	0.50	Medium-grained OAN	Hm-Ilm + Mt	n=4	34.9	4.0	27.9	1236.2	117.7	1.4	0.3	0.4
MX106-1	5.00	Medium-grained OAN	Hm-Ilm + Mt	n=4	68.7	76.7	0.9	187.2	122.8	1.2	n.a	0.1
MX108-6	3.00	Semi-massive Oxides	Hm-Ilm + Mt	n=4	61.8	148.3	0.6	134.0	130.6	0.8	n.a	0.5
MX114-1	8.50	Fine-grained ferrodiorite	Hm-Ilm + Mt	n=4	19.9	38.3	4.2	762.9	113.7	1.2	0.4	3.5
MX-115	16.50	Semi-massive Oxides	Hm-Ilm + Mt	n=4	52.0	356.6	0.8	42.3	87.6	0.9	n.a	0.2
MX-117	13.50	Massive Oxides	Hm-Ilm + Mt	n=4	86.6	496.4	1.9	139.9	117.7	0.6	n.a	0.4

Major elements in wt.%, FeO and Fe2O3 recalculated from FeOt by charge balance equations; trace element in ppm; OAN = Oxide-apatite norite; Hm-ilm = hemo-ilmenite; Ilm = ilmenite; Mt = magnetite.

Appendix 3.1.9 Complete LA-ICP-MS results of apatite

Sample	Depth (m)	Lithology	Location	Oxide Mineralogy	# analysis	La_2O_3	Ce_2O_3	Pr_2O_3	Nd_2O_3	CaO	P_2O_5	FeO_t	Total
20PM06B	-	Medium-grained OAN	Surface Outcrop	Hm-Ilm + Mt	n=6	0.02	0.06	0.01	0.05	54.67	41.84	0.34	97.01
20PM07	-	Nelsonite	Surface Outcrop	Ilm + Mt	n=6	0.04	0.11	0.02	0.08	54.58	43.88	0.28	98.98
20PM08B1	-	Medium-grained OAN	Surface Outcrop	Hm-Ilm + Mt	n=6	0.05	0.14	0.02	0.12	54.76	43.39	0.27	98.75
20PM08B2	-	Medium-grained OAN	Surface Outcrop	Hm-Ilm + Mt	n=6	0.05	0.13	0.02	0.11	53.91	46.48	0.09	100.79
20PM18B	-	Medium-grained OAN	Surface Outcrop	Hm-Ilm + Mt	n=6	0.07	0.18	0.03	0.13	51.96	46.62	0.24	99.21
20PM19A		Fine-grained ferrodiorite	Surface Outcrop	Hm-Ilm + Mt	n=6	0.07	0.22	0.03	0.18	54.43	48.44	0.06	103.42
20PM19B	-	Fine-grained jotunite	Surface Outcrop	Hm-Ilm + Mt	n=6	0.14	0.44	0.07	0.34	54.43	48.29	0.10	103.81
CM1001A	-	Fine-grained ferrodiorite	Surface Outcrop	Hm-ilm	n=4	0.14	0.39	0.06	0.27	54.43	48.99	0.27	104.54
CM1007	-	Medium-grained OAN	Surface Outcrop	Hm-Ilm + Mt	n=4	0.05	0.15	0.02	0.12	54.43	49.24	0.20	104.22
CM1012	-	Medium-grained OAN	Surface Outcrop	Hm-ilm	n=4	0.07	0.20	0.03	0.14	54.43	48.29	0.17	103.32
CM1013	-	Medium-grained OAN	Surface Outcrop	Hm-Ilm + Mt	n=4	0.05	0.14	0.02	0.11	54.43	48.52	0.13	103.41
CM1038	-	Medium-grained OAN	Surface Outcrop	Hm-Ilm + Mt	n=4	0.07	0.18	0.03	0.14	54.43	48.52	0.56	103.94
CM1045	-	Medium-grained OAN	Surface Outcrop	Hm-Ilm + Mt	n=4	0.05	0.12	0.02	0.09	54.43	48.33	0.18	103.22
CM1047	-	Medium-grained OAN	Surface Outcrop	Hm-Ilm + Mt	n=4	0.06	0.16	0.02	0.11	54.43	49.82	0.27	104.88
CM1050	-	Medium-grained OAN	Surface Outcrop	Hm-Ilm + Mt	n=4	0.03	0.09	0.01	0.07	54.43	49.58	0.37	104.59
CM1051	-	Medium-grained OAN	Surface Outcrop	Hm-Ilm + Mt	n=4	0.04	0.11	0.02	0.08	54.43	49.18	0.29	104.15
CM1052	-	Medium-grained OAN	Surface Outcrop	Hm-Ilm + Mt	n=4	0.04	0.11	0.02	0.08	54.43	49.38	0.15	104.20
CM1053	-	Medium-grained OAN	Surface Outcrop	Hm-Ilm + Mt	n=4	0.05	0.13	0.02	0.12	54.43	49.60	0.28	104.63
CM1060	-	Fine-grained ferrodiorite	Surface Outcrop	Hm-Ilm + Mt	n=4	0.08	0.19	0.03	0.13	54.43	48.55	0.18	103.59
CM1063B	-	Medium-grained OAN	Surface Outcrop	Hm-ilm	n=4	0.06	0.17	0.02	0.12	54.43	48.59	0.22	103.61
CM1064	-	Nelsonite	Surface Outcrop	Ilm + Mt	n=4	0.05	0.12	0.02	0.09	54.43	50.12	0.24	105.06
CM1067	-	Nelsonite	Surface Outcrop	Ilm + Mt	n=4	0.04	0.10	0.02	0.08	54.43	51.47	0.24	106.37
CM1076B	-	Fine-grained ferrodiorite	Surface Outcrop	Hm-Ilm + Mt	n=4	0.06	0.16	0.02	0.12	54.43	52.83	0.40	108.08
CM1110	-	Fine-grained ferrodiorite	Surface Outcrop	Hm-Ilm + Mt	n=4	0.04	0.09	0.01	0.07	54.43	47.62	0.19	102.44
MX102-3	13.50	Fine-grained ferrodiorite	Borehole MX-102	Hm-Ilm + Mt	n=4	0.07	0.19	0.03	0.14	54.43	47.23	0.36	102.45
MX102-5	21.00	Medium-grained OAN	Borehole MX-102	Hm-Ilm + Mt	n=4	0.07	0.20	0.03	0.15	54.43	47.27	0.26	102.40
MX105-1	0.50	Medium-grained OAN	Borehole MX-105	Hm-Ilm + Mt	n=4	0.05	0.13	0.02	0.11	54.43	46.45	0.17	101.35
MX106-1	5.00	Medium-grained OAN	Borehole MX-106	Hm-Ilm + Mt	n=4	0.05	0.12	0.02	0.09	54.43	48.83	0.18	103.72
MX108-6	3.00	Semi-massive Oxides	Borehole MX-108	Hm-Ilm + Mt	n=4	0.04	0.12	0.02	0.09	54.43	48.22	0.28	103.21
MX108-4	12.00	Fine-grained OAN	Borehole MX-108	Hm-ilm	n=4	0.02	0.05	0.01	0.04	54.43	47.17	0.19	101.89

MX114-1	8.50	Fine-grained OAN dyke	Borehole MX-114	Hm-Ilm + Mt	n=4	0.05	0.14	0.02	0.10	54.43	48.70	0.23	103.68

Appendix 3.1.9 (Cont.) Complete LA-ICP-MS results of apatite

Detection Limits (33-55µm bean size)					0.53 - 2.08	1.41 - 3.29	0.93-2.40	0.05-0.28	0.10-0.28	156.10 - 494.82	31.22 - 76.59	41.77 - 117.80	9.20-50.29	0.11 - 0.32	0.23-0.63	0.02 - 0.05	0.48 - 1.47
Sample	Depth (m)	Lithology	Oxide Mineralogy	# analysis	Li	B	Na	Mg	Al	Si	S	Cl	K	Sc	Ti	V	Cr
20PM06B	-	Medium-grained OAN	Hm-Ilm + Mt	n=6	2.9	46.4	631.1	543.9	498.2	2317.2	758.4	1483.8	65.4	5.4	90.0	8.7	1.8
20PM07	-	Nelsonite	Ilm + Mt	n=6	n.a	25.1	605.8	657.2	29.9	448.1	578.1	873.0	23.5	4.8	15.3	5.9	n.a
20PM08B1	-	Medium-grained OAN	Hm-Ilm + Mt	n=6	n.a	28.6	487.4	195.4	15.9	723.6	416.5	785.8	20.1	4.5	17.0	2.8	n.a
20PM08B2	-	Medium-grained OAN	Hm-Ilm + Mt	n=6	n.a	n.a	415.4	194.1	17.8	n.a	498.4	983.0	n.a	-0.3	0.0	2.4	1.8
20PM18B	-	Medium-grained OAN	Hm-Ilm + Mt	n=6	0.6	6.7	594.8	837.3	600.7	2105.5	766.0	929.0	n.a	1.2	3.5	6.9	n.a
20PM19A		Fine-grained ferrodiorite	Hm-Ilm + Mt	n=6	n.a	6.0	331.1	142.2	6.5	1615.9	441.0	1561.9	30.0	0.9	0.8	3.1	n.a
20PM19B	-	Fine-grained jotunite	Hm-Ilm + Mt	n=6	1.4	6.3	792.8	223.5	39.3	2788.1	818.1	2179.3	13.7	1.2	2.6	6.4	0.5
CM1001A	-	Fine-grained ferrodiorite	Hm-ilm	n=4	2.7	4.8	777.6	803.0	738.7	3745.4	966.1	1797.3	n.a	0.6	3.6	7.6	n.a
CM1007	-	Medium-grained OAN	Hm-Ilm + Mt	n=4	0.7	4.9	407.6	486.5	368.6	2055.0	350.2	922.9	13.6	0.7	8.1	3.5	n.a
CM1012	-	Medium-grained OAN	Hm-ilm	n=4	0.6	5.9	665.0	270.5	1206.4	4392.1	319.5	1259.0	64.5	0.5	1.1	3.2	0.5
CM1013	-	Medium-grained OAN	Hm-Ilm + Mt	n=4	n.a	4.5	379.3	214.7	371.8	1138.1	395.3	903.1	n.a	0.5	34.1	4.4	n.a
CM1038	-	Medium-grained OAN	Hm-Ilm + Mt	n=4	2.0	9.1	732.7	673.6	1656.6	4569.3	853.0	966.6	88.0	0.5	3.0	6.1	n.a
CM1045	-	Medium-grained OAN	Hm-Ilm + Mt	n=4	n.a	5.9	460.6	288.2	441.5	1620.3	372.3	839.9	17.9	0.7	10.6	4.4	n.a
CM1047	-	Medium-grained OAN	Hm-Ilm + Mt	n=4	0.8	6.1	413.8	278.3	895.8	1875.5	534.3	946.7	n.a	0.5	1.0	6.7	n.a
CM1050	-	Medium-grained OAN	Hm-Ilm + Mt	n=4	1.2	19.6	3483.0	887.0	14690.0	25892.7	543.5	876.5	138.3	1.1	5.6	4.7	n.a
CM1051	-	Medium-grained OAN	Hm-Ilm + Mt	n=4	0.7	8.4	473.7	407.3	465.1	3471.3	587.9	971.3	14.5	0.5	2.5	6.6	n.a
CM1052	-	Medium-grained OAN	Hm-Ilm + Mt	n=4	0.6	6.0	404.1	272.0	384.3	980.0	442.3	827.4	9.7	0.4	1.6	5.6	n.a
CM1053	-	Medium-grained OAN	Hm-Ilm + Mt	n=4	n.a	8.6	402.3	418.1	522.7	2664.4	308.7	724.3	21.6	0.6	16.2	2.3	n.a
CM1060	-	Fine-grained ferrodiorite	Hm-Ilm + Mt	n=4	1.1	7.7	1903.1	335.3	3267.6	10532.4	1019.0	1233.8	92.7	0.6	2.3	10.4	n.a
CM1063B	-	Medium-grained OAN	Hm-ilm	n=4	1.1	10.7	513.5	433.5	1002.8	3428.6	657.5	1048.3	35.8	0.5	4.6	6.9	n.a
CM1064	-	Nelsonite	Ilm + Mt	n=4	0.7	7.7	610.9	653.3	136.5	1723.0	890.9	937.4	n.a	0.7	5.4	8.7	n.a
CM1067	-	Nelsonite	Ilm + Mt	n=4	n.a	6.7	634.9	887.5	121.2	749.8	835.8	923.3	n.a	0.9	0.5	6.4	11.6

CM1076B	-	Fine-grained ferrodiorite	Hm-Ilm + Mt	n=4	0.6	9.5	339.7	272.9	245.2	2581.0	440.8	1088.0	19.1	0.8	294.0	4.8	n.a
CM1110	-	Fine-grained ferrodiorite	Hm-Ilm + Mt	n=4	0.7	7.1	1057.3	299.6	2096.5	6119.4	423.7	1115.4	30.4	0.3	5.8	5.7	n.a
MX102-3	13.50	Fine-grained ferrodiorite	Hm-Ilm + Mt	n=4	0.5	3.2	490.2	469.8	168.6	1594.2	388.6	1864.7	n.a	0.4	1.8	6.9	n.a
MX102-5	21.00	Medium-grained OAN	Hm-Ilm + Mt	n=4	0.6	3.5	510.1	421.5	148.1	1881.8	401.2	2042.2	n.a	0.4	1.5	7.0	n.a
MX105-1	0.50	Medium-grained OAN	Hm-Ilm + Mt	n=4	0.6	2.9	605.3	259.8	922.2	3308.2	355.5	813.6	22.0	0.7	4.0	3.8	n.a
MX106-1	5.00	Medium-grained OAN	Hm-Ilm + Mt	n=4	0.5	3.5	383.4	282.2	62.3	1081.6	443.3	840.1	n.a	0.4	1.2	5.4	n.a
MX108-6	3.00	Semi-massive Oxides	Hm-Ilm + Mt	n=4	0.6	3.2	432.1	603.0	293.9	1442.9	431.9	613.8	n.a	0.7	4.9	3.2	n.a
MX108-4	12.00	Fine-grained OAN	Hm-ilm	n=4	0.5	3.4	439.4	516.1	37.8	606.4	776.0	543.1	n.a	0.6	8.2	9.1	n.a
MX114-1	8.50	Fine-grained OAN dyke	Hm-Ilm + Mt	n=4	0.7	4.0	758.7	342.1	538.5	3438.4	572.5	885.2	27.5	0.4	2.0	7.3	n.a

Appendix 3.1.9 (Cont.) Complete LA-ICP-MS results of apatite

Detection Limits (33-55µm bean size)					0.32-0.72	0.49-1.07	0.01 - 0.04	0.17 - 0.31	0.12 - 0.27	0.10-0.26	0.03 - 0.07	0.19-0.34	0.11 - 0.25	0.01-0.07	0.01-0.02	0.01 - 0.02	0.004 - 0.007
Sample	Depth (m)	Lithology	Oxide Mineralogy	# analysis	Mn	Fe	Co	Ni	Cu	Zn	Ga	Ge	As	Sr	Y	Zr	Nb
20PM06B	-	Medium-grained OAN	Hm-Ilm + Mt	n=6	320.8	2621.6	3.9	4.5	1.9	1.7	0.8	9.1	3.6	943.4	200.2	0.7	0.0
20PM07	-	Nelsonite	Ilm + Mt	n=6	519.1	2141.4	3.4	3.6	0.3	1.1	0.3	13.1	4.2	1339.9	306.2	1.7	0.0
20PM08B1	-	Medium-grained OAN	Hm-Ilm + Mt	n=6	354.2	2077.8	3.4	3.2	0.1	1.1	0.5	19.2	6.3	1200.1	456.2	0.8	0.0
20PM08B2	-	Medium-grained OAN	Hm-Ilm + Mt	n=6	314.6	723.6	0.2	n.a	0.2	4.5	21.9	3.6	5.5	1246.7	402.1	0.6	0.0
20PM18B	-	Medium-grained OAN	Hm-Ilm + Mt	n=6	327.9	1826.8	0.7	1.0	0.2	9.5	1.6	69.5	21.9	712.2	493.0	0.8	0.0
20PM19A		Fine-grained ferrodiorite	Hm-Ilm + Mt	n=6	542.9	454.8	0.2	0.3	0.1	1.3	1.2	84.7	27.2	779.2	746.4	0.9	0.0
20PM19B	-	Fine-grained jotunite	Hm-Ilm + Mt	n=6	616.8	812.8	0.2	0.3	0.3	2.9	3.0	178.8	56.7	618.1	1350.7	0.5	0.0
CM1001A	-	Fine-grained ferrodiorite	Hm-ilm	n=4	384.0	2137.2	0.8	0.7	0.3	3.3	30.2	6.8	12.6	560.9	1251.5	1.0	0.1
CM1007	-	Medium-grained OAN	Hm-Ilm + Mt	n=4	333.5	1526.3	0.5	0.3	0.6	2.2	13.1	3.2	6.1	936.4	506.2	0.5	0.0
CM1012	-	Medium-grained OAN	Hm-ilm	n=4	299.9	1283.6	0.3	0.2	0.3	1.3	17.0	3.8	7.6	766.8	569.3	0.4	0.0
CM1013	-	Medium-grained OAN	Hm-Ilm + Mt	n=4	260.2	1035.1	0.4	0.3	0.2	1.2	11.7	2.9	5.4	862.8	443.4	0.5	0.0
CM1038	-	Medium-grained OAN	Hm-Ilm + Mt	n=4	329.8	4359.8	0.8	0.4	1.9	4.6	17.0	3.7	7.6	830.9	540.5	0.5	0.0
CM1045	-	Medium-grained OAN	Hm-Ilm + Mt	n=4	278.4	1367.8	0.4	0.3	0.5	8.8	10.3	2.3	4.3	882.2	350.0	0.7	0.0
CM1047	-	Medium-grained OAN	Hm-Ilm + Mt	n=4	367.1	2091.0	0.5	1.5	4.8	2.5	13.5	3.0	5.5	832.0	431.0	0.8	0.0
CM1050	-	Medium-grained OAN	Hm-Ilm + Mt	n=4	368.5	2866.8	3.3	17.8	27.7	10.1	11.9	2.1	3.9	1005.0	292.4	0.7	0.0
CM1051	-	Medium-grained OAN	Hm-Ilm + Mt	n=4	269.2	2220.5	0.5	0.5	1.5	3.1	10.2	2.2	4.7	888.4	335.7	0.9	0.0
CM1052	-	Medium-grained OAN	Hm-Ilm + Mt	n=4	249.9	1179.7	1.0	2.6	3.8	3.0	9.6	2.0	4.4	839.6	280.9	3.4	0.0
CM1053	-	Medium-grained OAN	Hm-Ilm + Mt	n=4	390.4	2152.8	1.1	0.4	1.0	6.8	13.7	3.2	6.2	909.7	465.1	1.1	0.0
CM1060	-	Fine-grained ferrodiorite	Hm-Ilm + Mt	n=4	330.9	1419.3	0.6	0.8	1.7	3.4	16.9	3.5	6.6	768.4	522.2	1.0	0.0
CM1063B	-	Medium-grained OAN	Hm-ilm	n=4	211.8	1693.7	0.7	2.3	2.2	5.0	16.3	3.4	7.3	684.8	476.8	0.6	0.0
CM1064	-	Nelsonite	Ilm + Mt	n=4	633.1	1853.8	0.5	0.8	0.3	5.0	11.8	2.4	4.9	1295.9	347.4	2.0	0.0
CM1067	-	Nelsonite	Ilm + Mt	n=4	547.5	1877.8	0.4	0.6	0.2	141.7	9.8	2.1	4.3	1310.5	309.0	2.6	0.0

CM1076B	-	Fine-grained ferrodiorite	Hm-Ilm + Mt	n=4	348.8	3116.9	0.7	0.9	0.9	8.4	15.9	3.5	7.2	809.4	483.1	0.5	0.2
CM1110	-	Fine-grained ferrodiorite	Hm-Ilm + Mt	n=4	237.7	1444.5	0.4	0.4	1.1	1.3	8.6	1.8	3.4	1021.3	235.4	0.8	0.0
MX102-3	13.50	Fine-grained ferrodiorite	Hm-Ilm + Mt	n=4	387.4	2784.4	0.5	0.3	0.2	3.5	15.6	3.6	8.4	669.7	609.9	1.2	0.0
MX102-5	21.00	Medium-grained OAN	Hm-Ilm + Mt	n=4	376.7	1983.8	0.4	0.3	0.2	3.7	16.5	3.8	9.0	669.6	638.9	1.4	0.0
MX105-1	0.50	Medium-grained OAN	Hm-Ilm + Mt	n=4	312.0	1288.7	0.5	0.2	0.6	19.1	11.4	2.7	4.9	886.5	426.6	0.6	0.0
MX106-1	5.00	Medium-grained OAN	Hm-Ilm + Mt	n=4	318.5	1410.0	0.6	0.6	0.3	6.2	11.1	2.5	4.6	887.5	360.8	0.7	0.0
MX108-6	3.00	Semi-massive Oxides	Hm-Ilm + Mt	n=4	571.2	2185.7	1.7	6.3	1.9	8.2	11.0	2.6	4.5	742.1	401.9	1.3	0.0
MX108-4	12.00	Fine-grained OAN	Hm-ilm	n=4	303.2	1446.1	0.4	0.9	0.3	10.1	4.4	1.0	1.9	1054.3	155.7	0.6	0.0
MX114-1	8.50	Fine-grained OAN dyke	Hm-Ilm + Mt	n=4	289.1	1785.7	0.3	1.9	0.1	2.5	12.9	2.9	4.9	825.6	418.1	1.4	0.0

Appendix 3.1.9 (Cont.) Complete LA-ICP-MS results of apatite

Detection Limits (33-55µm bean size)					0.02-0.05	0.05 - 0.17	0.02 - 0.04	0.02 - 0.06	0.003 - 0.014	0.003 - 0.012	0.002 - 0.008	0.012 - 0.030	0.013 - 0.021	0.003 - 0.009	0.015 - 0.057	0.002 - 0.004	0.008 - 0.014
Sample	Depth (m)	Lithology	Oxide Mineralogy	# analysis	Mo	Sn	Sb	Ba	La	Ce	Pr	Nd	Sm	Eu	Gd	Tb	Dy
20PM06B	-	Medium-grained OAN	Hm-Ilm + Mt	n=6	0.0	0.0	n.a	2.8	190.1	514.7	85.4	469.7	98.9	24.4	98.2	9.8	46.8
20PM07	-	Nelsonite	Ilm + Mt	n=6	0.0	0.0	n.a	0.8	355.0	903.5	135.9	695.6	143.2	34.5	135.9	14.4	71.1
20PM08B 1	-	Medium-grained OAN	Hm-Ilm + Mt	n=6	0.0	0.0	n.a	2.1	413.7	1180.0	193.5	1050.9	229.0	58.5	218.9	23.3	111.3
20PM08B 2	-	Medium-grained OAN	Hm-Ilm + Mt	n=6	0.0	0.0	n.a	1.4	391.7	1094.4	177.5	924.1	201.5	51.3	175.0	19.2	93.1
20PM18B	-	Medium-grained OAN	Hm-Ilm + Mt	n=6	0.0	0.1	n.a	0.6	568.4	1528.0	231.0	1099.1	219.2	48.3	187.2	21.7	112.5
20PM19A		Fine-grained ferrodiorite	Hm-Ilm + Mt	n=6	0.0	0.1	n.a	0.3	577.7	1843.3	297.5	1518.0	318.5	51.0	272.9	32.3	170.4
20PM19B	-	Fine-grained jotunite	Hm-Ilm + Mt	n=6	0.0	0.0	n.a	0.2	1222.7	3740.0	594.9	2891.7	597.7	83.8	476.8	58.1	311.8
CM1001A	-	Fine-grained ferrodiorite	Hm-ilm	n=4	0.0	n.a	n.a	0.8	1194.5	3302.4	491.8	2284.6	483.5	94.1	410.9	51.0	272.9
CM1007	-	Medium-grained OAN	Hm-Ilm + Mt	n=4	0.0	0.0	n.a	1.0	442.4	1267.4	203.5	1055.9	227.6	49.9	203.3	22.6	115.4
CM1012	-	Medium-grained OAN	Hm-ilm	n=4	0.0	0.0	n.a	3.8	621.3	1679.5	254.3	1240.0	253.1	46.8	218.6	25.1	130.5
CM1013	-	Medium-grained OAN	Hm-Ilm + Mt	n=4	0.0	n.a	n.a	1.8	433.1	1197.0	187.8	937.6	200.4	44.1	175.9	19.8	100.8
CM1038	-	Medium-grained OAN	Hm-Ilm + Mt	n=4	0.0	0.0	n.a	14.7	600.2	1569.2	241.4	1200.3	247.7	58.1	214.4	23.8	122.6
CM1045	-	Medium-grained OAN	Hm-Ilm + Mt	n=4	0.0	n.a	n.a	7.4	407.6	1051.8	158.9	794.4	164.2	39.5	143.9	15.8	79.4
CM1047	-	Medium-grained OAN	Hm-Ilm + Mt	n=4	0.0	0.0	n.a	105.4	545.9	1366.2	199.5	966.4	193.4	44.5	166.0	18.6	95.5
CM1050	-	Medium-grained OAN	Hm-Ilm + Mt	n=4	0.0	0.7	n.a	15.4	278.7	767.9	122.1	637.4	139.6	35.0	125.4	13.7	67.2
CM1051	-	Medium-grained OAN	Hm-Ilm + Mt	n=4	0.0	n.a	n.a	9.2	362.1	948.7	143.7	712.9	145.9	35.5	129.2	14.6	75.1
CM1052	-	Medium-grained OAN	Hm-Ilm + Mt	n=4	0.0	n.a	n.a	1.3	363.2	926.8	136.9	673.5	133.1	33.2	115.7	12.4	62.0
CM1053	-	Medium-grained OAN	Hm-Ilm + Mt	n=4	0.4	0.0	n.a	1.5	404.5	1131.6	184.6	989.0	215.8	55.0	197.9	21.8	110.1
CM1060	-	Fine-grained ferrodiorite	Hm-Ilm + Mt	n=4	0.0	n.a	n.a	88.7	645.0	1650.8	242.6	1155.7	229.7	48.6	197.0	22.7	118.9
CM1063B	-	Medium-grained OAN	Hm-ilm	n=4	0.0	0.1	n.a	0.9	533.7	1413.7	210.6	1014.4	203.8	38.2	179.2	20.8	107.7
CM1064	-	Nelsonite	Ilm + Mt	n=4	0.0	n.a	n.a	1.1	398.5	1030.1	153.9	757.9	154.0	36.0	135.9	15.2	77.7
CM1067	-	Nelsonite	Ilm + Mt	n=4	0.0	0.1	n.a	0.8	335.7	872.7	132.2	662.8	136.9	33.6	121.0	13.5	68.6
CM1076B	-	Fine-grained ferrodiorite	Hm-Ilm + Mt	n=4	0.0	n.a	n.a	1.8	518.0	1381.2	212.6	1058.6	212.5	47.6	186.4	20.9	106.3

CM1110	-	Fine-grained ferrodiorite	Hm-Ilm + Mt	n=4	0.0	0.1	n.a	6.2	300.0	788.2	118.1	578.3	116.9	27.5	100.5	10.7	53.7
MX102-3	13.50	Fine-grained ferrodiorite	Hm-Ilm + Mt	n=4	0.0	n.a	n.a	1.2	595.7	1616.2	250.1	1216.5	250.5	53.4	219.3	25.6	133.9
MX102-5	21.00	Medium-grained OAN	Hm-Ilm + Mt	n=4	0.0	n.a	n.a	0.6	635.8	1708.3	261.5	1265.2	260.8	54.9	227.2	26.8	140.9
MX105-1	0.50	Medium-grained OAN	Hm-Ilm + Mt	n=4	0.0	0.1	0.1	4.6	385.5	1112.3	176.9	924.0	196.7	48.6	176.9	19.4	96.6
MX106-1	5.00	Medium-grained OAN	Hm-Ilm + Mt	n=4	0.0	n.a	n.a	0.8	404.9	1044.3	157.2	768.8	156.9	37.8	136.8	15.5	79.5
MX108-6	3.00	Semi-massive Oxides	Hm-Ilm + Mt	n=4	0.0	0.0	n.a	1.8	377.4	1050.0	162.8	810.5	170.4	32.4	150.9	17.2	89.4
MX108-4	12.00	Fine-grained OAN	Hm-ilm	n=4	#DIV/0!	n.a	n.a	125.4	146.5	402.8	65.5	349.9	74.3	18.2	67.6	7.0	33.9
MX114-1	8.50	Fine-grained OAN dyke	Hm-Ilm + Mt	n=4	0.0	n.a	0.5	4.5	457.2	1186.7	180.5	892.4	183.0	43.3	160.8	18.1	92.8

Appendix 3.1.9 (Cont.) Complete LA-ICP-MS results of apatite

Detection Limits (33-55µm bean size)					0.002-0.003	0.006-0.015	0.002-0.004	0.009-0.027	0.002-0.003	0.010-0.036	0.006-0.036	0.004-0.022	0.004-0.007	0.003-0.008
Sample	Depth (m)	Lithology	Oxide Mineralogy	# analysis	Ho	Er	Tm	Yb	Lu	W	Pb	Bi	Th	U
20PM06 B	-	Medium-grained OAN	Hm-Ilm + Mt	n=6	7.7	17.0	1.8	9.5	1.3	n.a	0.8	0.0	1.7	0.5
20PM07	-	Nelsonite	Ilm + Mt	n=6	12.0	28.1	3.1	16.6	2.2	n.a	3.4	0.0	3.3	1.0
20PM08 B1	-	Medium-grained OAN	Hm-Ilm + Mt	n=6	18.3	42.4	4.4	22.5	3.0	n.a	1.1	0.0	3.2	1.3
20PM08 B2	-	Medium-grained OAN	Hm-Ilm + Mt	n=6	15.7	35.3	3.5	19.4	2.4	n.a	1.2	0.0	3.1	1.3
20PM18 B	-	Medium-grained OAN	Hm-Ilm + Mt	n=6	19.0	46.2	5.2	28.1	3.8	n.a	1.7	0.0	4.4	2.0
20PM19 A		Fine-grained ferrodiorite	Hm-Ilm + Mt	n=6	29.2	69.9	7.8	43.4	5.5	n.a	2.8	0.1	22.1	5.5
20PM19 B	-	Fine-grained jotunite	Hm-Ilm + Mt	n=6	54.0	131.2	15.6	85.7	11.2	n.a	2.6	0.0	1.5	1.0
CM1001 A	-	Fine-grained ferrodiorite	Hm-ilm	n=4	48.1	118.7	14.1	78.6	10.6	0.1	4.5	0.0	21.4	6.4
CM1007	-	Medium-grained OAN	Hm-Ilm + Mt	n=4	19.4	44.9	4.9	25.9	3.4	n.a	2.3	0.0	5.8	1.9
CM1012	-	Medium-grained OAN	Hm-ilm	n=4	22.3	52.9	6.0	33.0	4.3	0.1	2.8	0.0	14.4	3.9
CM1013	-	Medium-grained OAN	Hm-Ilm + Mt	n=4	17.1	39.6	4.4	23.5	3.1	n.a	2.2	0.0	5.7	1.9
CM1038	-	Medium-grained OAN	Hm-Ilm + Mt	n=4	20.6	47.7	5.2	27.5	3.6	n.a	2.1	0.0	7.5	2.4
CM1045	-	Medium-grained OAN	Hm-Ilm + Mt	n=4	13.5	31.1	3.3	17.8	2.4	n.a	1.5	0.0	3.9	1.9
CM1047	-	Medium-grained OAN	Hm-Ilm + Mt	n=4	16.3	38.3	4.3	23.8	3.1	n.a	2.9	0.0	8.9	2.1
CM1050	-	Medium-grained OAN	Hm-Ilm + Mt	n=4	11.1	24.2	2.5	12.7	1.6	n.a	1.5	0.0	1.8	0.9
CM1051	-	Medium-grained OAN	Hm-Ilm + Mt	n=4	12.9	30.4	3.4	18.6	2.4	n.a	1.5	0.0	5.2	2.4
CM1052	-	Medium-grained OAN	Hm-Ilm + Mt	n=4	10.4	24.1	2.6	14.0	1.9	n.a	1.2	0.0	2.9	1.0
CM1053	-	Medium-grained OAN	Hm-Ilm + Mt	n=4	18.5	42.1	4.5	23.4	3.1	n.a	1.4	0.0	4.8	1.5
CM1060	-	Fine-grained ferrodiorite	Hm-Ilm + Mt	n=4	20.6	49.6	5.6	31.0	4.1	n.a	2.1	0.0	4.7	1.7
CM1063 B	-	Medium-grained OAN	Hm-ilm	n=4	18.5	44.1	5.0	27.7	3.6	n.a	2.0	0.0	10.3	3.1
CM1064	-	Nelsonite	Ilm + Mt	n=4	13.3	31.3	3.5	19.3	2.6	n.a	2.1	0.0	2.9	0.9
CM1067	-	Nelsonite	Ilm + Mt	n=4	11.7	27.6	3.1	16.8	2.2	n.a	3.0	0.0	3.1	0.9
CM1076 B	-	Fine-grained ferrodiorite	Hm-Ilm + Mt	n=4	18.0	42.5	4.7	25.9	3.4	n.a	1.4	0.0	1.9	0.8

CM1110	-	Fine-grained ferrodiorite	Hm-Ilm + Mt	n=4	8.9	20.0	2.1	11.7	1.5	n.a	1.5	n.a	2.4	0.8
MX102-3	13.50	Fine-grained ferrodiorite	Hm-Ilm + Mt	n=4	23.3	56.6	6.5	36.6	4.9	0.1	2.8	0.1	5.4	2.4
MX102-5	21.00	Medium-grained OAN	Hm-Ilm + Mt	n=4	24.5	59.2	6.8	38.0	5.1	0.1	3.2	0.1	7.2	2.6
MX105-1	0.50	Medium-grained OAN	Hm-Ilm + Mt	n=4	16.4	37.9	4.1	21.6	2.9	n.a	4.4	0.0	3.3	1.3
MX106-1	5.00	Medium-grained OAN	Hm-Ilm + Mt	n=4	13.5	31.9	3.6	19.7	2.6	n.a	3.3	0.0	5.2	1.6
MX108-6	3.00	Semi-massive Oxides	Hm-Ilm + Mt	n=4	15.3	36.3	4.1	22.2	2.9	n.a	2.1	0.0	3.7	1.4
MX108-4	12.00	Fine-grained OAN	Hm-ilm	n=4	5.7	12.9	1.4	7.9	1.1	n.a	17.5	0.0	0.9	0.4
MX114-1	8.50	Fine-grained OAN dyke	Hm-Ilm + Mt	n=4	15.8	37.6	4.2	23.0	3.1	n.a	1.6	0.1	3.3	1.0

[La/Yb]n and Eu/Eu* = (Eu)n/[(Sm)n x (Gd)n]0.5 calculated with Chondrite normalization values of Sun & McDonough (1989). OAN = Oxide-apatite norite; Hm-ilm = hemo-ilmenite; Ilm = ilmenite; Mt = magnetite.

Appendix 3.1.10 Compilation of whole-rock analysis of ferrodiorite dykes

Sample	Rock Type	Location	SiO_2	TIO_2	Al_2O_3	Fe_2O_3	FeO	MnO	MgO	CaO	Na_2O	K_2O	P_2O_5	Total	V	Cr	Co
20PM19A	Ferrodiorite dyke	Lac Mirepoix - Canada	51.8	1.3	21.7	6.4	-	0.1	1.5	8.5	4.7	1.3	0.8	100.0	71.3	23.0	12.1
20PM19B	Jotunite dyke	Lac Mirepoix - Canada	58.0	2.0	14.8	9.4	-	0.1	2.1	5.5	3.1	3.5	1.4	100.0	99.5	19.2	15.6
MX102-3	Ferrodiorite dyke	Lac Mirepoix - Canada	40.4	4.6	12.5	19.6	-	0.2	5.5	9.1	2.9	0.8	3.7	100.0	337.2	22.1	53.7
MX114-1	Ferrodiorite dyke	Lac Mirepoix - Canada	28.0	6.5	8.8	32.4	-	0.3	5.4	9.8	1.6	0.4	6.0	100.0	661.9	40.1	83.2
CM1001A	Ferrodiorite dyke	Lac Mirepoix - Canada	46.8	3.1	13.5	14.9	-	0.2	4.3	7.7	3.2	2.0	2.4	98.1	113.1	-	21.9
CM1060	Ferrodiorite dyke	Lac Mirepoix - Canada	39.1	4.0	12.3	21.2	-	0.2	5.4	10.3	2.2	0.5	3.6	98.9	210.2	-	20.5
CM1076B	Ferrodiorite dyke	Lac Mirepoix - Canada	39.0	4.0	12.6	21.1	-	0.2	5.1	10.7	2.0	0.5	3.5	98.8	197.5	-	21.9
CM1110	Ferrodiorite dyke	Lac Mirepoix - Canada	29.7	7.0	6.6	27.1	-	0.3	8.9	11.4	0.9	0.2	7.0	99.0		18.7	17.6
LO-06[#]	Ferrodiorite dyke	Lac a L'Orignal - Canada	34.6	5.1	10.9	23.7	-	0.3	6.3	10.2	2.2	0.4	5.3	100.0	297.6	49.2	48.5
LO-08[#]	Ferrodiorite dyke	Lac a L'Orignal - Canada	41.8	5.2	13.5	19.3	-	0.2	4.6	8.8	3.2	0.7	2.7	100.0	341.3	32.6	57.4
89115[a]	Evolved Jotunite	Rogaland Province - Norway	46.5	4.0	13.2	15.7	-	0.2	3.3	7.8	3.5	1.8	2.4	98.4	109.0	—	48.9
8925[a]	Evolved Jotunite	Rogaland Province - Norway	46.9	4.1	13.2	15.6	-	0.2	3.4	7.7	3.3	1.5	2.6	98.5	187.0	—	56.9
75202F[a]	Evolved Jotunite	Rogaland Province - Norway	46.9	3.6	13.5	15.4	-	0.2	3.2	8.4	3.4	1.8	2.5	98.8	159.0	66.0	34.7
8926[a]	Evolved Jotunite	Rogaland Province - Norway	47.2	3.6	13.8	15.7	-	0.2	3.4	7.2	3.6	1.7	2.3	98.6	164.0	—	51.1
7355[a]	Evolved Jotunite	Rogaland Province - Norway	47.9	3.5	13.4	16.0	-	0.3	3.4	7.8	3.7	1.5	2.0	99.4	231.0	—	49.6
75204[a]	Varberg Dyke	Rogaland Province - Norway	49.3	3.4	13.5	15.0	-	0.2	2.8	7.1	3.4	2.2	2.1	99.1	116.0	65.7	30.9

T2[a]	Tellnes Dyke	Rogaland Province - Norway	49.5	3.1	13.5	15.3	-	0.3	2.7	6.3	3.1	3.4	2.0	99.3	87.0	48.8	27.1
T221[a]	Tellnes Dyke	Rogaland Province - Norway	51.2	3.1	13.3	14.8	-	0.2	2.8	6.5	3.1	3.0	1.8	99.8	66.0	-	30.8
78211[a]	Eivatn Dyke	Rogaland Province - Norway	49.8	3.2	13.1	15.0	-	0.2	2.7	7.2	3.0	2.5	2.2	98.8	142.0	-	47.1
91141[a]	Primitive Jotunite	Rogaland Province - Norway	50.4	4.6	14.7	13.2	-	0.2	5.0	7.0	3.5	1.1	0.7	100.3	284.0	-	72.9
145–937[b]	Ferrodiorite dyke	Grader Intrusion - Canada	39.0	4.6	13.7	20.9	-	0.2	4.3	10.4	2.4	0.5	3.3	99.2	250.0	15.6	58.0
145–938[b]	Ferrodiorite dyke	Grader Intrusion - Canada	38.5	4.4	13.1	21.8	-	0.2	4.5	10.5	2.5	0.5	3.3	99.2	287.0	28.5	54.0
223–601[b]	Ferrodiorite dyke	Grader Intrusion - Canada	39.7	3.9	12.7	21.9	-	0.2	4.9	11.2	2.5	0.4	2.7	100.1	251.0	5.9	57.0
223–604[b]	Ferrodiorite dyke	Grader Intrusion - Canada	39.5	6.2	15.0	16.8	-	0.1	5.3	9.4	2.9	0.5	3.1	98.7	337.0	42.4	51.0
225–135[b]	Ferrodiorite dyke	Grader Intrusion - Canada	37.7	5.2	11.9	21.0	-	0.2	5.2	11.2	2.2	0.3	3.9	98.8	233.0	6.3	54.0
145–648[b]	Ferrodiorite dyke	Grader Intrusion - Canada	40.1	4.6	13.6	19.9	-	0.2	5.1	9.5	2.7	0.5	2.9	99.1	283.0	24.0	54.0
225–302[b]	Ferrodiorite dyke	Grader Intrusion - Canada	52.5	4.3	13.4	14.5	-	0.2	2.8	5.1	3.3	2.2	0.8	99.0	150.0	7.6	34.0
7252[c]	Evolved Jotunite	Rogaland Province - Norway	47.3	3.6	12.8	16.0	-	0.2	3.4	7.4	3.5	2.3	2.7	99.4	128.0	22.0	36.0
80123[d]	Primitive Jotunite	Rogaland Province - Norway	49.4	3.7	15.8	13.1	-	0.1	4.5	6.9	3.5	1.0	0.7	98.7	216.0	28.0	49.0
7234[e]	Primitive Jotunite	Rogaland Province - Norway	49.5	3.8	14.5	13.7	-	0.2	4.9	6.0	3.5	2.0	0.9	99.0	300.0	31.8	46.5
BA13[f]	Jotunite/ Mangerite	Rogaland Province - Norway	54.5	2.8	13.9	3.0	9.7	0.2	3.4	5.0	4.2	2.5	0.7	99.9	-	-	23.7
BA8[f]	Jotunite/ Mangerite	Rogaland Province - Norway	54.9	2.1	14.2	3.4	9.2	0.2	2.0	5.2	4.7	3.7	1.0	100.5	-	-	15.3
BA26[f]	Jotunite/ Mangerite	Rogaland Province - Norway	55.5	1.9	14.4	3.1	9.0	0.2	2.0	4.9	4.6	3.7	0.9	100.1	-	-	18.4

Appendix 3.1.10 (Cont.) Compilation of whole-rock analysis of ferrodiorite dykes

Sample	Rock Type	Location	Ni	Cu	Zn	Ga	Rb	Sr	Y	Zr	Nb	Ba	La	Ce	Pr	Nd	Sm
20PM19A	Ferrodiorite dyke	Lac Mirepoix - Canada	13.1	5.1	101.2	25.4	10.2	1637.0	17.6	70.7	7.0	1364.9	28.1	62.5	8.5	38.2	7.5
20PM19B	Jotunite dyke	Lac Mirepoix - Canada	11.8	10.7	140.9	29.3	46.0	1034.3	61.9	1173.2	25.3	3074.9	101.6	235.0	32.3	140.3	27.0
MX102-3	Ferrodiorite dyke	Lac Mirepoix - Canada	55.8	34.2	285.5	25.2	7.1	1001.1	59.6	255.5	18.0	1047.4	73.6	179.8	25.8	120.3	23.9
MX114-1	Ferrodiorite dyke	Lac Mirepoix - Canada	70.7	47.1	398.9	30.5	1.7	779.6	56.5	360.9	12.7	486.9	64.6	164.2	24.3	121.1	24.4
CM1001A	Ferrodiorite dyke	Lac Mirepoix - Canada	31.5	3.9	219.9	24.5	21.4	909.5	78.5	437.9	25.9	1991.6	-	170.6	-	-	-
CM1060	Ferrodiorite dyke	Lac Mirepoix - Canada	44.3	12.4	244.5	16.6	9.7	1013.5	63.7	194.8	19.7	870.3	-	132.0	-	-	-
CM1076B	Ferrodiorite dyke	Lac Mirepoix - Canada	44.7	19.3	244.9	16.5	9.5	902.9	51.4	133.6	13.7	607.5	-	124.7	-	-	-
CM1110	Ferrodiorite dyke	Lac Mirepoix - Canada	57.1	4.1	224.6	6.0	10.8	587.7	51.2	159.9	19.2	234.1	51.8	134.0	18.9	99.1	20.4
LO-06[#]	Ferrodiorite dyke	Lac a L'Orignal - Canada	52.7	98.3	353.8	24.4	4.5	1024.9	52.5	386.2	23.3	765.6	69.3	165.2	22.8	101.6	19.6
LO-08[#]	Ferrodiorite dyke	Lac a L'Orignal - Canada	68.6	55.4	421.2	25.1	2.9	906.3	45.9	107.2	10.7	862.0	53.5	135.4	19.9	97.5	19.4
89115[a]	Evolved Jotunite	Rogaland Province - Norway	-	-	214.0	31.6	10.6	465.0	64.0	253.0	39.9	1602.0	65.3	130.0	19.6	92.1	21.7
8925[a]	Evolved Jotunite	Rogaland Province - Norway	-	-	226.0	30.7	12.7	463.0	69.0	203.0	43.6	1435.0	60.7	142.0	21.4	99.0	22.4
75202F[a]	Evolved Jotunite	Rogaland Province - Norway	16.0	-	190.0	—	10.6	415.0	72.0	191.0	26.0	1362.0	48.8	112.0	-	-	14.1
8926[a]	Evolved Jotunite	Rogaland Province - Norway	-	-	233.0	36.1	12.6	465.0	57.0	402.0	22.6	1400.0	50.8	119.0	17.7	78.6	18.9
7355[a]	Evolved Jotunite	Rogaland Province - Norway	-	-	—	30.4	16.6	412.0	107.0	509.0	32.5	1130.0	79.9	180.0	26.5	119.0	27.7
75204[a]	Varberg Dyke	Rogaland Province - Norway	25.0	-	212.0	—	20.4	375.0	87.0	250.0	27.0	1009.0	63.7	151.0	-	-	16.9

T2[a]	Tellnes Dyke	Rogaland Province - Norway	23.0	-	258.0	—	25.4	342.0	95.0	687.0	29.0	1541.0	55.8	131.0	-	96.0	17.8
T221[a]	Tellnes Dyke	Rogaland Province - Norway	3.0	-	223.0	—	19.2	349.0	78.0	598.0	28.0	1542.0	54.7	121.0	-	-	18.8
78211[a]	Eivatn Dyke	Rogaland Province - Norway	-	-	—	32.1	28.5	341.0	70.0	473.0	27.2	1346.0	58.0	132.0	19.4	89.5	21.4
91141[a]	Primitive Jotunite	Rogaland Province - Norway	-	-	133.0	21.7	5.8	461.0	33.0	241.0	21.9	801.0	14.8	31.0	4.9	24.1	6.2
145–937[b]	Ferrodiorite dyke	Grader Intrusion - Canada	27.0	56.0	222.0	31.0	3.2	688.0	50.6	190.0	17.3	305.0	51.1	134.0	20.9	82.5	18.4
145–938[b]	Ferrodiorite dyke	Grader Intrusion - Canada	30.0	55.0	261.0	35.0	3.1	718.0	66.6	197.0	20.4	394.0	56.6	145.0	22.8	96.2	21.9
223–601[b]	Ferrodiorite dyke	Grader Intrusion - Canada	50.0	84.0	263.0	36.0	1.2	637.0	59.8	147.0	17.2	309.0	40.6	108.0	16.0	74.1	16.1
223–604[b]	Ferrodiorite dyke	Grader Intrusion - Canada	93.0	31.0	85.0	38.0	3.0	669.0	66.4	163.0	19.2	301.0	54.3	141.0	22.4	91.2	18.3
225–135[b]	Ferrodiorite dyke	Grader Intrusion - Canada	28.0	66.0	213.0	30.0	0.3	698.0	47.1	147.0	17.6	235.0	49.9	122.0	19.0	90.8	18.7
145–648[b]	Ferrodiorite dyke	Grader Intrusion - Canada	56.0	77.0	200.0	25.0	3.0	592.0	54.0	151.0	21.6	325.0	58.0	144.0	20.7	91.2	18.6
225–302[b]	Ferrodiorite dyke	Grader Intrusion - Canada	27.0	33.0	207.0	27.0	30.0	642.0	25.0	376.0	19.2	945.0	34.2	81.0	11.8	50.8	13.2
7252[c]	Evolved Jotunite	Rogaland Province - Norway	6.6	-	197.0	-	17.0	354.0	79.0	442.0	27.0	1212.0	54.7	138.0	-	106.0	20.4
80123[d]	Primitive Jotunite	Rogaland Province - Norway	60.0	-	144.0	-	18.0	530.0	22.0	262.0	-	470.0	23.9	58.0	-	39.0	8.5
7234[e]	Primitive Jotunite	Rogaland Province - Norway	55.0	-	—	-	43.0	382.0	-	300.0	-	580.0	35.3	82.0	-	52.9	11.5
BA13[f]	Jotunite/ Mangerite	Rogaland Province - Norway	-	-	204.0	-	32.0	319.0	72.0	701.0	50.0	872.0	44.9	91.0	-	74.0	15.0
BA8[f]	Jotunite/ Mangerite	Rogaland Province - Norway	-	-	217.0	-	44.0	259.0	82.0	461.0	30.0	1084.0	48.4	106.0	-	88.0	18.3
BA26[f]	Jotunite/ Mangerite	Rogaland Province - Norway	-	-	241.0	-	46.0	269.0	78.0	445.0	28.0	1154.0	45.0	113.0	-	78.0	18.5

Appendix 3.1.10 (Cont.) Compilation of whole-rock analysis of ferrodiorite dykes

Sample	Rock Type	Location	Eu	Gd	Tb	Dy	Ho	Er	Tm	Yb	Lu	Hf	Ta	W	Pb	Th	U
20PM19A	Ferrodiorite dyke	Lac Mirepoix - Canada	3.3	6.1	0.7	3.8	0.7	1.7	0.2	1.2	0.2	2.0	`	-	14.7	-	-
20PM19B	Jotunite dyke	Lac Mirepoix - Canada	6.0	20.7	2.5	13.8	2.4	6.2	0.8	4.7	0.7	23.9	-	-	30.2	-	-
MX102-3	Ferrodiorite dyke	Lac Mirepoix - Canada	6.9	22.9	2.5	13.0	2.3	5.8	0.7	4.1	0.6	7.3	-	-	7.8	-	-
MX114-1	Ferrodiorite dyke	Lac Mirepoix - Canada	6.4	23.7	2.6	12.7	2.2	5.1	0.6	3.2	0.5	8.5	-	-	3.0	-	-
CM1001A	Ferrodiorite dyke	Lac Mirepoix - Canada	-	-	-	-	-	-	-	-	-	-	-	-	35.0	-	-
CM1060	Ferrodiorite dyke	Lac Mirepoix - Canada	-	-	-	-	-	-	-	-	-	-	-	-	28.0	-	-
CM1076B	Ferrodiorite dyke	Lac Mirepoix - Canada	-	-	-	-	-	-	-	-	-	-	-	-	29.0	-	-
CM1110	Ferrodiorite dyke	Lac Mirepoix - Canada	5.0	17.3	2.0	10.0	1.8	3.7	0.4	2.5	0.3	-	-	-	34.0	-	-
LO-06[#]	Ferrodiorite dyke	Lac a L'Orignal - Canada	5.2	16.2	2.1	11.1	1.9	5.1	0.6	3.7	0.5	9.5	1.1	-	10.8	1.1	0.6
LO-08[#]	Ferrodiorite dyke	Lac a L'Orignal - Canada	5.4	16.7	1.9	9.7	1.7	4.0	0.4	2.5	0.3	3.0	0.5	-	5.0	0.6	0.2
89115[a]	Evolved Jotunite	Rogaland Province - Norway	7.9	18.6	2.7	12.5	2.3	5.2	0.7	3.5	0.5	5.2	1.7	-	8.6	-	-
8925[a]	Evolved Jotunite	Rogaland Province - Norway	7.6	19.6	2.9	13.3	2.5	5.5	0.7	4.0	0.5	4.4	2.2	-	8.0	-	-
75202F[a]	Evolved Jotunite	Rogaland Province - Norway	7.5	-	2.2	-	-	-	-	3.6	-	-	-	-	—	-	-
8926[a]	Evolved Jotunite	Rogaland Province - Norway	7.1	16.0	2.3	10.9	2.1	4.6	0.6	3.3	0.4	6.9	1.0	-	7.1	-	-
7355[a]	Evolved Jotunite	Rogaland Province - Norway	7.3	26.0	3.7	18.8	4.0	9.8	1.3	8.1	1.2	9.6	1.3	-	8.7	1.2	-
75204[a]	Varberg Dyke	Rogaland Province - Norway	7.4	-	2.6	-	-	-	-	4.8	-	5.4	1.8	-	—	1.2	-
T2[a]	Tellnes Dyke	Rogaland Province - Norway	7.7	-	2.4	-	-	-	-	4.3	0.8	16.2	1.7	-	20.0	0.7	0.2
T221[a]	Tellnes Dyke	Rogaland Province - Norway	7.5	-	2.4	-	-	-	-	4.8	-	12.2	1.8	-	10.0	0.7	0.4
78211[a]	Eivatn Dyke	Rogaland Province - Norway	7.4	25.6	2.7	13.2	2.5	5.8	0.8	4.4	0.6	8.8	2.1	-	11.0	0.2	-
91141[a]	Primitive Jotunite	Rogaland Province - Norway	2.8	4.5	1.0	5.0	1.2	2.9	0.5	2.9	0.4	5.5	0.8	-	8.1	-	-
145–937[b]	Ferrodiorite dyke	Grader Intrusion - Canada	4.2	14.9	2.2	11.6	2.1	4.4	0.5	2.9	0.4	4.6	1.2	-	6.5	1.1	0.2
145–938[b]	Ferrodiorite dyke	Grader Intrusion - Canada	5.4	17.2	2.3	13.0	2.2	4.9	0.5	3.3	0.4	4.3	1.1	-	13.4	1.5	0.2
223–601[b]	Ferrodiorite dyke	Grader Intrusion - Canada	4.3	15.4	2.2	11.7	2.1	4.7	0.5	3.1	0.4	4.3	0.9	-	2.3	0.6	0.1
223–604[b]	Ferrodiorite dyke	Grader Intrusion - Canada	4.2	17.0	2.6	12.7	2.4	5.1	0.6	3.2	0.4	5.3	1.5	-	6.7	1.2	0.0
225–135[b]	Ferrodiorite dyke	Grader Intrusion - Canada	5.2	15.1	2.0	10.0	1.9	4.0	0.5	2.6	0.4	4.3	1.1	-	2.2	0.8	0.1
145–648[b]	Ferrodiorite dyke	Grader Intrusion - Canada	4.5	16.4	2.1	10.7	2.0	4.5	0.5	3.0	0.4	4.4	1.2	-	3.0	1.3	0.1
225–302[b]	Ferrodiorite dyke	Grader Intrusion - Canada	4.1	9.5	1.3	6.5	1.1	2.3	0.3	1.4	0.2	9.5	1.4	-	11.2	1.3	0.3
7252[c]	Evolved Jotunite	Rogaland Province - Norway	7.4	-	2.4	-	-	-	-	3.8	-	11.0	1.7	-	-	0.8	0.3
80123[d]	Primitive Jotunite	Rogaland Province - Norway	2.9	-	1.1	-	-	-	-	2.0	0.3	6.5	1.3	-	-	0.5	0.2
7234[e]	Primitive Jotunite	Rogaland Province - Norway	3.3	-	1.6	-	-	-	-	3.6	0.5	7.3	1.2	-	-	3.6	1.2
BA13[f]	Jotunite/ Mangerite	Rogaland Province - Norway	4.6	-	2.1	-	-	-	-	6.4	-	19.0	3.3	-	20.0	0.9	0.5
BA8[f]	Jotunite/ Mangerite	Rogaland Province - Norway	6.4	-	2.5	-	-	-	-	6.0	-	11.1	1.9	-	14.0	1.4	0.6
BA26[f]	Jotunite/ Mangerite	Rogaland Province - Norway	6.4	-	2.2	-	-	-	-	7.2	-	10.0	1.7	-	14.0	0.7	0.4

Appendix 3.1.10 (Cont.) Compilation of whole-rock analysis of ferrodiorite dykes

Sample	Rock Type	Location	SiO_2	TIO_2	Al_2O_3	Fe_2O_3	FeO	MnO	MgO	CaO	Na_2O	K_2O	P_2O_5	Total	V	Cr	Co
MY4[f]	Jotunite/ Mangerite	Rogaland Province - Norway	57.6	1.7	15.1	2.6	7.6	0.2	1.0	2.9	5.3	5.4	0.3	99.6	-	-	6.7
88.4[f]	Jotunite/ Mangerite	Rogaland Province - Norway	58.0	1.3	15.5	10.7	N.D	0.1	1.0	3.1	5.0	5.6	0..44	100.9	-	-	16.6
BA15[f]	Jotunite/ Mangerite	Rogaland Province - Norway	59.1	1.2	15.7	3.3	6.6	0.2	0.7	3.5	4.2	5.5	0.4	100.3	-	-	7.8
BA17[f]	Jotunite/ Mangerite	Rogaland Province - Norway	60.7	1.1	15.5	2.3	6.5	0.2	0.7	2.9	5.3	5.5	0.3	100.9	-	-	5.5
022A (Morin)[g]	Jotunite	Morin Anorthosite - Canada	46.7	3.7	16.1	15.5	-	0.2	3.2	10.3	3.3	0.6	1.6	101.1	207.0	5.0	22.2
25 (Morin)[g]	Jotunite	Morin Anorthosite - Canada	48.4	3.2	14.4	15.5	-	0.3	2.8	8.7	3.0	1.1	1.5	98.9	143.0	7.0	25.4
907 (Morin)[g]	Jotunite	Morin Anorthosite - Canada	50.4	2.5	16.3	12.7	-	0.2	2.4	8.6	2.8	1.4	1.2	98.5	120.0	<8	22.2
45 (Morin)[g]	Jotunite	Morin Anorthosite - Canada	51.6	1.9	18.9	9.9	-	0.3	2.2	8.9	3.9	1.3	1.1	99.9	57.0	5.0	14.3
23 (Morin)[g]	Jotunite	Morin Anorthosite - Canada	54.3	2.0	17.2	11.1	-	0.2	1.8	7.5	3.6	1.9	0.9	100.4	45.0	3.2	14.4
752 (St.Urbain)[g]	Jotunite	Saint Urbain Anorthosite - Canada	44.1	4.2	13.9	17.9	-	0.2	3.3	9.0	3.2	0.9	2.6	99.3	144.0	12.6	38.4
738 (St.Urbain)[g]	Jotunite	Saint Urbain Anorthosite - Canada	47.8	4.1	14.2	15.8	-	0.2	4.7	7.7	3.3	1.2	0.8	99.7	197.0	46.6	48.6
712 (St.Urbain)[g]	Jotunite	Saint Urbain Anorthosite - Canada	47.9	3.3	13.0	16.2	-	0.3	3.2	8.3	3.3	1.7	2.2	99.3	113.0	<4	31.2
729 (St.urbain)[g]	Jotunite	Saint Urbain Anorthosite - Canada	51.7	2.5	15.6	12.6	-	0.2	2.6	7.6	4.1	1.6	1.6	100.1	110.0	<5	22.8
96A (St.Urbain)[g]	Jotunite	Saint Urbain Anorthosite - Canada	54.1	2.5	14.5	12.4	-	0.2	2.5	7.0	3.6	2.1	1.4	100.3	92.0	<4	22.2
271 (Lbr)[g]	Jotunite	Labrieville Alkaline Anorthosite - Canada	43.6	3.9	12.4	19.5	-	0.3	4.0	9.0	3.1	1.1	2.4	99.2	193.0	<4	42.7
303 (Lbr)[g]	Jotunite	Labrieville Alkaline Anorthosite - Canada	46.2	3.1	13.4	17.0	-	0.4	3.7	7.7	3.5	1.8	2.2	99.0	<16	5.6	14.6
327 (Lbr)[g]	Jotunite	Labrieville Alkaline Anorthosite - Canada	49.5	2.9	14.4	16.3	-	0.2	2.5	6.6	3.5	1.9	1.8	99.7	64.0	7.6	27.7
194 (Lbr)[g]	Jotunite	Labrieville Alkaline Anorthosite - Canada	52.2	2.1	15.1	12.5	-	0.2	2.5	6.4	3.9	2.6	1.4	99.0	62.0	<2	21.8
242 (Lbr)[g]	Jotunite	Labrieville Alkaline Anorthosite - Canada	55.3	1.7	15.5	10.2	-	0.3	1.9	5.0	4.1	3.6	1.0	98.7	<15	4.2	5.8
T13[h]	High-Zr Jotunite	Rogaland Province - Norway	48.0	2.5	15.6	17.3	-	0.2	2.6	8.4	4.1	1.0	1.1	99.9	81.0	17.0	20.0
84.2[h]	High-Zr Jotunite	Rogaland Province - Norway	48.3	2.5	16.6	16.9	-	0.3	2.5	7.9	4.1	0.9	1.2	100.1	157.0	22.0	27.0
T11[h]	High-Zr Jotunite	Rogaland Province - Norway	48.6	2.3	16.1	16.7	-	0.2	2.6	8.3	4.3	0.9	0.9	99.9	88.0	19.0	23.0
T12[h]	High-Zr Jotunite	Rogaland Province - Norway	49.0	2.5	16.1	16.5	-	0.3	2.6	8.2	4.2	1.1	1.0	100.4	70.0	28.0	20.0
T20-1[h]	High-Zr Jotunite	Rogaland Province - Norway	49.6	2.2	16.3	16.2	-	0.2	2.5	7.9	3.8	1.3	1.0	100.1	72.0	19.0	21.0

93BN56[h]	High-Zr Jotunite	Rogaland Province - Norway	54.3	1.9	14.6	15.1	-	0.2	1.1	5.0	3.5	3.2	0.7	98.7	55.0	b25	15.0
93BN61[h]	High-Zr Jotunite	Rogaland Province - Norway	57.4	1.6	16.0	12.0	-	0.2	1.1	4.6	4.3	3.7	0.6	100.5	54.0	b25	14.0
93BN50[h]	High-Zr Jotunite	Rogaland Province - Norway	61.1	1.5	13.7	11.6	-	0.2	1.0	3.1	4.6	4.3	0.4	100.6	32.0	b25	12.0
75.54.2[h]	High-Zr Jotunite	Rogaland Province - Norway	52.0	2.1	15.0	15.1	-	0.2	2.1	6.2	4.1	2.7	1.0	99.6	66.0	17.0	21.0
76.27[h]	High-Zr Jotunite	Rogaland Province - Norway	51.5	2.3	15.0	15.6	-	0.3	2.2	6.3	4.2	2.6	1.1	100.8	79.0	13.0	25.0
78.32.3[h]	High-Zr Jotunite	Rogaland Province - Norway	50.6	3.9	8.9	27.4	-	0.3	2.2	5.7	0.7	1.4	1.3	100.7	112.0	20.0	24.0
BM-21[h]	High-Zr Jotunite	Rogaland Province - Norway	45.3	3.5	8.3	28.3	-	0.5	3.4	7.1	2.1	0.5	1.3	100.3	90.0	17.0	-
BM-22[h]	High-Zr Jotunite	Rogaland Province - Norway	48.0	3.0	11.3	23.1	-	0.4	2.7	6.9	3.0	0.7	1.0	100.1	86.0	14.0	-
PM-618[h]	High-Zr Jotunite	Rogaland Province - Norway	39.9	4.0	8.1	32.3	-	0.6	2.9	9.2	1.6	0.3	1.2	100.0	144.0	22.0	-
PM436[h]	High-Zr Jotunite	Rogaland Province - Norway	59.4	0.7	14.7	8.7	-	0.2	0.2	3.8	3.7	4.8	0.2	97.6	-	7.0	-
MPK60[h]	High-Zr Jotunite	Rogaland Province - Norway	57.0	0.9	15.1	11.8	-	0.3	0.5	4.5	4.1	4.7	0.2	99.2	-	-	-
AA-41[h]	High-Zr Jotunite	Rogaland Province - Norway	58.8	1.4	13.8	12.4	-	0.2	0.6	4.5	3.5	4.5	0.4	100.2	-	-	-

Appendix 3.1.10 (Cont.) Compilation of whole-rock analysis of ferrodiorite dykes

Sample	Rock Type	Location	Ni	Cu	Zn	Ga	Rb	Sr	Y	Zr	Nb	Ba	La	Ce	Pr	Nd	Sm
MY4[f]	Jotunite/ Mangerite	Rogaland Province - Norway	-	-	217.0	-	115.0	188.0	106.0	748.0	50.0	1275.0	82.2	198.0	-	—	26.3
88.4[f]	Jotunite/ Mangerite	Rogaland Province - Norway	-	-	218.0	-	85.0	294.0	93.0	####	18.0	1555.0	61.4	115.0	-	97.0	23.9
BA15[f]	Jotunite/ Mangerite	Rogaland Province - Norway	-	-	170.0	33.0	82.0	143.0	46.0	795.0	13.0	1359.0	33.4	69.0	-	50.0	11.4
BA17[f]	Jotunite/ Mangerite	Rogaland Province - Norway	-	-	133.0	-	98.0	154.0	59.0	446.0	39.0	1362.0	36.1	72.0	-	67.0	12.0
022A (Morin)[g]	Jotunite	Morin Anorthosite - Canada	<9	<11	156.0	29.5	2.6	670.0	51.4	58.0	5.8	437.0	23.5	58.3	-	44.0	11.8
25 (Morin)[g]	Jotunite	Morin Anorthosite - Canada	<11	<12	262.0	24.9	10.1	585.0	92.8	391.0	17.9	373.0	56.7	136.3	-	76.0	22.3
907 (Morin)[g]	Jotunite	Morin Anorthosite - Canada	<8	<10	172.0	25.5	7.4	625.0	58.2	97.0	10.2	710.0	34.5	82.7	-	53.0	13.6
45 (Morin)[g]	Jotunite	Morin Anorthosite - Canada	<8	<9	180.0	25.7	41.1	636.0	75.6	127.0	11.9	431.0	46.9	112.8	-	69.0	16.6
23 (Morin)[g]	Jotunite	Morin Anorthosite - Canada	<8		197.0	27.3	18.5	616.0	55.0	476.0	9.4	2029.0	34.3	78.6	-	56.0	13.3
752 (St.Urbain)[g]	Jotunite	Saint Urbain Anorthosite - Canada	19.0	20.0	393.0	33.3	4.7	795.0	87.3	1300.0	56.1	1074.0	165.0	370.0	-	234.0	40.6
738 (St.Urbain)[g]	Jotunite	Saint Urbain Anorthosite - Canada	46.0	17.0	207.0	29.6	10.2	830.0	21.1	269.0	27.0	563.0	35.0	82.7	-	48.0	10.8
712 (St.Urbain)[g]	Jotunite	Saint Urbain Anorthosite - Canada	<10	<11	340.0	33.0	16.7	663.0	110.7	791.0	32.1	1429.0	98.7	235.0	-	127.0	34.8
729 (St.urbain)[g]	Jotunite	Saint Urbain Anorthosite - Canada	6.0	<10	243.0	28.6	15.6	716.0	76.9	506.0	21.8	1024.0	79.2	188.0	-	99.0	24.8
96A (St.Urbain)[g]	Jotunite	Saint Urbain Anorthosite - Canada	<9	55.0	222.0	26.7	11.6	643.0	67.6	438.0	19.9	1629.0	58.7	139.7	-	70.0	20.9
271 (Lbr)[g]	Jotunite	Labrieville Alkaline Anorthosite - Canada	<13	<27	322.0	27.0	5.3	943.0	62.3	263.0	20.1	1100.0	66.3	159.0	-	113.0	23.7
303 (Lbr)[g]	Jotunite	Labrieville Alkaline Anorthosite - Canada	<10	<12	632.0	37.0	7.4	1225.0	98.6	1411.0	38.8	3455.0	135.3	332.0	-	222.0	47.9
327 (Lbr)[g]	Jotunite	Labrieville Alkaline Anorthosite - Canada	<10	<11	345.0	27.1	9.1	661.0	54.7	1604.0	36.2	1841.0	67.4	164.0	-	96.0	22.5
194 (Lbr)[g]	Jotunite	Labrieville Alkaline Anorthosite - Canada	<15	<10	237.0	29.6	15.0	1025.0	54.4	507.0	15.8	2479.0	61.4	144.0	-	87.0	19.9
242 (Lbr)[g]	Jotunite	Labrieville Alkaline Anorthosite - Canada	10.0	<10	532.0	37.4	29.9	1050.0	91.9	2162.0	47.4	4603.0	144.0	335.0	-	235.0	44.1
T13[h]	High-Zr Jotunite	Rogaland Province - Norway	16.0	-	253.0	-	4.6	494.0	270.0	####	39.0	488.0	163.0	462.0	61.0	296.0	55.0
84.2[h]	High-Zr Jotunite	Rogaland Province - Norway	52.0	-	280.0	-	2.7	532.0	295.0	1863.0	26.0	562.0	164.0	412.0	27.0	227.0	58.0
T11[h]	High-Zr Jotunite	Rogaland Province - Norway	26.0	-	342.0	-	3.9	453.0	240.0	2197.0	35.0	466.0	154.0	415.0	43.0	361.0	51.0
T12[h]	High-Zr Jotunite	Rogaland Province - Norway	11.0	-	225.0	-	3.7	494.0	263.0	2166.0	46.0	507.0	157.0	412.0	121.0	263.0	50.0
T20-1[h]	High-Zr Jotunite	Rogaland Province - Norway	9.0	-	279.0	-	7.8	476.0	271.0	####	28.0	883.0	190.0	451.0	-	122.0	53.0

93BN56[h]	High-Zr Jotunite	Rogaland Province - Norway	b25	-	322.0	-	67.0	257.0	301.0	####	50.0	1382.0	255.0	592.0	-	161.0	75.0
93BN61[h]	High-Zr Jotunite	Rogaland Province - Norway	b25	-	235.0	-	72.0	287.0	228.0	2114.0	52.0	1682.0	191.0	424.0	-	189.0	51.0
93BN50[h]	High-Zr Jotunite	Rogaland Province - Norway	b25	-	227.0	-	80.0	149.0	129.0	1609.0	52.0	1106.0	80.0	175.0	-	187.0	28.0
75.54.2[h]	High-Zr Jotunite	Rogaland Province - Norway	b10	-	221.0	-	42.0	347.0	144.0	1591.0	41.0	1613.0	102.0	254.0	-	154.0	39.0
76.27[h]	High-Zr Jotunite	Rogaland Province - Norway	14.0	-	350.0	-	37.0	304.0	183.0	1480.0	73.0	1400.0	122.0	288.0	-	125.0	42.0
78.32.3[h]	High-Zr Jotunite	Rogaland Province - Norway	10.0	-	906.0	-	11.0	82.0	199.0	5110.0	39.0	393.0	91.0	275.0	-	176.0	43.0
BM-21[h]	High-Zr Jotunite	Rogaland Province - Norway	21.0	-	460.0	-	4.7	171.0	140.0	1880.0	-	425.0	110.0	284.0	-	19.0	40.0
BM-22[h]	High-Zr Jotunite	Rogaland Province - Norway	10.0	-	377.0	-	2.0	242.0	111.0	1967.0	-	269.0	97.0	244.0	-	-	31.0
PM-618[h]	High-Zr Jotunite	Rogaland Province - Norway	36.0	-	425.0	-	143.0	179.0	85.0	3135.0	-	395.0	52.0	146.0	-	-	28.0
PM436[h]	High-Zr Jotunite	Rogaland Province - Norway	7.0	-	267.0	-	72.0	157.0	136.0	2143.0	-	1282.0	208.0	343.0	-	-	33.0
MPK60[h]	High-Zr Jotunite	Rogaland Province - Norway	8.0	-	247.0	-	83.0	276.0	112.0	####	-	3400.0	63.0	156.0	-	-	9.0
AA-41[h]	High-Zr Jotunite	Rogaland Province - Norway	-	-	-	-	-	247.0	-	1904.0	-	1171.0	-	-	-	-	24.0

Appendix 3.1.10 (Cont.) Compilation of whole-rock analysis of ferrodiorite dykes

Sample	Rock Type	Location	Eu	Gd	Tb	Dy	Ho	Er	Tm	Yb	Lu	Hf	Ta	W	Pb	Th	U
MY4[f]	Jotunite/ Mangerite	Rogaland Province - Norway	5.5	-	3.0	-	-	-	-	7.7	-	23.5	2.7	-	23.0	3.4	0.8
88.4[f]	Jotunite/ Mangerite	Rogaland Province - Norway	5.7	-	3.3	-	-	-	-	7.8	-	46.0	0.2	-	18.0	0.7	-
BA15[f]	Jotunite/ Mangerite	Rogaland Province - Norway	5.4	-	1.5	-	-	-	-	4.2	-	17.1	0.8	-	25.0	1.6	0.7
BA17[f]	Jotunite/ Mangerite	Rogaland Province - Norway	5.7	-	1.7	-	-	-	-	5.4	-	11.1	2.0	-	24.0	1.0	0.4
022A (Morin)[g]	Jotunite	Morin Anorthosite - Canada	3.8	-	1.8	-	-	-	-	4.1	0.6	2.0	0.4	<1.7	<7	0.4	0.2
25 (Morin)[g]	Jotunite	Morin Anorthosite - Canada	5.8	-	3.3	-	-	-	-	8.5	1.2	10.0	0.9	<2	<11	1.0	0.4
907 (Morin)[g]	Jotunite	Morin Anorthosite - Canada	4.3	-	2.1	-	-	-	-	5.1	0.7	3.9	0.6	<0.8	<12	0.7	0.3
45 (Morin)[g]	Jotunite	Morin Anorthosite - Canada	4.2	-	2.6	-	-	-	-	8.7	1.3	4.4	0.6	<2	<8	1.2	1.4
23 (Morin)[g]	Jotunite	Morin Anorthosite - Canada	5.1	-	2.0	-	-	-	-	5.3	0.8	13.8	0.5	<1.2	<8	0.9	0.4
752 (St.Urbain)[g]	Jotunite	Saint Urbain Anorthosite - Canada	8.0	-	3.9	-	-	-	-	5.7	0.8	36.8	2.9	<2	12.8	1.7	0.7
738 (St.Urbain)[g]	Jotunite	Saint Urbain Anorthosite - Canada	3.3	-	1.2	-	-	-	-	1.5	0.2	8.3	2.0	—	<9	0.4	<0.3
712 (St.Urbain)[g]	Jotunite	Saint Urbain Anorthosite - Canada	7.8	-	4.3	-	-	-	-	8.1	1.1	21.7	1.7	<8	13.1	1.3	0.8
729 (St.urbain)[g]	Jotunite	Saint Urbain Anorthosite - Canada	5.7	-	3.1	-	-	-	-	6.0	0.8	14.0	1.3	<3	16.8	1.6	0.7
96A (St.Urbain)[g]	Jotunite	Saint Urbain Anorthosite - Canada	5.5	-	2.6	-	-	-	-	5.4	0.8	11.8	1.1	<2	12.1	0.8	0.4
271 (Lbr)[g]	Jotunite	Labrieville Alkaline Anorthosite - Canada	6.8	-	2.7	-	-	-	-	4.3	0.6	7.2	1.1	<1.1	<14	0.3	0.3
303 (Lbr)[g]	Jotunite	Labrieville Alkaline Anorthosite - Canada	14.8	-	4.8	-	-	-	-	6.3	0.9	35.1	2.0	<11	15.9	0.4	<0.9
327 (Lbr)[g]	Jotunite	Labrieville Alkaline Anorthosite - Canada	7.3	-	2.4	-	-	-	-	4.7	0.7	36.9	1.8	<1	11.0	0.3	0.3
194 (Lbr)[g]	Jotunite	Labrieville Alkaline Anorthosite - Canada	6.7	-	2.3	-	-	-	-	4.2	0.6	14.2	0.8	<1.9	12.3	0.4	0.3
242 (Lbr)[g]	Jotunite	Labrieville Alkaline Anorthosite - Canada	15.0	-	4.4	-	-	-	-	6.6	0.9	51.4	2.2	<3	28.2	1.1	0.5
T13[h]	High-Zr Jotunite	Rogaland Province - Norway	7.1	51.0	7.1	39.0	8.0	21.0	2.7	20.0	2.3	57.0	1.3	-	14.0	3.0	0.6
84.2[h]	High-Zr Jotunite	Rogaland Province - Norway	6.0	27.0	7.5	24.0	5.0	13.0	1.7	16.0	3.6	57.0	0.9	-	17.0	2.7	0.8
T11[h]	High-Zr Jotunite	Rogaland Province - Norway	6.3	39.0	6.5	34.0	7.0	17.0	2.3	18.0	2.5	54.0	1.2	-	14.0	2.6	0.5
T12[h]	High-Zr Jotunite	Rogaland Province - Norway	6.7	39.0	6.2	28.0	7.4	13.0	6.4	15.0	1.8	52.0	1.6	-	16.0	3.3	0.4
T20-1[h]	High-Zr Jotunite	Rogaland Province - Norway	6.8	28.0	7.1	22.0	-	11.0	-	23.0	2.1	58.0	0.9	-	22.0	5.0	0.6
93BN56[h]	High-Zr Jotunite	Rogaland Province - Norway	7.0	30.0	9.7	20.0	-	9.2	-	24.0	2.1	57.0	1.7	-	42.0	15.0	2.0
93BN61[h]	High-Zr Jotunite	Rogaland Province - Norway	6.7	28.0	7.4	25.0	-	13.0	-	17.0	0.3	49.0	1.7	-	19.0	7.2	1.3
93BN50[h]	High-Zr Jotunite	Rogaland Province - Norway	4.5	-	4.2	-	-	-	-	11.0	1.7	45.0	2.3	-	11.0	2.5	1.4
75.54.2[h]	High-Zr Jotunite	Rogaland Province - Norway	7.2	-	5.3	-	-	-	-	13.0	1.6	39.0	1.9	-	-	2.1	0.5
76.27[h]	High-Zr Jotunite	Rogaland Province - Norway	7.1	-	5.4	-	-	-	-	15.0	1.8	25.0	1.9	-	-	2.7	0.8
78.32.3[h]	High-Zr Jotunite	Rogaland Province - Norway	5.1	-	5.9	-	-	-	-	16.0	-	124.0	3.4	-	-	1.4	0.5
BM-21[h]	High-Zr Jotunite	Rogaland Province - Norway	3.3	-	14.0	-	-	-	-	12.0	-	44.0	2.2	-	-	2.0	
BM-22[h]	High-Zr Jotunite	Rogaland Province - Norway	3.4	-	3.9	-	-	-	-	10.0	-	-	-	-	-	-	-
PM-618[h]	High-Zr Jotunite	Rogaland Province - Norway	3.4	-	-	-	-	-	-	7.5	-	-	-	-	-	-	-
PM436[h]	High-Zr Jotunite	Rogaland Province - Norway	6.0	-	-	-	-	-	-	13.0	-	-	-	-	-	-	-

MPK60[h]	High-Zr Jotunite	Rogaland Province - Norway	17.0	-	-	-	-	-	-	12.0	-	-	-	-	-	-	-
AA-41[h]	High-Zr Jotunite	Rogaland Province - Norway	4.5	-	-	-	-	-	-	-	-	-	-	-	-	-	-

Miloski et al. 2023a; a Vander Auwera et al. (1998); b Charlier et al. (2008); c Wilmart et al. (1989); d Duchesne & Hertogen (1988); e Duchesne et al. (1974); f Duchesne & Wimart (1996); g Owens et al. (1993); h Duchesne & Liegeois (2015).

Appendix 3.1.11 fO_2 Calculations of fine-grained dykes

Dyke sample		MX114-1 (primitive ferrodiorite)		20PM19B (evolved jotunite)		CM1060		CM1076B		CM1110		MX102-3		LO-06* (Lac à l'Orignal ferrodiorite dyke)	
Temp. (°C)	Pressure (bar)	ΔFMQ	fO_2	ΔFMQ	fO_2	ΔFMQ	fO_2	ΔFMQ	fO_2	ΔFMQ	fO_2	ΔFMQ	fO_2	ΔFMQ	fO_2
1100	1	0.64	-8.91	2.09	-7.46	1.66	-7.90	1.42	-8.13	-0.27	-9.82	0.46	-9.10	1.71	-7.85
1200	1	0.11	-8.22	1.78	-6.55	1.28	-7.05	1.01	-7.32	-0.91	-9.23	-0.99	-8.43	1.34	-6.99
1100	1000	0.56	-8.90	2.01	-7.46	1.58	-7.89	1.34	-8.13	-0.35	-9.82	0.38	-9.09	1.63	-7.84
1200	1000	0.03	-8.22	1.70	-6.55	1.20	-7.05	0.93	-7.32	-0.98	-9.23	0.18	-8.42	1.26	-6.99
1100	5000	0.25	-8.88	1.70	-7.43	1.26	-7.87	1.03	-8.10	-0.66	-9.79	0.06	-9.07	1.31	-7.82
1200	5000	-0.27	-8.20	1.40	-6.53	0.90	-7.03	0.63	-7.30	-1.28	-9.21	-0.47	-8.41	0.96	-6.97
1100	7000	0.09	-8.87	1.54	-7.42	1.11	-7.86	0.87	-8.09	-0.82	-9.78	-0.09	-9.05	1.16	-7.80
1200	7000	-0.42	-8.19	1.26	-6.52	0.76	-7.02	0.49	-7.29	-1.43	-9.20	-0.62	-8.40	0.82	-6.96

Note that applying the QUILF-equilibrium without fixing the temperature, for a pressure of 1Kbar, unrealistic FMQ values of fO2 around – 20.95 and +7.78 are obtained. As expected, these calculated values reflect the modification of Fe-Ti oxides primary compositions (especially the loss of Ti content on magnetite) with exchange of elements between the oxides and silicates in subsolidus re-equilibration (Charlier et al. 2009), and do not reflect the parental magma conditions. * Dyke sample from Miloski et al. (2023a).

Appendix 3.1.12 EMPA analyses of plagioclase in the Lac Mirepoix Fe-Ti-P mineralization

Sample	Lithology	SiO2	Al_2O_3	CaO	FeO	Na_2O	K_2O	Total	%An	%Ab	%Or	An*
20PM07	Nelsonite	58.51	26.64	8.15	0.16	6.94	0.04	100.44	39.27	60.51	0.22	39.36
20PM08B1	Oxide Apatite Norite (OAN)	56.47	27.81	9.76	0.11	5.80	0.26	100.20	47.44	51.06	1.49	48.16
CM1081	Anorthosite	56.54	27.58	9.50	0.12	5.96	0.32	100.02	45.97	52.18	1.85	46.84
CM1063B	Anorthosite	55.43	26.87	8.85	1.43	5.75	0.42	98.75	44.75	52.76	2.49	45.89
CM1045	Oxide Apatite Norite (OAN)	57.26	27.24	8.92	0.09	6.29	0.30	100.10	43.17	55.09	1.74	43.93
CM1099	Anorthosite	56.55	27.64	9.55	0.11	6.08	0.25	100.17	45.82	52.78	1.41	46.47
CM1077	Semi-massive oxides	54.97	28.36	10.66	0.00	5.27	0.00	99.47	52.76	47.23	0.01	52.76
CM1063	Anorthosite	56.70	27.10	9.28	-	5.96	0.46	99.67	45.03	52.33	2.64	46.26
CM1060	Oxide Apatite Norite (OAN)	57.36	26.61	8.35	0.00	6.44	0.00	99.01	41.71	58.28	0.01	41.72
CM1053B	Oxide Apatite Norite (OAN)	58.81	26.70	8.19	0.00	6.57	0.00	100.47	40.76	59.23	0.01	40.76
CM1053C	Oxide Apatite Norite (OAN)	56.94	27.48	9.22	0.00	6.08	0.00	100.04	45.58	54.41	0.01	45.58
CM1052	Oxide Apatite Norite (OAN)	56.60	27.56	9.30	0.00	6.01	0.00	99.64	46.54	53.45	0.01	46.54
CM1110	Oxide Apatite Norite (OAN)	56.30	28.33	9.92	0.00	5.79	0.00	100.33	48.60	51.40	0.01	48.60
CM1045	Oxide Apatite Norite (OAN)	57.26	27.24	8.92	-	6.29	0.30	100.10	43.17	55.09	1.74	43.93

An= 100*Ca/(Ca+Na+K); Ab=100*Na/(Ca+Na+K); Or=100*K/(CA+Na+K); An*=An/(An+Ab). "CM" analysis from Morisset (2001).

Appendix 3.1.13 pXRF analyses of plagioclase in the Lac Mirepoix Fe-Ti-P mineralization

Sample	Lithology	Si	Al	Ca	K	%An	Sr *	Ba *
20PM05C	Anorhtosite	28.16	15.14	5.68	0.63	36.81	1679	827
20PM08B2	Anorhtosite	27.60	15.08	6.71	0.31	43.08	2847	1938
MX-102-6	Anorhtosite	27.87	15.18	7.53	0.31	46.99	2606	1452
MX-105-3	Anorhtosite	26.23	13.30	6.96	0.35	46.24	2380	949
MX-108-8	Anorhtosite	28.50	14.69	5.41	0.68	34.95	1499	1516
MX-109-7	Anorhtosite	27.36	14.65	6.20	0.86	40.57	2003	1471

Si, Al, Ca, K cationic values in %. Sr and Ba in ppm.

APPENDIX 3.2 SUPPLEMENTARY FIGURES (CHAPTER 3)

Appendix 3.2.1. CL Images of selected analyzed zircons

GC-LMX-01

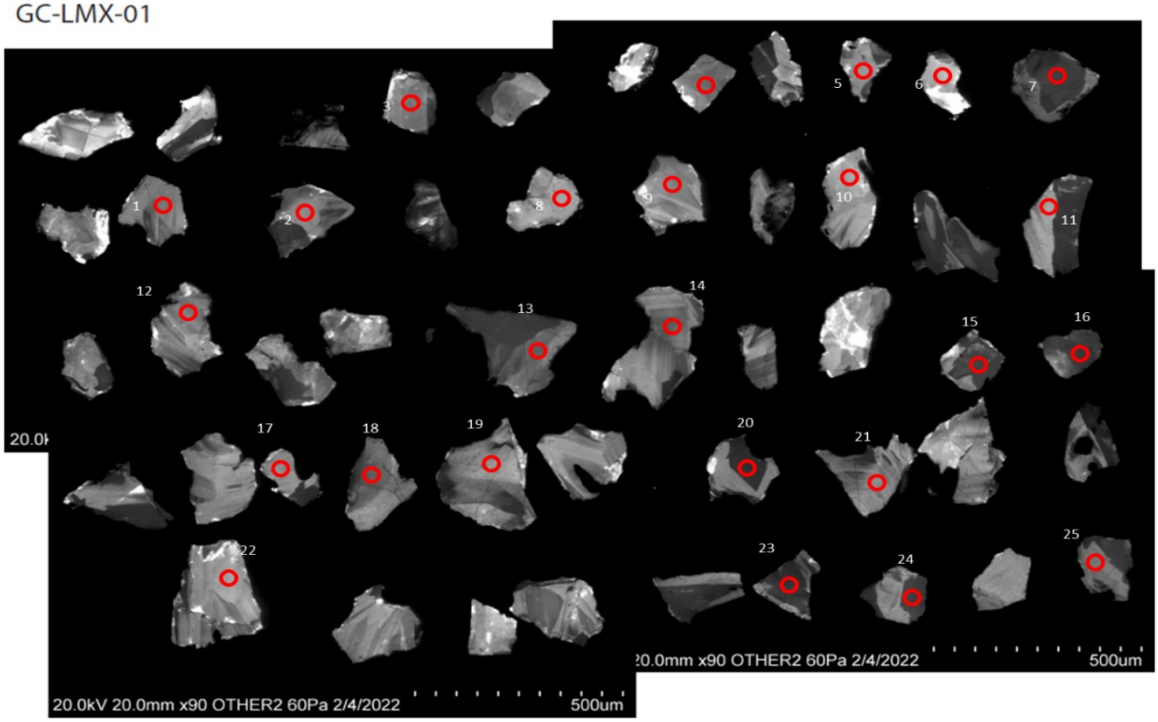

GC-LMX-02

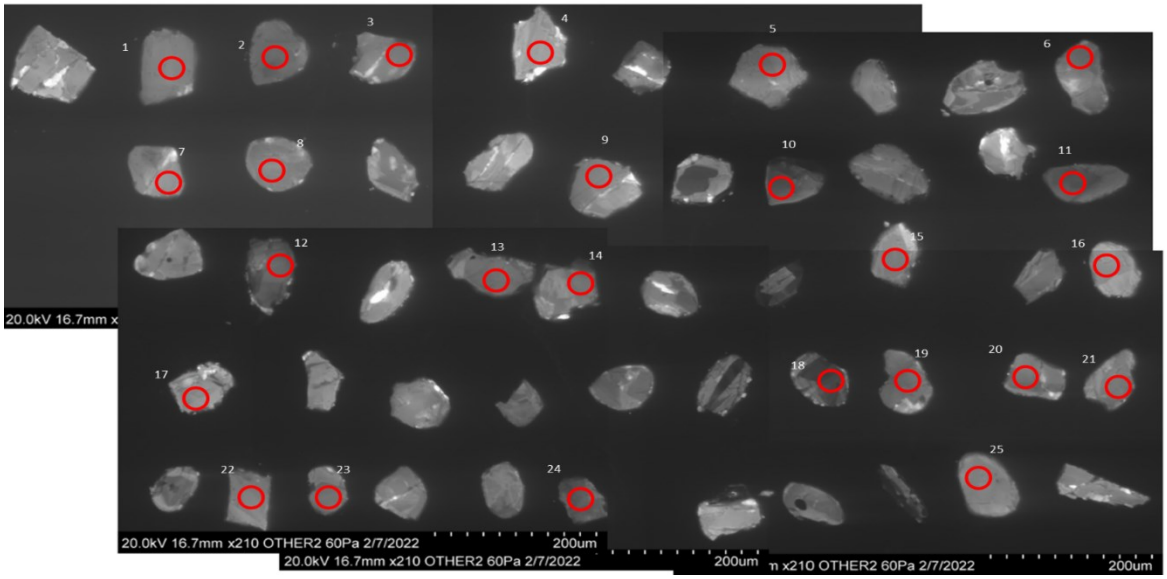

Appendix 3.2.2. Cartography map of the Lac Mirepoix area (after Morisset, 2001)

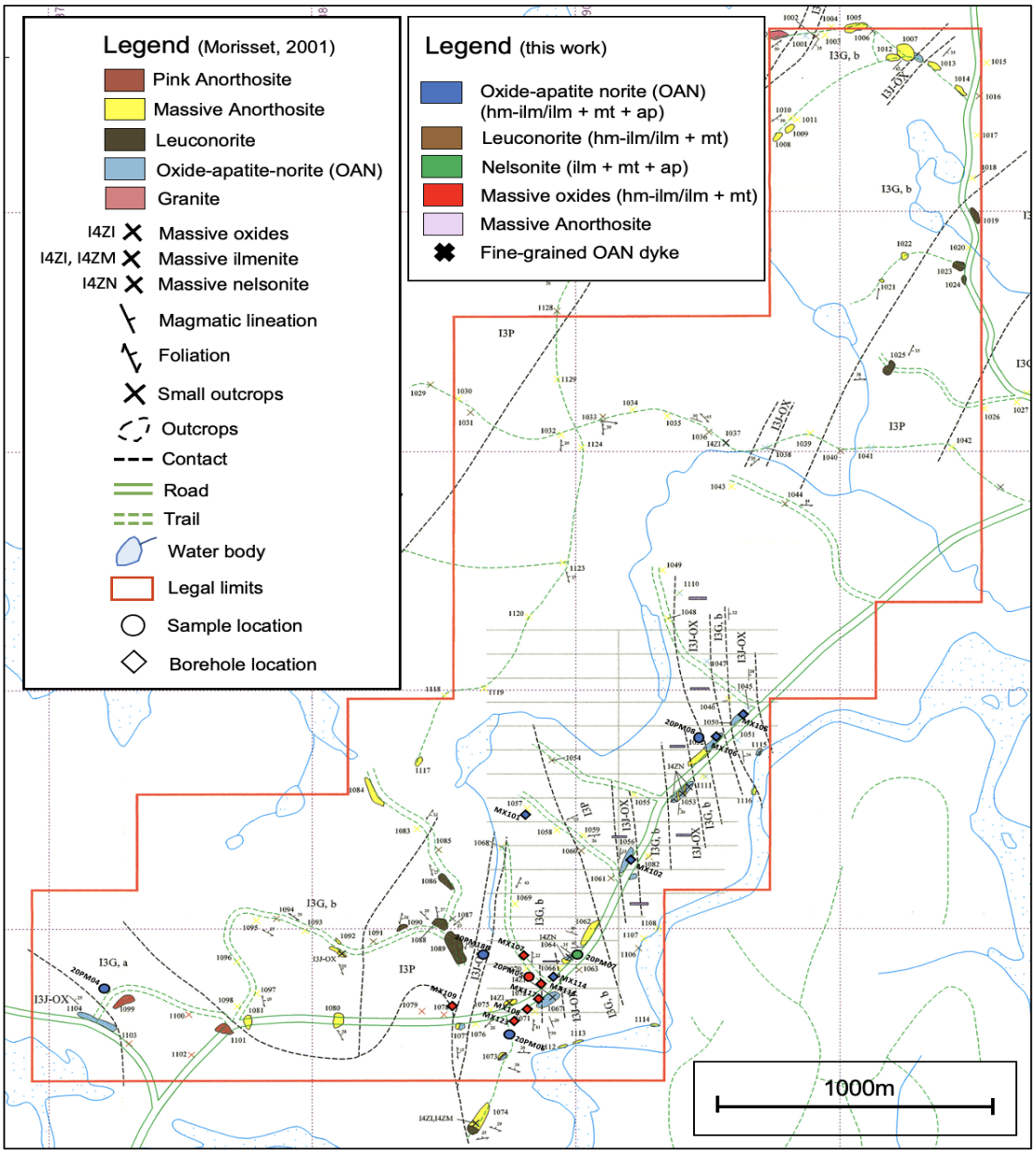

Appendix 3.2.3. µXRF-maps sample MX-105-1 showing the different proportions of oxides an apatite from the Lac Mirepoix Fe-Ti-P mineralized zone. Apatite is white. Ilmenite is blue, where as hematite-rich part of ilmenite is cyan. Magnetite is bright green. Orthopyroxene/biotite is dark green

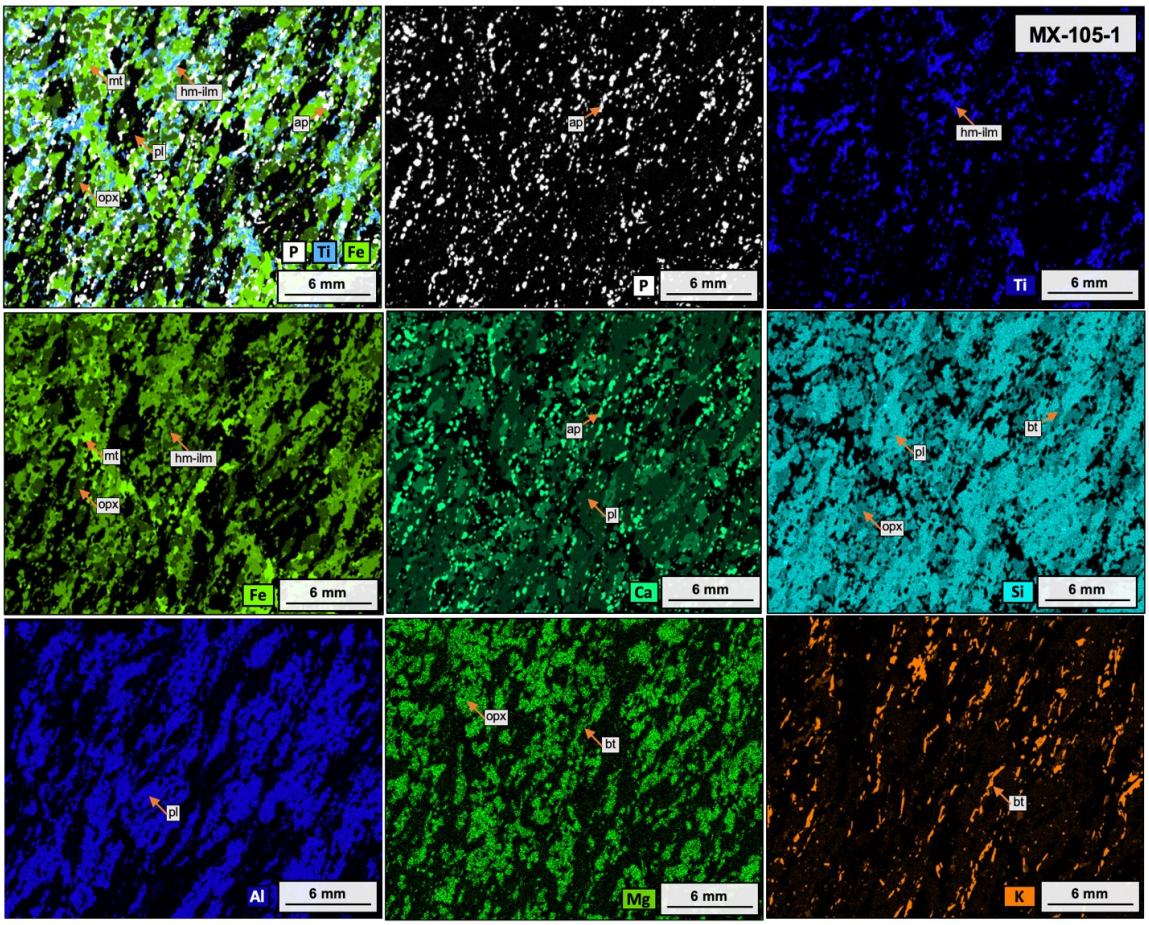

Appendix 3.2.4. µXRF-maps sample MX-114-1 showing the different proportions of oxides an apatite from the Lac Mirepoix Fe-Ti-P mineralized zone. Apatite is white. Ilmenite is blue, where as hematite-rich part of ilmenite is cyan. Magnetite is bright green. Orthopyroxene/biotite is dark green

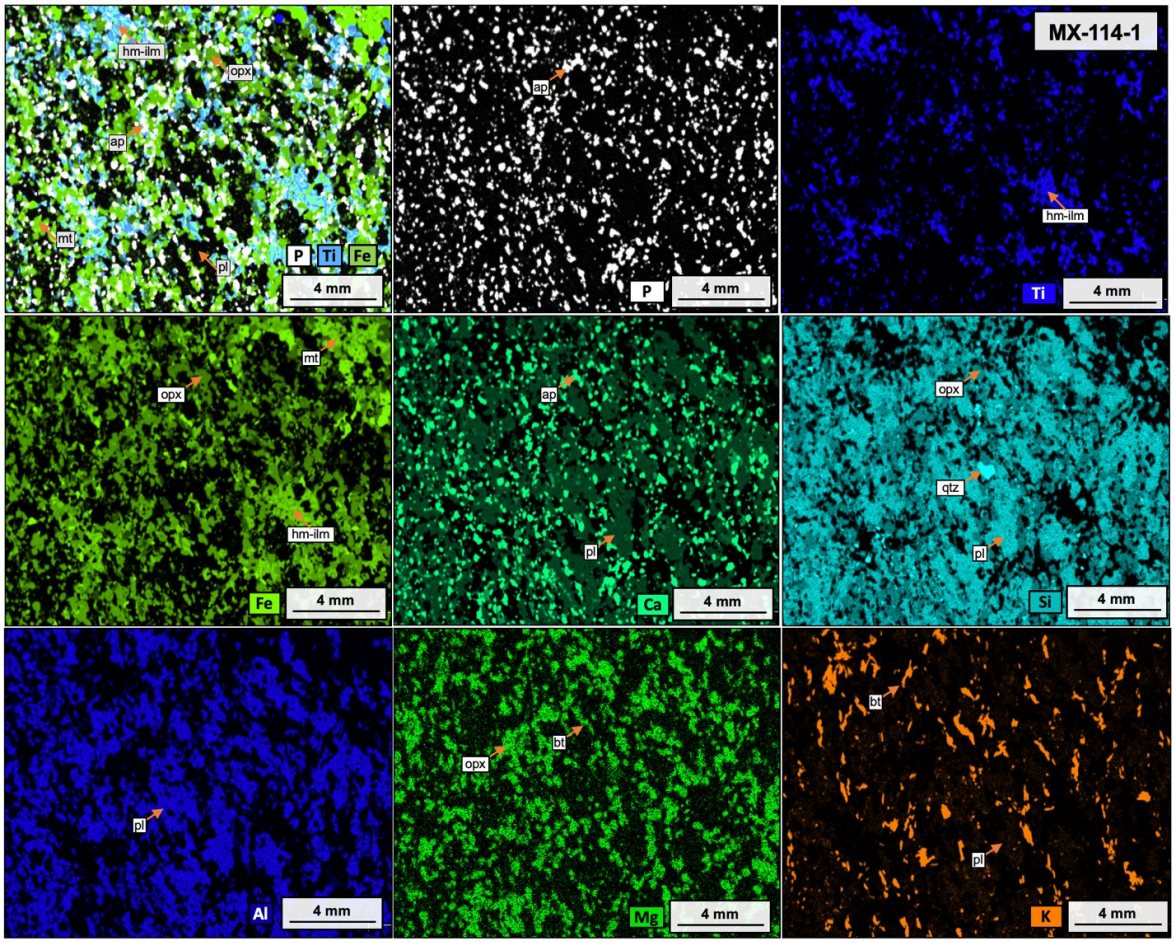

Appendix 3.2.5. µXRF-maps sample 20PM19-B showing the different proportions of oxides an apatite from the Lac Mirepoix Fe-Ti-P mineralized zone. Apatite is white. Ilmenite is blue, where as hematite-rich part of ilmenite is cyan. Magnetite is bright green. Orthopyroxene/biotite is dark green

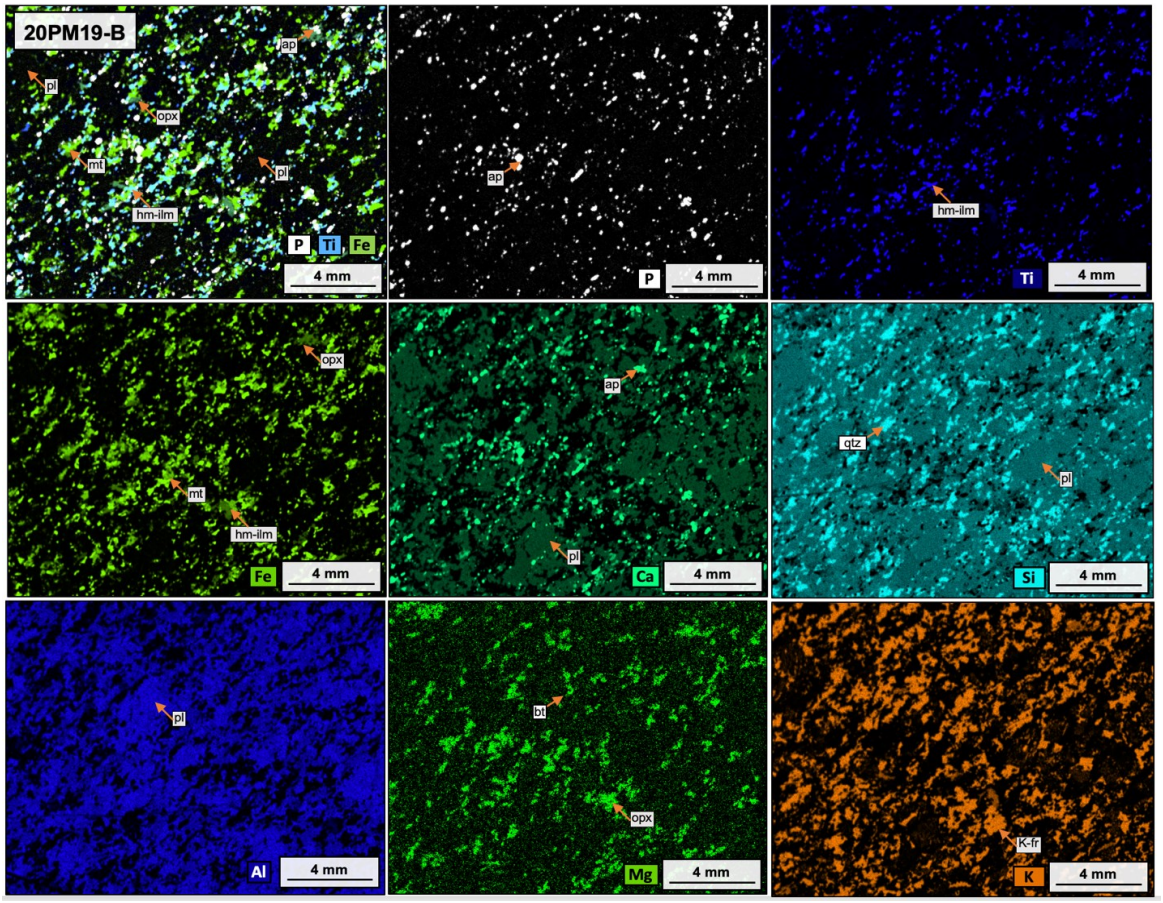

Appendix 3.2.6. µXRF-maps sample 20PM05-A showing the different proportions of oxides an apatite from the Lac Mirepoix Fe-Ti-P mineralized zone. Apatite is white. Ilmenite is blue, where as hematite-rich part of ilmenite is cyan. Magnetite is bright green. Orthopyroxene/biotite is dark green

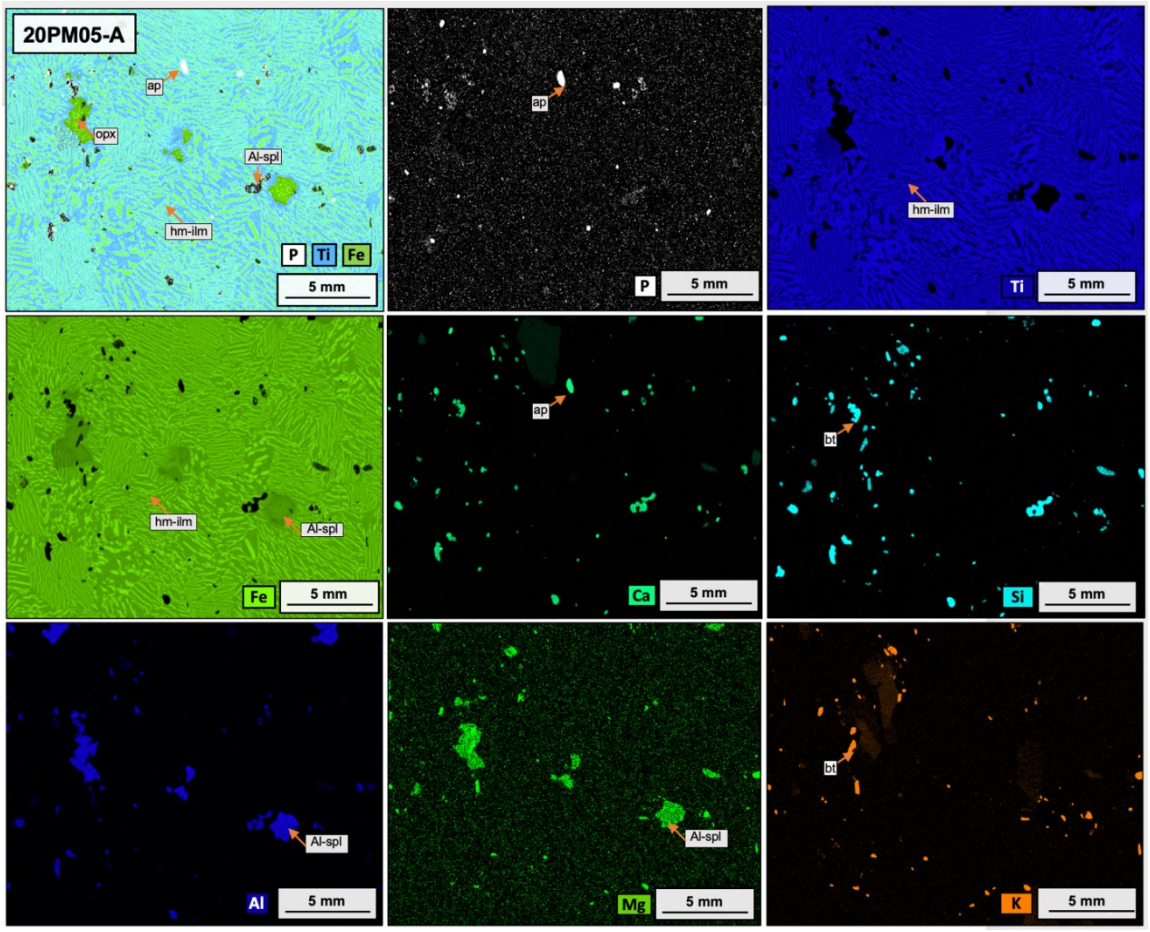

Appendix 3.2.7. µXRF-maps sample 20PM07 showing the different proportions of oxides an apatite from the Lac Mirepoix Fe-Ti-P mineralized zone. Apatite is white. Ilmenite is blue, where as hematite-rich part of ilmenite is cyan. Magnetite is bright green. Orthopyroxene/biotite is dark green

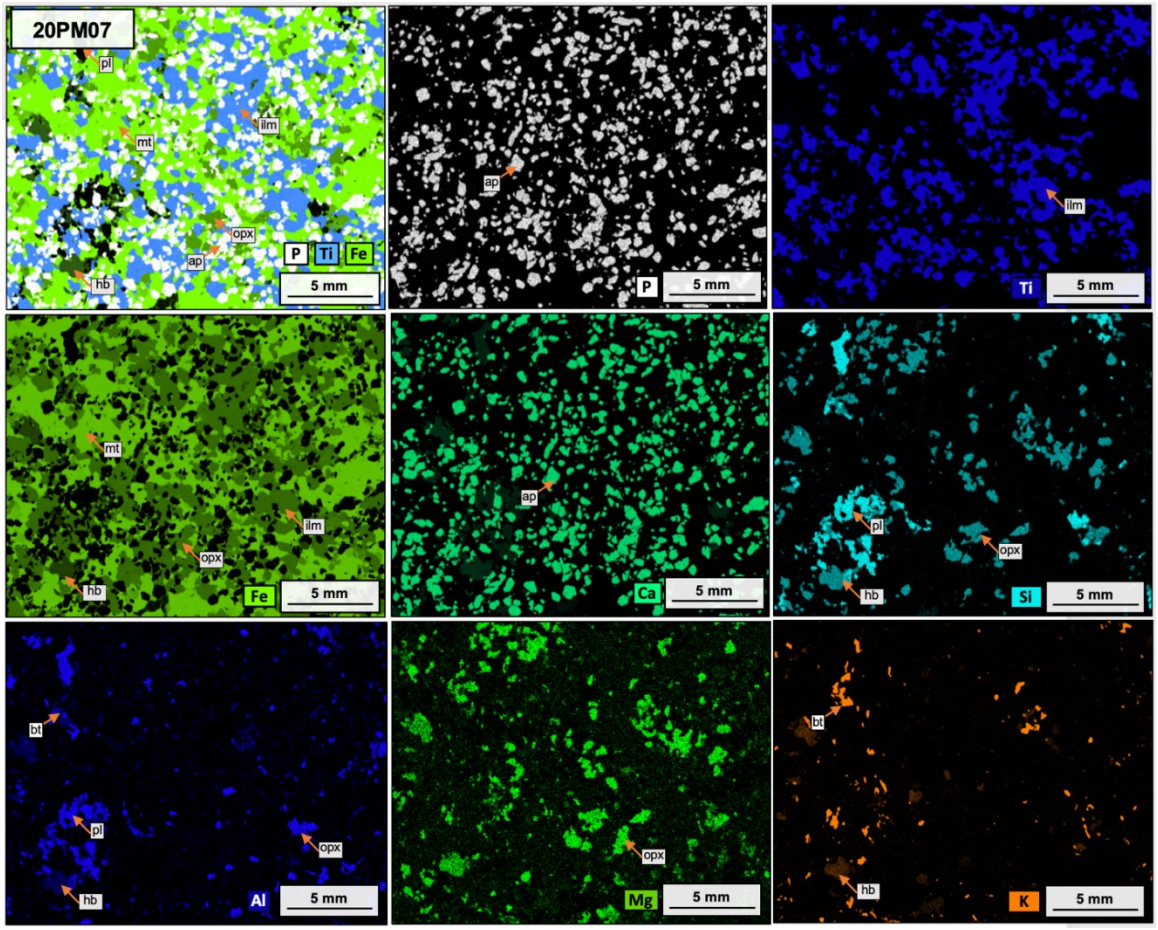

Appendix 3.2.8. µXRF-maps sample 20PM04-B showing the different proportions of oxides an apatite from the Lac Mirepoix Fe-Ti-P mineralized zone. Apatite is white. Ilmenite is blue, where as hematite-rich part of ilmenite is cyan. Magnetite is bright green. Orthopyroxene/biotite is dark green

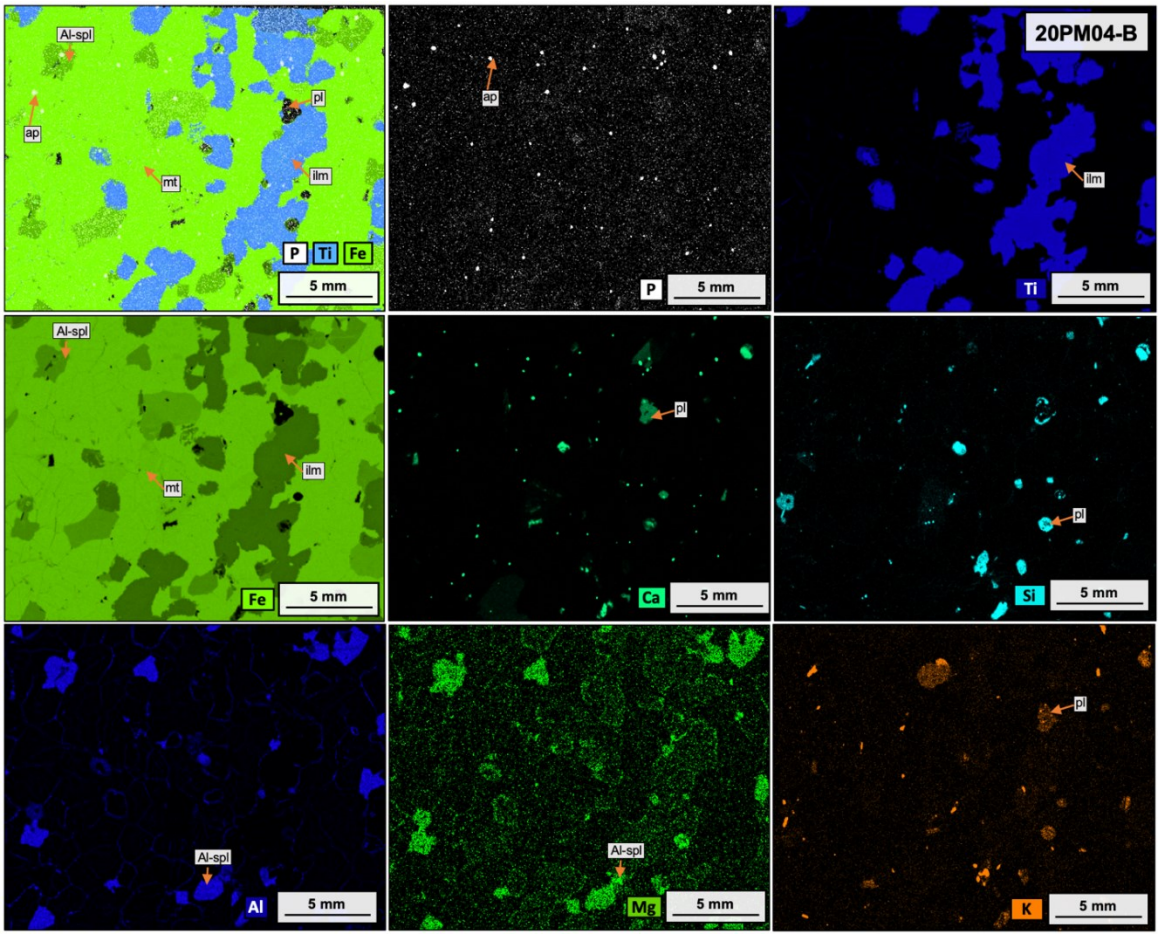

Appendix 3.2.9. µXRF-maps sample 20PM06-B showing the different proportions of oxides an apatite from the Lac Mirepoix Fe-Ti-P mineralized zone. Apatite is white. Ilmenite is blue, where as hematite-rich part of ilmenite is cyan. Magnetite is bright green. Orthopyroxene/biotite is dark green

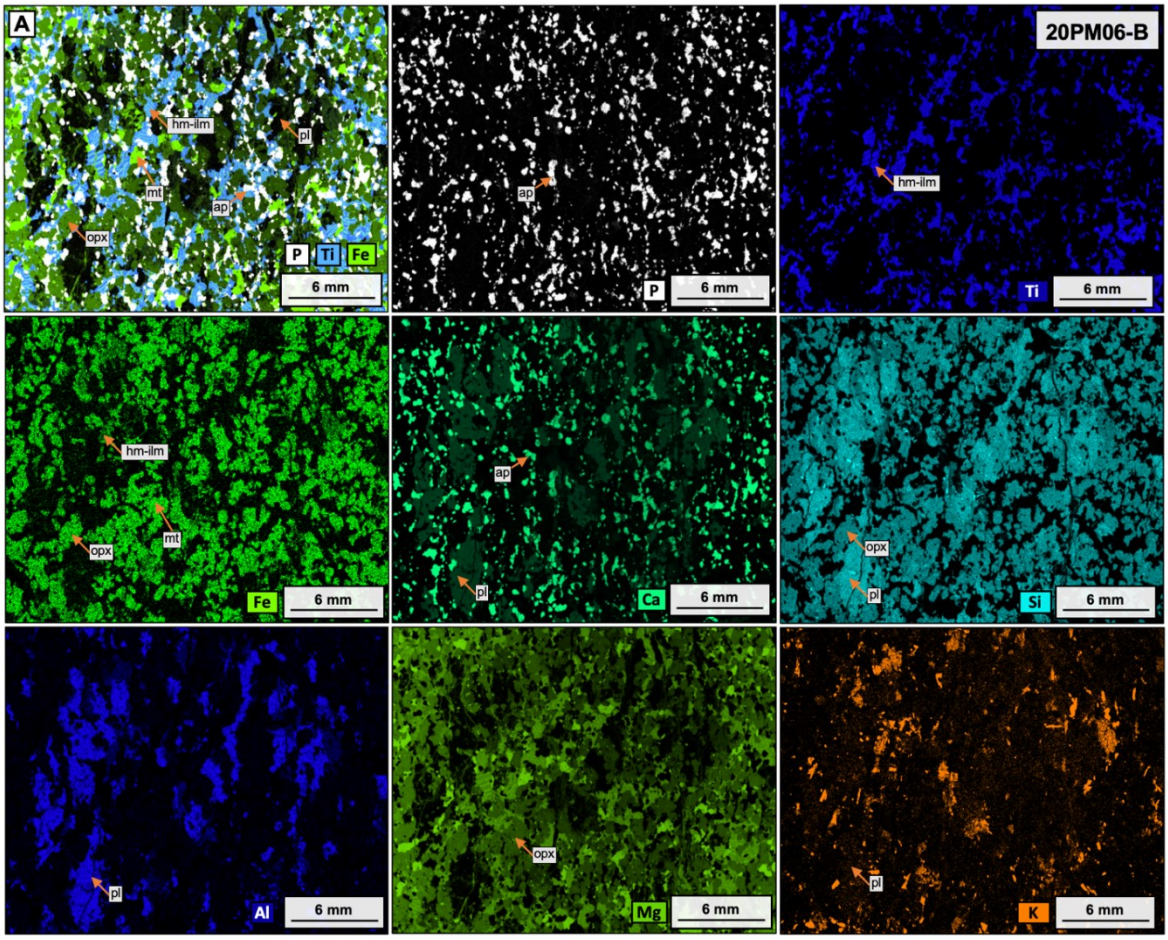

Appendix 3.2.10. µXRF-maps sample 20PM08-B1 showing the different proportions of oxides an apatite from the Lac Mirepoix Fe-Ti-P mineralized zone. Apatite is white. Ilmenite is blue, where as hematite-rich part of ilmenite is cyan. Magnetite is bright green. Orthopyroxene/biotite is dark green

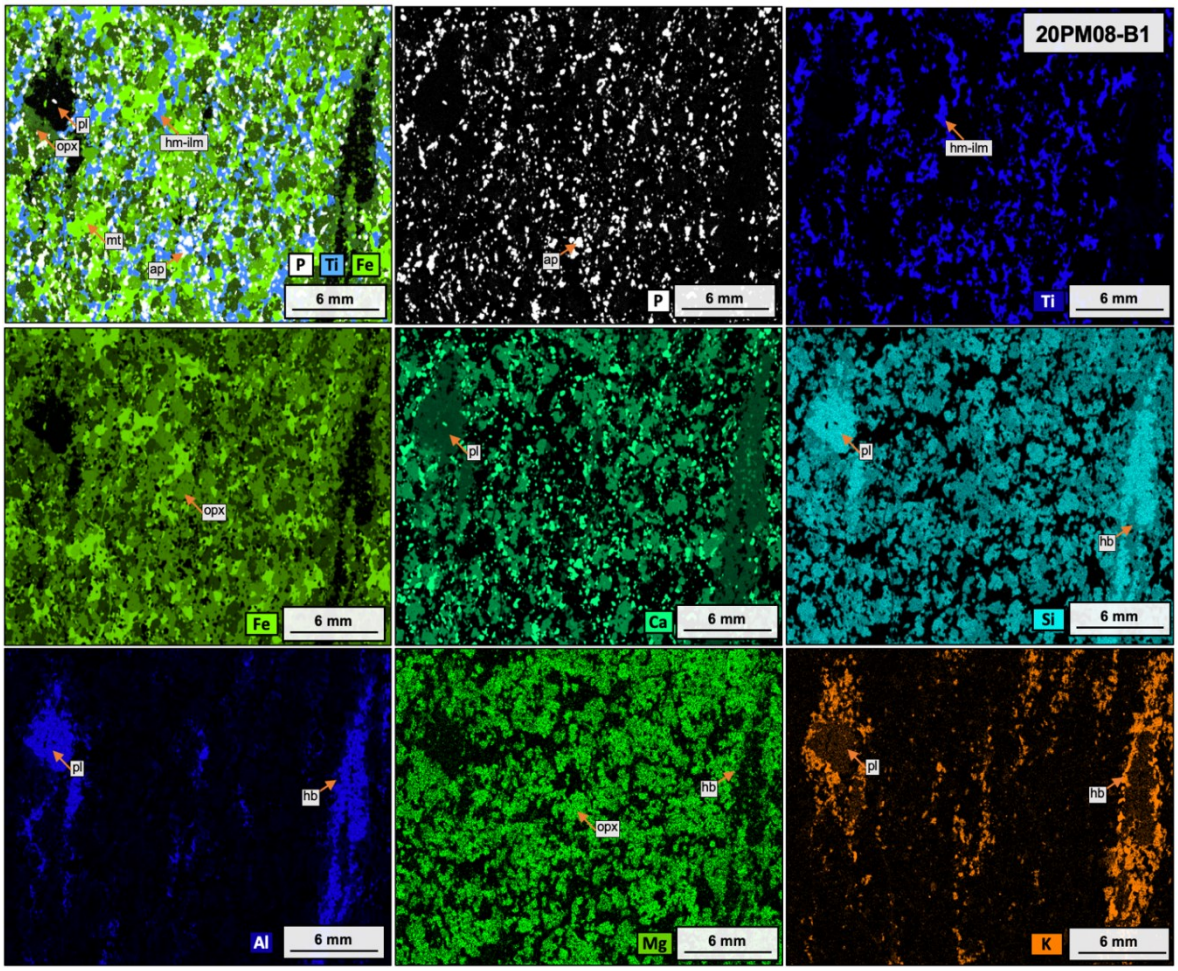

Appendix 3.2.11. µXRF-maps sample MX-109-2 showing the different proportions of oxides an apatite from the Lac Mirepoix Fe-Ti-P mineralized zone. Apatite is white. Ilmenite is blue, where as hematite-rich part of ilmenite is cyan. Magnetite is bright green. Orthopyroxene/biotite is dark green

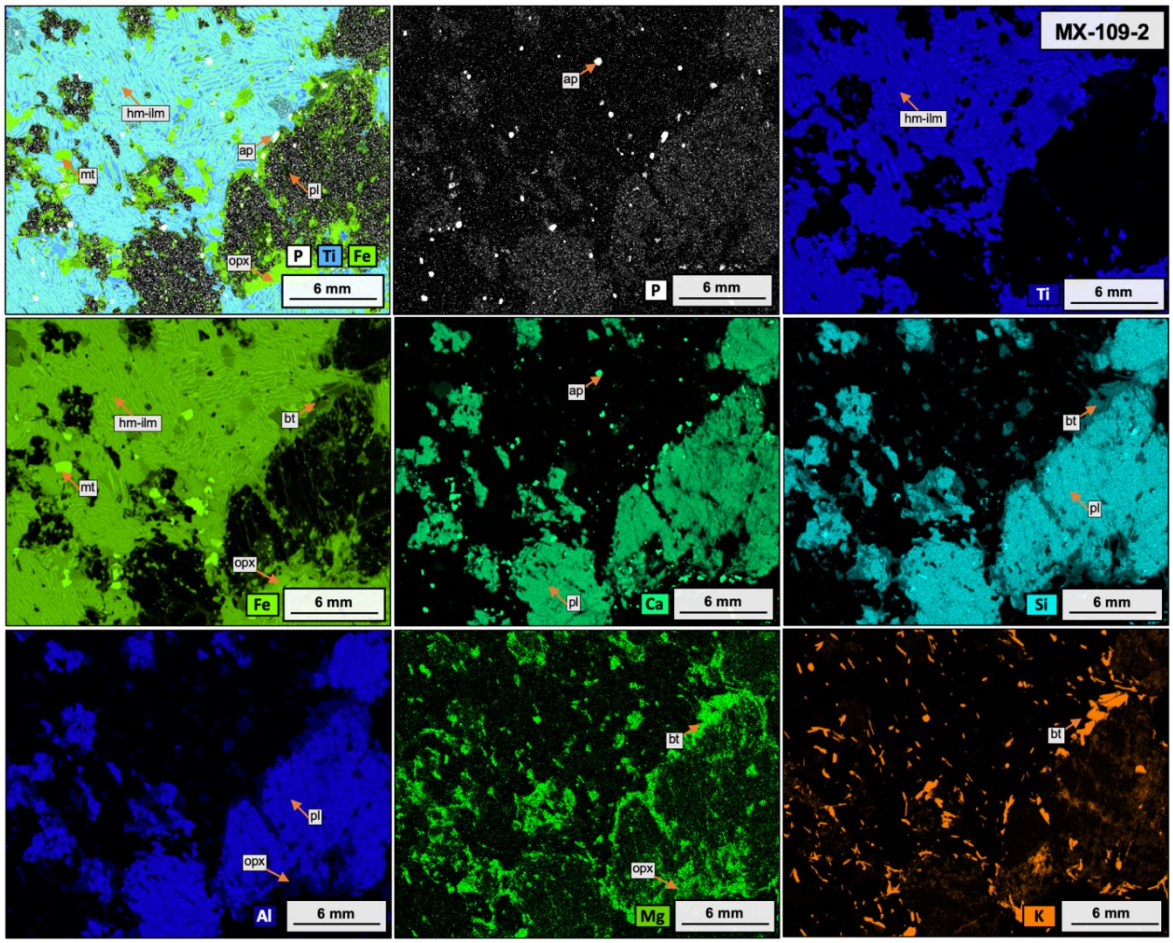

Appendix 3.2.12. µXRF-maps sample MX-108-4 showing the different proportions of oxides an apatite from the Lac Mirepoix Fe-Ti-P mineralized zone. Apatite is white. Ilmenite is blue, where as hematite-rich part of ilmenite is cyan. Magnetite is bright green. Orthopyroxene/biotite is dark green

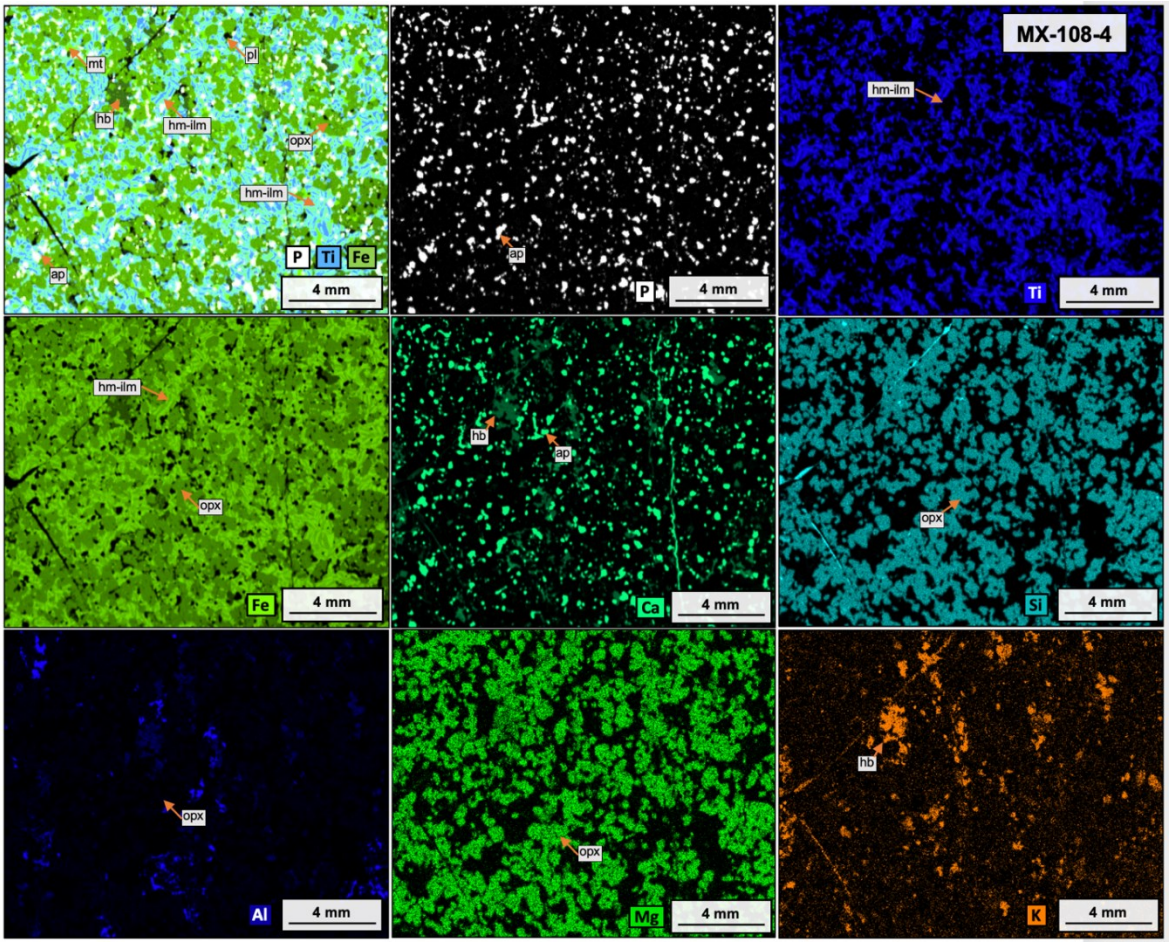

Appendix 3.2.13. Geochemical variation of whole-rock compositions in the Lac Mirepoix Fe-Ti-P mineralization along the section a-b. Abbreviations: OAN: oxide-apatite-norite

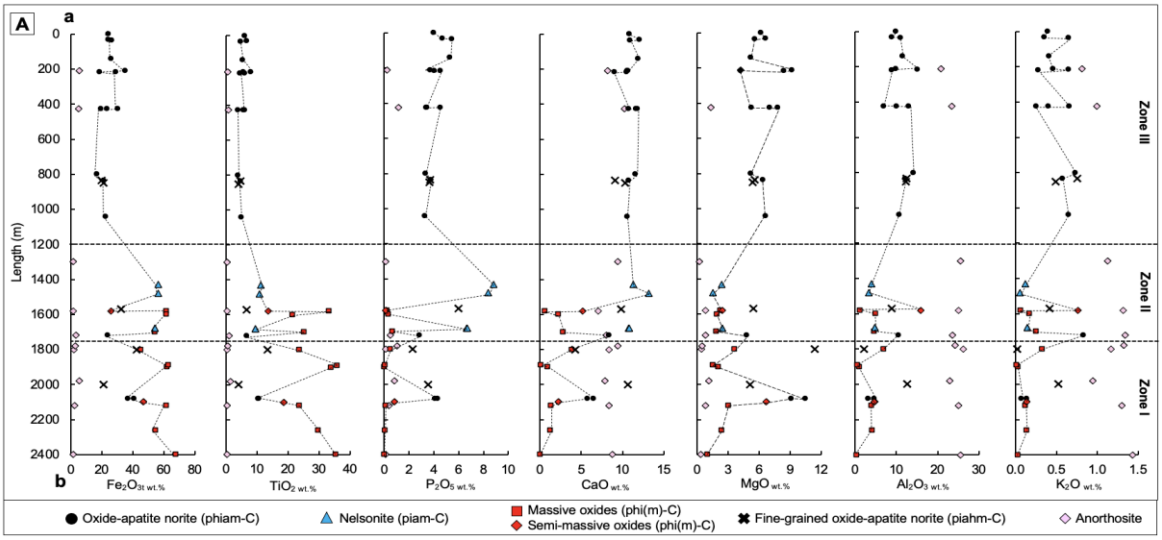

Appendix 3.2.14. Geochemical variation of apatite compositions in t he Lac Mirepoix Fe-Ti-P mineralization along the section a-b. Error bars = 1 standard deviation and représentas the natural variation within the thin section

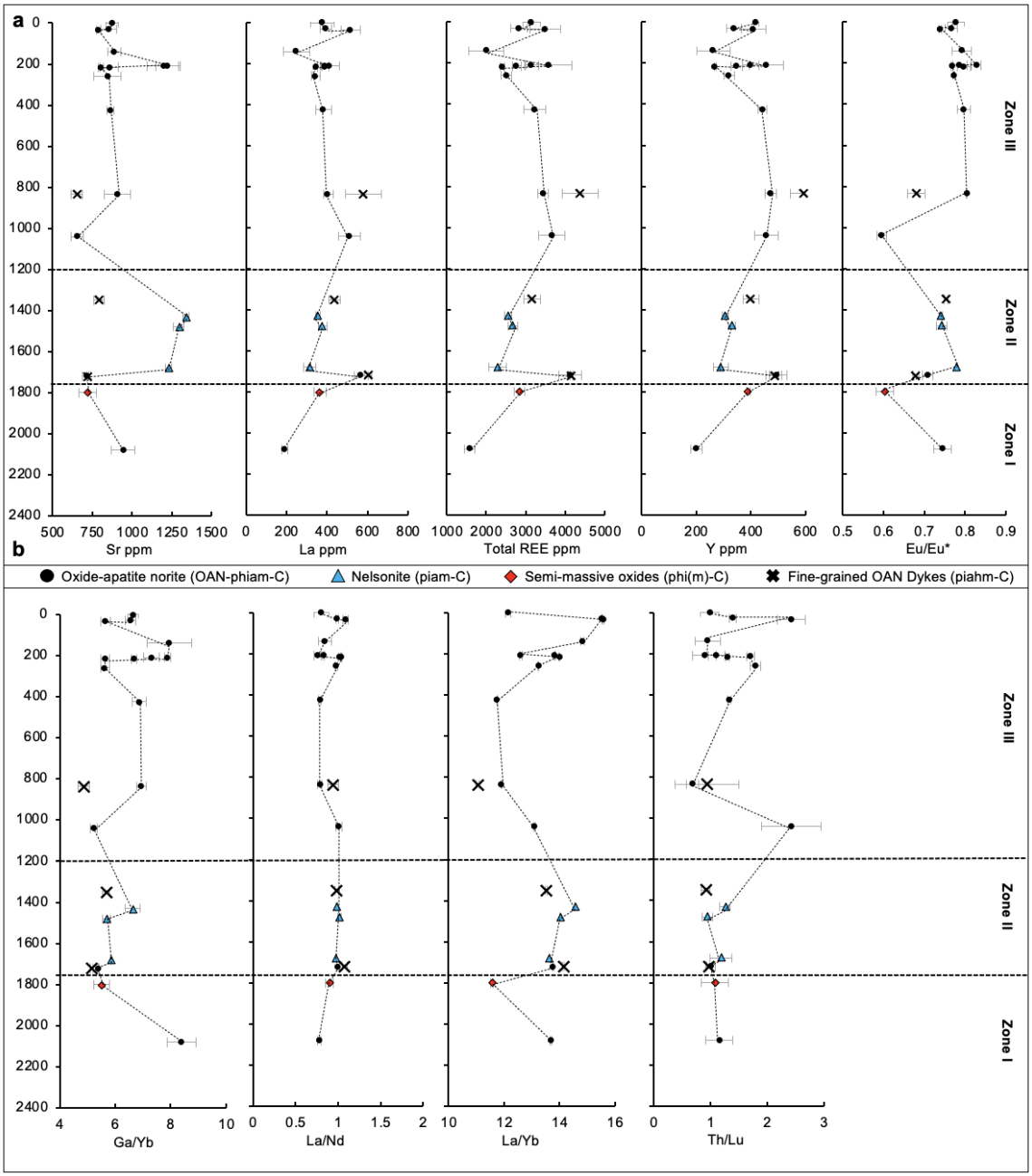

Appendix 3.2.15. Geochemical variation of ilmenite compositions in the Lac Mirepoix Fe-Ti-P mineralization along the section a-b. Error bars = 1 standard deviation and represents the natural variation within the thin section

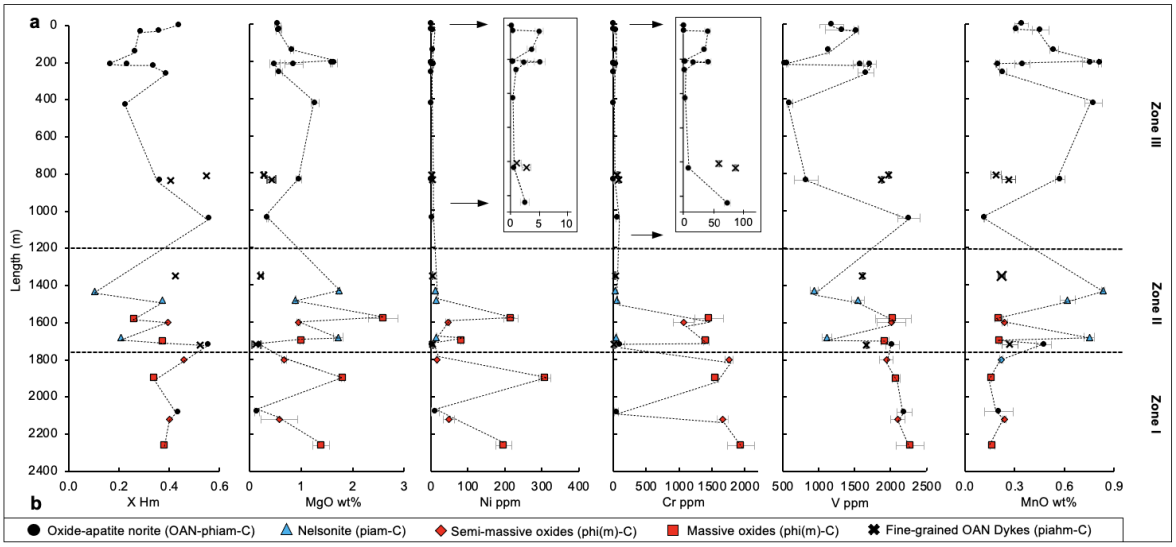

Appendix 3.2.16 Compilation of bulk whole-rock compositions of fine-grained lithologies interpreted as liquidus compositions in the Grenville Province, Quebec (Owens *et al.* (1993), Charlier *et al.* (2008)), including the nearby Lac à l'Orignal Fe-Ti-P mineralization (Miloski *et al.* 2022), the Rogaland Anorthosite Province, Norway (Duchesne *et al.* (1974); Duchesne & Hertogen (1988); Wilmart *et al.* (1989); Duchesne & Wilmart (1996); Vander Auwera *et al.* (1998)) and the Sept Iles Layered Intrusion (Namur *et al.* 2011), applying: A. The AFM ($A=Na_2O + K_2O$, $F = FeO + 0.8998 \times Fe_2O_3$, M=MgO, in wt.%) diagram (Le Maitre, 2002), with curves from Irvine & Baragar (1971). B. The total alkalis versus silica (TAS; in wt.%) discrimination and classification diagram (Le Bas *et al.* 1986). C. Whole-rock variation diagrams

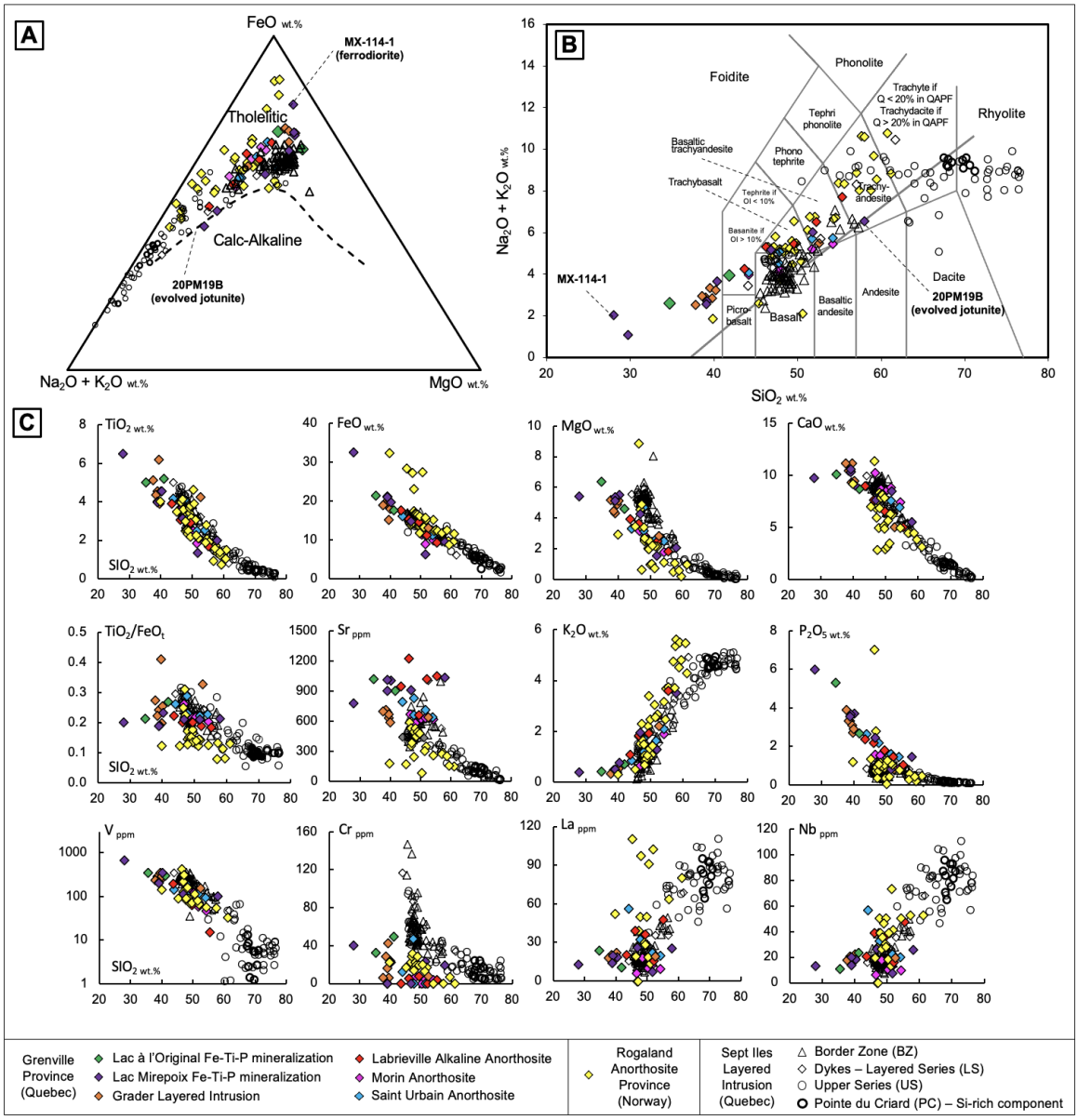

Appendix 3.2.17 Bulk whole-rock compositions of fine-grained lithologies projected into ternary diagrams for liquid immiscibility evaluation in the Sept Iles Layered Intrusion. A. Composition of the proposed liquid line of descent (after Charlier & Grove, 2012). B. Fine dashed line corresponds to outer boundaries of immiscibility fields from 1 atm experiments (Tollari et al. 2006); thick dashed line corresponds to 400 MPa (Bogaerts & Schmidt, 2006) experiments; the intermediate dashed line corresponds to the extrapolated immiscibility field at 200 MPa and grey zones correspond to the immiscibility fields of Roedder (1951). C-F. Tie lines for various conjugate immiscible melt pairs (after Charlier *et al.* 2011). Grey fields of low-temperature immiscibility field in system leucite-fayalite-SiO2 (Roedder, 1978). C: Immiscible ferrobasalts and granitic liquids obtained from melt inclusion compositions in the Sept Iles layered intrusion. D: Experimental immiscible pairs in lunar basalts (Longhi, 1990). E: Natural immiscible pairs of glassy globules in tholeiitic basalts (Philpotts,1982). F: Experimental immiscible ferrobasalt and granitic liquids (Dixon and Rutherford, 1979). Grey projection of low-tem- perature immiscibility field in system leucite-fayalite-SiO2 (Roedder, 1978)

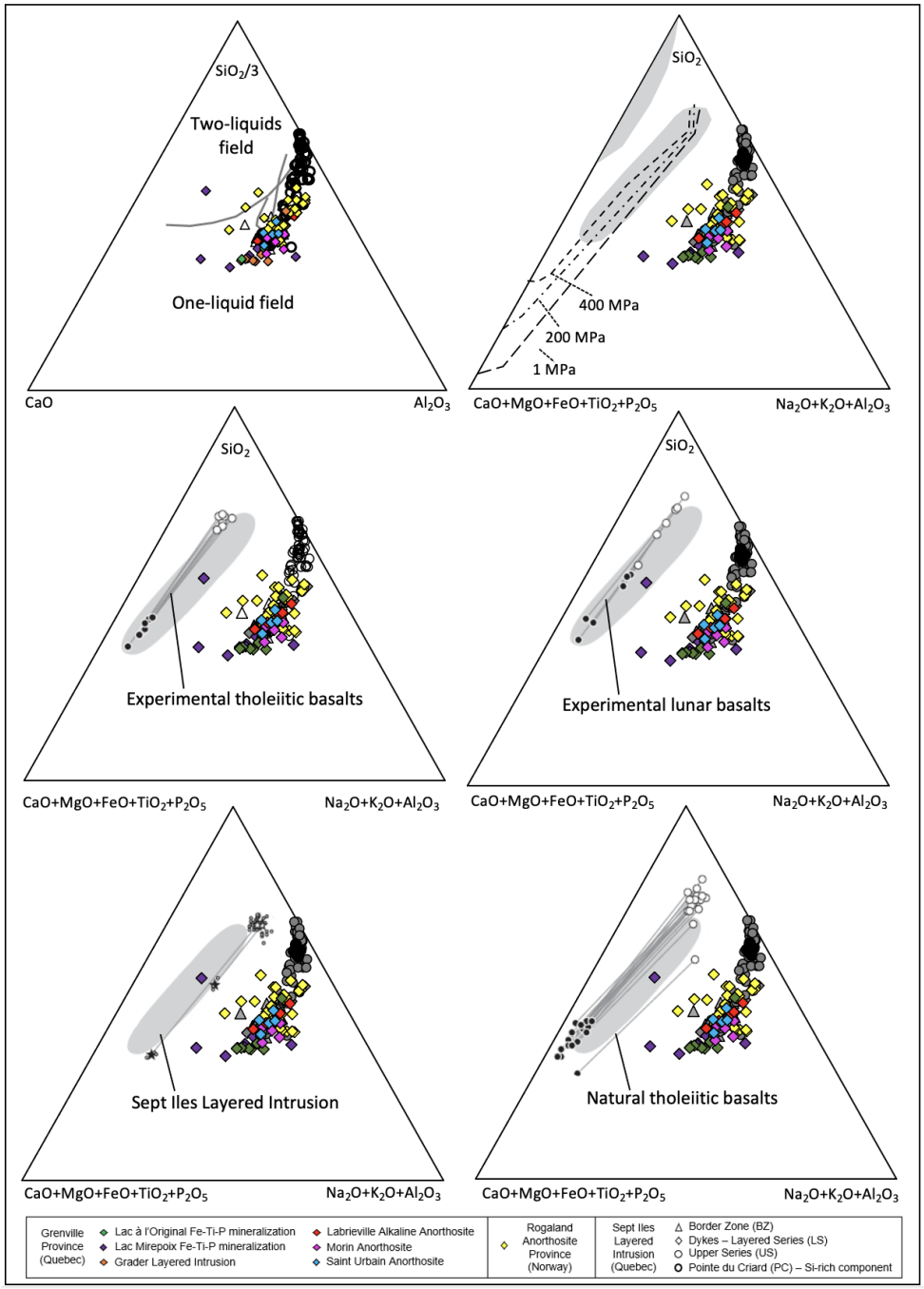

APPENDIX 3.3 METHODOLOGY (CHAPTER 3)

Appendix 3.3.1 Whole rock lithogeochemistry by fusion-LA-ICP-MS

See details for similar methodology on Appendix 2.2.1

Appendix 3.3.2 Mineral chemistry by LA-ICP-MS

See details for similar methodology on Appendix 2.2.2

Appendix 3.3.3 Electron microprobe

See details for similar methodology on Appendix 2.2.4

Appendix 3.3.4 U-Pb geochronology

See details for similar methodology on Appendix 2.2.5

Appendix 3.3.5 Portable XRF (pXRF)

Analyses of Ca, Si, Al, K, Ba and Sr were determined in plagioclase crystals of cut-slabs (10 x 10cm) of anorthosite by portable (p)XRF (Niton XL3t, Thermo Scientific) at LabMaTer, UQAC, following the protocol developed at UQAC by Tondoh (2021) and Mercier (2022). 3-5 grains of plagioclase were analyzed for each sample. Due to the coupled substitution of Ca-Na and Al-Si in plagioclase, the Anorthite contents were calculated from the Ca/Si ratio following the method of Tondoh (2021). Matrix-matched plagioclase reference materials, which were characterised using LA-ICP-MS and EMPA at UQAC, were used to correct the instrumental bias of Si, Ca and Sr values of the pXRF method. Repeated analysis of these reference materials indicates that the pXRF method is accurate and precise to within 2 – 5% (Tondoh 2021; Mercier 2022). The comparison between LA-ICP-MS and pXRF results obtained for An content, Sr and Ba in this study (Figure A2) show a good correlation between the two methods, especially for An content and Sr.

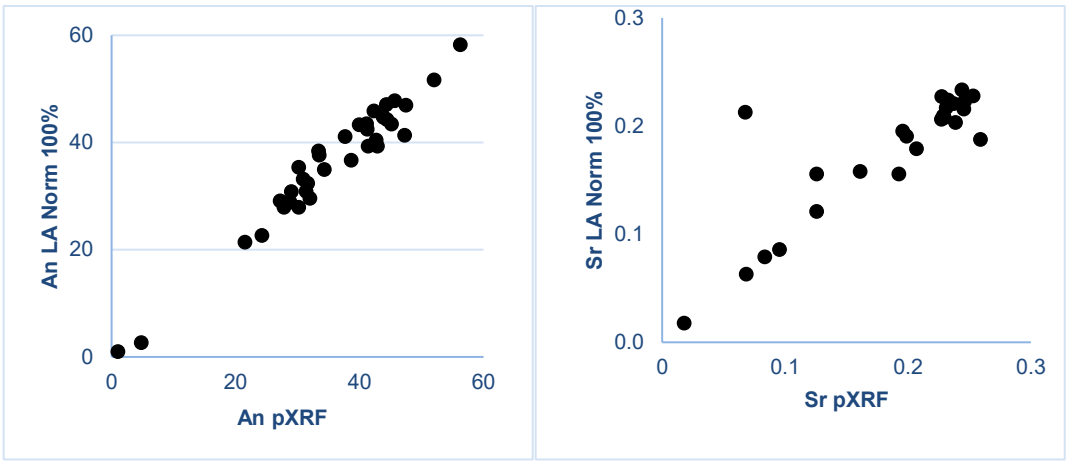

Figure 1. Comparison between LA-ICP-MS and pXRF results obtained for plagioclase (both reference materials and samples).

APPENDIX 4.1 METHODOLOGY (CHAPTER 4)

Appendix 4.1.1 Whole rock lithogeochemistry by fusion-LA-ICP-MS

See details for similar methodology on Appendix 2.2.1

Appendix 4.1.2 Mineral chemistry by LA-ICP-MS

See details for similar methodology on Appendix 2.2.2

Appendix 4.1.3 Portable XRF (pXRF)

See details for similar methodology on Appendix 3.3.5

Appendix 4.1.4 U-Pb geochronology

See details for similar methodology on Appendix 2.2.5

Appendix 4.1.5 Hf isotopes

Hf isotope measurements were carried out at the University of Geneva, Switzerland, using a Termo Neptune Plus multi-collector-ICP-MS coupled to a NWR 193 HE laser ablation system, following a procedure similar to that described in Ruiz et al., (2022). Zircons were ablated with a fluence of 3.5 J/cm2 fluence, a repetition rate of 5 Hz and a spot size of 40 µm. Helium gas was used to carry the ablated particles through the two volume ablation cell, and this gas was mixed with a small amount of N2 (6m/min), before entering the Ar-plasma torch, the nitrogen gas was used to enhance sensitivity. All of the measurements were performed at low mass resolution, 120 cycles of 1 second were collected, however sample measurements typically only lasted for between 100 and 120 cycles depending on the zircon thickness. To assess if any offsets between the measured values and reference values were present, we measured a series of reference materials after every 20 sample measurements, blanks were measured after ever sample or standard. The zircon reference materials we used were Mud Tank (176Hf/177Hf=0.282507; Woodhead & Hergt, 2005), Plešovice (176Hf/177Hf=0.282482; Slama et al., 2008), GJ-1 (176Hf/177Hf=0.282000; Morel et al., 2008), and synthetic MUN (176Hf/177Hf=0.282135; Fisher et al., 2014). Data reduction was conducted offline using an in-house Excel spreadsheet. It involved blank

subtractions, removal of isobaric interferences associated with the 176Lu and 176Yb masses on the 176Hf mass (e.g., Fisher et al. 2014), and correction of the resulting 176Hf/177Hf ratio for mass bias (Albarède et al., 2004). The βHf and βYb mass bias coefficients were calculated from the measured 179Hf/177Hf and 173Yb/171Yb using the reference values of Patchett & Tatsumoto (1980) (179Hf/177Hf=0.7325) and Thirlwall & Anczkiewicz (2004) (173Yb/171Yb=1.1234), respectively. Isobaric interferences of 176Yb and 176Lu with 176Hf were corrected using 176Yb/173Yb=0.786954 and 176Lu/175Lu=0.02645 (Thirlwall & Anczkiewicz, 2004). 176Hf/177Hf vs. Time plots were used to identify any heterogeneities with the zircon e.g. areas that have different 176Hf/177Hf ratios due to inclusions, metamorphic overgrowth, inherited cores, and only non-perturbed spectra were retained. Initial 176Hf/177Hf ratios and εHf values were calculated using the 207Pb/206Pb date of the sample or the age of the individual age of the inherited zircon xenocryst, the present-day chondritic values of Lizuka et al., (2015) (176Hf/177Hf=0.282793 and 176Lu/177Hf=0.0336), and λ176Lu=1.87×10–11 a−1 (Söderlund et al., 2004) were used. All values are presented in ESM2.

References

Albarède, F., Desaulty, A. M., & BLICHERT-TOFT, J. (2012). A geological perspective on the use of Pb isotopes in archaeometry. Archaeometry, 54(5), 853-867.

Bodorkos S, Stern R.A, Kamo S, Corfu F, Hickman AH. 2009. OG1: a natural reference material for quantifying SIMS instrumental mass fractionation of Pb Isotopes during zircon dating. InAGU Fall Meeting Abstracts 2009 Dec (Vol. 2009, pp. V33B-2044).

Barnes, S. J., Mansur, E. T., Pagé, P., Meric, J., & Arguin, J. P. 2020. Major and trace element compositions of chromites from the Stillwater, Bushveld and Great Dyke intrusions compared with chromites from komatiites, boninites and large igneous provinces.

Fisher, C. M., Vervoort, J. D., & Hanchar, J. M. (2014). Guidelines for reporting zircon Hf isotopic data by LA-MC-ICPMS and potential pitfalls in the interpretation of these data. Chemical geology, 363, 125-133.

Norman, M., Robinson, P., & Clark, D. 2003. Major-and trace element analysis of sulfide ores by laser-ablation ICP–MS, solution ICP–MS, and XRF: new data on international reference materials. The Canadian Mineralogist, 41(2), 293-305.

Paton, C., Hellstrom, J., Paul, B., Woodhead, J., & Hergt, J. (2011). Iolite: Freeware for the visualisation and processing of mass spectrometric data. Journal of Analytical Atomic Spectrometry, 26(12), 2508-2518.

Patchett, P. J., & Tatsumoto, M. (1980). Hafnium isotope variations in oceanic basalts. Geophysical Research Letters, 7(12), 1077-1080.

Perkins, W. T., Pearce, N. J. G., & Jeffries, T. E. 1993. Laser ablation inductively coupled plasma mass spectrometry: a new technique for the determination of trace and ultra-trace element in silicates. Geochimica et Cosmochimica Acta, 57(2), 475-482.

Perrot, M., Tremblay, A., David, J., 2017. Detrital zircon U-Pb geochronology of the Magog Group, southern Quebec–stratigraphic and tectonic implications for the Quebec Appalachians. Am. J. Sci. 317 (10), 1049–1094

Rocha, B.C, Davies J.H.F.L., Janasi V.A., Schaltegger U, Nardy A.J.R., Greber N.D, Lucchetti A.C.F,. Polo L.A. 2020. Rapid eruption of silicic magmas from the Paraná magmatic province (Brazil) did not trigger the Valanginian event. Geology; 48 (12): 1174–1178. doi: https://doi.org/10.1130/G47766.1

Ruiz, M., Schaltegger, U., Gaynor, S. P., Chiaradia, M., Abrecht, J., Gisler, C., ... & Wiederkehr, M. (2022). Reassessing the intrusive tempo and magma genesis of the late Variscan Aar batholith: U–Pb geochronology, trace element and initial Hf isotope composition of zircon. Swiss Journal of Geosciences, 115(1), 1-24.

Sláma J, Košler J, Condon DJ, Crowley JL, Gerdes A, Hanchar JM, Horstwood MS, Morris GA, Nasdala L, Norberg N, Schaltegger U. 2008. Plešovice zircon—a new natural reference material for U–Pb and Hf isotopic microanalysis. Chemical Geology. Mar 30;249(1-2):1-35.

Söderlund, U., Patchett, P. J., Vervoort, J. D., & Isachsen, C. E. (2004). The 176Lu decay constant determined by Lu–Hf and U–Pb isotope systematics of Precambrian mafic intrusions. Earth and Planetary Science Letters, 219(3-4), 311-324.

Thirlwall, M. F., & Anczkiewicz, R. (2004). Multidynamic isotope ratio analysis using MC–ICP–MS and the causes of secular drift in Hf, Nd and Pb isotope ratios. International Journal of Mass Spectrometry, 235(1), 59-81.

Vermeesch, P., 2018, IsoplotR: a free and open toolbox for geochronology. Geoscience Frontiers, v.9, p.1479-1493, doi:10.1016/j.gsf.2018.04.001.

Woodhead, J. D., & Hergt, J. M. (2005). A preliminary appraisal of seven natural zircon reference materials for in situ Hf isotope determination. Geostandards and Geoanalytical Research, 29(2), 183-195

APPENDIX 4.2 SUPPLEMENTARY TABLES (CHAPTER 4)

Appendix 4.2.1 Whole-rock reference materials (separate excel sheet)

Appendix 4.2.2 Mineral chemistry reference materials (separate excel sheet)

Appendix 4.2.3 Petrographic modal proportions

Sample	UTM-E	UTM-N	Lithology	Modal Proportions (%)									Ilmenite/ Magnetite ratio
				Plagioclase	OPX	Hemo-ilmenite	Ilmenite	Magnetite	Al-spinel	Apatite	Biotite/ Hornblende	K-feldspar + Quartz	
20PM09A	403222	5431875	Medium-grained OAN	45	5		6	4		10	30		1.5
20PM09B	403222	5431875	Medium-grained OAN	20	60		5	2		10	3		2.5
20PM23C	403226	5432881	Medium-grained OAN	35	35		6	4		10	10		1.5
20PM25	403226	5432418	Medium-grained OAN	40	35		4	4		7	10		1.0
20PM26A	402636	5433515	Medium-grained leuconorite	60	25		2	3		3	5		0.7
20PM24	403214	5432851	Medium-grained leuconorite	70	15		3	2		5	5		1.5
20PM26B	402636	5433515	Medium-grained leuconorite	65	20		3	2		5	5		1.5
20PM46E	392299	5432637	Medium-grained OAN	55	15	5		5		5	15		1.0
20PM46A	392299	5432637	Medium-grained nelsonite	5	7		30	30		25	3		1.0
20PM47	392270	5432656	Medium-grained nelsonite	5	5		25	20		30	5		1.3
20PM12-C2	389480	5424110	Medium-grained leuconorite	70	10		5	5		5	5		1.0
20PM12B	389480	5424110	Medium-grained leuconorite	60	30		8			2			-
20PM12D	389480	5424110	Medium-grained leuconorite	60	30		8			2			-
21PM11-B	376707	5418903	Medium-grained OAN	55	20		7	3		10	5		2.3
21PM18-B	382116	5422795	Medium-grained oxide-norite	30	55		15						-
21PM19	382889	5422795	Medium-grained oxide-norite	30	45		25						-
20PM32A	433018	5459507	Medium-grained leuconorite	65	30	5							-
20PM42A	418253	5471028	Medium-grained OAN	30	50	8		4		8			2.0
20PM42B	418253	5471028	Fine-grained-leuconorite	80	15	3				2			-
20PM32B	433018	5459507	Massive oxides	98					2				-
20PM33B	430892	5463836	Massive oxides	5		93			2				-
20PM37	429782	5470490	Massive oxides	95	4				1				-
20PM38A	429698	5470593	Medium-grained nelsonite	20	10	40				30			-
20PM38C	429698	5470593	Medium-grained nelsonite	3	7	58			2	30			-
21PM06	363669	5417435	Oxide-apatite-rich mangerite	48	25		4	4		7	<3	10	1.0
21PM07	363763	5417085	Oxide-apatite-rich mangerite	32	45		6	6		3	<3	5	1.0
21PM08	360627	5425240	Oxide-apatite-rich mangerite	47	25		6	4		10	<3	5	1.5
21PM09	360627	5425240	Oxide-apatite-rich mangerite	37	35		5	3		12	<3	5	1.7

21PM57	364912	5425682	Oxide-apatite-rich mangerite	52	25		3	5		10	<3	<5	0.6
21PM53-A	371910	5435680	Massive oxides				40	50	10				0.8
21PM53-B	371910	5435680	Medium-grained leuconorite	55	25		8	7			5		1.1
21PM55	364953	5434038	Medium-grained leuconorite	25	50		3	2			20		1.5

Appendix 4.2.4 Complete LA-ICP-MS whole-rock results

Sample	Lithology	Oxides	UTM-E	UTM-N	SiO_2	TiO_2	Al_2O_3	Fe_2O_{3t}	MnO	MgO	CaO	Na_2O	K_2O	P_2O_5	LOI	Total
Lac Périgny Fe-Ti-P mineralization																
20PM09A	Medium-grained OAN	Ilm + Mt	403222	5431875	40.1	4.1	15.8	16.6	0.2	4.9	9.9	3.1	1.1	3.8	0.3	100.0
20PM09B	Medium-grained OAN	Ilm + Mt	403222	5431875	38.5	4.8	11.1	20.5	0.3	8.9	8.1	1.6	2.1	4.0	0.1	100.0
20PM23C	Medium-grained OAN	Ilm + Mt	403226	5432881	37.1	4.4	15.2	17.8	0.2	4.5	11.8	2.8	0.5	5.7	0.0	100.0
20PM25	Medium-grained OAN	Ilm + Mt	403226	5432418	39.2	3.7	13.0	21.0	0.4	4.8	9.9	2.6	0.9	4.5	0.0	100.0
20PM26A	Medium-grained leuconorite	Ilm + Mt	402636	5433515	45.0	3.2	15.8	16.6	0.2	4.2	8.9	3.2	0.5	2.2	0.1	100.0
20PM24	Medium-grained leuconorite	Ilm + Mt	403214	5432851	49.0	1.4	22.1	8.7	0.1	2.9	9.2	4.0	0.9	1.3	0.4	100.0
20PM26B	Medium-grained leuconorite	Ilm + Mt	402636	5433515	49.9	1.6	18.9	10.9	0.2	3.7	9.0	3.7	0.5	1.0	0.6	100.0
Lac de L'Abbondance Fe-Ti-P mineralization																
20PM46E	Medium-grained OAN	Hm-ilm	392299	5432637	44.3	3.1	17.6	13.9	0.2	4.1	9.0	4.5	1.0	2.2	0.0	100.0
20PM46A	Medium-grained nelsonite	Ilm + Mt	392299	5432637	4.0	11.4	5.4	65.4	0.2	2.7	5.8	0.3	0.1	4.2	0.0	100.0
20PM47	Medium-grained nelsonite	Ilm + Mt	392270	5432656	3.0	11.1	4.8	65.7	0.2	2.4	6.8	0.2	0.1	5.2	0.0	100.0
Mattawa Anorthosite (Fe-Ti-(P) mineralization occurrences)																
20PM12-C2	Medium-grained leuconorite	Hm-ilm + Mt	389480	5424110	42.2	5.4	12.7	19.4	0.2	3.1	8.8	3.3	1.1	3.3	0.5	100.0
20PM12B	Medium-grained leuconorite	Hm-ilm + Mt	389480	5424110	37.1	5.0	11.8	23.2	0.2	5.2	9.6	2.3	0.6	4.1	0.9	100.0
20PM12D	Medium-grained leuconorite	Hm-ilm + Mt	389480	5424110	44.9	4.8	12.9	17.2	0.2	3.7	8.3	3.3	1.1	2.6	1.0	100.0
21PM11-B	Medium-grained OAN	Ilm + Mt	376707	5418903	47.9	2.4	14.8	15.3	0.2	3.2	7.0	4.1	2.1	2.7	0.3	100.0
21PM18-B	Medium-grained oxide-norite	Hm-ilm + Mt	382116	5422795	30.4	14.4	4.7	34.5	0.2	7.3	7.2	1.1	0.2	0.0	-0.2	100.0
21PM19	Medium-grained oxide-norite	Hm-ilm + Mt	382889	5422795	30.1	14.7	4.3	35.0	0.2	7.6	7.0	0.9	0.1	0.0	-0.4	100.0
21PM12	Medium-grained leuconorite	Hm-ilm + Mt	375331	5420378	53.0	2.7	13.6	13.9	0.2	2.2	5.7	3.6	2.6	1.8	0.6	100.0
21PM11-A	Medium-grained leuconorite	Hm-ilm + Mt	376707	5418903	49.7	2.5	14.9	14.6	0.2	2.9	6.0	4.2	2.5	2.2	0.3	100.0
Labrieville Anorthosite (Fe-Ti-(P) mineralization occurrences)																
20PM32A	Medium-grained leuconorite	Hm-ilm + Mt	433018	5459507	35.9	7.6	7.7	27.5	0.3	6.8	8.7	1.8	0.4	3.3	0.0	100.0
20PM42A	Medium-grained OAN	Hm-ilm + Mt	418253	5471028	35.3	7.1	7.4	28.0	0.3	6.5	9.6	1.8	0.4	3.5	0.0	100.0
20PM42B	Fine-grained leuconorite	Hm-ilm	418253	5471028	55.9	2.2	13.7	12.6	0.2	2.2	5.4	3.3	3.1	1.6	0.0	100.0
20PM32B	Massive oxides	Hm-ilm	433018	5459507	1.0	34.1	2.0	59.0	0.1	2.5	0.5	0.0	0.0	0.1	0.0	100.0
20PM33B	Massive oxides	Hm-ilm	430892	5463836	6.7	31.2	3.3	54.6	0.1	1.5	1.2	0.7	0.2	0.1	0.0	100.0
20PM37	Massive oxides	Hm-ilm	429782	5470490	0.8	34.1	1.3	59.6	0.1	2.1	0.8	0.0	0.0	0.4	0.0	100.0
20PM38A	Medium-grained nelsonite	Hm-ilm	429698	5470593	0.8	30.7	1.0	60.7	0.1	1.3	2.9	0.0	0.0	2.1	0.0	100.0
20PM38C	Medium-grained nelsonite	Hm-ilm	429698	5470593	6.3	17.7	2.8	33.5	0.1	1.1	20.5	0.5	0.1	17.1	0.0	100.0
La Hache Mangerite (Fe-Ti-(P) mineralization occurrences)																
21PM06	Oxide-apatite-rich mangerite	Ilm + Mt	363669	5417435	37.0	5.6	8.3	26.3	0.5	6.4	9.7	2.0	0.7	3.5	-0.1	100.0
21PM07	Oxide-apatite-rich mangerite	Ilm + Mt	363763	5417085	34.8	6.0	7.8	30.0	0.6	5.9	8.9	2.0	1.0	3.0	-0.6	100.0
21PM08	Oxide-apatite-rich mangerite	Ilm + Mt	360627	5425240	37.9	3.9	11.6	23.4	0.3	5.2	9.7	2.7	0.6	4.7	0.0	100.0
21PM09	Oxide-apatite-rich mangerite	Ilm + Mt	360627	5425240	12.5	7.0	4.9	46.9	0.3	2.9	13.2	0.8	0.3	11.1	-0.2	100.0
21PM57	Oxide-apatite-rich mangerite	Ilm + Mt	364912	5425682	50.6	1.8	16.7	11.8	0.3	3.1	6.9	4.6	2.1	1.9	0.2	100.0
L'Etang Fe-Ti mineralization																
21PM53-A	Massive oxides	Ilm + Mt	371910	5435680	3.3	27.5	3.6	61.6	0.4	3.0	0.5	0.1	0.0	0.0	-3.1	100.0
21PM53-B	Medium-grained leuconorite	Ilm + Mt	371910	5435680	41.2	3.6	17.9	21.4	0.2	5.2	6.9	3.0	0.5	0.0	0.2	100.0
21PM55	Medium-grained leuconorite	Ilm + Mt	364953	5434038	43.9	0.8	12.9	17.9	0.2	16.2	5.1	1.9	0.4	0.2	0.5	100.0

Appendix 4.2.4 (cont.) Complete LA-ICP-MS whole-rock results

Sample	Lithology	Oxides	^{45}Sc	^{51}V	^{53}Cr	^{59}Co	^{60}Ni	^{63}Cu	^{66}Zn	^{69}Ga	^{85}Rb	^{88}Sr	^{89}Y	^{90}Zr	^{93}Nb	^{137}Ba	^{139}La	^{140}Ce
20PM09A	Medium-grained OAN	Ilm + Mt	13.6	174.1	25.1	44.1	24.9	56.6	118.7	19.0	29.3	547.7	47.8	63.9	10.2	271.0	29.2	75.7
20PM09B	Medium-grained OAN	Ilm + Mt	17.0	178.4	24.9	78.5	29.4	88.7	168.1	15.2	200.1	320.9	69.2	75.5	24.5	237.7	44.5	114.6
20PM23C	Medium-grained OAN	Ilm + Mt	11.7	179.2	16.0	55.8	26.7	34.1	141.1	20.3	6.1	592.3	76.2	53.0	9.9	229.2	42.1	117.4
20PM25	Medium-grained OAN	Ilm + Mt	20.5	101.8	12.3	37.7	11.9	21.8	269.9	19.8	22.2	441.9	81.0	370.3	15.5	384.0	48.2	123.8
20PM26A	Medium-grained leuconorite	Ilm + Mt	21.7	226.0	82.4	39.7	37.7	32.7	160.6	21.8	2.0	490.5	41.2	72.4	14.0	221.6	32.3	80.8
20PM24	Medium-grained leuconorite	Ilm + Mt	5.3	102.1	44.7	30.3	22.9	17.4	74.7	22.0	15.3	721.2	16.0	47.1	2.6	321.9	12.1	30.9
20PM26B	Medium-grained leuconorite	Ilm + Mt	17.9	60.1	39.9	24.6	12.0	15.6	129.5	18.8	1.8	553.8	33.3	49.7	11.1	273.3	20.8	51.6
20PM46E	Medium-grained OAN	Hm-ilm	15.5	206.1	47.9	34.1	56.8	17.8	173.0	24.4	12.7	####	22.4	60.7	5.4	801.3	25.4	63.1
20PM46A	Medium-grained nelsonite	Ilm + Mt	12.4	###	784.0	207.3	443.1	180.3	600.7	50.7	0.8	232.5	20.2	53.0	2.7	64.1	20.8	56.4
20PM47	Medium-grained nelsonite	Ilm + Mt	12.6	###	851.6	166.4	341.4	127.4	615.2	50.7	0.8	218.6	23.6	30.7	2.6	60.7	24.0	65.0
20PM12-C2	Medium-grained leuconorite	Hm-ilm + Mt	24.8	282.3	42.9	43.2	36.8	48.4	209.9	23.4	4.1	889.6	66.0	218.4	35.7	835.3	60.7	156.3
20PM12B	Medium-grained leuconorite	Hm-ilm + Mt	30.4	351.5	24.7	52.3	30.0	27.4	276.5	27.2	1.9	959.6	56.8	206.3	15.2	755.4	67.0	166.5
20PM12D	Medium-grained leuconorite	Hm-ilm + Mt	25.2	249.0	34.9	40.0	31.9	40.4	198.2	22.8	3.8	893.1	59.1	207.4	29.0	832.1	52.4	132.3
21PM11-B	Medium-grained OAN	Ilm + Mt	26.4	80.7	4.0	30.8	23.2	34.7	257.3	31.0	6.0	####	41.3	39.7	16.7	2039.3	42.5	107.2
21PM18-B	Medium-grained oxide-norite	Hm-ilm + Mt	36.3	###	63.1	58.5	35.5	32.6	201.4	16.2	0.7	183.5	11.9	73.2	17.8	108.2	2.0	7.2
21PM19	Medium-grained oxide-norite	Hm-ilm + Mt	35.8	###	63.1	74.7	47.7	66.9	210.7	16.6	0.5	144.4	11.5	128.7	17.9	77.7	1.8	6.4
21PM12	Medium-grained leuconorite	Hm-ilm + Mt	29.5	108.5	4.5	24.8	13.5	36.7	259.8	28.8	9.4	787.6	46.5	819.8	25.8	2104.5	55.8	131.0
21PM11-A	Medium-grained leuconorite	Hm-ilm + Mt	28.0	57.9	3.0	23.5	4.7	16.6	292.3	31.0	7.5	####	45.2	62.8	20.6	3238.6	45.8	116.4
20PM32A	Medium-grained leuconorite	Hm-ilm + Mt	31.6	394.4	26.8	52.6	18.0	11.1	197.2	19.1	1.5	589.5	37.7	97.1	12.4	294.5	24.2	66.7
20PM42A	Medium-grained OAN	Hm-ilm + Mt	33.8	450.7	13.5	49.2	10.2	15.3	244.8	22.6	1.8	568.1	48.1	169.5	13.9	292.5	34.9	90.8
20PM42B	Fine-grained leuconorite	Hm-ilm	18.8	100.5	36.5	21.2	18.8	16.7	248.7	27.7	20.8	743.2	47.5	1204.9	19.1	3477.6	66.7	156.7
20PM32B	Massive oxides	Hm-ilm	23.9	###	369.3	129.1	128.1	11.5	235.4	24.0	-	11.7	1.1	131.4	24.2	21.3	1.1	2.7
20PM33B	Massive oxides	Hm-ilm	23.0	###	314.9	101.2	75.1	14.3	167.0	16.9	0.8	234.3	1.3	198.7	26.6	112.0	1.1	2.5
20PM37	Massive oxides	Hm-ilm	26.4	###	651.4	114.0	72.0	10.4	201.5	21.5	-	17.0	2.8	163.6	31.5	19.1	2.1	6.0
20PM38A	Medium-grained nelsonite	Hm-ilm	27.1	###	351.7	210.5	164.9	202.0	372.4	24.4	-	63.4	12.0	140.4	38.5	10.2	9.4	26.6
20PM38C	Medium-grained nelsonite	Hm-ilm	16.5	988.1	201.7	49.9	60.6	45.7	87.2	15.9	-	576.8	93.9	87.9	22.3	110.7	76.6	214.5
21PM06	Oxide-apatite-rich mangerite	Ilm + Mt	45.5	156.3	7.2	42.1	8.6	15.5	466.3	27.0	2.3	770.7	60.4	95.3	11.6	960.9	65.3	174.1
21PM07	Oxide-apatite-rich mangerite	Ilm + Mt	52.9	85.5	6.2	30.5	24.4	25.3	566.3	23.9	3.4	541.5	57.3	65.9	9.5	1395.0	50.5	143.0
21PM08	Oxide-apatite-rich mangerite	Ilm + Mt	26.9	193.2	7.2	42.1	11.7	18.8	382.2	32.5	3.7	####	55.3	133.8	11.1	766.9	62.8	164.2
21PM09	Oxide-apatite-rich mangerite	Ilm + Mt	13.7	621.8	4.2	123.5	12.9	53.2	782.6	50.1	2.5	621.5	97.6	79.3	14.9	305.5	119.1	349.1
21PM57	Oxide-apatite-rich mangerite	Ilm + Mt	32.6	10.6	13.0	12.1	4.5	9.7	355.1	34.6	9.5	####	49.8	147.2	12.4	4040.1	73.1	176.3
21PM53-A	Massive oxides	Ilm + Mt	22.4	###	269.4	162.4	127.5	48.4	484.6	43.1	0.5	3.7	1.2	153.1	25.6	15.5	0.1	0.5
21PM53-B	Medium-grained leuconorite	Ilm + Mt	21.3	784.8	112.7	66.8	95.5	27.2	171.5	28.4	4.0	470.2	2.0	17.3	1.8	174.0	1.5	2.8

21PM55	Medium-grained leuconorite	Ilm + Mt	18.8	45.4	28.6	108.5	430.1	23.1	130.2	10.5	2.7	377.8	4.3	32.8	3.0	152.7	5.0	11.0

Appendix 4.2.4 (cont.) Complete LA-ICP-MS whole-rock results

Sample	Lithology	Oxides	^{141}Pr	^{146}Nd	^{147}Sm	^{153}Eu	^{157}Gd	^{159}Tb	^{163}Dy	^{165}Ho	^{166}Er	^{169}Tm	^{172}Yb	^{175}Lu	^{174}Hf	^{208}Pb	^{232}Th	^{238}U
20PM09A	Medium-grained OAN	Ilm + Mt	11.6	59.7	14.3	4.3	14.2	1.8	9.6	1.8	4.4	0.5	2.8	0.4	1.9	10.5	0.6	0.3
20PM09B	Medium-grained OAN	Ilm + Mt	17.1	84.0	19.9	4.0	19.7	2.5	14.1	2.5	6.4	0.8	4.4	0.6	2.3	10.0	1.8	1.6
20PM23C	Medium-grained OAN	Ilm + Mt	18.8	98.9	24.2	5.5	24.7	3.0	16.1	2.9	6.8	0.7	4.1	0.5	1.4	8.9	0.6	0.3
20PM25	Medium-grained OAN	Ilm + Mt	18.7	93.6	23.2	5.9	22.6	2.9	16.2	3.0	7.5	0.9	5.3	0.8	8.2	5.4	2.7	0.8
20PM26A	Medium-grained leuconorite	Ilm + Mt	11.3	52.1	11.9	3.0	11.7	1.5	8.3	1.6	4.1	0.5	3.0	0.4	2.0	5.9	0.7	0.4
20PM24	Medium-grained leuconorite	Ilm + Mt	4.4	21.7	5.3	2.6	5.0	0.6	3.3	0.6	1.5	0.2	1.0	0.1	1.2	6.1	0.3	0.1
20PM26B	Medium-grained leuconorite	Ilm + Mt	7.4	33.2	8.0	3.1	7.7	1.1	6.6	1.2	3.4	0.5	3.0	0.4	1.5	6.5	0.6	0.4
20PM46E	Medium-grained OAN	Hm-ilm	9.9	46.2	9.5	3.1	8.5	0.9	5.0	0.8	1.9	0.2	1.3	0.2	1.8	4.7	0.2	0.1
20PM46A	Medium-grained nelsonite	Ilm + Mt	8.8	45.8	9.6	2.4	8.9	0.9	4.6	0.7	1.7	0.2	0.9	0.1	1.6	1.1	0.2	0.1
20PM47	Medium-grained nelsonite	Ilm + Mt	10.2	53.2	11.3	2.7	10.0	1.1	5.2	0.9	2.0	0.2	1.0	0.1	1.3	1.1	0.2	0.1
20PM12-C2	Medium-grained leuconorite	Hm-ilm + Mt	23.6	115.1	25.1	6.0	21.8	2.7	14.4	2.5	6.3	0.8	4.4	0.6	5.9	4.9	0.3	0.2
20PM12B	Medium-grained leuconorite	Hm-ilm + Mt	24.6	118.8	24.3	6.4	20.6	2.4	12.2	2.2	5.3	0.6	3.4	0.5	5.6	5.1	0.4	0.1
20PM12D	Medium-grained leuconorite	Hm-ilm + Mt	19.5	93.1	20.2	4.8	17.9	2.2	12.2	2.3	5.5	0.7	4.0	0.6	5.8	5.0	0.2	0.1
21PM11-B	Medium-grained OAN	Ilm + Mt	16.0	78.3	17.7	7.2	17.5	2.0	9.9	1.6	3.8	0.4	2.4	0.3	1.7	5.4	0.3	0.1
21PM18-B	Medium-grained oxide-norite	Hm-ilm + Mt	1.4	8.6	2.9	0.9	3.4	0.5	2.6	0.5	1.3	0.1	1.0	0.1	3.1	0.7	0.1	0.0
21PM19	Medium-grained oxide-norite	Hm-ilm + Mt	1.3	7.9	2.8	0.8	3.2	0.4	2.7	0.5	1.2	0.2	1.0	0.1	4.4	2.7	0.0	0.0
21PM12	Medium-grained leuconorite	Hm-ilm + Mt	18.5	88.7	18.3	6.7	17.6	2.0	10.7	1.8	4.5	0.6	3.3	0.5	17.4	11.7	0.2	0.1
21PM11-A	Medium-grained leuconorite	Hm-ilm + Mt	17.4	85.6	19.0	8.7	18.2	2.1	10.3	1.8	4.1	0.5	2.7	0.4	2.0	6.3	0.2	0.1
20PM32A	Medium-grained leuconorite	Hm-ilm + Mt	10.7	57.7	13.8	3.7	13.2	1.5	8.2	1.4	3.4	0.4	2.2	0.3	3.0	1.3	0.1	0.1
20PM42A	Medium-grained OAN	Hm-ilm + Mt	13.9	71.6	16.9	4.6	15.9	1.9	10.3	1.8	4.5	0.5	3.1	0.4	4.7	1.7	0.2	0.1
20PM42B	Fine-grained leuconorite	Hm-ilm	22.4	102.1	20.6	6.8	16.8	2.0	10.7	1.8	4.7	0.6	3.5	0.5	27.9	19.2	0.2	0.1
20PM32B	Massive oxides	Hm-ilm	0.4	2.0	0.5	0.1	0.4	0.0	0.3	0.0	0.1	0.0	0.1	0.0	5.4	0.2	0.1	0.0
20PM33B	Massive oxides	Hm-ilm	0.4	1.7	0.4	0.2	0.4	0.0	0.3	0.1	0.2	0.0	0.2	0.0	6.6	0.6	0.0	0.1
20PM37	Massive oxides	Hm-ilm	0.9	4.7	1.1	0.3	1.2	0.1	0.7	0.1	0.2	0.0	0.2	0.0	5.8	0.3	0.0	0.0
20PM38A	Medium-grained nelsonite	Hm-ilm	4.2	22.5	5.1	1.5	4.9	0.5	2.6	0.5	1.0	0.1	0.6	0.1	6.0	1.6	0.1	0.0
20PM38C	Medium-grained nelsonite	Hm-ilm	34.7	184.8	43.0	12.2	38.8	4.2	21.1	3.4	7.7	0.8	4.2	0.5	3.2	0.9	0.3	0.2
21PM06	Oxide-apatite-rich mangerite	Ilm + Mt	26.9	136.5	30.4	8.6	28.2	3.1	15.1	2.5	5.5	0.6	3.3	0.4	3.0	2.9	0.4	0.2
21PM07	Oxide-apatite-rich mangerite	Ilm + Mt	23.7	126.0	28.6	8.9	26.7	3.0	14.6	2.3	5.0	0.6	3.0	0.4	2.2	2.3	0.3	0.2
21PM08	Oxide-apatite-rich mangerite	Ilm + Mt	25.2	126.9	27.6	7.8	26.0	2.7	13.5	2.2	4.9	0.5	3.0	0.4	3.7	4.4	0.5	0.2
21PM09	Oxide-apatite-rich mangerite	Ilm + Mt	47.7	240.7	50.9	13.0	47.8	5.1	24.3	3.8	8.2	0.9	4.7	0.6	2.3	3.1	0.7	0.3

21PM57	Oxide-apatite-rich mangerite	Ilm + Mt	25.6	122.6	25.5	13.6	23.2	2.6	12.4	2.0	4.6	0.5	2.8	0.4	4.0	12.7	0.3	0.1
21PM53-A	Massive oxides	Ilm + Mt	0.1	0.5	0.2	0.1	0.2	0.0	0.2	0.0	0.1	0.0	0.2	0.0	4.2	0.2	0.0	0.0
21PM53-B	Medium-grained leuconorite	Ilm + Mt	0.4	1.7	0.4	0.9	0.5	0.1	0.4	0.1	0.2	0.0	0.3	0.0	0.6	1.0	0.1	0.0
21PM55	Medium-grained leuconorite	Ilm + Mt	1.4	6.0	1.2	0.9	1.2	0.2	0.9	0.2	0.5	0.1	0.5	0.1	1.0	2.3	0.2	0.1

Appendix 4.2.5 (cont.) Complete LA-ICP-MS results of plagioclase

Sample	Lithology	Oxide Mineralogy	# analysis	SiO_2	Al_2O_3	CaO	Na_2O	K_2O	Total	An	Ab	Or
Lac Périgny Fe-Ti-P mineralization												
20PM09A	Medium-grained OAN	Ilm + Mt	n=5	57.5	29.0	8.5	6.2	0.1	101.3	42.9	56.3	0.8
20PM23C	Medium-grained OAN	Ilm + Mt	n=5	59.5	26.3	7.3	6.1	0.1	99.3	39.3	59.7	0.9
20PM24	Medium-grained leuconorite	Ilm + Mt	n=5	56.4	28.5	9.5	5.0	0.1	99.6	50.7	48.7	0.6
20PM25	Medium-grained OAN	Ilm + Mt	n=5	58.8	26.5	7.8	5.7	0.2	99.1	42.5	56.4	1.1
20PM26A	Medium-grained leuconorite	Ilm + Mt	n=5	57.7	27.4	8.6	5.0	0.2	99.1	47.8	50.5	1.7
Lac de L'Abbondance Fe-Ti-P mineralization												
20PM46E	Medium-grained OAN	Hm-ilm	n=5	58.1	27.4	8.0	5.7	0.0	99.2	43.5	56.2	0.3
Mattawa Anorthosite (Fe-Ti-(P) mineralization occurrences)												
20PM13B	Medium-grained OAN	Hm-ilm + Mt	n=5	58.4	24.9	5.7	6.5	2.6	98.6	27.9	57.0	15.1
21PM18B	Medium-grained OAN	Hm-ilm + Mt	n=5	58.0	25.5	5.9	6.1	2.7	98.5	29.2	54.9	16.0
21PM19	Medium-grained OAN	Hm-ilm + Mt	n=5	55.8	27.6	7.9	6.7	0.3	98.5	38.9	59.5	1.6
21PM11B	Medium-grained OAN	Ilm + Mt	n=5	59.7	23.9	4.0	5.5	5.1	98.9	19.7	49.9	30.3
Labrieville Anorthosite (Fe-Ti-(P) mineralization occurrences)												
20PM32A	Medium-grained leuconorite	Hm-ilm + Mt	n=5	60.4	25.5	6.8	5.8	0.4	99.0	38.4	59.1	2.5
20PM42A	Medium-grained OAN	Hm-ilm + Mt	n=5	60.5	25.7	6.6	5.9	0.3	99.1	37.7	60.5	1.8
20PM42B	Fine-grained-leuconorite	Hm-ilm	n=5	63.0	24.2	5.0	6.9	0.3	99.5	28.2	70.1	1.8
La Hache Mangerite (Fe-Ti-(P) mineralization occurrences)												
21PM06	Oxide-apatite-rich mangerite	Ilm + Mt	n=5	58.4	25.2	5.5	7.0	2.1	98.7	26.7	60.9	12.5
21PM07	Oxide-apatite-rich mangerite	Ilm + Mt	n=5	59.5	24.0	4.4	6.1	4.1	99.0	21.5	54.3	24.2
21PM08	Oxide-apatite-rich mangerite	Ilm + Mt	n=5	56.3	27.2	7.5	6.8	0.6	98.5	36.7	59.7	3.6
21PM09	Oxide-apatite-rich mangerite	Ilm + Mt	n=5	56.8	26.7	7.2	6.6	1.0	98.5	35.4	58.5	6.1
21PM57	Oxide-apatite-rich mangerite	Ilm + Mt	n=5	59.1	24.5	4.4	5.9	4.3	99.2	21.7	53.1	25.3
21PM59	Oxide-apatite-rich mangerite	Ilm + Mt	n=5	59.0	25.2	5.6	8.1	0.3	98.4	27.1	71.5	1.4
21PM56	Oxide-apatite-rich mangerite	Ilm + Mt	n=5	63.4	20.0	0.5	3.9	10.4	98.4	2.7	35.2	62.0
L'Etang Fe-Ti mineralization												
21PM52A	Medium-grained leuconorite	Ilm + Mt	n=5	49.7	32.2	12.3	4.1	0.1	98.6	61.9	37.6	0.5
21PM53B	Medium-grained leuconorite	Ilm + Mt	n=5	53.0	29.8	10.0	5.6	0.1	98.5	49.3	50.0	0.8
21PM55	Medium-grained leuconorite	Ilm + Mt	n=5	53.6	29.4	9.5	5.9	0.1	98.5	46.7	52.6	0.6

Appendix 4.2.5 (cont.) Complete LA-ICP-MS results of plagioclase

Detection Limits (33-55µm)				0.165 - 2.006	0.191 - 1.473	19.622 - 216.80	0.042 - 0.243	0.091 - 0.218	0.063 - 0.165	0.515-0.809	0.005 - 0.013	0.003 - 1.838	0.008 - 0.476	0.010 - 0.057	0.005 - 0.058	0.001 - 0.023	
Sample	Lithology	Oxide Mineralogy	# analysis	^{69}Ga	^{72}Ge	^{85}Rb	^{89}Y	^{90}Zr	^{93}Nb	^{137}Ba	^{139}La	^{140}Ce	^{141}Pr	^{146}Nd	^{147}Sm	^{153}Eu	Total REE
20PM09A	Medium-grained OAN	Ilm + Mt	n=5	16.6	0.7	-	0.2	0.1	0.0	36.2	3.4	5.0	0.5	1.3	0.0	1.5	11.7
20PM23C	Medium-grained OAN	Ilm + Mt	n=5	28.8	0.0	-	0.0	0.0	0.0	127.0	3.8	6.2	0.3	0.7	0.0	1.1	12.1
20PM24	Medium-grained leuconorite	Ilm + Mt	n=5	22.9	0.0	-	0.0	0.0	0.0	68.0	3.8	6.3	0.6	1.5	0.0	1.6	13.9
20PM25	Medium-grained OAN	Ilm + Mt	n=5	48.5	0.2	65.9	0.0	0.0	0.0	271.8	5.7	8.6	0.6	2.2	0.0	3.4	20.5
20PM26A	Medium-grained leuconorite	Ilm + Mt	n=5	36.3	0.0	126.6	0.0	0.0	0.0	176.4	4.4	6.7	0.5	0.8	0.0	1.6	14.0
20PM46E	Medium-grained OAN	Hm-ilm	n=5	50.6	0.0	-	0.0	0.0	0.0	352.4	5.3	7.2	0.6	0.7	0.0	0.9	14.7
20PM13B	Medium-grained OAN	Hm-ilm + Mt	n=5	170.8	0.9	7.6	0.3	0.1	0.0	2197.8	6.6	10.1	0.9	3.0	0.3	2.3	23.6
21PM18B	Medium-grained OAN	Hm-ilm + Mt	n=5	108.1	0.8	9.7	0.1	0.1	0.0	1350.6	2.2	3.3	0.3	1.2	0.1	1.2	8.4
21PM19	Medium-grained OAN	Hm-ilm + Mt	n=5	49.4	0.7	2.1	0.2	0.1	0.0	385.3	4.0	5.7	0.5	1.8	0.2	1.4	13.8
21PM11B	Medium-grained OAN	Ilm + Mt	n=5	391.3	1.0	13.9	0.1	0.1	0.0	5063.6	5.4	6.3	0.5	1.8	0.2	4.8	19.3
20PM32A	Medium-grained leuconorite	Hm-ilm + Mt	n=5	44.7	0.0	199.4	0.0	0.0	0.0	233.7	3.2	4.8	0.4	0.0	0.0	1.1	9.4
20PM42A	Medium-grained OAN	Hm-ilm + Mt	n=5	101.3	0.0	79.6	0.0	0.2	0.0	861.8	4.2	6.2	0.5	1.0	0.0	2.0	14.0
20PM42B	Fine-grained-leuconorite	Hm-ilm	n=5	90.4	0.0	132.8	0.2	0.2	0.0	852.9	16.8	20.9	1.6	4.1	0.0	3.9	47.3
21PM06	Oxide-apatite-rich mangerite	Ilm + Mt	n=5	205.5	1.1	6.9	0.2	0.5	0.1	2529.5	9.7	12.9	1.2	3.9	0.4	6.7	31.9
21PM07	Oxide-apatite-rich mangerite	Ilm + Mt	n=5	433.3	1.2	11.1	0.2	0.4	0.0	5845.0	7.7	10.8	1.0	3.4	0.3	8.3	31.8
21PM08	Oxide-apatite-rich mangerite	Ilm + Mt	n=5	70.4	1.0	1.1	0.3	0.0	0.0	590.4	6.7	9.7	0.9	3.3	0.3	3.4	24.7
21PM09	Oxide-apatite-rich mangerite	Ilm + Mt	n=5	78.9	0.9	14.3	0.1	0.0	0.0	782.3	6.3	8.4	0.7	2.5	0.2	3.1	21.5
21PM57	Oxide-apatite-rich mangerite	Ilm + Mt	n=5	626.5	1.3	16.7	0.5	0.3	0.0	7787.3	18.8	23.5	2.1	6.6	0.7	10.3	62.6
21PM59	Oxide-apatite-rich mangerite	Ilm + Mt	n=5	69.5	1.2	-	0.3	0.1	0.0	554.6	23.6	29.8	2.6	7.9	0.6	11.6	76.5
21PM56	Oxide-apatite-rich mangerite	Ilm + Mt	n=5	115.7	1.3	137.0	0.0	0.1	0.0	1466.5	17.5	17.9	1.1	2.8	0.1	3.7	43.1
21PM52A	Medium-grained leuconorite	Ilm + Mt	n=5	25.5	0.4	0.2	0.1	0.1	0.0	136.3	1.7	2.2	0.2	0.6	0.1	0.5	5.4

21PM53 B	Medium-grained leuconorite	Ilm + Mt	n=5	27.8	0.7	-	0.0	0.1	0.0	152.4	2.0	2.6	0.2	0.6	0.1	0.9	6.6
21PM55	Medium-grained leuconorite	Ilm + Mt	n=5	34.8	0.8	-	0.0	0.0	0.0	323.7	9.1	9.9	0.7	1.5	0.1	0.8	22.2

Appendix 4.2.6 Complete LA-ICP-MS results of ilmenite

Sample	Lithology	Oxide Mineralogy	# analysis	SiO_2	TiO2	Al_2O_3	FeO_t	Fe_2O_3	FeO	MnO	MgO	Total
Lac Périgny Fe-Ti-P mineralization												
20PM09	Medium-grained OAN	Ilm + Mt	n=8	0.0	50.2	0.0	48.0	4.9	43.7	0.8	0.4	100.1
20PM24	Medium-grained leuconorite	Ilm + Mt	n=3	0.7	47.3	0.1	49.5	8.3	42.1	0.7	0.2	99.2
20PM23C	Medium-grained OAN	Ilm + Mt	n=3	0.6	50.2	0.0	49.5	6.9	43.3	0.3	1.1	102.4
20PM25	Medium-grained OAN	Ilm + Mt	n=3	0.5	49.1	0.1	49.5	7.8	42.5	1.0	0.4	101.4
20PM26A	Medium-grained leuconorite	Ilm + Mt	n=3	0.4	45.0	0.1	52.7	14.5	39.7	0.6	0.5	101.0
Lac de L'Abbondance Fe-Ti-P mineralization												
20PM46A	Medium-grained nelsonite	Ilm + Mt	n=3	0.0	44.5	0.0	50.2	14.5	37.1	0.8	1.3	98.4
20PM47	Medium-grained nelsonite	Ilm + Mt	n=3	0.1	43.5	0.1	51.0	16.9	35.8	0.9	1.5	98.9
20PM46E	Medium-grained OAN	Hm-ilm	n=3	0.2	41.0	0.1	56.6	23.5	35.5	1.5	0.1	101.9
Mattawa Anorthosite (Fe-Ti-(P) mineralization occurrences)												
20PM12B	Medium-grained leuconorite	Hm-ilm + Mt		0.4	36.3	0.1	62.3	34.2	31.5	0.4	0.7	103.6
20PM12C	Medium-grained leuconorite	Hm-ilm + Mt	n=3	0.1	34.8	0.1	63.5	36.3	30.9	0.4	0.2	102.9
20PM12D	Medium-grained leuconorite	Hm-ilm + Mt	n=3	0.1	35.9	0.1	62.8	34.5	31.7	0.4	0.2	103.1
21PM50	Medium-grained OAN	Hm-ilm + Mt	n=3	0.0	41.5	0.1	55.4	5.1	50.9	0.2	2.0	100.0
21PM13B	Medium-grained OAN	Hm-ilm + Mt	n=3	0.0	44.6	0.0	54.4	3.9	50.8	0.3	0.1	99.9
21PM17A	Medium-grained OAN	Hm-ilm + Mt	n=3	0.1	38.2	0.1	59.2	5.7	54.1	0.3	1.4	100.1
21PM16D	Medium-grained OAN	Hm-ilm + Mt	n=3	0.1	38.6	0.1	58.4	5.6	53.4	0.2	1.6	100.0
21PM18B	Medium-grained OAN	Hm-ilm + Mt	n=3	0.0	38.7	0.1	59.3	5.7	54.2	0.2	0.9	100.1
21PM19	Medium-grained OAN	Hm-ilm + Mt	n=3	0.0	38.5	0.1	59.4	5.5	54.5	0.2	0.9	100.0
21PM11B	Medium-grained leuconorite	Ilm + Mt	n=3	0.1	48.6	0.1	49.6	2.5	47.3	0.7	0.4	99.7
Labrieville Anorthosite (Fe-Ti-(P) mineralization occurrences)												
20PM32B	Massive oxides	Hm-ilm	n=3	0.2	36.9	0.1	56.3	29.7	29.6	0.1	2.2	99.1
20PM33A	Massive oxides	Hm-ilm + Mt	n=3	-	37.6	0.1	58.9	31.1	31.0	0.2	1.7	101.9
20PM34	Massive oxides	Hm-ilm	n=3	0.1	37.5	0.1	59.8	31.8	31.2	0.2	1.5	102.7
20PM37A	Massive oxides	Hm-ilm	n=3	0.0	37.4	0.1	60.2	32.8	30.6	0.2	1.8	103.4
20PM38A	Medium-grained nelsonite	Hm-ilm	n=3	0.1	37.0	0.1	62.4	33.3	32.5	0.1	0.5	103.8
20PM38C	Medium-grained nelsonite	Hm-ilm	n=3	0.8	37.7	0.1	61.9	33.1	32.1	0.1	1.2	105.0
20PM32A	Medium-grained leuconorite	Hm-ilm	n=3	0.4	37.2	0.1	62.8	33.7	32.4	0.3	0.7	104.9
20PM42A	Medium-grained OAN	Hm-ilm + Mt	n=3	-	39.2	0.1	59.1	28.9	33.0	0.4	1.1	103.0
20PM42B	Fine-grained-leuconorite	Hm-ilm	n=3	0.1	41.5	0.1	55.8	23.6	34.5	1.0	1.1	102.0
La Hache Mangerite (Fe-Ti-(P) mineralization occurrences)												
21PM08	Oxide-apatite-rich mangerite	Ilm + Mt	n=3	0.0	49.0	0.1	50.0	6.3	44.3	0.8	0.7	101.3
21PM09	Oxide-apatite-rich mangerite	Ilm + Mt	n=3	0.0	49.2	0.1	49.9	6.3	44.2	0.7	0.7	101.3
21PM57	Oxide-apatite-rich mangerite	Ilm + Mt	n=3	0.1	50.5	0.1	47.4	4.6	43.3	1.5	0.7	100.8
21PM06	Oxide-apatite-rich mangerite	Ilm + Mt	n=3	0.0	52.2	0.0	45.3	1.3	44.1	1.1	0.8	99.6
21PM07	Oxide-apatite-rich mangerite	Ilm + Mt	n=3	0.1	50.3	0.0	48.8	8.2	41.4	1.3	0.9	102.2
21PM59	Oxide-apatite-rich mangerite	Ilm + Mt	n=3	0.3	47.4	0.1	51.4	8.3	44.0	1.3	0.5	102.0
21PM56	Oxide-apatite-rich charnockite	Ilm + Mt	n=3	0.3	48.9	0.0	50.5	7.0	44.3	1.1	0.1	101.6
L'Etang Fe-Ti mineralization												
21PM53A	Massive oxides	Ilm + Mt	n=3	0.0	49.7	0.1	47.3	2.7	44.9	0.5	1.7	99.9
21PM52A	Medium-grained leuconorite	Ilm + Mt	n=3	0.1	47.0	0.1	50.4	3.4	47.4	0.4	1.3	100.0
21PM53B	Medium-grained leuconorite	Ilm + Mt	n=3	0.2	50.4	0.1	47.2	2.8	44.7	0.6	1.2	99.9
21PM55	Medium-grained leuconorite	Ilm + Mt	n=3	0.1	51.1	0.0	46.1	2.9	43.4	0.6	1.8	100.0

Appendix 4.2.6 Complete LA-ICP-MS results of ilmenite

Detection Limits (33-55µm)				280.87-1450.82	66.62-124.50	0.205-1.345	0.035-0.296	0.252-3.179	0.025-0.220	0.251-1.198	0.335-0.745	0.761-1.438
Sample	Lithology	Oxide Mineralogy	# analysis	^{27}Al	^{44}Ca	^{45}Sc	^{51}V	^{53}Cr	^{59}Co	^{60}Ni	^{63}Cu	^{66}Zn
20PM09	Medium-grained OAN	Ilm + Mt	n=8	105.8	19.9	13.8	254.5	0.9	58.5	3.8	2.8	48.4
20PM24	Medium-grained leuconorite	Ilm + Mt	n=3	344.3	1142.5	17.0	455.4	53.7	70.1	9.8	4.2	83.8
20PM23C	Medium-grained OAN	Ilm + Mt	n=3	215.6	820.0	9.3	455.1	28.1	69.1	6.0	4.7	52.6
20PM25	Medium-grained OAN	Ilm + Mt	n=3	308.4	####	29.8	154.8	51.9	38.0	2.2	4.3	39.6
20PM26A	Medium-grained leuconorite	Ilm + Mt	n=3	351.0	307.3	45.5	974.7	75.5	39.5	4.6	4.3	69.3
20PM46A	Medium-grained nelsonite	Ilm + Mt	n=3	167.5	-	33.1	1136.8	113.4	60.4	26.2	1.7	7.4
20PM47	Medium-grained nelsonite	Ilm + Mt	n=3	574.9	17.0	39.5	991.7	242.1	80.9	67.3	1.8	4.6
20PM46E	Medium-grained OAN	Hm-ilm	n=3	439.8	50.3	19.3	1010.5	23.8	22.7	21.2	2.1	230.4
20PM12B	Medium-grained leuconorite	Hm-ilm + Mt		473.8	30.9	54.1	1422.4	11.9	23.3	3.9	4.7	83.8
20PM12C	Medium-grained leuconorite	Hm-ilm + Mt	n=3	506.2	23.1	67.9	1343.3	47.0	24.1	4.6	1.9	143.3
20PM12D	Medium-grained leuconorite	Hm-ilm + Mt	n=3	474.3	10.7	68.8	1330.3	46.5	24.1	6.7	4.1	160.5
21PM50	Medium-grained OAN	Hm-ilm + Mt	n=3	449.6	2.3	26.3	1956.3	67.4	117.8	35.4	0.7	24.1
21PM13B	Medium-grained OAN	Hm-ilm + Mt	n=3	156.0	34.1	41.7	782.2	9.0	107.8	4.2	0.8	167.4
21PM17A	Medium-grained OAN	Hm-ilm + Mt	n=3	473.0	15.2	31.4	2005.1	521.0	38.2	53.5	1.8	36.3
21PM16D	Medium-grained OAN	Hm-ilm + Mt	n=3	714.5	9.6	27.0	2154.1	211.0	112.6	60.5	0.6	51.8
21PM18B	Medium-grained OAN	Hm-ilm + Mt	n=3	555.9	5.0	31.1	1910.6	125.5	36.3	14.5	1.6	189.5
21PM19	Medium-grained OAN	Hm-ilm + Mt	n=3	413.8	4.5	30.2	2121.1	127.9	51.3	14.4	0.7	132.4
21PM11B	Medium-grained leuconorite	Ilm + Mt	n=3	370.7	19.0	62.6	211.6	1.2	42.7	0.2	0.7	71.9

20PM32B	Massive oxides	Hm-ilm	n=3	343.1	210.1	26.0	2156.1	300.1	110.1	90.3	2.9	6.9
20PM33A	Massive oxides	Hm-ilm + Mt	n=3	403.1	109.0	28.0	2116.7	277.0	112.4	44.3	2.3	17.6
20PM34	Massive oxides	Hm-ilm	n=3	482.8	-	29.9	1846.0	232.3	111.1	40.8	1.1	20.2
20PM37A	Massive oxides	Hm-ilm	n=3	290.9	-	30.0	2311.2	724.9	85.4	149.9	1.0	38.5
20PM38A	Medium-grained nelsonite	Hm-ilm	n=3	377.9	331.5	32.5	####	335.5	38.7	34.0	2.3	163.5
20PM38C	Medium-grained nelsonite	Hm-ilm	n=3	502.7	1211.9	33.1	1932.0	305.8	38.2	9.0	3.7	93.6
20PM32A	Medium-grained leuconorite	Hm-ilm	n=3	454.6	-252.0	36.1	####	42.9	41.4	18.2	3.0	111.0
20PM42A	Medium-grained OAN	Hm-ilm + Mt	n=3	529.5	-160.9	51.9	1334.3	6.7	37.7	3.0	1.6	74.7
20PM42B	Fine-grained-leuconorite	Hm-ilm	n=3	657.1	74.0	96.0	535.4	5.2	26.4	0.4	1.7	192.7
21PM08	Oxide-apatite-rich mangerite	Ilm + Mt	n=3	432.8	-	68.8	382.0	2.6	39.2	0.6	1.0	73.7
21PM09	Oxide-apatite-rich mangerite	Ilm + Mt	n=3	341.4	19.5	71.0	410.4	0.9	35.0	1.0	0.8	26.1
21PM57	Oxide-apatite-rich mangerite	Ilm + Mt	n=3	461.1	65.8	73.2	17.6	0.3	20.6	0.0	0.8	64.6
21PM06	Oxide-apatite-rich mangerite	Ilm + Mt	n=3	159.5	7.6	50.2	51.8	0.6	27.8	0.6	1.1	21.4
21PM07	Oxide-apatite-rich mangerite	Ilm + Mt	n=3	131.5	201.2	73.3	31.4	0.7	19.9	0.4	1.0	34.3
21PM59	Oxide-apatite-rich mangerite	Ilm + Mt	n=3	503.2	197.1	52.0	60.3	0.8	16.9	0.1	0.9	133.0
21PM56	Oxide-apatite-rich charnockite	Ilm + Mt	n=3	126.7	42.6	12.4	6.1	0.9	16.2	0.1	0.8	128.5
21PM53A	Massive oxides	Ilm + Mt	n=3	551.1	-2.2	42.0	987.6	29.5	120.5	39.2	1.3	13.5
21PM52A	Medium-grained leuconorite	Ilm + Mt	n=3	378.0	37.1	15.4	1442.8	345.1	87.4	43.9	0.9	45.6
21PM53B	Medium-grained leuconorite	Ilm + Mt	n=3	462.9	39.0	27.6	735.8	51.5	91.0	30.6	0.8	18.4
21PM55	Medium-grained leuconorite	Ilm + Mt	n=3	219.9	65.8	6.0	70.8	15.0	122.8	191.0	1.1	11.4

Appendix 4.2.6 Complete LA-ICP-MS results of ilmenite

Detection Limits (33-55µm)				0.151-0.365	0.079-0.309	0.019-0.055	0.038-0.056	0.022-0.027	0.074-0.345	0.03	0.073-0.089	0.051-0.062	0.013-0.015	0.075-0.095	0.051-0.078
Sample	Lithology	Oxide Mineralogy	# analysis	^{69}Ga	^{72}Ge	^{89}Y	^{90}Zr	^{93}Nb	Sn	^{139}La	^{172}Yb	^{178}Hf	^{181}Ta	^{182}W	^{208}Pb
Lac Périgny Fe-Ti-P mineralization															
20PM09	Medium-grained OAN	Ilm + Mt	n=8	1.3	0.1	0.0	119.7	133.3	2.1	0.0	0.0	4.5	9.2	7.8	0.2
20PM24	Medium-grained leuconorite	Ilm + Mt	n=3	2.0	-	-	51.3	130.3	3.6	-	-	3.4	9.4	15.7	3.1
20PM23C	Medium-grained OAN	Ilm + Mt	n=3	2.6	-	-	75.0	124.6	1.9	-	-	5.6	9.5	4.8	1.6
20PM25	Medium-grained OAN	Ilm + Mt	n=3	2.0	-	-	32.2	230.6	3.5	-	-	3.0	11.1	2.3	1.2
20PM26A	Medium-grained leuconorite	Ilm + Mt	n=3	2.7	-	0.2	19.0	130.8	3.7	-	-	2.8	7.6	1.7	2.2
Lac de L'Abbondance Fe-Ti-P mineralization															
20PM46A	Medium-grained nelsonite	Ilm + Mt	n=3	1.7	0.2	0.1	11.0	9.8	5.8	-	-	2.4	0.6	0.0	0.3
20PM47	Medium-grained nelsonite	Ilm + Mt	n=3	11.0	0.2	-	14.4	9.7	5.3	-	-	2.8	0.4	0.0	0.3
20PM46E	Medium-grained OAN	Hm-ilm	n=3	4.4	0.3	0.3	12.6	59.1	7.0	0.2	-	0.7	3.3	2.0	1.0
Mattawa Anorthosite (Fe-Ti-(P) mineralization occurrences)															
20PM12B	Medium-grained leuconorite	Hm-ilm + Mt		8.0	-	0.1	15.4	175.7	17.2	-	-	2.6	8.1	0.0	0.4
20PM12C	Medium-grained leuconorite	Hm-ilm + Mt	n=3	8.4	0.3	0.2	27.1	245.5	20.3	0.0	-	5.8	11.4	0.3	6.8
20PM12D	Medium-grained leuconorite	Hm-ilm + Mt	n=3	9.6	-	0.2	13.3	231.1	16.8	-	-	4.6	10.1	0.0	1.1
21PM50	Medium-grained OAN	Hm-ilm + Mt	n=3	8.1	0.1	0.1	12.0	51.1	6.3	-	0.1	1.1	3.5	0.1	1.7
21PM13B	Medium-grained OAN	Hm-ilm + Mt	n=3	4.0	0.1	0.1	16.7	163.6	13.5	0.1	0.1	1.8	8.2	0.3	2.5
21PM17A	Medium-grained OAN	Hm-ilm + Mt	n=3	12.2	0.1	0.1	13.3	51.1	7.8	0.1	0.1	1.0	2.9	0.1	9.3

21PM16D	Medium-grained OAN	Hm-ilm + Mt	n=3	11.7	0.2	0.1	78.9	50.5	6.6	0.0	0.2	5.2	3.3	0.1	4.0
21PM18B	Medium-grained OAN	Hm-ilm + Mt	n=3	10.9	0.1	0.0	10.6	45.0	5.6	-	0.1	0.9	2.9	0.0	1.2
21PM19	Medium-grained OAN	Hm-ilm + Mt	n=3	10.5	0.1	0.1	11.2	42.8	5.9	-	0.1	1.0	2.8	0.0	4.3
21PM11B	Medium-grained leuconorite	Ilm + Mt	n=3	3.1	0.1	0.1	63.4	288.1	13.7	0.1	0.1	9.6	14.0	0.3	5.0
Labrieville Anorthosite (Fe-Ti-(P) mineralization occurrences)															
20PM32B	Massive oxides	Hm-ilm	n=3	6.4	-	-	13.6	26.9	4.2	-	-	3.5	1.6	0.0	-
20PM33A	Massive oxides	Hm-ilm + Mt	n=3	11.5	-	-	18.3	32.7	4.4	-	-	2.7	2.1	0.0	0.5
20PM34	Massive oxides	Hm-ilm	n=3	10.7	-	-	17.4	39.1	5.0	-	-	2.9	2.4	0.0	0.3
20PM37A	Massive oxides	Hm-ilm	n=3	13.5	-	-	10.8	32.1	5.0	-	-	2.8	2.1	0.0	3.1
20PM38A	Medium-grained nelsonite	Hm-ilm	n=3	13.1	-	-	15.9	48.1	5.5	-	-	3.0	2.7	0.0	-
20PM38C	Medium-grained nelsonite	Hm-ilm	n=3	12.2	-	-	31.7	49.2	5.3	-	-	4.4	2.8	0.0	0.9
20PM32A	Medium-grained leuconorite	Hm-ilm	n=3	11.0	-	-	14.9	39.2	5.4	-	-	2.1	2.2	0.0	-
20PM42A	Medium-grained OAN	Hm-ilm + Mt	n=3	7.8	-	0.1	37.5	83.9	8.4	-	-	6.9	4.3	0.0	2.8
20PM42B	Fine-grained-leuconorite	Hm-ilm	n=3	6.9	0.3	0.2	6.3	458.1	33.1	-	-	0.5	17.5	0.3	1.4
La Hache Mangerite (Fe-Ti-(P) mineralization occurrences)															
21PM08	Oxide-apatite-rich mangerite	Ilm + Mt	n=3	4.3	0.1	0.2	21.9	116.3	11.4	0.1	-	1.9	5.8	0.3	8.4
21PM09	Oxide-apatite-rich mangerite	Ilm + Mt	n=3	3.1	0.1	0.0	19.7	175.3	15.6	0.1	-	2.0	9.4	1.4	8.3
21PM57	Oxide-apatite-rich mangerite	Ilm + Mt	n=3	6.2	0.1	0.3	35.8	372.9	5.1	0.3	0.1	2.7	16.3	0.3	6.3
21PM06	Oxide-apatite-rich mangerite	Ilm + Mt	n=3	0.4	0.3	0.1	346.8	94.6	1.0	-	0.4	12.5	4.9	0.1	8.3
21PM07	Oxide-apatite-rich mangerite	Ilm + Mt	n=3	0.4	0.1	0.3	470.8	77.4	0.5	0.1	0.6	11.7	3.5	0.1	9.2

21PM59	Oxide-apatite-rich mangerite	Ilm + Mt	n=3	5.4	0.2	0.2	14.2	568.9	11.1	0.5	-	1.3	25.8	0.8	1.7
21PM56	Oxide-apatite-rich charnockite	Ilm + Mt	n=3	2.1	0.2	0.6	52.2	4378.5	5.0	0.3	0.4	2.1	165.2	0.6	3.9
L'Etang Fe-Ti mineralization															
21PM53A	Massive oxides	Ilm + Mt	n=3	2.1	0.1	0.0	72.5	46.0	2.0	-	-	4.4	3.4	1.6	7.1
21PM52A	Medium-grained leuconorite	Ilm + Mt	n=3	2.4	0.1	0.1	96.5	14.4	0.9	-	-	2.9	1.5	0.7	6.7
21PM53B	Medium-grained leuconorite	Ilm + Mt	n=3	1.7	0.1	0.1	48.9	25.0	1.5	-	-	2.0	1.7	2.7	2.6
21PM55	Medium-grained leuconorite	Ilm + Mt	n=3	0.5	-	-	38.2	142.0	1.0	0.1	-	1.5	15.4	4.1	4.3

Appendix 4.2.7 Complete LA-ICP-MS results of magnetite

Detection Limits (33-55µm)												0.2	0.9	300.0	10.0	76.0	0.3	0.9	0.0
Sample	Lithology	Oxide Mineralogy	# analysis	SiO_2	TiO_2	Al_2O_3	Fe_2O_3	FeO	MnO	MgO	Total	^{25}Mg	^{27}Al	^{29}Si	^{31}P	^{44}Ca	^{45}Sc	^{49}Ti	^{51}V
Lac Périgny Fe-Ti-P mineralization																			
20PM09	Medium-grained OAN	Ilm + Mt	n=8	0.6	0.4	0.5	69.9	29.5	0.0	0.1	101.2	656.5	2872.8	2811.4	-	-	0.3	2432.4	990.9
20PM24	Medium-grained leuconorite	Ilm + Mt	n=3	1.1	0.2	0.8	72.5	26.8	0.0	0.2	102.3	1370.9	4194.2	5000.3	58.1	1173.3	0.3	967.7	3345.4
20PM23C	Medium-grained OAN	Ilm + Mt	n=3	0.6	0.6	1.1	72.6	26.7	0.0	0.2	102.5	1019.0	6056.8	2655.9	107.9	-	0.4	3775.0	3859.7
20PM25	Medium-grained OAN	Ilm + Mt	n=3	0.8	2.9	2.4	80.3	19.7	0.1	0.1	106.7	816.3	12676.6	3908.2	92.7	607.4	2.6	17514.1	1359.6
20PM26A	Medium-grained leuconorite	Ilm + Mt	n=3	0.8	0.1	0.6	70.5	28.5	0.0	0.1	101.4	748.1	3308.3	3907.8	-	338.8	0.8	471.5	3789.1
Lac de L'Abbondance Fe-Ti-P mineralization																			
20PM46A	Medium-grained nelsonite	Ilm + Mt	n=3	0.0	0.1	0.5	67.7	31.1	0.0	0.1	100.1	513.0	2489.5	-	11.4	-	0.4	480.3	3220.8
20PM47	Medium-grained nelsonite	Ilm + Mt	n=3	0.1	0.0	0.4	67.5	31.2	0.0	0.1	100.1	645.1	2102.0	340.9	-	-	0.7	295.7	3200.9
20PM46E	Medium-grained OAN	Hm-ilm	n=3	0.2	0.1	0.4	67.1	31.6	0.0	0.1	99.8	523.5	2238.8	857.3	15.8	90.9	0.6	484.8	1920.3
Mattawa Anorthosite (Fe-Ti-(P) mineralization occurrences)																			
20PM12B	Medium-grained leuconorite	Hm-ilm + Mt	n=3	0.5	0.1	0.5	68.2	30.6	0.0	0.1	100.3	494.9	2641.4	2256.0	94.2	-	1.1	547.3	2096.3
20PM12C	Medium-grained leuconorite	Hm-ilm + Mt	n=3	0.1	0.1	0.4	66.9	31.8	0.0	0.0	99.8	246.5	2284.3	592.6	-	90.7	1.6	583.9	2274.0
20PM12D	Medium-grained leuconorite	Hm-ilm + Mt	n=3	0.2	0.1	0.3	66.8	31.9	0.0	0.0	99.7	186.9	1830.7	304.5	18.1	-	1.1	366.2	2055.8
20PM11B	Medium-grained leuconorite	Ilm + Mt	n=3	0.3	0.6	0.0	66.6	32.0	0.0	0.1	99.8	750.2	6244.9	1458.4	45.3	-	2.1	3451.3	1110.1
21PM50												3089.9	3721.8	4729.6	-	88.0	0.5	520.5	3924.6
21PM13B	Medium-grained OAN	Hm-ilm + Mt	n=3	0.2	0.1	0.0	65.4	33.1	0.0	0.1	99.2	378.8	2101.8	1046.8	37.2	106.8	0.7	557.2	1965.8
Labrieville Anorthosite (Fe-Ti-(P) mineralization occurrences)																			
20PM33A	Massive oxides	Hm-ilm + Mt	n=3	0.3	0.0	0.5	68.6	30.2	0.0	0.2	100.5	1052.2	2445.2	613.5	16.0	-	-	297.7	3143.9
20PM42A	Medium-grained OAN	Hm-ilm + Mt	n=3	1.7	0.1	0.5	72.9	26.4	0.0	0.1	102.6	512.5	2489.5	7702.3	19.6	4345.6	2.0	517.4	2554.1
20PM42B	Fine-grained-leuconorite	Hm-ilm	n=3	0.3	0.1	0.4	67.2	31.5	0.0	0.1	99.8	769.3	2175.5	1244.1	12.6	107.6	1.4	440.8	1059.3
La Hache Mangerite (Fe-Ti-(P) mineralization occurrences)																			
21PM06	Oxide-apatite-rich mangerite	Ilm + Mt	n=3	0.2	9.1	0.0	72.2	21.3	0.4	0.3	103.7	1471.2	18884.5	1079.8	65.7	-	7.6	54416.7	1079.1
21PM07	Oxide-apatite-rich mangerite	Ilm + Mt	n=3	0.3	9.8	0.0	74.8	14.8	0.6	0.4	104.2	1900.9	17446.2	968.4	-	27517.5	10.8	59007.5	676.3

21PM59	Oxide-apatite-rich mangerite	Ilm + Mt	n=3	0.7	0.9	0.0	68.5	30.4	0.1	0.2	100.7	1084.6	3370.5	3337.7	-	313.1	1.7	5492.0	276.9
21PM08	Oxide-apatite-rich mangerite	Ilm + Mt	n=3	0.7	0.3	0.0	67.4	31.4	0.0	0.1	100.1	927.4	5071.9	3345.1	151.0	174.2	1.9	1709.7	1457.5
21PM09	Oxide-apatite-rich mangerite	Ilm + Mt	n=3	0.3	0.7	0.0	69.6	29.4	0.0	0.2	101.2	964.7	5524.5	1663.7	7502.7	4175.3	2.1	4320.1	1684.8
21PM57	Oxide-apatite-rich mangerite	Ilm + Mt	n=3	0.3	2.3	0.0	70.6	28.5	0.1	0.2	102.1	1386.5	9355.5	1533.4	-	97.2	4.4	13897.1	164.2
21PM56	Oxide-apatite-rich charnockite	Ilm + Mt	n=3	0.7	1.6	0.0	69.2	29.7	0.1	0.0	101.3	270.4	2547.5	3231.0	10.7	276.6	0.7	9542.2	54.9
L'Etang Fe-Ti mineralization																			
21PM53A	Massive oxides	Ilm + Mt	n=3	0.1	1.0	0.1	70.2	28.8	0.0	0.3	101.7	1908.3	7504.9	-	-	-	1.7	6391.5	7585.3
21PM52A	Medium-grained leuconorite	Ilm + Mt	n=3	0.5	0.4	0.8	72.6	26.7	0.0	0.2	102.8	1318.4	5159.8	2627.3	10.7	117.4	0.5	2433.1	6674.7
21PM53B	Medium-grained leuconorite	Ilm + Mt	n=3	0.2	1.0	0.2	70.3	28.8	0.0	0.3	101.7	1696.4	9950.1	883.7	-	-	1.1	6048.8	6289.9
21PM55	Medium-grained leuconorite	Ilm + Mt	n=3	0.2	1.5	0.0	69.9	29.0	0.0	0.4	101.5	2615.3	7278.9	737.0	41.6	1430.6	-	9258.5	527.7

Appendix 4.2.7 (cont.) Complete LA-ICP-MS results of magnetite

Detection Limits (33-55µm)				1.5	0.6	0.0	0.7	0.4	0.8	0.1	0.1	0.0	0.5	0.0	0.1	0.0	0.1	0.1
Sample	Lithology	Oxide Mineralogy	# analysis	^{53}Cr	^{55}Mn	^{59}Co	^{60}Ni	^{63}Cu	^{66}Zn	^{69}Ga	^{72}Ge	^{89}Y	^{90}Zr	^{93}Nb	^{178}Hf	^{181}Ta	^{182}W	^{208}Pb
Lac Périgny Fe-Ti-P mineralization																		
20PM09	Medium-grained OAN	Ilm + Mt	n=8	5.7	193.8	26.0	14.8	1.5	40.6	46.9	0.9	0.1	2.0	-	-	-	-	0.4
20PM24	Medium-grained leuconorite	Ilm + Mt	n=3	###	164.8	73.8	61.1	0.5	53.4	99.0	1.2	-	-	-	-	-	-	1.2
20PM23C	Medium-grained OAN	Ilm + Mt	n=3	50.6	103.5	52.1	35.3	13.9	59.8	128.4	1.3	-	0.9	-	-	-	-	1.4
20PM25	Medium-grained OAN	Ilm + Mt	n=3	37.8	852.0	63.7	14.0	1.9	970.7	93.0	1.8	-	1.0	-	-	-	-	0.9
20PM26A	Medium-grained leuconorite	Ilm + Mt	n=3	790.4	83.6	36.7	22.9	0.8	32.8	86.3	1.7	0.2	-	-	-	-	-	1.3
Lac de L'Abbondance Fe-Ti-P mineralization																		
20PM46A	Medium-grained nelsonite	Ilm + Mt	n=3	1451.3	151.7	53.3	213.2	0.3	4.5	48.6	0.6	-	-	-	-	-	-	0.2
20PM47	Medium-grained nelsonite	Ilm + Mt	n=3	###	153.5	63.2	245.6	0.3	5.1	48.2	0.7	-	-	-	-	-	-	0.5
20PM46E	Medium-grained OAN	Hm-ilm	n=3	92.4	191.6	30.4	53.6	0.6	51.7	74.4	0.8	0.1	-	-	-	-	-	0.8
Mattawa Anorthosite (Fe-Ti-(P) mineralization occurrences)																		
20PM12B	Medium-grained leuconorite	Hm-ilm + Mt	n=3	78.4	67.4	27.9	22.6	2.3	81.6	77.3	1.0	-	-	-	-	-	-	0.2
20PM12C	Medium-grained leuconorite	Hm-ilm + Mt	n=3	130.9	56.9	27.5	28.6	0.4	73.4	81.7	1.0	-	-	-	-	-	-	3.3
20PM12D	Medium-grained leuconorite	Hm-ilm + Mt	n=3	193.5	38.4	26.2	29.3	-0.6	80.4	75.2	1.0	-	-	-	-	-	-	0.7
20PM11B	Medium-grained leuconorite	Ilm + Mt	n=3	-	249.2	49.5	1.4	0.3	939.0	123.0	1.4	0.1	-	0.6	-	-	-	4.3
21PM50				514.6	51.4	113.2	231.1	3.5	15.5	103.6	0.6	-	-	-	-	-	-	1.4
21PM13B	Medium-grained OAN	Hm-ilm + Mt	n=3	44.9	105.2	74.3	14.9	2.2	491.0	113.6	1.3	-	-	0.0	-	-	-	2.4
Labrieville Anorthosite (Fe-Ti-(P) mineralization occurrences)																		
20PM33A	Massive oxides	Hm-ilm + Mt	n=3	###	26.7	109.4	301.9	8.6	20.3	128.0	-	-	-	-	-	-	-	-
20PM42A	Medium-grained OAN	Hm-ilm + Mt	n=3	92.8	92.3	37.3	11.1	1.1	23.0	85.0	0.5	-	-	-	-	-	-	1.2
20PM42B	Fine-grained-leuconorite	Hm-ilm	n=3	8.0	135.5	26.0	4.8	0.3	18.3	107.0	1.3	0.0	-	-	-	-	-	0.7

La Hache Mangerite (Fe-Ti-(P) mineralization occurrences)																		
21PM06	Oxide-apatite-rich mangerite	Ilm + Mt	n=3	31.7	####	62.5	6.7	0.5	711.3	104.3	1.5	0.2	9.9	0.3	0.8	-	-	7.9
21PM07	Oxide-apatite-rich mangerite	Ilm + Mt	n=3	31.4	####	40.2	2.7	0.5	1324.6	103.8	2.0	15.0	13.5	1.1	0.9	-	-	8.3
21PM59	Oxide-apatite-rich mangerite	Ilm + Mt	n=3	4.7	520.6	20.2	1.0	1.7	1832.1	151.4	2.5	0.2	-	2.4	-	0.1	0.1	4.1
21PM08	Oxide-apatite-rich mangerite	Ilm + Mt	n=3	25.3	180.8	35.7	6.2	17.4	438.8	110.7	1.3	0.2	-	-	-	-	-	13.9
21PM09	Oxide-apatite-rich mangerite	Ilm + Mt	n=3	3.3	272.7	47.3	3.3	1.1	436.3	113.0	1.1	5.0	-	0.1	-	-	-	6.8
21PM57	Oxide-apatite-rich mangerite	Ilm + Mt	n=3	2.0	958.1	25.7	-	0.4	1147.3	130.3	1.7	0.4	0.7	0.0	-	-	-	4.4
21PM56	Oxide-apatite-rich charnockite	Ilm + Mt	n=3	2.9	576.2	15.4	-	0.6	878.5	166.5	5.9	2.8	0.6	0.8	-	-	-	3.6
L'Etang Fe-Ti mineralization																		
21PM53A	Massive oxides	Ilm + Mt	n=3	720.0	310.7	126.6	234.7	0.3	48.5	76.3	1.2	-	-	0.1	-	-	-	4.7
21PM52A	Medium-grained leuconorite	Ilm + Mt	n=3	###	177.2	95.6	322.2	161.8	294.8	82.9	1.0	0.0	-	0.0	-	-	0.4	7.6
21PM53B	Medium-grained leuconorite	Ilm + Mt	n=3	###	281.2	105.9	202.4	16.8	185.1	96.8	1.2	-	0.6	-	-	-	-	2.6
21PM55	Medium-grained leuconorite	Ilm + Mt	n=3	222.2	302.5	143.8	1325.6	1.1	40.1	22.2	1.5	-	0.8	0.0	-	-	-	3.0

Appendix 4.2.8 Complete LA-ICP-MS results of apatite

Detection Limits (33-55µm bean size)												0.53 - 2.08	0.93-2.40	0.05-0.28	0.10-0.28	156.10-494.82	9.20 - 50.29	0.11 - 0.32	0.23 - 0.63
Sample	Lithology	Oxide Mineralogy	# analysis	La_2O_3	Ce_2O_3	Pr_2O_3	Nd_2O_3	CaO	P_2O_5	FeO_t	Total	Li	Na	Mg	Al	Si	K	Sc	Ti
Lac Périgny Fe-Ti-P mineralization																			
20PM23C	Medium-grained OAN	Ilm + Mt	n=5	0.0	0.1	0.0	0.1	54.4	48.8	0.1	103.6	-	542.9	289.6	7.2	1425.6	35.8	0.8	1.1
20PM24	Medium-grained leuconorite	Ilm + Mt	n=5	0.0	0.1	0.0	0.1	54.4	49.3	0.1	104.0	0.9	312.3	302.9	57.8	770.2	30.1	0.8	0.5
20PM25	Medium-grained OAN	Ilm + Mt	n=5	0.1	0.1	0.0	0.1	54.4	48.8	0.1	103.6	0.6	307.7	148.7	39.8	1032.3	39.2	0.8	1.2
20PM26A	Medium-grained leuconorite	Ilm + Mt	n=5	0.0	0.1	0.0	0.1	54.4	50.5	0.1	105.3	-	211.4	162.5	77.0	763.7	33.0	0.8	2.4
20PM09A	Medium-grained OAN	Ilm + Mt	n=5	0.0	0.1	0.0	0.1	54.1	45.2	0.3	99.8	1.2	387.3	289.2	167.0	709.5	26.4	4.7	11.3
Lac de L'Abbondance Fe-Ti-P mineralization																			
20PM46A	Medium-grained nelsonite	Ilm + Mt	n=5	0.0	0.1	0.0	0.1	54.4	51.0	0.1	105.7	-	546.5	541.9	3.4	-	27.9	0.9	1.9
20PM47A	Medium-grained nelsonite	Ilm + Mt	n=5	0.0	0.1	0.0	0.1	54.4	51.5	0.3	106.4	-	498.7	648.2	844.2	1202.8	27.6	1.0	8.9
20PM46E	Medium-grained OAN	Hm-ilm	n=5	0.0	0.1	0.0	0.1	54.4	50.5	0.0	105.2	0.6	342.8	110.0	27.1	933.3	25.4	0.8	1.3
Mattawa Anorthosite (Fe-Ti-(P) mineralization occurrences)																			
20PM11B	Medium-grained OAN	Ilm + Mt	n=5	0.1	0.2	0.0	0.1	54.4	47.9	0.2	102.9	0.6	447.0	164.6	263.8	2309.3	70.7	0.4	2.4
Labrieville Anorthosite (Fe-Ti-(P) mineralization occurrences)																			
20PM38A	Medium-grained nelsonite	Hm-ilm	n=5	0.0	0.1	0.0	0.1	54.4	65.8	0.6	121.0	0.7	664.8	3184.6	43.2	1796.6	-	7.1	5.3
20PM38C	Medium-grained nelsonite	Hm-ilm	n=5	0.0	0.1	0.0	0.1	54.4	53.9	0.5	109.0	-	744.2	3260.6	5.2	-	-	3.8	4.5
20PM42A	Medium-grained OAN	Hm-ilm + Mt	n=5	0.1	0.1	0.0	0.1	54.4	50.9	0.1	105.8	-	308.3	127.8	28.6	398.8	-	2.1	1.4
20PM42B	Fine-grained-leuconorite	Hm-ilm	n=5	0.2	0.4	0.1	0.3	54.4	45.4	0.3	101.1	-	1463.1	457.8	2632.6	9263.4	102.6	3.0	9.8
La Hache Mangerite (Fe-Ti-(P) mineralization occurrences)																			
21PM06	Oxide-apatite-rich mangerite	Ilm + Mt	n=5	0.1	0.2	0.0	0.2	54.4	46.8	0.3	102.0	-	702.1	244.8	335.1	1831.6	72.5	0.7	3.6
21PM07	Oxide-apatite-rich mangerite	Ilm + Mt	n=5	0.1	0.2	0.0	0.2	54.4	47.0	0.5	102.4	-	631.8	625.5	117.7	2258.4	-	0.4	1.9
21PM08	Oxide-apatite-rich mangerite	Ilm + Mt	n=5	0.1	0.2	0.0	0.1	54.4	46.1	0.4	101.3	0.8	1076.4	356.2	1180.4	4496.1	68.0	0.7	3.6

21PM09	Oxide-apatite-rich mangerite	Ilm + Mt	n=5	0.1	0.2	0.0	0.1	54.4	46.7	0.3	101.8	0.6	290.9	447.4	143.4	1452.5	12.0	0.4	1.4
21PM57	Oxide-apatite-rich mangerite	Ilm + Mt	n=5	0.2	0.4	0.1	0.3	54.4	48.0	0.2	103.6	0.6	651.9	606.7	79.0	2399.5	11.1	0.4	44.3
21PM59	Oxide-apatite-rich mangerite	Ilm + Mt	n=5	0.1	0.2	0.0	0.2	54.4	46.1	0.2	101.2	-	94.5	230.1	63.6	2700.2	5.7	0.7	4.4

Appendix 4.2.8 (cont.) Complete LA-ICP-MS results of apatite

Detection Limits (33-55µm bean size)				0.02 - 0.05	0.48 - 1.47	0.32-0.72	0.49-1.07	0.01 - 0.04	0.17 - 0.31	0.12 - 0.27	0.10 - 0.26	0.03 - 0.07	0.19 - 0.34	0.11 - 0.25	0.01-0.07	0.01-0.02	0.01 - 0.02	0.004 - 0.007	0.02 - 0.06
Sample	Lithology	Oxide Mineralogy	# analysis	V	Cr	Mn	Fe	Co	Ni	Cu	Zn	Ga	Ge	As	Sr	Y	Zr	Nb	Ba
Lac Périgny Fe-Ti-P mineralization																			
20PM23C	Medium-grained OAN	Ilm + Mt	n=5	0.3	0.6	217.3	1119.2	0.3	0.3	0.6	2.0	0.8	40.1	18.4	654.3	227.7	2.4	-	0.4
20PM24	Medium-grained leuconorite	Ilm + Mt	n=5	0.4	-	467.6	1135.0	0.3	0.3	-	0.6	0.6	30.1	24.5	436.1	378.4	1.2	-	0.5
20PM25	Medium-grained OAN	Ilm + Mt	n=5	0.3	-	400.6	745.4	0.4	0.4	0.3	1.3	1.0	48.5	18.2	430.7	623.8	0.9	-	0.6
20PM26A	Medium-grained leuconorite	Ilm + Mt	n=5	2.2	0.8	307.9	720.4	0.3	0.5	0.4	2.3	0.9	38.9	12.1	353.5	599.7	0.4	-	0.0
20PM09A	Medium-grained OAN	Ilm + Mt	n=5	0.5	0.0	605.9	2211.2	3.7	3.3	1.4	1.8	0.3	10.8	4.3	503.0	320.1	2.4	-	0.4
Lac de L'Abbondance Fe-Ti-P mineralization																			
20PM46A	Medium-grained nelsonite	Ilm + Mt	n=5	2.1	-	466.9	745.3	0.2	0.8	0.2	0.5	0.6	24.5	7.7	2113.9	191.2	0.7	-	0.4
20PM47A	Medium-grained nelsonite	Ilm + Mt	n=5	3.2	1.2	431.7	2173.3	0.9	3.7	2.0	2.4	3.1	21.1	6.6	1839.1	182.1	0.5	-	0.6
20PM46E	Medium-grained OAN	Hm-ilm	n=5	3.0	-	541.8	356.0	0.2	0.7	0.1	1.6	0.7	31.0	11.1	988.6	207.3	0.5	-	0.5
Mattawa Anorthosite (Fe-Ti-(P) mineralization occurrences)																			
20PM11B	Medium-grained OAN	Ilm + Mt	n=5	1.1	-	316.1	1226.1	0.3	0.2	0.1	6.3	16.3	3.9	6.7	975.7	621.6	1.8	0.0	8.5
Labrieville Anorthosite (Fe-Ti-(P) mineralization occurrences)																			
20PM38A	Medium-grained nelsonite	Hm-ilm	n=5	1.5	15.7	1307.6	4748.8	0.5	0.7	0.6	2.9	9.2	2.2	2.5	1305.1	267.9	2.6	-	3.0
20PM38C	Medium-grained nelsonite	Hm-ilm	n=5	0.5	-	1156.6	3898.5	0.3	-	0.6	1.9	10.1	2.0	2.0	1295.8	265.0	2.7	-	3.8
20PM42A	Medium-grained OAN	Hm-ilm + Mt	n=5	4.1	0.7	225.1	547.8	0.1	0.2	0.7	1.3	18.6	3.6	4.0	940.2	554.8	0.3	-	-
20PM42B	Fine-grained-leuconorite	Hm-ilm	n=5	3.1	5.9	514.4	1994.8	0.3	1.2	1.1	3.4	50.9	10.1	8.7	440.9	1115.9	0.0	-	4.4
La Hache Mangerite (Fe-Ti-(P) mineralization occurrences)																			
21PM06	Oxide-apatite-rich mangerite	Ilm + Mt	n=5	0.5	-	409.6	2135.5	0.8	0.4	0.5	9.3	19.4	4.6	7.5	1020.1	572.2	6.2	0.0	2.0
21PM07	Oxide-apatite-rich mangerite	Ilm + Mt	n=5	0.1	-	322.2	3701.9	0.5	0.3	29.8	22.2	19.4	4.9	8.1	794.4	628.3	3.5	0.0	2.0
21PM08	Oxide-apatite-rich mangerite	Ilm + Mt	n=5	3.7	1.3	325.3	2827.6	1.0	0.4	4.6	10.2	14.3	3.4	6.4	851.3	464.8	0.5	0.0	3.0

21PM09	Oxide-apatite-rich mangerite	Ilm + Mt	n=5	3.5	-	318.4	2518.2	0.4	0.2	0.7	5.3	13.6	3.1	6.6	761.2	436.8	0.7	0.0	1.0
21PM57	Oxide-apatite-rich mangerite	Ilm + Mt	n=5	0.1	-	578.0	1748.5	0.4	0.2	0.7	13.1	32.4	7.6	13.3	1049.5	834.8	0.5	0.1	2.4
21PM59	Oxide-apatite-rich mangerite	Ilm + Mt	n=5	0.1	-	556.3	1243.6	0.2	0.2	-	3.5	20.7	6.7	11.4	1053.5	1445.8	1.0	0.0	1.5

Appendix 4.2.8 (cont.) Complete LA-ICP-MS results of apatite

Detection Limits (33-55µm bean size)				0.003 - 0.014	0.003 - 0.012	0.002 - 0.008	0.012 - 0.030	0.013 - 0.021	0.003 - 0.009	0.015 - 0.057	0.002 - 0.004	0.008 - 0.014	0.002 - 0.003	0.006 - 0.015	0.002 - 0.004	0.009 - 0.027	0.002 - 0.003	0.004 - 0.007	c
Sample	Lithology	Oxide Mineralogy	# analysis	La	Ce	Pr	Nd	Sm	Eu	Gd	Tb	Dy	Ho	Er	Tm	Yb	Lu	Th	U
Lac Périgny Fe-Ti-P mineralization																			
20PM23C	Medium-grained OAN	Ilm + Mt	n=5	296.0	829.6	128.7	667.3	147.2	28.4	137.9	14.4	64.6	8.7	14.6	1.0	3.5	0.3	6.7	4.6
20PM24	Medium-grained leuconorite	Ilm + Mt	n=5	255.1	712.8	108.2	556.0	126.9	26.2	128.8	15.2	81.1	14.3	33.3	3.5	18.3	2.5	10.6	3.7
20PM25	Medium-grained OAN	Ilm + Mt	n=5	467.8	1248.0	183.1	897.8	199.8	37.5	194.6	23.9	131.5	23.5	55.4	6.1	32.3	4.4	17.5	6.8
20PM26A	Medium-grained leuconorite	Ilm + Mt	n=5	377.4	1019.0	151.4	762.1	174.8	31.4	175.9	21.7	119.6	22.0	54.0	6.1	33.4	4.6	9.6	4.7
20PM09A	Medium-grained OAN	Ilm + Mt	n=5	290.8	767.6	114.4	573.0	123.6	27.1	126.9	13.7	68.4	11.8	27.6	3.0	15.6	2.2	9.4	5.8
Lac de L'Abbondance Fe-Ti-P mineralization																			
20PM46A	Medium-grained nelsonite	Ilm + Mt	n=5	222.3	604.7	94.4	483.8	97.3	24.1	86.3	9.0	44.5	7.3	15.7	1.6	7.6	0.9	2.2	0.6
20PM47A	Medium-grained nelsonite	Ilm + Mt	n=5	202.9	562.6	87.4	449.7	90.8	23.0	81.0	8.6	41.5	7.0	14.9	1.5	7.6	1.0	1.3	0.7
20PM46E	Medium-grained OAN	Hm-ilm	n=5	322.6	834.4	120.9	593.6	110.2	26.9	93.8	9.6	47.3	7.8	17.2	1.8	9.4	1.3	2.0	1.0
Mattawa Anorthosite (Fe-Ti-(P) mineralization occurrences)																			
20PM11B	Medium-grained OAN	Ilm + Mt	n=5	623.7	1643.3	249.6	1251.5	274.8	58.8	248.0	28.4	143.8	23.7	54.2	5.8	30.3	3.8	3.7	1.7
Labrieville Anorthosite (Fe-Ti-(P) mineralization occurrences)																			
20PM38A	Medium-grained nelsonite	Hm-ilm	n=5	222.0	609.6	100.3	527.3	121.8	34.9	112.0	12.0	60.6	10.0	21.9	2.3	11.8	1.5	0.6	0.2
20PM38C	Medium-grained nelsonite	Hm-ilm	n=5	214.7	593.7	97.9	516.0	120.2	34.2	109.8	12.1	60.9	10.1	22.4	2.3	12.4	1.6	0.6	0.3
20PM42A	Medium-grained OAN	Hm-ilm + Mt	n=5	460.1	1195.9	184.1	924.1	210.6	49.3	197.7	22.9	123.3	21.2	50.7	5.5	29.7	3.8	2.1	1.1
20PM42B	Fine-grained-leuconorite	Hm-ilm	n=5	1498.8	3674.8	557.3	2641.1	529.8	93.3	424.9	50.7	257.6	43.7	102.7	11.1	64.7	8.0	2.4	0.9
La Hache Mangerite (Fe-Ti-(P) mineralization occurrences)																			
21PM06	Oxide-apatite-rich mangerite	Ilm + Mt	n=5	789.2	2066.2	312.9	1548.2	316.6	60.8	266.5	28.4	135.0	21.2	46.1	4.6	23.5	2.9	6.0	2.4
21PM07	Oxide-apatite-rich mangerite	Ilm + Mt	n=5	710.7	1979.5	318.3	1672.3	351.0	70.2	303.9	31.8	150.3	23.5	50.1	4.9	24.3	3.1	4.3	2.1
21PM08	Oxide-apatite-rich mangerite	Ilm + Mt	n=5	498.3	1351.9	209.6	1072.8	231.2	53.8	202.0	22.2	109.2	17.5	39.7	4.2	22.4	2.9	4.7	1.5

21PM09	Oxide-apatite-rich mangerite	Ilm + Mt	n=5	534.5	1396.2	209.3	1046.5	221.6	51.6	191.5	20.9	102.4	16.3	36.7	3.9	21.4	2.8	6.7	3.1
21PM57	Oxide-apatite-rich mangerite	Ilm + Mt	n=5	1331.1	3375.3	512.7	2488.3	482.4	98.3	395.7	42.5	205.0	32.2	70.8	7.3	37.5	4.7	3.9	1.9
21PM59	Oxide-apatite-rich mangerite	Ilm + Mt	n=5	448.5	1656.7	346.4	2141.4	596.5	180.8	568.8	67.2	339.6	55.4	127.1	13.7	73.9	9.6	3.3	2.9

APPENDIX 4.3 SUPPLEMENTARY FIGURES (CHAPTER 4)

Appendix 4.3.1 CL Images of selected analyzed zircons

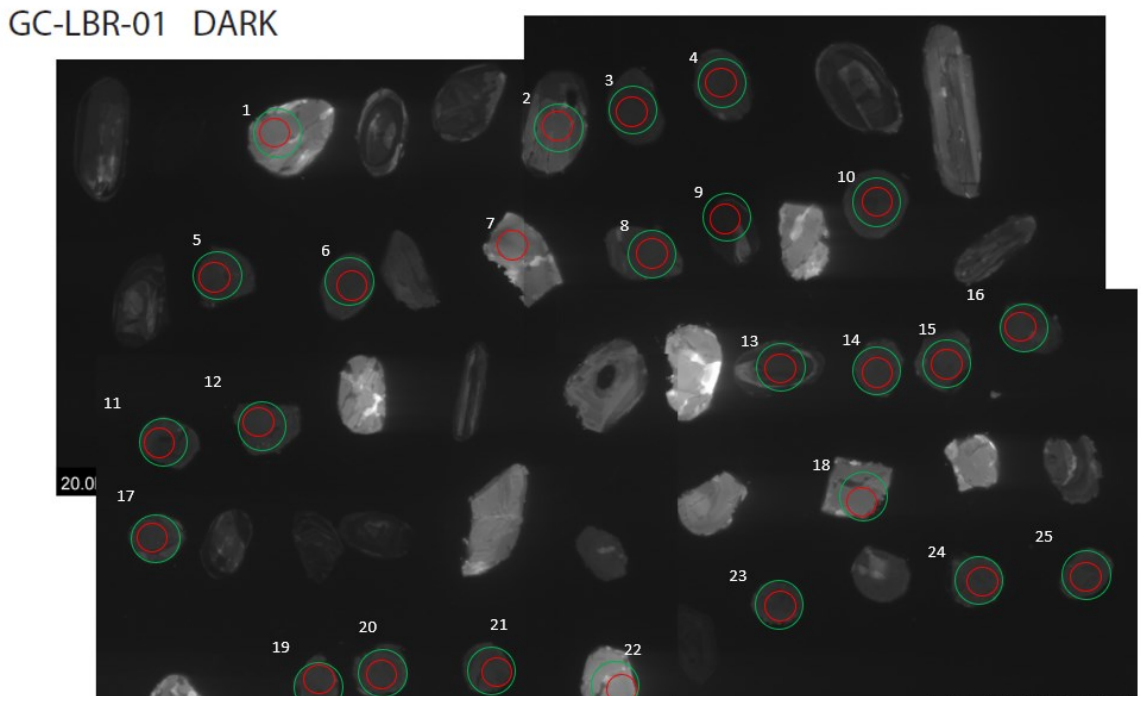

GC-LAB-01

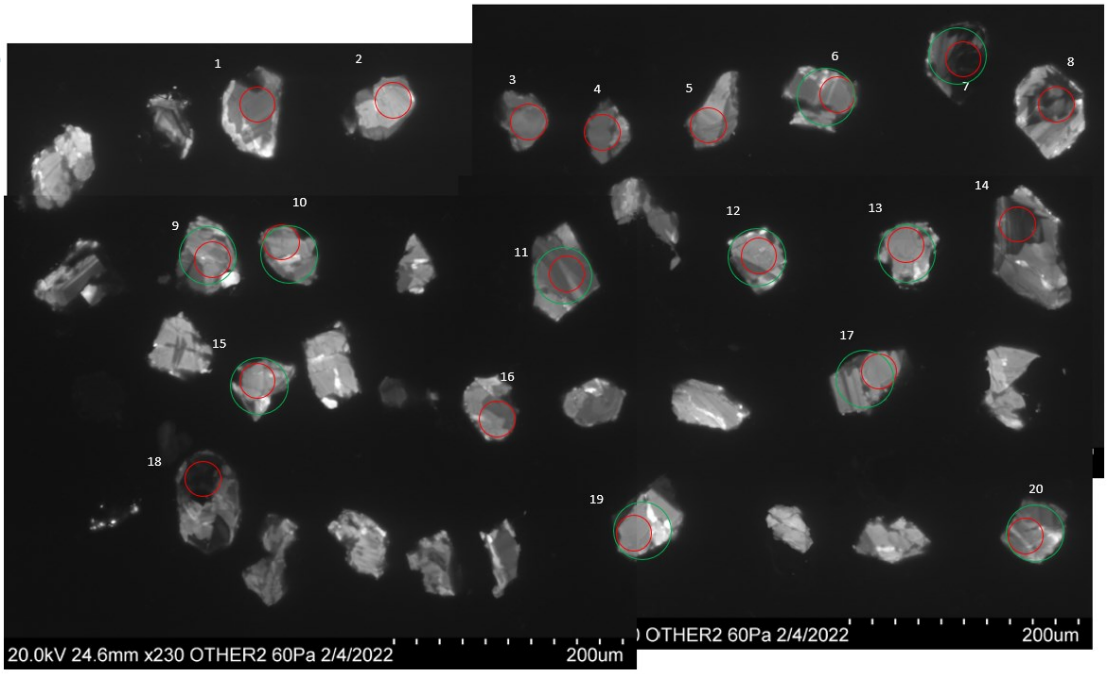

GC-LET-01

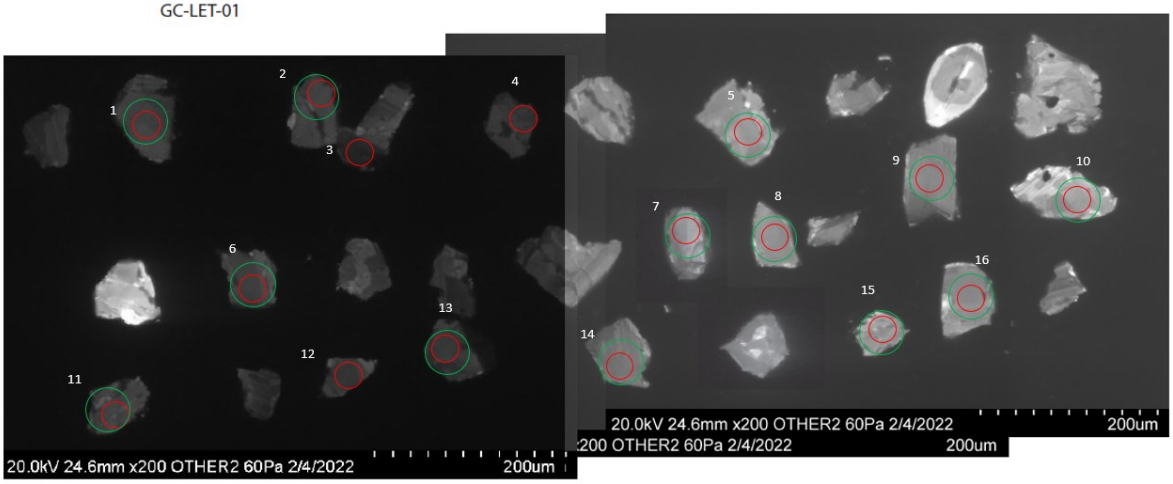

GC-LHC-01

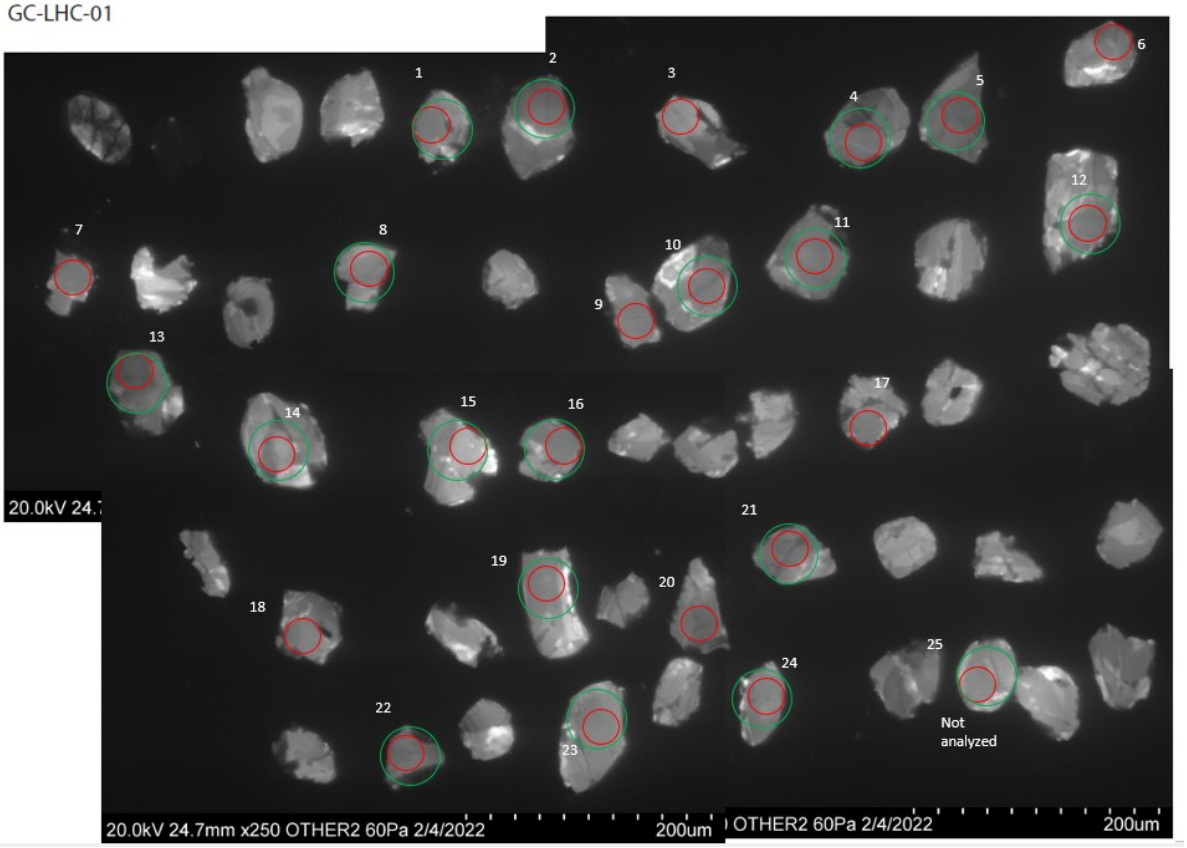

GC-LMX-01

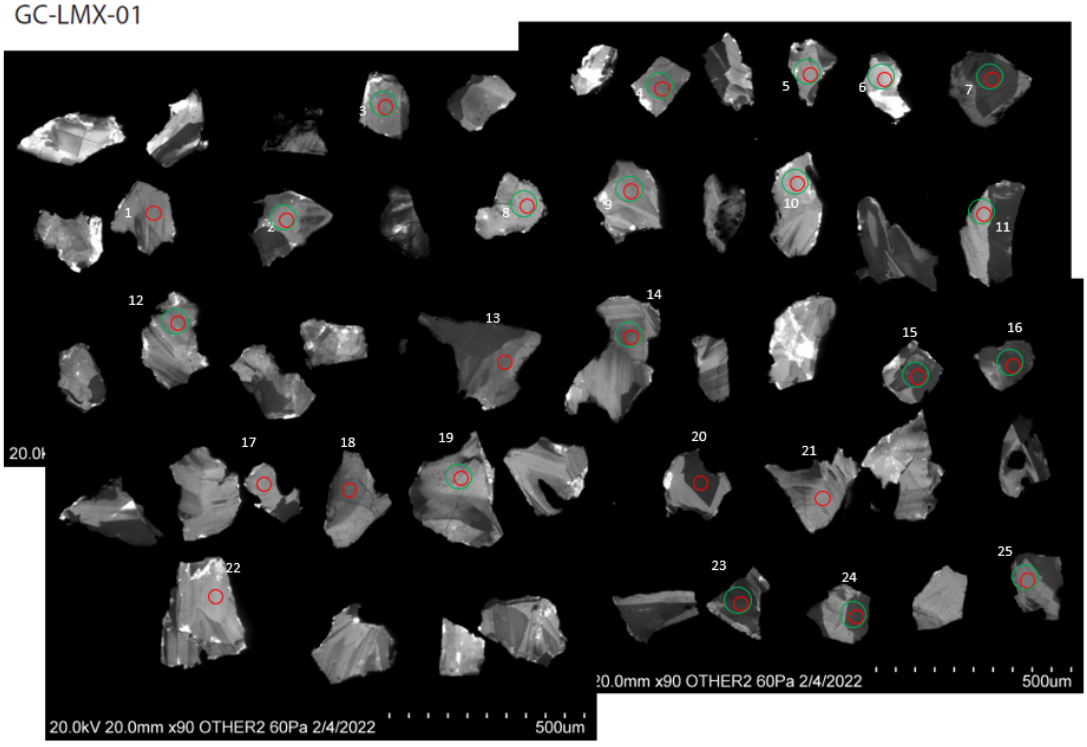

GC-LMX-02

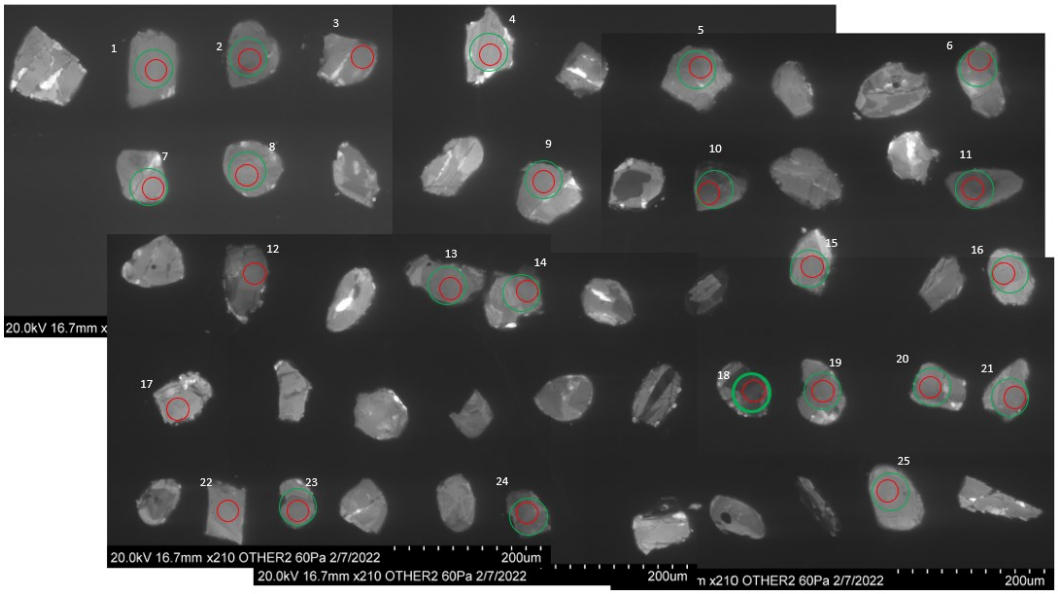

GC-LOR-01

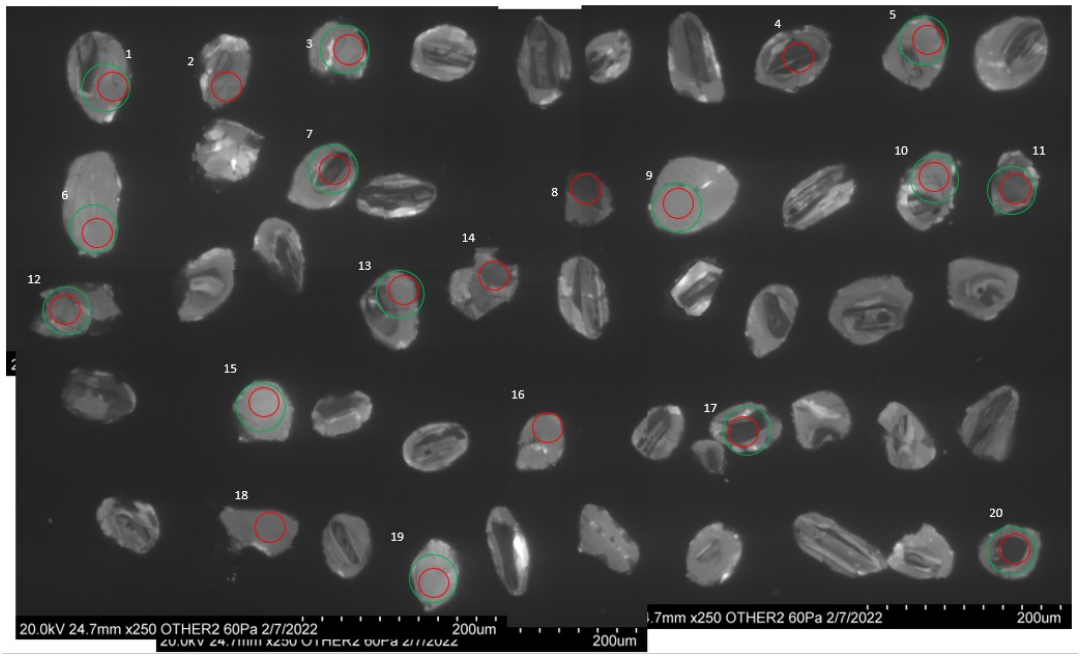

GC-LOR-02

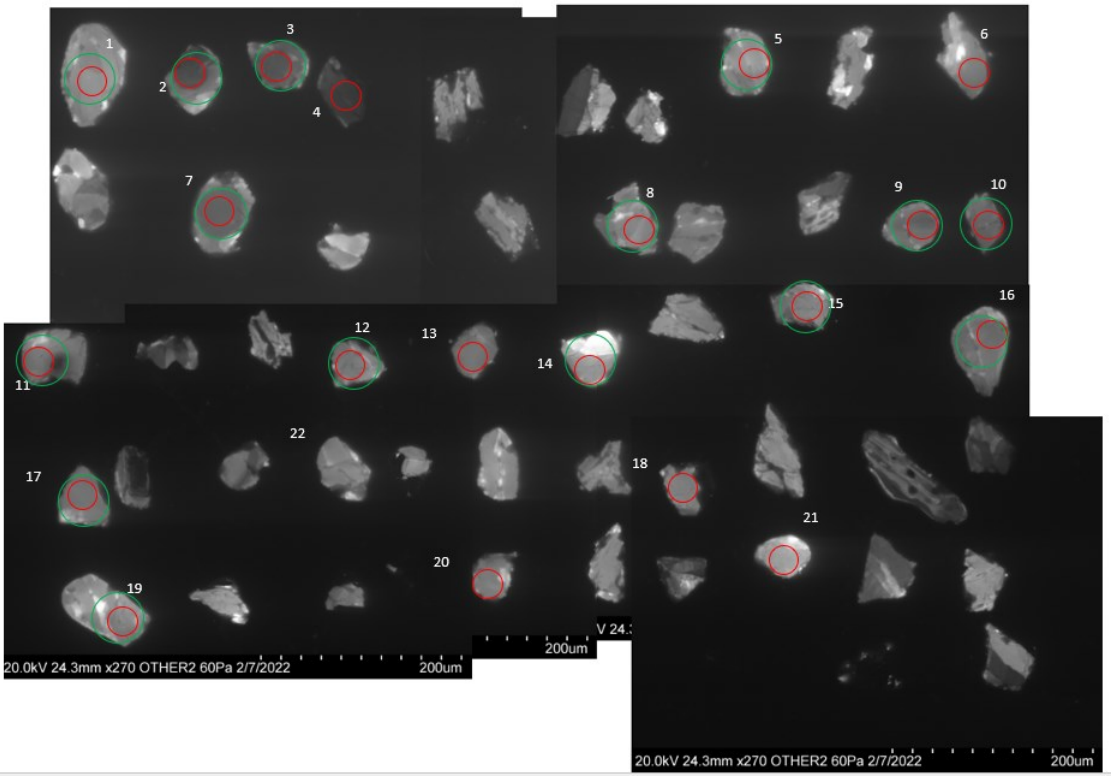

GC-LPR-01

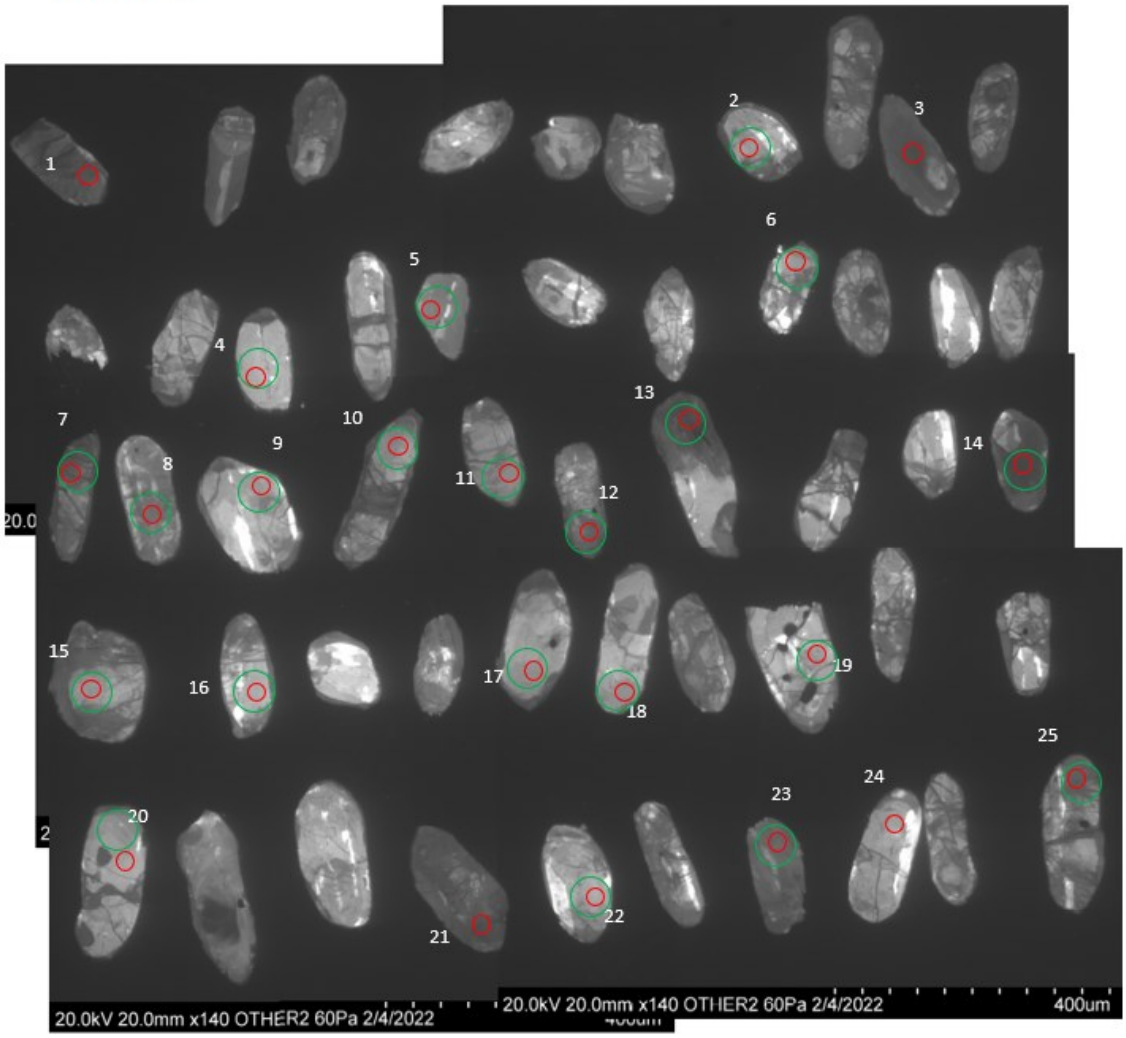
1
2
3
4
5
6
7
8
9
10
11
12
13
14
15
16
17
18
19
20
21
22
23
24
25
20.0kV 20.0mm x140 OTHER2 60Pa 2/4/2022
20.0kV 20.0mm x140 OTHER2 60Pa 2/4/2022
400um

GC-MAT-01

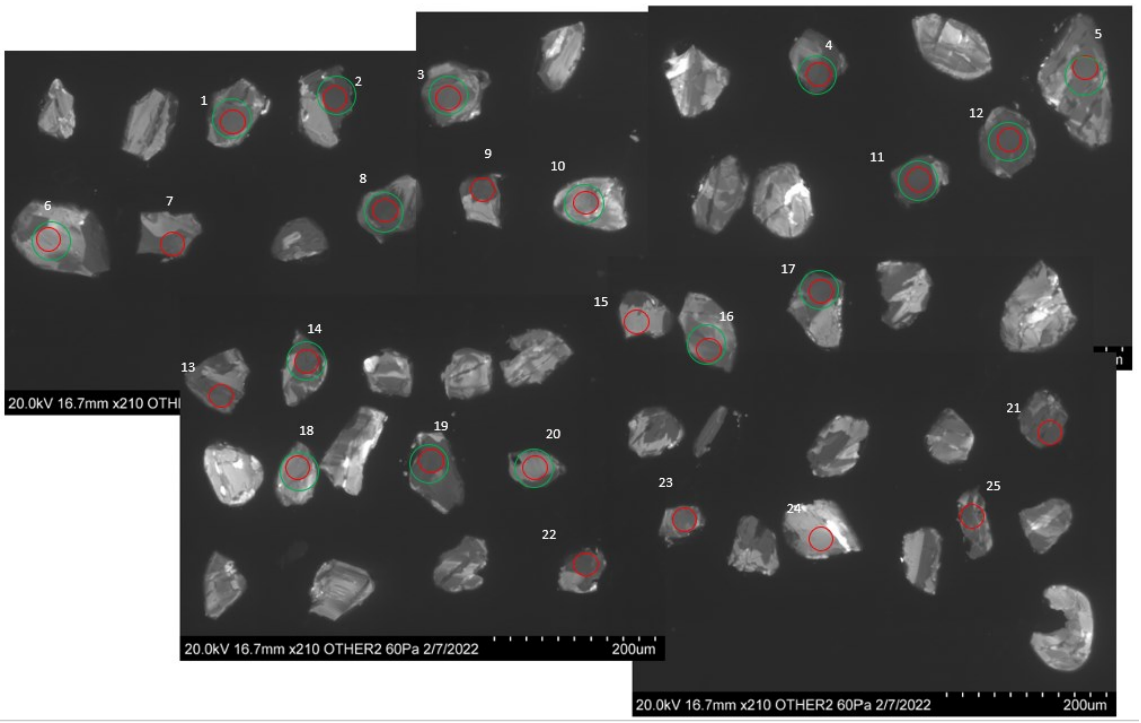
1
2
3
4
5
6
7
8
9
10
11
12
13
14
15
16
17
18
19
20
21
22
23
24
25
20.0kV 16.7mm x210 OTHE
20.0kV 16.7mm x210 OTHER2 60Pa 2/7/2022
200um
20.0kV 16.7mm x210 OTHER2 60Pa 2/7/2022
200um

Appendix 4.3.2 Weighted mean diagrams for LA-ICP-MS U–Pb analysis in zircon of Fe-Ti-(P) mineralization in the Central Grenville Province, Quebec. Each bar represents the result of the analysis of a single grain

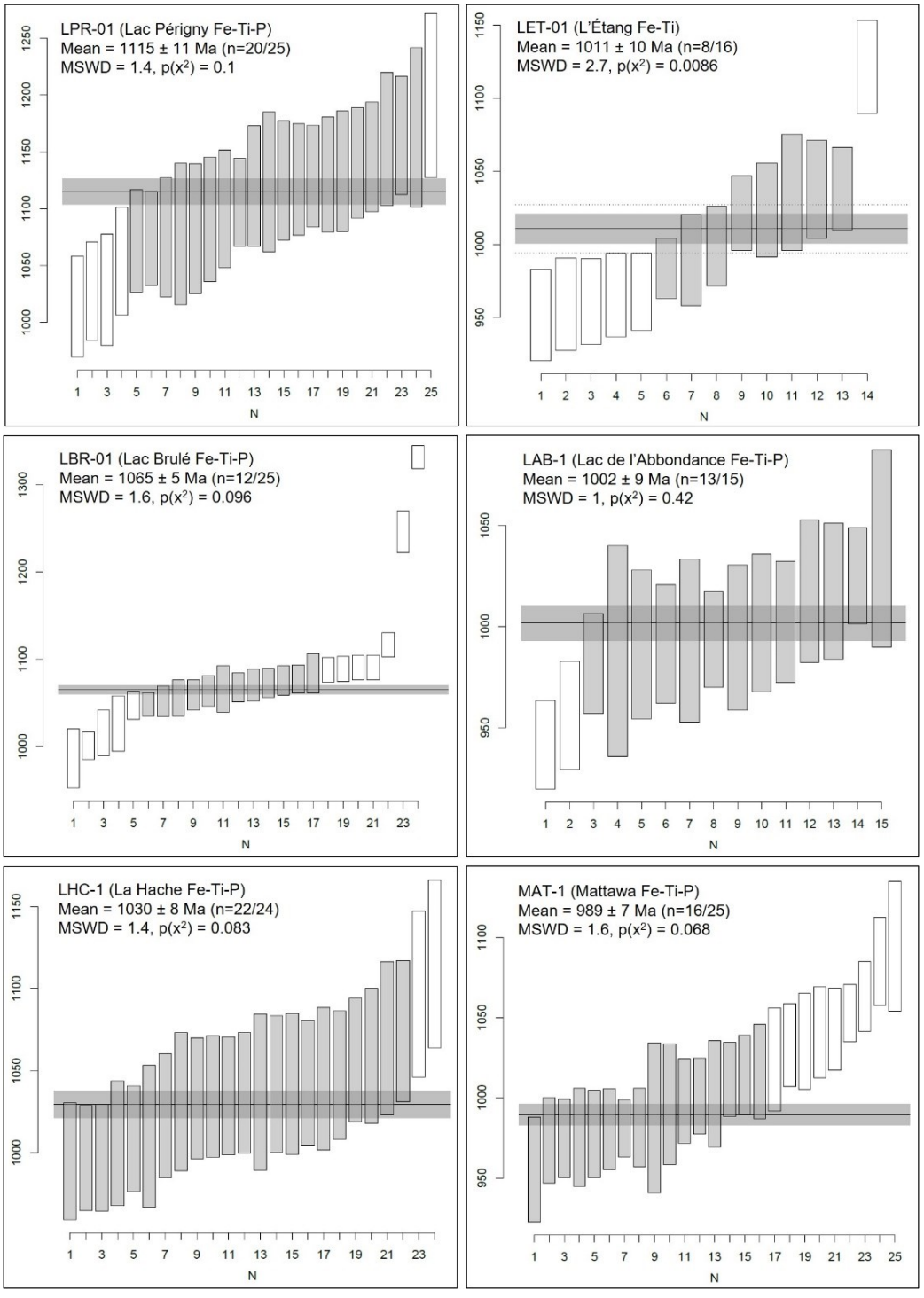

Appendix 4.3.3 µXRF-maps, combining P (white), Ti (blue) and Fe (green), showing the different proportions of oxides and apatite for the different Fe-Ti-(P) mineralization analyzed. Ilmenite is blue, where hematite-rich part of ilmenite is cyan. Magnetite is bright green. Orthopyroxene is dark green. A. Massive nelsonite dominated by magnetite and ilmenite (hematite exsolutions-free) (20PM47, Lac de l'Abbondance). B. Massive nelsonite dominated by coarse-grained apatite and hemo-ilmenite (20PM47, Lac Brulé/Labrieville). C. Massive ilmenitite with coarse hemo-ilmenite crystals and absence of cumulus magnetite and apatite (20PM05, Lac Mirepoix). D. Oxide-apatite-rich mangerite with high concentration of magnetite and minor ilmenite (hematite exsolutions-free) (21PM09, La Hache mangerite). E. Oxide-apatite norite (OAN) with equal proportions of hemo-ilmenite and magnetite (21PM18B, Mattawa Anorthosite). F. Leuconorite lens in andesine-anorthosite, dominated by magnetite and hemo-ilmenite (21PM11B, Mattawa Anorthosite). Mineral abbreviations: opx – orthpopyroxene; pl – plagioclase; hm-ilm – hemo-ilmenite; mt – magnetite; ap – apatite; ilm – ilmenite; K-fp – K-feldspar. Previously published data: Lac à l'Orignal Fe-Ti-P deposit (Miloski et al. 2023a) and the Lac Mirepoix Fe-Ti-P mineralization (Miloski et al. 2023 *in review*)

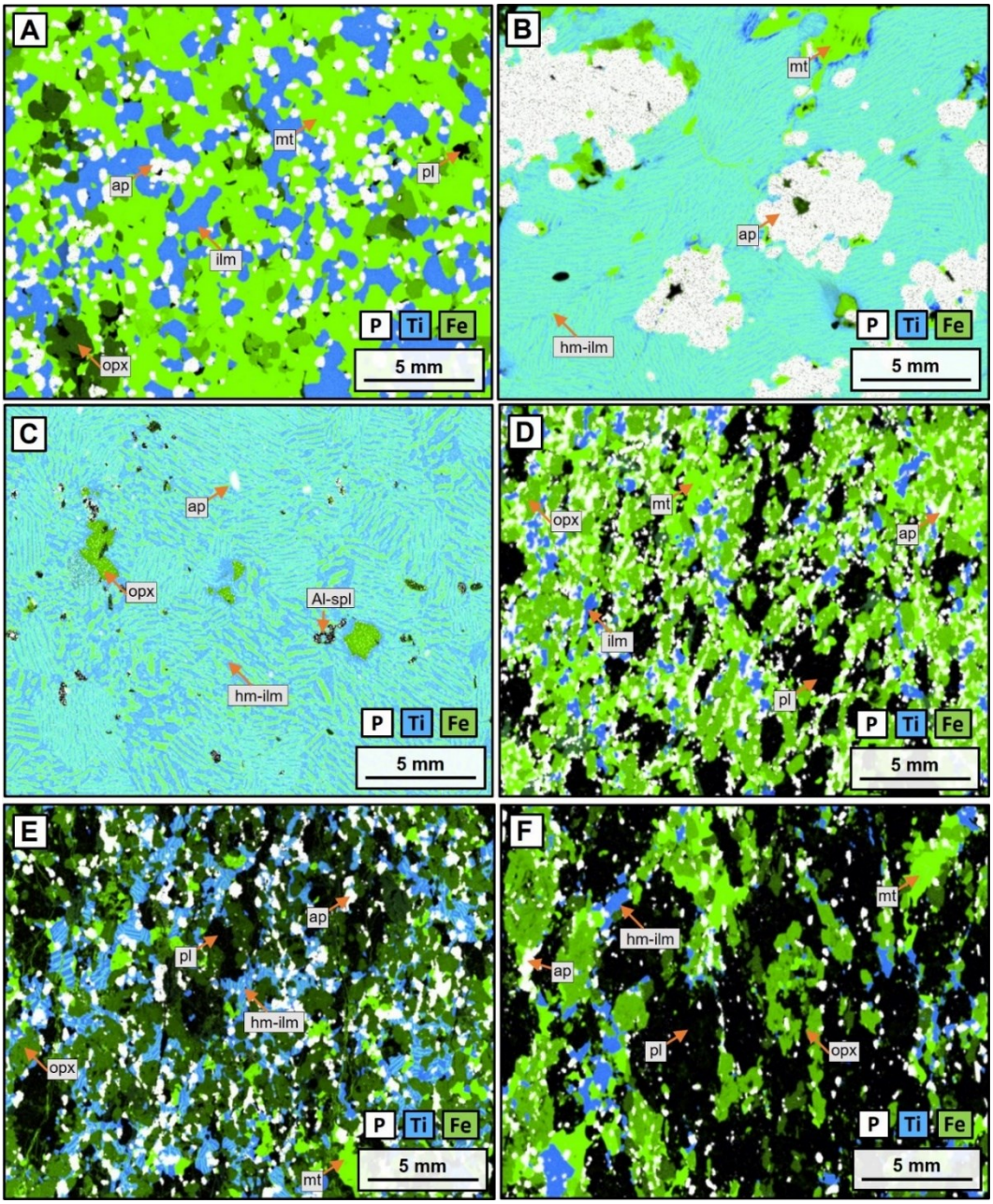

Appendix 4.3.4 Whole-rock variation diagrams for mineralized lithologies in the different Fe-Ti-(P) mineralization of the Central Grenville Province, with the major mineral compositions by electron microprobe, including the dataset of Morisset (2001). A. Harker diagrams. B. Fe_2O_3 x TiO_2 diagram. Previously published data: Lac à l'Orignal Fe-Ti-P deposit (Miloski et al. 2023a) and the Lac Mirepoix Fe-Ti-P mineralization (Miloski et al. 2023 *in review*)

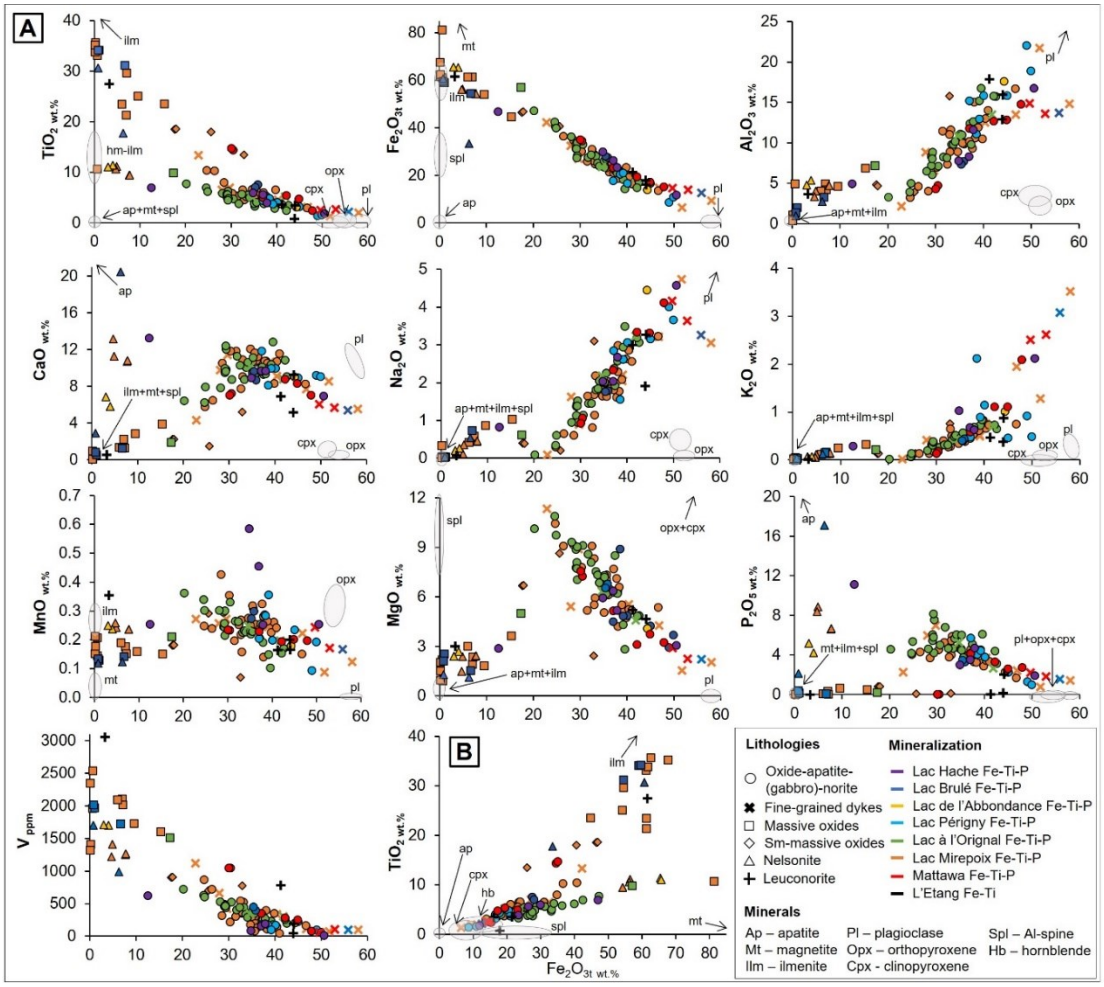

Appendix 4.3.5 Geochemical variation diagrams of plagioclase and apatite data of Fe-Ti-P mineralization and associated AMCG-host in the Central Grenville Province. Comparison with data of the Grader Fe-Ti-P, Quebec (Charlier *et al.* 2008). Previously published data: Lac à l'Orignal Fe-Ti-P deposit (Miloski et al. 2023a) and the Lac Mirepoix Fe-Ti-P mineralization (Miloski et al. 2023 *in review*)